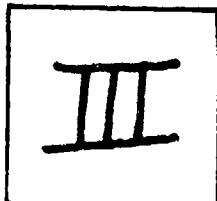


PHOTOGRAPH THIS SHEET

AD-E200 704

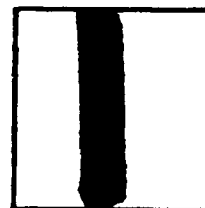
AD A100508

DTIC ACCESSION NUMBER



LEVEL

Dikewood Industries, Inc.
Albuquerque, NM



INVENTORY

Rept. No. DC-EH-1289
Contract F29601-76-C-0149
DOCUMENT IDENTIFICATION Final Rept., Dec. 80
AFWL-TR-80-402

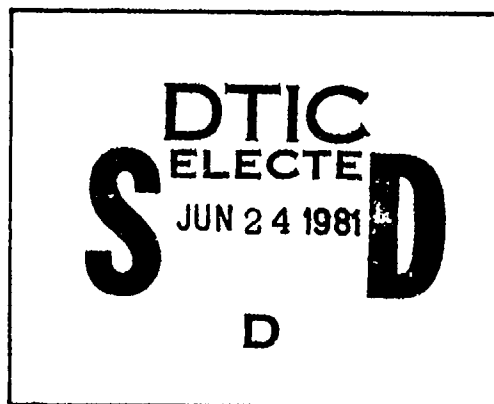
DISTRIBUTION STATEMENT A

Approved for public release;
Distribution Unlimited

DISTRIBUTION STATEMENT

ACCESSION FOR	
NTIS	GRA&I
DTIC	TAB
UNANNOUNCED	
JUSTIFICATION	
BY	
DISTRIBUTION /	
AVAILABILITY CODES	
DIST	AVAIL AND/OR SPECIAL
A	

DISTRIBUTION STAMP



DATE ACCESSIONED

816 22 007

DATE RECEIVED IN DTIC

PHOTOGRAPH THIS SHEET AND RETURN TO DTIC-DDA-2

AFWL-TR-80-402

AD-E200704

WL
TR
80-402
c.3

EMP INTERACTION:

PRINCIPLES, TECHNIQUES AND REFERENCE DATA

(A COMPLETE CONCATENATION OF TECHNOLOGY
FROM THE EMP INTERACTION NOTES)

EMP INTERACTION 2.1

December 1980

APPROVED FOR PUBLIC RELEASE. DISTRIBUTION UNLIMITED.

AIR FORCE WEAPONS & SUPPORT
AIR FORCE SYSTEMS COMMAND

81 6

22

007

AD A100508

This final report was prepared by Dikewood Industries, Inc., Albuquerque, New Mexico, under Contract F29601-76-C-0149, Job Order 37630132 with the Air Force Weapons Laboratory, Kirtland Air Force Base, New Mexico. J. Philip Castillo (NTMT) was the Laboratory Project Officer-in-Charge.

When US Government drawings, specifications, or other data are used for any purpose other than a definitely related Government procurement operation, the Government thereby incurs no responsibility nor any obligation whatsoever, and the fact that the Government may have formulated, furnished, or in any way supplied the said drawings, specifications, or other data, is not to be regarded by implication or otherwise, as in any manner licensing the holder or any other person or corporation, or conveying any rights or permission to manufacture, use, or sell any patented invention that may in any way be related thereto.

This report has been authored by a contractor of the United States Government. Accordingly, the United States Government retains a nonexclusive, royalty-free license to publish or reproduce the material contained herein, or allow others to do so, for the United States Government purposes.

This report has been reviewed by the Public Affairs Office and is releasable to the National Technical Information Service (NTIS). At NTIS, it will be available to the general public, including foreign nations.

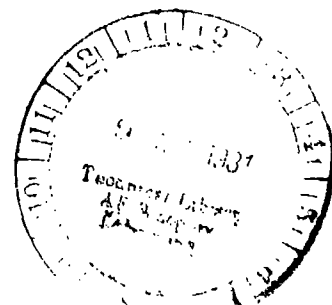
This technical report has been reviewed and is approved for publication.

FOR THE DIRECTOR

J. Philip Castillo
J. PHILIP CASTILLO, PhD
Project Officer

Norman K. Blocker
NORMAN K. BLOCKER
Colonel, USAF
Chief, Applied Physics Division

DO NOT RETURN THIS COPY. RETAIN OR DESTROY.



UNCLASSIFIED

SECURITY CLASSIFICATION OF THIS PAGE (When Data Entered)

REPORT DOCUMENTATION PAGE		READ INSTRUCTIONS BEFORE COMPLETING FORM
1. REPORT NUMBER AFWL-TR-80-402	2. GOVT ACCESSION NO.	3. RECIPIENT'S CATALOG NUMBER
4. TITLE (and Subtitle) EMP INTERACTION: PRINCIPLES, TECHNIQUES AND REFERENCE DATA (A COMPLEAT CONCATENATION OF TECHNOLOGY FROM THE EMP INTERACTION NOTES) EMP INTERACTION 2-1		5. TYPE OF REPORT & PERIOD COVERED Final Report
7. AUTHOR(s) K.S.H. Lee, Editor		6. PERFORMING ORG. REPORT NUMBER DC-EH-1289
9. PERFORMING ORGANIZATION NAME AND ADDRESS Dikewood Industries, Inc. 1009 Bradbury Drive, S. E. Albuquerque, New Mexico 87106		8. CONTRACT OR GRANT NUMBER(s) F29601-76-C-0149
11. CONTROLLING OFFICE NAME AND ADDRESS Air Force Weapons Laboratory (NTMT) Kirtland AFB, New Mexico 87117		10. PROGRAM ELEMENT, PROJECT, TASK AREA & WORK UNIT NUMBERS 64711F/37630132
14. MONITORING AGENCY NAME & ADDRESS (if different from Controlling Office)		12. REPORT DATE December 1980
		13. NUMBER OF PAGES 762
		15. SECURITY CLASS. (of this report) Unclassified
		15a. DECLASSIFICATION/DOWNGRADING SCHEDULE
16. DISTRIBUTION STATEMENT (of this Report) Approved for public release; distribution unlimited.		
17. DISTRIBUTION STATEMENT (of the abstract entered in Block 20, if different from Report)		
18. SUPPLEMENTARY NOTES		
19. KEY WORDS (Continue on reverse side if necessary and identify by block number) Aerospace System Ground Based Systems Aircraft Interaction Application Missile Coupling Satellites EMP		
20. ABSTRACT (Continue on reverse side if necessary and identify by block number) This work is divided into three parts. The first part, Principles and Techniques, concerns general concepts and calculational procedures from electro- magnetic theory relevant to EMP interaction. This contains a discussion of the concept of electromagnetic topology which is used to divide complex systems into somewhat natural smaller parts in an ordered way. This concept is fundamental to the organization and understanding of this work and is expected to lead to further insights and computational techniques [2-8]. Of course, there are many (over)		

DD FORM 1473
1 JAN 73

UNCLASSIFIED

SECURITY CLASSIFICATION OF THIS PAGE (When Data Entered)

UNCLASSIFIED

SECURITY CLASSIFICATION OF THIS PAGE(When Data Entered)

20. ABSTRACT (continued)

other concepts and techniques which play important roles and which are discussed in this part. The reader might consult a recent review paper [9] to put these in perspective including some concepts of potential future significance.

The second part, Formulas and Data, considers the information concerning the pieces of the system. The organization of this part is based on the system topology, specifically the hierarchical topology which divides the system into layers. Each layer is further divided into three ordered parts: coupling, propagation, and penetration. Within each category the various individual (or canonical) types of boundary-value problems are considered. As one might expect, the bulk of the material is contained in this section.

Having considered, first, the general concepts and techniques for EMP interaction and, second, the specific information concerning the pieces, we come to the third part, System Applications. This part attempts to illustrate the use of the previous parts in analyzing the EMP interaction with complex systems. Hypothetical system examples are chosen to illustrate the topological decomposition of the problem for selected signal paths, and the subsequent approximate calculation of the internal signals.

UNCLASSIFIED

SECURITY CLASSIFICATION OF THIS PAGE(When Data Entered)

EMP INTERACTION:

PRINCIPLES, TECHNIQUES AND REFERENCE DATA

(A COMPLETE CONCATENATION OF TECHNOLOGY FROM
THE EMP INTERACTION NOTES)

K.S.H. LEE, Editor

FOREWORD

A. Background

It has been some years now since the publication of something comparable to the present work concerning the interaction of the nuclear electromagnetic pulse (EMP) with complex systems. The most recent document of this kind is Electromagnetic Pulse Handbook for Missiles and Aircraft in Flight, EMP Interaction 1-1, September 1972; it was several years in the making, and the present document likewise was a lengthy undertaking.

Recent years have witnessed some considerable effort and associated advances in the state of the art of EMP interaction modeling. This development has been spurred by experimental observations of the EMP response characteristics of complex systems and by analytical and computational advances concerning the solution of appropriate types of electromagnetic boundary-value problems. Related to these advances, but extending beyond them in significance, are the fundamental insights which have been developed concerning the general properties of the EMP response of complex systems; these insights have led to ways of reducing somewhat the complexity of the interaction problem by decomposing it in certain "natural" ways into smaller subproblems and subresponses, each of these smaller entities being somewhat simpler than the total interaction problem and associated complex response.

There has also been a significant increase in the number of researchers, engineers and system designers involved in applying EMP interaction models developed mainly by theorists to military systems. These models are usually only applicable to highly idealized problems and/or may be described by very complicated mathematics not easily used to solve day-to-day practical problems. Consequently, a gap has appeared between the theoretical models and the practical applications. This document is meant to help bridge this gap.

B. Applicability

In organizing and compiling a work of this nature it is necessary to determine for whom this work is constructed and how such persons are to use it.

This document is intended to be used by engineers responsible for EMP hardening and testing of real military systems. Such is the fundamental purpose of all the EMP interaction research: to develop better information and techniques for ultimate use in making better (EMP hard) systems.

The rationale for studying the problem of EMP interaction with a system is to try to understand and quantify the characteristics of the penetrating EMP at the subsystem levels. This information when coupled with test data results in an insight into how much the EMP energy may have to be reduced so as to preclude functional upset or damage. The application of data, formulas, etc. from this document to a system can aid the analyst in making preliminary order-of-magnitude estimates of responses at a point in a system but does not in itself result in predictions for use in determining system hardening requirements. However, when used with high-quality data resulting from EMP testing a measure of the degree of hardening and hardening approaches necessary can be obtained. It is important to stress at this point that in designing and/or assessing the EMP hardness of a system high-quality system-level test data are absolutely indispensable, which are not contained in this document. It is also important to point out that this volume does not address the reliability/confidence error intervals (which are usually quite large, for example, a factor of 20 for 90/90 interval [1]) that one encounters in making an assessment of aircraft survivability to EMP. The error estimates presented in Chap. 1.6 and Sec. 3.2.5 of Chap. 3.2 are those that arise from physical modeling, mathematical approximation and laboratory scale-model measurements. They are generally small in comparison with the reliability/confidence error intervals.

The reader may ask: "How can something as complicated as electromagnetic theory ever be used by a multitude of engineers to design anything?" To answer this question one must first observe that there is not much choice in the matter. Design means to take some body of knowledge and apply it to making something with desired performance characteristics. EMP implies electromagnetics, and the distilled statement of electromagnetic phenomena, as we best understand it, is electromagnetic theory. One can always question whether a particular form of the description of an electromagnetic phenomenon is the best possible description or is optimally communicable to neophytes in electromagnetic

theory. Nevertheless, any description adopted must be at least approximately correct (i.e., in agreement with experimental fact). This rules out attempts at oversimplification; there are some concepts which will have to be learned in order to be able to effectively apply electromagnetic theory to EMP system interaction problems.

A secondary use of the document is for the electromagnetic theory community. In the process of organizing and writing such a work one gets a better picture of the state of the art and deficiencies become more apparent. This in turn can serve as a partial guide for future research. It must be emphasized, however, that even though the electromagnetic theory research community is of necessity the group providing the basic information for this volume, this work is not intended primarily for their use; its intended use is for the applicators. This does not necessarily mean the applicators at their current state of skills and knowledge, but the applicators raised to some basic level of required electromagnetic knowledge for the applications problem.

C. Technical Concept

In constructing this kind of work summarizing the state of the art of EMP interaction modeling, one might just list all the physical quantities and topics and have brief sections concerning each. However, these things are not unrelated to each other; one can make use of these relations in order to create a more coherent whole. This document is thus organized in some sense from the top down instead of from the bottom up. A consistent overall structure and notation has been created and the various pieces have been selected to fit into the overall concept.

This work is divided into three parts. The first part, Principles and Techniques, concerns general concepts and calculational procedures from electromagnetic theory relevant to EMP interaction. This contains a discussion of the concept of electromagnetic topology which is used to divide complex systems into somewhat natural smaller parts in an ordered way. This concept is fundamental to the organization and understanding of this work and is expected to lead to further insights and computational techniques [2-8]. Of course there are many other concepts and techniques which play important

roles and which are discussed in this part. The reader might consult a recent review paper [9] to put these in perspective including some concepts of potential future significance.

The second part, Formulas and Data, considers the information concerning the pieces of the system. The organization of this part is based on the system topology, specifically the hierarchical topology which divides the system into layers. Each layer is further divided into three ordered parts: coupling, propagation, and penetration. Within each category the various individual (or canonical) types of boundary-value problems are considered. As one might expect, the bulk of the material is contained in this section.

Having considered, first, the general concepts and techniques for EMP interaction and, second, the specific information concerning the pieces, we come to the third part, System Applications. This part attempts to illustrate the use of the previous parts in analyzing the EMP interaction with complex systems. Hypothetical system examples are chosen to illustrate the topological decomposition of the problem for selected signal paths, and the subsequent approximate calculation of the internal signals.

As appropriate to any large task this was a cooperative one involving many individuals and organizations. AFWL personnel were concerned with the overall technical organization and contractual administration of the effort. This was accomplished by a set of memos termed EIH (EMP Interaction Handbook) memos in three parts [10-12] which addressed outlines, notations, summaries of particular problems, etc. Particular thanks are given to MSgt. Harris Goodwin of AFWL for his efficient administration of this effort.

D. Future Evolution

While in our opinion some significant advances are reflected in this EMP interaction document, the present work should not be regarded as definitive. As was expected, the process of producing this document revealed various deficiencies to the participants. We believe that with time additional improvements will become apparent to us and to you, the user. With proper aging, as in the case of good wine, we will be able to form mature judgments concerning an

improved version of this volume. Presumably such an improved version will involve generalizations and simplifications of the basic concepts and techniques as well as more specific data and examples. When the technology allows for significant such improvements, a new version of this work is called for.

Air Force Weapons Laboratory
Albuquerque, New Mexico
September, 1979

C.E. BAUM
J.P. CASTILLO
J.H. DARRAH

REFERENCES

- [1] J.V. Locasso, et al, "EC-135 EMP assessment program, assessment error analysis," AFWL-TR-77-254, April 1978.
- [2] C.E. Baum, "How to think about EMP interaction," Proc. 1974 Spring FULMEN meeting, April 1974, pp. 12 - 23.
- [3] F.M. Tesche, M.A. Morgan, B. Fishbine, and E.R. Parkinson, "Internal interaction analysis: topological concepts and needed model improvements," IN 248, July 1975.
- [4] E.F. Vance, "Shielding and grounding topology for interference control," IN 306, April 1977.
- [5] F.M. Tesche, "Topological concepts for internal EMP interaction," AP-26, January 1978, pp. 60 - 64, and also EMC-20, February 1978, pp. 60 - 64.
- [6] C.E. Baum, "The role of scattering theory in electromagnetic interference problems," in P.L.E. Uslenghi (ed.), Electromagnetic Scattering, Academic Press, 1978.
- [7] C.E. Baum, "The use of topology as a means of subdividing complex electromagnetic scatterers and controlling the entry of electromagnetic energy," IEEE EMC Symposium, Atlanta, Georgia, 20 - 22 June 1978.
- [8] C.E. Baum, "Topological concepts for ordering electromagnetic interaction with complex systems," National Radio Science Meeting, Boulder, Colorado, 5 - 10 November 1978.
- [9] C.E. Baum, "Emerging technology for transient and broad-band analysis and synthesis of antennas and scatterers," IN 300, and also Proc. IEEE, November 1976, pp. 1598 - 1616.
- [10] J.P. Castillo (ed.), EMP Interaction Handbook (EIH) Memos, Part A: Administrative, 1976 ff.
- [11] C.E. Baum (ed.), EMP Interaction Handbook (EIH) Memos, Part B: Format Issues, 1976 ff.
- [12] C.E. Baum (ed.), EMP Interaction Handbook (EIH) Memos, Part C: Specific Technical Issues, 1976 ff.

A NOTE FROM THE EDITOR

This document is the product of a project undertaken by the Air Force Weapons Laboratory to compile a comprehensive, up-to-date, standard reference on EMP interaction. While this documentation should be useful to the entire community of EMP research workers, it is specifically aimed at providing in one volume the best currently-available technical data to engineers who are engaged in hardening military aircraft, missiles, and satellite communications systems against EMP penetration. To ensure accurate and expert coverage of every topic in EMP interaction, the contributors to this volume have been selected from among the nation's foremost EMP specialists who have been actively participating in EMP interaction analysis and experiment.

The body of technical data collected in this document is largely drawn from results obtained under AFWL-sponsored EMP research efforts directed by John Darrah, Carl Baum and Phil Castillo. These results have appeared in the AFWL EMP note series and in various AFWL technical reports. However, many of the results presented here were worked out during the making of this document and have never before appeared elsewhere.

During the last three years I worked very closely with Phil Castillo and H.A. Goodwin of AFWL on every aspect of the project. They had given me continued encouragement and advice, and helped overcome all the difficult problems that stood in the way. Their unstinting assistance and unabated interest in the project were essential to its completion. Carl Baum of AFWL was very much involved in the technical aspect of the project. He had continuously and generously given me comments and ideas to improve the content of the document. The entire technical staff of Dikewood, Santa Monica, not only has contributed a large amount of material to this document, but also proofread the typescript. In particular, Kendall Casey and F.C. Yang helped me rewrite and integrate many sections of the document. Ed Vance of SRI, Clay Taylor of the Mississippi State University, and several members of the technical staff of RDA have made numerous valuable suggestions regarding the suitability and

accuracy of the material in the document. Needless to say, the contributions from the twenty-four authors are the building blocks of the project. Their efforts and cooperation have made this document possible. Finally, my sincere appreciation goes to Diane DiFranco for her patience, assistance and skills in the preparation of the entire typescript.

Dikewood Industries, Inc.
Santa Monica, California
September, 1979

K.S.H. LEE

CONTRIBUTORS

The contributors are listed alphabetically below, together with their affiliations and the sections in which their contributions have been incorporated.

C.E. Baum (Air Force Weapons Laboratory)	1.1.1.3 through 1.1.1.5
C.M. Butler (University of Mississippi)	2.1.3.2
K.F. Casey (Dikewood Santa Monica)	1.6; 2.1.3.3; 2.4.1; 3.2.4; 3.2.5
J.P. Castillo (Air Force Weapons Laboratory)	2.1.2.3.1; 2.1.3.1.5
T.T. Crow (Mississippi State University)	2.1.2.3.2
L.B. Felsen (Polytechnic Institute of New York)	1.4.3.1 through 1.4.3.4
S. Frankel (Sidney Frankel and Associates)	1.3.2
D.F. Higgins (Mission Research Corporation)	1.1.1.1; 1.1.1.2; 1.1.2
R.W.P. King (Harvard University)	1.3.1.6; 2.1.2.1.2
R.G. Kouyoumjian (Ohio State University)	1.4.3.5; 2.1.2.2
J. Lam (Dikewood Santa Monica)	1.3.1.1 through 1.3.1.5; 1.4.2; 2.2.1.2; 2.2.2; 2.2.3
K.S.H. Lee (Dikewood Santa Monica)	1.3.3; 1.4.1; 2.1.3.1; 2.3
V.V. Liepa (University of Michigan)	1.5
C.L. Longmire (Mission Research Corporation)	1.1.1.1; 1.1.1.2; 1.1.2
L. Marin (Dikewood Santa Monica)	2.1.2.3.1; 2.1.3.1
R. Mittra (University of Illinois)	2.3.2.1
C.T.C. Mo (R & D Associates)	1.6
D.L. Sengupta (University of Michigan)	1.5
T.B.A. Senior (University of Michigan)	1.5

C.D. Taylor (Mississippi State University)	2.1.1; 2.1.2.1
F.M. Tesche (Science Applications, Inc.)	1.2; 1.3.2; 2.4.2; 2.1.2.3.2
E.F. Vance (Stanford Research Institute)	2.1.2.3.3; 3.1; 3.2.1 through 3.2.4
D.R. Wilton (University of Mississippi)	2.2.1.1
F.C. Yang (Dikewood Santa Monica)	2.3.2.1

CONTENTS

Foreword	iii
A Note From the Editor	ix
Contributors	xi
A Note on References	xxiv
Symbols and Notation	xxv

PART 1: PRINCIPLES AND TECHNIQUES

<u>Chapter</u>	<u>Page</u>
1.1 Introduction	1
1.1.1 History of EMP	2
1.1.1.1 Discovery of EMP	2
1.1.1.2 Early Activities	5
1.1.1.3 Sensor Development	7
1.1.1.4 Simulator Development	8
1.1.1.5 Notes on EMP and Related Subjects	9
1.1.2 Physics of EMP	10
1.1.2.1 Basic Mechanisms	13
1.1.2.1.1 Radiation Source Terms	13
1.1.2.1.2 Source Currents	16
1.1.2.1.3 The Air Conductivity	20
1.1.2.1.4 The Spherically Symmetric Case	23
1.1.2.2 Types of Electromagnetic Pulse	25
1.1.2.2.1 EMP From High-Altitude Bursts	25
1.1.2.2.2 EMP From Surface Bursts	31
1.1.2.2.3 EMP From Low-Altitude Bursts	38
1.1.2.2.4 Dispersed EMP	39
1.1.2.2.5 MHD EMP	39
1.1.2.2.6 SGEMP/IENTP	40
1.1.2.3 Computational Techniques	41
1.1.2.3.1 Analytic Methods	41
1.1.2.3.2 Numerical Methods	41
1.1.2.3.3 Comparison of Theory With Data	43
1.1.2.3.4 Unknowns	44
References	45

<u>Chapter</u>	<u>Page</u>
1.2 Topological Decomposition of Systems	48
1.2.1 Basic Decomposition Concepts	48
1.2.2 Decomposition of Layers	53
1.2.3 Hardening Concepts	64
References	66
1.3 Formulation of Interaction Problems	67
1.3.1 Integral-Equation Approach	67
1.3.1.1 Magnetic-Field Integral Equation	68
1.3.1.2 Electric-Field Integral Equation	75
1.3.1.3 Thin-Wire Integral Equation	77
1.3.1.4 Time-Domain Integral Equations	80
1.3.1.4.1 Time-Domain Magnetic-Field Integral Equation	81
1.3.1.4.2 Time-Domain Electric-Field Integral Equation	84
1.3.1.4.3 Time-Domain Thin-Wire Integral Equation	86
1.3.1.5 Aperture-Penetration Integral Equation	87
1.3.1.6 Intersecting Cylinders	91
1.3.1.6.1 Orthogonally Intersecting, Electrically Thin ($ka \leq 0.1$) Cylinders	92
1.3.1.6.2 Non-Orthogonally Intersecting, Electrically Thin ($ka \leq 0.1$) Cylinders	95
1.3.2 Transmission-Line Approach	100
1.3.2.1 The Two-Conductor Line	101
1.3.2.1.1 Line Excitation	103
1.3.2.1.2 Line Differential Equations	104
1.3.2.2 Multiconductor Lines and Cables	109
1.3.2.2.1 Multiconductor Line With Lossy Conductors	112
1.3.2.2.2 Multiconductor Transmission Line Modes	113
1.3.2.2.3 Load Voltage and Current Responses	115

<u>Chapter</u>	<u>Page</u>
1.3.2.3 Analysis of Transmission Line Networks	119
1.3.2.4 Determination of Line Parameters	125
1.3.2.4.1 Line Capacitance, Conductance and Inductance	125
1.3.2.4.2 Effects of Conductor Losses, Discontinuities and Inhomogeneities	127
1.3.2.4.3 Experimental Determination of Line Parameters	129
1.3.2.5 External Coupling Parameters	131
1.3.2.5.1 Incident Field Components Transverse to a Two-Conductor Line	132
1.3.2.5.2 Transverse Field Coupling to a Coaxial Cable Near a Perfectly Conducting Ground	134
1.3.2.5.3 Axial Field Coupling to Transmission Lines	134
1.3.2.5.4 Field Coupling to a Multi-conductor Line	135
1.3.3 Circuit Approach	137
1.3.3.1 Circuit Theory via Maxwell's Equations in Integral Form	138
1.3.3.2 Circuit Theory via Scalar and Vector Potentials	143
1.3.3.3 Circuit Properties of an Object in Free Space	146
1.3.3.3.1 Complex Poynting's Theorem	147
1.3.3.3.2 Natural Frequencies	149
1.3.3.3.3 Positive Real Functions	151
1.3.3.3.4 Energy Functions	153
1.3.3.4 Circuit Description of Modes and Discontinuities	157
1.3.3.4.1 Modes	157
1.3.3.4.2 Discontinuities	160
References	162
1.4 Frequency and Time-Domain Methods	170
1.4.1 Low-Frequency, Late-Time Region	170

<u>Chapter</u>	<u>Page</u>
1.4.1.1 Rayleigh Series	171
1.4.1.2 Properties of \vec{J}_0 and \vec{J}_1	176
1.4.1.3 Small Objects on a Large Structure	179
1.4.1.4 Dipoles and Polarizabilities	182
1.4.1.4.1 Object in Free Space	183
1.4.1.4.2 Aperture in Ground Plane	184
1.4.1.4.3 Boss on Ground Plane	186
1.4.1.4.4 Depression in Ground Plane	187
1.4.1.5 Quasi-Stationary, Late-Time Considerations	189
1.4.2 Intermediate-Frequency, Intermediate-Time Region	194
1.4.2.1 Singularity Expansion Method	194
1.4.2.1.1 Transient Analysis of a Lumped Network Circuit	194
1.4.2.1.2 Generalization	198
1.4.2.2 s-Plane Singularities in Transmission-Line Analysis	202
1.4.2.2.1 Finite Transmission Line	202
1.4.2.2.2 Infinite Transmission Line	209
1.4.2.3 s-Plane Singularities in Scattering Analysis	211
1.4.2.4 Expansion Parameters for Simple Natural-Frequency Poles	217
1.4.2.5 Numerical Approach	222
1.4.3 High-Frequency, Early-Time Region	223
1.4.3.1 Ray Method	223
1.4.3.2 Equations for the Ray-Optical Field, and Their Solution	232
1.4.3.2.1 Derivation of the Equations	232
1.4.3.2.2 Ray Trajectories	235
1.4.3.2.3 Phase and Amplitude	235
1.4.3.2.4 Ray-Optical Field	236
1.4.3.2.5 Evanescent Fields	237
1.4.3.3 Asymptotic Methods	241
1.4.3.3.1 Asymptotic Expansions	241
1.4.3.3.2 Asymptotic Evaluation of Integrals	243

<u>Chapter</u>	<u>Page</u>
1.4.3.4 Alternative Formulations of Diffraction Problems	243
1.4.3.4.1 Induced Current Formulation	243
1.4.3.4.2 Plane Wave Spectral Formulation	244
1.4.3.4.3 High-Frequency Approximations	245
1.4.3.5 The GTD Vector Fields	246
1.4.3.5.1 Reflection	250
1.4.3.5.2 Edge Diffraction	251
1.4.3.5.3 Vertex Diffraction	254
1.4.3.5.4 Surface Diffraction	255
References	262
1.5 Scale Modeling	267
1.5.1 Theoretical Background	267
1.5.2 Scale-Model Measurements	270
References	276
1.6 Error Estimation	277
1.6.1 General Considerations	278
1.6.2 Error Specification for Stimulus and Transfer Functions	283
1.6.3 Error Analysis for an Elementary Response	286
1.6.4 Error Analysis for Non-Elementary Responses	288
1.6.4.1 Series Interaction Paths	289
1.6.4.2 Parallel Interaction Paths	291
1.6.5 Confidence Bounds	292
References	295
PART 2: FORMULAS AND DATA	
2.1 External Interaction	297
2.1.1 Coupling	297

<u>Chapter</u>	<u>Page</u>
2.1.3.3 Metallic and Advanced Composite Walls	454
2.1.3.3.1 Homogeneous Conducting Walls	457
2.1.3.3.2 Mesh-Shielded Nonconductive Walls	460
2.1.3.3.3 Mesh-Shielded Conductive Walls	463
References	467
2.2 Intermediate Internal Interaction, I: Line Conductors	475
2.2.1 Coupling	475
2.2.1.1 Line Conductors Near Apertures	475
2.2.1.1.1 Line Conductors Near a Single Aperture	475
2.2.1.1.2 Line Conductors Near Periodic Arrays of Apertures	479
2.2.1.1.3 Line Conductors Inside a Triangular Waveguide With Periodic Apertures	482
2.2.1.2 Line Conductors Near a Conducting Surface	484
2.2.2 Propagation	486
2.2.2.1 Lumped Circuit Elements of Discontinuities	488
2.2.2.1.1 Abrupt Cable Bend	489
2.2.2.1.2 Circular Cable Bend	490
2.2.2.1.3 Cable Clamp	490
2.2.2.1.4 Circular Aperture on Ground Plane	493
2.2.2.1.5 Thin Rib on Ground Plane	494
2.2.2.1.6 Periodic Discontinuities	494
2.2.2.2 Distributed Impedances of a Wire Over a Finitely Conducting Surface	499
2.2.3 Penetration	501
2.2.3.1 Cable Conduit	501
2.2.3.2 Conduit Junction	506
References	510

<u>Chapter</u>		<u>Page</u>
2.3	Intermediate Internal Interaction, II: Cavities	512
2.3.1	Coupling	512
2.3.1.1	Coupling via Apertures	512
2.3.1.1.1	Aperture in a Curved Surface	514
2.3.1.1.2	Aperture With a Back-up Ground Plane	515
2.3.1.1.3	Aperture With a Back-up Cavity	517
2.3.1.1.4	Aperture With Other Modifications	518
2.3.1.2	Coupling via Diffusion	518
2.3.1.2.1	Cavities With Electrically Thin Walls	521
2.3.1.2.2	Shells of Arbitrary Electrical Thickness	521
2.3.2	Propagation	522
2.3.2.1	Cavity Excitation via Apertures	522
2.3.2.1.1	Parallel-Plate Cavities	523
2.3.2.1.2	Infinite Circular Cylindrical Cavities	530
2.3.2.1.3	Simply-Connected Cavities	536
2.3.2.1.4	Coaxial Cavities	547
2.3.2.1.5	Depressions	548
2.3.2.2	Diffusive Penetration Into Cavities	555
2.3.2.2.1	Physical Considerations of Shielding	555
2.3.2.2.2	Simple-Shaped Enclosures	557
2.3.2.2.3	Arbitrarily Shaped Enclosures	565
2.3.2.2.4	Enclosures With Other Wall Materials	566
2.3.3	Penetration	566
	References	570
2.4	Cable Interaction	574
2.4.1	Shielded Cables	574

<u>Chapter</u>	<u>Page</u>
2.4.1.1 Coupling to Coaxial Cables	575
2.4.1.1.1 Distributed Voltage and Current Sources per Unit Length	575
2.4.1.1.2 Discrete Voltage and Current Sources	587
2.4.1.2 Propagation	589
2.4.1.2.1 Series Impedance and Shunt Admittance per Unit Length	589
2.4.1.2.2 Solutions of the Transmission-Line Equations	592
2.4.1.3 Penetration	599
2.4.1.3.1 Penetration Resulting From Distributed Excitation	599
2.4.1.3.2 Penetration Resulting From Discrete Excitation	600
2.4.2 Open Transmission Lines	602
2.4.2.1 Determination of Line Parameters	602
2.4.2.1.1 Isolated Transmission Lines	602
2.4.2.1.2 Transmission Line Over a Ground Plane	604
2.4.2.2 Coupling to Open Lines	608
2.4.2.2.1 Transmission Line Illuminated by Plane Wave	608
2.4.2.2.2 Excitation of Transmission Line by a Parallel Line	613
2.4.2.2.3 Transmission Lines Excited Through Apertures	615
2.4.2.3 ^m Propagation Along Open Transmission Lines	616
2.4.2.3.1 Two-Wire Line Response to Plane Waves	616
2.4.2.3.2 Two-Wire Line Response to Localized Sources	621
2.4.2.3.3 Multiconductor Line Response	623
2.4.2.4 Penetration	627

<u>Chapter</u>	<u>Page</u>
2.4.2.4.1 Two-Conductor Transmission Line	630
2.4.2.4.2 Multiconductor Lines	630
References	632

PART 3: SYSTEM APPLICATIONS

3.1	Assessment and Hardening	635
3.1.1	The Assessment and Hardening Problem	635
3.1.1.1	Severity of the Problem	636
3.1.1.2	Shielding Surfaces	638
3.1.1.3	Penetration of Shields	639
3.1.1.4	Coupling and Propagation	640
3.1.2	Hardening Concepts	641
3.1.2.1	System Topology	641
3.1.2.2	Penetrating Conductors	642
3.1.2.3	Aperture Control	648
3.2	Illustrative System Examples	651
3.2.1	Rocket Vehicles in Flight	651
3.2.1.1	System Topology	654
3.2.1.2	External Interaction	656
3.2.1.3	Penetration of First Shield and Intermediate Interaction	660
3.2.1.3.1	Diffusion Through Skin	663
3.2.1.3.2	Leakage Through Joints	664
3.2.1.3.3	Voltage on Connector Pins	666
3.2.1.4	Penetration of Second Shield and Internal Interaction	667
3.2.1.4.1	Cable Shield Parameters	669
3.2.1.4.2	Internal Wire Voltage	670
3.2.2	Aircraft	671
3.2.2.1	General Description of Aircraft	671
3.2.2.1.1	Airframe and Equipment	671
3.2.2.1.2	Power Plant and its Derivatives	672

<u>Chapter</u>	<u>Page</u>
3.2.2.1.3 Flight Control	673
3.2.2.1.4 Radio Systems	674
3.2.2.1.5 Environmental Control Systems	676
3.2.2.2 Aircraft Topology	676
3.2.2.3 External Interaction	680
3.2.2.3.1 Airframe	680
3.2.2.3.2 UHF Antenna	685
3.2.2.3.3 HF Fixed-Wire Antennas	688
3.2.2.4 Internal Interaction	691
3.2.2.4.1 Fixed-Wire Cable Crosstalk	691
3.2.2.4.2 Wires Near Aperture	692
3.2.2.5 Hardening Approaches	694
3.2.3 Ground-Based System	695
3.2.3.1 System Topology	696
3.2.3.2 External Interaction	698
3.2.3.2.1 AC Overhead Power Lines	698
3.2.3.2.2 Buried Communication Cable	704
3.2.3.2.3 Communication Antenna and Feed	707
3.2.3.2.4 Summary of Penetration Currents	711
3.2.3.2.5 Lid Excitation	711
3.2.3.3 Internal Interaction	714
3.2.4 Satellites	717
3.2.4.1 EMP Environment for Satellites	718
3.2.4.2 EMP Interaction	719
3.2.5 Error-Analysis Examples	724
3.2.5.1 Induced Voltage on Rocket Raceway Cable	724
3.2.5.2 Aircraft HF Fixed-Wire Antenna Response	727
3.2.5.3 Satellite Cable-Bundle Induced Open-Circuit Voltage	728

A NOTE ON REFERENCES

The following abbreviations for references are used throughout the document:

AFWL-TR	Air Force Weapons Laboratory Technical Report
IN	Interaction Notes
SSN	Sensor and Simulation Notes
TN	Theoretical Notes
AP	IEEE Transactions on Antennas and Propagation
EMC	IEEE Transactions on Electromagnetic Compatibility
MTT	IEEE Transactions on Microwave Theory and Techniques

All references to classified documents have been omitted.

SYMBOLS AND NOTATION

Symbol Modifiers

In this handbook certain standard modifiers are used in conjunction with the symbols representing various quantities. These modifiers and their functions are listed below.

<u>Modifying Function</u>	<u>Symbol Modifier</u>
per unit length	' (prime as superscript)
surface (from volume quantity)	s (subscript)
source	(s) (superscript)
incident	(i) (superscript)
diffracted	(d) (superscript)
radiated	(r) (superscript)
scattered	(sc) (superscript)
reflected	(re) (superscript)
open circuit	oc (subscript)
short circuit	sc (subscript)
complex frequency domain	~ (directly above in highest position)
three-space vector	+ (directly above)
three-space dyad	‡ or ↔ (directly above)
total	t (subscript)
transfer	T (subscript)
electric	e (or absent) (subscript)
magnetic	m (subscript)
equivalent	eq (subscript)
effective	ef (subscript)

Superscripts may also be enclosed in parentheses if there exists the possibility of confusion with an exponent. It should also be noted that the tilde (~) denoting a quantity in the frequency domain may be omitted if the quantity is expressed explicitly as a function of frequency.

List of Symbols

In the following list of symbols are given the complete forms of the symbols used, their meanings, and abbreviated or alternate forms of these symbols.

LIST OF SYMBOLS

Symbol	Definition	Abbreviated or Alternate Forms; Remarks
$F(s) = \int_{-\infty}^{\infty} f(t)e^{-st}$ $e^{j\omega t}$ $\vec{u}, \vec{v}, \text{ etc.}$ $\vec{i}_x, \vec{i}_y, \text{ etc.}$ $\vec{u}, \vec{v} \text{ or } \vec{u}, \vec{v}$ $\vec{i} \text{ or } \vec{i}$	<p>time-harmonic factor</p> <p>vectors</p> <p>unit vectors</p> <p>dyads</p> <p>unit dyad</p> <p>symmetric product of scalars</p> <p>electric field, electric displacement</p> <p>magnetic field, magnetic induction</p> <p>incident electric, magnetic field</p> <p>reflected electric, magnetic field</p>	<p>two-sided Laplace transform</p> <p>ω denotes the real radian frequency ($s = j\omega$)</p> <p>$\vec{a}_x, \vec{a}_y; \vec{e}_x, \vec{e}_y; \vec{u}_x, \vec{u}_y; \vec{i}, \vec{j}; \hat{x}, \hat{y}$</p> <p>$\vec{i} \text{ or } \vec{i}$</p> <p>$\vec{E}^i, \vec{H}^i$; used in this handbook</p> <p>\vec{E}^r, \vec{H}^r; used in this handbook</p>

LIST OF SYMBOLS (Cont'd.)

Symbol	Definition	Abbreviated or Alternate Forms; Remarks
$\vec{E}^{(sc)}, \vec{H}^{(sc)}$	scattered electric, magnetic field	\vec{E}^s, \vec{H}^s ; used in this handbook
$\vec{E}_{sc}, \vec{H}_{sc}$	short-circuit electric, magnetic field	
\vec{A}, ϕ	magnetic vector, electric scalar potential	
\vec{A}_m, ϕ_m	electric vector, magnetic scalar potential	
ϕ	magnetic flux	
\vec{j}	volume electric current density	Used only in Sec. 1.1.2
\vec{j}_s, \vec{j}_{sm}	surface electric, magnetic current density	$\vec{K}, \vec{K}_m; \vec{j}, \vec{j}_m$; the latter used throughout this handbook except in Sec. 1.1.2 because no occasion arises in other sections dealing with volume current densities.
ρ_s, ρ_{sm}	surface electric, magnetic charge density	ρ, ρ_m used throughout this handbook because no occasion arises dealing with volume charge densities.

LIST OF SYMBOLS (Cont'd.)

Symbol	Definition	Abbreviated or Alternate Forms; Remarks
$\epsilon_0 \approx 8.85 \times 10^{-12} \text{ F/m}$	free-space permittivity	
$\mu_0 = 4\pi \times 10^{-7} \text{ H/m}$	free-space permeability	
$Z_0' \approx 377 \Omega$	free-space wave impedance	
$c \approx 3 \times 10^8 \text{ m/s}$	vacuum speed of light	
σ	conductivity	
ϵ_r	relative permittivity	
μ_r	relative permeability	
k	wave number	$k = \omega/c$
$\gamma = jk$	complex propagation constant	$\gamma = s/c$
τ_d	diffusion time	
τ_r	e-fold rise time	

LIST OF SYMBOLS (Cont'd.)

Symbol	Definition	Abbreviated or Alternate Forms; Remarks
τ_f	e-fold fall time	
$\dot{\phi}_\gamma$	γ -ray flux	
$\dot{\phi}_e$	electron number flux	
\dot{D}_e	dose rate	
λ_a	absorption length	
R_{mf}	mean forward range	
$\vec{P}_{eq}, \vec{M}_{eq}$	equivalent electric, magnetic dipole moment	\vec{P}, \vec{M} used throughout this handbook
$\vec{P}_{eq}, \vec{M}_{eq}$ or $\vec{P}_{eq}, \vec{M}_{eq}$	equivalent electric, magnetic polarizability	\vec{P}, \vec{M} used throughout this handbook
$\vec{P}_{ai}, \vec{M}_{ai}$	imaged aperture electric, magnetic dipole moment	
$\vec{\alpha}_e$ or $\vec{\alpha}_e$	imaged aperture electric polarizability	$\vec{P}_{ai} = \epsilon_0 \vec{\alpha}_e \cdot \vec{E}_{sc}$

LIST OF SYMBOLS (Cont'd.)

Symbol	Definition	Abbreviated or Alternate Forms; Remarks
$\vec{\alpha}_m$ or $\vec{\alpha}_m^{\leftrightarrow}$	imaged aperture magnetic polarizability	$\vec{\alpha}_m^{\leftrightarrow} = -\vec{\alpha}_m^{\leftrightarrow} \cdot \vec{H}_{sc}$
A_{ef}, A_{eq}	effective, equivalent area	
s_α	complex natural frequency of the α th mode	
η_α	coupling coefficient of the α th mode	
ν_α	α th natural mode	
μ_α	α th coupling mode	
ψ	eikonal	
ξ	arc length along a ray	
Z_T	transfer impedance	
Ω_T	charge transfer frequency	

LIST OF SYMBOLS (Concl'd.)

Symbol	Definition	Abbreviated or Alternate Forms; Remarks
Z_c	characteristic impedance	
Z'	impedance per unit length	
Y'	admittance per unit length	
$\vec{f}(\vec{r},s)$	vector function of position and complex frequency	$\vec{f}(\vec{r},s)$ used throughout this handbook
$(a_{m,n})$	matrix of elements $a_{m,n}$	(a_{mn}) ; comma between subscripts omitted if no possibility for confusion exists
(b_n)	column vector of elements b_n	

PART 1

PRINCIPLES AND TECHNIQUES

CHAPTER 1.1

INTRODUCTION

The interaction of the nuclear electromagnetic pulse (EMP) with a large aeronautical or communication system is not limited to coupling with the system's external structure. EMP energy can penetrate through the system's outer surface, propagate in its interior or along cables, and finally appear as electric currents and voltages at the sensitive components of electronic subsystems. The goal of EMP hardness engineering is to suppress these currents and voltages to levels below the components' damage and upset thresholds. The primary objective of this document is to provide quantitative data, both analytical and experimental, on EMP interaction (which comprises coupling, propagation and penetration) for typical system geometries, for use in system hardness design and implementation.

The material of this document is organized in three parts. Part 1 presents the fundamental concepts of EMP interaction and the methods of its formulation and analysis. The general process of EMP penetration into a large system is generically viewed as one of EMP energy transfer across successive substrata (intersurfaces) of a layered topological model. The outermost surface of the model is the system's external skin; the innermost surface consists of the shields of internal electrical cables. The crossing of each surface can be quantified by a transfer function. Each transfer function is to a large extent dependent on the local surface geometry and can be determined by solving an appropriate boundary-value problem in electromagnetic theory. The analytical methods for formulating and solving these electromagnetic boundary-value problems are described in detail.

Part 2 presents the analytical formulas as well as numerical and experimental data on EMP coupling, propagation and penetration. These formulas and data are organized according to the surfaces of the topological model to which they apply. Those pertaining to the outermost surface of the model describe the EMP interaction with the external structures of aeronautical and communication systems. Those pertaining

to the intermediate surfaces describe the excitation of wire-like conductors and cavities lying behind these surfaces. Those pertaining to the innermost surface describe the penetration of cable shields and the excitation of shielded or unshielded wires.

Part 3 presents a number of system examples to demonstrate the application of the formulas and data in Part 2. These examples are designed to illustrate typical EMP interactions with aircraft, missiles, satellites and ground communication facilities. Engineering techniques for hardening these systems are discussed. Finally, the errors in the calculations of the system examples are described.

1.1.1 HISTORY OF EMP

There are a number of reasons that make it difficult to compile even a brief history of EMP. Among these are the following: (1) much of the early work was never written down or documented in readily available sources; (2) EMP studies were carried out independently by persons and organizations (AEC, AFWL, DASA, etc.) in a number of locations both within the U.S. and overseas (e.g., U.K., U.S.S.R.); (3) much of the work was classified, making open literature surveys somewhat incomplete and possibly misleading; and (4) scientists and engineers were busy trying to solve technical problems rather than recording historical details. Thus, the brief history presented here may contain errors or have omitted important contributions by certain groups or individuals, but all in all is factual.

A partial list of events important to the history of EMP is given in table 1. The list includes nuclear test information and the first interests in system vulnerability and EMP simulation issues. The events are listed in chronological order to show the historical (although not necessarily the most logical) development.

1.1.1.1 Discovery of EMP

It is reported that Fermi realized that any nuclear explosion would create electromagnetic fields. The exact mechanisms that he had in mind

TABLE 1. IMPORTANT EVENTS IN THE HISTORY OF EMP

1945	TRINITY EVENT; electronic equipment shielded reportedly because of Fermi's expectations of EM signals from a nuclear burst
1951- 1952	First deliberate EMP observations made by Shuster, Cowan and Reines
1952- 1953	First British atomic tests; instrumentation failures attributed to "radioflash"
1954	Garwin of LASL proposes prompt gamma-produced Compton currents as primary sources of EMP
1957	Bethe makes estimate of high-altitude EMP signals using electric dipole model (early-time peak incorrect)
1957	Haas makes magnetic field measurements for PLUMBBOB test series (interest in EMP possibly setting off magnetic mines)
1958	Joint British/U.S. meeting begins discussions of system EMP vulnerability and hardness issues
1958	Kompaneets (USSR) publishes open literature paper on EMP from atomic explosion
1959	Pomham and Taylor of the U.K. present a theory of "radioflash"
1959	First interest in EMP coupling to underground cables of Minuteman missile
1962	FISHBOWL high-altitude tests; EMP measurements driven off scale; first indications of the magnitude of the high-altitude EMP signal
1962	SMALL BOY ground burst EMP test
1962	Karzas and Latter publish two open literature papers on using EMP signals for detections of nuclear tests; bomb case EMP and hydromagnetic EMP considered

TABLE 1. IMPORTANT EVENTS IN THE HISTORY OF EMP (Cont'd)

1963	Open literature calls for EMP hardening of military systems begin to appear
1963- 1964	First EMP system tests carried out by Air Force Weapons Laboratory (AFWL)
1963- 1964	Longmire gives a series of EMP lectures at AFWL; presents detailed theory of ground burst EMP and shows that the peak of the high-altitude EMP signals is explained by magnetic field turning (magnetic dipole signal)
1964	First note in the LASL/AFWL EMP notes series published
1965	Karzas and Latter publish first open literature paper giving high-frequency approximation for the high-altitude magnetic dipole signal
1967	Construction of ALECS as the first guided-wave simulator is completed for EMP simulation on missiles
1967	AJAX underground nuclear test
1969	Close-in EMP mechanisms recognized and evaluated by Graham and Schaefer
1970	EMP underground test feasibility recognized and preliminary design presented by Schaefer
1973	First joint nuclear EMP meeting at AFWL
1974	MING BLADE underground EMP test for confirmation of near surface burst EMP models
1975	DINING CAR underground EMP test as the first system hardware EMP test
1975	MIGHTY EPIC underground EMP test
1978	Special joint issue on the nuclear EMP in IEEE Transactions on Antennas and Propagation and also on Electromagnetic Compatibility
1978	Nuclear EMP meeting in Albuquerque under IEEE sponsorship

were apparently not recorded, but electromagnetic shielding techniques were applied to the various instruments used on the TRINITY event in 1945. The first deliberate EMP measurements were apparently made in 1951 through 1952. The goal was to obtain diagnostic information describing weapon output. Early U.S. tests also reportedly often used the EMP signal to trigger oscilloscopes and other recording equipment.

Standard shielding practices used by U.S. experimenters apparently kept EMP signals from interfering with diagnostics on the early nuclear tests. The British were less fortunate, however. In the first British atomic tests in 1952 through 1953, a number of instrumentation failures occurred, apparently due to EMP and the absence of any shielding. Thus, the British developed an early interest in "radioflash" (the British label for EMP).

1.1.1.2 Early Activities

The fact that nuclear explosions generate electromagnetic signals was experimentally well known by the mid-1950's when theoretical explanations of the effect began to appear. In 1954 Garwin of Los Alamos correctly proposed that the Compton current produced by prompt gamma radiation was a major source term for Maxwell's equations, while in 1958 Kompaneets [1] of the U.S.S.R. published one of the first papers in open literature on EMP. Also, in 1959 Pomham and Taylor of the U.K. presented a paper entitled "A Theory of Radioflash" [2].

The early theories were often incomplete and sometimes incorrect. Emphasis was placed on ground bursts or low-altitude explosions. Much of the interest was in nearby (but outside the source region) diagnostic measurements or long-range detection and observation of foreign tests. VLF and other low-frequency effects were of particular interest, since good quality high-frequency EMP measurements had not been made in the early tests.

The first glimmerings of the strategic and tactical importance of EMP effects began to appear about 1957 when Haas made a series of magnetic field measurements during the PLUMBOB test series. One goal of these measurements was to determine if EMP could set off nearby buried magnetic mines. In 1958

discussions between the U.K. and the U.S. took place regarding the EMP vulnerability and hardening of military systems (perhaps motivated by British test instrumentation problems), and in 1959 people began to worry about EMP coupling to the silos and buried cables of the Minute-man system.

Both experimental and theoretical work continued to be carried out at Los Alamos during this period, notably by Partridge, Suydam [3,4] and Malik. Some interest in high-altitude EMP began to appear in 1957 when Bethe made some estimates of the high-altitude signal using an electric dipole model. Unfortunately, this model is incorrect for the large, early-time peak and, as a result, a number of measurements attempted during the 1962 high-altitude test series were driven off-scale.

In 1962 a number of EMP measurements were attempted at the SMALL BOY nuclear test in Nevada. The goal was to obtain data on the close-in EMP environment of a ground burst. Unfortunately, many of the attempted measurements were unsuccessful due to instrumentation and other problems.

The somewhat surprising results of the high-altitude test series, combined with an atmospheric test ban, created a great deal of interest in EMP in the early 1960's. Karzas and Latter published two papers [5,6] on EMP theory in the open literature in 1962, their investigations being at least partially aimed at detection of nuclear test ban violations. In 1963 through 1964 Longmire gave a series of lectures at AFWL which presented a fairly detailed theory of source region surface-burst EMP and showed that electron turning effects due to the earth's magnetic field would produce the large early-time signals from high-altitude EMP seen in the 1962 test series. This "high-frequency approximation" was first presented in the open literature by Karzas and Latter in 1965 [7]. Significant theoretical work and computer code development were also carried out during this period at AFWL and in the U.K. Also, 1963 through 1964 apparently marked the beginning of EMP testing of military systems when Henderson, Graham, and Cikotas of AFWL first used a distribution of loops, a fast switch, and a large capacitor bank to carry out EMP tests.

Since the mid-1960's, both interest in and knowledge of EMP phenomena have greatly expanded, and an adequate history of this period is beyond the scope of this brief discussion. As a result of numerous efforts over this time period, there now exist a wide variety of simple analytical models and very complex computer codes used for calculating EMP environment. A number of EMP simulators have been built and simulation tests carried out. Interests in system vulnerabilities have also expanded from missiles to aircraft, satellites, and communication systems.

A good idea of present EMP interests can be gained by examining the recent special joint issue of two IEEE journals on the Nuclear Electromagnetic Pulse [8].

1.1.1.3 Sensor Development

After the SMALL BOY test in 1962 it was apparent that instrumentation for measuring the EMP physical parameters was inadequate, especially in the nuclear source region. The conventional sensors, which convert electric fields, magnetic fields, current densities, etc. to analog electrical signals on data cables and circuit elements, had fundamental physics problems in that their response in EMP source regions was unknown, and hence they were not designed to operate with acceptable and known accuracy. Problems associated with Compton (source) current density, nonlinear and time-changing air/soil conductivity, and other nuclear radiation effects were not familiar to antenna designers. These problems had to be solved if any experimental progress was to be made concerning the EMP source as well as the EMP interaction with objects in such source regions.

As a part of the nuclear test readiness program AFWL, with DASA funding, initiated a sensor development effort for source-region applications. Design concepts were developed based on the physical processes in EMP source regions (described by Baum in the early Sensor and Simulation Notes) and prototype sensors were built primarily by EG & G with the early E-field sensors being built by SRI. These first models were fielded

on the AJAX underground nuclear test in 1967 and several subsequent EMP experiments. Also during this period some air conductivity measurements were made on underground nuclear tests (by Baran, Baum and Ekman) using X-band double-interferometer techniques on irradiated air in a rectangular waveguide.

With the growth of EMP testing and the concomitant design of EMP simulators, accurate broadband sensors were needed for measuring both simulator performance and various response parameters of the system under test. For this application several designs have evolved which have found widespread use in both American and European agencies.

Both the source-region and source-free-region sensors are reviewed in a recent paper in the special joint issue on the Nuclear Electromagnetic Pulse authored by the principal contributors to this technology [9].

1.1.1.4 Simulator Development

From an EMP interaction viewpoint a military system such as a missile, aircraft, communication center, etc. is extremely complex, implying a low confidence in the results of an EMP interaction analysis as it affects the many possible electronic vulnerabilities. It was therefore apparent that a test capability was required. To perform these tests on any extensive basis required special test facilities producing EMP-like environments. This led to the need for what are referred to as EMP simulators.

There are two fundamental points to be considered in deciding if something is an EMP simulator (in the strict sense) or not: the accuracy of the form of the fields in the absence of the test object (spatial, temporal, frequency content, etc.), and an acceptably small interaction of the simulator itself with the test object (thereby changing the response characteristics of the test object [10]). The beginning of EMP simulation is related to the quantification of both of these points with designs accounting for them.

While some preliminary tests of military equipment were begun in 1963 through 1964 on some computer equipment and later on missiles, the

first EMP simulator in the strict sense was ALECS. This was first proposed by Partridge [11] as a three-plate parallel-plate transmission line for testing EMP instrumentation. This facility was changed (after construction as a three-plate facility) into a two-plate facility for testing missiles. The latter was completed in 1967 using calculations of Baum [12,13] and was intended to simulate a threat-like plane-wave EMP environment appropriate to in-flight systems (away from the earth's surface but below the atmospheric source region from a high-altitude (exoatmospheric) nuclear detonation). Given its 12.75 meter plate spacing ALECS is strictly an EMP simulator with respect to "in-flight" test objects of somewhat smaller dimensions in order that simulator/object interaction not be too severe.

Another important early development in EMP simulation concerns the source region of a near-surface burst. After some preliminary tests of missile silo systems subjected to somewhat arbitrary EM excitation, a simulator known as SIEGE was developed to simulate the magnetic field distribution produced near the ground surface by a near-surface burst. This simulator incorporated two concepts: the buried transmission line [14] and the surface transmission line [15]. In 1968 low-level testing was begun with the SIEGE simulator.

By now EMP simulation has evolved into an extensive field in its own right, with various simulator types available for various EMP environments. AFWL has pioneered in the development of EMP simulator concepts and has contracted the construction of the largest number of these. However, various other American agencies including DNA, Naval Surface Weapons Center, and Harry Diamond Laboratories have built some as well. Various European agencies have also built some EMP simulators, generally somewhat smaller than those in the U.S. For a review of the various EMP simulators, including both existing simulators and those that as yet exist only conceptually, the reader is referred to [10].

1.1.1.5 Notes on EMP and Related Subjects

An important stimulus for the development of EMP technology was begun in 1964 by Partridge of LASL. This was the Sensor and Simulation Note

series begun by Partridge to stimulate thinking about EMP sensor and simulation design problems. In 1966 the editorship was turned over to Baum at AFWL who was by that time the major contributor. Various individuals at AFWL (some being now at RDA) had contributed to the expansion of the note series to include various other aspects of EMP technology.

Currently, the editor has divided the note series on EMP and related subjects (or "EMP Notes" for short) into three major categories: EMP (Electromagnetic Pulse), PEP (Pulsed Electrical Power), and ACT (Analytical and Computational Techniques) encompassing over a thousand individual papers. These represent most of basic EMP-related technology. A majority were printed directly as notes, but some existing reports have been only assigned note numbers. Various indices have been published and the most extensive one (including detailed subject division) was published in 1973 [16]. A previous extensive index was published by Quested of AWRE in the United Kingdom in 1971 [17].

The Notes have functioned as a journal of the EMP community with important contributions from agencies and contractors in the U.S. and U.K. Publication has been supported primarily by AFWL, but many other agencies have made some contribution to this effort. The recent special joint issue on the Nuclear Electromagnetic Pulse [8] is based primarily on material that can be found in the Notes.

In addition to the individual notes, thirty volumes (about 400 pages each) or so have been published beginning in 1970 by AFWL to compile the early notes. The first few volumes were first published by DASA (now DNA) in 1968. In addition, a few special documents (handbooks) have been published as volumes in this series.

1.1.2 PHYSICS OF EMP

Although the fact that a nuclear explosion produces an electromagnetic pulse (EMP) was recognized as early as 1945 (see Sec. 1.1.1), it was some time before the mechanisms of EMP generation were understood well enough to make possible reasonably accurate predictions of signal amplitudes

and waveforms. EMP is now recognized by many as a potentially damaging nuclear weapon effect, and yet relatively few people have more than a rudimentary knowledge of the physics of EMP generation. Hopefully, this section may help to alleviate that situation.

It should be noted that a systems engineer or interaction analyst may never even see the results of a "real" EMP calculation. This is because calculated EMP waveforms can be sensitive functions of weapon design, burst location, and observer-burst orientation. Thus an EMP criterion signal is often defined. This criterion signal often represents an envelope that includes most or all EMP signals of a given type. Working with such a criterion signal greatly simplifies interaction analyses, but it should be remembered that the criterion and an actual threat signal are usually not identical.

Similarly, detailed predictions of EMP waveforms will not be presented here, partly because such waveforms are usually classified, but also because the interaction analyst will probably be supplied with an EMP criterion signal specific to the problem of interest. Instead, the presentation here is aimed at giving the reader some idea of the basic mechanisms of EMP.

A flow chart outlining the various steps of the EMP generation process is shown in Fig. 1. The process starts with a nuclear explosion. This nuclear burst creates photons with a large range of energies.

For understanding EMP phenomena one is primarily interested in the gamma-rays (photons with energies of about 1 MeV) and the X-rays (photons with energies of a few keV) created by the burst [18]. These photons interact with the material through which they pass (e.g., the bomb casing, the atmosphere, or the wall of a satellite) by Compton and/or photoeffect processes [19], creating free electrons and positive ions. The moving electrons then create spatial current densities which serve as source terms for Maxwell's equations. These fast electrons will also slow down by ionizing the medium through which they move, creating numerous secondary electrons. The low-energy secondaries will drift along the local electric field lines and are thus often treated in terms of an effective conductivity.

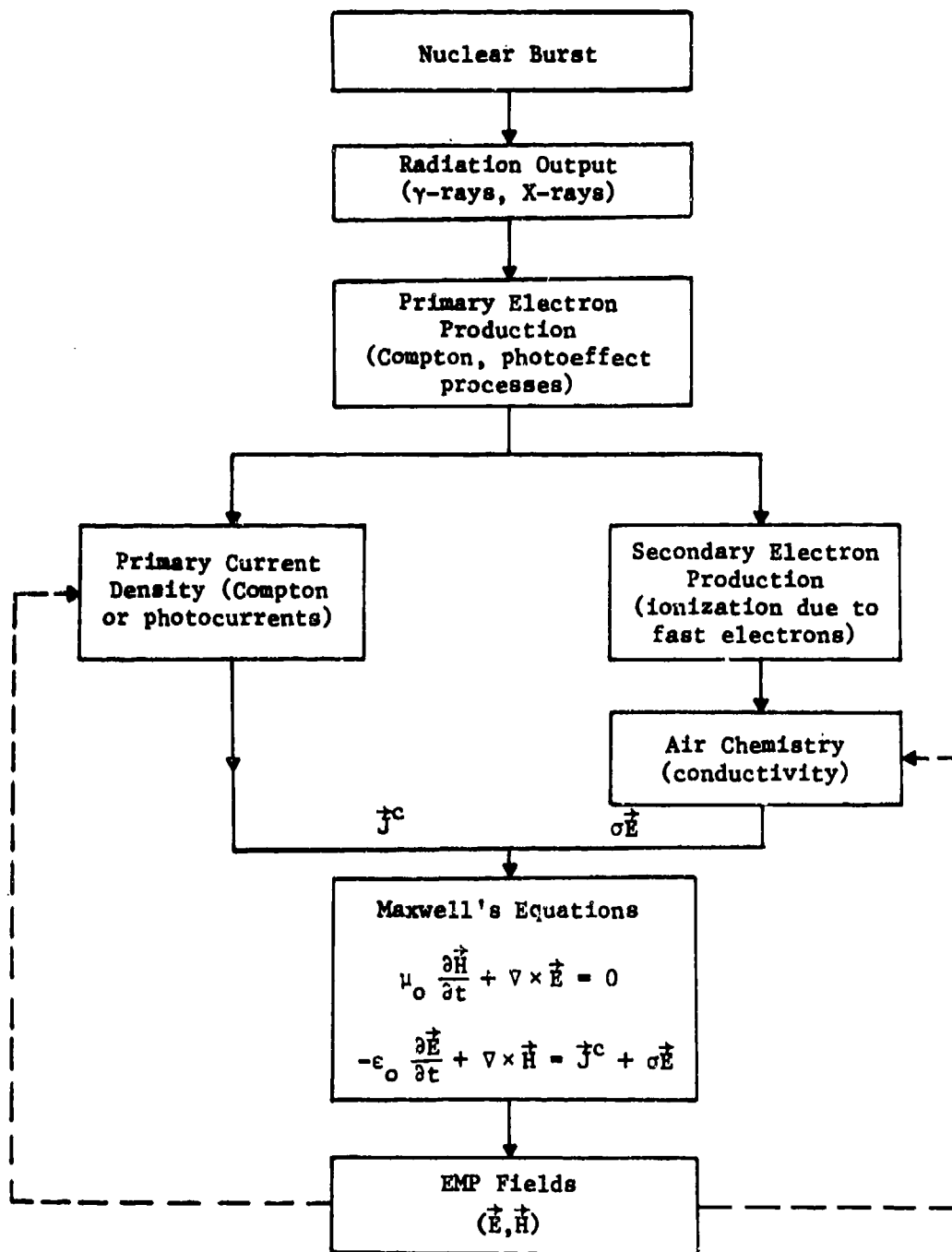


Fig. 1. Flow diagram of EMP production mechanisms.

A conduction current is then created, which tends to cancel any electric field set up by the primary current density. Once these current densities are known, the magnitude and waveform of the EMP are determined by Maxwell's equations.

The basic mechanisms outlined in the flow chart of Fig. 1 will first be individually discussed in the following subsection. The various types of EMP will then be described in terms of these basic mechanisms. Finally, calculational techniques, unknowns and uncertainties will be briefly addressed.

1.1.2.1 Basic Mechanisms

1.1.2.1.1 Radiation Source Terms

a. The Gamma Source

The primary source of most types of EMP is the gamma-ray output of a nuclear burst. Consider first a nuclear explosion in the air just above the ground surface (surface burst). A hypothetical but not atypical example of the gamma source strength from a 1-megaton surface burst is shown in Fig. 2 [20]. The total source is the sum of several components, each with its characteristic decay time [18]. The prompt gamma pulse comes directly out of the nuclear device, has a rise time of several nanoseconds (ns), and decays in a few tens of ns. The other gammas are made by neutrons that leave the device and interact with the air and ground. Fast neutrons striking solid objects (e.g., the ground) very near the device make inelastic scatter gammas in the same time frame as the prompt gammas. Fast neutrons (energy > 6 MeV) make air inelastic gammas by inelastic scattering in air. Ground capture gammas are made by neutrons which slow down and are captured in the ground. Air capture gammas, made by the same process in air, last longer because of the low density of air compared with ground. Fission product gammas, the longest lived source, are emitted by fission debris following the lingering beta decay of fission fragments.

For a burst somewhat above the ground, some time is required for the neutrons to reach the ground, so that ground inelastic and capture sources are delayed somewhat. At increasing burst altitudes, the intensities

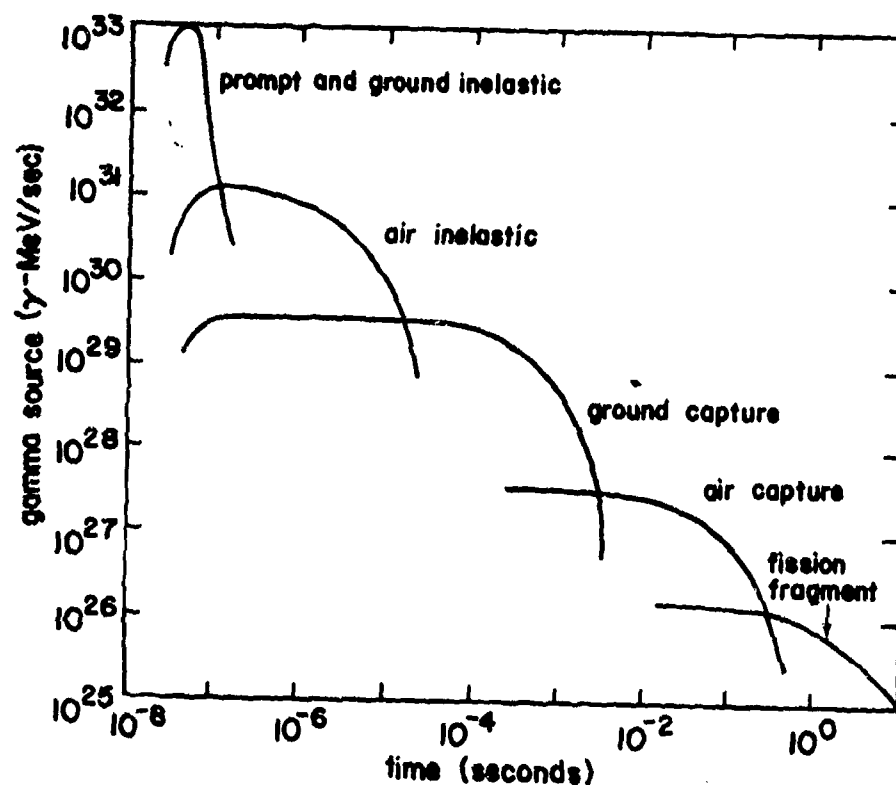


Fig. 2. Total gamma source strength versus time for a nominal 1-megaton surface burst.

of the air inelastic and air capture sources decrease, and their lifetimes increase, due to decreasing air density. For bursts at very high altitudes, the ground sources are absent and the air sources delayed until neutrons can reach the sensible atmosphere at altitudes of the order of 30 km. The speed of the fastest neutrons is about 5×10^7 m/sec.

While the prompt gamma source can be regarded as a point source, the size of the air and ground sources obviously depends on the burst geometry. In sea-level air, neutron mean free paths are of the order of 100 meters, and the air sources have dimensions of a few mean free paths.

Approximate average γ -ray energies and effective absorption lengths in the air are listed in table 2 for the various sources [19].

TABLE 2. APPROXIMATE AVERAGE ENERGIES AND EFFECTIVE ABSORPTION LENGTHS IN AIR OF GAMMA SOURCE COMPONENTS

Component	Energy (MeV)	Absorption Length (gm/cm ²)
Prompt	1.5	40
Air Inelastic	4	52
Ground Capture	3	38
Air Capture	6	58
Fission Fragment	1	37

Estimates of the gamma flux $\dot{\phi}_\gamma$ at distance r from the burst can be made by using spherical dilution and attenuation factors, e.g., in uniform air

$$\dot{\phi}_\gamma \sim e^{-r/\lambda_a} / 4\pi r^2 \quad (1)$$

where λ_a is the effective absorption length.

b. The X-ray Source

Because X-rays are more easily attenuated than gamma rays, they are often of secondary importance in EMP generation even though the nuclear burst generates much more energy in the X-ray energy range than in the γ -ray energy range. One major exception to this statement is the case of an exoatmospheric system of interest (e.g., SGEMP effects on a satellite).

The X-ray output of a nuclear burst can be reasonably well understood by just considering the debris as a thermal radiator with a temperature of roughly 10^7 °K [18]. If one treats the debris as a blackbody radiator, then one expects Planckian X-ray spectra with characteristic energies of the order of 1 keV. Time histories have characteristic times similar to those of the prompt γ -ray output (i.e., rise time ~ 10 ns), while the absorption length for a 10 keV X-ray in air is only 0.25 gm/cm^2 (i.e., several hundred times less than that of a prompt gamma ray).

1.1.2.1.2 Source Currents

a. The Compton Current

At γ -ray energies, the primary process by which free electrons are produced is Compton scattering [19]. In this scattering process, an incident gamma is scattered by an atomic electron, and the electron recoils somewhat like a struck billiard ball. The angular distribution of the recoil electrons peaks in the forward direction, so that a net electric current results. The average kinetic energy of the recoil electrons is of the order of one-half the incident gamma energy.

As the recoil electrons move through the air or other material medium, they gradually lose energy to other atomic electrons through collisions, dislodging some from their atoms and thus producing ionization. The energy loss is sufficient to bring the recoil electron to rest within a distance (track length) of a few meters in sea-level air. In addition, the recoil electrons suffer many small-angle scatterings (multiple scattering), largely in collisions with atomic nuclei. The multiple scattering reduces the mean forward range of recoil electrons to about two-thirds of the track length [21].

The geomagnetic field deflects the Compton recoil electrons, leading to components of Compton current in directions other than the direction of the incident gammas. This effect is relatively small at sea level, for the Larmor radius of the recoil electrons in the geomagnetic field is 50 to 100 meters, which is long compared with the mean forward range at sea level. However, at 30-km altitude, the center of the source region for high-altitude EMP, the mean forward range is comparable to the Larmor radius. Thus the deflected (transverse) Compton current is comparable to the radial current and is the principal source of the high-altitude EMP.

The Compton recoil electrons are also affected by the EMP fields. EMP calculations which include this effect are called self-consistent, since the fields are allowed to affect the Compton current which produces the fields. Such calculations are non-linear and are usually performed on a high-speed digital computer.

It is easy to understand the general magnitude of the Compton current. A steady flux $\dot{\phi}_\gamma$ of collimated gammas will produce a steady flux of recoil electrons in the same direction, according to the relation

$$\dot{\phi}_e = \dot{\phi}_\gamma \frac{R_{mf}}{\lambda_s} \approx 0.007 \dot{\phi}_\gamma^{[2]} \quad (2)$$

where λ_s is the scattering mean free path of the gammas, R_{mf} is the mean forward range of the recoil electron, $\dot{\phi}_e$ is the electron number flux, $\dot{\phi}_\gamma^{[1]}$ is the gamma number flux (gammas per unit area per unit time), and $\dot{\phi}_\gamma^{[2]}$ is the gamma energy flux in units of γ -MeV/cm²-sec. A dose rate of 1 rad/sec corresponds to a gamma energy flux of about 2×10^9 gamma-MeV/cm²-sec. Thus in terms of the dose rate \dot{D}_e the radial Compton current density J_r^C is*

$$J_r^C (\text{amps/m}^2) \approx 2 \times 10^{-8} \dot{D}_e (\text{rads/sec}) \quad (3)$$

This formula is valid from sea level up to about 30-km altitude, where the geomagnetic field limits the mean forward range. The transverse, geomagnetically deflected Compton current density is

$$J_t^C \approx J_r^C (R_{mf}/2R_L) \quad (4)$$

where R_L is the Larmor radius. At 30-km altitude J_t^C and J_r^C are comparable.

At sea level the effective lifetime (before stopping) of a Compton recoil electron is a few ns. Thus the waveform of the Compton current will be approximately the same as that of the gamma flux. At 30-km altitude the

*In this chapter \vec{J} is used to denote the volume current density, whereas in all other chapters \vec{J} denotes exclusively the surface current density.

lifetime is about 1 microsecond (μs), as is also the Larmor period. Here the current waveform is stretched by the recoil electron dynamics in the early part of the gamma pulse. Fig. 3 shows typical radial and transverse

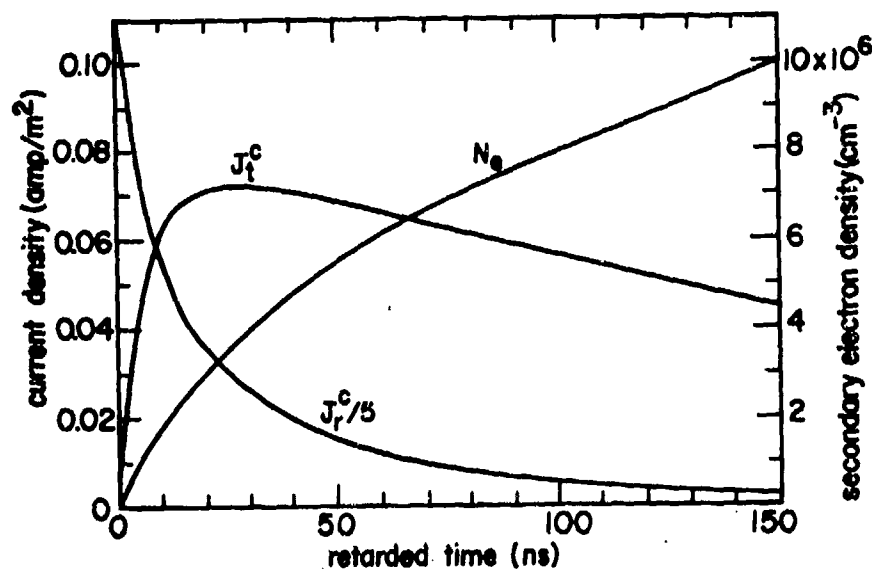


Fig. 3. Radial and transverse Compton currents J_r^C and J_t^C , and secondary electron density N_e versus retarded time at 31.4-km altitude for a delta-function pulse of 4.62×10^9 (1.5-MeV) gammas per cm^2 , perpendicular to a geomagnetic field of 0.6 gauss.

currents for a very short (delta-function) pulse of gammas [20]. The currents are plotted as functions of retarded time $t_{\text{ret}} = \tau/c$, where

$$\tau = ct - r \quad (5)$$

for convenience in understanding the solution of Maxwell's equations. Note that if a recoil electron starting at $t = 0$ moved outwards with speed c (the speed of light) its retarded time would remain equal to zero. The

fact that the recoil electrons do move outwards with speeds close to c accounts for the relatively large amplitude of J_r^C and J_t^C at early retarded times.

b. Photoeffect Currents

At X-ray energies the dominant electron production process is the photoeffect [19]. In this case, the incident X-ray photon disappears with part of its energy going to free an electron from a bound state near a nucleus and the rest of its energy going into kinetic energy of the free electron.

Photoeffect currents are of secondary importance for EMP except for observation points very near a nuclear burst or at vacuum/material interfaces (i.e., SGEMP source currents). The subject of electron emission from vacuum/material interfaces is too complicated to treat in detail here. As an example, however, typical electron yields for various blackbody X-ray spectra incident upon several materials are listed in table 3 [22].

TABLE 3. BACKSCATTERED ELECTRON YIELDS FOR SEVERAL BLACK-BODY SPECTRA

Incident Photon Blackbody Temperature (keV)	Aluminum (electrons/ calorie)	Gold (electrons/ calorie)	Silicon Dioxide (electrons/ calorie)
1	3.04 (13)	1.16 (14)	2.30 (13)
2	1.25 (13)	7.21 (13)	8.86 (12)
3	6.49 (12)	4.66 (13)	4.49 (12)
5	2.57 (12)	2.50 (13)	1.74 (12)
8	1.03 (12)	1.33 (13)	6.94 (11)
10	6.49 (11)	9.71 (12)	4.35 (11)

1.1.2.1.3 The Air Conductivity

A Compton recoil electron makes approximately one secondary electron-ion pair for each 85 eV lost by it in collisions with atoms. Most of the secondary electrons have energies of the order of 10 eV, but a few have larger energies, approaching one-half that of the original electron. The more energetic secondary electrons produce tertiaries, etc. When all the ionization is completed, there is approximately one electron-ion pair for each 34 eV lost by the original Compton recoil electron [23]. Thus a 1 MeV electron will produce eventually about 30,000 electron-ion pairs. The effects of these electron-ion pairs are often modeled by an equivalent conductivity.

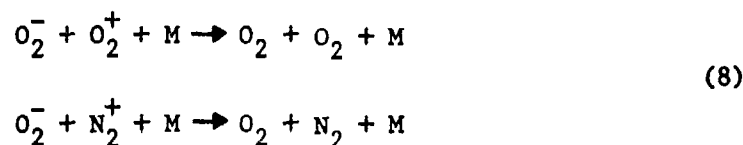
Both electrons and ions contribute to the conductivity, so that it is necessary to keep track of their densities. At low altitudes free electrons are removed predominantly by the attachment process



which produces the negative oxygen ion. At very high electron and ion densities, dissociative recombination removes both electrons and positive ions



Positive and negative ions remove each other by mutual neutralization, with the help of a third molecule M (either O_2 or N_2)



Both O_2^+ and N_2^+ are produced along with e in the original ionization. Since the conductivity properties of O_2^+ and N_2^+ are nearly the same, it is not necessary to keep track of both species separately. The common treatment defines densities N_e , N_+ , and N_- of electrons, positive and negative ions respectively, which satisfy the differential equations

$$\begin{aligned}\frac{dN_e}{dt} &= S_e - k_1 N_e - k_2 N_e N_+ \\ \frac{dN_+}{dt} &= S_e - k_2 N_e N_+ - k_3 N_+ N_- \\ \frac{dN_-}{dt} &= k_1 N_e - k_3 N_+ N_-\end{aligned}\tag{9}$$

Here S_e is the rate of production of electron-ion pairs. The rate constants k_1 , k_2 , k_3 are for the reactions (6), (7) and (8), respectively [24]. Typical values of these constants at sea level and their scaling with air density ρ_a are

$$\begin{aligned}k_1 &\approx 10^8/\text{sec}, & k_1 &\sim \rho_a^2 \\ k_2 &\approx 2 \times 10^{-7} \text{cm}^3/\text{sec}, & &\text{indep. of } \rho_a \\ k_3 &\approx 2 \times 10^{-6} \text{cm}^3/\text{sec}, & k_3 &\sim \rho_a\end{aligned}\tag{10}$$

The value of k_1 is affected by the presence of an electric field. Also, the complete recombination chemistry is somewhat more complicated than described here, especially in the presence of water vapor [24].

Simple approximate solutions to (9) are often useful. For example, the reaction (7) is usually negligible compared with (6). At early times, then, for an ionization source S_e which changes slowly in a time interval compared to $1/k_1$, the electron density is approximately

$$N_e \approx S_e/k_1\tag{11}$$

For a source which rises exponentially, $S_e \sim e^{\alpha t}$ (as for fission chain reactions), the solution is

$$N_e = S_e / (\alpha + k_1) \quad (12)$$

For a source which falls more slowly than t^{-2} , the late-time ion densities are

$$N_- \approx N_+ \approx \sqrt{S_e / k_3} \quad (13)$$

Finally, for a source which falls more rapidly than t^{-2} , the late-time ion densities are

$$N_- \approx N_+ \approx (k_3 t)^{-1} \quad (14)$$

The ionization source S_e can be related to the dose rate \dot{D}_e . Since one rad is defined as depositing 100 ergs/gram, and since 34 eV are required to make one electron-ion pair, one has the relation

$$S_e \left(\frac{\text{elect.}}{\text{cm}^3 \text{-sec}} \right) = 2.2 \times 10^9 \left(\frac{\rho_a}{\rho_{ao}} \right) \dot{D}_e \left(\frac{\text{rads}}{\text{sec}} \right) \quad (15)$$

Here $\rho_{ao} = 1.23$ grams/liter is the density of sea-level air. This relation assumes that all ionization is completed in times short compared with the variation of \dot{D}_e .

The mobility μ_e or μ_i of an electron or ion is defined as the ratio of its drift velocity to the electric field causing the drift. Typical values of the mobilities at sea level and their scaling with air density ρ_a are

$$\begin{aligned} \mu_e \left(\frac{\text{m}}{\text{sec}} \right) / \left(\frac{\text{V}}{\text{m}} \right) &\approx 0.3 \frac{\rho_{ao}}{\rho_a} \\ \mu_i \left(\frac{\text{m}}{\text{sec}} \right) / \left(\frac{\text{V}}{\text{m}} \right) &\approx 2.5 \times 10^{-4} \frac{\rho_{ao}}{\rho_a} \end{aligned} \quad (16)$$

Small differences between the mobilities of various ions are usually neglected. The electron mobility is not independent of the electric field, and is affected by water vapor [23,24].

Since the mobility of electrons is much larger than that of ions, electrons dominate the conductivity at early times when the densities of electrons and ions are comparable. In this circumstance the air conductivity is

$$\sigma = e N_e \mu_e \quad (17)$$

where $-e$ is the electron charge. Using (12) and other data stated above, we can relate the conductivity to the dose rate and find

$$\sigma \left(\frac{\text{mho}}{\text{m}} \right) = \frac{1 \times 10^{-4}}{(\alpha + k_1)} \dot{D}_e \left(\frac{\text{rads}}{\text{sec}} \right) \quad (18)$$

This result is independent of air density, except through the term k_1 . It should be noted, however, that variation of the ionization completion time with ρ_a and the dependence of μ_e on E/ρ_a (E = electric field) make the results only approximate.

At late times, when the electrons are almost all attached in O_2^- , ion conductivity can dominate.

1.1.2.1.4 The Spherically Symmetric Case

In Sec. 1.1.2.1.2 an expression for the spatial current density \vec{J}^c due to primary Compton electrons was derived and a conductivity σ was calculated in Sec. 1.1.2.1.3. One then has the information necessary to solve the Maxwell equations

$$\mu_0 \frac{\partial \vec{H}}{\partial t} + \nabla \times \vec{E} = 0 \quad (19)$$

$$-\epsilon_0 \frac{\partial \vec{E}}{\partial t} + \nabla \times \vec{H} = \vec{J}^c + \sigma \vec{E} \quad (20)$$

Eq.(19) indicates that $\partial \vec{H} / \partial t$ is zero if $\nabla \times \vec{E}$ is zero. Thus, the magnetic field will remain at its initial value (usually assumed to be zero) if the electric field is curl-free. The spherically symmetric geometry is one such case. For this case, $\nabla \times \vec{H} = 0$ in (20), and if \vec{J}^c has only a radial component centered at the burst location, then (20) becomes

$$\epsilon_0 \frac{\partial E_r}{\partial t} + \sigma E_r = - J_r^c \quad (21)$$

Note that in this case the electric field is purely radial and non-zero only within the source region where J_r^c is non-zero.

The solution of (21) is easy to understand. At early times, J_r^c and σ begin at arbitrarily small values, and increase. Therefore, E_r also begins at arbitrarily small values. Thus at sufficiently early times, the term σE_r is negligible. In this time regime, the solution of (21) is

$$E_r \approx - \frac{1}{\epsilon_0} \int_{-\infty}^t J_r^c dt \quad (22)$$

which indicates that J_r^c is creating the electric field E_r in space, which will rise exponentially if J_r^c does. At some time, the conduction current σE_r may become comparable to the displacement current $\epsilon_0 \partial E_r / \partial t$. If after this time we neglect the latter, we obtain

$$E_r \approx - \frac{J_r^c}{\sigma} \equiv E_s \quad (23)$$

From (3) and (18) we see that E_s is independent of the dose rate \dot{D}_e , since J_r^c and σ are proportional to \dot{D}_e . Thus E_r becomes constant at the saturated value E_s .

From (3) and (18) we find

$$E_s \left(\frac{V}{m} \right) \approx 2 \times 10^{-4} (\alpha + k_1) (\text{sec}^{-1}) \quad (24)$$

With $\alpha = 2 \times 10^8$ (not atypical), this formula gives $E_s = 6 \times 10^4$ V/m at sea level where $k_1 = 1 \times 10^8$, and $E_s = 4 \times 10^4$ V/m at higher altitudes where k_1 is negligibly small compared with α .

After the gamma pulse and the Compton current reach their peaks, the value of α effectively goes to zero. Eq.(24) indicates that E_s will then fall to about 2×10^4 V/m at sea level. The displacement current remains negligible, and E_r follows E_s . At sea level, within some kilometers from the nuclear burst, this value is maintained for some tens of μ s, after which the dominance of ion conductivity causes E_r to fall gradually, approximately as $\sqrt{S_e}$. This behavior can be deduced from the approximate solutions(13) and (3).

It should again be noted that for the spherically symmetric geometry just considered, there are no radiated EMP fields (i.e., no fields beyond the source region). If radiated EMP signals are to be created, there must be some asymmetry in the source current distribution. The magnitude and time history of radiated EMP signals can be very sensitive functions of the source asymmetry; thus, much of the early work on the physics of EMP was aimed at determining the most important sources of asymmetry.

1.1.2.2 Types of Electromagnetic Pulse

1.1.2.2.1 EMP From High-Altitude Bursts

One important type of EMP is generated by a nuclear burst above the atmosphere at altitudes of 100 kilometers or greater. In this case the prompt gamma output is the most important radiation source since these gammas will penetrate farthest into the atmosphere.

As indicated in Fig. 4, the downgoing gammas will begin to interact appreciably with the air at altitudes between 40 and 20 kilometers creating a Compton current in this EMP source region. The Compton current has two components. First, the component in the direction radial from the burst produces principally a radial electric field. However, since only part of the gamma shell intersects the atmosphere, we do not have complete spherical symmetry. Thus some transverse fields, principally of electric-

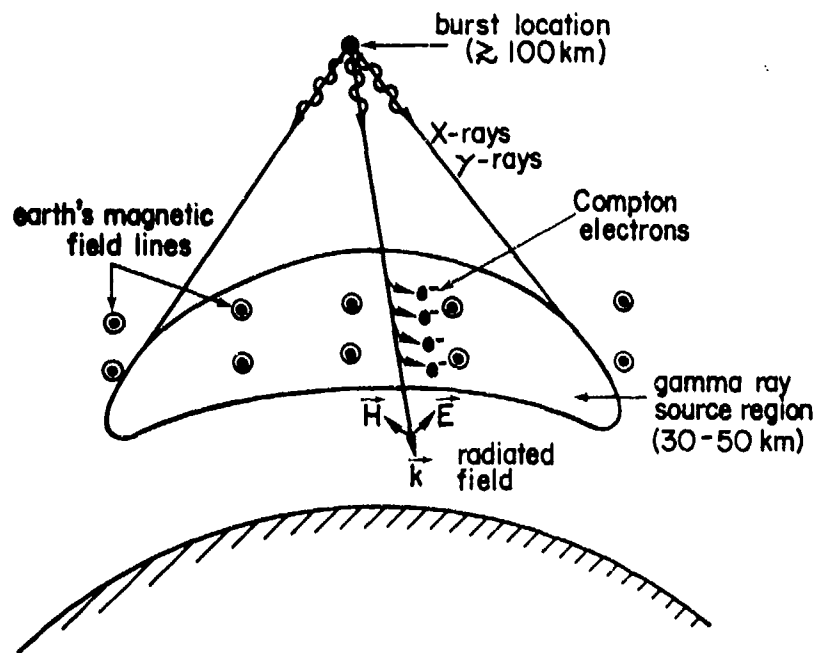


Fig. 4. Schematic representation of high-altitude EMP generation.

dipole type, are generated by the radial current. Second, the geomagnetic field causes the Compton current to have a transverse component perpendicular to the radial direction. This component directly generates outgoing and ingoing transverse fields, principally of magnetic-dipole type. It is this turning of Compton electrons in the earth's magnetic field that creates the very large, early-time peak in the EMP signal from a high-altitude burst. This mechanism was not anticipated prior to the 1962 nuclear test series. As a result, many attempted EMP measurements were driven off-scale. This magnetic-dipole signal was first explained by Longmire, and Karzas and Latter [7] in 1964.

From a simple point of view, the large magnetic-dipole signal is due primarily to the fact that the Compton source current moves radially outward at the speed of light. The net result is that the fields radiated by the various current elements (as shown in Fig. 5) will add in phase, resulting in a large total signal. The situation is similar to a phased array of antennas.

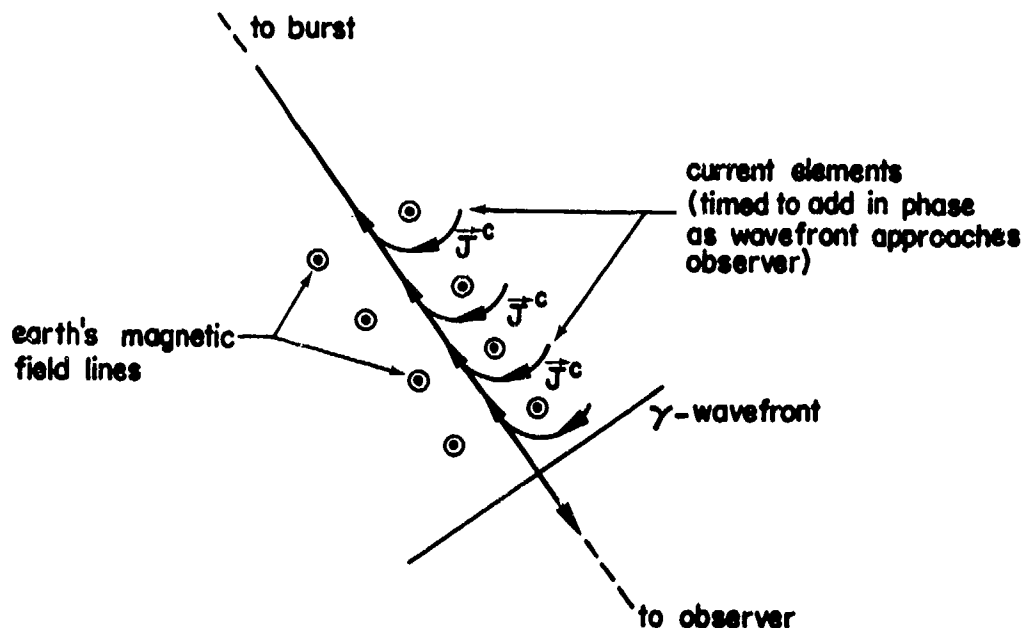


Fig. 5. Diagram indicating the current elements due to geomagnetic turning and how they add in-phase to give a large outgoing wave.

Because there has been a good deal of misunderstanding about the various aspects of high-altitude EMP, it is useful to give a brief mathematical explanation of the phenomenon. For simplicity, consider a planar pulse of gamma rays approaching a flat earth with a flat exponential atmosphere from the vertical direction. Let the vertical coordinate z increase downward, i.e., z is essentially the same as the radial coordinate from the burst, which is imagined to be very far away. Let the geomagnetic field be in the y -direction, so that the Compton current will have components J_z^c and J_x^c . We will have field components E_z , E_x and H_y , which depend only on z and t . Maxwell's equations become

$$\mu_0 \frac{\partial H_y}{\partial t} = - \frac{\partial E_x}{\partial z} \quad (25)$$

$$\epsilon_0 \frac{\partial E_x}{\partial t} + \sigma E_x + J_x^c = - \frac{\partial H_y}{\partial z} \quad (26)$$

$$\epsilon_0 \frac{\partial E_z}{\partial t} + \sigma E_z + J_z^c = 0 \quad (27)$$

It is now convenient to transform variables to retarded time τ and outgoing and incoming fields F and G , where

$$\tau = ct - z \quad (28)$$

$$F = E_x + Z_0 H_y \quad (29)$$

$$G = E_x - Z_0 H_y \quad (30)$$

where Z_0 is the impedance of free space. Thus

$$E_x = (F + G)/2 \quad (31)$$

$$H_y = (F - G)/(2Z_0) \quad (32)$$

and under the retarded-time transformation, the partial derivatives are replaced by

$$\frac{1}{c} \frac{\partial}{\partial t} \rightarrow \frac{\partial}{\partial \tau} \quad (33)$$

$$\frac{\partial}{\partial z} \rightarrow \frac{\partial}{\partial z} - \frac{\partial}{\partial \tau} \quad (34)$$

As a result of these transformations, Maxwell's equations become

$$\frac{\partial F}{\partial z} + \frac{\sigma Z_0 F}{2} = -Z_0 J_x^c - \frac{\sigma Z_0 G}{2} \quad (35)$$

$$\frac{\partial G}{\partial \tau} + \frac{\sigma Z_0 G}{4} = \frac{1}{2} \frac{\partial G}{\partial z} - \frac{Z_0 J_x^c}{2} - \frac{\sigma Z_0 F}{4} \quad (36)$$

$$\frac{\partial E_z}{\partial \tau} + \sigma Z_0 E_z = -Z_0 J_z^c \quad (37)$$

It is to be noted that the differential equation for E_z is uncoupled from the other field components and that this equation has the same form as the spherically symmetric field equation treated in Sec. 1.1.2.1.4. The nature of the solution is thus the same as was previously discussed. At early times, E_z is proportional to the time integral of J_z^C , and if the total charge displacement is sufficient, E_z saturates at the value $-J_z^C/\sigma$. The condition that saturation be reached while the Compton current pulse is still rising as $e^{\alpha t}$ is that the peak conductivity reach the value

$$\sigma \geq \epsilon_0 \alpha \approx 10^{-3} \text{ mho/m} \quad (38)$$

Here we have used $\alpha \approx 10^8/\text{sec}$. Using (18) as an estimate, we find that dose rates of about 10^9 rads/sec are needed to produce saturation of the radial electric field. For a nominal 1-megaton burst, saturation would occur only within slant distances of about 50 km between the burst point and the EMP source region. We will see that it is much easier to saturate the outgoing field F .

Now assume, as will be verified later, that G is small compared with F . One can thus neglect the $\sigma Z_0 G$ term in (35). When this term is dropped, the equation for F has the same form as the equation for E_z just discussed except that the derivative is with respect to distance z rather than the retarded time τ . Thus, for small σ ,

$$F(z, \tau) \approx -Z_0 \int_{-\infty}^z J_x^C(z', \tau) dz' \quad (39)$$

while if σ is large enough, F will saturate at the value

$$F = -\frac{2J_x^C}{\sigma} \quad (40)$$

In an exponential atmosphere, both J_x^C and σ increase as $\exp(z/h)$, where h is the atmospheric scale height. Saturation will thus occur when

$$\sigma \geq \frac{2}{Z_0 h} \approx 10^{-6} \text{ mho/m} \quad (41)$$

This is much smaller than the value needed to saturate E_z as given in (38). One can see that the transverse field will saturate at distances some 30 times farther from a burst than the radial field, or up to 1500 km for a nominal 1-megaton burst.

The reason F is more easily saturated than E_z is that F integrates J_x^c over a scale height, while E_z integrates J_z^c over the rise time multiplied by c . The latter distance is of the order of a few meters, while the former is about 7 km. It is for the same reason that G is small compared with F as is indicated by (36) that G integrates J_x^c in time. Moreover, once F saturates, the source term $Z_0 J_x^c/2 + \sigma Z_0 F/4$ effectively vanishes in the G -equation. In this regime the outgoing wave F induces a conduction current which effectively cancels J_x^c , leaving no net current to drive ingoing waves. The smallness of the incoming wave G compared with the outgoing wave F implies that

$$E_x \approx Z_0 H_y, \quad F \approx 2E_x \quad (42)$$

so that (35) is approximately

$$2 \frac{\partial E_x}{\partial z} + Z_0 \sigma E_x = -Z_0 J_x^c \quad (43)$$

This equation, which is known as the outgoing-wave approximation or the high-frequency approximation, is the basic equation of high-altitude EMP theory. It was derived in Cartesian coordinates (as here) by Longmire in 1963, while the equivalent expression in spherical coordinates was presented by Karzas and Latter in 1964 [7].

The behavior of the solution of (43) for E_x is the same as that discussed above for F . For a given retarded time τ , E_x increases as $\exp(z/h)$ at very high altitudes. If the source is sufficiently strong, E_x will saturate at

$$E_x = -\frac{J_x^c}{\sigma} \equiv E_s \approx 6 \times 10^4 \text{ V/m} \quad (44)$$

and remains saturated until the wave reaches an altitude below about 30 km where, due to absorption of the gammas, both σ and J_x^c fall away. Below this altitude, called the altitude of desaturation, (43) indicates that $\partial E_x / \partial z \approx 0$, or $E_x \approx \text{constant}$; the EMP propagates as a free wave. Actually, of course, E_x will fall as $1/r$.

At very early retarded times, J_x^c and σ are very small and saturation does not occur at all. The rise of the final EMP is similar to the rise of the Compton current before saturation. The duration of the final EMP is not longer than the duration of the Compton current pulse at the desaturation altitude.

Many details of high-altitude EMP theory neglected in the above discussion have been studied over the years and no serious problems with the high-frequency approximation have been discovered. Both detailed numerical [25] and theoretical [26] studies have been carried out.

1.1.2.2.2 EMP From Surface Bursts

For a nuclear burst in the air just above the ground or ocean surface, a Compton current density and air conductivity are produced as described previously. In this case, however, the source region is primarily hemispherical, since radiation created by the burst will not appreciably penetrate into the earth below the burst point. Also, soil conductivities are of the order of 10^{-2} mho/m and the ocean conductivity is about 4 mho/m. These values are higher than the air conductivities over most of the EMP space-time source region. Thus, the ground shorts out the radial electric field near it, and is often approximated by a perfect conductor. The net result is that a radially directed Compton current is generated in the hemisphere above the ground, resulting in a radial electric field as discussed in Sec. 1.1.2.1.4. The asymmetry introduced by the ground, however, creates transverse field components which can radiate to distances large compared to dimensions of the source region.

One simple model for understanding surface-burst EMP is illustrated in Fig. 6. The net effect (ignoring retardation) of radially directed

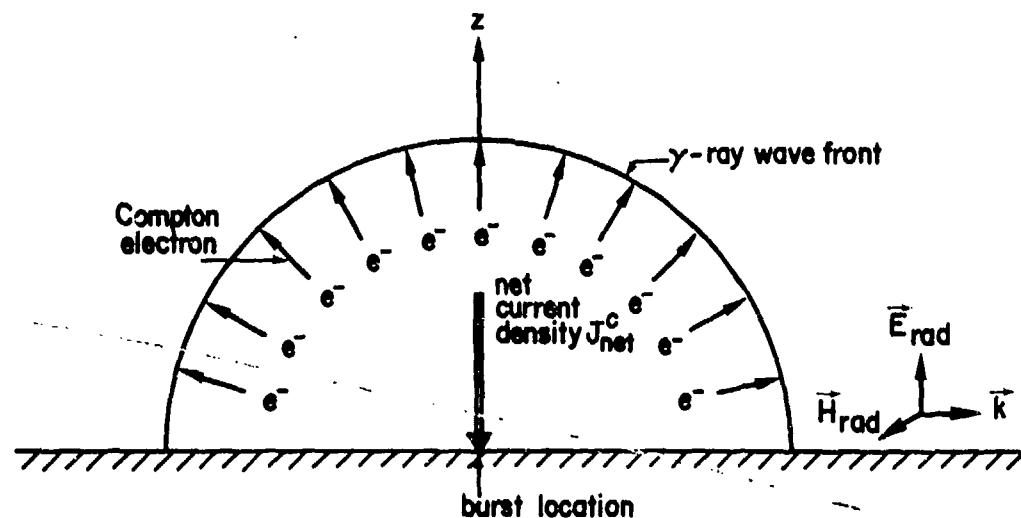


Fig. 6. Surface burst geometry showing Compton electrons and net current density, J_{net}^c . Radiated fields are approximately proportional to dJ_{net}^c/dt (electric-dipole fields).

current densities over a hemisphere is a composite current perpendicular to the ground. This current is just proportional to the time derivative of an effective electric dipole moment. The radiated fields seen by a distant observer can thus be approximated by the radiated fields of an electric dipole, and is proportional to the second time derivative of the dipole moment (i.e., the first time derivative of the net current).

Another simple model useful for understanding how a surface burst generates close-in magnetic fields is illustrated by the toroidal geometry shown in Fig. 7. As noted previously, when the burst occurs, Compton electrons flow radially away in the air creating a charge displacement. Because of the relatively large ground conductivity, equilibrium near the ground/air interface will be established by conduction current (σE) flow through the ground. The net result is a toroidal positive current flow toward the burst point in the air and away from the burst in the ground. It is clear that this toroidal current flow will create a strong, azimuthal magnetic field near the air/ground interface.

A basic theory of ground-burst EMP, including most of the important physical mechanisms, was presented by Longmire in 1963. More detailed

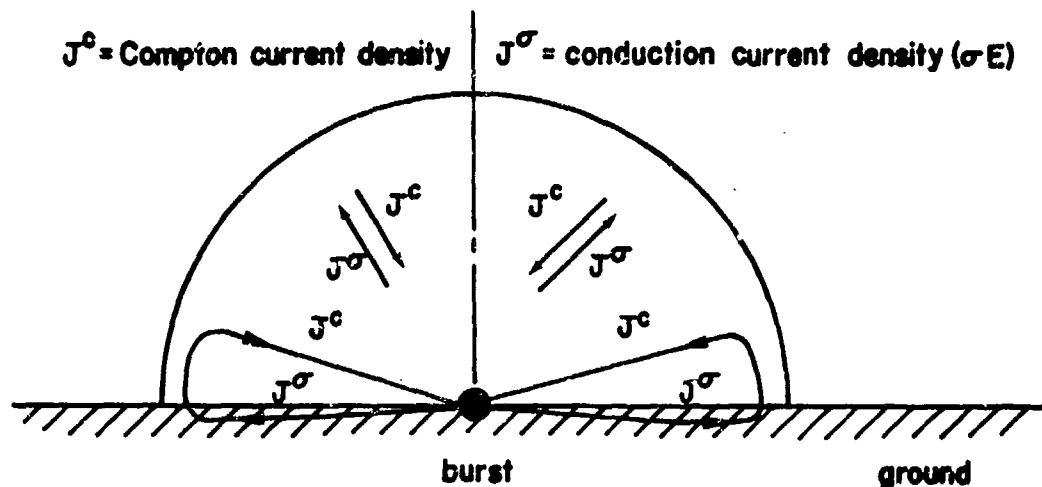


Fig. 7. Surface-burst geometry at intermediate times when Compton electrons created near the ground flow back to the burst through the highly conducting ground, creating a toroidal current loop. Both Compton currents and conduction currents are nearly radial close to vertical axis.

analytical treatments and complex numerical calculations have since been carried out, and a complete theory is obviously quite complicated. Thus, only a brief outline of parts of the physics of ground-burst EMP will be sketched in the following paragraphs.

The surface-burst EMP can be understood in terms of three phases. The first is the wave phase, in which the conduction current is small compared with the displacement current. This phase corresponds to the time before saturation and Maxwell's equations are approximately linear in this phase. The diffusion phase is entered at saturation, when the conduction current exceeds the displacement current and the latter can be neglected. During this phase, the return conduction current (which, in the spherically symmetric case, tries to cancel the Compton current) shifts to the ground from the air just above it. Thus current loops are formed and an azimuthal magnetic field is produced near the ground surface. This field diffuses up into the air and down into the ground by the familiar skin effect process. When the skin depth in the air

reaches to an angular elevation of about 1 radian (referred to the burst point), the diffusion is completed and the final, quasi-static phase is entered. During this final phase the induction (transverse) part of the electric field is small compared with the electrostatic (longitudinal) part, and the Compton and conduction currents are approximately in steady balance.

In mathematical terms, these various phases can be understood by considering a spherical coordinate system, centered at the burst with the polar axis perpendicular to the air/ground interface. In the air, Maxwell's two time-dependent equations reduce to

$$\mu_o \frac{\partial H_\phi}{\partial t} = -\frac{1}{r} \frac{\partial}{\partial r} (r E_\theta) + \frac{1}{r} \frac{\partial}{\partial \theta} E_r \quad (45)$$

$$\epsilon_o \frac{\partial E_\theta}{\partial t} + \sigma E_\theta + J_\theta^c = -\frac{1}{r} \frac{\partial}{\partial r} (r H_\phi) \quad (46)$$

$$\epsilon_o \frac{\partial E_r}{\partial t} + \sigma E_r + J_r^c = \frac{1}{r \sin \theta} \frac{\partial}{\partial \theta} (\sin \theta H_\phi) \quad (47)$$

During the early-time wave phase, it is convenient to transform these equations to retarded time and introduce outgoing and incoming fields, as was done for the high-altitude EMP case. As before, the incoming field G is small compared to the outgoing field F , and at early times the conduction current σE is small compared to the displacement current. One can thus obtain the approximate wave-phase equations to be

$$\frac{\partial F_r}{\partial r} + \frac{Z_o \sigma}{2} F_r = \frac{\partial E_r}{\partial \theta} \quad (48)$$

$$\frac{\partial E_r}{\partial \tau} = -Z_o J_r^c + \frac{1}{2r^2} \frac{\partial F_r}{\partial \theta} \quad (49)$$

where

$$F_r = r(E_\theta + Z_o H_\phi) \quad (50)$$

$$r = ct - r \quad (51)$$

J_θ^c has been assumed to be small compared to J_r^c , and $\sin \theta$ has been replaced by unity since F_r is confined to angles near the ground surface.

An examination of these equations indicates that the outgoing wave F_r is confined to a region near the air/ground interface (since $\partial E_r / \partial \theta$ is largest there) and the field produced near the ground spreads upward as it propagates outward.

At somewhat later times, during the diffusion phase, it is convenient to return to the real-time equations (45) - (47). During this phase, the conductivity has become large enough that the time-derivative terms in (46) to (47) can be dropped (i.e., the displacement current is much smaller than the conduction current). Since the magnetic field is confined to points near the ground surface, one can introduce the local vertical coordinate $z = r(\pi/2 - \theta)$. Eqs. (45) and (47) can then be combined to give

$$\mu_0 \frac{\partial H_\phi}{\partial t} = \frac{\partial}{\partial z} \left(\frac{J_r^c}{\sigma} \right) + \frac{\partial}{\partial z} \left(\frac{1}{\sigma} \frac{\partial}{\partial z} H_\phi \right) \quad (52)$$

Note that this equation is just the standard diffusion equation for the skin effect which can be solved under various assumptions for the time dependence of σ , and hence the name "diffusion phase."

Rather than investigate the diffusion phase by directly studying (52), a somewhat more intuitive approach using the geometry shown in Fig. 8 will be taken. If one ignores the displacement current, then

$$\nabla \times \vec{H} = \vec{J} \quad (53)$$

where \vec{J} includes both the Compton and conduction current. The integral form of this equation, using Stokes' law, is

$$\oint \vec{H} \cdot d\vec{\ell} = \int_S \vec{J} \cdot d\vec{S} \quad (54)$$

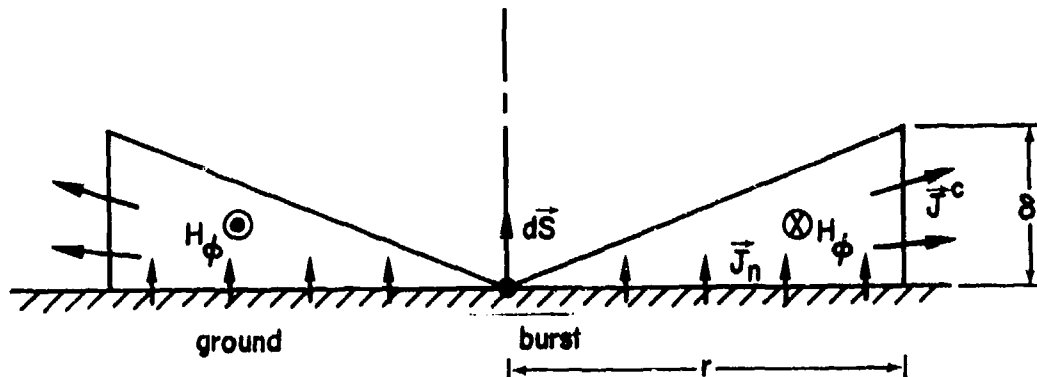


Fig. 8. Geometry for estimating surface-burst magnetic fields.

One can choose the line integral to be at a constant radius r and the surface S to be on the air/ground interface. One then obtains

$$2\pi r H_\phi = \pi r^2 J_n \quad (55)$$

where J_n is the normal current density through the air/ground interface. Thus

$$H_\phi = \frac{I}{2\pi r} \quad (56)$$

where I is the total current flowing normally through the surface. Hence, the magnetic field at a given radius can be found from a knowledge of the total current flowing vertically through the surface inside that radius.

One can estimate the total current through the ground in the following manner. Consider the wedge shown in Fig. 8 through which the Compton current flows to reach an observer at radius r . Assume that all currents within a skin depth of the surface flow back through the ground and that all currents above this flow back radially. If there is no charge build-up, the total vertical current will then equal the total current through the right-hand vertical end of the wedge, i.e.,

$$I = 2\pi r \delta J^c \quad (57)$$

and

$$H_{\phi} = \delta J^C \quad (58)$$

where J^C is the Compton current at radius r and the skin depth δ of a plasma is given by

$$\delta = \sqrt{2/\omega\mu_0\sigma} \quad (59)$$

where ω is the frequency of an oscillatory waveform.

At early times one often assumes that the current rises as $e^{\alpha t}$. A characteristic skin depth is then

$$\delta = \sqrt{2/\alpha\mu_0\sigma} \quad (60)$$

and

$$H_{\phi} \approx \sqrt{\frac{2}{\alpha\mu_0}} \frac{J^C}{\sqrt{\sigma}} \quad (61)$$

Since σ and J^C are both rising as $e^{\alpha t}$, it follows from (61) that

$$H_{\phi} \sim e^{\alpha t/2} \quad (62)$$

At later times, one can assume

$$\delta \sim \sqrt{t/\sigma} \quad (63)$$

so that

$$\begin{aligned} H_{\phi} &\sim J^C \sqrt{t/\sigma} \\ &\sim \frac{J^C}{\sigma} \sqrt{\sigma t} \end{aligned} \quad (64)$$

This last expression is useful since J^C/σ is just the saturated electric field, which is approximately a constant. Thus, the time history of H_{ϕ} in this regime depends upon $\sqrt{\sigma t}$. The peak H_{ϕ} will then occur near the peak of the gamma pulse and Compton current. After the peak, H_{ϕ} varies

only as the square root of gamma flux. As a result, H_ϕ does not decrease much during the remainder of the diffusion phase.

In the quasi-static phase, the divergence of the total current density must vanish, and \vec{E} must be derivable from a potential ϕ which must satisfy

$$\nabla \cdot (\sigma \nabla \phi) = \nabla \cdot \vec{J}^c \quad (65)$$

Longmire has shown that the solution of this problem is such that the electric field and the conduction current are very nearly in the θ direction. Thus while the Compton current flows outward radially, the return conduction current flows down to the ground in the θ direction.

We have not discussed here the EMP problem in the ground, which is dominated by conductivity [27,28]. Soil conductivities and permittivities typically vary substantially with frequency and the water content of the soil.

1.1.2.2.3 EMP From Low-Altitude Bursts

For low-altitude nuclear bursts, the basic physics of EMP generation is quite similar to the mechanisms already discussed — the geometry and relative timing of the various effects are more complicated, however.

For higher bursts (e.g., 30 - 50 km) the geomagnetic turning signal will be important, as it is for high-altitude bursts. However, as the altitude of the burst decreases, the magnitude of the geomagnetic turning signal also decreases because the increasing air density decreases Compton electron ranges and lifetimes. The air density gradient will still give an electric-dipole EMP following the magnetic-dipole signal.

At lower altitudes, the magnetic turning effects are small and the weak electric dipole source caused by the air density gradient becomes the dominant radiation mechanism. As the burst altitude is lowered still further, the gamma deposition region begins to intersect the ground, and the situation is similar to the ground-burst case discussed previously.

The nature of low-altitude EMP thus changes from nearly a high-altitude EMP signal to a ground-burst signal as the altitude of the burst is lowered. As this transition is made, the magnitude of the radiated EMP becomes quite small. Low-altitude effects are thus often ignored in favor of the more severe system threats posed by the high altitude or ground-burst signal.

1.1.2.2.4 Dispersed EMP

The term "dispersed EMP" (DEMP) has been applied to describe the case where the radiated signal from a high-altitude nuclear burst misses the earth (e.g., when the ray is tangent to the earth's surface) and travels out into space after traversing the ionosphere. Since the ionosphere is a dispersive medium (i.e., different frequencies will travel at different velocities), the dispersed pulse leaving the ionosphere will be considerably different from the pulse entering. Calculations show that a monopolar high-altitude EMP signal will be converted to a much longer pulse that resembles a swept CW waveform [29].

1.1.2.2.5 MHD EMP

Thus far, all of the various types of EMP discussed have resulted in early-time signals with characteristic times related to the radiation output of the nuclear device (i.e., milliseconds or less). Electromagnetic signals are also generated at much later times (tens of seconds after the burst) due to the hydromagnetic motion of the atmosphere and device debris. For simplicity, all such very late-time EMP signals are referred to here as magnetohydrodynamic electromagnetic pulse (MHD EMP).

A simple explanation which illustrates the basic ideas of MHD EMP is known as the magnetic bubble model. A nuclear burst will ionize the region of air surrounding it. This highly ionized region will also be heated and thus rise and expand as time progresses, according to the laws of hydrodynamics. Because it is highly conducting, this "bubble" will also force out any nearby geomagnetic field lines as it expands. A simple calculational model is thus a perfectly conducting sphere with a time varying radius immersed in the earth's magnetic field. The net

effect is a change in the electromagnetic field due to the earth's magnetic field being pushed out.

This mechanism for generating EM signals has been postulated for some time [6]. Current theories are more complex and include such effects as motion of regions of the ionosphere. In any case, it appears that the resulting fields are quite low but they can exist over long time periods and large areas. There has thus been some recent concern with coupling to very long communication lines. Work on detailed MHD EMP calculations is presently underway.

1.1.2.2.6 SGEMP/IEMP

System-generated EMP (SGEMP) and internal EMP (IEMP) differ from other types of EMP previously discussed in that the current densities that drive the Maxwell equations are created by the interaction of the incident radiation (X-rays or gamma rays) with the system itself, rather than air or ground near the burst. The system of interest whether a satellite, missile, or ground vehicle, must therefore be close enough to the burst to intercept some of the emitted radiation.

One common example is an orbiting satellite within a direct line-of-sight of an exoatmospheric nuclear burst [30]. In this case the only radiation attenuation is the r^{-2} geometric fall-off and X-rays will be the dominant source of electron emission from external surfaces of the satellite. The radiation will also penetrate the structure, and both X-rays and γ -rays will create free electrons inside the satellite. Because source currents can be generated anywhere within the system, simple hardening concepts such as external electromagnetic shielding may be much less effective than for other types of EMP.

A detailed discussion of the physics of SGEMP/IEMP would be too lengthy to include here. Calculated fields, currents and charges tend to be very system-specific and highly dependent upon assumed parameters of the incident radiation. General comments are thus difficult to make.

One point that should be made, however, is that SGEMP calculations often require a self-consistent treatment for the current densities used to drive Maxwell's equations. Here "self-consistent" means that the effects of the resulting electromagnetic fields on the subsequent motion of electrons which make up the source current density must be included. The driving current density is thus coupled to the resulting fields, making the problem highly non-linear. This self-consistent effect is especially important for SGEMP because many of the electrons are produced by incident X-rays and thus have low energies [31]. The motion of these low-energy photoelectrons is more easily influenced by the fields than higher-energy Compton electrons produced by incident gammas. Note that for other types of EMP, self-consistent effects are usually a minor correction but for SGEMP such effects may be dominant.

1.1.2.3 Calculational Techniques

1.1.2.3.1 Analytical Methods

Analytical methods are quite useful for gaining a general understanding of a phenomenon and for determining just what parameters are important. Approximate analytical techniques have thus been used previously to explain the basic physics of different types of EMP. Such methods as variable transformations and ignoring certain terms in differential equations have been used to make the problem tractable and to identify the phases of the problem when certain physical effects are dominant.

As with most areas of physics, however, purely analytical techniques are limited in terms of the complexity of the problems which are soluble. Problems for which analytical solutions can be found are often far from realistic.

In the case of EMP, the combined set of differential equations used to describe the Compton source current, the air chemistry, and the resulting electromagnetic fields is obviously quite complex and complete analytical solutions can be found for such simple cases as those with spherical symmetry.

1.1.2.3.2 Numerical Methods

An alternative to analytical solutions is the use of numerical methods.

Numerical techniques using large, fast computers enable one to calculate the response of models which are much more realistic than can be treated with purely analytical methods. Computer calculations can be thought of as "numerical experiments." These "experiments" can be complicated and involved, depending upon the degree of realism desired. Numerical calculations can have the disadvantage of generating massive amounts of output data. Checking and understanding such results can be a difficult and time-consuming task. Errors are thus easily made and results are often misinterpreted.

Work on EMP computer codes started at about the same time as the detailed analytical studies did [32,33]. The early work and almost all subsequent numerical studies have been based on finite-difference equivalents of the various differential equations presented earlier. EMP codes are thus typically based on some time-stepping procedure combined with a spatial grid. Sometimes one spatial dimension is suppressed by expansion techniques, e.g., using spherical harmonics to represent the angular dependence of a spherical geometry. Such time-domain, finite-difference calculations make good sense when one remembers that the source current densities and the conductivities used in Maxwell's equations are strong functions of space and time. In fact, the rapid variation of such functions near the gamma wave front makes it often advisable to finite-difference the retarded-time equations, rather than to work in real time. It has been discovered, however, that numerical solutions in retarded time can have stability problems [34] that require special numerical techniques.

Such EMP computer codes have been used to investigate the accuracy of various approximations made in analytical investigations. For example, the CHAP code has tested the accuracy of the high-frequency approximation (43) by including the ingoing wave in Maxwell's equations. Computer results show that the high-frequency approximation is indeed usually valid. Code calculations have also included detailed radiation sources, the full set of air chemistry equations, X-ray in addition to gamma ray effects, and self-consistent source current calculations. These effects

do, of course, change the details of the EMP signal produced. In general, however, such numerical studies have verified the overall accuracy of the general picture presented here.

Computer calculations also have certain limitations. Reasonable amounts of computer time and storage allocations mean that most EMP environment calculations assume a two-dimensional spatial geometry. Running such time-stepping codes to late times can also be a problem because of stability and accuracy limitations.

1.1.2.3.3 Comparison of Theory With Data

In the 1962 high-altitude test series there was at least one successful measurement of the high-altitude EMP waveform. The measurement was made by Wakefield of Los Alamos Scientific Laboratory. The result is shown in Fig. 9 along with a calculated EMP waveform and the same waveform after

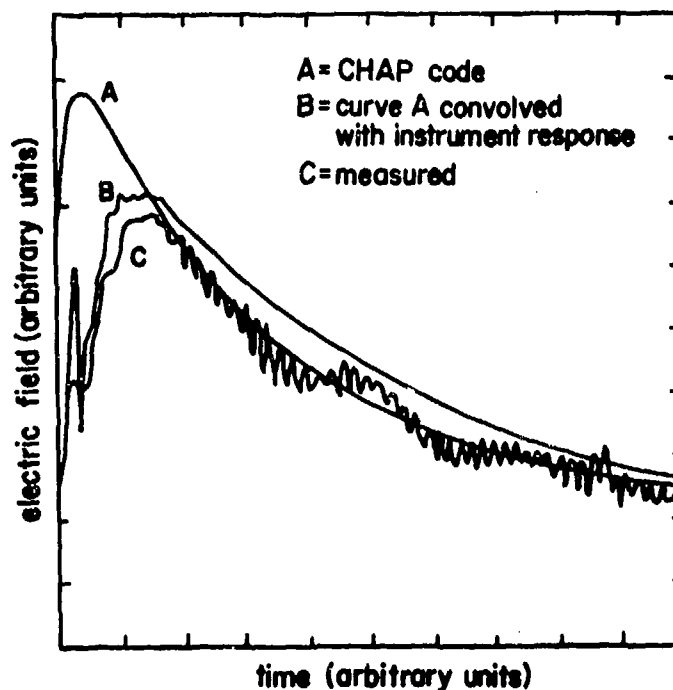


Fig. 9. Comparisons of experimental and theoretical EMP waveforms.

being convolved with the instrumentation response function. The agreement between the two waveforms is fairly good, considering that the instrumentation response function is somewhat uncertain. Existing ground-burst EMP data also appears to be consistent with analytical and numerical predictions. The agreement between theory and measured data tends to indicate that our understanding of the physics of EMP is reasonably well developed.

1.1.2.3.4 Unknowns

Although the overall physics of EMP is fairly well understood, there are still areas of uncertainty. Also, specific system vulnerability issues are continually resulting in the need for further environment calculations and increased accuracy.

Among the major unknowns at the present time are certain details of air chemistry reaction rates, the nature of late-time radiation sources, and the entire problem of late-time (i.e., times greater than 100 msec) EMP. Research into these areas is presently underway.

REFERENCES

- [1] A.S. Kompaneets, "Radio emission from an atomic explosion," JETP, December 1958.
- [2] Pomham and Taylor, "A theory of radioflash," AWRE 0-33/59.
- [3] B.R. Suydam, "Electromagnetic signal from a bomb burst in vacuo," TN 86, November 1961.
- [4] B.R. Suydam, "Computations of the parameter values inside of the E.M. source," TN 88, September 1961.
- [5] W.J. Karzas and R. Latter, "Electromagnetic radiation from a nuclear explosion in space," Physical Review, vol. 126, no. 6, June 15, 1962, and also TN 27, October 1961.
- [6] W.J. Karzas and R. Latter, "The electromagnetic signal due to the interaction of nuclear explosions with the earth's magnetic field," Journal of Geophysical Research, vol. 67, no. 12, November 1962, and also TN 28, December 1961.
- [7] W.J. Karzas and R. Latter, "Detection of electromagnetic radiation from nuclear explosions in space," Physical Review, vol. 137, no. 58, March 8, 1964, and also TN 40, October 1964.
- [8] IEEE Transactions on Antennas and Propagation, AP-26, January 1978, and also IEEE Transactions on Electromagnetic Compatibility, EMC-20, February 1978.
- [9] C.E. Baum, E.L. Breen, J.C. Giles, J. O'Neill, and G.D. Sower, "Sensors for electromagnetic pulse measurements both inside and away from nuclear source regions," AP-26, January 1978, pp. 22 - 35, and also EMC-20, February 1978, pp. 22 - 35.
- [10] C.E. Baum, "EMP simulators for various types of nuclear EMP environments: an interim categorization," AP-26, January 1978, pp. 35 - 53, and also EMC-20, February 1978, pp. 35 - 53 (adapted from SSN 151, July 1972).
- [11] R.E. Partridge, "EMP testing facility," SSN 1, February 1964.

- [12] C.E. Baum, "Impedance and field distribution for parallel plate transmission line simulators," SSN 21, June 1966.
- [13] C.E. Baum, "The conical transmission line as a wave launcher and terminator for a cylindrical transmission line," SSN 31, January 1967.
- [14] C.E. Baum, "The capacitor driven, open circuited, buried-transmission-line simulator," SSN 44, June 1967.
- [15] C.E. Baum, "The single-conductor, planar, uniform surface transmission line, driven from one end," SSN 46, July 1967.
- [16] C.E. Baum, "The complete guide to the notes, index 1 - 1," AFWL-TR-73-52, February 1973.
- [17] D.R. Quested, "Bibliography number twenty on the nuclear electromagnetic pulse as an environment for electronic equipment: catalogue of Baum notes," Technical Publication B-20, AWRE, UKAEA, Aldermaston, U.K., 1971.
- [18] S. Glasstone (ed.), The Effects of Nuclear Weapons, Department of Defense, U.S. Government Printing Office, April 1962.
- [19] R.D. Evans, The Atomic Nucleus, McGraw-Hill, New York, 1955.
- [20] C.L. Longmire, "On the electromagnetic pulse produced by nuclear explosions," AP-26, January 1978, pp. 3 - 13.
- [21] C.L. Longmire and H.J. Longley, "Improvements in the treatment of Compton current and air conductivity in EMP problems," Mission Research Corporation, DNA-3192T, October 1971, and also TN 128, October 1971.
- [22] N.J. Carron, "Characteristic steady-state electron emission properties for parametric blackbody X-ray spectra on several materials," Mission Research Corporation, MRC-N-221, DNA 3931T, February 1976, and also TN 280, February 1976.
- [23] C.E. Baum, "Electron thermalization and mobility in air," TN 12, July 1965.
- [24] Reaction Rate Handbook, Defense Nuclear Agency, DNA 1948H, March 1972.

- [25] J.E. Brau, G. Canavan, and L. Wittwer, "CHEMP: A code for calculation of high-altitude EMP," TN 198, March 1974.
- [26] D.F. Higgins, C.L. Longmire, and A. O'Dell, "A method for estimating X-ray produced electromagnetic pulse observed in the source region of a high-altitude burst," TN 181, February 1973.
- [27] C.L. Longmire and H.J. Longley, "Time domain treatment of media with frequency-dependent electrical parameters," Mission Research Corporation, DNA 3167F, March 1971.
- [28] C.L. Longmire and K.S. Smith, "A universal impedance for soils," Mission Research Corporation, DNA 3788T, October 1975, and also TN 247, October 1975.
- [29] K.C. Chen and J. Martinez, "EMP propagation in the ionosphere," TN 192, July 1974.
- [30] C.L. Longmire, "External system-generated EMP on some types of satellite structure," TN 124, August 1971.
- [31] N.J. Carron and C.L. Longmire, "On the structure of the steady state space-charge-limited boundary layer in one dimension," Mission Research Corporation, MRC-R-240, DNA 3928T, November 1975, and also TN 281, November 1975.
- [32] P.M. Livingston, "Spherical coordinate expansion of Maxwell's equations for computer solution," TN 22, April 1963.
- [33] W.R. Graham, "The electromagnetic fields produced by a general current distribution in a conductive environment under certain symmetry conditions," TN 21, January 1965.
- [34] H.J. Longley and C.L. Longmire, "Development and testing of LEMP 1," Los Alamos Scientific Laboratory, LA-4036, December 1969, and also TN 75, April 1970.

CHAPTER 1.2

TOPOLOGICAL DECOMPOSITION OF SYSTEMS

The EMP analysis of a large system is complicated by not only the physical and electrical complexity of the system but also the electrical properties of many system components that are not well understood throughout the EMP spectrum. To carry out the analysis it is often convenient conceptually to define a series of transfer functions (or, more precisely, operators) which relate the incident EMP signal to a response somewhere within the system.

One approach to determining these transfer functions for a large system is to subdivide, if possible, the system into a number of smaller, less complicated, and relatively independent pieces. The analyses of these smaller independent pieces are much easier to carry out, and the response of the entire system may then be constructed from the analyses of these pieces.

In order to facilitate the partitioning of a large system it is convenient to view the entire system as being constructed from a large number of conducting surfaces which attenuate or shield, to a certain degree, the incident electromagnetic wave as it propagates into the system. Thus, it is helpful to have a description of the electromagnetic shield topology, or a description of how the shielding surfaces of the system are configured, to perform such a decomposition of the system.

1.2.1 BASIC DECOMPOSITION CONCEPTS

The concept of shielding topology (or geometry) and its application to EMP analysis has been described in a number of reports [1-4]. One first defines a number of shield surfaces through which EMP energy penetrates at discrete or localized areas. The most obvious of such surfaces is, for example, the exterior skin of an all-metal aircraft with its windows, skin joints and antennas being points for energy penetration. Upon penetrating this outer skin additional surfaces

may be encountered, which serve to further enhance the shielding of the system. Smaller metallic enclosed areas in an aircraft, such as conduits and equipment housings, are examples of such additional surfaces. Similarly, inside these surfaces, another conducting surface may be evident in the form of shielding on cables.

For each of these surfaces one may define a number of fundamental problems for the determination of the energy penetration into and through the shielding regions. These problems include field penetration through apertures, direct energy propagation along insulated conductors piercing the shield and diffusion through the imperfectly conducting shield surfaces. Similarly, a number of mechanisms can be identified for energy propagation within a particular shielded region. For this internal propagation problem the transmission-line propagation is usually the most important mechanism.

As an example of the decomposition of a large problem into a set of smaller problems, consider a simplified interaction problem of a cable located inside a highly conducting shield with an aperture in it (Fig. 1).

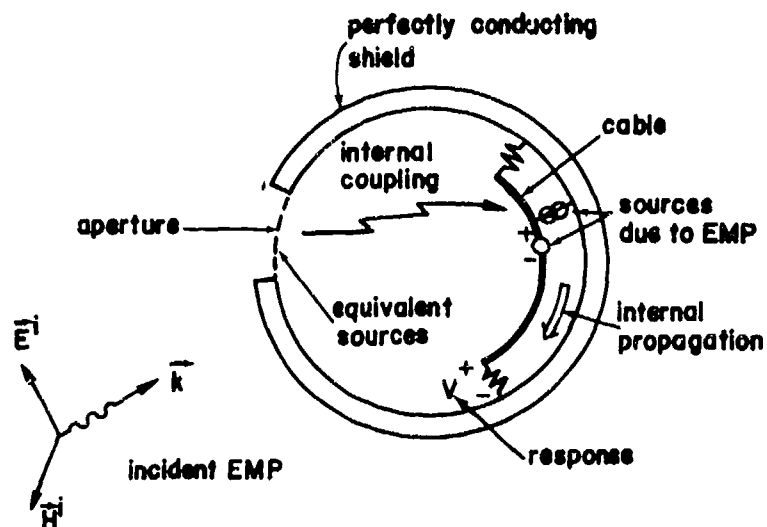


Fig. 1. Simplified internal interaction problem with one port of entry for EMP energy.

Note that the shield could represent the skin of an aircraft, the outer surface of a shielded room, or any other reasonably well-shielded region. The steps in carrying out the internal interaction analysis depicted in Fig. 1 are solving the following elementary problems:

- (1) Determine the equivalent sources within the aperture in terms of the surface current and charge densities on the exterior surface of the shield with the aperture completely covered up by perfect conductors. To do this often requires the assumptions that the aperture is electrically small and its dimensions are smaller than the local radii of curvature.
- (2) With the equivalent sources determined in (1) compute the fields within the cavity.
- (3) From the cavity fields determine the voltage and current sources exciting the cable.
- (4) With the cable sources found in (3) compute the distribution of cable currents and voltages.

At this point, it may be necessary to repeat steps (1) through (4) if the cable in the problem happens to be a shielded cable with additional conductors within the shield.

As may be noted from this example, under certain assumptions the overall problem may be broken up into simpler, independent and tractable pieces, and the electromagnetic geometry or topology of the system provides the rationale for how the problem should be subdivided. It should be remembered, however, that this approach of treating the interaction problem is only approximate.

Once each of the subproblems in the above example, i.e. ((a) relating the incident \vec{E}^i, \vec{H}^i fields to the outer surface charge and current, (b) relating the cable sources to a voltage or current (V,I) on the cable at a particular observation point) has been solved, an approximate solution to the overall problem may be expressed via a series of transfer functions or operators as

$$(V, I) = Z^{\text{cable}} \cdot Z^{\text{int}} \cdot Z^{\text{ext}} \cdot (\vec{E}^i, \vec{H}^i) \quad (1)$$

which may be written as

$$(V, I) = \left(\prod_i Z_i \right)_{\text{ap}} (\vec{E}^i, \vec{H}^i) \quad (2)$$

where the product \prod is over all the Z 's comprising the path taken by the EMP energy. Note that the Z 's depend on the location as well as the nature of the source. The subscript "ap" serves to remind one of the fact that the point of entry for EMP energy is the aperture. The notation (V, I) indicates that either V or I is the quantity being calculated.

In the preceding example there was only one path for the EMP fields to excite the cable. In an actual system, however, there may be many parallel paths simultaneously contributing to the response at a load. Consider the same cavity/cable problem previously examined, but now with a penetrating conductor (perhaps an antenna) which couples additional energy into the cavity, as illustrated in Fig. 2. This more complex

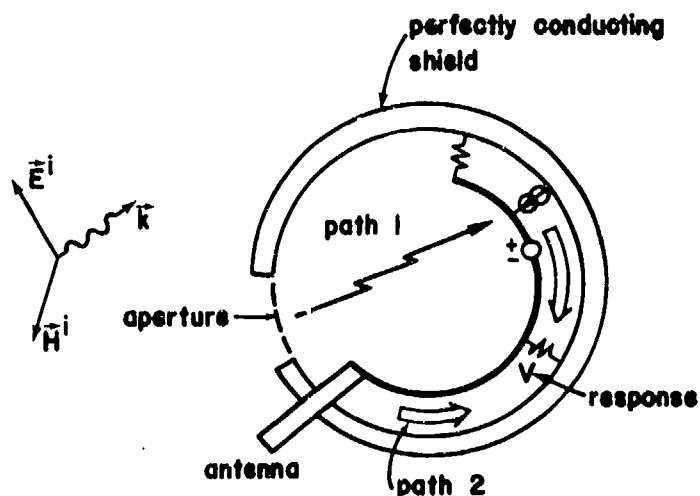


Fig. 2. Simplified internal interaction problem with two ports of entry for EMP energy.

problem can be solved by superimposing the result for the aperture penetration (path 1) with the result for the newly added coupling path (path 2). Similarly, the latter can be expressed as

$$(V, I)_{\text{path 2}} = \left(\prod_i Z_i \right)_{\text{ant}} \cdot (\vec{E}^1, \vec{H}^1) \quad (3)$$

The total approximate solution for the two linear, independent paths has the form

$$(V, I) = \left[\left(\prod_i Z_i \right) \cdot (\vec{E}^1, \vec{H}^1) \right]_{\text{ap}} + \left[\left(\prod_i Z_i \right) \cdot (\vec{E}^1, \vec{H}^1) \right]_{\text{ant}} \quad (4)$$

This concept may be generalized for any number j of linear, independent coupling paths to the following relation

$$(V, I)_{\text{total}} = \sum_{\text{path } j} \left(\prod_i Z_i \right)_j \cdot (\vec{E}^1, \vec{H}^1) \quad (5)$$

In the preceding examples, three basic phenomena have been illustrated. It will be useful to summarize these here, since these concepts will be employed throughout this document. The first phenomenon is coupling of EMP energy. By this is meant the determination of local driving source terms, either voltage and current sources, or equivalently, \vec{E} and \vec{H} which induce currents and charges on the surface of a shielded enclosure. The enclosure may be the skin of an aircraft with the exciting field being the incident EMP, or it may be a cable shield with the exciting field being a cavity field.

The second concept is that of propagation. This refers to the movement of the induced currents and charges and/or electric and magnetic fields throughout some volume or shielding layer. Propagation is then the solution to the equations in response to the coupling sources.

The third mechanism, penetration, relates to the excitation of the interior of a shielded region by the charges and currents residing on

the exterior surface of the region. These currents and charges may penetrate the surface through small apertures, penetrating conductors or by diffusion. This mechanism, then, refers to the conversion of the solution to the propagation problem into forms appropriate to be sources in the next shielding layer.

This entire process is referred to as EMP interaction within the particular region in question. If the problem involves the first shielding layer of a system, the term external interaction is often employed. Internal interaction is used to denote the EMP interaction process which occurs within the shielded regions inside the system. From this viewpoint the EMP interaction calculation for an entire system consists of a sequence of calculations of coupling, propagation and penetration within each shielding layer of the system. The results of an interaction calculation at one layer of the system thus serve as a starting point for another internal interaction calculation performed in a smaller, better shielded region. It must be emphasized again that the validity of this viewpoint lies in the assumption that each shielding layer is a very good shield.

1.2.2 DECOMPOSITION OF LAYERS

As discussed in the previous section, a large system may be divided into a number of smaller, relatively independent pieces for an approximate EMP analysis. The method of determining precisely how the system should be divided is based upon a study of the topology of the system. This, then, is essentially an investigation of the configuration and properties of the geometric volumes which comprise the system and which remain unchanged under deformation of the system, so long as no surface passes through another.

To permit a precise description of the structure of a large system, it is necessary to define a convention for labeling the various volumes and surfaces comprising the system. The following notation will be used throughout this section:

V_γ = volumes of the system

S_ξ = surfaces representing boundaries between various volumes

The subscripts γ and ξ can represent one or more integers which serve to distinguish the various volumes and surfaces of the system. Generally, the subscript γ is of the form (j,k) and ξ is of the form $(j,k;l,m)$. However, for simple systems γ and ξ may comprise fewer numbers.

As an example, consider the schematic diagram of a simple system shown in Fig. 3. For this particular case, the volume exterior to the

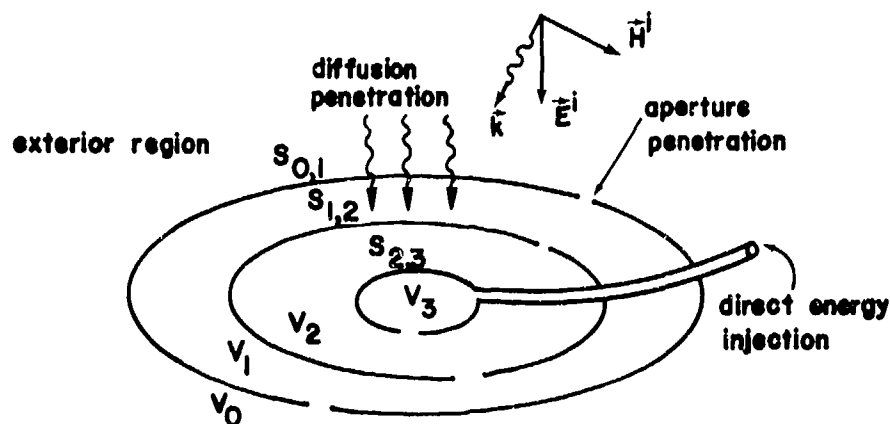


Fig. 3. Simplified shield topology.

system will be denoted by V_0 , with the value of the subscript increasing by unity upon moving into the system. Each surface $S_{j,k}$ separates the volumes V_j and V_k . This diagram, representing the conducting surfaces of the system, is referred to as the topological model of the system.

Thus, with this notation the surface $S_{0,1}$ represents the exterior surface of the system. Upon penetrating this surface, EMP energy propagates within volume V_1 , penetrates surface $S_{1,2}$, propagates within volume V_2 , etc., until it reaches the component level within

the system. The total number of shielding surfaces penetrated in this fashion is said to be the shielding level of the system.

In a conventional metal-skin aircraft, $S_{0,1}$ refers to the aircraft skin, and the $S_{1,2}$ shielding layer is often simply the braided shields of coaxial cables or the metallic shields surrounding electronic components. The B-1 aircraft is an example of a system with a possible shielding level of 3, the three surfaces being the aircraft skin, the conduit enclosure designed for additional EMP protection, and the outer conductor of shielded cables (if any) within the conduit.

It is to be noted that the above definition may not be sufficient to describe a complex system. An actual aircraft will have additional compartments located inside the $S_{0,1}$ surface, but which are part of V_1 . These compartments, such as the bomb bay, wheel wells and equipment bays, can act much like a shielded enclosure and may be referred to as elementary volumes or subvolumes. The formalism applied to the analysis of the shielding properties of the $S_{1,j}$ surfaces can also be used for treating these enclosures.

Because all of these elementary volumes occupy part of the same principal volume V_j , it is necessary to employ another subscript k to distinguish the various regions. Thus, the k th subvolume within the j th region will be denoted $V_{j,k}$ with the subscript k being dropped if no subvolumes exist. Fig. 4 shows a hypothetical example of a more complete version of a shielded system. Within the V_1 region, it is noted that there are four subvolumes denoted by $k=1,2,3$ and 4. These volumes can be identified as $V_{1,1}$, $V_{1,2}$, etc. Since a particular volume within a system can be labeled by two indices, j and k , it is convenient to refer to these indices as the longitudinal and transverse shielding numbers, respectively.

In this case, it is necessary to expand slightly the index on the term S_ξ to permit a precise definition of the various surfaces. The surface dividing volumes $V_{j,k}$ and $V_{l,m}$ may be described as $S_{j,k;l,m}$. Some of these surfaces are indicated in Fig. 4.

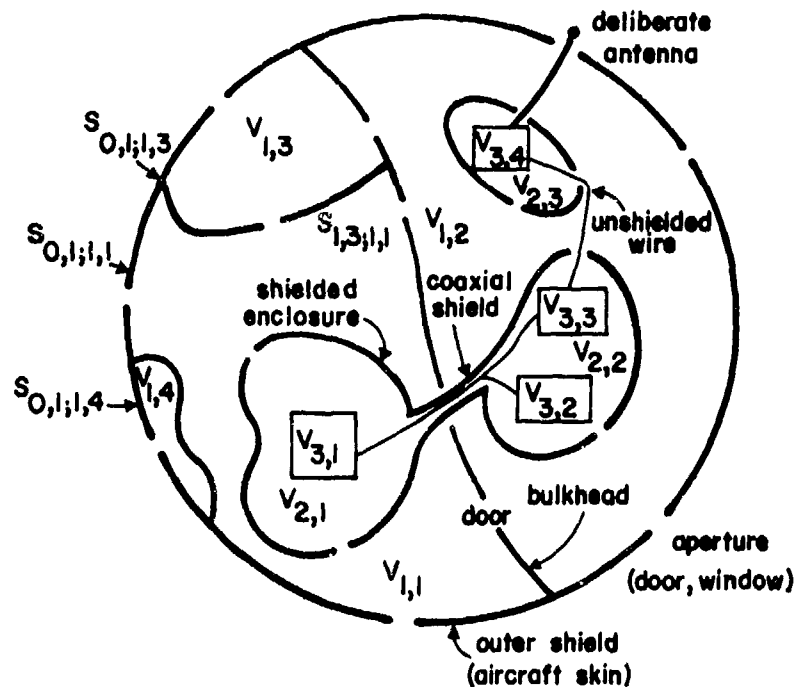


Fig. 4. A more general topological model.

Referring back to Fig. 3 the term external interaction can now be regarded as the determination of the currents and charges induced on the surface $S_{0,1}$ of a system due to external sources in V_0 . The response may be either in the time or frequency domain and is calculated by solving an appropriate boundary-value problem. The results of the external-interaction calculation on $S_{0,1}$ are then used to determine equivalent electromagnetic sources on this surface. These sources will radiate into V_1 and induce currents and charges over $S_{1,2}$. Internal interaction within a typical volume V_j , therefore, may be formally defined as the excitation and propagation of charge and current on an internal longitudinal layer or surface $S_{j,j+1}$ due to sources on surface $S_{j-1,j}$ or within the volume V_j .

It is also desirable to introduce the concept of the order of the internal interaction, which may simply be denoted by the j -index of the

volume in which the internal interaction is being considered, or by the j -index of the surface $S_{i,j}$ for considerations of surface penetration. Thus, exterior penetrations (from V_0 to V_1 through $S_{0,1}$) are described as penetrations of first order, and internal interaction within V_1 is also said to be of first order. The maximum shielding order possible on a system is defined to be the level of shielding.

Another concept for analyzing large system problems is the interaction sequence diagram. This is a diagram of all possible interaction paths from one volume to another in the system topological model. A portion of the interaction sequence diagram for the geometry of Fig. 4 is illustrated in Fig. 5. The dotted lines represent the configuration

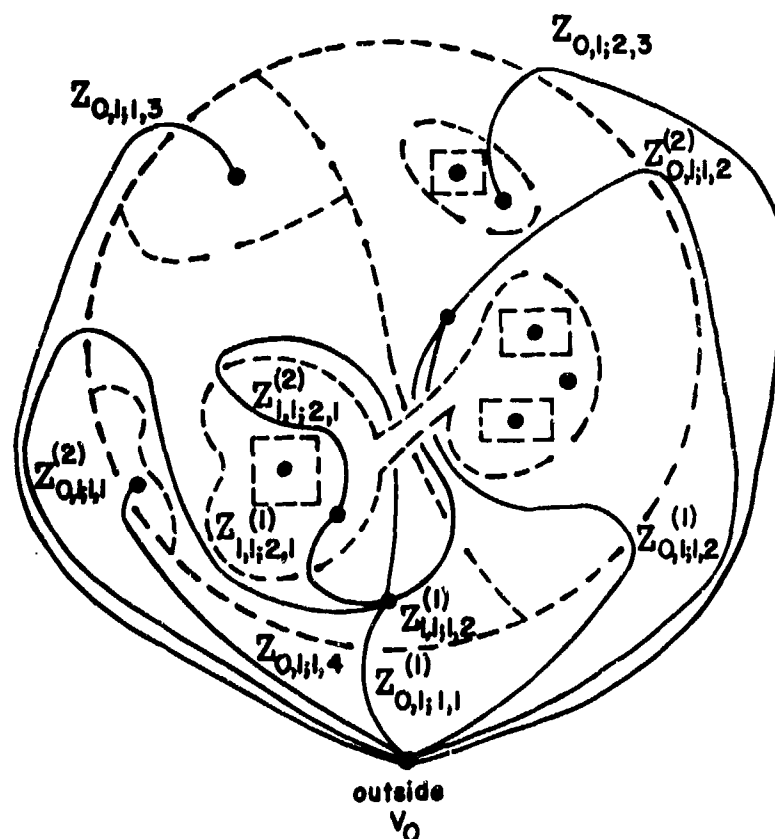


Fig. 5. Interaction sequence diagram.

of the system and the solid lines are the interaction paths from the outside volume V_0 to various volumes inside. The transfer operator for a particular path connecting the $V_{j,k}$ to the $V_{l,m}$ is denoted by $Z_{j,k;l,m}$. For more than one point of entry, a superscript (1), (2), etc., will distinguish the different transfer operators if more than one path exists from one volume to another.

It is useful to examine a few possible types of interaction sequence diagrams for hypothetical systems. Fig. 6 shows this diagram for a system of shielding order of 0. Fig. 7 is for a system of shielding order of 1 with the cable shields as the shielding layer, and Fig. 8 is for a system with the same shielding order but with the external skin being the shielding layer. Fig. 9 represents a case with a shielding order of 2 with the shielding layers being external skin and cable shielding.

In many practical cases, the largest contribution to a response within the system is due to transmission lines which provide a direct propagation path from one point to another. If only the direct connections are kept in the interaction sequence diagram, the result is a transmission-line network consisting of a number of junctions J_n , connected by various transmission lines, either single wire or multiconductor, forming a bundle or "tube," $T_{n,m}$, which connect junctions J_n and J_m . Fig. 10 illustrates a hypothetical transmission-line network which is similar to that encountered in EMP analysis problems.

The configuration of the transmission-line network thus formed from the interaction sequence diagram is similar to that of a low-frequency, lumped-element circuit. Fig. 11 illustrates the corresponding linear graph for a circuit, where there are a number of interconnected branches $B_{n,m}$ connecting nodes N_n and N_m . The only difference between this graph and that for the network of transmission lines in Fig. 10 is that the voltage and current relationships at the nodes and branches are described in a different manner. The graph configuration remains the same.

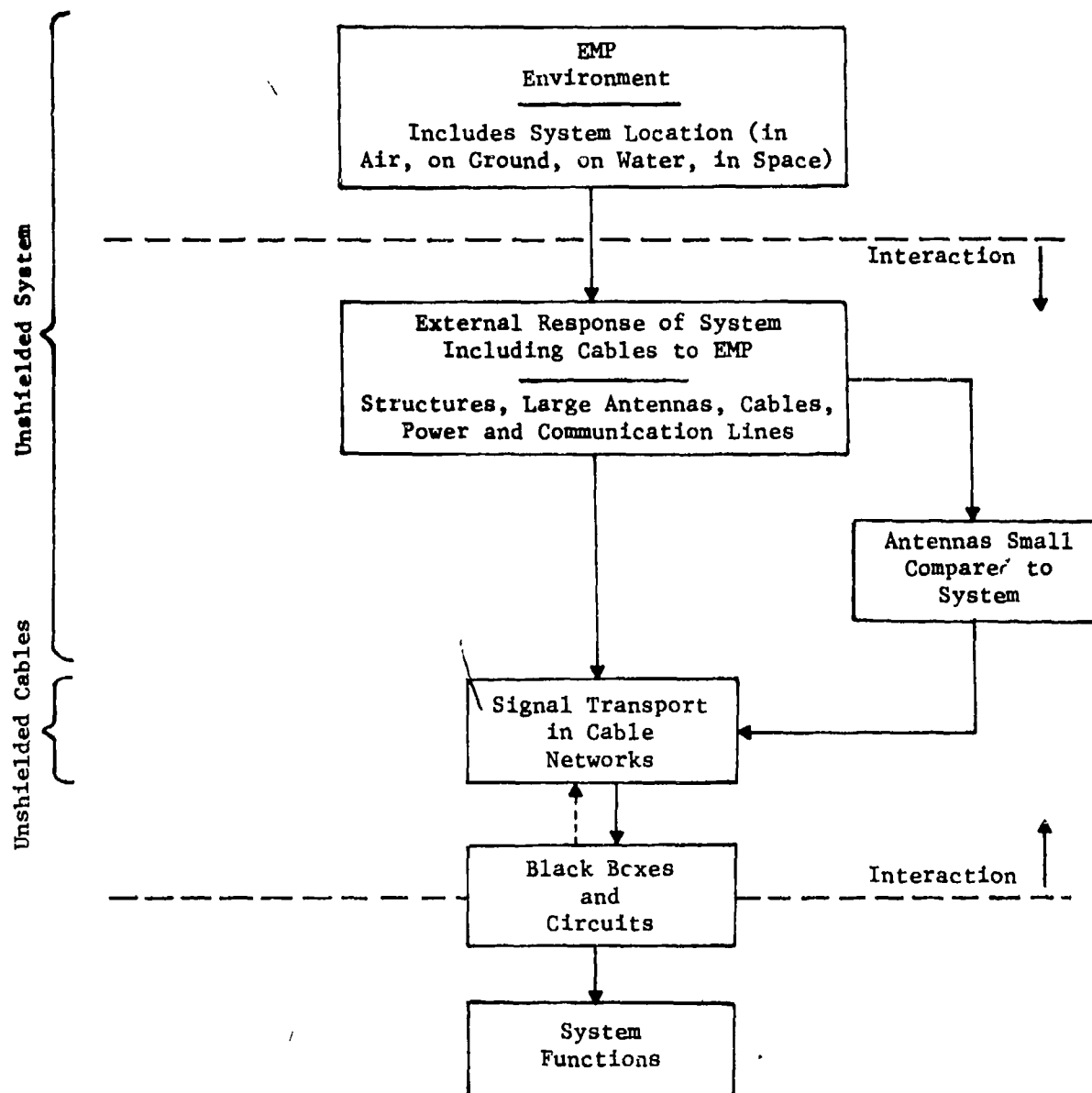


Fig. 6. EMP interaction sequence for unshielded system with unshielded cables: shielding order = 0.

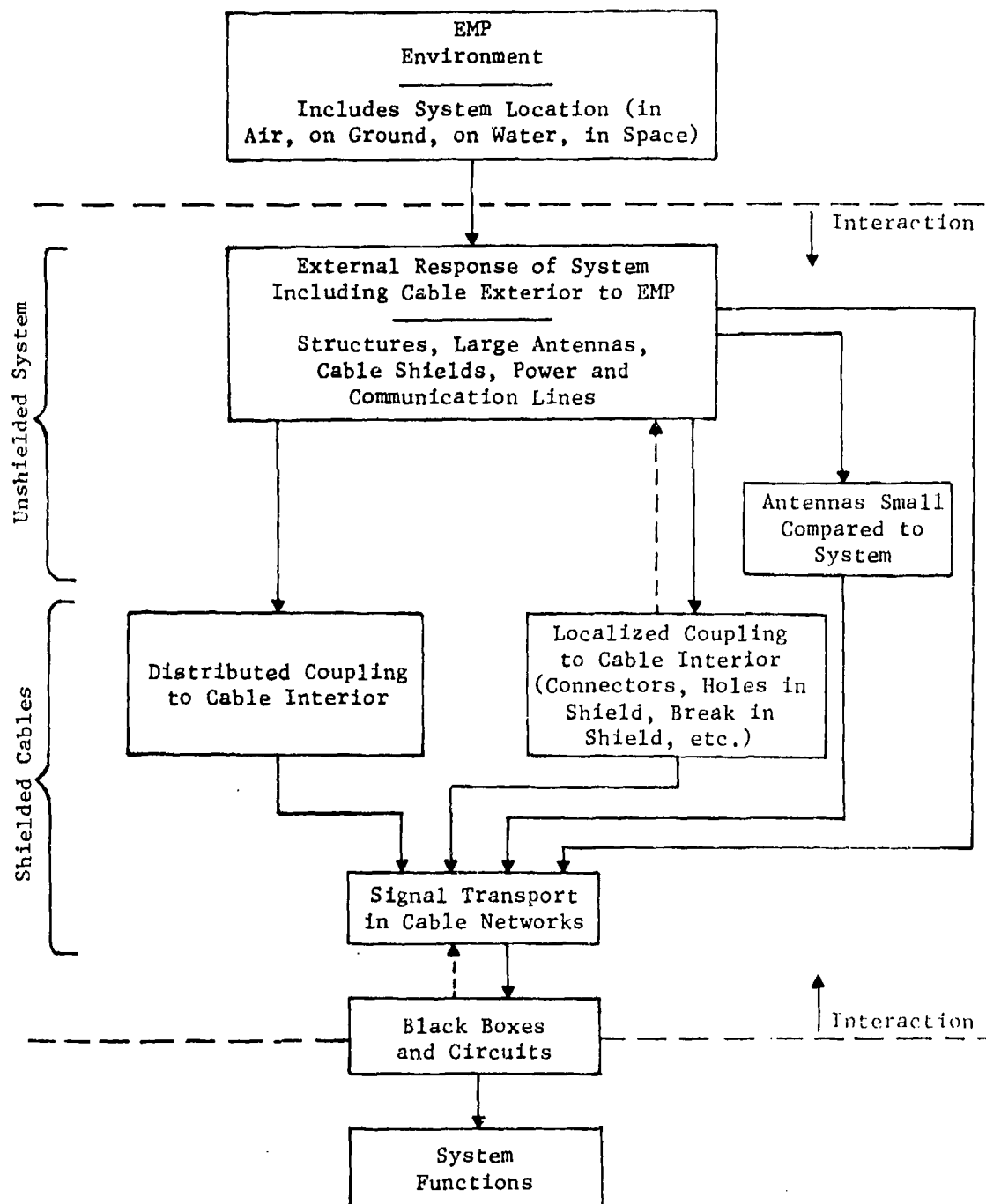


Fig. 7. EMP interaction sequence for unshielded system with shielded cables: shielding order = 1.

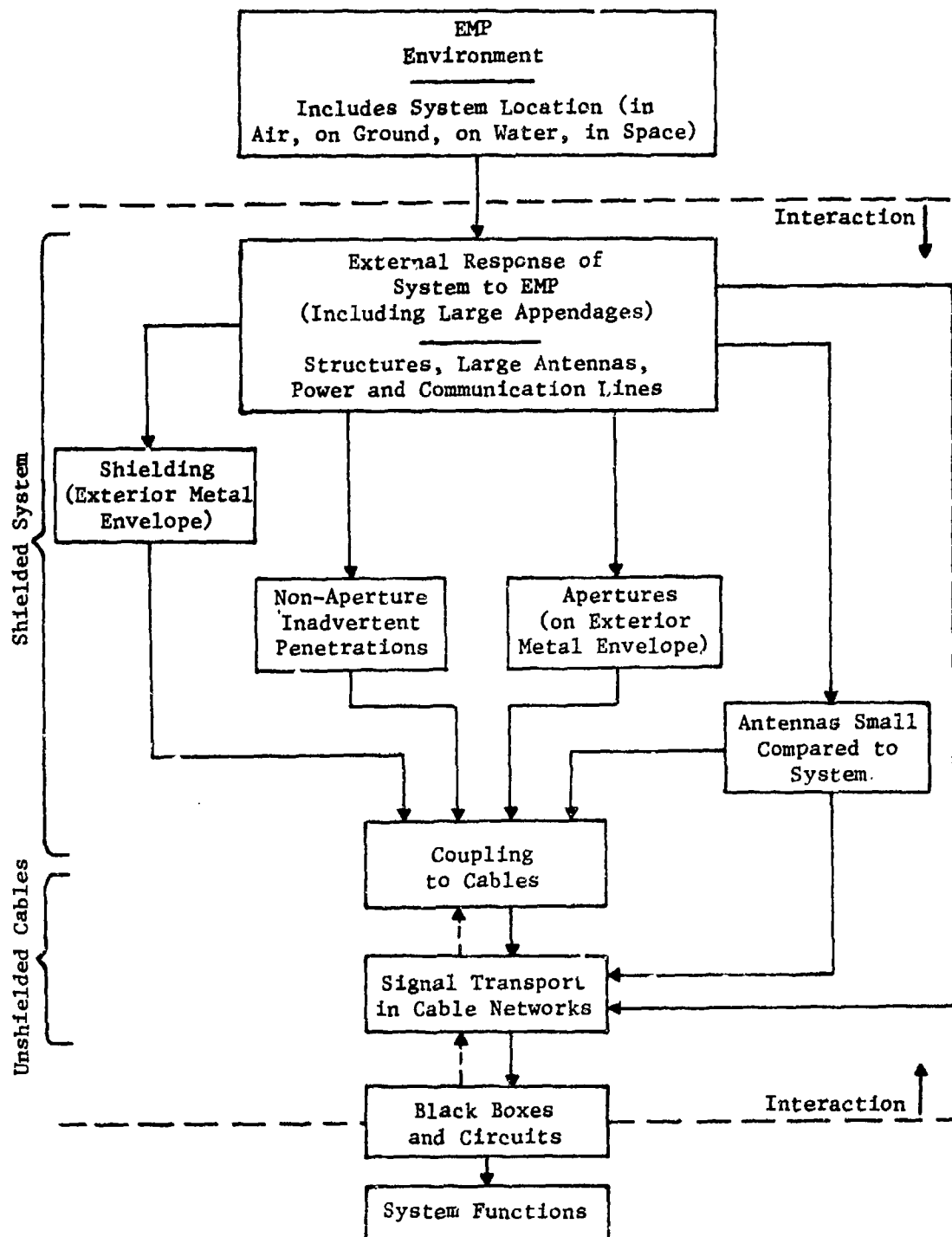


Fig. 8. EMP interaction sequence for shielded system with unshielded cables:
shielding order = 1

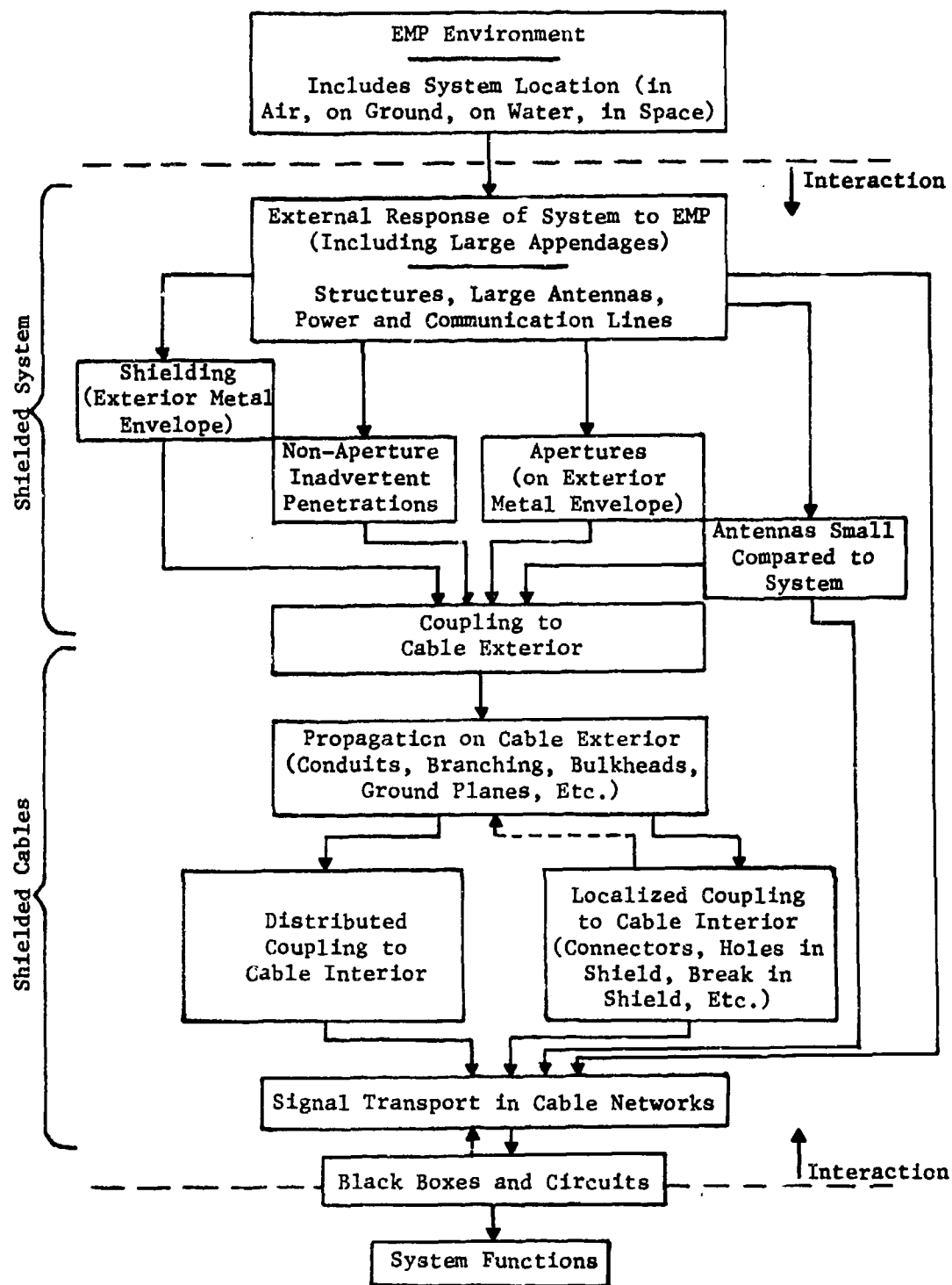


Fig. 9. EMP interaction sequence for shielded system with shielded cables: shielding order = 2.

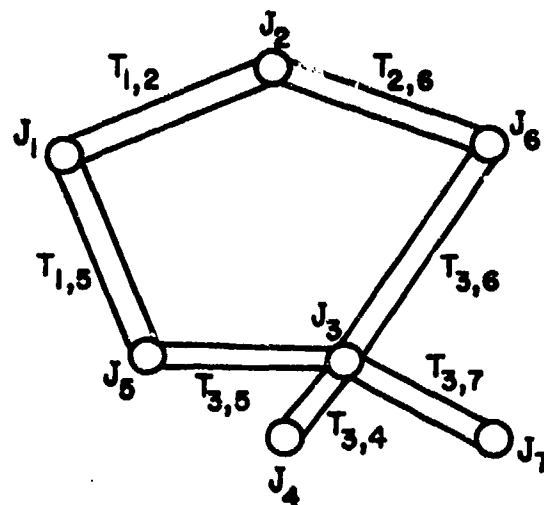


Fig. 10. Topology of interconnected transmission-line network.

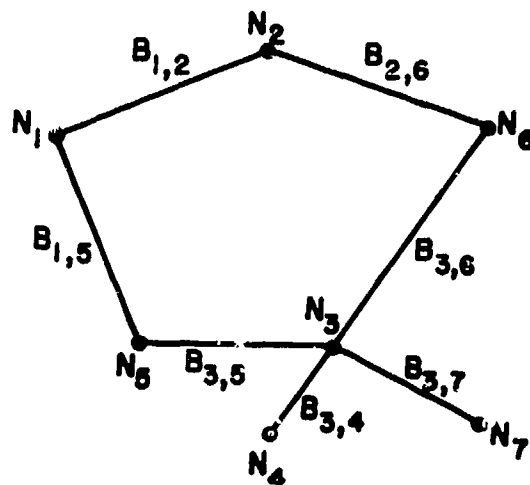


Fig. 11. Topology of lumped element circuit.









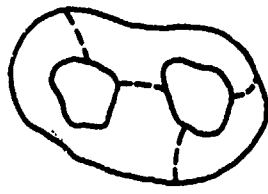


The relation between the fundamental elements of various network graphs discussed above and the interconnecting topological quantities of the system is illustrated in table 1. Note that the first two cases summarized in the table pertain to the propagation mechanisms of signals throughout the system, whereas the latter two describe the physical structure of the system.

1.2.3 HARDENING CONCEPTS

When a large system is viewed as being composed of a number of shielding layers, as described in the previous section, the conceptual approach to hardening such a system becomes apparent. By eliminating all electromagnetic energy penetration through one particular shielding surface, none of the shielded regions within this perfect shield will be affected by the incident EMP. Expressed in terms of (5) this requirement implies that one element Z_j for each of the j interaction paths should be zero.

An actual system, however, does not have a perfect electromagnetic shield and, thus, one must settle for trying to control the signals induced within the system. For a large system which has been decomposed into appropriate pieces one possible hardening approach is to examine the various terms of (5) to determine which interaction paths are most important in providing the excitation to the interior of the system. This will aid the analyst in determining his priorities in hardening the system. A detailed discussion of hardness design and implementation on actual systems will be given in Part 3 of this document.

TABLE 1. CORRESPONDENCE AMONG VARIOUS TOPOLOGICAL QUANTITIES

Topology	Basic Topological Quantity and Symbol	Interacting Topological Quantity and Symbol	Diagrammatic Form of Topology
Circuit	Node N_j ●	Branch $B_{j,k}$ —	
Transmission Line Network	Junction J_j ○	Tube $T_{j,k}$ 	
System	Volume V_j 	Surface $S_{j,k}$ 	
Hierarchical System	Principal Volume V_j 	Principal Surface (Closed but Sometimes in More than One Part) $S_{j,k}$ 	
	Elementary Volume $V_{j,k}$ 	Elementary Surface (Usually Open but Sometimes Closed) $S_{j,k;l,m}$ 	

REFERENCES

- [1] C.E. Baum, "How to think about EMP interaction," Proceedings of the 1974 Spring FULMEN Meeting, AFWL, April 16 and 17, 1974.
- [2] C.E. Baum, "The role of scattering theory in electromagnetic interference problems," presented at the National Conference on Electromagnetic Scattering, University of Illinois, Chicago, 15-18 June 1976. To be published in Electromagnetic Scattering, Academic Press, 1978.
- [3] F.M. Tesche, M.A. Morgan, D. Fishbine, and E.R. Parkinson, "Internal interaction analysis: topological concepts and needed model improvements," IN 248, July 1975.
- [4] F.M. Tesche, "Topological concepts for internal EMP interaction," AP-26, January 1978, pp. 60-63.

CHAPTER 1.3

FORMULATION OF INTERACTION PROBLEMS

The analysis of the interaction between a nuclear EMP and an aeronautical system often results in solving boundary-value problems for the Maxwell equations. These boundary-value problems can be formulated by the powerful integral-equation approach which is in no way restricted to those problem geometries that can be fitted into simple coordinate systems. Sec. 1.3.1 will discuss various types of integral equations that have been employed in the analysis of EMP interaction problems.

In the case where the interaction exhibits a unique direction for energy transport, the Maxwell equations will degenerate into a simpler set of coupled partial differential equations involving only one spatial variable, the so-called telegraphist's equations for transmission lines. Sec. 1.3.2 is devoted to the discussion of the transmission-line approach to EMP interaction problems.

Very often one is concerned with the interaction problem in which the dimensions of the interaction geometry are much smaller than the wavelengths of interest. In this case the spatial variations of the interaction problem are unimportant and the Maxwell equations, after all spatial coordinates are integrated out, reduce to the Kirchhoff circuit laws. Sec. 1.3.3 will show how the circuit approach can be applied to the formulation of EMP interaction problems.

1.3.1 INTEGRAL-EQUATION APPROACH

The integral-equation approach has several advantages which make it an attractive approach to solving EMP interaction boundary-value problems. The most noticeable advantage of the approach is its geometrical generality. This catholicity is precisely what is most needed to handle the complex system configurations of EMP interaction problems. The second advantage of the integral-equation approach is its compactness. An integral equation is a concise statement comprising both the equations of motion of the

electromagnetic fields and the initial or boundary conditions. This compactness has more than mere economical appeal since, when it comes to making approximations on the integral equation, the approximations will be simultaneously compatible with all aspects of the problem. The third advantage of the integral-equation method is its computability. The integral equations for electromagnetic boundary-value problems are linear. They are mathematically equivalent to systems of linear algebraic equations. Their properties are well known from linear algebra, and they can be solved numerically by standard computational methods.

The objective of this section is to present in detail the derivations of certain general integral equations that have found extensive application in EMP interaction analysis.

1.3.1.1 Magnetic-Field Integral Equation

The scattering of electromagnetic waves by good conductors is a common problem in the analysis of practical situations. A general mathematical method to treat this type of calculation is therefore of great practical value. It will be shown below that this scattering problem can be formulated in terms of a surface integral equation of the second kind which is particularly suitable for numerical solution.

Consider the situation depicted in Fig. 1. A perfect conductor of finite extent in free space is illuminated by an incident electromagnetic wave which is generated by known sources located either at finite distances from the conductor or at infinity. The incident wave is considered to be time-harmonic with angular frequency ω . Its time variation is given by the time factor $e^{j\omega t}$.

The quantities of interest in this situation are the induced surface current and charge densities, \vec{J} and ρ , which give rise to a scattered wave. If the surface of the conductor fits into an orthogonal coordinate system in which the Helmholtz equation is separable, the scattered wave can be determined by the well-known method of separation of variables. One need only expand the scattered wave into a complete set of appropriate eigen-

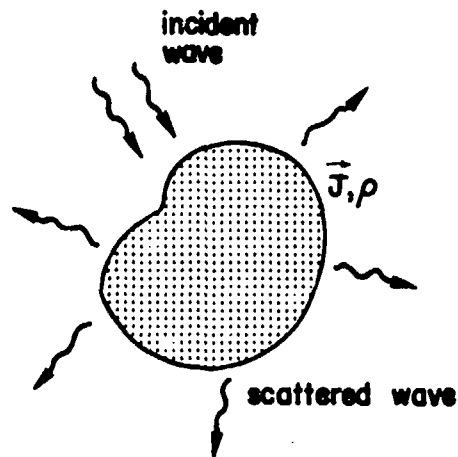


Fig. 1. Scattering of an incident electromagnetic wave by a perfectly conducting body.

functions of the Helmholtz equation and then determine the expansion coefficients by matching boundary and asymptotic conditions. But, simple as this method is, its applicability is severely limited by the stringent demand of equation separability, and only a handful of coordinate systems can meet this requirement.

By contrast, the integral-equation approach is of great geometrical universality and, in principle, not restricted to a particular coordinate system. The integral equation to be derived presently is an equation for the induced surface current density. A knowledge of the surface current density is sufficient to determine the scattered wave. The equation is called a magnetic-field integral equation because its derivation rests on an integral representation of the magnetic field.

The time-harmonic fields \vec{E} and \vec{H} satisfy the following Maxwell equations in free space

$$\begin{aligned} \nabla \cdot \vec{E} &= 0, & \nabla \times \vec{E} &= -j\omega\mu\vec{H} \\ \nabla \cdot \vec{H} &= 0, & \nabla \times \vec{H} &= j\omega\epsilon\vec{E} \end{aligned} \quad (1)$$

In solving specific problems, it is often expedient to introduce a scalar potential ϕ and a vector potential \vec{A} such that

$$\vec{E} = -\nabla\phi - j\omega\vec{A}, \quad \vec{H} = \frac{1}{\mu} \nabla \times \vec{A} \quad (2)$$

If one imposes on the potentials the Lorentz condition

$$\nabla \cdot \vec{A} + j\omega\mu\epsilon\phi = 0 \quad (3)$$

then one finds from (1) that the potentials individually satisfy the Helmholtz equation

$$(\nabla^2 + k^2)\phi = 0, \quad (\nabla^2 + k^2)\vec{A} = 0 \quad (4)$$

with

$$k^2 = \omega^2\mu\epsilon \quad (5)$$

The source of ϕ turns out to be the electric charge distribution ρ , and that of \vec{A} the electric current distribution \vec{J} .

In the interaction problem shown in Fig. 1, one can express the vector potential \vec{A}^s of the scattered wave as a surface integral over its source, namely, the electric current density \vec{J} on the surface of the conductor

$$\vec{A}^s(\vec{r}) = \mu \int_S \vec{J}(\vec{r}') G(\vec{r}, \vec{r}') dS' \quad (6)$$

where G is a free-space Green's function of the Helmholtz equation (4), satisfying the outgoing-wave condition at infinity

$$G(\vec{r}, \vec{r}') = \frac{1}{4\pi|\vec{r} - \vec{r}'|} e^{-jk|\vec{r} - \vec{r}'|} \quad (7)$$

In (6), \vec{r} refers to a field point exterior to the conductor; \vec{r}' refers to a source point on the conductor's surface denoted by S ; and the surface integral extends over all the source points \vec{r}' on S . Therefore the total

magnetic field \vec{H} in free space, being the sum of the incident and the scattered magnetic fields, has the following integral representation

$$\vec{H}(\vec{r}) = \vec{H}^1(\vec{r}) + \int_S \nabla \times [\vec{J}(\vec{r}') G(\vec{r}, \vec{r}')] dS' \quad (8)$$

where the operator ∇ acts on the field-point position vector \vec{r} .

An integral equation for the surface current density \vec{J} can be derived by letting the field point \vec{r} approach the conductor's surface S . One has in this limit the well-known relation between the tangential component of the total magnetic field and the surface current density on a perfect conductor

$$\vec{J}(\vec{r}) = \vec{I}_n(\vec{r}) \times \vec{H}(\vec{r}) \quad \text{on } S \quad (9)$$

where $\vec{I}_n(\vec{r})$ denotes the unit normal vector on S at \vec{r} pointing into free space. Combining (8) and (9), one obtains an integral equation for \vec{J}

$$\vec{J}(\vec{r}) = \vec{I}_n(\vec{r}) \times \vec{H}^1(\vec{r}) + \lim_{\vec{r}'' \rightarrow \vec{r}} \int_S \vec{I}_n(\vec{r}) \times \nabla'' \times [\vec{J}(\vec{r}') G(\vec{r}'', \vec{r}')] dS' \quad (10)$$

where \vec{r} and \vec{r}' both lie on S and the operator ∇'' acts on the dummy variable \vec{r}'' .

Eq.(10) cannot be regarded as the final form of the integral equation, inasmuch as the limiting process indicated therein has yet to be performed. The limit cannot be evaluated by a simple substitution of \vec{r} for \vec{r}'' because the expression so obtained has an infinity in the integrand for \vec{r}' equal to \vec{r} , and is by itself utterly meaningless. However, by carefully analyzing the behavior of the integral as \vec{r}'' approaches \vec{r} , one can show that a well-defined limit does exist.

Fig. 2 shows a portion of the conductor's surface S containing the point \vec{r} . The field point \vec{r}'' , exterior to the conductor, can be taken to approach \vec{r} along the unit outward normal vector $\vec{I}_n(\vec{r})$ at \vec{r} . When \vec{r}'' is

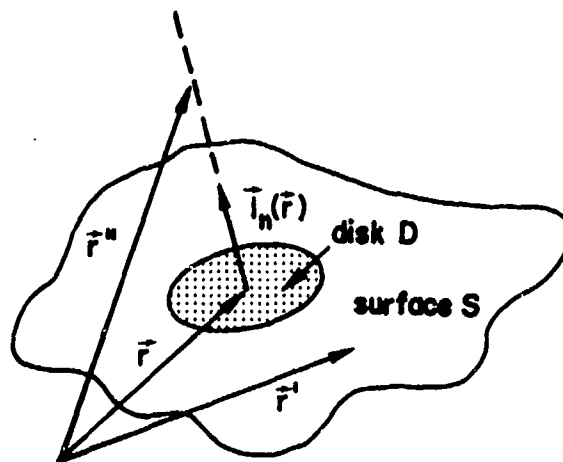


Fig. 2. Portion of the conductor's surface S around the point \vec{r} . The field point \vec{r}'' is to approach \vec{r} on S along the unit normal vector $\vec{I}_n(\vec{r})$ to S at \vec{r} . D is a small circular disk on S centered at \vec{r} . The source point \vec{r}' lies on S.

very close to \vec{r} , the integrand in (10), considered as a function of \vec{r}' , can be seen to develop a sharp peak at $\vec{r}' = \vec{r}$. For the purpose of evaluating the surface integral over S, it is expedient to break the integral up into two parts. One part extends over a small circular disk D centered at \vec{r} , as shown in Fig. 2. The other part extends over the remaining surface denoted by S - D. That is,

$$\int_S \vec{I}_n(\vec{r}) \times \nabla'' \times [\vec{J}(\vec{r}') G(\vec{r}'', \vec{r}')] dS' = \int_D + \int_{S-D} \quad (11)$$

The integral over D will capture most of the contribution from the peak in the integrand. Consider first the integral over the disk D

$$\int_D = \int_D \vec{I}_n(\vec{r}) \times \nabla'' \times [\vec{J}(\vec{r}') G(\vec{r}'', \vec{r}')] dS' \quad (12)$$

When D is sufficiently small, the current density $\vec{J}(\vec{r}')$ can be regarded as uniform throughout D and replaceable by its value $\vec{J}(\vec{r})$ at \vec{r} . Then, since

$\vec{I}_n(\vec{r}) \cdot \vec{J}(\vec{r}) = 0$, one obtains from (12) the expression

$$\int_D = - \vec{J}(\vec{r}) \int_D \vec{I}_n(\vec{r}) \cdot \nabla G(\vec{r}'', \vec{r}') dS' \quad (13)$$

Because both D and $|\vec{r}'' - \vec{r}|$ are small, one has, to leading order in $|\vec{r}'' - \vec{r}|$,

$$\nabla G(\vec{r}'', \vec{r}') = \frac{1}{4\pi} \nabla \left(\frac{1}{|\vec{r}'' - \vec{r}'|} \right) = \frac{-1}{4\pi} \frac{\vec{r}'' - \vec{r}'}{|\vec{r}'' - \vec{r}'|^3} \quad (14)$$

Substituting (14) into (13) one obtains

$$\int_D = \frac{1}{4\pi} \vec{J}(\vec{r}) \Omega_D(\vec{r}'') \quad (15)$$

where $\Omega_D(\vec{r}'')$ is simply the solid angle subtended by the disk D at the point \vec{r}'' .

With (15) established, one can proceed to take the limit $\vec{r}'' \rightarrow \vec{r}$. Furthermore, since the size of the disk D is arbitrary, one can append to this operation a second limiting process consisting of letting the radius of D shrink to 0, that is,

$$\lim_{\vec{r}'' \rightarrow \vec{r}} \int_S = \lim_{D \rightarrow 0} \lim_{\vec{r}'' \rightarrow \vec{r}} \left(\int_D + \int_{S-D} \right) \quad (16)$$

Under this double limit, one sees that

$$\lim_{D \rightarrow 0} \lim_{\vec{r}'' \rightarrow \vec{r}} \int_D = \frac{1}{2} \vec{J}(\vec{r}) \quad (17)$$

since the solid angle $\Omega_D(\vec{r}'')$ tends to 2π , and that

$$\begin{aligned} \lim_{D \rightarrow 0} \lim_{\vec{r}'' \rightarrow \vec{r}} \int_{S-D} &= \lim_{D \rightarrow 0} \int_{S-D} \vec{I}_n(\vec{r}) \times \nabla \times [\vec{J}(\vec{r}') G(\vec{r}, \vec{r}')] dS' \\ &= P \int_S \vec{I}_n(\vec{r}) \times \nabla \times [\vec{J}(\vec{r}') G(\vec{r}, \vec{r}')] dS' \end{aligned} \quad (18)$$

by definition of the Cauchy principal value of a two-dimensional integral denoted symbolically by the prefix P.

To examine the exact nature of the integrand of (18) at $\vec{r}' = \vec{r}$ one recalls that, when the field point \vec{r}'' approaches the point \vec{r} on the surface S, as illustrated in Fig. 2, the integrand of the surface integral over S in (10) develops a sharp peak at $\vec{r}' = \vec{r}$. Furthermore, it has been shown in (17) that, in the limit $\vec{r}'' \rightarrow \vec{r}$, this peak actually yields a finite contribution to the integral even when the integral is evaluated only over a disk of vanishingly small area centered at the point \vec{r} . This result clearly indicates that, in the limit $\vec{r}'' \rightarrow \vec{r}$, the peak evolves into a two-dimensional δ -function situated at \vec{r} . In fact, the findings from (11) to (18) can be summed up by the following formula with the symbol P treated as an operator

$$\lim_{\vec{r}'' \rightarrow \vec{r}} \vec{I}_n(\vec{r}) \times \nabla \times [\vec{J}(\vec{r}') G(\vec{r}'', \vec{r}')] = \frac{1}{2} \vec{J}(\vec{r}) \delta^{(2)}(\vec{r} - \vec{r}') + P\{\vec{I}_n(\vec{r}) \times \nabla \times [\vec{J}(\vec{r}') G(\vec{r}, \vec{r}')]\} \quad (19)$$

where \vec{r}'' is to approach \vec{r} from the outside of the closed surface S, and $\delta^{(2)}$ denotes the two-dimensional δ -function. This formula shows that, in the limit $\vec{r}'' \rightarrow \vec{r}$, the integrand in (10) is the superposition of a δ -function at $\vec{r}' = \vec{r}$ and a background designated by the symbol P. It can be shown that the latter function without the symbol P vanishes as \vec{r}' approaches \vec{r} , and hence the principal-value integral symbol P is not needed in (18) and the final form of the magnetic-field integral equation is

$$\frac{1}{2} \vec{J}(\vec{r}) - \int_S \vec{I}_n(\vec{r}) \times [\vec{J}(\vec{r}') \times \nabla' G(\vec{r}, \vec{r}')] dS' = \vec{I}_n(\vec{r}) \times \vec{H}^1(\vec{r}) \quad (20)$$

Of graver concern to the numerical analyst is the question of uniqueness. The magnetic-field integral equation (20) is a nonhomogeneous linear equation. Therefore, for any given solution of the equation, one can construct a second solution by adding to the first one a solution of the homogeneous equation

$$\frac{1}{2} \vec{J}(\vec{r}) - \int_S \vec{t}_n(\vec{r}) \times [\vec{J}(\vec{r}') \times \nabla' G(\vec{r}, \vec{r}')] ds' = 0 \quad (21)$$

Consequently, a necessary condition for (20) to have a unique solution is that the solution of (21) be identically zero. The latter condition indeed holds for almost all values of the frequency. However, there do exist an infinite number of discrete, real values of k for which (21) has nontrivial solutions. These values correspond to the frequencies of certain eigenmodes of the cavity enclosed by the surface S . One can show that, except at those special k -values, the solution of (20) is indeed unique.

But the numerical analyst is hard hit by the existence of k -values, albeit discrete, for which the homogeneous equation (21) has nonzero solutions. In general, a numerical solution of the integral equation (20) consists of a conversion to a system of linear algebraic equations and a subsequent matrix inversion. When the frequency of the incident wave approaches one of the cavity eigenfrequencies, the matrix to be inverted becomes progressively close to being singular, resulting in a serious loss of numerical accuracy. The situation is all the more painful since the precise distribution of these eigenfrequencies is not known without first solving the eigenvalue problem (21).

Examples of the application of the magnetic-field integral equation to EMP interaction problems can be found in [1-5].

1.3.1.2 Electric-Field Integral Equation

The problem of the scattering of a monochromatic electromagnetic wave by a conductor, as depicted in Fig. 1, can be formulated in terms of yet another equation. This formulation is generalizable to the case of a finitely conducting scatterer. It is based on an integral representation of the electric field. The equation so derived is called an electric-field integro-differential equation.

One can express the electric field $\vec{E}^s(\vec{r})$ of the scattered wave at a field point \vec{r} in terms of the vector potential $\vec{A}^s(\vec{r})$ by eliminating the scalar potential between (2) and (3)

$$\vec{E}^s(\vec{r}) = -j\omega \left(\vec{I} + \frac{1}{k^2} \nabla \nabla \right) \cdot \vec{A}^s(\vec{r}) \quad (22)$$

where \vec{I} is the unit dyad. The vector potential \vec{A}^s is a linear functional of the induced surface current density \vec{J} flowing on the surface S of the scatterer, as given in (6). Denoting the electric field of the incident wave by \vec{E}^i , one obtains the following integral representation for the total electric field $\vec{E}(\vec{r})$ at a field point \vec{r} exterior to the scatterer

$$\vec{E}(\vec{r}) = \vec{E}^i(\vec{r}) - j\omega \left(\vec{I} + \frac{1}{k^2} \nabla \nabla \right) \cdot \int_S \vec{J}(\vec{r}') G(\vec{r}, \vec{r}') dS' \quad (23)$$

Let the field point \vec{r} approach the conductor's surface S . In this limit the integral representation (23) for the electric field does not require any special treatment, unlike in the case of the integral representation (8) for the magnetic field. Although the Green's function G displays in this limit a linear infinity at $\vec{r}' = \vec{r}$, this singularity occurs under a surface integral and can be removed by a simple change of integration variables. Therefore, for \vec{r} lying on S , (23) is an integral representation of the total electric field on the surface of the scatterer. Note that one should not bring the dyadic operator $\nabla \nabla$ inside the integral since, after the two differentiations, the integrand would become too singular at $\vec{r}' = \vec{r}$.

An integral equation for the induced surface current density \vec{J} is derived by imposing the appropriate boundary condition on the total electric field on the surface of the scatterer. For a perfectly conducting scatterer, the tangential component of the total electric field on the surface must vanish. This condition is satisfied if

$$\vec{I}_n(\vec{r}) \times \vec{E}(\vec{r}) = 0 \quad \text{for } \vec{r} \text{ on } S \quad (24)$$

Upon substitution of (23) into (24), the following equation results

$$j\omega \vec{I}_n(\vec{r}) \times \left(\vec{I} + \frac{1}{k^2} \nabla \nabla \right) \cdot \int_S \vec{J}(\vec{r}') G(\vec{r}, \vec{r}') dS' = \vec{I}_n(\vec{r}) \times \vec{E}^i(\vec{r}) \quad (25)$$

Inasmuch as the differential operators are outside the integral, (25) is really an integro-differential equation. Its numerical solution is subject to the same difficulty arising from nonuniqueness as that encountered previously with the magnetic-field integral equation. Essentially, uniqueness of solution does not hold for (25) whenever the homogeneous equation, obtained by setting $\vec{E}^1 = 0$, possesses nonzero solutions. This happens at an infinite set of discrete, real values of k . Each k -value corresponds to the frequency of an eigenmode of the cavity bounded by the surface S . These cavity eigenmodes satisfy the Maxwell equations (1) and the boundary condition $\vec{I}_n \times \vec{E} = 0$ on S .

Eq.(25) can be generalized to accommodate a scatterer with less-than-perfect, albeit good, conductivity. On the surface of a good conductor, one can impose the surface impedance boundary condition

$$Z_s(\vec{r})\vec{J}(\vec{r}) = -\vec{I}_n(\vec{r}) \times [\vec{I}_n(\vec{r}) \times \vec{E}(\vec{r})] \quad (26)$$

where $Z_s(\vec{r})$ is the scalar surface impedance of the scatterer at \vec{r} . Substituting (23) into (26), one obtains the following integro-differential equation

$$\begin{aligned} Z_s(\vec{r})\vec{J}(\vec{r}) - j\omega\mu\vec{I}_n(\vec{r}) \times [\vec{I}_n(\vec{r}) \times \left(\vec{I} + \frac{1}{k^2} \nabla\nabla \right) \cdot \int_S \vec{J}(\vec{r}') G(\vec{r}, \vec{r}') dS'] \\ = -\vec{I}_n(\vec{r}) \times [\vec{I}_n(\vec{r}) \times \vec{E}^1(\vec{r})] \end{aligned} \quad (27)$$

Its solution is unique since the surface impedance generally has a dissipative part, and this implies that cavity eigenmodes cannot occur at real frequencies.

Examples of the application of the electric-field integral equation to EMP interaction problems can be found in [6-8].

1.3.1.3 Thin-Wire Integral Equation

When the scatterer is a thin wire, the electric field integro-differential equation becomes practically one-dimensional. In this reduced form it is

applied extensively to the analysis of the wire antennas. The calculation is relatively simple for the case of a straight thin wire, and can be performed with a minimum of approximations. The following analysis will be confined to the straight-wire geometry.

Fig. 3 illustrates a straight wire scatterer. The wire lies along the

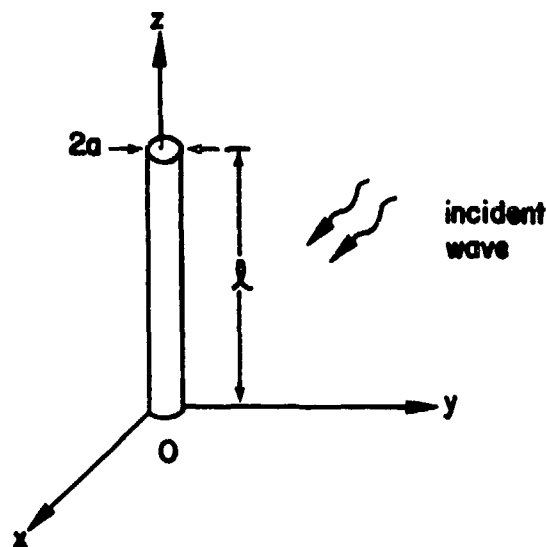


Fig. 3. Scattering of an incident electromagnetic wave by a thin, straight, conducting wire of length l and cross-sectional radius a .

z -axis of a cylindrical coordinate system from $z=0$ to $z=l$. It has a circular cross-section of radius a which, for a thin wire, is much smaller than both l and the wavelength of the incident wave.

The induced surface current density on the thin wire has mainly an axial component J_z . The circumferential component J_ϕ and the radial component J_ρ on the two ends are negligible. In this limit the vector integral equation (27) simplifies to the following scalar equation for just the component J_z

$$Z_s J_z(\phi, z) + j\omega\mu \left(1 + \frac{1}{k^2} \frac{\partial^2}{\partial z^2}\right) \int_0^{2\pi} d\phi' \int_0^L dz' J_z(\phi', z') G(\phi, z; \phi', z') = E_z^1(a, \phi, z) \quad (28)$$

where

$$G(\phi, z; \phi', z') = \frac{e^{-jk \sqrt{4a^2 \sin^2[(\phi - \phi')/2] + (z - z')^2}}}{4\pi \sqrt{4a^2 \sin^2[(\phi - \phi')/2] + (z - z')^2}} \quad (29)$$

and the impedance Z_s is assumed to be uniform over the wire's surface.

The integral equation (28) is two-dimensional, and involves the two coordinates ϕ and z . One can derive from it a one-dimensional integral equation for the total current $I(z)$ on the wire defined as

$$I(z) = \int_0^{2\pi} d\phi J_z(\phi, z) \quad (30)$$

by integrating (28) over ϕ from 0 to 2π . One then obtains the integral equation for a thin straight wire

$$Z_s' I(z) + j\omega\mu \left(1 + \frac{1}{k^2} \frac{d^2}{dz^2}\right) \int_0^L dz' I(z') \bar{G}(z - z') = \bar{E}_z^1(z) \quad (31)$$

where Z_s' is the series impedance per unit length of the wire given by

$$Z_s' = \frac{Z_s}{2\pi a} \quad (32)$$

The kernel $\bar{G}(z - z')$ is the definite integral

$$\bar{G}(z - z') = \frac{1}{\pi} \int_0^\pi d\psi \frac{e^{-jk \sqrt{(2a \sin \psi)^2 + (z - z')^2}}}{4\pi \sqrt{(2a \sin \psi)^2 + (z - z')^2}} \quad (33)$$

which has only a logarithmic singularity at $z = z'$, and $\bar{E}_z^1(z)$ is the angular average of $E_z^1(z)$, namely

$$\bar{E}_z^1(z) = \frac{1}{2\pi} \int_0^{2\pi} d\phi E_z^1(a, \phi, z) \quad (34)$$

The thin-wire integro-differential equation (31) can be converted into a genuine integral equation by integrating out the differential part analytically, viz.,

$$\begin{aligned} \int_0^L dz' I(z') \bar{G}(z - z') + \frac{Z_0'}{jZ_0} \int_0^z dz' I(z') \sin k(z - z') \\ = C_1 e^{-jkz} + C_2 e^{jkz} + \frac{1}{jZ_0} \int_0^z dz' \bar{E}_z^1(z') \sin k(z - z') \end{aligned} \quad (35)$$

where C_1 and C_2 are two arbitrary constants and Z_0 is the impedance of free space. Eq.(35) is a mixture of a Fredholm and a Volterra integral equation. The two constants C_1 and C_2 are determined to satisfy the following two end conditions for the wire current

$$I(0) = I(L) = 0 \quad (36)$$

Eq.(35) is an integral equation for the electric current induced on a thin straight wire by an incident electromagnetic wave. If the wire is a transmitting antenna, the averaged external field \bar{E}_z^e is prescribed on the surface of the wire. In this case one simply replaces \bar{E}_z^1 in (35) by $-\bar{E}_z^e$.

Examples of the application of the thin-wire integral equation can be found in [9 - 11].

1.3.1.4 Time-Domain Integral Equations

The integral equations derived so far are applicable to scattering and radiation calculations in the frequency domain. They describe the excitation of conductors by time-harmonic sources. In principle, they can also be used to solve problems involving aperiodic and transient sources, such as an EMP or pulse generator. This is done through the powerful technique of the Fourier or Laplace transform. In practice,

however, a frequency-domain approach to a transient problem necessitates the construction of a solution of the integral equation involved that is valid over a wide range of frequencies. Sometimes it may prove easier to formulate and solve the transient problem directly in the time domain [12]. Indeed, the frequency-domain integral equations have their time-domain counterparts.

1.3.1.4.1 Time-Domain Magnetic-Field Integral Equation

Consider the scattering of a general electromagnetic wave by a perfect conductor, as depicted in Fig. 1. The incident wave can have an arbitrary variation in space and time. The electric and magnetic fields of the scattered wave satisfy the time-domain Maxwell equations in free space outside the conductor

$$\begin{aligned} \nabla \cdot \vec{E}^s &= 0, & \nabla \times \vec{E}^s &= -\mu \frac{\partial}{\partial t} \vec{H}^s \\ \nabla \cdot \vec{H}^s &= 0, & \nabla \times \vec{H}^s &= \epsilon \frac{\partial}{\partial t} \vec{E}^s \end{aligned} \quad (37)$$

These fields can be derived from a scalar potential ϕ^s and a vector potential \vec{A}^s such that

$$\vec{E}^s = -\nabla \phi^s - \frac{\partial}{\partial t} \vec{A}^s, \quad \vec{H}^s = \frac{1}{\mu} \nabla \times \vec{A}^s \quad (38)$$

If the potentials are made to obey the Lorentz condition

$$\nabla \cdot \vec{A}^s + \frac{1}{c} \frac{\partial}{\partial t} \phi^s = 0 \quad (39)$$

where c is the free-space light speed, then the scalar and vector potentials individually satisfy the wave equation

$$\left(\nabla^2 - \frac{1}{c^2} \frac{\partial^2}{\partial t^2} \right) \phi^s = 0, \quad \left(\nabla^2 - \frac{1}{c^2} \frac{\partial^2}{\partial t^2} \right) \vec{A}^s = 0 \quad (40)$$

The retarded solutions of the wave equations (40) are

$$\phi^s(\vec{r}, t) = \frac{1}{4\pi\epsilon} \int_S \frac{\rho(\vec{r}', t - |\vec{r} - \vec{r}'|/c)}{|\vec{r} - \vec{r}'|} dS' \quad (41)$$

$$\vec{A}^s(\vec{r}, t) = \frac{\mu}{4\pi} \int_S \frac{\vec{J}(\vec{r}', t - |\vec{r} - \vec{r}'|/c)}{|\vec{r} - \vec{r}'|} dS' \quad (42)$$

The charge and current densities, ρ and \vec{J} , satisfy the continuity equation

$$\frac{\partial}{\partial t} \rho + \nabla \cdot \vec{J} = 0 \quad (43)$$

Substituting (42) into (38), one arrives at the following integral representation of the scattered magnetic field $\vec{H}^s(\vec{r}, t)$ at a point \vec{r} exterior to the scatterer and at time t

$$\vec{H}^s(\vec{r}, t) = \frac{1}{4\pi} \int_S \left[\vec{J}(\vec{r}', \tau) \times \nabla' \left(\frac{1}{R} \right) - \frac{1}{cR^2} \vec{R} \times \frac{\partial}{\partial \tau} \vec{J}(\vec{r}', \tau) \right] dS' \quad (44)$$

where

$$\vec{R} = \vec{r} - \vec{r}', \quad R = |\vec{r} - \vec{r}'| \quad (45)$$

and τ is the retarded time defined by

$$\tau = t - \frac{1}{c} |\vec{r} - \vec{r}'| \quad (46)$$

The operator ∇' acts on the source point \vec{r}' . Eq.(44) expresses the magnetic field of the scattered wave at a point in space and time as a composition of excitations emanating from individual points of the scatterer's surface at specific retarded times

An integral equation for the surface current density \vec{J} is obtained by observing that, on the surface S of a perfectly conducting scatterer, the total magnetic field is related to the surface current density at all times through the equation

$$\vec{J}(\vec{r}, t) = \vec{I}_n(\vec{r}) \times [\vec{H}^i(\vec{r}, t) + \vec{H}^s(\vec{r}, t)] \quad (47)$$

In evaluating the scattered magnetic field \vec{H}^s on S, given in the form of the integral representation (44), one must exercise proper caution in handling the singularity in the integrand, just as in the derivation of the magnetic-field integral equation in the frequency domain.

It can be shown that as the field point \vec{r} approaches S, the singularity at $R=0$ in the second term of the integrand in (44) is integrable, and requires no special attention. The singularity in the first term, however, is more violent. It is in fact of the same type as that in (8). Consequently, the limiting value of the surface integral (44), as \vec{r} approaches S, must be evaluated with the method applied previously to (10). Taking the limit $\vec{r} \rightarrow S$ in (44) one obtains the following time-domain integral equation for the induced surface current density \vec{J} on the scatterer

$$\begin{aligned} \frac{1}{2} \vec{J}(\vec{r}, t) - \frac{1}{4\pi} \int_S \vec{I}_n(\vec{r}) \times \left[\vec{J}(\vec{r}', \tau) \times \nabla' \left(\frac{1}{R} \right) \right. \\ \left. - \frac{1}{cR^2} \vec{R} \times \frac{\partial}{\partial \tau} \vec{J}(\vec{r}', \tau) \right] dS' = \vec{I}_n(\vec{r}) \times \vec{H}^i(\vec{r}, t) \end{aligned} \quad (48)$$

At first glance, the time-domain magnetic-field integral equation (48) may appear to bear a close resemblance to its frequency-domain counterpart (20). This formal similarity, however, is actually quite deceptive. When it comes to solving the equations, each equation requires a totally different procedure. This difference in treatment is the reflection of a basic difference in the physical contents of the two equations. The frequency-domain integral equation describes a steady state of the scattering process, long after all transient effects are damped out. In this equilibrium condition, the current densities at different points on the scatterer's surface at one instant of time are closely interrelated. The integral equation is equivalent to a system of simultaneous linear algebraic equations. Its solution consists of a matrix inversion. On the other hand, the time-domain integral equation describes the transient excitation of the scatterer by an incident wave. Each part of the incident wave,

upon striking the scatterer's surface, creates a disturbance which then ripples out around the scatterer in the form of surface currents. The current density at a given point of the scatterer's surface at a given time is obtained by adding up all the disturbances reaching this point from all the points of the surface and generated at appropriate earlier times. A determination of the surface current density, that is to say, a solution of the time-domain integral equation, requires only integration and no matrix inversion. This difference in the solution procedure is a mathematical consequence of the fact that the frequency-domain Maxwell equations are of the elliptic type, while the time-domain Maxwell equations are of the hyperbolic type.

1.3.1.4.2 Time-Domain Electric-Field Integral Equation

Just as in the frequency domain, the time-domain scattering of an electromagnetic wave by a conductor can also be formulated in terms of an electric-field integral equation. The starting point of this formulation is an integral representation of the scattered electric field in the time domain. Using (38), (41) and (42), one can establish the following integral representation for the scattered electric field $\vec{E}^s(\vec{r}, t)$ at a point \vec{r} exterior to the scatterer and at the time t , in terms of the retarded values of the surface charge density ρ and the surface current density \vec{J} induced on the scatterer's surface S

$$\vec{E}^s(\vec{r}, t) = -\frac{1}{4\pi\epsilon} \nabla \int_S \frac{dS'}{R} \rho(\vec{r}', \tau) - \frac{\mu}{4\pi} \int_S \frac{dS'}{R} \frac{\partial}{\partial \tau} \vec{J}(\vec{r}', \tau) \quad (49)$$

Hence, if one now lets the field point \vec{r} approach the surface S and imposes the following boundary condition on S

$$\vec{n}(\vec{r}) \times [\vec{E}^i(\vec{r}, t) + \vec{E}^s(\vec{r}, t)] = 0 \quad (50)$$

one arrives at an integro-differential equation involving ρ and \vec{J}

$$\vec{I}_n(\vec{r}) \times \left[\frac{1}{4\pi\epsilon} \nabla \int_S \frac{dS'}{R} \rho(\vec{r}', \tau) + \frac{\mu}{4\pi} \int_S \frac{dS'}{R} \frac{\partial}{\partial \tau} \vec{J}(\vec{r}', \tau) \right] \\ = \vec{I}_n(\vec{r}) \times \vec{E}^i(\vec{r}, t) \quad (51)$$

Note that, with the operator ∇ kept outside of the integral in (51), the limit of the integral as \vec{r} approaches S can be taken without special ado.

Eq.(51) is equivalent to two scalar equations, but it contains three unknowns: ρ and the two components of \vec{J} . It must therefore be supplemented by the continuity equation (43). The latter can be applied to eliminate ρ from (51). Integrating (43) over time, one has

$$\rho(\vec{r}', \tau) = - \int_{-\infty}^{\tau} d\tau' \nabla' \cdot \vec{J}(\vec{r}', \tau') \quad (52)$$

One has also assumed that in the infinitely remote past, before the incident wave reached the scatterer, the scatterer was uncharged. Substituting (52) into (51), one obtains the following final form of the time-domain electric-field integro-differential equation for the induced surface current density \vec{J}

$$\vec{I}_n(\vec{r}) \times \left[- \frac{1}{4\pi\epsilon} \nabla \int_S \frac{dS'}{R} \int_{-\infty}^{\tau} d\tau' \nabla' \cdot \vec{J}(\vec{r}', \tau') + \frac{\mu}{4\pi} \int_S \frac{dS'}{R} \frac{\partial}{\partial \tau} \vec{J}(\vec{r}', \tau) \right] \\ = \vec{I}_n(\vec{r}) \times \vec{E}^i(\vec{r}, t) \quad (53)$$

This is a fearsome-looking equation, but can be handled numerically on the computer in a straightforward fashion. Again, because of the appearance of the retarded time τ on the left-hand side of the equation, no matrix inversion is involved in the solution.

If one wishes, one can easily extend (53) to cover the case of finite scatterer conductivity, as was done previously in the frequency domain.

1.3.1.4.3 Time-Domain Thin-Wire Integral Equation

The time-domain electric-field integral equation simplifies considerably when the scatterer is a thin straight wire. The thin-wire geometry makes it possible to go over from a two-dimensional problem to a one-dimensional one. Instead of taking the thin-wire limit of (53), it is easier to derive the time-domain thin-wire integral equation directly from the Maxwell equations.

From (38) and the Lorentz condition (39) one finds that

$$\frac{\partial}{\partial t} \vec{E}^s(\vec{r}, t) = c^2 \left(\nabla \nabla - \vec{1} \frac{\partial^2}{\partial t^2} \right) \cdot \vec{A}^s(\vec{r}, t) \quad (54)$$

With \vec{A}^s given by (42) and the boundary condition

$$\frac{\partial}{\partial t} \left[E_z^i(\vec{r}, t) + E_z^s(\vec{r}, t) \right] = 0 \quad (55)$$

imposed on the surface of the wire, one obtains the following time-domain thin-wire integro-differential equation for the total axial current I

$$\left(\frac{\partial^2}{\partial z^2} - \frac{1}{c^2} \frac{\partial^2}{\partial t^2} \right) \int_0^{\ell} dz' I \left(z', t - \frac{|z - z'|}{c} \right) g(z - z') = - \epsilon \frac{\partial}{\partial t} \vec{E}_z^i(z, t) \quad (56)$$

where the wire is taken to stretch from $z = 0$ to $z = \ell$. The kernel is defined by

$$g(z - z') = \frac{1}{\pi} \int_0^{\pi} \frac{d\phi}{4\pi \sqrt{(2a \sin \phi)^2 + (z - z')^2}} \quad (57)$$

which has a logarithmic singularity at $z = z'$, and the averaged \vec{E}_z^i is defined in the same way as (34).

Examples of the application of time-domain integral equations can be found in [13-16].

1.3.1.5 Aperture-Penetration Integral Equation

The need for calculating electromagnetic penetration through apertures arises frequently in the analysis of EMP interaction. The typical configuration of aperture penetration is illustrated in Fig. 4.

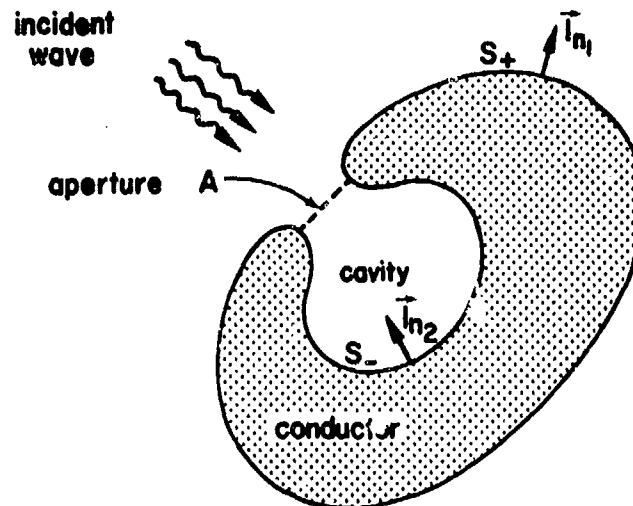


Fig. 4. Penetration of an incident electromagnetic wave through an aperture into the interior of a conducting body.

A shell made of perfectly conducting material is situated in free space, and encloses a cavity. The cavity opens onto the exterior of the shell by way of an aperture A. Let an electromagnetic wave be incident on the aperture from outside the shell. It is required to calculate the electromagnetic fields inside the cavity as a result of aperture penetration.

Suppose first the aperture A is completely plugged up by a perfectly-conducting, infinitely-thin cover. This cover therefore forms with the outer surface of the shell a closed, perfectly-conducting surface S_+ , while it forms with the cavity wall another closed, perfectly-conducting surface S_- . The incident electromagnetic wave, assumed time-harmonic with time factor $e^{j\omega t}$, is scattered by the external, closed surface S_+ . In the

aperture-penetration problem, the solution of this auxiliary scattering problem is assumed known.

Let the total external fields be

$$\vec{E}_{\text{ext}}(\vec{r}) = \vec{E}_{\text{sc}}(\vec{r}) + \vec{E}_1(\vec{r}), \quad \vec{H}_{\text{ext}}(\vec{r}) = \vec{H}_{\text{sc}}(\vec{r}) + \vec{H}_1(\vec{r}) \quad (58)$$

and the total internal fields be

$$\vec{E}_{\text{int}}(\vec{r}) = \vec{E}_2(\vec{r}), \quad \vec{H}_{\text{int}}(\vec{r}) = \vec{H}_2(\vec{r}) \quad (59)$$

where $\vec{E}_{\text{sc}}, \vec{H}_{\text{sc}}$ are the short-circuited fields with the aperture completely plugged up by a perfectly-conducting cover. One finds that [17]

$$\vec{H}_1(\vec{r}) = \int_{S_+} j\omega\epsilon \vec{\Gamma}_{\text{ext}}(\vec{r}, \vec{r}') \cdot [\vec{I}_{n_1}(\vec{r}') \times \vec{E}_1(\vec{r}')] dS' \quad (60)$$

with \vec{r} exterior to S_+ , and that

$$\vec{H}_2(\vec{r}) = \int_{S_-} j\omega\epsilon \vec{\Gamma}_{\text{int}}(\vec{r}, \vec{r}') \cdot [\vec{I}_{n_2}(\vec{r}') \times \vec{E}_2(\vec{r}')] dS' \quad (61)$$

with \vec{r} interior to S_- . The external dyadic Green's function $\vec{\Gamma}_{\text{ext}}$ characterizes the region exterior to S_+ , and the internal dyadic Green's function $\vec{\Gamma}_{\text{int}}$ characterizes the region interior to S_- . They both satisfy the differential equation

$$(\nabla \times \nabla \times - k^2) \vec{\Gamma}(\vec{r}, \vec{r}') = \vec{I} \delta(\vec{r} - \vec{r}') \quad (62)$$

and the following so-called boundary condition of the second kind, namely,

$$\begin{aligned} \vec{I}_{n_1}(\vec{r}) \times \nabla \times \vec{\Gamma}_{\text{ext}}(\vec{r}, \vec{r}') &= 0 \quad \text{for } \vec{r} \text{ on } S_+ \\ \vec{I}_{n_2}(\vec{r}) \times \nabla \times \vec{\Gamma}_{\text{int}}(\vec{r}, \vec{r}') &= 0 \quad \text{for } \vec{r} \text{ on } S_- \end{aligned} \quad (63)$$

The advantage of this boundary-condition assignment is that the tangential components of \vec{H}_1 and \vec{H}_2 on the surfaces S_+ and S_- now depend only on the tangential components of \vec{E}_1 and \vec{E}_2 .

The aperture-penetration integral equation is derived by matching the tangential components of the external and internal electromagnetic fields across the aperture A. The boundary conditions at A are

$$\vec{I}_{n_1}(\vec{r}) \times \vec{E}_1(\vec{r}) = -\vec{I}_{n_2}(\vec{r}) \times \vec{E}_2(\vec{r}) \quad (64)$$

$$\vec{I}_{n_1}(\vec{r}) \times [\vec{H}_{sc}(\vec{r}) + \vec{H}_1(\vec{r})] = -\vec{I}_{n_2}(\vec{r}) \times \vec{H}_2(\vec{r}) \quad (65)$$

The tangential component $\vec{I}_{n_1} \times \vec{E}_{sc}$ is identically zero. Substituting (60), (61) and (64) into (65) and noting the relation $\vec{I}_{n_1} = -\vec{I}_{n_2}$ on A, one finally arrives at the aperture-penetration integral equation in the form

$$\begin{aligned} j\omega\epsilon \vec{I}_{n_1}(\vec{r}) \times \int_A [\vec{\Gamma}_{ext}(\vec{r}, \vec{r}') + \vec{\Gamma}_{int}(\vec{r}, \vec{r}')] \cdot [\vec{I}_{n_1}(\vec{r}') \times \vec{E}_1(\vec{r}')] dS' \\ = -\vec{I}_{n_1}(\vec{r}) \times \vec{H}_{sc}(\vec{r}) \end{aligned} \quad (66)$$

It must be remarked that the integrand in (66) is actually non-integrable. The reason is that the Green's functions $\vec{\Gamma}_{ext}$ and $\vec{\Gamma}_{int}$ both contain double derivatives of the inverse distance $|\vec{r} - \vec{r}'|^{-1}$. In order to arrive at a meaningful limit as \vec{r} tends to \vec{r}' , it is necessary to bring the differential operators outside the integral, and (66) is to be interpreted in this sense. Eq.(66) is therefore an integro-differential equation for the tangential aperture electric field $\vec{I}_{n_1} \times \vec{E}_1$. Its solution can be used to calculate the total external and internal fields. It must be noted that, before one can apply the aperture-penetration equation (66) to a specific problem, one has first to determine the three quantities \vec{H}_{sc} , $\vec{\Gamma}_{ext}$ and $\vec{\Gamma}_{int}$ appearing therein for the aperture geometry concerned. Very often, this determination is an arduous task in itself.

However, when the aperture A lies in an infinite, conducting, thin plane screen between two half-spaces, (66) can be written out explicitly

in simple form. The infinite plane screen geometry, although an outright idealization, is actually a good approximation to many aperture configurations encountered in practice. Let the infinite plane screen be the x-y plane in a rectangular coordinate system, as shown in Fig. 5. Let

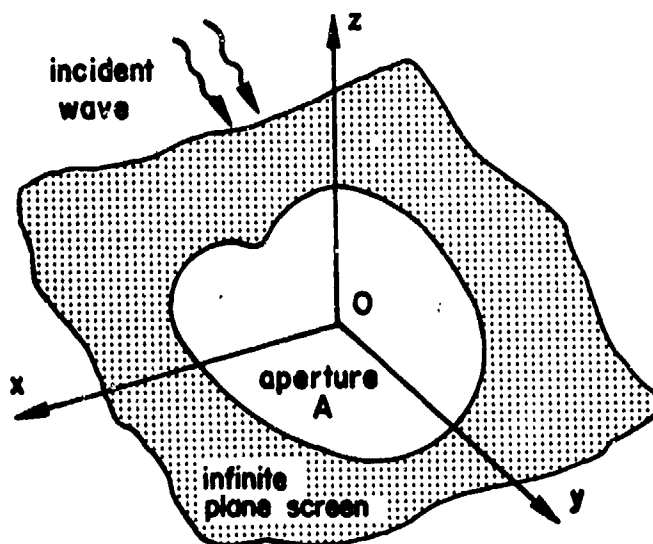


Fig. 5. Penetration of an incident electromagnetic wave through an aperture in a conducting, infinite, plane screen.

the incident electromagnetic wave impinge on the aperture A in the plane screen from the upper half-space $z > 0$. Therefore, the exterior region in this geometry is the upper half-space $z > 0$, and the interior region the lower half-space $z < 0$. The unit normal vector $\hat{\mathbf{n}}_1$ becomes simply $\hat{\mathbf{z}}$. The dyadic Green's function for a half-space satisfying the boundary condition of the second kind can be expressed in closed form

$$\begin{aligned} \vec{\mathbf{T}}(\vec{\mathbf{r}}, \vec{\mathbf{r}}') = & \left(\vec{\mathbf{I}} - \frac{1}{k^2} \nabla \nabla' \right) [G(\vec{\mathbf{r}}, \vec{\mathbf{r}}') + G(\vec{\mathbf{r}}, \vec{\mathbf{r}}'')] \\ & - 2 G(\vec{\mathbf{r}}, \vec{\mathbf{r}}'') \hat{\mathbf{z}} \hat{\mathbf{z}} \end{aligned} \quad (67)$$

where G is the free-space Green's function given by (7) and \vec{r}'' is the image of \vec{r}' . For the external Green's function \vec{r}_{ext} , one chooses positive z and z' . For the internal Green's function \vec{r}_{int} , one chooses negative z and z' . Upon substitution of (67) into (66), the following equation results

$$4j\omega\epsilon \vec{I}_z \times \left(\vec{I} + \frac{1}{k^2} \nabla_t \nabla_t \right) \cdot \iint_A dx' dy' G(x, y; x', y') [\vec{I}_z \times \vec{E}_1(x', y')] = -\vec{I}_z \times \vec{H}_{\text{sc}}(x, y) \quad (68)$$

where ∇_t is the tangential gradient operator

$$\nabla_t = \vec{I}_x \frac{\partial}{\partial x} + \vec{I}_y \frac{\partial}{\partial y} \quad (69)$$

Note that in (68) all differential operators occurring in the dyadic Green's functions have been taken out of the integral to ensure integrability, as has been discussed previously.

It must be pointed out that (66) is not the only possible integral-equation formulation of the aperture-penetration problem, although it is certainly one of the most general. Other versions do exist, especially when one restricts oneself to specific aperture geometries. Nevertheless, these different versions all share a common characteristic, in that they all select certain field quantities at the aperture opening as the unknowns of the problem, be they field components, their various derivatives or appropriate scalar potentials. Examples of the application of integral equations to the solution of aperture-penetration problems can be found in [18 - 21].

1.3.1.6 Intersecting Cylinders

Intersecting cylinders have been used to model many aeronautical systems for EMP interaction calculations. The most common applications of the model pertain to aircraft and satellites. In this section the basic

formulation of the two-intersecting-cylinder problem is discussed, while all relevant results are relegated to Part 2 of this document.

1.3.1.6.1 Orthogonally Intersecting, Electrically Thin ($ka \leq 0.1$) Cylinders

In Fig. 6 are shown two intersecting rods immersed in a time-harmonic

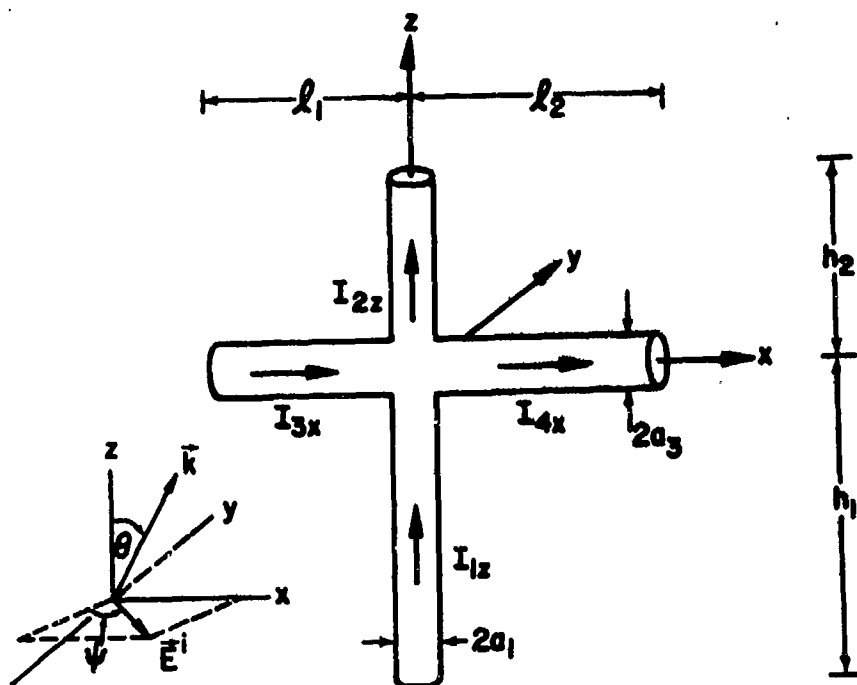


Fig. 6. Two orthogonally intersecting, electrically thin ($ka_1, ka_3 \leq 0.1$) cylinders in a time-harmonic plane wave. \vec{k} lies in the yz -plane.

plane wave whose electric field components are given by

$$E_x^i = E^i \sin \psi, \text{ (on horizontal wire)} \quad (70)$$

$$E_z^i = E^i \cos \psi \sin \theta e^{-jkz \cos \theta}, \text{ (on vertical wire)}$$

The total axial currents induced on the four sections of the rods are denoted by $I_{1z}(z)$, $I_{2z}(z)$, $I_{3x}(x)$ and $I_{4x}(x)$ which satisfy coupled integral equations subject to boundary conditions at the four ends and certain appropriate conditions at the junction. The boundary conditions at the ends of the four arms are

$$I_{1z}(-h_1) = I_{2z}(h_2) = I_{3x}(-l_1) = I_{4x}(l_2) = 0 \quad (71)$$

The conditions at the junction must relate the currents and the charges per unit length in the four arms. Strictly, the conditions must involve these quantities at electrically short distances from the junction, where the currents and charges are still rotationally symmetric. However, since with $ka \leq 0.1$ the electrical surface area of the junction region is very small (of the order $(ka)^2 \leq 0.01$), its shape is immaterial and the total charge on its surface is negligible. Accordingly, no significant error is introduced insofar as currents and charges at electrically very small distances away from the junction are concerned, if it is assumed that each arm and its rotationally symmetric current and charge per unit length extend to the junction point ($x=z=0$) as if concentrated along the axes of the conductors. The junction conditions can then be imposed at this point. For a vertical conductor with radius a_1 and a horizontal conductor with radius a_3 , the junction conditions include the Kirchhoff condition on the currents [22]

$$I_{1z}(0) - I_{2z}(0) + I_{3x}(0) - I_{4x}(0) = 0 \quad (72)$$

and the following three conditions on the charges q per unit length [23]

$$q_1(0)\psi_1 = q_2(0)\psi_2 = q_3(0)\psi_3 = q_4(0)\psi_4 \quad (73)$$

where, for conductors at least a quarter wavelength long,

$$\psi_1 = \psi_2 = 2[\ln(2/ka_1) - 0.5772], \quad \psi_3 = \psi_4 = 2[\ln(2/ka_3) - 0.5772] \quad (74)$$

Note that these parameters are independent of the lengths of the conductors. For shorter conductors, the length is of importance and

$$\psi_1 = \psi_2 = 2 \ln(\sqrt{h_1 h_2} / a_1), \quad \psi_3 = \psi_4 = 2 \ln(\sqrt{l_1 l_2} / a_3) \quad (75)$$

When the radii are equal ($a_1 = a_3 = a$), $\psi_1 = \psi_2 = \psi_3 = \psi_4$ in (73) and this reduces to the equality of charges per unit length.

The use of thin-cylinder theory is an acceptable approximation only when the following inequalities are satisfied

$$\begin{aligned} ka_1 &\ll 1; & a_1 &\ll h_1, & a_1 &\ll h_2 \\ ka_3 &\ll 1; & a_3 &\ll l_1, & a_3 &\ll l_2 \end{aligned} \quad (76)$$

The required coupled integral equations for I_x and I_z are readily derived from the following one-dimensional boundary conditions on the surface of the conductors [24,25]

$$\begin{aligned} E_z(z) = E_z^i - \partial\phi(z)/\partial z - j\omega A_z(z) &= 0, & -h_1 \leq z \leq h_2 \\ E_x(x) = E_x^i - \partial\phi(x)/\partial x - j\omega A_x(x) &= 0, & -l_1 \leq x \leq l_2 \end{aligned} \quad (77)$$

When the integrals for the scalar potential ϕ and the components of the vector potential \vec{A} are substituted in (77), the following pair of simultaneous integral equations is obtained for the unknown currents $I_x(x)$ and $I_z(z)$

$$\begin{aligned} \int_{-h_1}^{h_2} I_z(z') K(z, z') dz' - \frac{j\omega}{k^2} \frac{\partial}{\partial z} \left[\int_{-h_1}^{h_2} q(z') K(z, z') dz' + \int_{-l_1}^{l_2} q(x') K(z, x') dx' \right] \\ = -(j4\pi/\omega\mu) E_z^i(z) \end{aligned} \quad (78)$$

$$\int_{-l_1}^{l_2} I_x(x') K(x, x') dx' - \frac{j\omega}{k^2} \frac{\partial}{\partial x} \left[\int_{-l_1}^{l_2} q(x') K(x, x') dx' + \int_{-h_1}^{h_2} q(z') K(x, z') dz' \right] = -(j4\pi/\omega\mu) E_x^i \quad (79)$$

where $E_z^i(z)$ and $E_x^i(x)$ are given in (70). Note that $q(z) = (j/\omega) \partial I_z(z) / \partial z$ and $q(x) = (j/\omega) \partial I_x(x) / \partial x$. The kernels are defined as follows:

$$\begin{aligned} K(z, z') &= \exp(-jkR_z) / R_z, & K(x, x') &= \exp(-jkR_x) / R_x \\ K(z, x') &= \exp(-jkR_{cz}) / R_{cz}, & K(x, z') &= \exp(-jkR_{cx}) / R_{cx} \end{aligned} \quad (80)$$

with

$$\begin{aligned} R_z &= [(z - z')^2 + a_1^2]^{1/2}, & R_x &= [(x - x')^2 + a_3^2]^{1/2} \\ R_{cz} &= [z^2 + x'^2 + a_3^2]^{1/2}, & R_{cx} &= [x^2 + z'^2 + a_1^2]^{1/2} \end{aligned}$$

Eqs.(78) and (79) are to be solved for $I_z(z)$ and $I_x(x)$ subject to the four end conditions in (71) and the four junction conditions in (72) and (73).

Analytical solutions of these equations have been obtained when $a_1 = a_3 = a$ for two different cases, namely, (a) the case of a normally incident field with the electric vector parallel to the vertical conductor and arbitrary arm lengths [26], and (b) the case of a general incident field and equal arm lengths [27]. More general cases than these two are readily formulated and evaluated by analytical or numerical methods. Approximate currents and charges have been calculated for a wide range of arm lengths in [24,25,27]. Measured currents and charges are in [28]. Details of the analytic solution and explicit formulas for the coefficients are given in [29].

1.3.1.6.2 Non-Orthogonally Intersecting, Electrically Thin ($ka \leq 0.1$) Cylinders

The determination of the currents and charges on the surfaces of conductors intersecting at angles Δ other than 90° , as shown in Fig. 7,

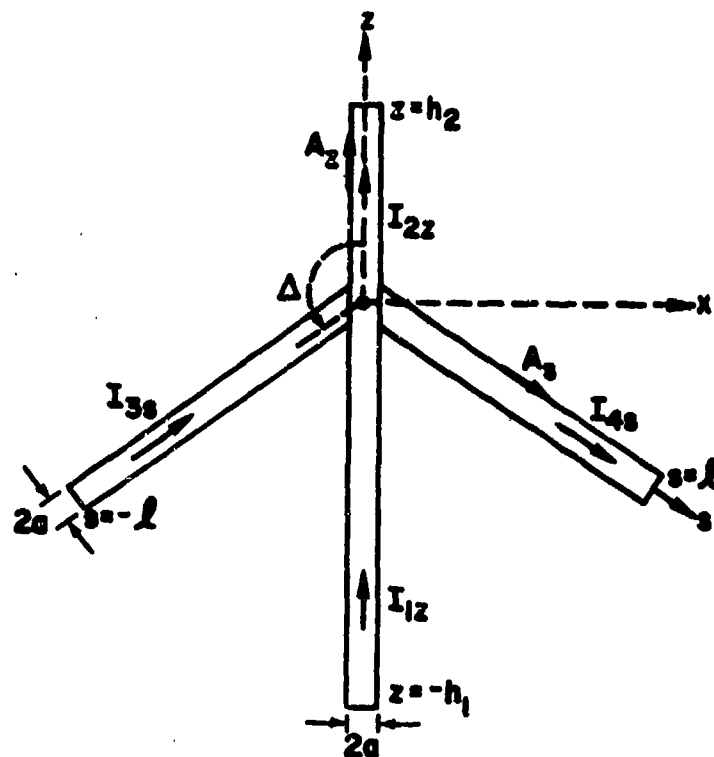


Fig. 7. Swept-wing thin-wire cross.

can be accomplished for electrically thin cylinders by a generalization of the analytical procedure described for orthogonal conductors. All of the thin-cylinder conditions previously imposed for $\Delta = 90^\circ$ must be satisfied and, in addition, a restriction of the angle Δ of intersection must be enforced. This is needed in order to keep the junction region electrically small enough to preserve the validity of the assumption that the total charge on its surfaces is negligible. The added condition is

$$|\sin \Delta| \gg ka \quad (81)$$

When $\Delta = 90^\circ$, this reduces to the previously imposed condition $ka \ll 1$.

The integral equations for the currents in the swept-wing configuration shown in Fig. 7 are derived in the same manner as those for the

orthogonal cross but several additional terms and integrals occur, since the crossed conductors are now coupled inductively as well as capacitively. In order to permit the ready correlation with the equations for the orthogonal cross, the notation shown in Fig. 7 is used. As before, the vertical member extends from $z = -h_1$ to $z = h_2$ with the junction at the origin. The arms are taken to be equal and of length l with the variable s ranging from $s = -l$ to $s = 0$ along the left arm and from $s = 0$ to $s = l$ along the right arm. Note that when $\Delta = 90^\circ$, s becomes x and the entire notation reduces to that of the orthogonal cross.

The boundary conditions requiring the vanishing of the tangential component of the electric field on the surfaces of the conductors, each with radius a , now have the form

$$E_z(z) = E_z^1 - \partial\phi(z)/\partial z - j\omega A_z(z) = 0, \quad -h_1 \leq z \leq h_2 \quad (82)$$

$$E_s(s) = -E_z^1 \cos \Delta - \partial\phi_3(s)/\partial s - j\omega A_{3s}(s) = 0, \quad -l \leq s \leq 0 \quad (83)$$

$$E_s(s) = E_z^1 \cos \Delta - \partial\phi_4(s)/\partial s - j\omega A_{4s}(s) = 0, \quad 0 \leq s \leq l \quad (84)$$

for a normally incident field, $\vec{E}^1 = \hat{z} E_z^1$. A consequence of symmetry is that the currents and charges, and the vector and scalar potentials on the two side arms satisfy the following relations:

$$I_{3s}(-s) = -I_{4s}(s), \quad q_3(s) = q_4(-s) \quad (85)$$

$$A_{3s}(-s) = -A_{4s}(s), \quad \phi_3(-s) = \phi_4(s)$$

Hence, it is necessary to determine only $I_{1z}(z)$, $I_{2z}(z)$, and $I_{4s}(s)$. With the relations (85), the vector and scalar potentials in (82) are

$$A_z(z) = (\mu/4\pi) \left\{ \int_{-h_1}^{h_2} I_z(z') K(z, z') dz' + 2 \cos \Delta \int_0^l I_s(s') K(z, s', \Delta) ds' \right\} \quad (86)$$

$$\phi(z) = (1/4\pi\epsilon) \left\{ \int_{-h_1}^{h_2} q(z')K(z,z')dz' + 2 \int_0^l q(s')K(z,s',\Delta)ds' \right\} \quad (87)$$

where

$$K(z,z') = \frac{e^{-jkR_z}}{R_z}, \quad K(z,s',\Delta) = \frac{e^{-jkR_{zs'}}}{R_{zs'}} \quad (88)$$

$$R_z = [(z-z')^2 + a^2]^{1/2}, \quad R_{zs'} = [z^2 + s'^2 - 2zs'\cos\Delta + a^2]^{1/2}$$

Similarly, in (84)

$$A_{4s}(s) = (1/4\pi) \left\{ \int_0^l I_s(s') [K(s,s') + K(s,s',\Delta)\cos 2\Delta] ds' + \cos\Delta \int_{-h_1}^{h_2} I_z(z')K(s,z',\Delta)dz' \right\} \quad (89)$$

$$\phi_4(s) = (1/4\pi\epsilon) \left\{ \int_0^l q(s') [K(s,s') + K(s,s',\Delta)] ds' + \int_{-h_1}^{h_2} q(z')K(s,z',\Delta)dz' \right\} \quad (90)$$

where

$$K(s,s') = \frac{e^{-jkR_s}}{R_s}, \quad K(s,s',\Delta) = \frac{e^{-jkR_{ss'}}}{R_{ss'}}, \quad K(s,z',\Delta) = \frac{e^{-jkR_{sz'}}}{R_{sz'}}$$

$$R_s = [(s-s')^2 + a^2]^{1/2} \quad (91)$$

$$R_{ss'} = [s^2 + s'^2 - 2ss'\cos 2\Delta + a^2]^{1/2}$$

$$R_{sz'} = [s^2 + z'^2 - 2|s|z'\cos\Delta + a^2]^{1/2}$$

When (86) - (90) are substituted in (82) and (84), the following simultaneous integral equations for the currents and charges are obtained after

integration by parts

$$\int_{-h_1}^{h_2} [\partial^2 I_z(z') / \partial z'^2 + k^2 I_z(z')] K(z, z', \Delta) dz' - F_2(z, \Delta) - F_3(z) - F_4(z, \Delta) = - \frac{j4\pi k^2}{\omega \mu} E_z^i \quad (92)$$

$$\int_0^l [\partial^2 I_s(s') / \partial s'^2 + k^2 I_s(s')] [K(s, s') - K(s, s', \Delta)] ds' - F_2(s, \Delta) - F_3(s, \Delta) - F_4(s, \Delta) - F_5(s, \Delta) = - \frac{j4\pi k^2}{\omega \mu} E_z^i \cos \Delta \quad (93)$$

where

$$F_2(z, \Delta) = 2j\omega(\partial/\partial z) \int_0^l q(s') K(z, s', \Delta) ds' \\ F_3(z) = -j\omega[q(h_2)K(z, h_2) - q(-h_1)K(z, -h_1)] \quad (94)$$

$$F_4(z, \Delta) = 2k^2 \cos \Delta \int_0^l I_s(s') K(z, s', \Delta) ds'$$

and

$$F_2(s, \Delta) = j\omega(\partial/\partial s) \int_{-h_1}^{h_2} q(z') K(s, z', \Delta) dz' \\ F_3(s, \Delta) = 2j\omega q(l) [K(s, l) - K(s, l, \Delta)] \\ F_4(s, \Delta) = k^2 \cos \Delta \int_{-h_1}^{h_2} I_z(z') K(s, z', \Delta) dz' \\ F_5(s, \Delta) = k^2 (1 + \cos 2\Delta) \int_0^l I_s(s') K(s, s', \Delta) ds' \quad (95)$$

Zero-order current and charge distributions for any Δ and normally incident fields have been obtained in [30] by solving (92) and (93) with the end conditions (71) and the junction conditions (72) and (73).

1.3.2 TRANSMISSION-LINE APPROACH

This section presents the formulation and solution of the basic differential equations describing the EMP induced voltages and currents on a group of conductors forming a transmission line. Throughout this section the cross-sectional dimensions of the transmission line are assumed to be small compared with a wavelength.

The propagation of a pure TEM mode on a two-conductor line is first discussed. Its simple concepts are then generalized to a multiconductor line. Energy propagation on a multiconductor line can be described by the propagation of a number of independent field configurations or modes.

Previous efforts in applying transmission-line theory to EMP problems have been restricted to simple transmission-line configurations, such as two cascaded sections or a simple branching of lines. Recently, work has begun on the development of a computer code for analyzing a network of arbitrarily interconnected transmission lines (both single and multiconductor lines). In this work a large matrix equation is derived for all of the unknown currents at each of the junctions, or nodes, of the transmission-line network, and then these currents are determined by matrix inversion. This process permits the inclusion of much more complex types of transmission-line networks, such as those having closed loops, than what has been previously analyzed.

In the case of lossy conductors an axial component of electric field exists in the vicinity of the conductors, so that propagation is only nearly TEM, or quasi-TEM. Deviation from strict TEM propagation also occurs when the dielectric medium, although homogeneous in the direction of propagation, displays inhomogeneous properties in the transverse plane. These departures from the ideal case can introduce severe analytical difficulties in solving transmission-line problems.

1.3.2.1 The Two-Conductor Line

Consider Fig. 8 in which the conductor axes of a uniform transmission line are parallel to the z-axis of a rectangular coordinate system. Assume the conductors to be lossless and embedded in a homogeneous isotropic dielectric with constitutive parameters ϵ , μ , σ . The integral form of one of Maxwell's equations gives

$$\oint_C \vec{E} \cdot d\vec{\ell} = -s\mu \int_A \vec{H} \cdot \vec{I}_n dA \quad (96)$$

where C is a curve enclosing the area A , and $s = j\omega$ on the $j\omega$ -axis of the complex frequency s -plane. If A lies completely in a plane transverse to the z -axis, then the fact that \vec{H} is transverse implies that

$$\oint_C \vec{E} \cdot d\vec{\ell} = 0 \quad (97)$$

which, in turn, implies that in any transverse plane, \vec{E} can be expressed as the negative gradient of a scalar potential ϕ

$$\vec{E} = -\nabla_t \phi = -\left(\frac{\partial \phi}{\partial x} \vec{I}_x + \frac{\partial \phi}{\partial y} \vec{I}_y \right) \quad (98)$$

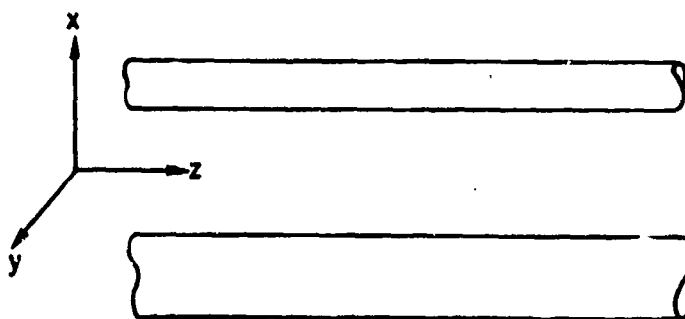


Fig. 8. Two-conductor line.

Since $\nabla \cdot \vec{E} = 0$, (98) becomes

$$\nabla \cdot \nabla_t \phi = \nabla_t^2 \phi = \frac{\partial^2 \phi}{\partial x^2} + \frac{\partial^2 \phi}{\partial y^2} = 0 \quad (99)$$

That is, in any transverse plane ϕ satisfies a two-dimensional Laplace's equation; hence, in any transverse plane \vec{E} appears at any instant as an electrostatic field. Such a field must originate and terminate on electric charges, and since there are none in the dielectric, they must appear on the conductors.

Differentiating (99) first with respect to x and then y and adding the results, one obtains

$$\frac{\partial^2 \vec{E}}{\partial x^2} + \frac{\partial^2 \vec{E}}{\partial y^2} = 0 \quad (100)$$

which, together with $\nabla^2 \vec{E} = \gamma^2 \vec{E}$, implies

$$\frac{\partial^2 \vec{E}}{\partial z^2} = \gamma^2 \vec{E} \quad (101)$$

where $\gamma = \sqrt{s\mu(\sigma + s\epsilon)}$. The solution of (101) is

$$\vec{E} = \vec{E}_1(x, y; s)e^{-\gamma z} + \vec{E}_2(x, y; s)e^{\gamma z} \quad (102)$$

where \vec{E}_1, \vec{E}_2 are arbitrary vector functions derivable from scalar potentials satisfying the two-dimensional Laplace equation (99). If Z_d denotes the dielectric-space impedance

$$Z_d = \frac{s\mu}{\gamma} = \left[\frac{s\mu}{\sigma + s\epsilon} \right]^{1/2} \quad (103)$$

then

$$\vec{H} = \pm Z_d^{-1} (\vec{i}_z \times \vec{E}) = \pm Y_d (\vec{i}_z \times \vec{E}) \quad (104)$$

with upper and lower signs for forward and back waves, respectively.

The charge Q' per unit length bounded by the electric field is

$$Q' = C'V \quad (105)$$

where C' is the capacitance per unit length between conductors. The current diverted through the dielectric is

$$I'_d = G'V \quad (106)$$

where G' is the leakage conductance per unit length. Finally, the magnetic intensity linking the conductors induces a counter-emf in series with the line given by

$$V'_L = s L' I \quad (107)$$

where L' is the inductance per unit length represented by the magnetic flux linkages, and I is the line current.

In Sec. 1.3.2.4 the line parameters C' , G' and L' will be discussed.

1.3.2.1.1 Line Excitation

A transmission line may be excited by an EMP field in a variety of ways. In the simplest case the line is in "free space" (i.e., far from other objects compared to its cross-sectional dimensions) and is excited by an electromagnetic wave. It may be situated above ground so distant that its propagation characteristics are unaffected by the ground parameters, but close enough that it is exposed to both incident and ground-reflected components of an EMP. It may be within the interior of a coaxial cable, which may have a solid shield or a braided shield for its outer conductor. In the latter case fields may be coupled locally into a line by incomplete shielding at cable connectors, at flanges joining sections of solid conduit enclosing the line, or at shield apertures that are required for other functions.

In all cases it is convenient to consider the incident field to be resolved into components transverse to the line and those parallel to it. The transverse components may be due to coupling from another distant line. The axial components of magnetic and electric field affect the line differently. The axial magnetic component induces currents that circulate around the peripheries of the conductors but produce no axial transmission line current. The axial electric field, on the other hand, induces antenna-mode currents on the conductors, which for the most part do not flow through the line terminations. However, because of the physical separation of the line conductors, there is generally a small difference in the excitation of the individual conductors by an axial electric field, which induces excitation sources in series with the line. This difference is entirely accounted for (via Faraday's induction law) by the transverse magnetic field.

1.3.2.1.2 Line Differential Equations

Two fundamental laws underlie the derivation of the line equations: Faraday's law (96) and the law of current continuity (43).

Fig. 9 represents a small increment of a two-conductor line. Although represented here as two conductors of finite cross section,

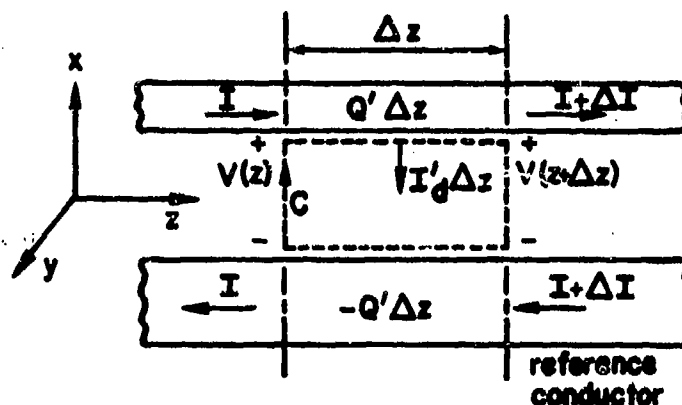


Fig. 9. Small increment of a two-conductor line.

it should be noted that one conductor could be an "infinite" ground plane. Alternatively, one conductor could be enclosed in the other, as in a coaxial line. To develop expressions for the line excitation for the special case of a two-conductor line, we begin by applying (96) to the contour C in Fig. 9. The right member of (96) is proportional to the magnetic flux Φ through the area A enclosed by C. The magnetic field \vec{H} is positive when directed as the translation of a right-hand screw turned clockwise. Thus, $-\Phi$ is positive when directed in the positive y direction.

The total magnetic flux linking the conductors has two sources: the incident magnetic field \vec{H}^i and the magnetic field due to the transmission line current.

Antenna-mode currents I_{c1} and I_{c2} are induced by the axial electric field. The total currents I_1 and I_2 in the conductors are, respectively,

$$\begin{aligned} I_1 &= I + I_{c1} \\ I_2 &= -I + I_{c2} \end{aligned} \quad (108)$$

Performing the integration indicated in the left-hand side of (96) we have

$$\oint_C \vec{E} \cdot d\vec{l} = -V(z) + 0 + V(z + \Delta z) + 0 = V(z + \Delta z) - V(z) = \Delta V \quad (109)$$

the integration along the conductors contributing nothing since $\vec{E} \cdot d\vec{l} = 0$ at the surface of lossless conductors.

For the two components of magnetic flux per unit length we introduce Φ'_L and Φ'_1 with

$$\Phi'_L \equiv L' I, \quad \Phi'_1 \equiv -L^i H_1^i \quad (110)$$

where L^i is a constant measured in henries, and H_1^i is the component of the incident magnetic field perpendicular to the plane containing the axes of two conductors of the line.

The total flux in the increment Δz is then given by

$$\phi' \Delta z = (L'I - L^i_{H_1} I^i) \Delta z \quad (111)$$

Substituting (109) and (111) in (96), dividing by Δz and passing to the limit, we obtain

$$\frac{\partial V}{\partial z} + sL'I = sL^i_{H_1} I^i \quad (112)$$

which is the first equation for the transmission line voltage and current in the s-domain.

To derive the second line equation we integrate the continuity equation and obtain (see Fig. 9)

$$\Delta I + I'_d \Delta z + sQ' \Delta z = 0$$

Rearranging, dividing by Δz and passing to the limit, we obtain

$$\frac{\partial I}{\partial z} + I'_d = -sQ' \quad (113)$$

which becomes, with the aid of (106),

$$\frac{\partial I}{\partial z} + G'V = -sQ' \quad (114)$$

The charge Q' has two sources: the TEM potential difference between conductors and the transverse impressed electric field. Calling these two charges Q'_V and Q'_1 we have

$$Q'_V = C'V \quad (\text{from line voltage } V) \quad (115)$$

$$Q'_1 = C^i E^i_1 \quad (\text{from incident electric field } E^i_1 \text{ perpendicular to the axes of conductors})$$

where C^i is a constant of proportionality measured in farads.

Thus, the second line equation becomes

$$\frac{\partial I}{\partial z} + (G' + sC')V = -sC_1^1 E_1^1 \quad (116)$$

The determination of the line parameters L' , C' , G' , and the coupling parameters L^1 and C^1 will be discussed in Sec. 1.3.2.4.

Finite conductivity of the line conductors affects the behavior of the line in two ways: it causes slight modifications in the line parameters, effects which are usually ignored at high frequencies; and it results in additional attenuation of waves on the line, thus affecting the value of the propagation constant. For the case of the two-conductor line, the second effect can be incorporated into the line equations without difficulty.

Eqs. (112) and (116) are the basic transmission line equations in the s -domain and they may be summarized in the following convenient form:

$$\begin{aligned} \frac{\partial V}{\partial z} + Z' I &= V'(s) \\ \frac{\partial I}{\partial z} + Y' V &= I'(s) \end{aligned} \quad (117)$$

where $V'(s)$ and $I'(s)$ are the per-unit-length sources to denote respectively the right-hand sides of (112) and (116), and Z' and Y' are the per-unit-length impedance and admittance of the line given by $Z' = R' + sL'$ and $Y' = G' + sC'$. Here, R' is the line resistance to be discussed in Sec. 1.3.2.4.

Recently, a new set of transmission-line equations has been proposed, which incorporates the effect of the "antenna-mode" currents [31]. Let I_1 and I_2 be the total currents on the two conductors and let I_d and I_c be defined by

$$I_d = \frac{1}{2} (I_2 - I_1), \quad I_c = \frac{1}{2} (I_2 + I_1) \quad (118)$$

It can be shown that for the case of an incident plane wave one has [31]

$$\frac{dV}{dz} + sL'I_d = -\mu s(\vec{h} \times \vec{I}_z) \cdot \vec{H}^i - sL'\alpha I_c \quad (119)$$

$$\frac{dI_d}{dz} + sC'V = -sC'\vec{h} \cdot \vec{E}^i + s\alpha Q'_c$$

where $Q'_c = - (1/s)(d/dz)I_c$, \vec{h} and α are given by (see Fig. 10)

$$h = |\vec{h}| = D \left[1 - \left(\frac{a+b}{D} \right)^2 \right]^{1/2} \left[1 - \left(\frac{a-b}{D} \right)^2 \right]^{1/2} \quad (120)$$

$$\alpha = C'(2\pi\epsilon)^{-1} [\operatorname{arccsch}(2b/h) - \operatorname{arccsch}(2a/h)]$$

for two conductors of circular cross-sections with radii a , b .

There are two points of paramount importance about (119). First, if one sets

$$I = I_d + \alpha I_c \quad (121)$$

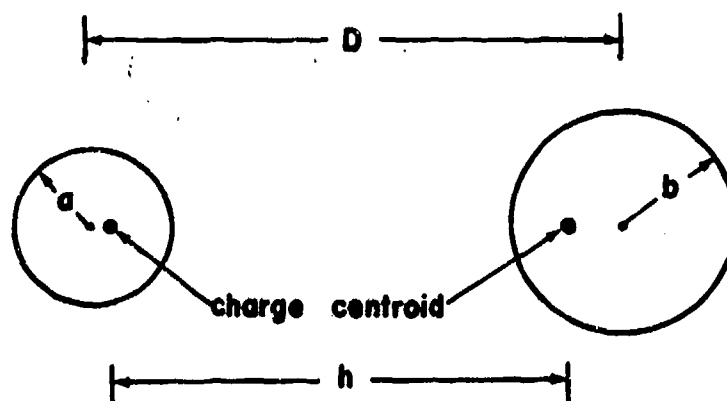


Fig. 10. Two-wire line of unequal radii.

where I is the line current of (117), then (119) reduces to (117). Secondly, the "common-mode" (or antenna-mode) current I_c defined by (118) is equal in magnitude and direction on both conductors, and hence is zero at the terminating impedances of a line of two equal-length conductors. In this case, I and I_c will have the same end conditions. (Note that one may define a common-mode current in such a way that it will not appear in (119).) This means that, as far as the currents at the terminating impedances are concerned, one may use (117) instead of (119). On the other hand, if one is interested in the total currents at other points along the line's conductors or the case where the line's conductors are of unequal length, one should resort to (119).

1.3.2.2 Multiconductor Lines and Cables

Fig. 11 depicts a multiconductor transmission line embedded in a homogeneous isotropic dielectric. For this case, the discussion in Sec. 1.3.2.1 up to and including (104) applies exactly here, except that we are now thinking in terms of $(N+1)$ conductors rather than two. The reasons for selecting a general line of $(N+1)$ conductors (rather than N) are two: first, among $(N+1)$ conductors there are only N independent potential differences; second, the total TEM current flowing in any cross section of the line must be zero, so

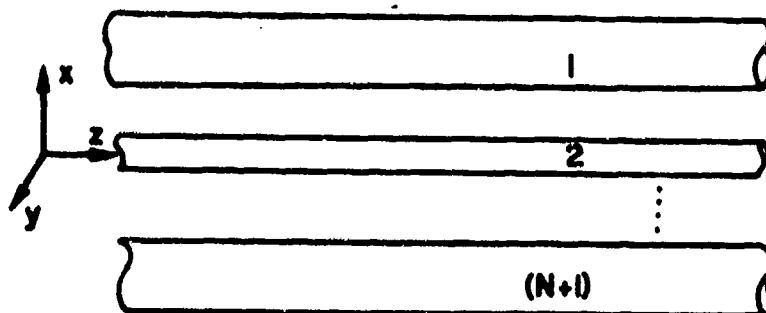


Fig. 11 $(N+1)$ -conductor line.

that one of the currents may be expressed as a linear sum of the remaining N , implying the existence of only N independent currents. Thus, the behavior of an $(N+1)$ -conductor line is characterized by N independent potentials and N independent currents. Such a line may then be referred to as an N -line. According to this definition the conventional two-conductor line is a 1-line characterized by a single potential difference and a single independent value of current.

Instead of speaking of potential differences it is convenient to choose one conductor as the reference or zero-potential conductor. The potential of any conductor is then its potential with respect to the reference or common conductor. When necessary, the reference conductor is called the "zeroth" conductor. Conductors other than the common conductor, when forced to zero potential, are said to be "grounded."

The potentials of the respective N conductors are denoted by the vector (V_n) . As before, in the transverse plane the potential ϕ satisfies Laplace's equation and the conductors are equipotentials. Consequently, electric charges Q'_n (for $n=1, \dots, N$) exist on the conductor surfaces, and standard theory relates these charges to the potentials by [32]

$$Q'_n = \sum_{m=1}^N C'_{nm} V_m \quad n=1, \dots, N \quad (122)$$

or, in matrix notation,

$$(Q'_n) = (C'_{nm})(V_m) \quad (123)$$

The quantities C'_{nm} are Maxwell's coefficients of capacitance with the following properties [33,34]

$$\begin{aligned} C'_{nn} &\geq 0 \text{ for every } n \\ C'_{nm} &\leq 0 \text{ for every } m \neq n \\ C'_{nm} &= C'_{mn} \text{ for every } n, m \end{aligned} \quad (124)$$

The quantities C'_{nm} are defined fundamentally as follows. Let V_k be different from zero, while $V_m = 0$, $m \neq k$; that is, suppose all conductors are grounded except the k th. Then (123) becomes

$$C'_{nk} = Q'_n / V_k, \quad n = 1, \dots, N \quad (125)$$

Evaluation of the C'_{nm} for specific configurations will be discussed in Chap. 2.4.

Because steady current flow in conductors obeys Laplace's equation with equipotential conditions on lossless conductors, analogous results apply to the currents flowing between conductors in a lossy dielectric, namely

$$(I'_{dn}) = (G'_{nm})(V_m) \quad (126)$$

where I'_{dn} is the total current per unit length in the dielectric leaving the n th wire, and G'_{nm} are coefficients of conductance with the properties

$$\begin{aligned} G'_{nn} &\geq 0 \text{ for every } n \\ G'_{nm} &\leq 0 \text{ for every } n \neq m \\ G'_{nm} &= G'_{mn} \text{ for every } n, m \end{aligned} \quad (127)$$

Furthermore, if $V_m = 0$ for $m \neq k$, then (126) gives

$$G'_{nk} = I'_{dn} / V_k, \quad n = 1, \dots, N \quad (128)$$

Finally, the magnetic flux ϕ'_{Ln} linking the n th conductor and ground is the resultant of currents flowing in the N independent conductors

$$\phi'_{Ln} = (L'_{nm})(I_m) \quad (129)$$

where the L'_{nm} , all positive or zero, are the line coefficients of inductance. Furthermore, the individual inductance coefficients are given by, with currents on all conductors being zero except the k th,

$$L'_{nk} = \Phi'_{L_n} / I_k, \quad n = 1, \dots, N \quad (130)$$

To derive the line equations for the total line voltage, one may visualize a generalization of Fig. 9 and then considers only the n th and reference conductors. The path C in Fig. 9 may be any path whose contour is confined to the z - and $(z + \Delta z)$ -planes and tangent to the n th and reference conductors. Following the same procedure that leads from (109) to (117) we get, in matrix form,

$$\frac{\partial}{\partial z} (V_n) + s(L'_{nm})(I_m) = s(L_n^{(1)})H_1^{(1)} \quad (131)$$

$$\frac{\partial}{\partial z} (I_n) + \left((G'_{nm}) + s(C'_{nm}) \right) (V_m) = -s(C_n^{(1)})E_1^{(1)}$$

1.3.2.2.1 Multiconductor Line With Lossy Conductors

In general, conductor losses depend on the distribution of current around the conductor peripheries. When the conductors are cylinders of small radii compared to conductor spacings, an extra term $(R'_{nm})(I_m)$ may be added to the left member of the first equation of (131), where (R'_{nm}) is a diagonal matrix in which R'_{nn} is the resistance (Ω/m) of the n th conductor, readily evaluated by standard means [32]. At frequencies sufficiently high that the conductor skin depth is small compared to the conductor radius of curvature, the effect of conductor losses can be accounted for by finding the peripheral current distributions on all conductors (assumed temporarily lossless) for a given current vector, and integrating the loss over all conductors. The attenuation constant representing these losses is then determined from

$$\alpha_c = -\frac{1}{2} \ln(1 - W_c/W_0) \quad (132)$$

where α_c is the part of the attenuation constant due to conductor losses (nepers/m); W_c is the total conductor power loss in one meter of line, and W_o is the total transmitted power at the point of conductor loss evaluation. An alternative expression is

$$\alpha_c = -\frac{1}{2W_o} \frac{dW_o}{dz} \quad (133)$$

Where the approximations used above are not justified, effective conductor resistance must be determined by complicated boundary-value procedures, generally requiring numerical analysis.

Further discussion on this subject appears in Sec. 1.3.2.4.

1.3.2.2.2 Multiconductor Transmission Line Modes

To solve a multiconductor transmission-line problem (131) subject to appropriate boundary (or load) conditions at the ends of the transmission line, one may first obtain the source-free solutions on the multiconductor line by solving the homogeneous version of (131) and one may then construct a particular solution with the excitation sources and loads present.

Let

$$\begin{aligned} (Z'_{nm}) &= s(L'_{nm}) \\ (Y'_{nm}) &= (G'_{nm}) + s(C'_{nm}) \end{aligned} \quad (134)$$

to be the series impedance-per-unit length and shunt admittance-per-unit-length matrices of the line. With no sources, (131) becomes

$$\begin{aligned} \frac{\partial}{\partial z} (V_n) + (Z'_{nm})(I_m) &= 0 \\ \frac{\partial}{\partial z} (I_n) + (Y'_{nm})(V_m) &= 0 \end{aligned} \quad (135)$$

from which one obtains

$$\frac{\partial^2}{\partial z^2} (I_n) = (Y'_{nm})(Z'_{nm})(I_n) \quad (136)$$

$$\frac{\partial^2}{\partial z^2} (V_n) = (Z'_{nm})(Y'_{nm})(V_n)$$

These equations seem difficult to solve at first, since the propagation matrices $(Y'_{nm})(Z'_{nm})$ and $(Z'_{nm})(Y'_{nm})$ are full matrices. It is possible, however, to diagonalize the propagation matrices by a transformation matrix (T_{nm}) consisting of the eigenvectors of the matrix $(Y'_{nm})(Z'_{nm})$, i.e.,

$$(T_{nm})^{-1}(Y'_{nm})(Z'_{nm})(T_{nm}) = (\gamma_{nn})^2 \quad (137)$$

where $(\gamma_{nn})^2$ is a diagonal matrix with elements equal to the corresponding eigenvalues.

Because (Z'_{nm}) and (Y'_{nm}) are symmetric, the matrix $(Z'_{nm})(Y'_{nm})$ can also be diagonalized by T_{nm} , viz.,

$$(T'_{nm})^T(Z'_{nm})(Y'_{nm})(T_{nm})^{-1} = (\gamma_{nn})^2 \quad (138)$$

where the superscript T denotes the transpose.

Let

$$(i_n) = (T_{nm})^{-1}(I_n), \quad (v_n) = (T_{nm})^T(V_n) \quad (139)$$

where i_n and v_n represent the modal amplitudes of the nth eigenmode. Then (136) can be put in the form

$$\frac{\partial^2}{\partial z^2} (i_n) = (\gamma_{nn})^2 (i_n) \quad (140)$$

$$\frac{\partial^2}{\partial z^2} (v_n) = (\gamma_{nn})^2 (v_n)$$

For a straight section of multiwire line consisting of perfect conductors immersed in a simple medium, the propagation matrix $(Y'_{nm})(Z'_{nm})$ has identical eigenvalues. In the case of an N-wire line plus a reference conductor, this matrix can be written as

$$(Y'_{nm})(Z'_{nm}) = s\mu(\sigma + s\varepsilon)(\delta_{nm}) = \gamma^2(\delta_{nm}) \quad (141)$$

where (δ_{nm}) is the unit matrix. This yields the value of γ as in (101). For this degenerate but extremely important case, any linearly independent set of modes may be used for describing the behavior of the multiconductor transmission line.

In the general case, however, the eigenvalues of the propagation matrix will be different. This occurs when the transmission-line cross section consists of a number of dielectrics with different parameters. When this is the case, the eigenvectors of $(Y'_{nm})(Z'_{nm})$ corresponding to a particular eigenvalue γ_{nn}^2 are uniquely determined (except for a scale factor) and are subsequently used to define the transformation matrix (T_{nm}) .

1.3.2.2.3 Load Voltage and Current Responses

The voltage and current modes derived in the last section can be used to calculate the currents on a driven multiconductor transmission line. Consider the case of an (N+1)-wire transmission line, as illustrated in Fig. 12. At a position z_s there are two vector sources $(V_n^{(s)})$ and $(I_n^{(s)})$, each consisting of N generators. For this line, there are N independent modes which propagate and contribute to the total current on the line. At each end of the transmission line there is a matrix load impedance (Z_{Lnm}) terminating the transmission line. The diagonal elements (Z_{Lnn}) correspond to the value of the impedance between the N wires and the reference conductor, and the off-diagonal terms Z_{Lij} correspond to the impedance elements between the ith and jth conductor.

On a section of multiconductor line with no sources the total current and voltage can be viewed as a combination of positive and negative traveling modes which must satisfy (140), the solution of which is given by

$$\begin{aligned} (i_n) &= e^{-(\gamma_{nn})z} (A_n) + e^{(\gamma_{nn})z} (B_n) \\ (v_n) &= e^{-(\gamma_{nn})z} (C_n) + e^{(\gamma_{nn})z} (D_n) \end{aligned} \quad (142)$$

where (A_n) , (B_n) , (C_n) and (D_n) are N-vectors which must be determined from the load and excitation conditions.

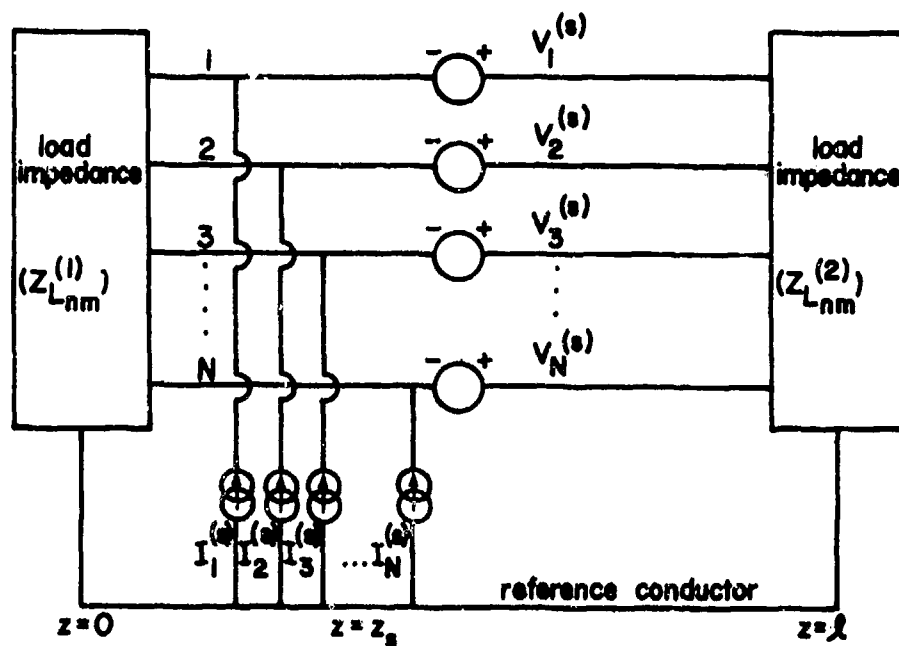


Fig. 12. A single length multiconductor transmission line with loads and lumped sources.

With the aid of (139), the total line currents and voltages on the source-free section of the line can be expressed as

$$\begin{aligned}(I_n) &= (T_{nm})e^{-(\gamma_{nn})z}(A_n) + (T_{nm})e^{(\gamma_{nn})z}(B_n) \\(V_n) &= (T_{nm})^{-1}e^{-(\gamma_{nn})z}(C_n) + (T_{nm})^{-1}e^{(\gamma_{nn})z}(D_n)\end{aligned}\quad (143)$$

By writing an equation in the form of (143) for each source-free section of the multiconductor line, and then using the impedance and source boundary conditions, as done in the case of the two-conductor line, the following matrix equation can be developed for the currents flowing at the matrix load impedances

$$\begin{bmatrix} (I_n(0)) \\ (I_n(l)) \end{bmatrix} = \begin{bmatrix} ((\delta_{nm}) + (\Gamma_{1nm})) & (0_{nm}) \\ (0_{nm}) & ((\delta_{nm}) + (\Gamma_{2nm})) \end{bmatrix} \quad (144)$$

$$\begin{bmatrix} (-\Gamma_{1nm}) & (T_{nm})e^{(\gamma_{nn})l}(T_{nm})^{-1} \\ (T_{nm})e^{(\gamma_{nn})l}(T_{nm})^{-1} & (-\Gamma_{2nm}) \end{bmatrix}^{-1} \begin{bmatrix} (\varphi_n)_1 \\ (\varphi_n)_2 \end{bmatrix}$$

where the terms $(\varphi_n)_q$, $q=1,2$ represent the source terms on the multiconductor line and are referred to as the combined current sources.

These terms are given by

$$\begin{aligned}(\varphi_n)_1 &= \frac{1}{2} (T_{nm})e^{(\gamma_{nn})z_s}(T_{nm})^{-1} \left((Z_{c_{nm}})^{-1}(V_n^{(s)}) + (I_n^{(s)}) \right) \\(\varphi_n)_2 &= \frac{1}{2} (T_{nm})e^{(\gamma_{nn})(l-z_s)}(T_{nm})^{-1} \left((Z_{c_{nm}})^{-1}(V_n^{(s)}) - (I_n^{(s)}) \right)\end{aligned}\quad (145)$$

Notice that the matrix equation in (144) has matrices as its elements. Thus it is referred to as a supermatrix equation.

The terms (Γ_{1nm}) and (Γ_{2nm}) are the generalized voltage reflection coefficients defined as

$$(\Gamma_{1nm}) = \left[(Z_{Lnm}^{(1)}) + (Z_{c_{nm}}) \right]^{-1} \left[(Z_{Lnm}^{(1)}) - (Z_{c_{nm}}) \right] \quad (146)$$

for the impedance load at $z=0$, and similarly for (Γ_{2nm}) at $z=l$ with $(Z_{Lnm}^{(2)})$ as the load impedance. In this equation, the term $(Z_{c_{nm}})$ represents the characteristic impedance matrix of the multiconductor line and is given by the relation

$$(Z_{c_{nm}}) = (Y'_{nm})^{-1} (T_{nm}) (Y_{nn}) (T_{nm})^{-1} \quad (147)$$

The treatment of distributed excitation, as opposed to the discrete excitation described above, can be regarded as a simple extension of the above formulae, by integrating over the $(V_n^{(s)})$ and $(I_n^{(s)})$ source distributions. For this case, the terms $(\vartheta_n)_1$ and $(\vartheta_n)_2$ in (145) take the form

$$(\vartheta_n)_1 = \frac{1}{2} \int_0^l (T_{nm}) e^{(Y_{nn})\xi} (T_{nm})^{-1} \left((Z_{c_{nm}})^{-1} (V_n^{(s)}(\xi)) + (I_n^{(s)}(\xi)) \right) d\xi \quad (148)$$

$$(\vartheta_n)_2 = \frac{1}{2} \int_0^l (T_{nm}) e^{(Y_{nn})(l-\xi)} (T_{nm})^{-1} \left((Z_{c_{nm}})^{-1} (V_n^{(s)}(\xi)) - (I_n^{(s)}(\xi)) \right) d\xi$$

which follows directly from superposition. Notice that now the voltage and current sources are per-unit-length quantities, and hence are denoted by a prime.

Once the transmission-line currents at the loads have been determined from (144) the line voltages at the loads can be determined as

$$(V_n(0)) = - (Z_{L_{nm}}^{(1)})(I_n(0)) \quad (149)$$

$$(V_n(l)) = (Z_{L_{nm}}^{(2)})(I_n(l))$$

Note that here, only the terminal responses of the multiconductor line have been discussed. The general line response for a multiconductor line can be evaluated using the same technique as for the two-wire line, but the results are generally not too useful for EMP applications.

It should be noted in passing that it is possible to develop an alternate formulation for the response of a multiconductor line, involving voltage reflection coefficients, the voltage eigenmodes and propagation constants, and the combined voltage sources. There is no reason for preferring one formulation to another, since each requires an equal amount of work for computations.

1.3.2.3 Analysis of Transmission Line Networks

The previous sections have discussed the solution for voltage and current of a single section of two-wire transmission line, and on a general multiconductor transmission line. In actual situations a single section of transmission line may not accurately model the physical configuration of conductors. Many cascaded transmission-line sections, branching transmission lines, or lines forming closed loops may be required for an accurate model of an electrical system.

As will be shown in this section, a general interconnected transmission-line network can be described by an equation similar to that of (144). By using the electrical properties of the individual transmission-line sections which comprise the transmission-line network (here referred to as transmission tubes), as well as details of the interconnection of the transmission lines at the junctions, it is possible to solve for the various load currents or voltages in a direct fashion, as discussed in [35 - 37].

Consider a multiconductor transmission-line network, with four interconnected uniform transmission lines and a common reference

conductor, as illustrated in Fig. 13a. It is desired to compute the voltage or current response at various junctions within the network. To facilitate the analysis, it is convenient to represent the network by a linear graph, consisting of junctions and tubes, as shown in Fig. 13b. This network can be described mathematically by one or more interconnection matrices [36] which indicate how the tubes and junctions are connected. For example, there are tube-tube, junction-junction, junction-tube and tube-junction matrices. Furthermore,

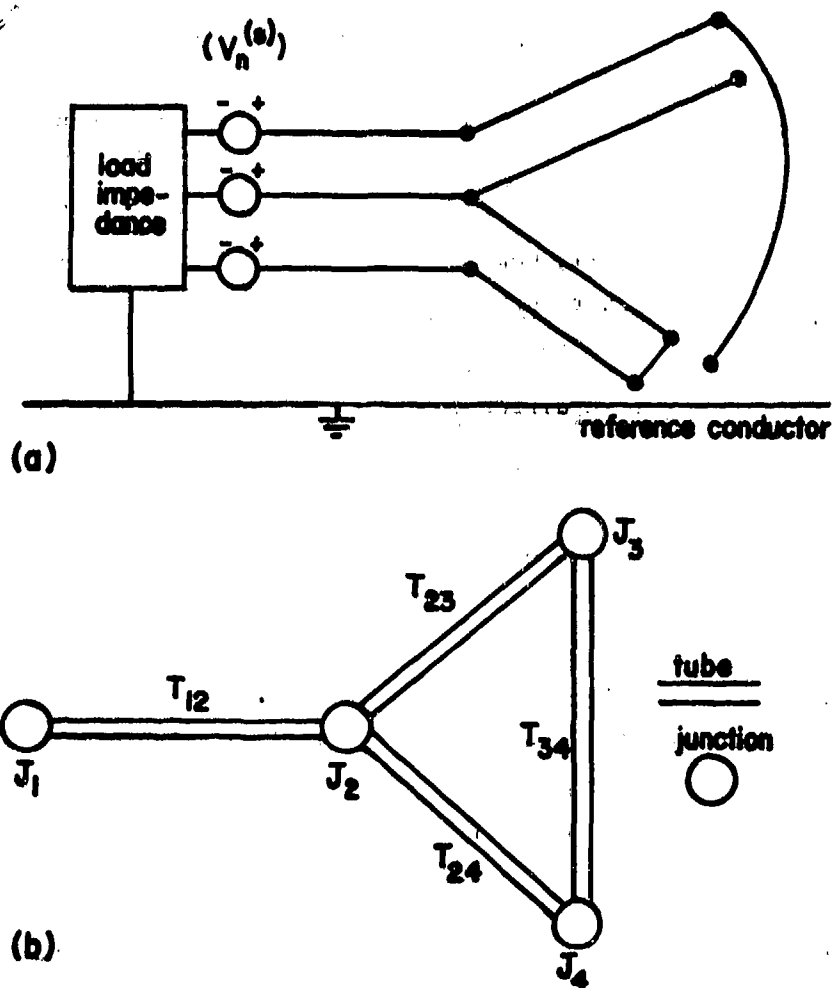


Fig. 13. (a) A simple multiconductor transmission-line network, and (b) its associated graph.

since the propagation analysis on the multiconductor tubes involves forward and backward propagating waves, it is possible to define a wave-wave interconnection matrix for which a typical element relates a particular incident wave at a junction to all the scattered waves at the same junction.

In Sec. 1.3.2.2.2 the propagation relations for voltage and current waves on a multiconductor line have been developed. A slightly different (but equivalent) method for determining these propagation relations has been developed in [36] and involves the concept of a combined voltage quantity, $(V_n)_q$, which is defined as

$$(V_n)_q = (V_n) + q(Z_{c_{nm}})(I_n) \quad (150)$$

The quantity q is $+1$ or -1 , depending on whether the combined voltage wave is forward or backward propagating, and (V_n) and (I_n) are the usual tube voltage and current vectors.

The combined voltage differential equation describing the propagation along the tube comes directly from the Telegrapher's equations and has the form

$$\frac{\partial}{\partial z} (V_n)_q + q(Z'_{nm})(Y'_{nm})(V_n)_q = (V'_n(s))_q \quad (151)$$

where $(V'_n(s))_q$ is a combined voltage source term involving the actual distributed voltage and current sources, $(V'_n(s))$ and $(I'_n(s))$, and is given by

$$(V'_n(s))_q = (V'_n(s)) + q(Z_{c_{nm}})(I'_n(s)) \quad (152)$$

Eq. (151) can be solved using the same diagonalization procedure used for (136) with the result that

$$\begin{aligned}
(V_n(z))_q &= (T_{nm})^T e^{-q(\gamma_{nm})z} (T_{nm})^{-1} (V_n(0))_q \\
&+ \int_0^z (T_{nm})^T e^{-q(\gamma_{nm})\xi} (T_{nm})^{-1} \\
&\times \left[(V'_n(s))(\xi) + q(Z_{c_{nm}})(I'_n(s))(\xi) \right] d\xi
\end{aligned} \tag{153}$$

Here the modal matrix (T_{nm}) and the diagonal eigenvalue matrix (γ_{nm}) are defined in (137) or (138).

Note that (153) relates the combined voltage at z to the same quantity at $z=0$ and to the distributed sources along the line. It is, essentially, a relation for forward and backward propagating voltage waves on the line. The total voltages on the line can then be determined as

$$(V_n) = \frac{1}{2} \left[(V_n)_+ + (V_n)_- \right] \tag{154}$$

and the line current is

$$(I_n) = (Z_{c_{nm}})^{-1} \frac{1}{2} \left[(V_n)_+ - (V_n)_- \right] \tag{155}$$

To apply (153) to the problem of analyzing a transmission-line network, it is possible to obtain two independent relations for the waves propagating away from the ends of the tubes in terms of the waves incident on the tube ends. For a single tube of length l , this takes the form

$$\begin{bmatrix} (V_n(0))_+ \\ (V_n(l))_- \end{bmatrix} = \begin{bmatrix} (0_{nm})(P_{nm}) \\ (P_{nm})(0_{nm}) \end{bmatrix} \begin{bmatrix} (V_n(l))_+ \\ (V_n(0))_- \end{bmatrix} + \begin{bmatrix} (V_n^{(s)})_+ \\ (V_n^{(s)})_- \end{bmatrix} \tag{156}$$

where the matrix (P_{nm}) is given by

$$(P_{nm}) = (T_{nm})^T e^{(\gamma_{nm})l} (T_{nm})^{-1} \quad (157)$$

and the source terms $(V_n^{(s)})_q$ are obtained from (153) with $z = l$ as

$$(V_n^{(s)})_+ = \int_0^l (T_{nm})^T e^{(\gamma_{nm})(l-\xi)} (T_{nm})^{-1} \times [V_n'(\xi, s) + (Z_{c_{nm}}) I_n'(\xi, s)] d\xi \quad (158)$$

$$(V_n^{(s)})_- = \int_0^l (T_{nm})^T e^{(\gamma_{nm})\xi} (T_{nm})^{-1} \times [V_n'(\xi, s) - (Z_{c_{nm}}) I_n'(\xi, s)] d\xi$$

Eq. (156), which is a matrix equation whose elements are themselves matrices, is called a supermatrix equation and can be written in a more compact form as

$$((V_n)_v) = ((P_{nm})_{uv}) : ((V_n)_u) + ((V_n^{(s)})_v) \quad (159)$$

where the subscripts $v=1,2$ and $u=1,2$, and the propagation supermatrix $((P_{nm})_{uv})$ denotes the sparse supermatrix containing the P terms in (156). For $v=1$ the term (V_n) represents the n -vector combined voltage reflected from the tube at $z=0$. Similarly, the $v=2$ term represents combined voltage reflected at $z=l$.

For a transmission-line network consisting of N_T tubes, there will be N_T equations like (156) describing the line currents. These may be expressed in supermatrix form as in (159) with $u, v = 1, 2, \dots, 2N_T$. In constructing this supermatrix equation, it should be noted that the wave-wave interconnection matrix describes the ordering of the individual block matrices, (P_{nm}) , within the supermatrix.

In addition to (159), it is necessary to develop a relationship between incident and reflected combined voltage waves at the network.

junctions to be able to solve for the network response. For a junction containing k tubes, the relationship between the reflected and scattered components can be expressed as

$$((V_n)_v) = ((S_{nm})_{uv}) : ((V_n)_u) \quad (160)$$

where the supervectors $((V_n)_u)$ and $((V_n)_v)$ consist of k vector components and the supermatrix $((S_{nm})_{uv})$ is a $k \times k$ block supermatrix. The elements of $((S_{nm})_{uv})$ depend upon the details of the interconnection between the various tubes at the junctions, the characteristic impedance of the tubes, as well as any impedance discontinuities (or loading) which may be present at the junction. This is discussed in more detail in [35].

The indices u and v here are not simply equal to $1, 2, \dots, k$, but depend on the values of u and v assigned to the k tubes connected to the junction under consideration, as described by the junction-wave interconnection matrix. Eq.(160) is also valid for the entire network by letting u and v run over all possible values found in the network, i.e., $u, v = 1, 2, \dots, 2N_T$.

After reordering the elements in the scattering equation (160), so as to correspond to the wave-wave interconnection matrix, it is possible to develop a single equation for all components of the combined incident voltages at the junctions of the network by equating $((V_n)_v)$ in (159) and (160). We then obtain

$$((V_n)_u) = [((S_{nm})_{uv}) - ((P_{nm})_{uv})]^{-1} ((V_n^{(s)})_v) \quad (161)$$

The total voltage at the ends of each tube in the network is then expressed via (154) and (160) as

$$((V_n)_k) = \frac{1}{2} [((V_n)_u) + ((V_n)_v)] = \frac{1}{2} [((\delta_{nm})_{uv}) + ((S_{nm})_{uv})] : [((S_{nm})_{uv}) - ((P_{nm})_{uv})]^{-1} ((V_n^{(s)})_v) \quad (162)$$

where $k=1,2,\dots,2N_T$ and N_T is the total number of tubes within the transmission-line network.

The expression in (162) is one form of the BLT equation, which has been named after the authors of [36]. Other variations of this formula may be written for the total current. The above BLT equation describes the voltage response at an arbitrary complex frequency s for the entire network. Transient results for the network can be obtained using Laplace or SEM methods.

1.3.2.4 Determination of Line Parameters

1.3.2.4.1 Line Capacitance, Conductance and Inductance

We have already seen that (C'_{nm}) can be determined by solving a two-dimensional electrostatic problem. It can be shown that (L'_{nm}) and (G'_{nm}) are simply related to (C'_{nm}) . The field coupling coefficients $(L_m^{(i)})$ and $(C_m^{(i)})$ can also be solved as electrostatic problems when the incident field is essentially uniform throughout the line cross section.

It is worthwhile, therefore, to devote some brief consideration to the solution of the two-dimensional electrostatic problem. For more detail one may consult [31-34, 38-48].

Three general methods of solution are available: mathematical, experimental and numerical. Mathematical methods depend on solving (122), or the inverse equation

$$V_n = \sum_{m=1}^N S'_{nm} Q'_m \quad n=1,\dots,N \quad (163)$$

where the S'_{nm} , called elastance coefficients, are defined by

$$S'_{nk} = V_n / Q'_k \quad n,k=1,\dots,N$$

$$Q'_m = 0 \text{ for } m \neq k$$

In matrix notation,

$$(V_n) = (S'_{nm})(Q'_m) \quad (164)$$

whence

$$(Q'_n) = (S'_{nm})^{-1} (V_m) \quad (165)$$

$$(C'_{nm})(S'_{nm}) = (S'_{nm})(C'_{nm}) = (\delta_{nm})$$

Some results of analysis are given in Chap. 2.4.

Capacitance may be measured directly by standard methods, or, if more convenient, a scaled model of the actual configuration may be used. Analog measurements using an electrolytic tank or a conductive sheet (Teledeltos paper) may be employed [43].

Numerical methods use high-speed digital computers to solve large sets of simultaneous linear equations derived by writing the Laplace differential equation as a finite difference equation, or to approximate the integral of Poisson's equation

$$V = \frac{1}{4\pi\epsilon} \int_S \frac{\rho}{r} dS'$$

as a finite sum [43-48]. Space limitation precludes discussion of this interesting subject in detail.

The conductance coefficients are readily determined from the capacitance coefficients. The relation is

$$(G'_{nm}) = \frac{\sigma}{\epsilon} (C'_{nm}) \quad (166)$$

In fact, (166) is the basis for determination of capacitance by the electrolytic tank and conductive sheet methods [38,43].

The inductance matrix (L'_{nm}) may also be computed from the capacitance matrix and the constitutive parameters. It may be shown that the matrices (L'_{nm}) and (C'_{nm}) obey the relationship

$$(L'_{nm})(C'_{nm}) = (C'_{nm})(L'_{nm}) = \mu\epsilon(\delta_{nm}) \quad (167)$$

for lines in homogeneous isotropic media.

For media varying in the cross-sectional dimensions of the line coefficients are frequently computed as though the system were electrostatic, while the inductance coefficients are determined as though the medium permittivity were uniform.

1.3.2.4.2 Effects of Conductor Losses, Discontinuities and Inhomogeneties

In some cases, the conductors comprising the transmission line cannot be considered to be perfectly conducting but are good conductors, defined by the inequality

$$\frac{\sigma}{\omega \epsilon} \gg 1 \quad (168)$$

A plane wave traveling over the surface of a semi-infinite plane conductor induces surface current J (A/m) in the conductor. The loss in a surface one meter wide and one meter long in the direction of propagation is

$$W_l = J^2 R_o \quad \text{watts/m}^2 \quad (169)$$

where R_o is the effective resistance in ohms per square of a section of the conductor one meter wide and one meter long. If δ is the skin depth, then

$$R_o = 1/(\sigma \delta) = \sqrt{\pi f \mu / \sigma} \quad (170)$$

For conductors with curvilinear cross sections, but with radii of curvature much greater than the skin depth, (170) is a good approximation for the peripheral unit resistance, and is commonly used. Thus, the resistance (Ω/m) of a solid round conductor of radius a is

$$R'_a \approx \frac{R_o}{2\pi a} = \frac{1}{2a} \sqrt{f \mu / \pi \sigma} \quad \Omega/m \quad (171)$$

If f is in MHz, a in mm, and $\sigma = 5.8 \times 10^7$ y/m for copper conductors, then

$$R'_a \approx 0.0415 \sqrt{f}/a \quad \Omega/m \quad (172)$$

Eq. (171) assumes that current is distributed uniformly around the conductor cross section. For a two-conductor line with conductor radii equal to a , the line resistance, assuming uniform current distribution, is $2R'_a$, i.e.,

$$R' = 2R'_a \approx \frac{1}{a} \sqrt{f\mu/\pi\sigma} \quad (173)$$

However, when the conductors are in close proximity, the current distribution is disturbed. In that case, we can derive the conductor resistance through the solution of an electrostatic problem. For instance, for a round conductor of radius a and a circumferential linear current density J , the conductor power loss per meter of line is

$$W'_c = aR_o \int_0^{2\pi} J^2 d\phi \quad (174)$$

The conductor resistance R' is then given by

$$R' = \frac{W'_c}{I^2} = \frac{aR_o}{Q'^2} \int_0^{2\pi} \rho^2 d\phi \quad (175)$$

where

$$Q' = a \int_0^{2\pi} \rho d\phi$$

and ρ is the conductor surface charge density along the circumference of the wire, determined as the solution of an electrostatic problem. For instance, the correct value for the two-conductor line resistance previously given by (173) is

$$R' = \frac{1}{a} \left(\frac{f\mu}{\pi\sigma} \right)^{\frac{1}{2}} \left[1 - \left(\frac{2a}{D} \right)^2 \right]^{-\frac{1}{2}} \quad (176)$$

where D is the separation of the lines.

Thus, given a system of conductors with an assigned set of conductor potentials, the various charge distributions Q'_n and therefore the effec-

tive resistances can be found. It must be emphasized that every different set of potentials results in a (generally) different set of charge distributions, therefore different values of line attenuation. The only exception is the two-conductor ($N=1$) line.

Line discontinuities may occur for a variety of reasons: (a) line terminations themselves constitute discontinuities; (b) the line may pass near one or more objects that constitute geometric disturbances in the uniformity of the line cross section; (c) cables may contain occasional holes or slots that disturb cross-section uniformity. All such disturbances give rise to higher-order modes of propagation which, because of the line's small electrical cross section, attenuate rapidly in the vicinity of the discontinuity. Their effect can be accounted for by a simple lumped-constant network at the point of discontinuity. A number of examples of such equivalent circuits is given in [49,50].

When a multiconductor line is embedded in an inhomogeneous dielectric, as occurs frequently, for instance, in a multiwire cable, propagation is no longer in a pure TEM or single mode. Strictly speaking, the use of static values of capacitance, inductance and conductance is erroneous; however, when the line cross section is small compared to a wavelength, the errors are not expected to be serious. Evaluation of such errors is generally very complicated. Some elementary cases have been analyzed to obtain information regarding the error order of magnitude to be expected [38].

1.3.2.4.3 Experimental Determination of Line Parameters

In many practical situations, it may be difficult to compute the transmission-line parameters from a knowledge of the geometrical properties of the line. An alternate approach is to measure voltages and/or currents on the line with various load configurations, and then to evaluate the line parameters. A description of various techniques for single and multiwire transmission lines is given in [51].

One approach to the problem of determining the parameters of a two-wire line, assumed to be lossless, is to perform transient measurements at one end of the transmission line with a time-domain reflectometer

(TDR). The TDR launches a very sharp voltage step into the line and then measures the total (reflected plus incident) voltage at the line's input as a function of time. The TDR records the instantaneous voltage reflection coefficient Γ_v given by

$$\Gamma_v = \frac{Z_c - Z_g}{Z_c + Z_g} \quad (177)$$

where Z_c is the characteristic line impedance seen by the TDR and Z_g is the internal impedance of the TDR. With a measurement of Γ_v from the TDR the impedance of the two-wire line being measured is given by

$$Z_c = Z_g \left(\frac{1 + \Gamma_v}{1 - \Gamma_v} \right) \quad (178)$$

For most TDR's the generator impedance Z_g is 50 Ω .

In addition to measuring the impedance level on the transmission line, the TDR can be used to determine the imaginary part of the propagation constant γ on the line. This is done by noting the time interval Δt between reflections at the near and far ends of the cable. For a line of length ℓ , this time is given by

$$\Delta t = \frac{2\ell}{v} \quad (179)$$

where v is the speed of propagation on the line. The imaginary part of the propagation constant can then be expressed as

$$\beta = \text{Im}(\gamma) = \frac{\omega}{v} = \omega \frac{\Delta t}{2\ell} \quad (180)$$

where ω is the angular frequency.

The imaginary part of the series impedance per unit length of the line is

$$\text{Im}(Z'(s)) = \text{Im}(\gamma)Z_c = \omega \frac{\Delta t}{2l} Z_c \quad (181)$$

which, together with (178), gives a series inductance per unit length as

$$L' = \frac{\Delta t}{2l} Z_g \left(\frac{1 + \Gamma_v}{1 - \Gamma_v} \right) \quad (182)$$

and a shunt capacitance per unit length

$$C' = \frac{\Delta t}{2l} \frac{1}{Z_g} \left(\frac{1 - \Gamma_v}{1 + \Gamma_v} \right) \quad (183)$$

For multiconductor lines, the TDR measurements are somewhat more complicated due to the fact that multiple propagation constants can exist on the line. In this case an alternate set of measurements in the frequency domain can be used to determine the parameters of a lossless multiconductor line [51]. This approach involves measuring the input impedance matrix (Z_{nm}^{sc}) of the line at one end with the other end shorted and the dual quantity, the input admittance matrix (Y_{nm}^{oc}), with the other end in an open circuit configuration. If the line is assumed lossless and the transmission line is electrically short, i.e., $\omega l/c \ll 1$, these open and short circuit measurements lead directly to the per-unit-length line parameters as

$$(L'_{nm}) = (Z_{in_{nm}}^{sc}) / j\omega l \quad (184)$$

$$(C'_{nm}) = (Y_{in_{nm}}^{oc}) / j\omega l$$

where l is the line length and the general complex frequency s has been replaced by $j\omega$.

1.3.2.5 External Coupling Parameters

Transmission lines and cables are excited by external fields in a variety of ways. Perhaps, the prototypical example is that of an isolated

two-conductor line subject to a plane wave at arbitrary incidence. Other situations include (a) distributed excitation of systems of one or more wires close to a metal surface or to conducting earth; (b) distributed excitation of the interiors of cables through penetration of solid or braided shields; (c) localized excitation of the interiors of cables through leaks at connectors; (d) "point" excitation of conduit interiors through leaks at conduit joints.

It is convenient to separate the incident electric and magnetic field into components parallel to the line axis and those transverse to the axis. Components transverse to the axis appear ordinarily to be most important in exciting the line, and will first be discussed below. By Faraday's induction law, variation in the axial component of electric intensity across the line is equivalent to the transverse magnetic field linking it.

1.3.2.5.1 Incident Field Components Transverse to a Two-Conductor Line

Because of the small transverse dimensions of the line it is possible to solve for the transverse coupling parameters, or to measure them experimentally, by treating them as electrostatic quantities, i.e., capacitances or combinations of capacitances. This situation can be appreciated intuitively by imagining the excitation fields to be the result of a wave on a parallel-plate transmission line enclosing the given line (Fig. 14). The parallel plates are sufficiently sepa-

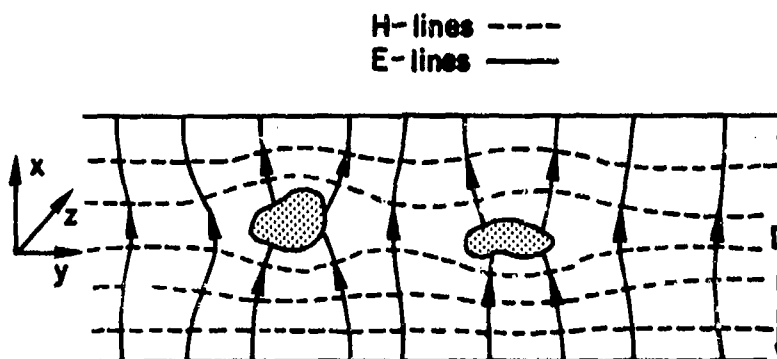


Fig. 14. Parallel-plate line enclosing two-wire line.

rated from the line, so that the reaction of currents and charges on the line does not affect the values of current and charge on the plates. Thus, the E-field coupling problem is reduced essentially to that of capacitance coupling between the two-conductor line and the plate line. The H-field coupling is one of inductive coupling, which is directly related to an electrostatic problem. Some problems using this concept are solved in [38].

An elegant theoretical approach starting with fundamental concepts is used in [31]. For a line of two conductors with arbitrary cross sections in a uniform field, the incident-field forcing functions of (117) are given by the first terms on the right side of (119). For a plane wave incident on an isolated two-conductor line, a simple relation exists between $V'(s)$ and $I'(s)$ of (117) if the Poynting vector of the incident wave makes an angle θ with the line axis, and the E-vector is parallel to the plane containing the conductors' axes. Then

$$\begin{aligned} V'(s) &= \gamma Z_0 H_0 h e^{-\gamma z \cos \theta} \\ I'(s) &= -\gamma \frac{E_0 h}{Z_c} \cos \theta e^{-\gamma z \cos \theta} \end{aligned} \quad (185)$$

where H_0 , E_0 are the magnetic and electric field incident on the line at $z=0$, Z_0 is the free-space impedance, and Z_c is the line characteristic impedance.

For a single conductor over a lossless ground plane, the above equations can also be used for determining the line excitation. Because of reflection from the ground, the effective values of H_0 and $E_0 \cos \theta$ are doubled in (185), while

$$h = D_g \left[1 - (a/D_g)^2 \right]^{1/2} \quad (186)$$

where a is the conductor radius and D_g is the height of the conductor center above the ground plane. The value of Z_c also changes accordingly.

1.3.2.5.2 Transverse Field Coupling to a Coaxial Cable Near a Perfectly Conducting Ground

One important transmission-line configuration often used for EMP analysis is a coaxial cable whose inner conductor is excited by an incident EMP. The EMP field is incident on the cable exterior, with coupling parameters computed as though it were a solid conductor. The induced current on the cable exterior gives rise to a series distributed voltage in the interior of the cable given by [52,53]

$$V'(s) = Z_T' I_t \quad (187)$$

where I_t is the total current flowing on the cable, and Z_T' is the transfer impedance which will be discussed in Chap. 2.4.

The geometry of a braided shield, however, is such as to preclude any possibility of a tractable mathematical model that resembles closely an actual shield. A number of ingenious approximate models have been suggested and analyzed [54 - 60] and, in at least one case, compared with measured data [54]. In spite of the fact that some of the experimental data had been based on partly erroneous concepts concerning the coupling mechanism [61] the calculated and measured values agreed within a factor of about 3 to 1. A developed section of a braided shield is shown in Fig. 15. As a result of the incomplete coverage of the criss-crossed wire braids, small diamond-shaped apertures occur through which both electric and magnetic fields can penetrate, the penetrability increasing with frequency. In addition, magnetic field diffuses through the solid portion of the shield, diminishing with increasing frequency. The determination of the distributed sources ($V_n^{(s)}$) and ($I_n^{(s)}$) can be found in Chap. 2.4.

1.3.2.5.3 Axial Field Coupling to Transmission Lines

For conductors with electrically small cross sections, an incident axial magnetic field component is of no practical importance. An axial electric field component, on the other hand, affects TEM transmission in two ways. First, the variation of this field component across the line

due primarily to space phase shift can be accounted for by the transverse magnetic field component, which has already been considered. Second, the average value of the axial electric intensity induces antenna-mode currents I_c and charges Q_c' on the conductors, as defined in (118). For more details the reader is referred to [31].

1.3.2.5.4 Field Coupling to a Multiconductor Line

The determination of the field excited sources $(V_n^{(s)})$ and $(I_n^{(s)})$ has been discussed recently in [62]. For a general coaxial multiconductor line these sources take the form

$$\begin{aligned} (V_n^{(s)}(z)) &= (Z_{T_n}'(z))I_t(z) + \sum_{m=1}^2 (Z_{T_n}'(z))_m (H_m^1(z)) \\ (I_n^{(s)}(z)) &= (\Omega_{T_n}'(z))Q_t'(z) + \sum_{m=1}^2 (\Omega_{T_n}'(z))_m (D_m^1(z)) \end{aligned} \quad (188)$$

In this relation I_t and Q_t' represent the total current and charge per unit length on the outer sheath of a coaxial multiconductor line. The other terms, which are summed over m (the three orthogonal vector

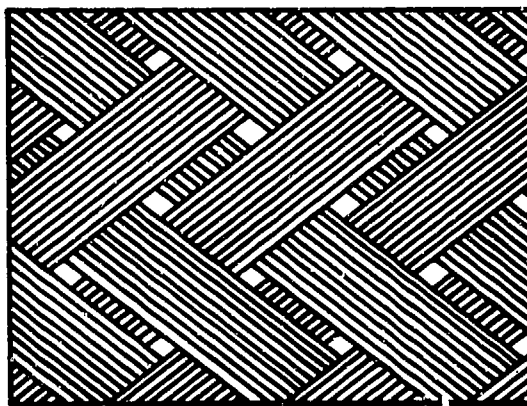


Fig. 15. Braid pattern developed on a plane.

directions, with $m=3$ corresponding to the direction of propagation on the line), relate the sources to the appropriate components of the incident \vec{H}^i and \vec{E}^i fields through the transfer impedance vectors $(Z_{Tn}(z))_m$ and the charge transfer functions $(Q_{Tn}(z))_m$.

The determination of the source terms for an open multiconductor transmission line has also been discussed in [38,63] for the special case of round conductors with radii small compared to their separation. Under this assumption of no interactions among the small conductors these source terms take the form

$$\begin{aligned} (V'_n(s)(z)) &= s\mu_0 \left(\int_0^{d_n} H_{1n}^i(\xi, z) d\xi \right) \\ (I'_n(s)(z)) &= -s(C'_{nm}) \left(\int_0^{d_m} E_{1n}^i(\xi, z) d\xi \right) \end{aligned} \quad (189)$$

where d_n represents the distance from the reference conductor to the n th conductor, H_{1n}^i is the perpendicular component of the incident magnetic field passing through the area between the reference and the n th conductor, and E_{1n}^i is the transverse component of the incident electric field between the conductors. For lines with cross sections small compared with a wavelength, such that \vec{H}^i and \vec{E}^i do not vary appreciably over the cross section, these terms can be approximated as

$$\begin{aligned} (V'_n(s)(z)) &= (s\mu_0 d_n H_{1n}^i(z)) \\ (I'_n(s)(z)) &= -s(C'_{nm})(d_m E_{1n}^i(z)) \end{aligned} \quad (190)$$

For a more general multiconductor cable whose wire radii may be comparable to the wire separation, (190) is not valid due to the non-uniform distribution of charges and currents around the wires. The above source terms for thick wire conductors as well as the antenna-mode

excitation for a multiconductor transmission line have not been investigated in detail, and remain an area open for future research.

An alternate approach to determining the external coupling vectors for a multiconductor cable is to measure them experimentally. This approach will require a generalization of the accepted technique of exciting the cable through an auxiliary coaxial cylinder surrounding it [64-66]. However, care must be taken that the results are interpreted properly [61].

1.3.3 CIRCUIT APPROACH

The circuit approach is essentially a low-frequency method useful for wavelengths much greater than the overall dimensions of the system under consideration. When this assumption holds, the electrical response of the system can be described by the conventional circuit theory. This theory is expressed in two laws, the Kirchhoff current and voltage laws. These two laws take extremely simple mathematical form, namely, the form of algebraic and ordinary differential equations. For this reason the circuit approach quickly leads to simple and physically interpretable results. Besides the analytical ease of this approach, the circuit concept is a powerful tool for qualitative thinking, often shedding valuable light on the many electromagnetic interactions taking place within a complex system. But two important points must be borne in mind in applying the circuit concept to EMP interaction problems. The circuit approach is an approximation to the transmission-line approach (Sec. 1.3.2) which, in turn, is an approximation to the integral-equation approach (Sec. 1.3.1). Another point is that the circuit approach is incomplete in the sense that it gives no information on the value of the lumped circuit elements (the resistance, inductance, and capacitance) of the object under consideration. These elements must be deduced from either field theory or experimental measurements.

In this section we will first discuss the relationship of Kirchhoff's circuit theory to Maxwell's field theory starting from Maxwell's equations in integral form. This relationship is then re-examined from the customary

viewpoint of the electrical engineer through the use of vector and scalar potentials. We then proceed to derive the circuit properties of an object in infinite space with the aid of the complex Poynting theorem expressed in terms of current and charge densities on the external surface of the object. With this theorem the positive real (p.r.) characteristics of the driving-point impedance or admittance can be proved, the resonance condition can be established, and the damping of each resonant (natural) mode by radiation can be calculated. This theorem also leads, at the low-frequency limit, to the concept of energy functions in terms of which the Kirchhoff voltage law can be re-derived by the Lagrangian method. To end this section we will briefly discuss the equivalent circuit representations of discontinuities in an otherwise uniform transmission line or waveguide, and the circuit descriptions of the dynamic behaviors of several different kinds of modes, such as the waveguide modes, the cavity modes, the leaky modes, and the natural modes.

1.3.3.1 Circuit Theory via Maxwell's Equations in Integral Form

A close relationship between circuit theory and field theory can be found in Maxwell's equations written in integral form [67-69]

$$\oint_C \vec{E} \cdot d\vec{l} = - \frac{d}{dt} \int_S \vec{B} \cdot d\vec{S} \quad (191)$$

$$\oint_C \vec{H} \cdot d\vec{l} = \frac{d}{dt} \int_S \vec{D} \cdot d\vec{S} + I \quad (192)$$

where the surface S spans the contour C (Fig. 16), I is the total conduction current crossing the surface S , and the circle through the integral sign is used to denote that the contour is a closed curve. Note that in (191) and (192) all spatial coordinates are integrated out, as is the case with Kirchhoff's laws in circuit theory.

To illustrate how (191) can be applied to EMP interaction problems we consider a conducting loop immersed in a slowly time-varying magnetic

field $\vec{B}^1(t)$ and calculate the induced current I in the loop (Fig. 17a). Let us take the contour C anywhere inside the loop. Then, using Ohm's law $\vec{J}_V = \sigma \vec{E}$, one gets from the left-hand side of (191)

$$\oint_C \vec{E} \cdot d\vec{l} = RI \quad (193)$$

where R is the loop's resistance and is given by

$$R = \oint_C \frac{dl}{\sigma A} \quad (194)$$

if \vec{J}_V is uniformly distributed over the cross-section A of the wire. The direction of the induced current I is dictated by Lenz's rule, which states that the direction of the induced current in the loop is such that it tends to oppose the change of flux linking the loop [67,70].

To evaluate the right-hand side of (191) we write \vec{B} as the sum of the incident and scattered magnetic fields, and obtain

$$\frac{d}{dt} \int_S \vec{B} \cdot d\vec{S} = \frac{d\phi^1}{dt} + \frac{d\phi^s}{dt} \quad (195)$$

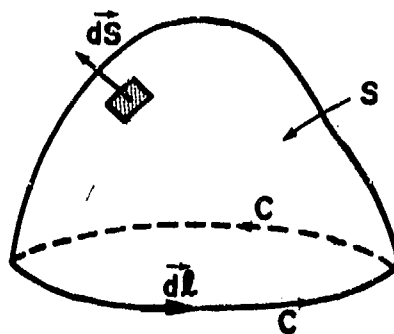


Fig. 16. A surface S spanning the closed curve C .

where ϕ^i and ϕ^s are, respectively, the total flux of the incident and scattered field \vec{B}^i and \vec{B}^s linking the loop, and ϕ^i is equal to \vec{B}^i times the effective area \vec{A}_{ef} of the loop, namely [71]

$$\phi^i = \vec{B}^i \cdot \vec{A}_{ef} \quad (196)$$

Since ϕ^s is proportional to the induced current I we write

$$\phi^s(t) = LI(t) \quad (197)$$

where the proportionality constant L is the so-called self-inductance of the loop. Substitution of (193), (195) and (197) in (191) gives

$$L \frac{dI}{dt} + RI = V_{oc} \quad (198)$$

$$V_{oc} \equiv - \frac{d\phi^i}{dt}$$

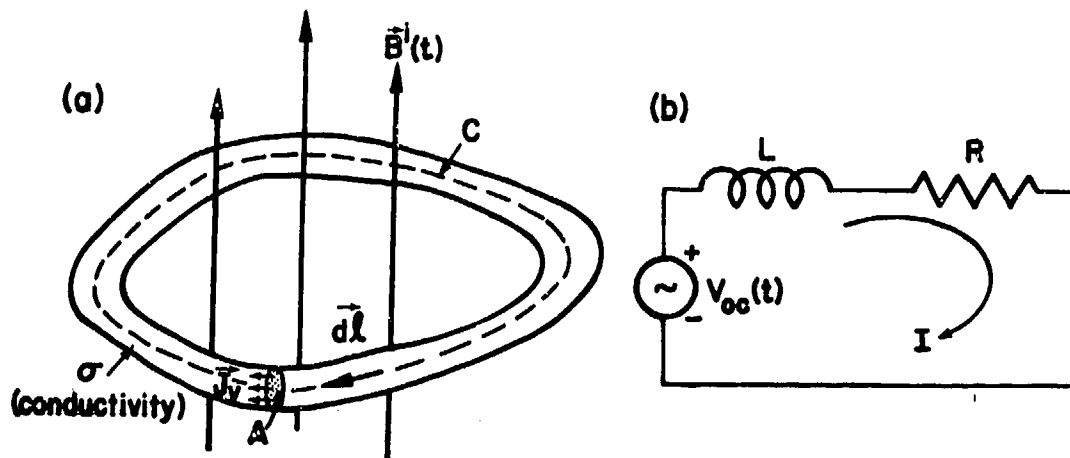


Fig. 17. (a) A conducting loop in a time-varying magnetic field, (b) Equivalent circuit of (a).

which expresses the Kirchhoff voltage law for a RL network that the total voltage drop around a closed loop is zero. The circuit representation of (198) is shown in Fig. 17b.

We now turn to (192) and see how it can be applied to calculate the induced voltage on a hatch in a large ground plane exposed to a slowly time-varying electric field (see Fig. 18a). We first split the contour C into $C_+ + C_-$ and the surface S into $S_+ + S_-$, where the subscripts \pm refer to the upper and lower surfaces of the geometry of the problem, as shown in Figs. 18a,b. With the direction of the conduction current I in the gasket as defined in the figures, the left-hand side of (192) gives

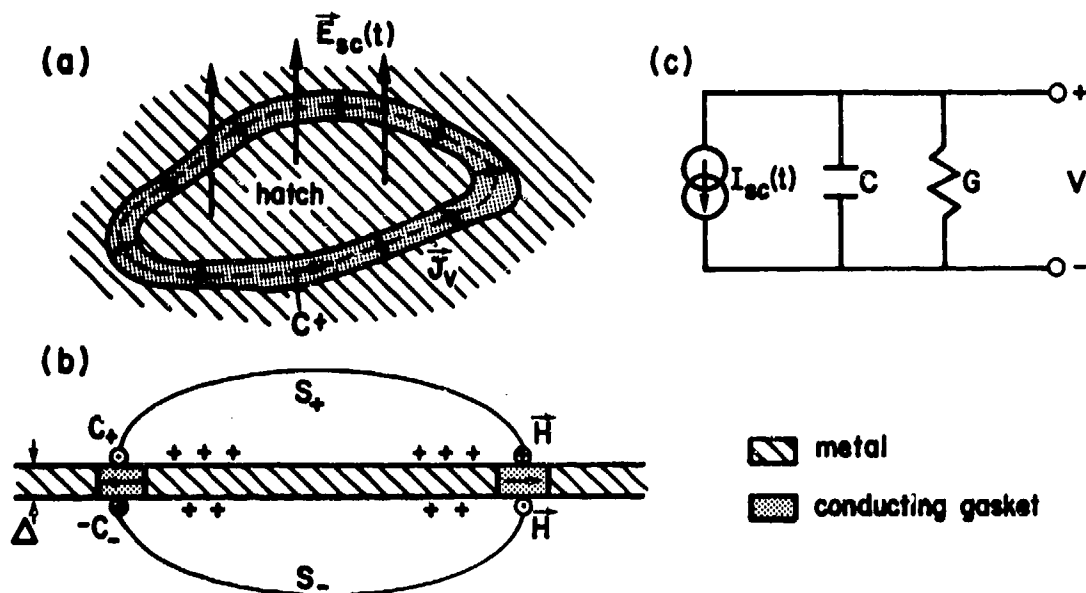


Fig. 18. (a) A hatch aperture with a conducting gasket in a time-varying electric field, (b) cross-sectional view of (a), in which $\odot(\bullet)$ points out(into)the pages, and (c) equivalent circuit of (a).

$$\oint_{C_+ + C_-} \vec{H} \cdot d\vec{l} = -I = -GV \quad (199)$$

where V is the induced voltage on the hatch with respect to the ground plane and G is the conductance of the hatch given approximately by

$$G = \frac{\Delta}{w} \oint_C \sigma dl \quad (200)$$

where w and Δ are the average width and thickness of the gasket and σ is the gasket's conductivity.

The right-hand side of (192) can be evaluated in the same manner as (195). Thus,

$$\begin{aligned} \frac{d}{dt} \int_S \vec{D} \cdot d\vec{S} &= \frac{d}{dt} \int_{S_+ + S_-} (\vec{D}_{sc} + \vec{D}^s) \cdot d\vec{S} \\ &= I_{sc} + \frac{dQ}{dt} \end{aligned} \quad (201)$$

where Q is the total charge on the hatch due to the scattered field \vec{D}^s alone and I_{sc} is equal to the equivalent area A_{eq} of the hatch multiplied by the short-circuit displacement current \vec{D}_{sc} , namely [71]

$$I_{sc} = A_{eq} \frac{d}{dt} D_{sc} \quad (202)$$

The charge Q is of course related to the induced voltage V through

$$Q(t) = C V(t) \quad (203)$$

and the constant C is just the capacitance of the hatch with respect to the ground plane. After substituting (199), (201) and (203) into (192) we obtain

$$C \frac{dV}{dt} + GV = -I_{sc} \quad (204)$$

which is the Kirchhoff current law stating that the total current flowing into or leaving a node is zero. The circuit representation of (204) is shown in Fig. 18c.

In circuit theory Fig. 18c is said to be the dual of Fig. 17b, and vice versa [72]. In field theory the duality is a direct consequence of certain symmetries in Maxwell's equations [73], manifesting itself in the principle of Babinet for a plane screen [74]. If the resistive loop of Fig. 17a is the exact complement of the impedance-loaded slot of Fig. 18a, the Babinet principle says that there exist definite relations between the quantities L, R, I, V_{oc}, A_{ef} of Fig. 17b and the quantities C, G, V, I_{sc}, A_{eq} of Fig. 18c. The relations are summarized in table 1 [75].

TABLE 1. RELATIONSHIP BETWEEN DUAL QUANTITIES

Quantities in Fig. 17b		Quantities in Fig. 18c
L	$=$	$(Z_o^2/4)C$
R	$=$	$(Z_o^2/4)G$
I	$=$	$(2/Z_o)V$
V_{oc}	$=$	$(Z_o/2)I_{sc}$
A_{ef}	$=$	A_{eq}

1.3.3.2 Circuit Theory via Scalar and Vector Potentials

In the preceding section we saw how an equivalent circuit can be constructed by integrating out all the spacial variables of Maxwell's equations. There is another method which leads to the Kirchhoff circuit

theory from the Maxwell field theory. This method, perhaps more appealing to the electrical engineer, is to make use of the electric scalar potential ϕ and the magnetic vector potential \vec{A} [76,77]. Consider, for example, a conducting loop immersed in an incident field \vec{E}^i , as shown in Fig. 19a. Within the conductor we have

$$\nabla \times \vec{H} = (\sigma + j\omega\epsilon)\vec{E} \quad (205)$$

which gives, upon integration over the cross-section S of the conductor,

$$I(\xi) = \int_S (\sigma + j\omega\epsilon) E_\xi dS \quad (206)$$

where I is the total current crossing S . Next, we split the total field E_ξ into the incident and scattered field E_ξ^i and E_ξ^s , and write

$$\begin{aligned} E_\xi &= E_\xi^i + E_\xi^s \\ &= E_\xi^i - j\omega A_\xi^s - \frac{\partial \phi^s}{\partial \xi} \end{aligned} \quad (207)$$

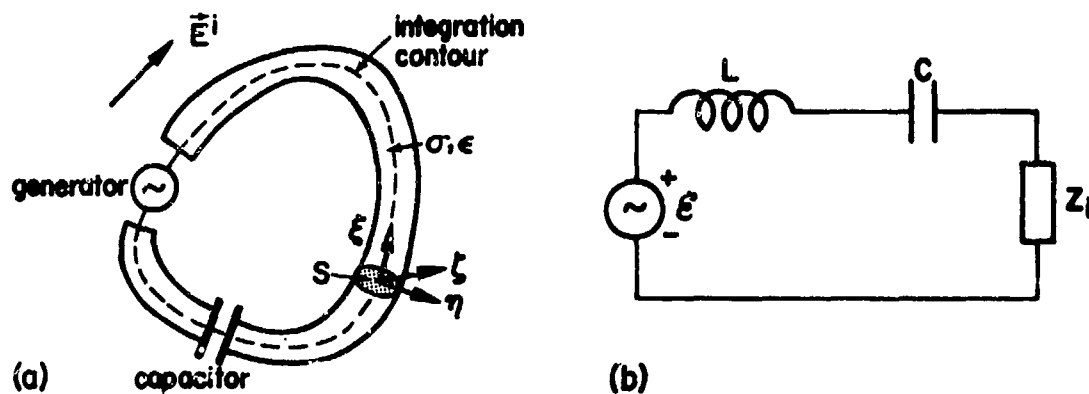


Fig. 19. (a) A conducting loop with capacitor and generator in an incident field, (b) equivalent circuit of (a).

If one makes the assumption that the ξ -dependence of a function can be separated out from its dependence on the transverse coordinates (η, ζ) , i.e., if one writes

$$\begin{aligned} A_{\xi}^s &= f(\eta, \zeta) \bar{A}_{\xi}^s(\xi) \\ \phi^s &= f(\eta, \zeta) \bar{\phi}^s(\xi) \end{aligned} \quad (208)$$

then one gets, by substituting (207) and (208) into (206),

$$j\omega \bar{A}_{\xi}^s + \frac{\partial \bar{\phi}^s}{\partial \xi} + Z_1' I = \bar{E}_{\xi}^1 \quad (209)$$

with the internal impedance Z_1' per unit length and the weighted incident field \bar{E}^1 given by

$$\begin{aligned} 1/Z_1'(\omega, \xi) &= \int_S (\sigma + j\omega\epsilon) f(\eta, \zeta) d\eta d\zeta \\ \bar{E}_{\xi}^1 &= \frac{\int_S (\sigma + j\omega\epsilon) E_{\xi}^1 d\eta d\zeta}{\int_S (\sigma + j\omega\epsilon) f(\eta, \zeta) d\eta d\zeta} \end{aligned} \quad (210)$$

When the cross-sectional dimensions of the conductor are electrically small, (210) can be replaced by

$$Z_1' \approx \frac{1}{\sigma S}, \quad \bar{E}_{\xi}^1 \approx E_{\xi}^1 \quad (211)$$

where S is the cross-sectional area of the conductor.

To obtain the Kirchhoff voltage law we integrate (209) around the loop (Fig. 19), and get

$$j\omega \oint \bar{A}_{\xi}^s d\xi + \oint \frac{\partial \bar{\phi}^s}{\partial \xi} d\xi + Z_1' I = \oint \bar{E}_{\xi}^1 d\xi \quad (212)$$

where I is assumed to have no variation along the loop, and Z_1 is the total internal impedance of the loop and, for all practical applications, is equal to R given by (194). The first term on the left-hand side of (212) can be identified with the voltage drop across an inductor and the second term represents the voltage drop across a capacitor or the voltage jump across a voltage generator. Any voltage generator can be combined with the right-hand side of (212) to form the total electromotive force \mathcal{E} . Thus, (212) is in fact the Kirchhoff voltage law

$$\left(j\omega L + \frac{1}{j\omega C} + Z_1 \right) I = \mathcal{E} \quad (213)$$

The circuit appropriate to (213) is shown in Fig. 19b.

One may also apply the above procedure to obtain an equivalent circuit for the complementary geometry of Fig. 18a, but the details are omitted here.

1.3.3.3 Circuit Properties of an Object in Free Space

The lumped circuit elements L and C are intimately associated with the total stored magnetic and electric energies, while the other lumped element R is a measure of the heat dissipated either through ohmic losses or by way of radiation. This interpretation of the lumped elements works well for a finite region of space such as the space confined by a cavity, but it meets with serious difficulty for an unbounded region, as in the case of an antenna radiating into an infinite space. The difficulty lies in the fact that the total electric and magnetic energies of a radiated field are infinite in an unbounded region because the field decays only as the inverse distance at infinity from the antenna or scatterer. One way out of this difficulty is to define the magnetic energy as arising from the interactions among the surface currents and the electric energy from the interactions among the surface charges. This definition avoids the consideration of field energy density distributed throughout the infinite space, and leads to the usual definition of magnetostatic and electrostatic energies. In the following we will first discuss this point with the aid of the complex Poynting theorem. With this theorem

we will establish that the total interaction energy is a positive-real function of which the driving-point impedance or admittance of an antenna is a special case.

1.3.3.3.1 Complex Poynting's Theorem

The complex Poynting theorem provides an essential link between the field theory and circuit theory. It has been often used by the field theorist to derive equivalent circuits for resonators, waveguides, and other microwave devices [78,79].

Let us start with the E-field equation for a perfect conductor in an incident field \vec{E}^i , viz.,*

$$\vec{I}_n \times \vec{E}^i = j\omega\mu \vec{I}_n \times \int_S \vec{J} G dS' + \frac{1}{\epsilon} \vec{I}_n \times \nabla \int_S \rho G dS' \quad (214)$$

where \vec{J} and ρ are the surface current and charge densities, G is the free-space Green's function, and \vec{I}_n is the outward unit vector normal to the surface S of the conductor. Scalarly multiplying (214) by \vec{H}^* , the complex conjugate of the magnetic intensity \vec{H} and integrating over S , we obtain

$$\begin{aligned} \frac{1}{2} \int_S \vec{E}^i \cdot \vec{J}^* dS &= \frac{j\omega\mu}{2} \int_S \int_S \vec{J}^*(\vec{r}) \cdot \vec{J}(\vec{r}') G(\vec{r}, \vec{r}') dS' dS \\ &\quad - \frac{j\omega}{2\epsilon} \int_S \int_S \rho^*(\vec{r}) \rho(\vec{r}') G(\vec{r}, \vec{r}') dS' dS \end{aligned} \quad (215)$$

where the factor 1/2 has been inserted, so that the left-hand side of (215) can be interpreted as a time-average quantity. Separating out the real and imaginary parts of the right-hand side of (215) we get

*We leave it to the interested reader to generalize expressions (214) through (223) to the complex s-plane.

$$\frac{1}{2} \int_S \vec{E}^1 \cdot \vec{J}^* dS = j 2\omega(\bar{W}_J - \bar{W}_\rho) + \bar{P} \quad (216)$$

with the total time-average energies, \bar{W}_J and \bar{W}_ρ , and the total time-average radiated or scattered power \bar{P} given by

$$\bar{W}_J = \frac{\mu}{4} \iint \vec{J}^*(\vec{r}) \cdot \vec{J}(\vec{r}') \frac{\cos kR}{4\pi R} dS' dS \quad (217)$$

$$\bar{W}_\rho = \frac{1}{4\epsilon} \iint \rho^*(\vec{r}) \rho(\vec{r}') \frac{\cos kR}{4\pi R} dS' dS \quad (218)$$

$$\bar{P} = \omega \iint \left[\frac{\mu}{2} \vec{J}^*(\vec{r}) \cdot \vec{J}(\vec{r}') - \frac{1}{2\epsilon} \rho^*(\vec{r}) \rho(\vec{r}') \right] \frac{\sin kR}{4\pi R} dS' dS \quad (219)$$

where $R = |\vec{r} - \vec{r}'|$. Eq.(216) has the following physical meaning: the time-average power that the incident field \vec{E}^1 spends in creating \vec{J} and ρ on the surface of a perfect conductor is equal to $j2\omega$ times the difference of the time-average energy associated with the surface current \vec{J} and the time-average energy associated with the surface charge ρ plus the total time-average power scattered by the conductor. Note that \bar{W}_J , \bar{W}_ρ and \bar{P} are all well-defined quantities and that for low frequencies $2\bar{W}_J$ and $2\bar{W}_\rho$ reduce respectively to the magnetostatic and electrostatic energies; that is, for $\omega \rightarrow 0$

$$2\bar{W}_J \rightarrow \frac{\mu}{8\pi} \iint \frac{\vec{J}(\vec{r}) \cdot \vec{J}(\vec{r}')}{|\vec{r} - \vec{r}'|} dS' dS \quad (220)$$

$$2\bar{W}_\rho \rightarrow \frac{1}{8\pi\epsilon} \iint \frac{\rho(\vec{r}) \rho(\vec{r}')}{|\vec{r} - \vec{r}'|} dS' dS \quad (221)$$

Before proceeding to the applications of (216) it should be mentioned that (216) is equivalent to the complex Poynting theorem expressed in the familiar form

$$\frac{1}{2} \int_S \vec{E}^i \cdot \vec{J}^* dS = \frac{j\omega}{2} \int_{V_\infty} (\vec{B}^s \cdot \vec{H}^{s*} - \vec{E}^s \cdot \vec{D}^{s*}) dV + \frac{1}{2} \int_{V_\infty} (\vec{E}^s \times \vec{H}^{s*}) \cdot \vec{I}_n dS \quad (222)$$

where the superscript s is used to denote scattered field, and V_∞ is the volume bounded by the surface S of the conductor and the surface S_∞ at infinity. It is important to note that unlike \bar{W}_J and \bar{W}_ρ the total time-average magnetic and electric energies of the scattered field, \bar{W}_m^s and \bar{W}_e^s , given by

$$\bar{W}_m^s = \frac{1}{4} \int_{V_\infty} \vec{B}^s \cdot \vec{H}^{s*} dV \quad (223)$$

$$\bar{W}_e^s = \frac{1}{4} \int_{V_\infty} \vec{E}^s \cdot \vec{D}^{s*} dV$$

are infinite as V_∞ becomes infinite. At the static limit, however, \bar{W}_m^s and \bar{W}_e^s respectively tend to \bar{W}_J and \bar{W}_ρ given by (220) and (221)

1.3.3.3.2 Natural Frequencies

As a first application of (215) we will show how it directly leads to a stationary expression for calculating the natural frequencies of a finite-sized object in free space. Corresponding to each natural frequency there is a RLC network, and hence the circuit properties of an object are characterized by its natural frequencies [80].

The condition for natural resonance or free oscillation of a body is given by (215) in the absence of the incident field \vec{E}^i . Thus,

$$\mu \iint \vec{J}^*(\vec{r}) \cdot \vec{J}(\vec{r}') G(\vec{r}, \vec{r}') dS' dS = \frac{1}{\epsilon} \iint \rho^*(\vec{r}) \rho(\vec{r}') G(\vec{r}, \vec{r}') dS' dS \quad (224)$$

Making use of the continuity equation

$$\nabla \cdot \vec{J} = -j\omega \rho \quad (225)$$

one obtains from (224)

$$\omega^2 = \frac{\iint \vec{J}^*(\vec{r}) \cdot [\nabla \nabla' G(\vec{r}, \vec{r}'; k)] \cdot \vec{J}(\vec{r}') dS' dS}{\mu \epsilon \iint \vec{J}^*(\vec{r}) \cdot \vec{J}(\vec{r}') G(\vec{r}, \vec{r}'; k) dS' dS} \quad (226)$$

The following points should be noted about (226) (see, for example, [81] for proofs):

- (a) Let $\mathfrak{J}[\vec{J}, \vec{J}^*]$ be the functional denoting the right-hand side of (226). One can show by the calculus of variations that the problem of maximizing or minimizing \mathfrak{J} is equivalent to solving the E-field equation (214) with $\vec{E}^i = 0$.
- (b) Eq. (226) is a stationary representation for ω^2 in the sense that a trial function \vec{J} or \vec{J}^* , which is good to first order, will yield an approximate ω^2 which is good to second order.
- (c) The functional \mathfrak{J} depends on the parameter k through the Green's function G . This parameter should be determined by the process of maximizing or minimizing \mathfrak{J} after evaluation of integrals for a chosen trial function.

For slender structures such as a thin rod or a stick-model aircraft the damping due to radiation can be treated as a perturbation. In this case (226) can be simplified considerably. Let s_n and \vec{J}_n be the natural frequency and natural current mode of the n th mode, and let

$$s_n = \alpha_n + j\omega_n \quad (227)$$

$$k_n = \omega_n / c$$

Then, a simple manipulation of (226) gives

$$\alpha_n = \frac{1}{2\omega_n \mu \epsilon} \frac{\iint \vec{J}_n^*(\vec{r}) \cdot \left[(k_n^2 \vec{I} - \nabla \nabla') \frac{\sin k_n R}{4\pi R} \right] \cdot \vec{J}_n(\vec{r}') dS' dS}{\iint \vec{J}_n^*(\vec{r}) \cdot \vec{J}_n(\vec{r}') \frac{\cos k_n R}{4\pi R} dS' dS} \quad (228)$$

where \vec{I} is the unit dyad, and the resonance angular frequency ω_n is calculated approximately from the simple transmission-line theory.

The approximate expression (228) for α_n can also be derived from the concept of Q , the so-called quality factor. Since the bandwidth of the n th mode is given by $2\alpha_n$, and [72]

$$2\alpha_n = \frac{\omega_n}{Q_n}, \quad Q_n = \frac{2\omega_n \bar{W}_{Jn}}{\bar{P}_n} \quad (229)$$

one has

$$\alpha_n = \frac{\bar{P}_n}{4\bar{W}_{Jn}} \quad (230)$$

where \bar{W}_{Jn} and \bar{P}_n are given by (217) and (219) for $k=k_n$, $\vec{J}=\vec{J}_n$, and $\rho=\rho_n$. Substituting the values of \bar{P}_n and \bar{W}_{Jn} in (230) one obtains (228).

For a thin rod expression (228) gives an α_n value identical to that obtained by the Hallén asymptotic antenna theory [82]. This expression has been used to calculate the damping constants of the natural modes of a stick-model aircraft [83].

1.3.3.3 Positive Real Functions

As a second application of (215) we will demonstrate that the driving-point impedance or admittance of an antenna is a positive real (p.r.) function. As is well known in circuit synthesis, the p.r. property of a function is a necessary and sufficient condition to ensure its physical realizability, by which it is meant that a p.r. function can be synthesized with passive lumped circuit elements [84]. A function is said to be p.r. if in the complex frequency s -plane

- (a) it is real for real values of s , and
- (b) it has a positive real part in the right half s -plane.

The requirement (b) can be replaced by the requirement that it be analytic in the right half s -plane and have a nonnegative real part on the $j\omega$ -axis.

Let $Z|I|^2$ denote the left-hand side of (215) with the proportionality factor $|I|^2$, i.e.,

$$Z(j\omega) \equiv \frac{1}{|I(j\omega)|^2} \int_S \vec{E}^1(\vec{r}, j\omega) \cdot \vec{J}^*(\vec{r}, j\omega) dS \quad (231)$$

Then, with s replacing $j\omega$ and $\vec{J}(-s)$, $\rho(-s)$ replacing $\vec{J}^*(j\omega)$, $\rho^*(j\omega)$ respectively in (215) we have

$$Z(s) = \frac{1}{I(s)I(-s)} \left[su \iint \vec{J}(\vec{r}, -s) \cdot \vec{J}(\vec{r}', s) G(\vec{r}, \vec{r}', s) dS' dS \right. \\ \left. - \frac{s}{c} \iint \rho(\vec{r}, -s) \rho(\vec{r}', s) G(\vec{r}, \vec{r}', s) dS' dS \right] \quad (232)$$

It is easy to see that Z is real when s is real, thanks to the symmetry of G in \vec{r} and \vec{r}' . On the $j\omega$ -axis the real part of Z is given by

$$\text{Re } Z(j\omega) = \frac{\bar{P}(j\omega)}{(1/2)|I(j\omega)|^2} \quad (233)$$

where \bar{P} is the total average scattered or radiated power given by (219) and is certainly nonnegative. Furthermore, Z is analytic in the right half s -plane because \vec{J} and ρ satisfy the causality condition. Thus, Z is a p.r. function and is physically realizable with passive lumped elements.

For a transmitting antenna energized by a sliced voltage generator, the incident field \vec{E}^1 in (231) takes the form

$$\vec{E}^1(\vec{r}, s) = V(s) \delta(\vec{r} - \vec{r}_0) \quad (234)$$

In this case the expression (232) for Z is the driving-point impedance. This expression has been used by some investigators as the starting point for a variational calculation of the driving-point impedance of a cylindrical antenna [85, 86].

1.3.3.3.4 Energy Functions

When the scatterer is electrically small, i.e., when $kR \ll 1$, one may expand $\cos kR$ and $\sin kR$ in powers of kR . One then obtains from (217), (218) and (219)

$$\bar{W}_J = \frac{\mu}{16\pi} \iint \frac{\vec{J}^*(\vec{r}) \cdot \vec{J}(\vec{r}')}{R} dS' dS + \dots \quad (235)$$

$$\bar{W}_\rho = \frac{1}{16\pi\epsilon} \iint \frac{\rho^*(\vec{r}) \rho(\vec{r}')}{R} dS' dS - \frac{k^2}{32\pi\epsilon} \iint \rho^*(\vec{r}) \rho(\vec{r}') R dS' dS + \dots \quad (236)$$

$$\bar{P} = \frac{\omega k \mu}{8\pi} \iint \vec{J}^*(\vec{r}) \cdot \vec{J}(\vec{r}') dS' dS + \frac{\omega k^3}{48\pi\epsilon} \iint \rho^*(\vec{r}) \rho(\vec{r}') R^2 dS' dS + \dots \quad (237)$$

where

$$\int \rho(\vec{r}) dS = 0 \quad (238)$$

has been used for a scatterer with no net charge. By using the continuity equation (225) one can show that with \hat{r}_R denoting the unit vector of \vec{R} one obtains

$$\iint \rho^*(\vec{r}) \rho(\vec{r}') R dS' dS = -\frac{1}{\omega} \iint \frac{1}{R} \vec{J}^*(\vec{r}) \cdot [\hat{r} - \hat{r}_R \hat{r}_R] \cdot \vec{J}(\vec{r}') dS' dS \quad (239)$$

$$\iint \rho^*(\vec{r}) \rho(\vec{r}') R^2 dS' dS = -\frac{2}{\omega^2} \iint \vec{J}^*(\vec{r}) \cdot \vec{J}(\vec{r}') dS' dS \quad (240)$$

Substitution of (240) into (237) gives

$$\bar{P} = \frac{\omega k \mu}{12\pi} \iint \vec{J}^*(\vec{r}) \cdot \vec{J}(\vec{r}') dS' dS \quad (241)$$

If one recalls the definition of the dipole moment \vec{p} [73]

$$\int \vec{J} dS = j\omega \vec{p}$$

then the expression (241) can be written as

$$\overline{P} = \frac{\omega^4 \mu \sqrt{\mu \epsilon}}{12\pi} |\vec{p}|^2 \quad (242)$$

which is the total time-average power radiated by a dipole [87].

Substituting (235), (236), (239) and (241) into (216) we get

$$\frac{1}{2} \int \vec{E}^1 \cdot \vec{J}^* dS = 2 j\omega(\overline{T} - \overline{V}) + 2\overline{P} \quad (243)$$

where \overline{T} , \overline{V} and \overline{P} are the so-called time-average energy functions in circuit theory [72] and are given by

$$\overline{T} = \frac{1}{4} \iint \frac{\mu}{8\pi R} \vec{J}^*(\vec{r}) \cdot [\vec{I} + \vec{I}_{RR}] \cdot \vec{J}(\vec{r}') dS' dS \quad (244)$$

$$\overline{V} = \frac{1}{4} \iint \frac{\rho^*(\vec{r}) \rho(\vec{r}')}{4\pi \epsilon R} dS' dS \quad (245)$$

$$\overline{P} = \frac{1}{4} \left(\frac{k^2 Z_0}{6\pi} \right) \iint \vec{J}^*(\vec{r}) \cdot \vec{J}(\vec{r}') dS' dS \quad (246)$$

where Z_0 is the free-space impedance. Note that \overline{T} consists of two parts: the part associated with \vec{I} can be identified as one-half the usual Neumann formula for magnetic energy, while the other part is one-half the Weber formula for magnetic energy, which is little known nowadays but was a subject of considerable controversy in the middle of last century until Helmholtz showed that the two formulas give the same result for closed circuits [88]. The total magnetic energy given in (244) is similar to the one derived by Lamb [89].

To find the counterpart of (243) in the time domain, one starts with the time domain E-field equation, scalarly multiplies with the total \vec{H} , integrates the resulting equation over the entire surface of the scatterer, and obtains

$$\int \vec{E}^1(\vec{r}, t) \cdot \vec{J}(\vec{r}, t) dS = \frac{\mu}{4\pi} \iint \frac{1}{R} \vec{J}(\vec{r}, t) \cdot \frac{\partial}{\partial t} \vec{J}(t - R/c, \vec{r}') dS' dS$$

$$+ \frac{1}{4\pi\epsilon} \iint \frac{1}{R} \rho(t - R/c, \vec{r}') \frac{\partial}{\partial t} \rho(\vec{r}, t) dS' dS \quad (247)$$

For times larger than the transit time R/c across the scatterer one may expand $\rho(t - R/c)$ and $\vec{J}(t - R/c)$ in Taylor's series about t . Hence, one obtains from (247)

$$\int \vec{E}^1(\vec{r}, t) \cdot \vec{J}(\vec{r}, t) dS = \frac{d}{dt} (T + V) + F \quad (248)$$

with the instantaneous magnetic energy T , electric energy V , and scattered power F given by

$$T = \frac{\mu}{16\pi} \iint \frac{1}{R} \vec{J}(\vec{r}, t) \cdot [\vec{I} + \vec{I}_R \vec{I}_R] \cdot \vec{J}(\vec{r}', t) dS' dS \quad (249)$$

$$V = \frac{1}{8\pi\epsilon} \iint \frac{1}{R} \rho(\vec{r}, t) \rho(\vec{r}', t) dS' dS \quad (250)$$

$$F = -\frac{\mu\sqrt{\mu\epsilon}}{12\pi} \iint \left[\vec{J}(\vec{r}, t) \cdot \frac{\partial^2}{\partial t^2} \vec{J}(\vec{r}', t) + \vec{J}(\vec{r}', t) \cdot \frac{\partial^2}{\partial t^2} \vec{J}(\vec{r}, t) \right] dS' dS \quad (251)$$

Note that the integrands in (249) - (251) are symmetric in \vec{r} and \vec{r}' . Now, if one approximates the integrals of (249) - (251) by some quadrature formulas, one may write these equations in a discrete form

$$T = \frac{1}{2} \sum_{j,k} L_{jk} i_j i_k \quad (252)$$

$$V = \frac{1}{2} \sum_{j,k} S_{jk} q_j q_k \quad (253)$$

$$F = \frac{1}{2} \sum_{j,k} R_{jk} \left(i_j \frac{d^2 i_k}{dt^2} + i_k \frac{d^2 i_j}{dt^2} \right) \quad (254)$$

where L_{ij} and S_{ij} are the elements of the inductance and elastance matrices, R_{ij} has the dimension of ohm-(second)² and is proportional to the cosine of the angle between $\vec{J}(\vec{r}_j)$ and $\vec{J}(\vec{r}_k)$, and q_j is the charge on the j th subarea of the scatterer.

We are now in a position to go directly to the Lagrangian description of the Kirchhoff voltage law. Let q_j be the generalized coordinate, \mathcal{L} be the Lagrangian defined by

$$\mathcal{L} = T - V \quad (255)$$

and F be the Rayleigh dissipation function. Then, the Euler-Lagrange equation is [90]

$$\frac{d}{dt} \left(\frac{\partial \mathcal{L}}{\partial \dot{q}_j} \right) - \frac{\partial \mathcal{L}}{\partial q_j} + \frac{\partial F}{\partial \dot{q}_j} = \mathcal{E}_j \quad (256)$$

where $\dot{q}_j = i_j$ and \mathcal{E}_j denotes all electromotive forces such as the incident electric field \vec{E}^i or the field due to a voltage generator on the surface of the scatterer. Use of (252) - (254) in (256) gives the Kirchhoff voltage law

$$\sum_{k=1}^n \left(L_{jk} \frac{di_k}{dt} + S_{jk} q_k + R_{jk} \frac{d^2 i_k}{dt^2} \right) = \mathcal{E}_j, \quad j=1,2,\dots,n \quad (257)$$

It should be noted that the dissipation term is proportional to the second time derivative of the current rather than the current itself as in the case of ohmic loss. The dissipation term in (257) is due to the radiation loss and is identical to the radiation reaction in the non-relativistic equation of motion of a charged particle [77].

1.3.3.4 Circuit Description of Modes and Discontinuities

In the preceding sections we saw the intimate connection between Maxwell's field theory and Kirchhoff's circuit theory, first in the integral form of Maxwell's equations, then through the scalar and vector potentials, and finally in the Lagrangian formulation. The common assumption we employed is that the wavelengths in the surrounding medium are much greater than the dimensions of the object under consideration. This, however, does not mean that the circuit approach is useful only for electrically small objects. In many instances, the electromagnetic behavior of an object, regardless of its electrical size, may be described by a set of independent modes $\phi_n(\vec{r})$, i.e.,

$$\psi(\vec{r}, s) = \sum_n a_n(s) \phi_n(\vec{r}) \quad (258)$$

in which the modal amplitudes $a_n(s)$ may be represented by equivalent circuits. We will discuss the types of modes often found in EMP interaction problems.

Another area where the equivalent-circuit approach has invariably been used is the problem of describing the effect of a discontinuity in a uniform wave-guiding structure on the dominant mode. The justification for such a description is that the energies of the higher-order modes created by the discontinuity are confined to the neighborhood of the discontinuity. In the following, several types of discontinuities commonly encountered in EMP interaction problems will be described.

1.3.3.4.1 Modes

Fig. 20 shows some typical structures on which the most common types of modes exist. They are the natural modes of a body in free space (Fig. 20a), the normal modes inside a cavity (Fig. 20b), the leaky modes on two parallel plates of finite width (Fig. 20c), and the waveguide modes within a coaxial cable (Fig. 20d).

Natural modes: They are the solutions of source-free Maxwell's equations subject to some prescribed boundary conditions on the surface of a body and the outgoing wave condition at infinity. The modal functions $\Phi_n(\vec{r})$ increase exponentially at infinity. The modal amplitudes $a_n(s)$ are meromorphic and holomorphic respectively in the left half and right half s -plane [91], which is to say, the only singularities of $a_n(s)$ are poles in the left half s -plane (Fig. 21). Corresponding to each pole there is an equivalent RLC circuit [80]. It should be remarked that the above consideration excludes the singularities of the excitation, if any, which may be contained in $a_n(s)$.

Cavity normal modes: These modes form a complete orthogonal set and are regular everywhere within the cavity. They are a special case of the natural mode. For a lossless cavity the modal amplitudes $a_n(s)$ have simple poles on the $j\omega$ -axis, each of which corresponds to an equivalent LC circuit (Fig. 21a).

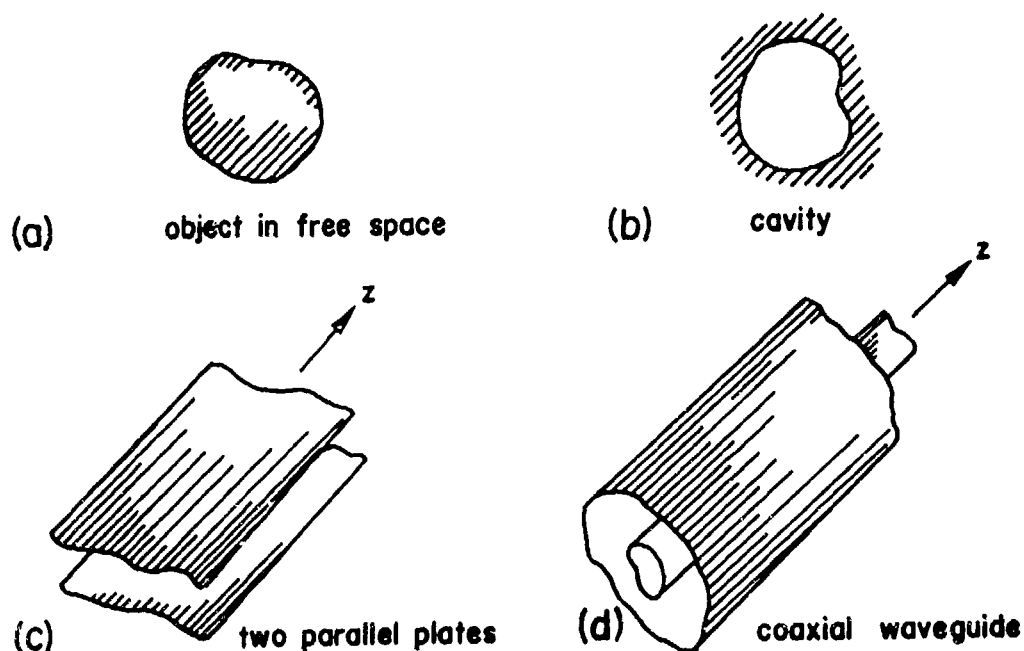


Fig. 20. Structures for: (a) natural modes, (b) normal modes, (c) leaky modes and, (d) waveguide modes.

Leaky modes: These modes are in many ways similar to the natural modes except that a leaky-mode structure is two-dimensional, while a natural-mode structure is three-dimensional. The modal functions $\phi_n(\vec{r})$, except for the TEM mode, increase exponentially along a direction transverse to the axis of the structure and decrease exponentially along the axial direction of the structure. Let z be the axial direction and x, y be the transverse directions. Then one may write

$$\phi_n(\vec{r}) = \phi_n(x, y) e^{\zeta_n z} \quad (259)$$

The singularities ζ_n are shown in Fig. 21b in the so-called improper (bottom) sheet of the double Riemann surface [92,93]. The other sheet

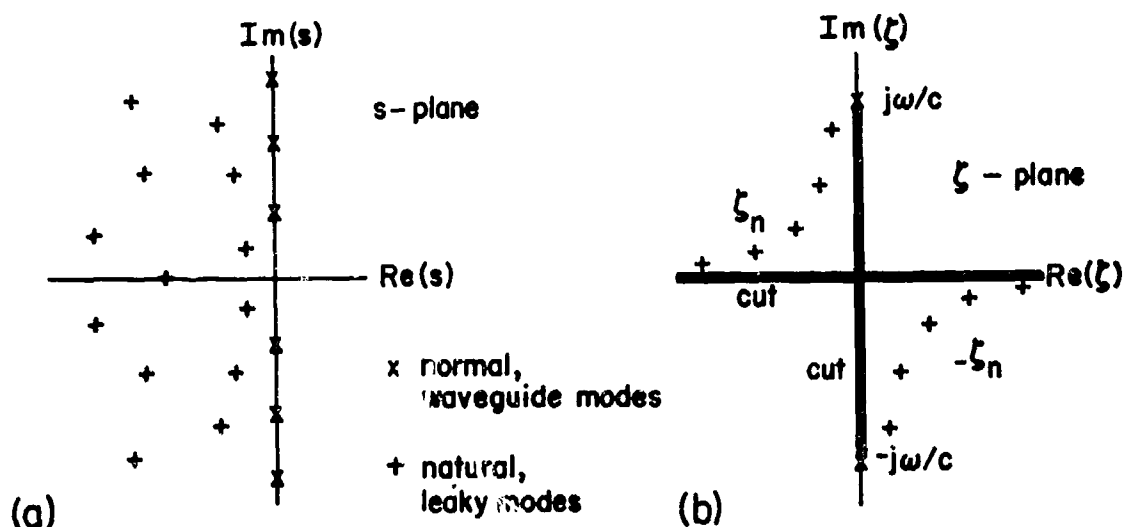


Fig. 21. (a) Natural and resonance frequencies of the natural and normal modes in the s-plane, (b) complex propagation constants ζ_n of leaky modes in the improper (bottom) sheet where the second and fourth quadrant are referred respectively to $+z$ and $-z$.

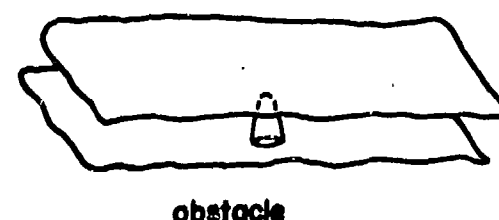
(the top sheet of Fig. 21b) is called the proper sheet in which the leaky modes are absent. For each mode it should be possible to construct a transmission-line analogue with the help of the complex Poynting vector theorem, in much the same way as in the case of a waveguide mode [79].

Waveguide modes: These modes form a complete orthogonal set and are regular everywhere within any cross section of a waveguide. They are a special case of the leaky modes. In the complex ζ -plane the only singularities are poles which are located either on the $j\omega$ -axis or the real axis. The $j\omega$ -axis poles correspond to propagating modes, whereas the real-axis poles are associated with evanescent modes along the z -axis (Fig. 20d) of the guide. For each mode there is a transmission-line analogue [79].

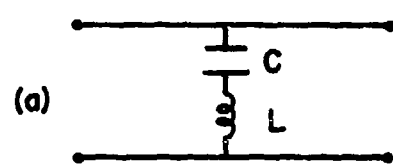
In addition to the four different types of modes discussed above there are other kinds of modes, such as the eigenmodes [94] and the characteristic modes [95]. Circuit synthesis of these modes has not yet been attempted.

1.3.3.4.2 Discontinuities

In Fig. 22 we show some typical discontinuities often encountered in EMP interaction problems. A discontinuity in a uniform wave-guiding structure may take the form of an obstacle (Fig. 22a), or simply a termination (Fig. 22d). The question usually asked is, what effect does a given discontinuity have on the dominant mode of a given guiding structure? The most popular (and rigorous) method to account for this effect is first to determine the equivalent circuit of the discontinuity. The lumped elements of this circuit can be either measured experimentally or calculated by one of the many analytical techniques appropriate to the problem at hand [49,96,97]. Alongside the discontinuities of Fig. 22 we show the equivalent circuits, some of which will be taken up for more detailed discussion in part 2.



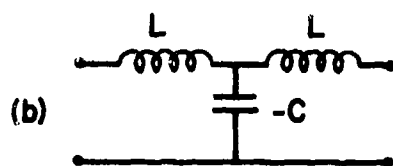
obstacle



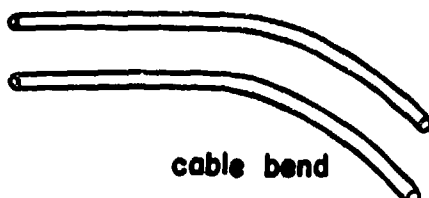
(a)



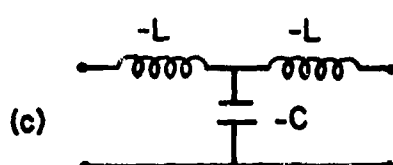
aperture



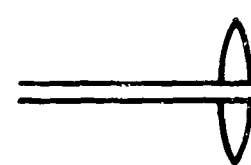
(b)



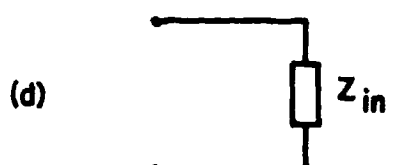
cable bend



(c)



antenna



(d)

Fig. 22. Some exemplary discontinuities and their equivalent circuits.

REFERENCES

- [1] R.W. Sassman, "The current induced on a finite, perfectly conducting, solid cylinder in free space by an electromagnetic pulse," IN 11, July 1967.
- [2] R.W. Latham and K.S.H. Lee, "Radiation of an infinite cylindrical antenna with uniform resistive loading," SSN 83, April 1969.
- [3] M.I. Sancer and A.D. Varvatsis, "Calculation of the induced surface current density on a perfectly conducting body of revolution," IN 101, April 1972.
- [4] L. Marin, "Natural-mode representation of transient scattering from rotationally symmetric, perfectly conducting bodies and numerical results for a prolate spheroid," IN 119, September 1972.
- [5] K.S.H. Lee and L. Marin, "Interaction of external system-generated EMP with space systems," IN 179, August 1973.
- [6] R.F. Harrington and J.R. Mautz, "Radiation and scattering from bodies of revolution," IN 188, July 1969.
- [7] C.D. Taylor and D.R. Wilton, "The extended boundary condition solution of the dipole antenna of revolution," IN 113, June 1972.
- [8] K.S.H. Lee, L. Marin and J.P. Castillo, "Limitations of wire-grid modeling of a closed surface," IN 231, May 1975.
- [9] C.M. Butler, "Integral equations for currents induced on a wire model of a parked aircraft," IN 139, January 1972.
- [10] F.M. Tesche, "On the singularity expansion method as applied to electromagnetic scattering from thin-wires," IN 102, April 1972.
- [11] L. Marin, "Natural modes of certain thin-wire structures," IN 186, August 1974.
- [12] L.B. Felsen (editor), Transient Electromagnetic Fields, Springer-Verlag, Berlin, 1976.

- [13] E.K. Miller, "Some computational aspects of transient electromagnetics," IN 143, September 1972.
- [14] R.A. Perala, "Integral equation solution for induced surface currents on bodies of revolution," IN 193, August 1973.
- [15] K.S.H. Lee and L. Marin, "SGEMP for resonant structures," TN 199, August 1974.
- [16] L. Marin and T.K. Liu, "A simple way of solving transient thin-wire problems," Radio Science 11, 1976, pp. 149 - 155.
- [17] C.T. Tai, Dyadic Green's Functions in Electromagnetic Theory, Intext Educational Publishers, Scranton, 1971, pp. 52 - 53.
- [18] R.W. Latham, K.S.H. Lee and R.W. Sassman, "Minimization of current distortions on a cylindrical post piercing a parallel-plate waveguide," SSN 93, September 1969.
- [19] J.N. Bombardt and L.F. Libelo, "Scattering of electromagnetic radiation by apertures," IN 244, April 1975.
- [20] J. Lam, "Analysis of EMP penetration through the B-1 cable conduit connector," AFWL-TR-77-91, July 1977.
- [21] K.S.H. Lee and F.C. Yang, "A wire passing by a circular aperture in an infinite ground plane," IN 317, February 1977.
- [22] T.T. Wu and R.W.P. King, "The tapered antenna and its application to the junction problem for thin wires," AP-24, January 1976, pp. 42 - 45.
- [23] R.W. Burton and R.W.P. King, "Induced currents and charges on thin cylinders in a time-varying electromagnetic field," EMC-17, August 1975, pp. 149 - 155.
- [24] R.W.P. King and T.T. Wu, "Analysis of crossed wires in a plane-wave field," EMC-17, November 1975, pp. 255 - 265.
- [25] R.W.P. King, "Currents induced in a wire cross by a plane wave incident at an angle," AP-25, November 1977, pp. 775 - 781.

- [26] R.F. Harrington, Field Computation by Moment Methods, Macmillan Co., New York, 1968, Fig. 4.11, p. 78.
- [27] R.W.P. King, "Current distribution in arbitrarily oriented receiving and scattering antenna," AP-20, March 1972, pp. 152 - 159.
- [28] R.W. Burton and R.W.P. King, "Measured currents and charges on thin crossed antennas in a plane-wave field," AP-23, September 1975, pp. 657 - 664.
- [29] C.M. Butler, "Currents induced on a pair of skew wires," AP-20, November 1972, pp. 731 - 736.
- [30] R.W.P. King, "Integral-equation solutions and measurements for currents and charges on tubular cylinders and intersecting cylinders; junction and boundary conditions," to be published as an AFWL-TR.
- [31] K.S.H. Lee, "Balanced transmission lines in external fields," IN 115, July 1972, and also EMC-20, May 1978, pp. 288 - 296.
- [32] S. Ramo and J.R. Whinnery, Fields and Waves in Modern Radio, Wiley, New York, 1944, Chap. 6.
- [33] J.H. Jeans, The Mathematical Theory of Electricity and Magnetism, Cambridge University Press, 1933.
- [34] W.R. Smythe, Static and Dynamic Electricity, McGraw-Hill, New York, 1939.
- [35] C.E. Baum, T.K. Liu, F.M. Tesche and S.K. Chang, "Numerical results for multiconductor transmission lines," IN 322, September 1977.
- [36] C.E. Baum, T.K. Liu and F.M. Tesche, "On the general analysis of multiconductor transmission line networks," IN 350, November 1978.
- [37] F.M. Tesche, "A general multiconductor transmission line model," presented at the 1976 URSI Meeting, Amherst, Mass.
- [38] S. Frankel, Multiconductor Transmission Line Analysis, Artech House, Dedham, Mass., 1978.

- [39] S. Frankel, "Characteristic impedance of parallel wires in rectangular troughs," Proc. I.R.E, Vol. 30, April 1942, pp. 182 - 190.
- [40] F. Oberhettinger and W. Magnus, Anwendung der Elliptischen Funktionen in Physik und Technik, Springer, Berlin, 1940.
- [41] M. Walker, The Schwarz-Christoffel Transformation and its Applications, Dover, New York, 1964.
- [42] H.P. Westman (ed.), Reference Data for Radio Engineers, Fifth Edition, Indianapolis, 1968.
- [43] D. Vitkovich (ed.), Field Analysis, Van Nostrand, New York, 1966.
- [44] F.B. Hildebrand, Introduction to Numerical Analysis, McGraw-Hill, New York, 1956.
- [45] E.G. Cristal, "Coupled circular cylindrical rods between parallel ground planes," MTT-12, July 1964, pp. 428 - 439.
- [46] D.H. Sinnott, "Upper and lower bounds on the characteristic impedance of TEM-mode transmission lines with curved boundaries," MTT-16, November 1968, pp. 971 - 972.
- [47] H.E. Green, "The numerical solution of some important transmission-line problems," MTT-13, September 1965, pp. 672 - 692.
- [48] M.V. Schneider, "Computation of impedance and attenuation of TEM lines by finite difference methods," MTT-13, November 1965, pp. 793 - 800.
- [49] N. Marcuvitz, Waveguide Handbook, M.I.T. Radiation Lab. Series, Vol. 10, McGraw-Hill, New York, 1948.
- [50] G.L. Matthaei, L. Young and E.M.T. Jones, Microwave Filters, Impedance-Matching Networks, and Coupling Structures, McGraw Hill, New York, 1964.
- [51] A.K. Agrawal, et al., "Experimental characterization of multi-conductor transmission lines in frequency domain," IN 311, June 1977.

- [52] S.A. Schelkunoff, "Theory of coaxial transmission lines and cylindrical shields," Bell System Technical Journal, Vol. 13, October 1934, pp. 532 - 579.
- [53] S.A. Schelkunoff and T.M. Odarenko, "Cross talk between coaxial lines," Bell System Technical Journal, Vol. 16, April 1937, pp. 144 - 164.
- [54] E.F. Vance, "Shielding effectiveness of braided-wire shields," IN 172, April 1974.
- [55] R.W. Latham, "Small holes in cable shields," IN 118, September 1972.
- [56] K.S.H. Lee and C.E. Baum, "Application of modal analysis to braided-shield cables," IN 132, January 1973, and also EMC-17, August 1975, pp. 159 - 169.
- [57] K.F. Casey, "On the effective transfer impedance of thin coaxial cable shields," IN 267, March 1976.
- [58] J.R. Wait, "Electromagnetic field analysis for a coaxial cable with periodic slots," IN 265, February 1976.
- [59] J.R. Wait, "Electromagnetic theory of the loosely braided coaxial cable part I," IN 266, February 1976.
- [60] L. Marin, "Effects of a dielectric jacket of a braided-shield cable on EMP coupling calculations," IN 178, May 1974.
- [61] S. Frankel, "Terminal response of braided-shield cables to external monochromatic electromagnetic fields," EMC-16, February 1974, pp. 4 - 16.
- [62] C.E. Baum, "Coupling into coaxial cables from currents and charges on the exterior," presented at the 1976 URSI Meeting, Amherst, Massachusetts.
- [63] C.R. Paul, "Frequency response of multiconductor transmission lines illuminated by an electromagnetic field," EMC-18, November 1976, pp. 183 - 190.

- [64] L. Krügel, "Shielding effectiveness of outer conductors of flexible coaxial cables" (Abschirmwirkung von Aussenleitern flexibler Koaxialkabeln), Telefunken-Zeitung, Vol. 29, December 1936, pp. 256 - 266.
- [65] E.D. Knowles and L.W. Olson, "Cable shielding effectiveness testing," EMC-16, February 1974, pp. 16 - 23.
- [66] J. Zorzy and R.F. Muehlberger, "RF leakage characteristics of popular coaxial cables and connectors," Microwave Journal, Vol. 4, November 1961, pp. 80 - 86.
- [67] A. Sommerfeld, Electrodynamics; Lectures on Theoretical Physics, Vol. IV, Academic Press, New York, 1952.
- [68] J.A. Stratton, Electromagnetic Theory, McGraw-Hill, New York, 1941.
- [69] S.A. Schelkunoff and H.T. Friis, Antennas, John Wiley & Sons, Inc., New York, 1966.
- [70] J.C. Maxwell, A Treatise on Electricity and Magnetism, Vol. II, Dover Publications, Inc., New York, 1954.
- [71] C.E. Baum, "Parameters for some electrically-small electromagnetic sensors," SSN 38, March 1967.
- [72] E.A. Guillemin, Introductory Circuit Theory, John Wiley & Sons, Inc. New York, 1955.
- [73] C.H. Papas, Theory of Electromagnetic Wave Propagation, McGraw-Hill, New York, 1965.
- [74] M. Born and E. Wolf, Principles of Optics, Pergamon Press, New York 1959.
- [75] F.C. Yang, K.S.H. Lee and L. Marin, "Analysis of EMP penetration into a weapons bay," AFWL-TR-77-133, December 1977.
- [76] R.W.P. King, Fundamental Electromagnetic Theory, Dover Publications, Inc., New York, 1963.
- [77] W. Pauli, Electrodynamics, MIT Press, Cambridge, 1973.

- [78] C.G. Montgomery, R.H. Dicke, and E.M. Purcell, Principles of Microwave Circuits, Dover Publications, Inc., New York, 1965.
- [79] F.E. Borgnis and C.H. Papas, Handbuch der Physik, Vol. XVI, Springer-Verlag, Berlin, 1958.
- [80] C.E. Baum, "Single port equivalent circuits for antennas and scatterers," IN 295, March 1975.
- [81] J. Mathews and R.L. Walker, Mathematical Methods of Physics, Benjamin, Inc., Menlo Park, California, 1970.
- [82] L. Marin, "Currents induced on the VLF/LF antenna wires on the E-4 in the resonance region of the aircraft," AFWL-TR-78-37, June 1978.
- [83] G. Bedrosian, "Stick-model characterization of the natural frequencies and natural modes of aircraft, IN 326, September 1977.
- [84] E.A. Guillemin, Synthesis of Passive Networks, John Wiley & Sons, New York, 1957.
- [85] J.E. Storer, "Variational solution to the problem of the symmetrical cylindrical antenna," Tech. Rept. No. 101, Cruft Laboratory, Harvard University, Massachusetts, 1950.
- [86] C.T. Tai, "A variational solution to the problem of cylindrical antennas," Tech. Rept. No. 12, SRI, California, 1950.
- [87] J.C. Slater and N.H. Frank, Electromagnetism, McGraw-Hill, New York, 1947.
- [88] E.T. Whittaker, Aether and Electricity, Vol. I, Humanities Press, New York, 1973.
- [89] H. Lamb, "On the mutual potential of two lines in space," Proc. Lond. Math. Soc. XIV, 1883.
- [90] H. Goldstein, Classical Mechanics, Addison-Wesley, Reading, Massachusetts, 1959.

- [91] L. Marin and R.W. Latham, "Analytical properties of the field scattered by a perfectly conducting finite body," IN 92, January 1972; and also Proc. IEEE 60, 1972.
- [92] L. Marin, "Transient electromagnetic properties of two parallel wires," SSN 173, March 1973.
- [93] N. Marcuvitz, "On field representations in terms of leaky modes or eigenmodes," AP-4, July 1956.
- [94] C.E. Baum, "On the eigenmode expansion method for electromagnetic scattering and antenna problems, Part I: Some basic relations for eigenmode expansions and their relation to the singularity expansion," IN 229, January 1975.
- [95] R.F. Harrington and J.R. Mautz, "Theory and computation of characteristic modes for conducting bodies," TN 195, December 1970, and also AP-19, 1971.
- [96] J. Schwinger and D.S. Saxon, Discontinuities in Waveguides, Gordon and Breach, New York, 1968.
- [97] R.W.P. King, Transmission-Line Theory, Dover Publications, Inc., New York, 1965.

CHAPTER 1.4

FREQUENCY AND TIME DOMAIN METHODS

The preceding chapter dealt with various approaches to the formulation of EMP interaction problems. In this chapter various methods based on frequency-domain considerations are discussed for solving EMP interaction problems. If the interaction between an object (e.g., an aircraft) and the nuclear EMP is viewed in the frequency domain, a crucial numerical parameter of this interaction is the ratio of the characteristic dimension a of the object to the characteristic wavelength λ of the incoming EMP. When the ratio a/λ is very small, the interaction is said to be in the low-frequency region, and an approximate procedure for calculating this interaction can be developed by expanding the quantities of interest in a power series of the small parameter a/λ . This case will be treated in Sec. 1.4.1. When the ratio a/λ is very large, the interaction is said to be in the high-frequency region, and the appropriate method of approximation is that of asymptotic expansion of the quantities of interest in the large parameter a/λ . Sec. 1.4.3 is devoted to the discussion of this region. In between the low-frequency and high-frequency regions lies the intermediate-frequency region for which the singularity expansion method offers one of the most efficient techniques to calculate the interaction. This method and its applications will be elucidated in Sec. 1.4.2. From the low-frequency, intermediate-frequency, and high-frequency solutions one can respectively derive by Laplace transforms the late-time, intermediate-time, and early-time behaviors of the interaction process in the time-domain description.

1.4.1 LOW-FREQUENCY, LATE-TIME REGION

When the wavelengths of an incident radiation are considerably greater than the relevant dimensions of the scatterer or when the external fields change slowly in a time interval comparable to the transit time of the scatterer, one then has an "almost static" situation. In this section we will discuss the interaction problem

under this low-frequency or slow time-variation assumption. We will begin with a rigorous formulation of the interaction problem via the magnetic-field integral equation, and from it develop the Rayleigh series for the induced current and charge densities. The first two terms of this series will be examined critically and their relation to the magnetic and electric dipoles discussed. We will then go on to examine small objects on a large structure (for example, a blade antenna or a window on an aircraft) and see how their interaction properties can be characterized by dipoles and how the polarizabilities of various objects are interrelated. Finally, we will discuss the behaviors of the induced current and charge densities in their late-time state, quasi-stationary state, and steady state and their relations to the low-frequency solution.

1.4.1.1 Rayleigh Series

The so-called Rayleigh series is a power series in frequency. In the s -plane, the Rayleigh series is a Taylor series about the origin $s = 0$. The fact that this series exists and possesses a finite radius of convergence has been proved for a smooth, finite, perfectly conducting object [1,2]. It is believed that the radius of convergence is equal to the absolute value of the lowest natural frequency of the object and, hence, within this circle of convergence the Rayleigh series should converge to the exact solution. However, one seldom goes beyond the first few terms which usually suffice for most practical purposes.

Consider a perfect conductor immersed in a time-harmonic field \vec{E}^i, \vec{H}^i . Let \vec{J} and ρ be the induced current and charge densities with the following low-frequency expansions

$$\begin{aligned}\vec{J} &= \vec{J}_0 + \vec{J}_1 + \vec{J}_2 + \dots \\ \rho &= \rho_0 + \rho_1 + \rho_2 + \dots\end{aligned}\tag{1}$$

where the ratio of two consecutive terms (e.g., ρ_1/ρ_0 , ρ_2/ρ_1 , etc.) is proportional to s .

To find $\vec{J}_0, \vec{J}_1, \rho_0$, etc. one may follow the approach of Stevenson [3,4], which starts with a low-frequency expansion of Maxwell's equations. Each term in the expansion requires only the solution of standard problems in potential theory from which $\vec{J}_0, \vec{J}_1, \rho_0$, etc. can be determined straightforwardly. An elegant, and perhaps most efficient, method is to start with the low-frequency expansion of the H-field integral equation. The shortcoming of this method, however, is that the H-field integral equation applies only to a perfect conductor with nonzero thickness. For a conductor with finite surface impedance or a perfect conductor of vanishingly small thickness (e.g., a thin metallic sheet) one may start with a low-frequency expansion of the E-field equation and arrive at a set of equations for the determination of $\vec{J}_0, \vec{J}_1, \rho_0$, and so on. As will be seen below, for a smooth finite body of infinite conductivity the set of equations resulting from the E-field equation is far more complicated than the set deduced from the H-field integral equation.

The integral-equation method has been utilized in the past to obtain a low-frequency expansion of the solution for a scalar boundary-value problem [5]. For the electromagnetic boundary-value problem the Helmholtz integral representation for the field has been employed to examine the low-frequency scattering and the equivalent dipole moments in terms of potential functions [6].

The point of departure is the H-field integral equation for the current density \vec{J} induced by an incident wave (\vec{E}^i, \vec{H}^i) on the surface of a perfect conductor (Fig. 1), namely

$$\frac{1}{2} \vec{J}(\vec{r}) - \int_S \vec{I}_n(\vec{r}) \times [\nabla G(\vec{r}, \vec{r}') \times \vec{J}(\vec{r}')] dS' = \vec{J}^i(\vec{r}) \quad (2)$$

where $\vec{J}^i = \vec{I}_n \times \vec{H}^i$, and the free-space Green's function G is given by

$$G(\vec{r}, \vec{r}') = \frac{e^{-jkR}}{4\pi R}, \quad R = |\vec{r} - \vec{r}'| \quad (3)$$

Expanding \vec{J}, \vec{J}^i in Rayleigh's series and ∇G in powers of k and equating terms of like orders of magnitude we obtain from (2)

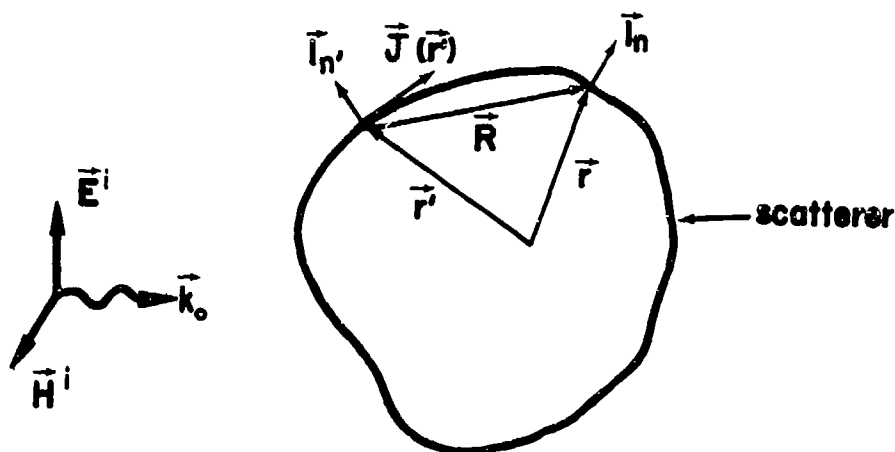


Fig. 1. A plane wave impinging upon a scatterer. \hat{n} is the outward unit normal.

$$\frac{1}{2} \hat{J}_0 - \int_S \hat{n} \times \left[\nabla \frac{1}{4\pi R} \times \hat{J}_0 \right] dS' = \hat{J}_0^1 \quad (4a)$$

$$\frac{1}{2} \hat{J}_1 - \int_S \hat{n} \times \left[\nabla \frac{1}{4\pi R} \times \hat{J}_1 \right] dS' = \hat{J}_1^1 \quad (4b)$$

⋮

$$\frac{1}{2} \hat{J}_p - \int_S \hat{n} \times \left[\nabla \frac{1}{4\pi R} \times \hat{J}_p \right] dS' = \hat{J}_p^1 \quad (4p)$$

$$- \sum_{m=2}^p \frac{m-1}{m!} (-jk)^m \int_S R^m \hat{n} \times \left[\nabla \frac{1}{4\pi R} \times \hat{J}_{p-m} \right] dS' \quad \vdots$$

In the case of an incident plane wave with propagation vector \vec{k}_0 and magnetic field \vec{H}^1 given by

$$\vec{H}^1 = \vec{H}_0 e^{-j\vec{k}_0 \cdot \vec{r}} \quad (5)$$

one has

$$\begin{aligned} \vec{J}_0^1 &= \vec{I}_n \times \vec{H}_0, \quad \vec{J}_1^1 = -j\vec{k}_0 \cdot \vec{r} \vec{I}_n \times \vec{H}_0, \dots \\ \vec{J}_p^1 &= \frac{1}{p!} (-j\vec{k}_0 \cdot \vec{r})^p \vec{I}_n \times \vec{H}_0, \dots \end{aligned} \quad (6)$$

The chain of equations (4) enables one to determine a Rayleigh series for \vec{J} from which the Rayleigh series for ρ follows via the continuity equation. There are several important points which should be noted about (4):

- (a) All orders \vec{J}_p satisfy the same integral equation except for the source terms on the right-hand sides.
- (b) Eq. (4a) is an integral formulation of the magnetostatic boundary-value problem, while (4b) contains the corresponding formulation of the electrostatic boundary-value problem. In fact, if one takes the surface divergence of (4b) and makes use of the continuity equation

$$\nabla_s \cdot \vec{J} = -s\rho \quad (7)$$

one obtains

$$\frac{1}{2} \rho_0 + \int_S \rho_0(\vec{r}') \frac{\partial}{\partial n} \left(\frac{1}{4\pi R} \right) dS' = \epsilon \vec{I}_n \cdot \vec{E}_0^1 \quad (8)$$

which is the formulation of an electrostatic boundary-value problem in terms of an integral equation of the second kind.

- (c) It can be shown from (4a) that

$$\nabla_s \cdot \vec{J}_0^1 = 0 \quad (9a)$$

if and only if $\nabla_s \cdot \vec{J}_0^1 = 0$. It is true that $\nabla_s \cdot \vec{J}_0^1 = 0$ for a plane-wave field but not for the field due to moving charged

particles [7]. If one substitutes the expansion (1) in the continuity equation (7) and equates terms of like orders of magnitude, one will see that the first term gives (9a) while the second term yields

$$\nabla_s \cdot \vec{J}_1 = -s\rho_0 \quad (9b)$$

Before we proceed to explore the properties of \vec{J}_0 and \vec{J}_1 , which are the most important quantities in low-frequency considerations, let us examine briefly what light the E-field formulation may shed on these two quantities. On the surface of a perfect conductor one has the well-known E-field equation

$$s\mu \vec{I}_n \times \int G \vec{J} dS' + \frac{1}{\epsilon} \vec{I}_n \times \nabla \int G \rho dS' = \vec{I}_n \times \vec{E}^i \quad (10a)$$

together with the continuity equation (7). However, (7) and (10a) are not well suited for low-frequency expansions. One way out of this difficulty is to abandon the continuity equation and to use instead the following integral relation between \vec{J} and ρ , namely

$$\frac{1}{2} \rho + \int \frac{\partial G}{\partial n} \rho dS' + s\mu \epsilon \vec{I}_n \cdot \int \vec{J} G dS' = \epsilon \vec{I}_n \cdot \vec{E}^i \quad (10b)$$

which can be obtained by taking the \vec{I}_n -dot of the Helmholtz integral representation of the E-field, in much the same way as (10a) can be obtained by taking the \vec{I}_n -cross of that representation [8]. Now making a low-frequency expansion of (10a) and (10b) one obtains

$$\left. \begin{aligned} \vec{I}_n \times \nabla \int \frac{1}{4\pi R} \rho_0 dS' &= \epsilon \vec{I}_n \times \vec{E}_0^i \\ \frac{1}{2} \rho_0 + \int \frac{\partial}{\partial n} \left(\frac{1}{4\pi R} \right) \rho_0 dS' &= \epsilon \vec{I}_n \cdot \vec{E}_0^i \end{aligned} \right\} \quad (11a)$$

$$\frac{1}{2} \rho_0 + \int \frac{\partial}{\partial n} \left(\frac{1}{4\pi R} \right) \rho_0 dS' = \epsilon \vec{I}_n \cdot \vec{E}_0^i \quad (11b)$$

$$s\mu\epsilon \vec{I}_n \times \int \frac{1}{4\pi R} \vec{J}_0 dS' + \vec{I}_n \times \nabla \int \frac{1}{4\pi R} \rho_1 dS' = \epsilon \vec{I}_n \times \vec{E}_1^1 \quad (12a)$$

$$\frac{1}{2} \rho_1 + \int \frac{\partial}{\partial n} \left(\frac{1}{4\pi R} \right) \rho_1 dS' + s\mu\epsilon \vec{I}_n \cdot \int \vec{J}_0 \frac{1}{4\pi R} dS' = \epsilon \vec{I}_n \cdot \vec{E}_1^1 \quad (12b)$$

and similar sets of coupled equations for (\vec{J}_1, ρ_2) , (\vec{J}_2, ρ_3) , and so on. Eqs. (11a) and (11b) can be recognized as the formulation of an electrostatic boundary-value problem, since (11a) leads to

$$\frac{1}{\epsilon} \int \frac{1}{4\pi R} \rho_0 dS' + \phi_0^1 = \text{constant} \quad (13a)$$

where ϕ_0^1 is the electrostatic potential of \vec{E}_0^1 and the constant is determined by (11b) which, upon integration over the surface of the body, gives

$$\int \rho_0 dS = 0 \quad (13b)$$

If one wishes, one can solve (11b) directly and it can be shown that the solution of (11b) will automatically satisfy (11a). On the other hand, (12a) and (12b) for (\vec{J}_0, ρ_1) , and similar equations for (\vec{J}_1, ρ_2) , etc., are sets of coupled equations with the number of equations equal to the number of unknowns.

It is evident from the above considerations that Rayleigh's series can be obtained with ease from the H-field formulation but not from the E-field formulation.

1.4.1.2 Properties of \vec{J}_0 and \vec{J}_1

We have just seen that the first two terms, \vec{J}_0 and \vec{J}_1 , in the Rayleigh series satisfy respectively the integral equations (4a) and (4b) and also the differential equations (9a) and (9b). Integration of (9a) and (9b) over the patch A, which is a part of the entire surface S of the body, gives (see Fig. 2)

$$\oint_C \vec{J}_0 \cdot \vec{I}_b d\ell = 0, \quad \oint_C \vec{J}_1 \cdot \vec{I}_b d\ell = -s \iint_A \rho_0 dS \quad (14)$$

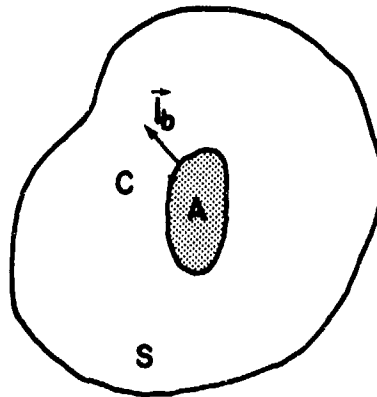


Fig. 2. Geometry for (14). \vec{t}_b = unit binormal tangent to S,
 C = closed curve on S bounding A, A = area of patch on S,
 S = surface of body.

These equations imply that the lines of \vec{J}_0 form closed loops on the surface S, whereas the lines of \vec{J}_1 terminate at charges. Thus, \vec{J}_0 has nothing to do with the total induced current flowing across any cross-section of the body [9], such as the total axial current on a cylinder.

As is evident from (9b), a knowledge of \vec{J}_1 is sufficient for the determination of ρ_0 but the reverse is generally not true. In certain special cases, however, \vec{J}_1 is obtainable directly from ρ_0 . For example, in the case of two-dimensional geometries, \vec{J}_1 and ρ_0 have the same peripheral distributions [10]. For three-dimensional bodies with rotational symmetry, such as the right circular cylinder, the prolate spheroid, the disk, etc., \vec{J}_1 may be obtained directly from ρ_0 via the second equation of (14) if the domain A (Fig. 2) of integration is appropriately chosen (see Figs. 3a - c).

In the case where the magnetic field and the propagation vector of an incident plane wave are respectively parallel and perpendicular to the axis of symmetry of a body as shown in Fig. 3d, one can relate \vec{J}_0 and ρ_0 by [11,12]

$$\frac{J_{0\phi}}{H_0} = - \frac{\rho_0}{2\epsilon E_0 \cos \phi} \quad (15)$$

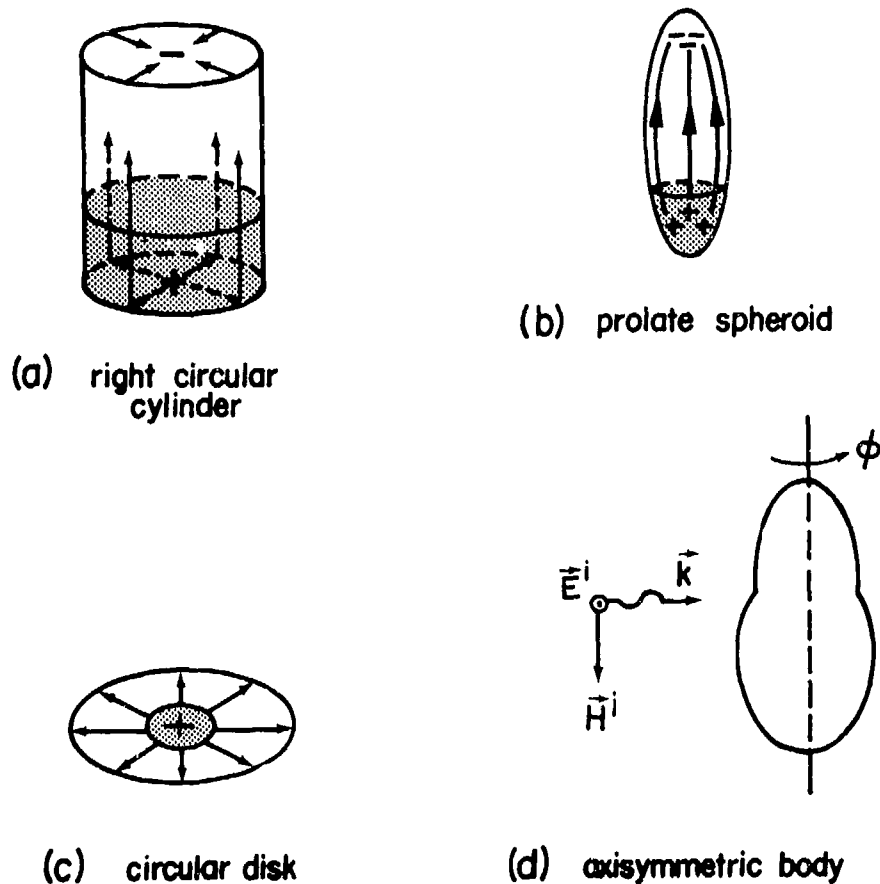


Fig. 3. Examples of axisymmetric geometries.

In this case the total axial current is zero. For the other polarization where the electric field and the propagation vector of the incident plane wave are respectively parallel and perpendicular to the axis of symmetry, no similar relationship exists between \vec{J}_0 and ρ_0 .

It is not unexpected that \vec{J}_0 and \vec{J}_1 give rise to a magnetic and an electric dipole respectively, since lines of \vec{J}_0 form closed loops while lines of \vec{J}_1 are terminated at charges. Recalling the usual definitions for magnetic dipole moment \vec{m} and electric dipole moment \vec{p} [13]

$$\begin{aligned}\vec{m} &= \frac{1}{2} \int_S \vec{r} \times \vec{J} dS \\ \vec{p} &= \int_S \vec{r} \rho dS = \frac{1}{s} \int_S \vec{J} dS\end{aligned}\tag{16}$$

one sees that \vec{J}_0 and \vec{J}_1 give respectively the static magnetic and electric dipole moments.

1.4.1.3 Small Objects on a Large Structure

On the surface of an aerospace vehicle such as an aircraft there are many small objects or inhomogeneities (see Fig. 4). These objects are

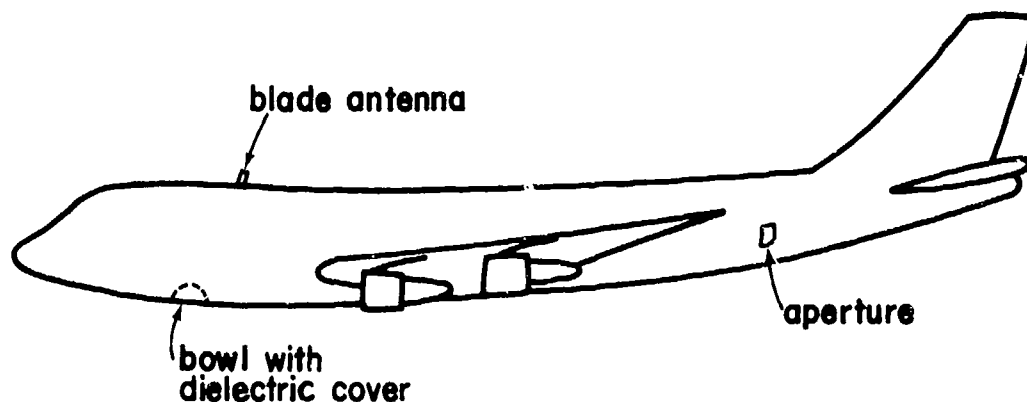


Fig. 4. Small objects on an aircraft.

physically small in comparison with the overall dimensions of the vehicle. In addition, they are electrically small over the important portion of a typical EMP spectrum. Hence, their mutual interactions as well as their perturbational effect on the overall external interaction of the entire structure with EMP can be characterized by their dipole moments [14].

To find the induced dipole moments for each object one will have to solve a magnetostatic and an electrostatic boundary-value problem which, among other things, involve the local geometry of the object. Fig. 5 shows the appropriate static boundary-value problems one needs to solve for a stub, a depression, and an aperture in an infinite ground plane. The approximation of the local geometry of the large structure by an infinite ground plane becomes better the larger the local radii

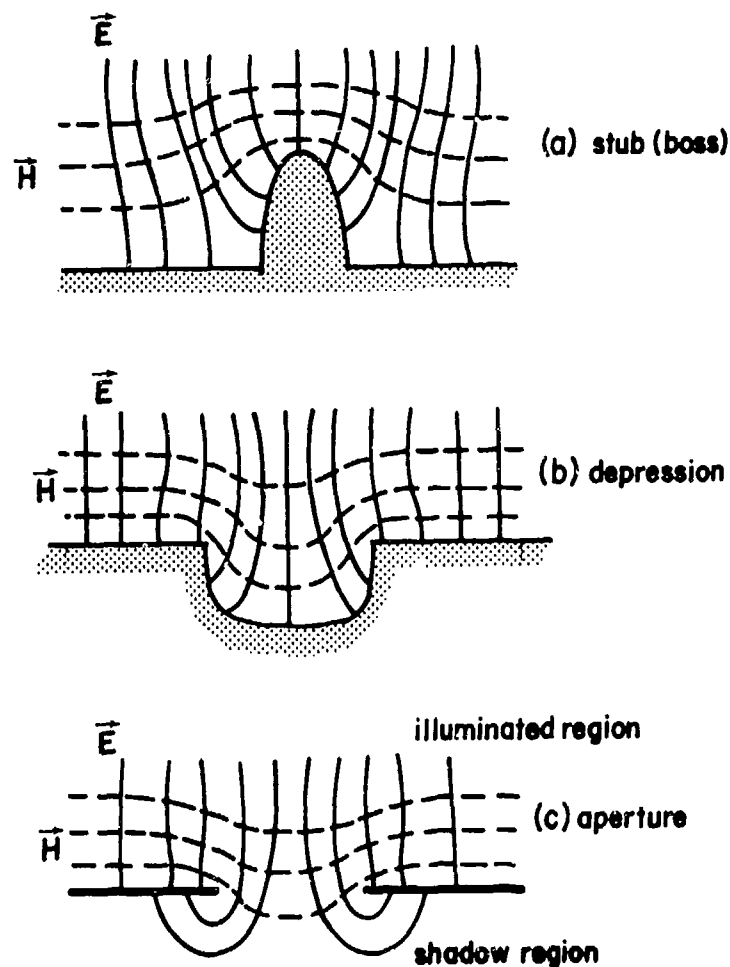


Fig. 5. Illustrations of static electric and magnetic field in the neighborhood of (a) a stub, (b) a depression, and (c) an aperture.

of curvature of the large structure are in comparison to the maximum dimension of the object. Generally one may have to use some canonical geometries of finite radii of curvature, such as a sphere, an infinite cylinder, or an ellipsoid, to model the local geometry of the large structure. But these canonical-shaped structures introduce an enormous amount of complexity to the analysis. On the other hand, an infinite

ground plane will not introduce any complexity to the problem at hand, and it will only lead to larger induced dipole moments.

There are two important points about the static boundary-value problems depicted in Fig. 5. The exciting fields are the "short-circuit" fields (\vec{E}_{sc} , \vec{H}_{sc}). By a "short-circuit" field we mean a field that would exist at the location of the scatterer if the scatterer were removed. This means that if the scatterer were an aperture or a depression, the aperture or the depression would be covered by isotropic conductors. In the language of boundary-value problems a "short-circuit" field is the total field far away from the scatterer on an infinite plane. This field is related to surface current density \vec{J} and surface charge density ρ by

$$\vec{E}_{sc} = \vec{I}_n \rho / \epsilon \quad (17a)$$

$$\vec{H}_{sc} = \vec{J} \times \vec{I}_n \quad (17b)$$

where \vec{I}_n is the outward unit vector normal to the surface of the large structure. To find \vec{J} and ρ one has to solve an external interaction problem in which all small objects are "removed" from the surface of the large structure. It is thus seen that \vec{E}_{sc} and \vec{H}_{sc} will contain those resonances of the large structure whose resonance-wavelengths are much greater than the dimensions of the small object.

To solve the static boundary-value problems of Fig. 5 for the dipole moments one may start with the Laplace equation for the magnetic scalar potential ϕ_m and the electric scalar potential ϕ , viz.,

$$\nabla^2 \phi_m = 0 \quad (18a)$$

$$\nabla^2 \phi = 0 \quad (18b)$$

with $\phi_m \rightarrow -\vec{r} \cdot \vec{H}_{sc}$ and $\phi \rightarrow -\vec{r} \cdot \vec{E}_{sc}$ for observation points \vec{r} far away from the object, and the usual boundary conditions that $(\partial/\partial n)\phi_m$ and ϕ vanish on the conductor's surface. There are many methods of solving (18). If

the surface of the object permits separation of variables, the eigenfunction expansion method is the natural one to use. If the object is of arbitrary shape, the integral equation method aided by numerical quadrature is more promising. The integral equations derived on the basis of (18) and the corresponding boundary conditions are scalar and, hence, are much simpler than their vector counterparts (4a) and (4b). But it must be emphasized that (18b) together with the corresponding boundary condition does not in general yield a complete information on \vec{J}_1 , the second term in the Rayleigh series. Eq.(18b) gives the information on the surface charge density which, however, is sufficient for the determination of the electric dipole moment and, of course, all electric multipoles.

The above considerations can be put on a firm mathematical basis by taking the low-frequency limit of the integral-equation formulation of the problem appropriate for Fig. 4. Such a formulation would involve the dyadic Green's functions of the first and second kind [15], \vec{G}_1 and \vec{G}_2 , which satisfy the boundary conditions

$$\vec{I}_n \times \vec{G}_1(\vec{r}, \vec{r}') = 0, \quad \vec{I}_n \times \nabla \times \vec{G}_2(\vec{r}, \vec{r}') = 0 \quad (19)$$

on the surface of the large structure. It suffices to mention here that \vec{G}_1 is useful for the problem of a small stub on a large structure, while \vec{G}_2 is appropriate for the problem involving an aperture or a depression in the surface of a large structure.

1.4.1.4 Dipoles and Polarizabilities

In this section formulas will be given to calculate the dipole moments and polarizabilities of an object in free space, an aperture in a ground plane, a boss on a ground plane and, finally, a depression in a ground plane. There exist certain important relationships among the components of the electric and magnetic polarizability tensors. These relationships, among other properties of the polarizabilities, will be discussed.

1.4.1.4.1 Object in Free Space

The static dipole moments of an object in free space are given by the static limit of the general definition (16), viz.,

$$\vec{m} = \frac{1}{2} \int_S \vec{r} \times \vec{J}_0 dS, \quad \vec{p} = \int_S \vec{r} \rho_0 dS \quad (20)$$

where S is the surface of the object. Since \vec{m} and \vec{p} are linearly related to the incident fields \vec{H}^i and \vec{E}^i respectively, one has the following general relationship

$$\vec{p} = \epsilon \overleftrightarrow{P} \cdot \vec{E}^i, \quad \vec{m} = \overleftrightarrow{M} \cdot \vec{H}^i \quad (21)$$

where \overleftrightarrow{P} and \overleftrightarrow{M} are respectively called the electric and magnetic polarizability tensors. No matter how tortuous the surface of the object may be so long as the object is composed of reciprocal material, \overleftrightarrow{P} and \overleftrightarrow{M} are always symmetric, i.e.,

$$P_{ij} = P_{ji}, \quad M_{ij} = M_{ji} \quad (i, j = 1, 2, 3) \quad (22)$$

This symmetry property follows from a general theorem on the "generalized susceptibility" [16]. Thus, in general there are only six independent components in P_{ij} or M_{ij} . Furthermore, since they are real and symmetric there always exists a coordinate system in which P_{ij} or M_{ij} is diagonalized; that is to say, there exists a coordinate system in which only three parameters are needed to characterize \overleftrightarrow{P} or \overleftrightarrow{M} .

In addition to the existence of many inequalities among the components of \overleftrightarrow{P} and \overleftrightarrow{M} [17,18], there are certain special cases where \overleftrightarrow{P} and \overleftrightarrow{M} are directly related to each other. For a body rotationally symmetric about, say, the 3-axis one has

$$\begin{aligned} P_{ij} &= M_{ij} = 0, \quad i \neq j \\ P_{11} &= P_{22}, \quad M_{11} = M_{22} \\ P_{11} &= 2M_{33} \end{aligned} \quad (23)$$

where the last relation follows from (15) and the first two are obvious from the symmetry of the problem. Even among the non-vanishing parameters of (23) there exist a number of conditions. For more detail the reader may consult [18].

For an ellipsoid, which can degenerate into a prolate spheroid, an oblate spheroid, a sphere, an elliptic disk, or a circular disk, there are many interesting relations among the P_{ij} and M_{ij} [19]. Let V denote the volume of the ellipsoid and let the coordinate axes be along the principal axes of the ellipsoid. Then [19]

$$\begin{aligned} P_{ij} &= M_{ij} = 0, \quad i \neq j \\ \frac{1}{P_{ii}} - \frac{1}{M_{ii}} &= \frac{1}{V} \\ \sum_{i=1}^3 \frac{1}{P_{ii}} &= \frac{1}{V} \end{aligned} \quad (24)$$

Eqs.(24) show that one needs only two independent parameters to characterize the low-frequency interaction properties of an ellipsoid.

Once \vec{p} and \vec{m} are known, the field can be calculated by [13]

$$\begin{aligned} \vec{E} &= -\frac{1}{\epsilon} \nabla \times (\vec{p} \times \nabla G) + j\omega\mu \vec{m} \times \nabla G \\ \vec{H} &= -\nabla \times (\vec{m} \times \nabla G) - j\omega \vec{p} \times \nabla G \end{aligned} \quad (25)$$

where G is the free-space Green's function given by (3).

1.4.1.4.2 Aperture in Ground Plane

The dipole moments of an aperture in an infinite ground plane are tricky to define because of the presence of the ground plane (Fig. 5c). For one thing, the ground plane divides the entire space into illuminated and shadow regions, making it necessary to have oppositely directed dipoles for the scattered field in each of these two regions. What is more, the

relevant excitation field in the low-frequency limit is the short-circuit field ($\vec{E}_{sc}, \vec{H}_{sc}$), implying that factors of 2 will crop up here and there [20].

In view of the duality between \vec{E} and \vec{H} in Maxwell's equations, one would naturally introduce \vec{p}_a and \vec{m}_a as

$$\begin{aligned}\vec{p}_a &= -\frac{\epsilon}{2} \int_A \vec{r} \times \vec{J}_m dS \\ \vec{m}_a &= \int_A \vec{r} \rho_m dS\end{aligned}\tag{26}$$

in complete analogy to the general definition (16). Here A is the surface of the aperture, and \vec{J}_m and ρ_m are the magnetic surface current and charge densities related to the total aperture electric field \vec{E}_a by

$$\vec{J}_m = 2 \vec{l}_n \times \vec{E}_a, \quad \rho_m = -\frac{1}{s} \nabla_s \cdot \vec{J}_m\tag{27}$$

where \vec{l}_n is the unit normal vector pointing into the illuminated region. With the definition (27) one can show that \vec{p}_a and \vec{m}_a , as defined by (26), give the correct total penetrant field in the shadow region via formula (25). Substituting (27) in (26) and taking the low-frequency limit one obtains a simpler working definition for \vec{p}_a and \vec{m}_a , namely

$$\begin{aligned}\vec{p}_a &= -2\epsilon \vec{l}_n \int_A \phi dS \\ \vec{m}_a &= -2 \int_A \vec{r} H_n dS\end{aligned}\tag{28}$$

where ϕ is the electrostatic potential and H_n is the normal component of the magnetic field [20].

Although \vec{p}_a and \vec{m}_a give the total penetrant field via the free-space dipole field formula (25), they are not too convenient to use for most interaction calculations because a cavity and/or cables often exist behind an aperture, in which cases the ground plane is part of the cavity

or part of the transmission line. This means that the dipole moments, \vec{p}_{ai} and \vec{m}_{ai} , defined in the presence of the ground plane, are preferable to \vec{p}_a and \vec{m}_a . They are related simply by

$$\vec{p}_{ai} = \frac{1}{2} \vec{p}_a, \quad \vec{m}_{ai} = \frac{1}{2} \vec{m}_a \quad (29)$$

Next, we introduce the electric and magnetic polarizabilities $\overleftrightarrow{\alpha}_e$ and $\overleftrightarrow{\alpha}_m$ through

$$\vec{p}_{ai} \equiv \epsilon \overleftrightarrow{\alpha}_e \cdot \vec{E}_{sc}, \quad \vec{m}_{ai} \equiv -\overleftrightarrow{\alpha}_m \cdot \vec{H}_{sc} \quad (30)$$

where the - sign in the second equation of (30) is needed, so that the components of $\overleftrightarrow{\alpha}_m$ are positive. Again, it is important to remember that \vec{p}_{ai} and \vec{m}_{ai} are defined for the shadow region and that their directions must be reversed for the illuminated region.

Since \vec{E}_{sc} is always perpendicular to the ground plane, $\overleftrightarrow{\alpha}_e$ has only one non-vanishing component. On the other hand, \vec{H}_{sc} may have two independent components for a given coordinate system, and hence $\overleftrightarrow{\alpha}_m$ is a two-dimensional symmetric dyad which can always be diagonalized by an orthogonal transformation. There exists a relationship between $(\overleftrightarrow{\alpha}_e, \overleftrightarrow{\alpha}_m)$ of an aperture and (\vec{P}, \vec{M}) of the complementary disk via the Babinet principle. It can be shown that [21]

$$\overleftrightarrow{\alpha}_e = -\frac{1}{4} \overleftrightarrow{M}_{disk}, \quad \overleftrightarrow{\alpha}_m = \frac{1}{4} \overleftrightarrow{P}_{disk} \quad (31)$$

Thus, the polarizabilities of an ellipsoid discussed previously can yield in its limiting forms the polarizabilities of an elliptical and a circular hole.

1.4.1.4.3 Boss on Ground Plane

A boss is a protrusion on a ground plane (Fig. 5a). The blade antennas on an aircraft are one such example. Let \vec{p}_b and \vec{m}_b be the dipole moments giving the total scattered field via the free-space dipole field

formula (25). Let \vec{p}_{bi} and \vec{m}_{bi} be the dipole moments radiating in the presence of an infinite ground plane. Then, with S_b denoting the surface of the boss one has

$$\begin{aligned}\vec{p}_b &= 2 \int_{S_b} \vec{r} \rho_o dS, & \vec{m}_b &= \int_{S_b} \vec{r} \times \vec{J}_o dS \\ \vec{p}_{bi} &= \frac{1}{2} \vec{p}_b & \vec{m}_{bi} &= \frac{1}{2} \vec{m}_b \\ \vec{p}_{bi} &\equiv \epsilon \vec{\beta}_e \cdot \vec{E}_{sc} & \vec{m}_{bi} &\equiv \vec{\beta}_m \cdot \vec{H}_{sc}\end{aligned}\quad (32)$$

If \vec{P} and \vec{M} are the polarizabilities in free space of the boss plus its image, then it is obvious that

$$\vec{\beta}_e = \frac{1}{2} \vec{P} \quad \vec{\beta}_m = \frac{1}{2} \vec{M} \quad (33)$$

1.4.1.4.4 Depression in Ground Plane

Flush-mounted antennas on aircraft are examples of depressions in a ground plane (see Fig. 5b). Except for a hemispherical bowl [22] there are no known solutions for other three-dimensional depressions. Let \vec{p}_d and \vec{m}_d be the dipole moments that give the total scattered field via formula (25) and let \vec{p}_{di} and \vec{m}_{di} be the dipole moments defined with the ground plane. The situation is similar to that of an aperture except that now there is only the illuminated region. Thus

$$\begin{aligned}\vec{p}_d &= -\frac{\epsilon}{2} \int_A \vec{r} \times \vec{J}_m dS, & \vec{m}_d &= - \int_A \vec{r} \rho_m dS \\ \vec{p}_{di} &= \frac{1}{2} \vec{p}_d & \vec{m}_{di} &= \frac{1}{2} \vec{m}_d \\ \vec{p}_{di} &\equiv \epsilon \vec{\gamma}_e \cdot \vec{E}_{sc} & \vec{m}_{di} &\equiv \vec{\gamma}_m \cdot \vec{H}_{sc}\end{aligned}\quad (34)$$

where A is the area of the depression's mouth. For a hemispherical depression $\vec{\gamma}_e$ has an exact closed form, whereas $\vec{\gamma}_m$ can be obtained only approximately [22]. As would be expected, the polarizability values are smaller than the corresponding values of a circular aperture. Thus, it is reasonable to assume that the polarizabilities of the aperture A in an infinite ground plane (i.e., when the volume of the depression becomes infinite while its opening remains unchanged) give the upper bounds of $\vec{\gamma}_e$ and $\vec{\gamma}_m$.

At this point it is a good idea to summarize the above results. The total fields \vec{E} , \vec{H} radiated by the dipoles \vec{p} , \vec{m} are given by (25). The values of \vec{p} and \vec{m} to be used in (25) for the four different situations discussed above are tabulated in table 1. It should be pointed out that

TABLE 1. DIPOLE MOMENTS TO BE USED IN EQUATIONS (25)

	Body in Free Space	Aperture in Ground Plane	Boss in Ground Plane	Depression in Ground Plane
\vec{p}	$\epsilon \vec{P} \cdot \vec{E}^i$	$2 \epsilon \vec{\alpha}_e \cdot \vec{E}_{sc}$	$2 \epsilon \vec{\beta}_e \cdot \vec{E}_{sc}$	$2 \epsilon \vec{\gamma}_e \cdot \vec{E}_{sc}$
\vec{m}	$\vec{M} \cdot \vec{H}^i$	$-2 \vec{\alpha}_m \cdot \vec{H}_{sc}$	$2 \vec{\beta}_m \cdot \vec{H}_{sc}$	$2 \vec{\gamma}_m \cdot \vec{H}_{sc}$

in the case of an aperture in a ground plane the values of \vec{p} and \vec{m} in table 1 when substituted in (25) give the total fields in the shadow region

The above discussions have been focused on three-dimensional objects and two-dimensional apertures. In the case of two-dimensional objects or one-dimensional apertures, the magnetic polarizability per unit length \vec{M} is directly related to the electric polarizability per unit length \vec{P} . The truth of this statement can be seen from the following simple considerations. Let the z -axis be the axis of a two-dimensional object, the y -axis be directed along the incident magnetic field \vec{H}^i and the

x-axis along the incident electric field \vec{E}^i . Then the electric and magnetic scalar potentials ϕ and ϕ_m form the complex potential W , namely [23]

$$W = \phi + j\phi_m \quad (35)$$

which satisfies the Laplace equation. From the theory of conjugate functions one can show that the electric polarizability tensor \vec{P}^i and the magnetic polarizability tensor \vec{M}^i are related by

$$\vec{P}^i = \vec{I}_z \times \vec{M}^i \quad (36)$$

The discussions thus far have been limited to perfectly conducting bodies. It should come as no surprise that the low-frequency interaction properties of a dielectric/permeable body are predominantly characterized by its electric and magnetic polarizabilities. For more detail the interested reader should refer to [24].

1.4.1.5 Quasi-Stationary, Late-Time Considerations

As is evident from (4) each term of the Rayleigh series for the current density is given by

$$\begin{aligned} \vec{J}_0 &= \vec{L} \cdot \vec{J}_0^i \\ \vec{J}_1 &= \vec{L} \cdot \vec{J}_1^i \\ \vec{J}_2 &= \vec{L} \cdot \left\{ \vec{J}_2^i + \frac{s^2}{c^2} \int \frac{\vec{I}_n \times (\vec{R} \times \vec{J}_0^i)}{8\pi R} ds' \right\} \end{aligned} \quad (37)$$

and so on, where \vec{L} is the static dyadic integral operator inverse to the integral operator on the left-hand side of (4). For separable surfaces, \vec{L} takes a very simple form. For example, in the case of an infinitely long cylinder (Fig. 6a) we have

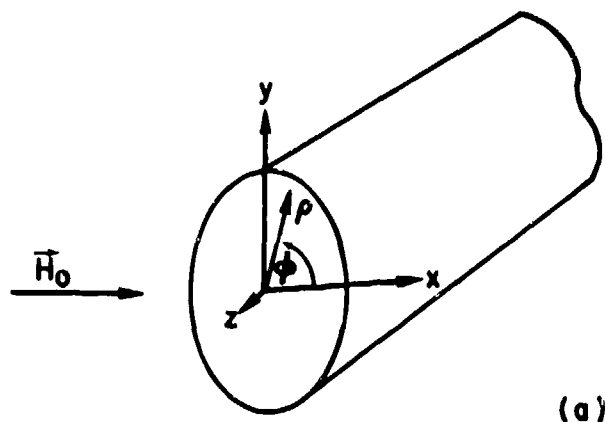


Fig. 6a. Incident magnetic field perpendicular to the axis of an infinite cylinder.

$$\vec{E} = 2\vec{I}_z\vec{I}_z, \quad \vec{J}_0^1 = -\vec{I}_z H_0 \sin \phi \quad (38)$$

and in the case of a sphere (Fig. 6b) we have

$$\vec{E} = \frac{3}{2}\vec{I}_\phi\vec{I}_\phi, \quad \vec{J}_0^1 = -\vec{I}_\phi H_0 \sin \theta \quad (39)$$

The time-domain series corresponding to (37) is

$$\begin{aligned} \vec{J}_0(t) &= \vec{E} \cdot \vec{J}_0^1(t) \\ \vec{J}_1(t) &= \vec{E} \cdot \vec{J}_1^1(t) \\ \vec{J}_2(t) &= \vec{E} \cdot \left\{ \vec{J}_2^1(t) + \frac{1}{8\pi c^2} \int \vec{I}_n \times (\vec{I}_R \times \ddot{\vec{J}}_0) dS' \right\} \end{aligned} \quad (40)$$

and so on, where the double dots denote two time-differentiations and \vec{I}_R is the unit vector in the direction of \vec{R} (see Fig. 1). The dependence of \vec{J}_0 , \vec{J}_1 , etc. on \vec{r} (the position on the surface of the object) should be understood and has been omitted for simplicity. It is reasonable to call

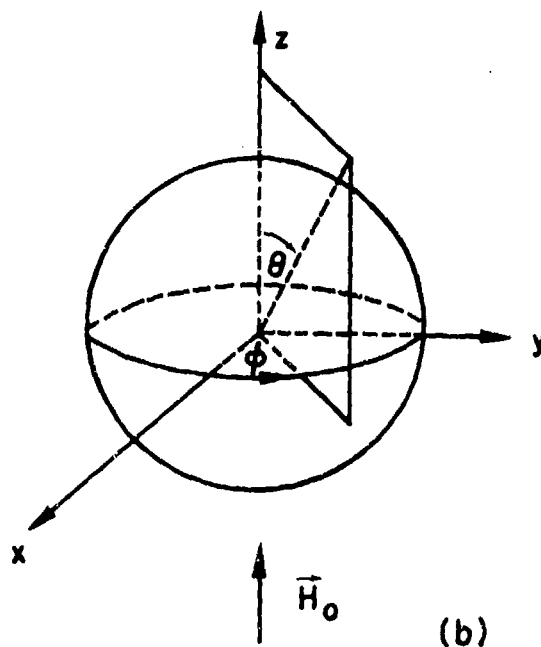


Fig. 6b. Incident magnetic field along the polar axis of a sphere.

(40) a quasi-stationary series, since this series holds true if the electromagnetic phenomena are slowly varying during a time interval comparable to the characteristic or transit time t_c of the body. In fact, the series (40) can also be obtained by expanding the time-domain H-field integral equation, the inverse Fourier transform of (2), in powers of t_c . Thus, the quasi-stationary series makes sense if the pulse width of the incident wave is much larger than t_c (Figs. 7a,b), or if the speeds of the charged particles are very small compared to the speed of light in the surrounding medium (see Fig. 7c), as is often the case in most SGEMP interaction problems. Of course, the prerequisite for the series to be valid is that all early-time transient effects have subsided; that is to say, the object is well immersed in the incident pulse or the charged particles have long ceased their violent motions. In this sense (40) may also be termed a late-time series.

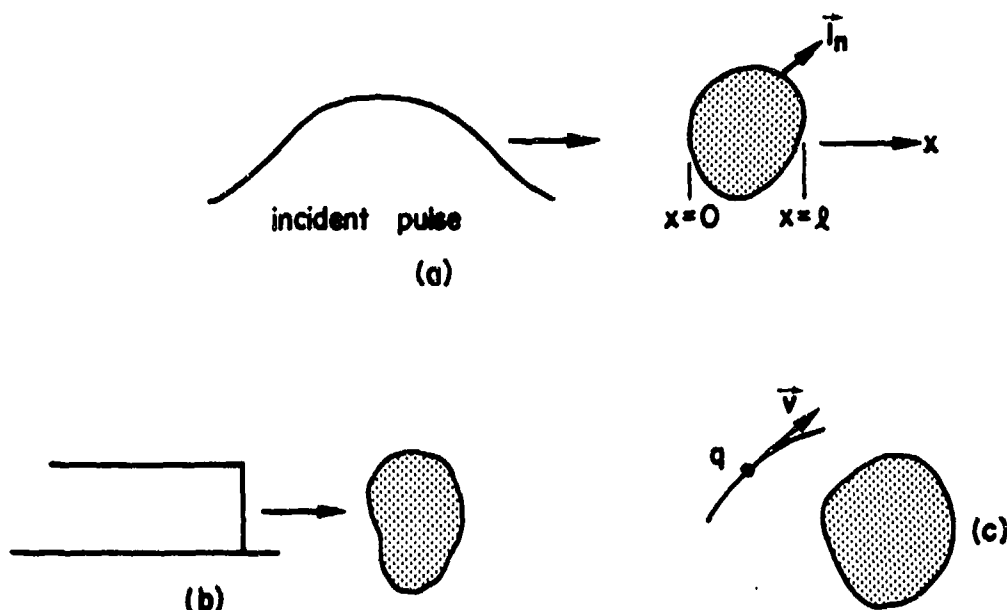


Fig. 7. (a) A pulse incident on a body, (b) a step-function wave incident on a body, and (c) a charged particle q moving with velocity \vec{v} near a body.

Let a plane-wave pulse travel along the positive x -direction and impinge on an object as shown in Fig. 7a. Then, the incident current $\vec{J}^i(\vec{r}, t)$ is given by

$$\vec{J}^i(\vec{r}, t) = \vec{I}_n \times \vec{H}^i f(t - x/c) \quad (41)$$

where x lies between $x=0$ and $x=l$. Expanding f in a Taylor series and introducing $t_c = l/c$ one gets

$$f(t - x/c) = f(t) - \frac{x}{l} t_c \dot{f}(t) + \frac{1}{2} \left(\frac{x}{l} \right)^2 t_c^2 \ddot{f}(t) + \dots \quad (42a)$$

which is a convergent series if

$$|f| > |t_c \dot{f}|, \quad |\dot{f}| > |t_c \ddot{f}|, \dots \quad (42b)$$

In physical terms this means that the incident waveform does not vary much during a time interval equal to the transit time t_c . When this condition is met one then has, according to (40),

$$\begin{aligned}
 \vec{J}_0(\vec{r}, t) &= \vec{C}_0(\vec{r}) f(t) \\
 \vec{J}_1(\vec{r}, t) &= \vec{C}_1(\vec{r}) \dot{f}(t) \\
 \vec{J}_2(\vec{r}, t) &= \vec{C}_2(\vec{r}) \ddot{f}(t) \\
 &\vdots \\
 \vec{J}_n(\vec{r}, t) &= \vec{C}_n(\vec{r}) f^{(n)}(t)
 \end{aligned} \tag{43}$$

where $f^{(n)}$ denotes the n th time derivative of f and \vec{C}_0, \vec{C}_1 , etc. are vector functions depending only on the observation point \vec{r} on the surface. If one reconstructs the waveform for the induced current $\vec{J}(\vec{r}, t)$ from the quasi-stationary or late-time series (43), \vec{J} will be different from the waveform of the incident pulse because the \vec{C}_n 's are generally different from the coefficients of the Taylor series (42a).

Fig. 7b depicts a step-function plane wave striking an object. In this case we have

$$f(t - x/c) = u(t - x/c) \tag{44}$$

where u is the unit step function. Clearly, after all the initial transient phenomena have subsided there remain

$$\begin{aligned}
 \vec{J}_0(\vec{r}, t) &= \vec{C}_0(\vec{r}) \\
 \rho_0(\vec{r}, t) &= -\nabla_s \cdot \vec{C}_1(\vec{r})
 \end{aligned} \tag{45}$$

where the second equation follows from integrating the time-domain version of the continuity equation (9b) from $-\infty$ to t with the help of the second equation of (43).

If the incident wave is, say, a step-function sine wave with angular frequency ω_0 , the induced current and charge densities will eventually oscillate at ω_0 with different phase shifts. This state of affairs is called the steady state, as is well known in all branches of the physical sciences. Of course, the static state (45) is a special case of the steady state.

1.4.2 INTERMEDIATE-FREQUENCY, INTERMEDIATE-TIME REGION

Following the low-frequency, late-time region is the intermediate-frequency, intermediate-time region which is characterized by the ratio a/λ (ratio of characteristic dimension of scatterer to characteristic wavelength of incoming EMP) that is neither very small nor very large compared to unity. Therefore a power series expansion or an asymptotic expansion in a/λ cannot be carried out to good advantage, if at all. On the other hand, the intermediate-frequency region can be very important in electromagnetic problems involving a broad-band source of excitation like an EMP. An efficient mathematical technique to calculate intermediate-frequency scattering and intermediate-time behavior is therefore much in demand for analyzing the EMP interaction. The singularity expansion method offers one such technique that is short of solving the interaction problem exactly [25 - 27].

1.4.2.1 Singularity Expansion Method

The singularity expansion method (sometimes known as SEM) consists of characterizing the physical quantities in EMP interaction problems by their singularities in the complex frequency plane. The idea has its origin in the classical analysis of the transient responses of lumped network circuits, and can be introduced in this connection.

1.4.2.1.1 Transient Analysis of a Lumped Network Circuit

Consider the simple LRC series shown in Fig. 8. It is driven by a transient voltage source $v(t)$. As a consequence the circuit develops a transient response in the form of a current $i(t)$. This time-dependent

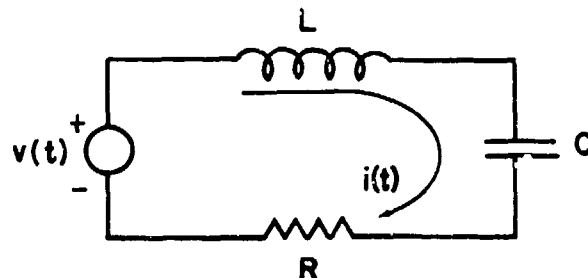


Fig. 8. A lumped LRC series circuit driven by a transient voltage source $v(t)$.

phenomenon is described by a second order, nonhomogeneous, linear differential equation in time

$$\left(L \frac{d^2}{dt^2} + R \frac{d}{dt} + \frac{1}{C} \right) i(t) = \frac{d}{dt} v(t) \quad (46)$$

The current $i(t)$ can be calculated by solving an initial-value problem.

The classical tool for analyzing initial-value problems is the Laplace transform. Let $f(t)$ be the time-domain response of a physical system, such as the LRC circuit, to a transient excitation. One can introduce a complex frequency s , and write the frequency-domain response $F(s)$ as the two-sided Laplace transform [28] of $f(t)$

$$F(s) = \int_{-\infty}^{\infty} e^{-st} f(t) dt \quad (47)$$

If $f(t)$ is reasonably smooth and vanishes sufficiently rapidly as $t \rightarrow \pm\infty$, $F(s)$ is an analytic function of s except at a set of singularities. The location, number, and type of the singularities are determined by the physical characteristics of the system and the excitation. In fact, most of these s -plane singularities can be put in a one-to-one correspondence with certain so-called natural oscillation frequencies of the system.

The inverse Laplace transform of (47) is given by

$$f(t) = \frac{1}{2\pi j} \int_{\Omega-j\infty}^{\Omega+j\infty} e^{st} F(s) ds \quad (48)$$

Here Ω is a real constant so chosen that the singularities of $F(s)$ all lie to the left of the path of integration. The confinement of the singularities of $F(s)$ to the left half-plane of the s -plane is guaranteed by the principle of causality. It follows from the identical vanishing of the response $f(t)$ before the arrival of the excitation.

Applying the Laplace transform to (46), one obtains the solution in the frequency domain

$$I(s) = Y(s)V(s) \quad (49)$$

where $Y(s)$ is the admittance of the LRC circuit at complex frequency s , given by

$$Y(s) = \frac{s}{Ls^2 + Rs + 1/C} \quad (50)$$

The singularities of $I(s)$ in the s -plane are contained in $Y(s)$ and $V(s)$. Eq.(50) shows that $Y(s)$ has two simple poles situated at $s = s_{\pm}$ with

$$s_{\pm} = -\frac{R}{2L} \pm \sqrt{\left(\frac{R}{2L}\right)^2 - \frac{1}{LC}} \quad (51)$$

Both these poles are located in the left half-plane, since $\text{Re } s_{\pm} < 0$. Depending on the sign of the discriminant in (51), s_{+} and s_{-} are either both real (in which case the poles both lie on the real axis) or they are complex conjugates (in which case the poles lie symmetrically with respect to the real axis). This symmetry in the pole distribution with respect to the real axis is a consequence of the fact that L , R and C are all real physical quantities.

The admittance $Y(s)$ in (50) can be rewritten in the following partial-fraction form

$$Y(s) = \frac{1}{L(s_+ - s_-)} \left[\frac{s_+}{s - s_+} - \frac{s_-}{s - s_-} \right] \quad (52)$$

This is in fact a singularity expansion of $Y(s)$. That is, $Y(s)$ is here expressed as a sum of terms, each one of which exhibits one of its singularities.

A singularity expansion of $V(s)$ can be performed in like manner. For definiteness, take $v(t)$ to be a step function:

$$v(t) = \begin{cases} 0, & t < 0 \\ V_0, & t > 0 \end{cases} \quad (53)$$

That is to say, the applied voltage source is switched on instantly at $t = 0$ to full strength V_0 , and maintained at this value for all time $t > 0$. Its Laplace transform is

$$V(s) = \frac{V_0}{s} \quad (54)$$

This expression is already in the form of a singularity expansion, showing a simple pole at $s = 0$.

The singularity expansion of $I(s)$, which is really what is most interesting as far as solving the transient-response problem is concerned, can be derived by combining (52) and (54). One obtains

$$I(s) = \frac{V_0}{L(s_+ - s_-)} \left[\frac{1}{s - s_+} - \frac{1}{s - s_-} \right] \quad (55)$$

This expansion shows two simple poles at $s = s_{\pm}$ corresponding to the two natural frequencies of the LRC series circuit. Note that in this particular

example the pole of $V(s)$ at $s = 0$ is eliminated by the factor s in the numerator of $Y(s)$ in (50), and does not figure in the singularity expansion of $I(s)$. But, in general, the source introduces singularities into the response, which do not correspond to natural frequencies of the system.

The transient response current $i(t)$ can be obtained by performing the inverse Laplace transform

$$i(t) = \frac{1}{2\pi j} \int_{\Omega-j\infty}^{\Omega+j\infty} e^{st} I(s) ds \quad (56)$$

In this case the constant Ω can be chosen equal to 0. The integral is easily evaluated by the method of residues, since the open straight contour can be closed by a right semi-circle at infinity for $t < 0$, and by a left semi-circle at infinity for $t > 0$. The result of the integration is

$$i(t) = \begin{cases} 0, & t < 0 \\ \frac{V_0}{L(s_+ - s_-)} [e^{s_+ t} - e^{s_- t}], & t > 0 \end{cases} \quad (57)$$

Each pole in $I(s)$ is seen to contribute a damped sinusoid to $i(t)$.

1.4.2.1.2 Generalization

The above transient-response analysis of a simple lumped network circuit by means of the Laplace transform contains practically all that there is to SEM. In the application of SEM to more advanced electromagnetic problems, certain complications will inevitably arise. But the basic features of the analysis will persist. One anticipated complication will be the appearance of spatial dependence. As soon as one goes beyond lumped-parameter circuits, one encounters distributed systems. These are described by partial differential equations or integral equations, which differ from the ordinary differential equation

(46) in the dependence on spatial coordinates. Another anticipated complication is that the number of natural frequencies will be much larger for a distributed system, and thus many more singularities will show up in the s -plane.

A feeling of the state of affairs in the s -plane representing the transient response of a distributed system, such as the response of an aircraft to an EMP, can be gleaned from the following somewhat simplistic picture. Nevertheless, this picture actually obtains when one uses approximate numerical methods to perform the singularity expansion. Let the applied excitation reach the system at time $t=0$, and let the system's response be denoted by a real function of space and time $f(\vec{r}, t)$. This function can either be a scalar (such as the surface charge density) or a vector (such as the surface current density) or some other more exotic physical entity. Its Laplace transform $F(\vec{r}, s)$ will be analytic in the right half-plane $\text{Re } s > 0$. Its singularities are confined to the left half-plane $\text{Re } s < 0$. Very often, they consist of a host of simple poles lying either along the real axis or occurring in complex-conjugate pairs as shown in Fig. 9. This symmetry of the singularity distribution with respect to the real axis is a consequence of the reality of $f(\vec{r}, t)$, so that one can deduce from (47), the Schwarz reflection principle

$$F^*(\vec{r}, s) = F(\vec{r}, s^*) \quad (58)$$

where the asterisk denotes the complex conjugate.

Let $F(\vec{r}, s)$ be written in the form of the following singularity expansion

$$F(\vec{r}, s) = \sum_{m=1}^M \left[\frac{R_m(\vec{r})}{s - s_m} + \frac{R_m^*(\vec{r})}{s - s_m^*} \right] \quad (59)$$

The natural frequencies s_m can be complex with $\text{Re } s_m < 0$ or real and negative. The residues R_m can be complex or real and are functions of

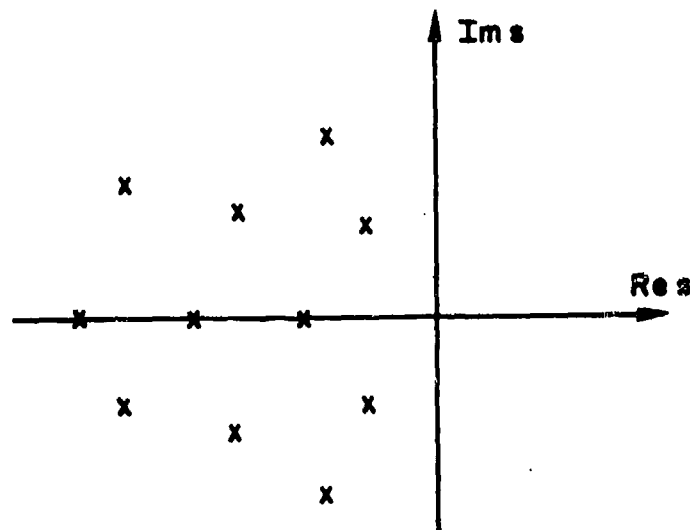


Fig. 9. Example of the complex-frequency-plane singularity pattern of a physical system.

position. They are proportional to the natural modes of oscillation of the system at the respective natural frequencies. The constants of proportionality measure the extent to which these modes are agitated by the source of excitation.

Eq.(59) is not the most general expansion for $F(\vec{r}, s)$. One can clearly add an arbitrary entire function to the right-hand side without affecting the singularity pattern in the finite s -plane. However, this entire function will alter the asymptotic behavior of $F(\vec{r}, s)$, making it approach a nonzero value as $s \rightarrow \infty$. Indeed, the entire function is closely related to the high-frequency response of the system. But if the excitation applied to the system is a pulse, its high-frequency components are vanishingly small. The response $F(\vec{r}, s)$ can be expected to approach zero as $s \rightarrow \infty$, as is the case in (59).

The inverse Laplace transform can again be performed by the method of residues, and one finds that for $t > 0$

$$f(\vec{r}, t) = \sum_{m=1}^M \left[R_m(\vec{r}) e^{s_m t} + K_m^*(\vec{r}) e^{s_m^* t} \right] \quad (60)$$

This shows the time-domain response $f(\vec{r}, t)$ as a sum of damped sinusoids. Each term describes the exponential decay of a natural mode after its excitation by the applied source.

Eq.(59) is an expression for studying the system's response to an intermediate-frequency excitation. The response of the system in the frequency domain is given by the value of $F(\vec{r}, s)$ along the $j\omega$ -axis of the s -plane. At real excitation frequency ω , the response is $F(\vec{r}, j\omega)$. From (59), it is clear that the contributions to $F(\vec{r}, j\omega)$ come mainly from those poles of $F(\vec{r}, s)$ that lie close to the point $s = j\omega$. In fact, a few nearest poles in the singularity expansion will generally represent the response with sufficient accuracy. Thus one sees that, at low and high excitation frequencies, the usual expansion of the frequency-domain response of a system is in terms of the ratio of the system dimension to the wavelength, whereas at intermediate excitation frequencies, a useful expansion is a singularity expansion in terms of the set of natural frequencies of the system.

Eq.(60) is valuable for studying the system's time-domain response at intermediate times. Each damped sinusoid appearing therein has its own characteristic damping constant which is directly proportional to the distance of the corresponding s -plane pole from the imaginary axis. The decay time of the corresponding natural mode is inversely proportional to this distance. At the very earliest times, immediately after the arrival of the applied excitation, the time-domain response $f(\vec{r}, t)$ is made up of contributions from each of the excited natural modes. However, as time goes on, the shorter-lived modes die out one by one, and progressively fewer terms need be retained in $f(\vec{r}, t)$, so that at late times none but the contribution from the pole closest to the imaginary axis survives. One therefore concludes that at an intermediate time t , only those poles with decay times comparable to or greater than t will contribute substantially to the time-domain response $f(\vec{r}, t)$.

The characterization of a system's response by a finite collection of simple poles, as exemplified by the singularity expansion of $F(\vec{r}, s)$

in (59), is a technique of great aesthetical appeal for studying transient electromagnetic problems. This type of basic singularity pattern is really what one comes up with when one approaches the singularity expansion by purely numerical methods. But, analytically, more complicated situations can conceivably arise. First, the number of natural frequencies of a distributed system is really infinite, so that the set of poles is actually infinite. The integer M in (59) should be replaced by ∞ . This raises the question of the convergence of the infinite sum; and one may have to perform appropriate rearrangements of the terms to achieve convergence. Second, some singularities of $F(\vec{r}, s)$ may appear as branch cuts. A branch cut is essentially a continuous one-dimensional distribution of poles, and turns up whenever the natural frequency spectrum of the system contains a continuous portion. Third, some singularities of $F(\vec{r}, s)$ may appear as multiple poles rather than simple poles; but this new feature can be easily accommodated in the singularity expansion. One suspects that multiple poles can occur only under the most fortuitous circumstances, when the parameters of a physical system are accidentally so interrelated that two or more simple poles coincide.

Before delving into the mechanics of singularity expansion, it is instructive to analyze in detail a number of exactly soluble electromagnetic problems in the context of complex-frequency-plane singularities.

1.4.2.2 s-Plane Singularities in Transmission-Line Analysis

A transmission line is an important electromagnetic system that is only one step removed from a lumped network circuit in order of complexity. Its behavior is described by a pair of partial differential equations involving one spatial dimension as well as time. These equations are often simple enough to permit exact solution. A close study of the exact solution can shed valuable light on the basic features of singularity expansion.

1.4.2.2.1 Finite Transmission Line

Consider a straight two-wire transmission line of finite length ℓ , open circuited at both ends. Let it lie in the z -direction from $z = 0$

to $z=l$, as shown in Fig. 10. The inductance, capacitance, resistance and conductance per unit length of the line are assumed constant. They are denoted respectively by L' , C' , R' and G' .

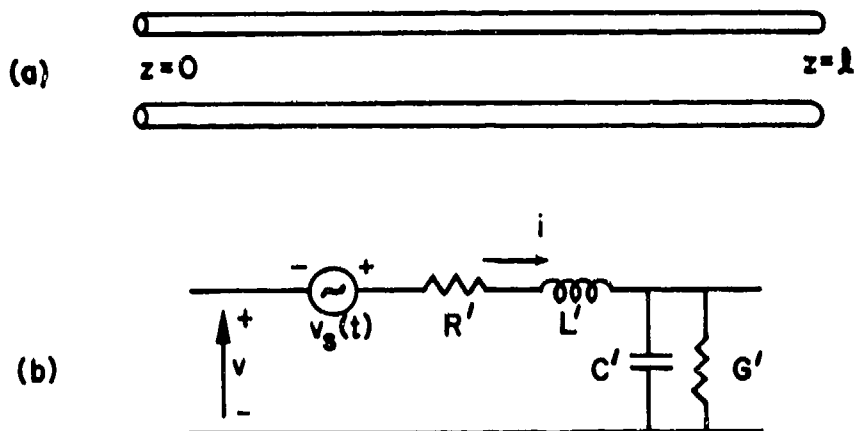


Fig. 10. A finite two-wire transmission line and its equivalent circuit per section.

Let the line be excited by a transient distributed voltage source $v_s(z,t)$. Then the shunt voltage $v(z,t)$ and the series current $i(z,t)$ vary along the line according to the following pair of coupled partial differential equations in space and time

$$\begin{aligned} \frac{\partial v}{\partial z} + \left(L' \frac{\partial}{\partial t} + R' \right) i &= v_s \\ \frac{\partial i}{\partial z} + \left(C' \frac{\partial}{\partial t} + G' \right) v &= 0 \end{aligned} \quad (61)$$

In the complex-frequency domain these equations become

$$\begin{aligned} \frac{dv}{dz} + Z'I &= v_s \\ \frac{dI}{dz} + Y'v &= 0 \end{aligned} \quad (62)$$

where Z' and Y' are respectively the series impedance and the shunt admittance per unit length given by

$$Z'(s) = L's + R', \quad Y'(s) = C's + G' \quad (63)$$

Eliminating V from (62), one obtains a nonhomogeneous second-order ordinary differential equation for I

$$\left(\frac{d^2}{dz^2} + k^2 \right) I = -Y' V_s \quad (64)$$

with

$$k^2(s) = -Y'(s)Z'(s) \equiv -\gamma^2(s) \quad (65)$$

The open-circuited line has the following homogeneous boundary conditions

$$I(z=0) = I(z=l) = 0 \quad (66)$$

The solution of (64) satisfying (66) can be expressed as

$$I(z,s) = Y'(s) \int_0^l G(z,z') V_s(z',s) dz' \quad (67)$$

where $G(z,z')$ is a Green's function determined by equation

$$\left(\frac{d^2}{dz^2} + k^2 \right) G(z,z') = -\delta(z-z') \quad (68)$$

and the boundary conditions

$$G(0,z') = G(l,z') = 0 \quad (69)$$

For the purpose of deriving a singularity expansion for I from (67), it is convenient to expand the Green's function $G(z,z')$ in terms of the eigenfunctions $\psi_n(z)$ of the Hermitian operator $-d^2/dz^2$

$$-\frac{d^2}{dz^2} \psi_n = k_n^2 \psi_n \quad (70)$$

The eigenfunctions which vanish at the ends $z=0$ and l are

$$\psi_n(z) = \sqrt{\frac{2}{l}} \sin(k_n z) \quad (71)$$

with the eigenvalues

$$k_n = \frac{n\pi}{l} \quad n = 1, 2, 3, \dots \quad (72)$$

These eigenfunctions are real and form a complete orthonormal set

$$\int_0^l \psi_n(z) \psi_m(z) dz = \delta_{nm} \quad (73)$$

so that one can expand $G(z, z')$ as

$$G(z, z') = \sum_{n=1}^{\infty} a_n \psi_n(z) \quad (74)$$

Substituting this expression in (68) and evaluating the coefficients a_n one obtains

$$G(z, z') = \sum_{n=1}^{\infty} \frac{\psi_n(z) \psi_n(z')}{k_n^2 - k^2} \quad (75)$$

Upon combining (67) and (75) the following explicit representation of the solution I of (64) results

$$I(z, s) = \sum_{n=1}^{\infty} \frac{Y'(s) X_n(s)}{k_n^2 - k^2(s)} \psi_n(z) \quad (76)$$

with

$$X_n(s) = \int_0^l V_s(z', s) \psi_n(z') dz' \quad (77)$$

The singularity expansion of $I(z,s)$ is readily derived from (76). From (63) and (65) one first obtains the following partial-fraction decomposition

$$\frac{Y'(s)}{k_n^2 - k^2(s)} = \frac{1}{L'C'} \frac{1}{(s_{n+} - s_{n-})} \left[\frac{Y'(s_{n+})}{s - s_{n+}} - \frac{Y'(s_{n-})}{s - s_{n-}} \right] \quad (78)$$

where s_{n+} and s_{n-} are the roots of the equation

$$k_n^2 - k^2(s) = 0 \quad (79)$$

or, more explicitly,

$$s_{n\pm} = -\frac{1}{2} \left(\frac{R'}{L'} + \frac{G'}{C'} \right) \pm \frac{1}{2} \sqrt{\frac{4n^2\pi^2}{L'^2 C'} - \left(\frac{R'}{L'} - \frac{G'}{C'} \right)^2} \quad (80)$$

Eq.(78) shows that $I(z,s)$ has simple poles at $s = s_{n\pm}$ in the s -plane. These complex frequencies are precisely those at which the homogeneous part of (64), with $V_s = 0$, has nontrivial solutions satisfying the boundary conditions (66). They are in fact the natural frequencies of the finite transmission line. The eigenfunctions ψ_n in (71) are the corresponding natural modes.

Besides the poles at the natural frequencies $s_{n\pm}$, $I(z,s)$ also contains the singularities of the factor $X_n(s)$ contributed by the source V_s . One can split up the singularity expansion of $I(z,s)$ into two parts

$$I(z,s) = I_1(z,s) + I_2(z,s) \quad (81)$$

such that I_1 contains all the natural-frequency singularities, and I_2 all the source singularities. One finds that

$$I_1(z,s) = \sum_{n=1}^{\infty} \frac{\psi_n(z)}{L'C' (s_{n+} - s_{n-})} \left[\frac{X_n(s_{n+})Y'(s_{n+})}{s - s_{n+}} - \frac{X_n(s_{n-})Y'(s_{n-})}{s - s_{n-}} \right] \quad (82)$$

and that

$$I_2(z, s) = \sum_{n=1}^{\infty} \frac{\psi_n(z)}{L'C'(s_{n+} - s_{n-})} \left[\frac{\{X_n(s) - X_n(s_{n+})\} Y'(s_{n+})}{s - s_{n+}} - \frac{\{X_n(s) - X_n(s_{n-})\} Y'(s_{n-})}{s - s_{n-}} \right] \quad (83)$$

If the square root in (80) is real for all n , then one has $s_{n-} = s_{n+}^*$ and (82) becomes

$$I_1(z, s) = \sum_{n=1}^{\infty} \left[\frac{R_n(z, s_{n+})}{s - s_{n+}} + \frac{R_n^*(z, s_{n+})}{s - s_{n+}^*} \right] \quad (84)$$

with

$$R_n(z, s_{n+}) = \frac{X_n(s_{n+}) Y'(s_{n+})}{L'C'(s_{n+} - s_{n+}^*)} \psi_n(z) \quad (85)$$

Use has been made of the relation

$$X_n(s_{n+}^*) = X_n^*(s_{n+}) \quad (86)$$

following from the fact that the source function $v_s(z, t)$ is real. It is clear from (80) that the poles of $I_1(z, s)$ all lie along a straight line parallel to the imaginary axis as shown in Fig. 11. If the square root in (80) is imaginary for some n , then some of the poles lie on the negative real axis. Note that the two terms inside the square brackets in (84) should be summed together as a single unit. If they are summed individually, the individual infinite sums may diverge.

The current $I_2(z, s)$ in (83) is analytic at the natural frequencies $s_{n\pm}$. Its singularities are due solely to the source V_s . Take, for definiteness, the source $v_s(z, t)$ in the form of a step function in time

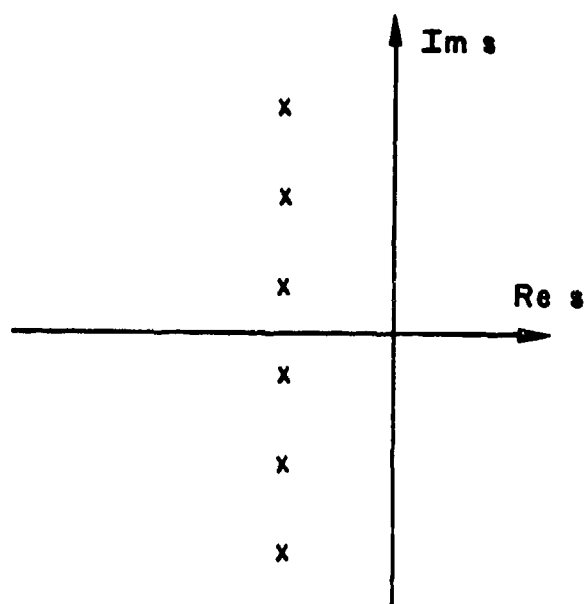


Fig. 11. Complex-frequency-plane singularity pattern of a finite open-circuit transmission line. The pattern consists of an infinite array of simple poles parallel to the imaginary axis.

$$v_s(z, t) = \begin{cases} 0 & t < 0 \\ g_o(z) & t > 0 \end{cases} \quad (87)$$

Its Laplace transform is

$$V_s(z, s) = \frac{g_o(z)}{s} \quad (88)$$

showing a simple pole at $s = 0$. The function $X_n(s)$ becomes

$$X_n(s) = \frac{W_n}{s} \quad (89)$$

with W_n being real and given by

$$W_n = \int_0^l g_o(z') \psi_n(z') dz' \quad (90)$$

Substituting (89) in (83) one finds that

$$I_2(z,s) = -\frac{1}{s} \sum_{n=1}^{\infty} \frac{\psi_n(z) W_n}{L'C' (s_{n+} - s_{n-})} \left[\frac{Y'(s_{n+})}{s_{n+}} - \frac{Y'(s_{n-})}{s_{n-}} \right] \quad (91)$$

showing the same simple pole at $s=0$ as V_s .

1.4.2.2 Infinite Transmission Line

Suppose now the transmission line in the above example becomes of infinite length. Its behavior is still governed by (61), but its range is extended to the infinite interval $-\infty < z < \infty$. Then (64) can be solved by using the Fourier integral. The solution is

$$I(z,s) = \int_{-\infty}^{\infty} \frac{Y'(s) X_p(s)}{p^2 - k^2(s)} \psi_p(z) dp \quad (92)$$

where now

$$\psi_p(z) = \frac{1}{\sqrt{2\pi}} e^{-j p z} \quad (93)$$

$$X_p(s) = \int_{-\infty}^{\infty} V_s(z',s) \psi_p^*(z') dz' \quad (94)$$

Eq.(92) is obviously a generalization of (76). In place of the infinite-sum representation in (76) for the current in the finite transmission line, one has here an infinite-integral representation when the length of the transmission line grows to infinity.

The s -plane singularities of $I(z,s)$ are a sum of those of the integrand in (92). As a function of s , the integrand has singularities at the zeros of the denominator $p^2 - k^2(s)$, in addition to whatever singularities the source factor $X_p(s)$ may contain. One has

$$p^2 - k^2(s) = L'C'(s - s_{p+})(s - s_{p-}) \quad (95)$$

with

$$s_{p\pm} = -\frac{1}{2} \left(\frac{R'}{L'} + \frac{G'}{C'} \right) \pm \frac{1}{2} \sqrt{\frac{4p^2}{L'C'} - \left(\frac{R'}{L'} - \frac{G'}{C'} \right)^2} \quad (96)$$

Thus the integrand has two simple poles at $s = s_{p+}$ and s_{p-} . The locations of the poles depend on the continuous integration variable p , instead of on an integer n in (80) for the finite line. Under integration, p varies continuously from $-\infty$ to ∞ . These poles then trace out a branch cut in the s -plane for $I(z,s)$, as shown in Fig. 12. The branch cut has an

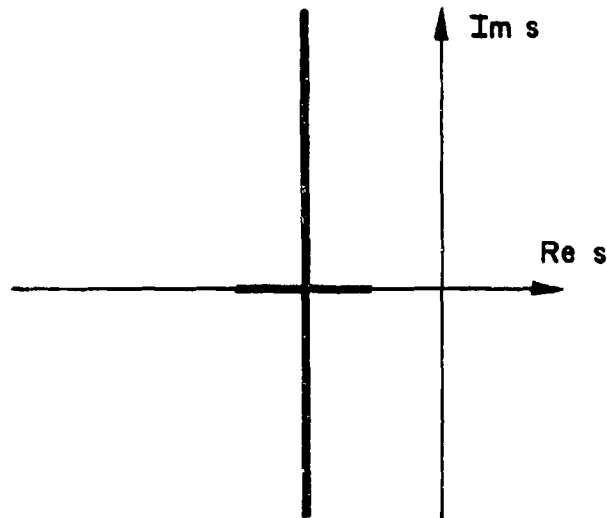


Fig. 12. s -plane singularity pattern of an infinite transmission line. The pattern consists of branch cuts.

infinite portion parallel to the imaginary axis, as well as a finite portion along the real axis. The latter portion is due to those values of p for which the square root in (96) is purely imaginary.

The existence of the branch cut for the infinite transmission line may well be deduced by letting the length l of the finite line tend to ∞

in (80). In this limit the poles of the finite line in the s -plane become densely crowded together. At infinite l , the pole array merges into a continuum and forms a branch cut.

The appearance of the branch cut for the infinite line is also to be expected from general considerations. There is a one-to-one correspondence between the s -plane singularities and the natural frequencies of a physical system. The poles correspond to a discrete natural-frequency spectrum, while a branch cut corresponds to a continuous spectrum. It is well known that a finite transmission line has a discrete spectrum, i.e., only at a discrete set of frequencies can excitations be produced along the line which satisfy the boundary conditions at the two ends of the line. By contrast, an infinite line has a continuous spectrum. At each and every frequency, excitations can propagate freely along the line; and the homogeneous transmission-line equations have nontrivial solutions at all frequencies.

The singularity expansion for the transmission-line voltage $V(z,s)$ can be derived from that for the current $I(z,s)$ by using (62).

1.4.2.3 s -Plane Singularities in Scattering Analysis

Of greater complexity than the transmission-line problem is the problem of transient electromagnetic scattering from a conductor. This scattering problem is central to the external interaction of an aircraft with an EMP. The response of the conductor to the incident electromagnetic transient is in the form of an induced surface current density. Just as for the current along a transmission line, this surface current density can be characterized by singularities in the complex frequency plane. These singularities are closely related to the properties of the conductor and the incident wave. Each singularity belonging to the conductor corresponds to the frequency of a certain natural mode of the conductor. The response in the frequency domain can be expanded in terms of these singularities. In the following the singularity expansion of the induced surface current density is derived and examined for an exactly soluble scattering problem.

Consider the scattering of an arbitrary incident electromagnetic wave by a perfectly conducting sphere of radius a and centered at the coordinate origin, as shown in Fig. 13. It is well known that this problem can be solved exactly by the method of separation of variables.

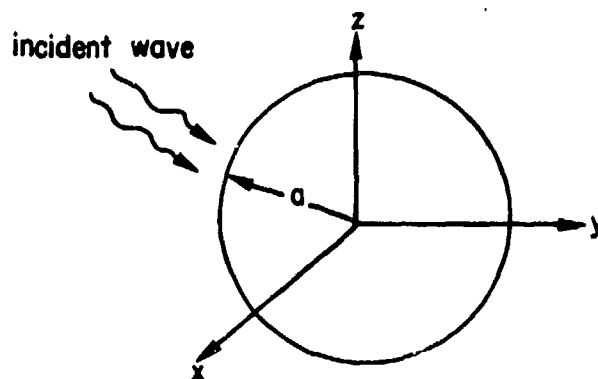


Fig. 13. Scattering of an arbitrary electromagnetic wave by a perfectly conducting sphere centered at the coordinate origin.

In the frequency domain the Maxwell equations in free space outside the sphere read

$$\begin{aligned} \nabla \cdot \vec{E}(\vec{r}, s) &= 0, & \nabla \times \vec{E}(\vec{r}, s) &= -s\mu_0 \vec{H}(\vec{r}, s) \\ \nabla \cdot \vec{H}(\vec{r}, s) &= 0, & \nabla \times \vec{H}(\vec{r}, s) &= s\varepsilon_0 \vec{E}(\vec{r}, s) \end{aligned} \quad (97)$$

The fields \vec{E} and \vec{H} can be derived from a pair of scalar Debye potentials U and V

$$\begin{aligned} \vec{E} &= -\nabla \times (jk\vec{r}U + \vec{r} \times \nabla V) \\ z_0 \vec{H} &= -\nabla \times (\vec{r} \times \nabla U - jk\vec{r}V) \end{aligned} \quad (98)$$

where

$$k = -j s/c \equiv -j\gamma \quad (99)$$

The Debye potentials are both solutions of the Helmholtz equation

$$(\nabla^2 + k^2)U = 0, \quad (\nabla^2 + k^2)V = 0 \quad (100)$$

U generates a TE wave and V a TM wave relative to the r-direction. They can be split up into an incident part and a scattered part

$$U = U^i + U^s, \quad V = V^i + V^s \quad (101)$$

The incident Debye potentials can be derived from the given fields of the incident wave. They have the following general expansions in terms of the spherical wave functions

$$\begin{aligned} U^i(\vec{r}, s) &= \sum_{\ell=1}^{\infty} \sum_{m=-\ell}^{\ell} A_{\ell m}(s) j_{\ell}(kr) Y_{\ell m}(\theta, \phi) \\ V^i(\vec{r}, s) &= \sum_{\ell=1}^{\infty} \sum_{m=-\ell}^{\ell} B_{\ell m}(s) j_{\ell}(kr) Y_{\ell m}(\theta, \phi) \end{aligned} \quad (102)$$

where j_{ℓ} is a spherical Bessel function and $Y_{\ell m}$ a spherical harmonic. The latter is defined by

$$Y_{\ell m}(\theta, \phi) = \sqrt{\frac{2\ell+1}{4\pi} \frac{(\ell-m)!}{(\ell+m)!}} P_{\ell}^m(\cos \theta) e^{jm\phi} \quad (103)$$

with P_{ℓ}^m denoting an associated Legendre function. $Y_{\ell m}$ satisfies the orthonormality relation

$$\int_0^{2\pi} d\phi \int_0^{\pi} d\theta \sin \theta Y_{\ell m}^*(\theta, \phi) Y_{\ell' m'}(\theta, \phi) = \delta_{\ell \ell'} \delta_{m m'}, \quad (104)$$

Note that in (102) the term $\ell=0$ is absent since it does not give rise to any fields.

The scattered Debye potentials are calculated by imposing the following boundary conditions at the surface of the sphere $r = a$

$$U^i + U^s = 0, \quad \frac{\partial}{\partial r} (rV^i + rV^s) = 0 \quad (105)$$

The results are

$$U^s(\vec{r}, s) = - \sum_{\ell=1}^{\infty} \sum_{m=-\ell}^{\ell} A_{\ell m}(s) \frac{j_{\ell}(ka)}{h_{\ell}^{(2)}(ka)} h_{\ell}^{(2)}(kr) Y_{\ell m}(\theta, \phi) \quad (106)$$

$$V^s(\vec{r}, s) = - \sum_{\ell=1}^{\infty} \sum_{m=-\ell}^{\ell} B_{\ell m}(s) \frac{\psi'_{\ell}(ka)}{\zeta'_{\ell}(ka)} h_{\ell}^{(2)}(kr) Y_{\ell m}(\theta, \phi)$$

where $h_{\ell}^{(2)}$ is a spherical Hankel function of the second kind, and

$$\psi_{\ell}(ka) = ka j_{\ell}(ka), \quad \zeta_{\ell}(ka) = ka h_{\ell}^{(2)}(ka) \quad (107)$$

The prime on ψ_{ℓ} and ζ_{ℓ} in (106) denotes differentiation with respect to the argument.

The surface current density \vec{J} induced on the sphere is related to the total magnetic field by

$$\vec{J} = \vec{I}_r \times (\vec{H}^i + \vec{H}^s) \quad (108)$$

From the Debye potentials calculated above one obtains after some algebra

$$J_{\theta}(\theta, \phi, s) = \frac{1}{aZ_0} \sum_{\ell=1}^{\infty} \sum_{m=-\ell}^{\ell} \left[A_{\ell m}(s) \frac{-j_{\ell}(ka)}{\zeta_{\ell}(ka)} \frac{1}{\sin \theta} \frac{\partial}{\partial \phi} Y_{\ell m}(\theta, \phi) + B_{\ell m}(s) \frac{1}{\zeta'_{\ell}(ka)} \frac{\partial}{\partial \theta} Y_{\ell m}(\theta, \phi) \right] \quad (109)$$

$$J_{\phi}(\theta, \phi, s) = \frac{1}{aZ_0} \sum_{\ell=1}^{\infty} \sum_{m=-\ell}^{\ell} \left[A_{\ell m}(s) \frac{j_{\ell}(ka)}{\zeta_{\ell}(ka)} \frac{\partial}{\partial \theta} Y_{\ell m}(\theta, \phi) + B_{\ell m}(s) \frac{1}{\zeta'_{\ell}(ka)} \frac{1}{\sin \theta} \frac{\partial}{\partial \phi} Y_{\ell m}(\theta, \phi) \right] \quad (110)$$

Eqs.(109) and (110) show that the s-plane singularities of both components of the induced surface current density \vec{J} are contained in the two types of factors $A_{\ell m}/\zeta_\ell$ and $B_{\ell m}/\zeta'_\ell$. The first factor originates from a TE mode, and the second from a TM mode. The singularities contributed by $A_{\ell m}$ and $B_{\ell m}$ are all due to the incident wave. Those contributed by $1/\zeta_\ell$ and $1/\zeta'_\ell$ correspond to the natural frequencies of the conducting sphere. By (99) and (107) and the definition of the spherical Hankel function, one has

$$\frac{1}{\zeta_\ell(ka)} = \frac{s^\ell e^{sa/c}}{(\text{polynomial of degree } \ell \text{ in } s)} \quad (111)$$

$$\frac{1}{\zeta'_\ell(ka)} = \frac{s^{\ell+1} e^{sa/c}}{(\text{polynomial of degree } \ell+1 \text{ in } s)} \quad (112)$$

Consequently $1/\zeta_\ell$ has ℓ simple poles, and $1/\zeta'_\ell$ has $\ell+1$ simple poles, in the finite s-plane. They both have an essential singularity at infinity, but tend to zero exponentially as $s \rightarrow \infty$ in the left half-plane.

Eqs.(109) and (110) display one feature of singularity expansion that is not found in the transmission-line analysis, namely, the appearance of degeneracy. By degeneracy is meant that several distinct natural modes all correspond to the same natural frequency. Each natural mode function of the surface current density on the sphere depends on the two integers ℓ and m , whereas each natural frequency depends on ℓ but not on m . The consequence is that each natural frequency is $(2\ell+1)$ -fold degenerate. On the other hand, it is also true that to each natural mode function there correspond several natural frequencies. Each mode function is multiplied into $1/\zeta_\ell$ or $1/\zeta'_\ell$, which contains more than one natural frequency pole.

In principle, it is possible to perform a partial-fraction decomposition of $1/\zeta_\ell$ and $1/\zeta'_\ell$ in terms of their poles, and hence obtain the explicit singularity expansions for J_θ and J_ϕ from (109) and (110). However, a general analytical formula for the pole location does not

exist. The poles must be located by numerical computation, as is done in [29]. Fig. 14 shows a plot of some of the natural-frequency poles of a conducting sphere, using the results of [29]. One gets the idea that these poles actually blanket the entire left half-plane, unlike in the case of the finite transmission line. Note also the symmetry of the pole distribution with respect to the real axis.

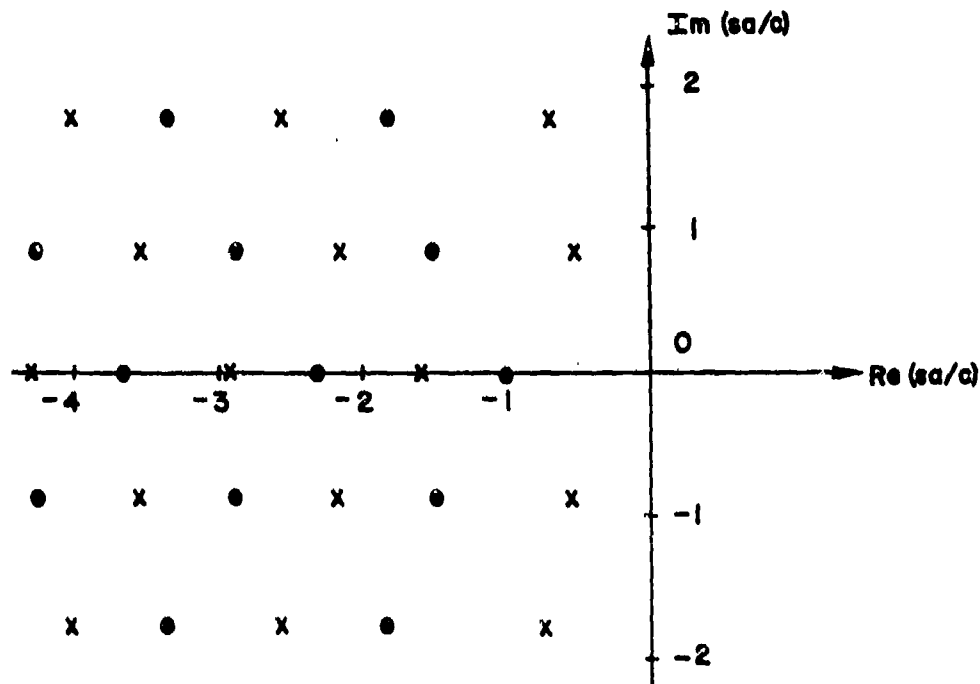


Fig. 14. Natural-frequency poles of a perfectly conducting sphere of radius a . A cross (\times) denotes a TM mode, while a heavy dot (\bullet) denotes a TE mode.

The induced surface current density on a conducting spherical scatterer is therefore a meromorphic function of the complex frequency s . It has been shown that this conclusion is actually true for all finite-sized conducting scatterers [30]. This result can perhaps be

understood by observing that a finite-sized scatterer is topologically equivalent to a sphere. If a sphere is gradually deformed into the shape of another scatterer, its natural frequencies are expected to change continuously and the corresponding poles are shifted around over the s -plane. It is observed that when a sphere is elongated to form a prolate spheroid, its line of poles closest to the imaginary axis moves even closer toward the imaginary axis, while the other poles move progressively farther away from it [31]. Thus, a very slender prolate spheroid must exhibit a singularity pattern consisting of an infinite linear array of poles close to the imaginary axis, which reminds one of the pole pattern of a finite transmission line, and an infinite cluster of poles far away in the left half-plane.

1.4.2.4 Expansion Parameters for Simple Natural-Frequency Poles

The exact solutions of simple electromagnetic problems are extremely valuable in providing insight into the intricate workings of singularity expansion. In practice, however, exact solutions are notoriously hard to come by. More often than not, one has to make do with approximate solutions. One can try to expand the frequency-domain response of a physical system in terms of only a partial set of the natural-frequency singularities. This subset is to be so chosen that the truncated singularity expansion still offers a good approximation to the exact expansion under the circumstances of interest. For this endeavor it is desirable to have at one's disposal a general prescription for calculating directly the singularity expansion parameters.

Practical physical systems all have finite geometrical dimensions. The exact solutions worked out above lead one to believe that the natural-frequency singularities of finite bodies consist only of simple poles in the finite s -plane. A simple pole is characterized completely by its location and residue. These two quantities can be calculated from the equations describing the frequency-domain response of the physical system.

The frequency-domain response of a linear electromagnetic system to an applied excitation can be described in the concise language of

abstract vector space. In this description the response and the excitation are represented by vectors $f(s)$ and $g(s)$, respectively, with s denoting the complex frequency. These vectors are related by a linear operator, or matrix, $L(s)$ characterizing the system

$$L(s)f(s) = g(s) \quad (113)$$

For a lumped network circuit, $L(s)$ is a multiplicative function. For a transmission line, $L(s)$ is a differential operator. In scattering problems, $L(s)$ usually appears as an integral operator.

In general, $L(s)$ has a set of eigenvectors v_α with corresponding eigenvalues s_α . They are determined from the nontrivial solutions of the homogeneous equation

$$L(s_\alpha)v_\alpha = 0 \quad (114)$$

The eigenvalues s_α are the natural frequencies of the system and the eigenvectors v_α represent the natural modes. As $L(s)$ is in general not Hermitian, the eigenvalues s_α are in general complex. The real part of s_α describes the decay of the natural mode due to radiation or ohmic losses.

One next introduces the transpose L^T of L obtained by interchanging the two matrix indices of L

$$(L^T)_{mn} = (L)_{nm} \quad (115)$$

L^T has its own set of eigenvalues and eigenvectors. Its eigenvalues turn out to be identical to those of L . They likewise consist of the set s_α . The eigenvector corresponding to the eigenvalue s_α will be denoted by μ_α , so that

$$L^T(s_\alpha)\mu_\alpha = 0 \quad (116)$$

as compared to (114). The eigenvector μ_α lies in a vector space dual to that of v_α . A scalar product between two vectors ψ and χ belonging to two mutually-dual vector spaces can be defined as

$$\langle \psi, \chi \rangle = \int \psi(x) \chi(x) dx \quad (117)$$

where the integration extends over the entire domain of definition of the eigenvectors, and x symbolically represents a general point of the domain.

Suppose the eigenvalue spectrum of L is discrete. Then the response $f(s)$ has a simple pole at every natural frequency s_α . Furthermore, suppose s_α is not degenerate, so that it corresponds to one and only one natural mode v_α . Then, when the frequency s is very close to s_α , the response $f(s)$ is predominantly in the resonant mode v_α . One can therefore put

$$f(s) \approx C_\alpha(s) v_\alpha \quad \text{for } s \approx s_\alpha \quad (118)$$

where C_α is a function of s . To evaluate C_α one substitutes (118) into (113), and takes the scalar product of the resulting expression with the dual eigenvector μ_α . The outcome is

$$C_\alpha = \frac{\langle \mu_\alpha, g(s) \rangle}{\langle \mu_\alpha, L(s) v_\alpha \rangle} \quad (119)$$

For $s \approx s_\alpha$, one can make the following approximation

$$L(s) \approx L(s_\alpha) + (s - s_\alpha) L'(s_\alpha) \quad (120)$$

where the prime on L denotes differentiation with respect to s . Substituting (120) into (119) and making use of (114), one obtains

$$C_\alpha = \frac{\langle \mu_\alpha, g(s_\alpha) \rangle}{(s - s_\alpha) \langle \mu_\alpha, L'(s_\alpha) v_\alpha \rangle} \quad (121)$$

where $g(s)$ has been replaced by its value $g(s_\alpha)$ at the pole. Eqs.(118) and (121) show that in the immediate neighborhood of the simple natural-frequency pole $s = s_\alpha$, the response $f(s)$ has the form

$$f(s) \approx \frac{\eta_\alpha v_\alpha}{s - s_\alpha} \quad (122)$$

where η_α is a coupling coefficient defined by

$$\eta_\alpha = \frac{\langle \mu_\alpha, g(s_\alpha) \rangle}{\langle \mu_\alpha, L'(s_\alpha) v_\alpha \rangle} \quad (123)$$

If, on the other hand, the natural frequency s_α is degenerate, the above calculation must be modified. Suppose s_α corresponds to n natural modes v_1, v_2, \dots, v_n . Then, by definition

$$L(s_\alpha) v_i = 0, \quad i = 1, 2, \dots, n \quad (124)$$

Similarly, the transpose operator L^T of L has an n -fold degenerate natural frequency s_α with corresponding natural modes $\mu_1, \mu_2, \dots, \mu_n$, so that

$$L^T(s_\alpha) \mu_i = 0, \quad i = 1, 2, \dots, n \quad (125)$$

When the frequency s is very close to s_α , the system response $f(s)$ will be predominantly distributed among the n degenerate resonant modes. One can put

$$f(s) \approx \sum_{i=1}^n C_i(s) v_i, \quad \text{for } s \approx s_\alpha \quad (126)$$

where each C_i is a function of s . Substituting (126) into (113) and taking scalar products successively with $\mu_1, \mu_2, \dots, \mu_n$, one obtains the following set of n linear equations

$$\sum_{j=1}^n C_j \langle \mu_i, L(s) v_j \rangle = \langle \mu_i, g(s) \rangle, \quad i = 1, 2, \dots, n \quad (127)$$

The solution of (127) becomes particularly simple if one chooses in advance the degenerate natural modes μ_i and v_j in such a way that the operator $L'(s_\alpha)$ is diagonal, that is,

$$\langle \mu_i, L'(s_\alpha) v_j \rangle = \langle \mu_i, L'(s_\alpha) v_i \rangle \delta_{ij} \quad (128)$$

Then, by (120), (124) and (128) one has

$$\langle \mu_i, L(s) v_j \rangle \approx (s - s_\alpha) \langle \mu_i, L'(s_\alpha) v_i \rangle \delta_{ij} \quad (129)$$

The solution of (127) becomes

$$c_i = \frac{\langle \mu_i, g(s_\alpha) \rangle}{(s - s_\alpha) \langle \mu_i, L'(s_\alpha) v_i \rangle} \quad (130)$$

where $g(s)$ has been replaced by $g(s_\alpha)$.

Therefore, when s is close to the n -fold degenerate natural frequency s_α , the response $f(s)$ has the form

$$f(s) \approx \frac{1}{s - s_\alpha} \sum_{i=1}^n \eta_i v_i \quad (131)$$

where the coupling coefficients η_i are

$$\eta_i = \frac{\langle \mu_i, g(s_\alpha) \rangle}{\langle \mu_i, L'(s_\alpha) v_i \rangle} \quad (132)$$

and the degenerate natural modes have been chosen to make the operator $L'(s_\alpha)$ diagonal.

Examples of the application of the formulas for simple-pole singularity expansion parameters can be found in [32,33].

1.4.2.5 Numerical Approach

The frequency-domain response of an electromagnetic system to an applied excitation can be described by a linear equation of the general form (113). The response is determined by constructing the inverse L^{-1} of L , so that the solution of (113) is

$$f(s) = L^{-1}(s)g(s) \quad (133)$$

It is clear that $f(s)$ has singularities at those values s_α of s that are eigenvalues of the operator L [see (114)]. When the inverse operator L^{-1} is expressed in terms of the eigenvalues and the eigenvectors of L , (133) becomes a singularity expansion of $f(s)$.

In most practical problems, it will not be possible to determine the inverse operator L^{-1} analytically. Approximate numerical techniques will have to be employed. In general, in a numerical approach, $f(s)$ and $g(s)$ in (113) are approximated by finite-dimensional vectors. One such approach is the so-called method of moments [34] in which a set of expansion basis functions $\{v_n\}$ is introduced. The unknown function $f(\vec{r}, s)$ is then approximated by

$$f(\vec{r}, s) = \sum_{n=1}^M f_n(s) v_n(\vec{r}) \quad (134)$$

Substituting (134) in (113) one obtains

$$\sum_{n=1}^M f_n(s) L(\vec{r}, s) v_n(\vec{r}) = g(\vec{r}, s) \quad (135)$$

Next, a set of testing functions $\{u_m\}$ is defined and the scalar product of (135) with each u_m is taken according to (117). Then

$$\sum_{n=1}^M f_n(s) \langle u_m, L(s) v_n \rangle = \langle u_m, g(s) \rangle, \quad m=1, 2, \dots, N \quad (136)$$

Under this scheme, L becomes a finite-dimensional square matrix whose elements are functions of s . Its inverse L^{-1} can be constructed by

standard methods of matrix inversion. The natural frequencies s_α are solutions of the equation

$$\det \langle u_m, L(s)v_n \rangle = 0 \quad (137)$$

and can be calculated numerically by iteration. The corresponding natural modes v_α and their duals u_α are then determined by (114) and (116). Knowing both the natural frequencies and the natural modes, one can calculate the coupling coefficients from (123) and obtain thereby the singularity expansion of $f(s)$.

Examples of numerical approaches to SEM can be found in [31,35]. For a comprehensive literature survey on SEM, the reader may consult [26].

1.4.3 HIGH FREQUENCY, EARLY-TIME REGION

At high frequencies, the electromagnetic fields away from source regions (whether actual, as on an antenna, or induced, as on a passive scatterer) can be approximated by equations that are simpler than the Maxwell vector field equations. The simplification arises from the fact that in the far zone of source distributions, the evanescent storage field can be neglected. The simplified equations are based on the assumption that $ka \gg 1$, where $k = 2\pi/\lambda$ (with λ representing the wavelength) is the wavenumber in the medium and a is a scale length describing characteristic observation distances, obstacle dimensions or medium inhomogeneities. The precise nature of a depends on the problem under consideration, and it is therefore convenient in the mathematical treatment to regard k by itself as the large parameter, keeping in mind that normalization in the combined form ka is intended eventually. This section will treat the high-frequency approximation methods based on the assumption that $ka \gg 1$.

1.4.3.1 Ray Method

The simplified equations resulting from $ka \gg 1$ are found to characterize the high-frequency field in terms of local propagation

phenomena involving propagation paths called rays. Thus, the field from an initial reference surface A to an observation point P can be tracked along a ray that passes through P and originates at point P' on A. The field at P is affected only by the initial field values in the vicinity of P' and by the medium properties in the vicinity of the ray. It is possible that several rays pass through P, either because of the nature of the field distribution on A or because the presence of obstacles or scatterers gives rise to other local fields (Fig. 15). In that event,

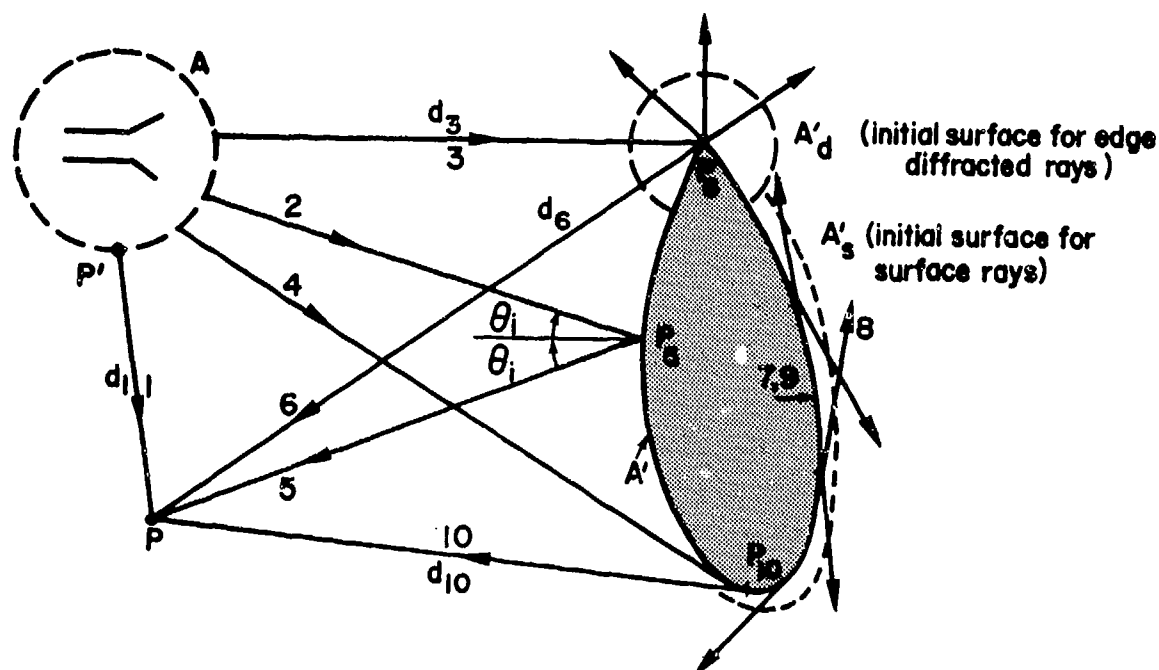


Fig. 15. Scattering by a composite obstacle with surface contour A'. Various ray species have been identified by numbers explained in the text. The following are initial surfaces: A for incident rays, A' for reflected rays, A'_d for tip diffracted rays, and A'_s for surface (creeping) rays.

the total field at P is synthesized by the sum of the fields reaching P along the various rays. The localization arises from the fact that high-frequency source distributions generate a spectrum of plane waves that interfere constructively along certain preferred directions, the rays, and thereby give rise to a strong field; along other directions that deviate from the rays, these waves interfere destructively and cause weak effects that can be ignored [36 - 38].

Along the ray trajectories, the constructively interfering plane waves can be characterized as a *local* plane wave. The local plane wave concept is central to the tracking of high-frequency fields. To understand what is involved, we consider the distinction between true and local plane waves. A true plane wave in a homogeneous medium has a plane phase front (equiphase surface) $A(\vec{r}) = A_0$ (constant) and an amplitude $u(\vec{r}) = u_0$ (constant), where \vec{r} is the position vector. The field propagates in the direction perpendicular to the phase front. These perpendicular trajectories, along which the phase front advances, point in the direction of $\nabla A(\vec{r})|_{A=A_0}$ and are the rays. For an observation point P along a ray, the field differs from that at P' on the initial surface A_0 only by the phase change $\exp(-jkd)$, where d is the distance between P' and P (Fig. 16). A local plane wave describes a field

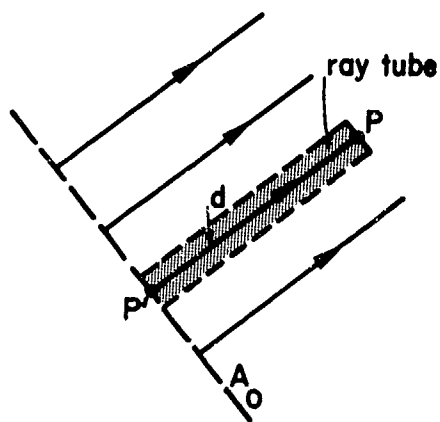


Fig. 16. True plane wave.

characterized by non-planar phase fronts. The simplest example is that of a spherical wave. Ignoring the vectorial properties, the scalar field in the far zone is given by

$$u(\vec{r}) \sim C \frac{e^{-jkr}}{kr} \quad (138)$$

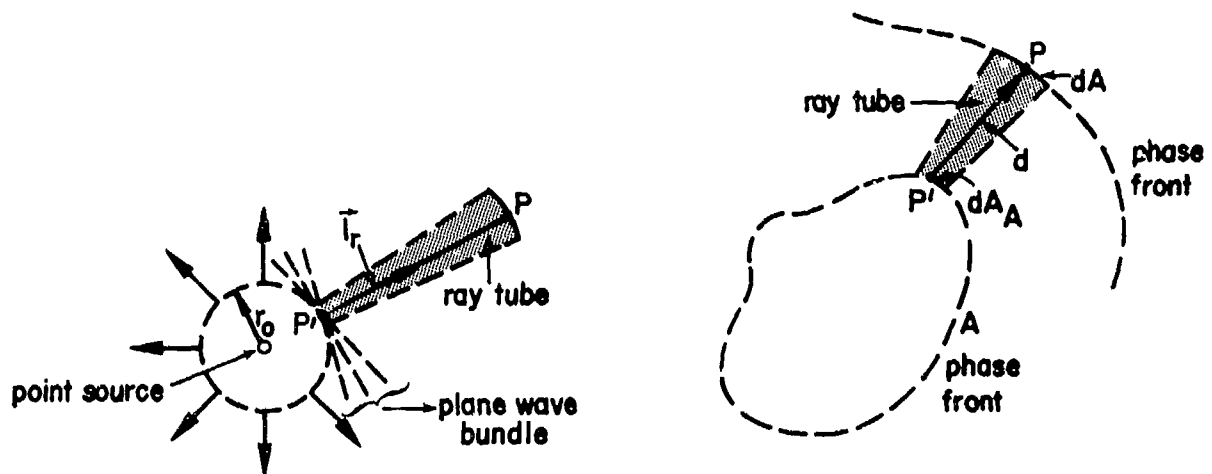
where C is a constant. If $r=r_0$ denotes the initial wave front, then the rays point in the direction $\nabla r|_{r=r_0} = \hat{r}$, where \hat{r} is a radial unit vector. The field at P along the ray originating at P' differs from the field at P' not only by the phase change $\exp(-jkd)$ as in a true plane wave, but also by the amplitude change $r_0/(r-r_0)$. This amplitude change identifies the field along the ray as a local plane wave field which is synthesized by constructive interference of a bundle or packet of true plane waves whose propagation directions are close to \hat{r} (Fig. 17a)

Since energy in the high-frequency field, as carried by the local plane waves, flows along the direction of the rays, energy is conserved in a tube of rays. Thus, the energy density is inversely proportional to the ray tube cross section dA . The field amplitude is proportional to the square root of the energy density and therefore varies inversely with \sqrt{dA} . For the spherical wavefront in Fig. 17a, the ray tube is conical and the cross section varies as r^2 ; the amplitude therefore decreases as $1/r$ as in (138). When the wavefront has a more general shape as in Fig. 17b, the ray tube cross section dA may have two principal radii of curvature R_1 and R_2 each centered on a surface called a caustic.

The preceding considerations lead to the following formulation of the local plane wave field carried along a ray [37]

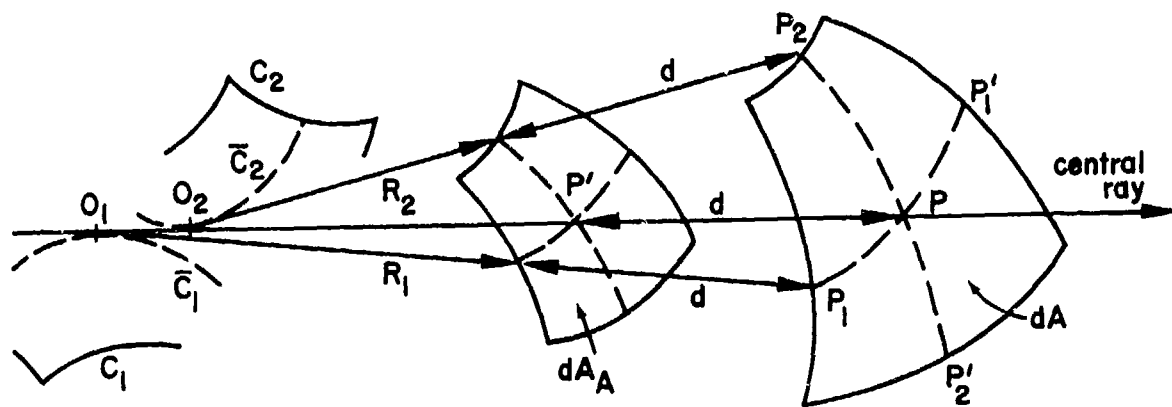
$$u(\vec{r}) \sim u_A \left(\frac{dA_A}{dA} \right)^{1/2} e^{-jkd}, \quad \frac{dA_A}{dA} = \frac{R_1 R_2}{(R_1 + d)(R_2 + d)} \quad (139)$$

where u_A is the initial field at P' on A (Fig. 17b), dA_A is the initial ray tube cross section, and d is the distance from P' to P . The expression for dA_A/dA in terms of R_1 and R_2 is inferred from Figs. 17b,c.



(a) spherical phase front

(b) arbitrary phase front



(c) Ray tube cross sections dA_A and dA for arbitrary phase front. The principal coordinate directions are shown dashed. The principal radii of curvature R_1 and R_2 are centered at the virtual foci O_1 and O_2 , respectively, from which emanate the rays passing through the points (P_1, P'_1) and (P_2, P'_2) . These rays are tangent to caustic surfaces C_1 and C_2 whereon lie the virtual foci descriptive of ray tubes cut out elsewhere on the phase front. The curves \bar{C}_1 and \bar{C}_2 on the caustic surfaces correspond to rays passing through extensions of the principal coordinate curves $P_1P'_1$ and $P_2P'_2$.

Fig. 17. Local plane waves, rays and ray tubes.

The local plane wave field along a ray can be calculated by (139) from a knowledge of the initial field value and the ray geometry. The initial field value must be determined independently by solution of *canonical problems*. In the canonical problem, the incident local plane wave field may be replaced by a true plane wave field, and the obstacle configuration by a simpler geometry that nevertheless retains the correct local scattering properties. For the incident field in Fig. 15 the initial values on A can be calculated from the known source distribution. The reflected field is caused by the incident rays (ray 2 in Fig. 15) reflected at the obstacle surface. The reflection laws for local plane waves on a curved surface are the same as for *true plane waves* on an *infinite plane surface* tangent to the curved surface at the point of impact of the incident ray (canonical problem). Thus, the incident and reflection angles θ_1 are equal. The initial value of the reflected field at P_5 is given by the incident field at P_5 multiplied by the plane wave reflection coefficient $\Gamma(\theta_1)$ descriptive of the reflecting properties of the boundary surface. The amplitude variation along ray 5, as determined by the ray tube cross section dA_{A5} , involves the surface curvature at P_5 , the curvature parameters for the incident wavefront, and the angle coordinates χ and χ_1 specifying the directions of the reflected and incident rays. Therefore, the reflected contribution to the field at P is given by (see ray 5 in Fig. 15)

$$u_5 \sim u_2 \Gamma(\theta_1) M(5,2) e^{-jkd_5}, \quad u_2 \sim u_{A2} \frac{e^{-jkd_2}}{kd_2} \quad (140)$$

where u_{A2} is the initial field for ray 2 on surface A. To simplify the notation here and subsequently, we have written

$$(dA_{A5}/dA)^{1/2} \equiv M(\chi_5, \chi_2) = M(5,2) \quad (141)$$

The incident local plane wave field along ray 3 striking the conical tip of the obstacle in Fig. 15 excites a spherical wave front and therefore a family of rays centered at the tip. The canonical problem for the

tip diffracted field is that of a plane wave incident on an infinite conical obstacle. That solution provides the *diffraction coefficient* $D^V(\chi, \chi_1)$, by which the incident ray field is modified upon emerging from the conical tip.* Here, χ and χ_1 denote, respectively, the angle coordinates specifying the directions of the diffracted and incident rays. Thus, the contribution at P due to the local plane wave along ray 6 is

$$u_6 \sim D^V(6,3) \frac{e^{-jkd_6}}{kd_6} u_3, \quad u_3 \sim u_{A3} \frac{e^{-jkd_3}}{kd_3} \quad (142)$$

where u_{A3} is the initial field for ray 3 on surface A. To simplify the notation here and subsequently, we have written

$$D^V(6,3) \equiv D^V(\chi_6, \chi_3) \quad (143)$$

Although the canonical problem yields the diffracted field on the initial surface A'_d in Fig. 15, the result can be expressed more conveniently as in (142) where relevant length parameters are measured from the tip.

When an incident ray grazes a smooth segment of a scatterer (ray 4 in Fig. 15), it excites a diffracted surface ray (also called creeping ray) that travels along a geodesic on the shadowed surface (ray 7) and sheds energy continuously (ray 8). The launching amplitude $L(\chi, \chi_1)$ of a surface ray field and its amplitude variation $M_s(d_7)$ along its geodesic path d_7 are determined from the canonical problem of plane wave diffraction by a smooth obstacle and have been found for special configurations. When a surface ray strikes the conical tip, it also gives rise to a spherical diffracted wave that adds a field u'_6 to the contribution at P arriving along ray 6. The canonical problem of surface ray field diffraction by

*While the problem of plane wave diffraction by a conical obstacle can be solved, no convenient form for the diffraction coefficient has as yet been developed.

the tip of a conical obstacle is still under study; it furnishes the diffraction coefficient $D_s(\chi, \chi_1)$. The field u'_6 is then given by

$$u'_6 \sim u_4 L(7,4) M_s(d_7) e^{-jkd_7} D_s(6,7) \frac{e^{-jkd_6}}{kd_6}, \quad u_4 \sim u_{A4} \frac{e^{-jkd_4}}{kd_4} \quad (144)$$

where d_7 is the surface ray path (geodesic) between the point of tangency of the incident ray 4 and the tip.

Tip diffraction due to incident ray 3 also gives rise to a surface ray (ray 9) that emerges at P_{10} to contribute to the field at P along ray 10. The initial surface A'_s for shed surface rays is displaced from the obstacle surface but in the formulation of the diffracted field, it is again convenient to measure distances from the obstacle surface. Thus

$$u_{10} \sim u_3 D_s(9,3) M_s(d_9) e^{-jkd_9} L(10,9) \frac{e^{-jkd_{10}}}{kd_{10}} \quad (145)$$

where u_3 is given in (142), d_9 denotes the geodesic length along ray 9 from the tip to the shedding point P_{10} , and $L(10,9)$ gives the shedding amplitude which can be normalized, so that it equals in form the launching amplitude. Although the surface rays 7 and 9 in Fig. 15 appear to coincide, they describe different trajectories since the points of tangency of ray 4 and departure of ray 10 are not identical.

The total ray-optical field at point P in Fig. 15 is now given by

$$u \sim u_1 + u_5 + u_6 + u'_6 + u_{10} \quad (146)$$

where

$$u_1 \sim u_{A1} \frac{e^{-jkd_1}}{kd_1} \quad (147)$$

denotes the field along the direct ray from the source, and the remaining contributions, given by (140) - (145), are due to the presence of the obstacle.

The result in (146) contains only the dominant contribution from each of the ray fields. Generally, each ray field has, in addition to this leading term, a series of higher-order terms that decay inversely with k . The field is therefore given by an asymptotic expansion in inverse powers of k . Validity of the leading term alone implies that the higher-order terms, in particular the second term, are small in comparison with the first. Some estimates of the accuracy of the asymptotically expanded field can be made on general grounds (see. Sec. 1.4.3.3.1) but for scattering problems encountered in practice, it is usually too difficult to apply them. Therefore, the range of parameters, for which formulas as in (146) are useful and valid, has been ascertained by comparison with canonical analytical solutions or with numerical solutions that can be generated independently. These considerations are illustrated in Sec. 2.1.2.2. For example, in transition regions near shadow boundaries, caustics, and foci where relevant ray field amplitudes tend to infinity, the use of uniform asymptotic methods provides a valid description.

By the very construction of the field in (146), it is evident that the ray method decomposes a complicated composite scattering problem into a sequence of simpler (canonical) problems via the following steps:

- (a) Determination of the incident field over an initial surface A.
- (b) Determination of the reflected and diffracted ray fields that contribute at an observation point P.
- (c) Identification of canonical problems that treat *separately* each of the ray reflection and diffraction problems. The solutions of these problems furnish the initial amplitudes along various species of reflected and diffracted rays.
- (d) Synthesis of composite scattering problem by interaction (along rays) between canonical constituents.

The various ray species arising in the diffraction problem of Fig. 15 have been associated with a perfectly conducting obstacle.

When the obstacle has other surface features (for example, edges) or when it is penetrable (lossless dielectric), additional diffraction mechanisms and corresponding ray fields may arise [36 - 38].

1.4.3.2 Equations for the Ray-Optical Field, and Their Solution [36 - 38]

1.4.3.2.1 Derivation of the Equations

The scalar field u in an inhomogeneous medium with refractive index n satisfies the scalar wave equation

$$[\nabla^2 + k^2(\vec{r})]u(\vec{r}) = 0, \quad k(\vec{r}) = k_0 n(\vec{r}) \quad (148)$$

where k_0 is the wavenumber in vacuum and k is the wavenumber in the medium. By assuming that u at high frequencies (large k_0) behaves like a local plane wave field, the wave equation can be simplified. In order to allow for corrections to the local plane wave assumption, we write u in the form of an asymptotic expansion (see Sec. 1.4.3.3.1) in inverse powers of k_0 , wherein the local plane wave field represents the dominant ($m=0$) term

$$u(\vec{r}) \sim u_0(\vec{r}) \exp[-jk_0 \psi(\vec{r})] + \exp[-jk_0 \psi(\vec{r})] \sum_{m=1}^{\infty} \frac{u_m(\vec{r})}{(-jk_0)^m} \quad (149)$$

The amplitude functions u_m , $m=0,1,2,\dots$, and the phase function ψ , are assumed to be independent of k_0 . Substitution of (149) into (148) gives

$$\sum_{m=0}^{\infty} Q_m(\vec{r}) (-jk_0)^{2-m} = 0 \quad (150)$$

Since this equation must be satisfied for arbitrary (though large) k_0 , one equates to zero the coefficients Q_m to obtain from $Q_0 = 0$

$$[\nabla \psi(\vec{r})]^2 = n^2(\vec{r}) \quad (\text{eikonal equation}) \quad (151)$$

A unit vector

$$\hat{\mathbf{i}}_{\xi} = \frac{\nabla \psi(\vec{r})}{|\nabla \psi(\vec{r})|} = \frac{\nabla \psi(\vec{r})}{n(\vec{r})} \quad (152)$$

compatible with (151) then points in the direction of the normal to the equiphase surfaces $\psi(\vec{r}) = \text{constant}$, and may therefore be identified as the ray vector tangent to the ray trajectories. Since

$$\vec{l}_\xi = \frac{d\vec{r}}{d\xi} \quad (153)$$

if $\vec{r} = \vec{r}(\xi)$ denotes points on the ray trajectory and ξ measures distance along a ray (Fig. 18), one may write (152) as

$$\frac{d}{d\xi} \left[n(\xi) \frac{d\vec{r}}{d\xi} \right] = \nabla n(\xi) \quad (154)$$

to obtain the ray equation. The notation $n(\xi)$ implies that the observation points \vec{r} are constrained to lie along a ray.

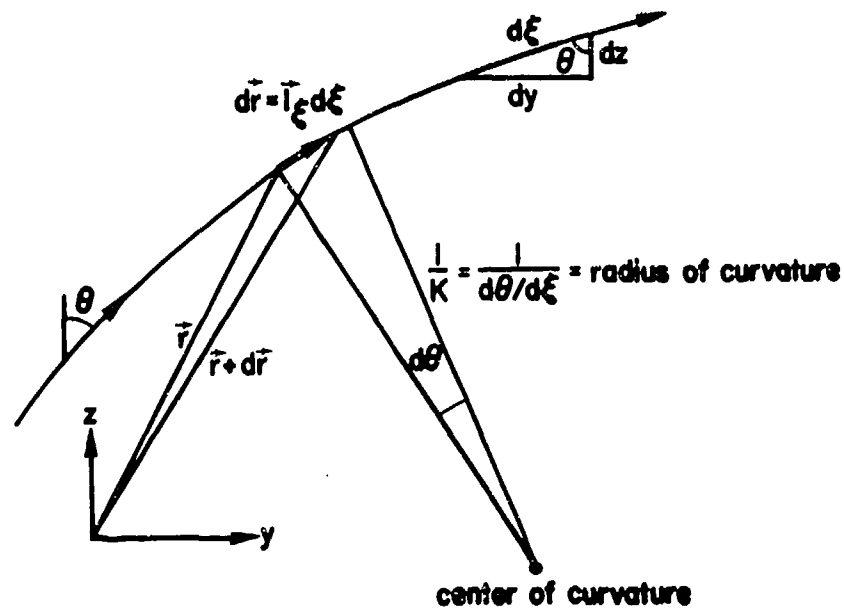


Fig. 18. Ray parameters.

The next term in (150) gives $Q_1 = 0$, that is,

$$[\nabla^2 \psi(\vec{r}) + 2\nabla \psi(\vec{r}) \cdot \nabla] u_0(\vec{r}) = 0 \quad (\text{transport equation}) \quad (155)$$

which is equivalent to

$$\nabla \cdot [|u_0^2(\vec{r})| n(\vec{r}) \hat{\xi}] = 0 \quad (156)$$

with the quantity inside the square brackets being proportional to the energy flux density in the local plane wave field flowing along the rays. Eq. (156) therefore represents an energy flux conservation theorem, which has already been applied in Sec. 1.4.3.1 on physical grounds (within a tube of rays) for the determination of u_0 along a ray.

From $Q_m(\vec{r}) = 0$, $m \geq 2$, in (150) one obtains the transport equations for the higher-order amplitude coefficients that correct the local plane wave field. These equations are

$$[\nabla^2 \psi(\vec{r}) + 2\nabla \psi(\vec{r}) \cdot \nabla] u_{m-1}(\vec{r}) = -\nabla^2 u_{m-2}(\vec{r}), \quad m \geq 2 \quad (157)$$

These recursive equations are more complicated than that for the dominant term u_0 , and it is usually impractical to effect a solution for the higher-order coefficients u_m , $m \geq 2$. However, these equations are useful for providing estimates on the range of validity of the local plane wave field assumption, which requires that $|u_1| k_0^{-1} \ll |u_0|$ (see Sec. 1.4.3.3.1). From this requirement, one may deduce the restriction

$$\frac{|\nabla n(\vec{r})|}{n(\vec{r})} \frac{1}{k_0 n(\vec{r})} \ll 1 \quad (158)$$

which states that the relative change in the refractive index over an interval of the local wavelength λ in the medium must be small; that is to say, the medium must be "slowly varying" on the local wavelength scale.

1.4.3.2.2 Ray Trajectories

The ray trajectories are obtained by solving (154) subject to prescribed initial conditions. In a homogeneous medium with $n(\xi) = \text{constant}$, (154) reduces to $d\vec{r}/d\xi = \text{constant}$, or $\vec{r}(\xi) = \vec{A}\xi + \vec{B}$, where \vec{A} and \vec{B} are constant vectors. Therefore, the rays are straight lines.

In an inhomogeneous medium, the rays are generally smoothly curved. It may be shown that the curvature K of the ray is given by

$$K(\xi) = \frac{1}{n(\xi)} \frac{dn(\xi)}{d\ell} \quad (159)$$

where ℓ is the coordinate perpendicular to ξ and hence lies on a wavefront. Therefore, the ray is curved whenever the refractive index n varies along a wavefront, and the ray bends toward the direction of increasing n . This behavior is in accord with the application of Snell's law of refraction when the continuously varying medium is approximated by a sequence of locally homogeneous layers. In a plane stratified medium where the refractive index $n(\vec{r}) = n(z)$ varies along the rectilinear coordinate z only, the rays may be shown to be plane curves. A typical ray $y = y(z)$ lying in the $x = 0$ plane (Fig. 18) has the functional form

$$y - y_0 = \eta \int_{z_0}^z \frac{d\zeta}{[n^2(\zeta) - \eta^2]^{1/2}} \quad (160)$$

where (y_0, z_0) is the initial point on the ray, and $\eta \equiv n(z) \sin \theta(z) = \text{constant}$, with θ defined in Fig. 18, is the ray parameter. By choosing different values of η according to different initial conditions, one may generate the entire ray family. The condition $\eta = \text{constant}$ is a statement of Snell's refraction law when applied to a continuously varying medium.

1.4.3.2.3 Phase and Amplitude

The local plane wave phase ψ is determined from (152) by integration along a ray

$$\psi(\vec{r}) - \psi(\vec{r}_0) = \int_{\vec{r}_0}^{\vec{r}} n(\xi) d\xi \quad (161)$$

where \vec{r}_0 and \vec{r} are the initial and observation point along the same ray, and $\psi(\vec{r}_0)$ is the initial phase.

In a homogeneous medium with constant $n(\vec{r}) = n_0$, where the rays are straight lines,

$$\psi(\vec{r}) - \psi(\vec{r}_0) = n_0 |\vec{r} - \vec{r}_0| = n_0 d \quad (162)$$

as already noted in Sec. 1.4.3.1 from physical considerations pertaining to the local plane wave field. In a plane stratified inhomogeneous medium with $n(\vec{r}) = n(z)$, (161) yields for the ray in (160)

$$\psi(\vec{r}) - \psi(\vec{r}_0) = n(y - y_0) + \int_{z_0}^z [n^2(\zeta) - n^2]^{1/2} d\zeta \quad (163)$$

The local plane wave amplitude u_0 is determined by (155) or (156). By applying Gauss' divergence theorem to a volume contained within a tube of rays, (156) may be reduced to

$$|u_0(\vec{r})| \sim |u_0(\vec{r}_0)| \left[\frac{n(\vec{r}_0) dA(\vec{r}_0)}{n(\vec{r}) dA(\vec{r})} \right]^{1/2} \quad (164)$$

where $dA(\vec{r}_0)$ and $dA(\vec{r})$ are, respectively, the ray tube cross sections containing the initial point and the observation point along the same ray. For a spherical wavefront in a homogeneous medium, (164) reduces to the result in Sec. 1.4.3.1.

1.4.3.2.4 Ray-Optical Field

The ray-optical (local plane wave) field $u_0 \exp(-jk\psi)$ in an inhomogeneous medium can be constructed by combining the results from (161) and (164) to give

$$u(\vec{r}) \sim u(\vec{r}_0) \left[\frac{n(\vec{r}_0) dA(\vec{r}_0)}{n(\vec{r}) dA(\vec{r})} \right]^{1/2} \exp \left[-jk_0 \int_{\vec{r}_0}^{\vec{r}} n(\xi) d\xi \right] \quad (165)$$

The validity of (165) is confined to slowly varying media, which are given by the condition (158). It is also restricted by the condition

$$dA(\vec{r}) \neq 0 \quad (166)$$

i.e., to the exterior of focusing regions where ray crossings occur. Ignoring (166) would lead to the incorrect conclusion of infinite fields at caustics and foci. To accommodate focusing regions where the ray-optical field is invalid, it is necessary to employ transition functions that are derived by a more sophisticated set of equations than those in (151) and (155).

1.4.3.2.5 Evanescent Fields [39,40]

Evanescent fields decay exponentially along certain directions, even in a lossless medium, and are therefore usually ignored in the presence of non-evanescent fields. However, situations arise where evanescent fields, though weak, are the only fields to be observed, and their propagation and diffraction characteristics then become important. Configurations where the total field is evanescent include the interior of cutoff waveguides, the exterior of dielectric slabs or rods guiding trapped waves, the transmitting medium when an incident field is totally reflected at an interface, the "dark" side of caustics confining focused fields, and the off-axis regions of strongly focused beams.

Like non-evanescent fields, high-frequency evanescent fields can be tracked by invoking the notion of local evanescent plane waves. Such waves are defined by the first term in (149) except that the phase ψ is now complex just like the amplitude u_0 . Thus, one writes for the local evanescent plane wave field

$$u(\vec{r}) \sim u_0(\vec{r}) \exp[-jk_0 \psi(\vec{r})] \quad (167)$$

with

$$\psi(\vec{r}) = R(\vec{r}) - jI(\vec{r}), \quad u_0(\vec{r}) = \exp[w(\vec{r}) - jv(\vec{r})] \quad (168)$$

where R , I , w and v are real functions of \vec{r} . The phase fronts $R(\vec{r}) = \text{constant}$ advance along the direction of the unit vectors

$$\vec{l}_\xi = \frac{\nabla R(\vec{r})}{\beta(\vec{r})}, \quad \beta \equiv |\nabla R| \quad (169)$$

while the field decays along the direction of the unit vector

$$\vec{l}_t = \frac{\nabla I(\vec{r})}{\alpha(\vec{r})}, \quad \alpha \equiv |\nabla I| \quad (170)$$

On surfaces $I(\vec{r}) = \text{constant}$, the field has constant exponential amplitude.

When (167) and (168) are substituted into the wave equation (148), the reduced equations (151) and (155) remain valid. On separating into real and imaginary parts, one obtains from (151) the dispersion equation

$$\beta^2(\vec{r}) - \alpha^2(\vec{r}) = n^2(\vec{r}) \quad (171)$$

and also the condition $\nabla R \cdot \nabla I = 0$, indicating that the surfaces of constant phase and constant exponential amplitude are orthogonal. Thus, the coordinates ξ and t form an orthogonal grid, with the ξ -trajectories (on which $I = \text{constant}$) referred to as "phase paths" and the t -trajectories (on which $R = \text{constant}$) referred to as "attenuation paths" (Fig. 19). The phase paths should not be confused with rays since the former are generally curved, even in a homogeneous medium. Whenever α varies along an attenuation path (i.e., on a phase front) so that $d\alpha/dt \neq 0$, then in view of (171) β will likewise vary along a phase front, even when $n = \text{constant}$. Since $\beta = \omega/V$,

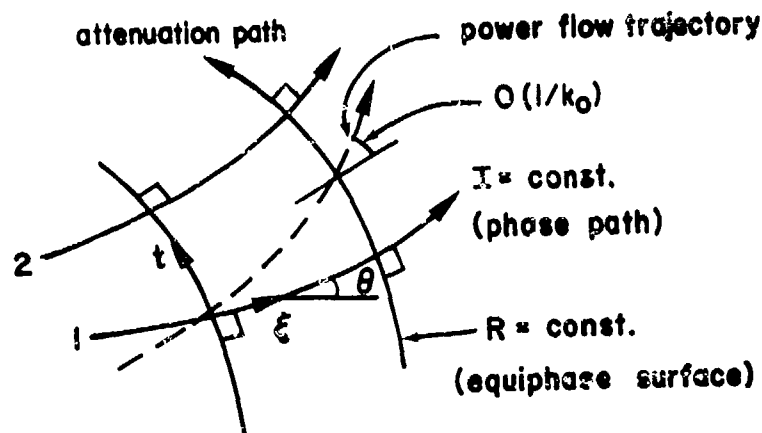


Fig. 19. Surfaces of constant phase and amplitude.

where ω is the wave frequency and V the phase propagation speed, different portions of the phase front propagate at different speeds. Hence, an originally plane phase front will become non-planar, and the phase paths orthogonal thereto become curved. Moreover, as indicated in Fig. 19, the power flow in the local evanescent plane wave field does not exactly follow the phase paths but deviates from them by an angle of $O(1/k_0)$.

From (169) and (170) the equations for the phase paths and attenuation paths are

$$\frac{d}{d\xi} [\beta(\vec{r}) \vec{l}_\xi] = \nabla \beta(\vec{r}), \quad \frac{d}{dt} [\alpha(\vec{r}) \vec{l}_t] = \nabla \alpha(\vec{r}) \quad (172)$$

Each of these equations, which must be solved simultaneously subject to (171), has the form of the ray equation (154) for the geometric-optical field. It also follows from (169) and (170) and the fact that $I = \text{constant}$ on a phase path while $R = \text{constant}$ on an attenuation path that

$$\alpha(\vec{r}) = \alpha(\vec{r}_0) \frac{dt(\vec{r}_0)}{dt(\vec{r})} \quad (173)$$

$$\beta(\vec{r}_1) = \beta(\vec{r}_0) \frac{d\xi(\vec{r}_0)}{d\xi(\vec{r}_1)} \quad (174)$$

In (173) \vec{r}_0 and \vec{r} are the initial point and observation point, respectively, along the same phase path, while $dt(\vec{r}_0)$ and $dt(\vec{r})$ are the spacings between corresponding neighboring phase paths (Fig. 20). Similarly, in (174) \vec{r}_0

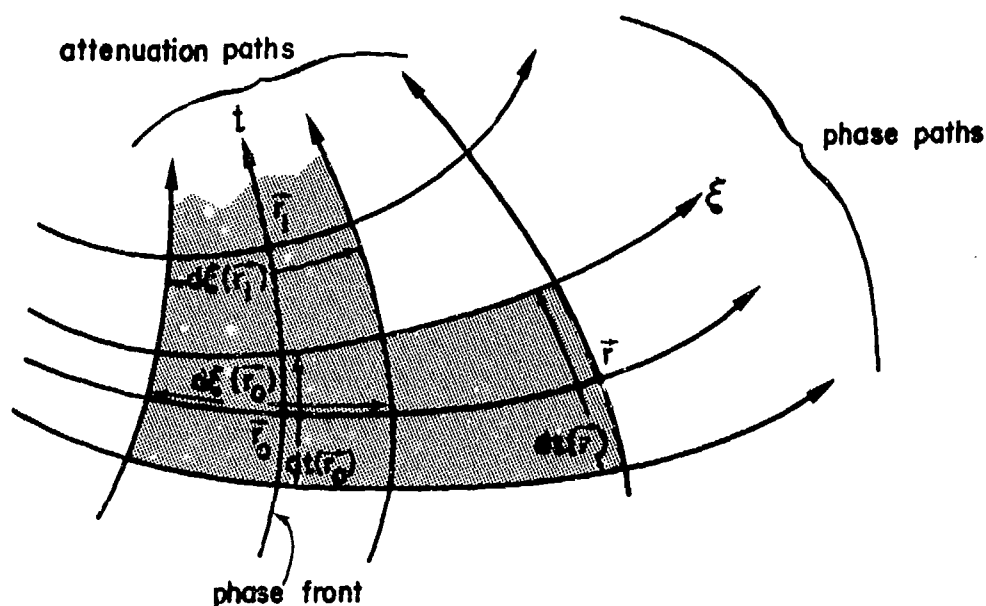


Fig. 20. Tracking of α and β along phase and attenuation paths.

and \vec{r}_1 are the initial and observation points, respectively, along the same attenuation path, while $d\xi(\vec{r}_0)$ and $d\xi(\vec{r}_1)$ are the spacings between corresponding neighboring attenuation paths (Fig. 20). Thus, as for the geometric-optical field, the (ξ, t) trajectory grid for the evanescent field provides the information required for the tracking of the phase gradient β and attenuation gradient α .

When (155) is separated into real and imaginary parts, there result two coupled transport equations for w and v in (168)

$$\nabla^2 R(\vec{r}) + 2\beta(\vec{r}) \frac{dw(\vec{r})}{d\xi} - 2\alpha(\vec{r}) \frac{dv(\vec{r})}{d\xi} = 0 \quad (175)$$

$$\nabla^2 I(\vec{r}) + 2\beta(\vec{r}) \frac{dv(\vec{r})}{d\xi} - 2\alpha(\vec{r}) \frac{dw(\vec{r})}{d\xi} = 0 \quad (176)$$

For weakly evanescent fields with small α , the above equations can be solved by perturbation methods. Since $\beta^{(0)} \approx n$ (see (171)), where the superscript denotes the order of the perturbation, one observes from (154) and the first equation in (172) that the unperturbed phase paths coincide with the geometric-optical rays for non-evanescent fields. One then calculates $\alpha^{(0)}$ along a phase path from (173), and thereafter $\beta^{(1)} = (n^2 + [\alpha^{(0)}]^2)^{1/2}$. Using $\beta^{(1)}$, the phase paths can now be corrected from (172), and $R^{(1)}$ can be calculated by integrating $\beta^{(1)} = dR^{(1)}/d\xi$ along a phase path. The exponential attenuation function I along a phase path remains constant at its initial value. The transport equations in (175) and (176) can be solved in a similar manner. It should be noted that due to the need for tracking two functions α and β along mutually perpendicular trajectories, the propagation characteristics of high-frequency evanescent fields are less local than those of non-evanescent fields.

1.4.3.3 Asymptotic Methods [41]

1.4.3.3.1 Asymptotic Expansions

Approximate evaluations of fields in the high-frequency regime commonly generate expansions in inverse powers of the wavenumber k , based on the assumption that k is large. An example is provided by the field representation in (149), wherein the leading term describes the local plane wave field. Expansions of this type, called "asymptotic expansions," generally do not converge; i.e., for a fixed value of the parameters (k_0 and \vec{r} in (149)), the series diverges because the expansion coefficients ($u_m(\vec{r})$ in (149)) grow as $m \rightarrow \infty$. Nevertheless, these series, although divergent in the strict mathematical sense, are useful because they can be employed to approximate the field provided that only a finite number of terms is included. Loosely speaking, a calculation involving the first M terms in the expansion is legitimate provided that the $(M+1)$ th term is smaller in magnitude than the M th term. For a given M , this can always be accomplished by choosing the asymptotic-expansion parameter ($1/k_0$ in (149)) large enough. A good indication of the quality of the

approximation can be obtained from the recognition that the error between the asymptotic representation involving M terms and the true value of the field is roughly equal to the magnitude of the $(M+1)$ th term. Based on these considerations one can deduce the necessary restrictions on the parameters in a function represented by an asymptotic series. For example, validation of the local plane wave (ray-optical) field in (149), as given by the first term, requires at the very least that $|u_1/k_0| \ll |u_0|$. Improvement of the local plane wave field by inclusion of the $m=1$ term requires at the very least that $|u_2/k_0| \ll |u_1|$, etc. In view of the error criterion cited above, it is evidently dangerous to push an asymptotic expansion containing a few terms, and especially if only the leading term is retained, near the limit where the first omitted term equals in magnitude the last term retained.

The preceding considerations can be phrased mathematically. Regarding k_0 as the large parameter, a function $F(\vec{r}, k_0)$ (for example, the field in (149)) can be represented rigorously as follows

$$F(\vec{r}, k_0) = \sum_{m=0}^M F_m(\vec{r}) k_0^{-m} + R_M(\vec{r}, k_0) \quad (177)$$

where R_M is a remainder term. Making k_0 large enough, one can reduce R_M to as small a value as desired (a good estimate of R_M is given by $|F_{M+1}(\vec{r}) k_0^{-M-1}|$). Thus asymptotic series are not usually written in the form (177); instead, letting $k_0 \rightarrow \infty$, the summation is extended over all values of m

$$F(\vec{r}, k_0) \sim \sum_{m=0}^{\infty} F_m(\vec{r}) k_0^{-m}, \quad k_0 \rightarrow \infty \quad (178)$$

and it is implied that for any m

$$\frac{F_{m+1}(\vec{r})}{k_0 F_m(\vec{r})} \rightarrow 0, \quad \text{as } k_0 \rightarrow \infty \quad (179)$$

However, for practical calculations involving fixed k_0 and \vec{r} , the series in (178) is to be understood in the sense of (177).

1.4.3.3.2 Asymptotic Evaluation of Integrals

Field formulations exterior to actual or induced source distributions generally involve integrals that extend either over a surface or volume in physical coordinate space, or over wavenumber space in a spectral representation (see Sec. 1.4.3.4). Such integrals are typically of the form

$$I(\Omega) = \int_D f(\vec{\tau}) e^{-j\Omega q(\vec{\tau})} d\vec{\tau} \quad (180)$$

where $\vec{\tau} = (\tau_x, \tau_y, \tau_z)$ denotes the integration variable in a three-dimensional coordinate space, D is the domain of integration, $f(\vec{\tau})$ and $q(\vec{\tau})$ are analytical functions of $\vec{\tau}$ (with isolated singularities), and Ω is a positive parameter (if Ω is complex, one writes $\Omega = |\Omega| \exp(-j \arg \Omega)$ and combines $\arg \Omega$ with q). When Ω is large, the exponential term is rapidly oscillating for real q or rapidly decaying for negative imaginary q . Assuming that f varies slowly by comparison with $\exp(-j\Omega q)$, one concludes that the major contribution to the integral arises from those regions in the τ -space where q is slowly varying when real, or where $(\text{Im } q)$ has a maximum when q is complex. These observations form the basis for approximate methods for evaluating I , which may be found in [42].

1.4.3.4 Alternative Formulations of Diffraction Problems

Diffraction problems of the type schematized in Fig. 15 can be formulated in various ways. Let the obstacle be perfectly conducting. The secondary field generated by the induced surface currents can be represented either in terms of the direct radiation from the elementary currents distributed over the obstacle surface A' , or in terms of a superposition of modal fields excited by these currents. One important example of the latter procedure involves modal plane-wave fields and results in the "plane-wave spectral representation." Both of these are formulated below.

1.4.3.4.1 Induced Current Formulation

Referring to Fig. 15, the total vector electric field \vec{E} may be decomposed into a specified incident part \vec{E}^i , which would exist in the

absence of the obstacle, and a secondary part \vec{E}^s due to the induced obstacle surface current

$$\vec{E} = \vec{E}^i + \vec{E}^s \quad (181)$$

The radiation from each current element \vec{J} can be expressed in terms of the free-space dyadic Green's function $\vec{G}(\vec{r}, \vec{r}')$. Thus

$$\vec{E}^s(\vec{r}) = \int_{A'} \vec{G}(\vec{r}, \vec{r}') \cdot \vec{J}(\vec{r}') d\vec{r}' \quad (182)$$

The surface currents must be such as to ensure vanishing of the tangential electric field on A' , i.e.

$$\vec{I}_n \times \vec{E}(\vec{r}) = 0, \quad \vec{r} \text{ on } A' \quad (183)$$

where \vec{I}_n is the unit vector normal to A' . Thus, these currents are specified implicitly by the integral equation

$$\vec{I}_n \times \vec{E}^i(\vec{r}) = -\vec{I}_n \times \int_{A'} \vec{G}(\vec{r}, \vec{r}') \cdot \vec{J}(\vec{r}') d\vec{r}', \quad \vec{r} \text{ on } A' \quad (184)$$

1.4.3.4.2 Plane-Wave Spectral Formulation

The incident and secondary fields may be expressed by modal superposition. In a basis involving plane-wave modes, one obtains

$$\vec{E}^i(\vec{r}) = \iint_{-\infty}^{\infty} \vec{e}^i(\xi, \eta) \exp \left[-jk(\xi x + \eta y + \sqrt{1 - \xi^2 - \eta^2} z) \right] d\xi d\eta \quad (185)$$

$$\vec{E}^s(\vec{r}) = \iint_{-\infty}^{\infty} \vec{e}^s(\xi, \eta) \exp \left[-jk(\xi x + \eta y + \sqrt{1 - \xi^2 - \eta^2} z) \right] d\xi d\eta \quad (186)$$

where $z = 0$ is a suitably chosen reference plane. Here, ξ, η and $\sqrt{1 - \xi^2 - \eta^2}$ are the normalized wave numbers of the modal plane waves

along the x, y and z directions, respectively. The modal amplitudes $\vec{e}^{\pm 1}$ for the known incident field are obtained by Fourier inversion of (185). The modal amplitudes $\vec{e}^{\pm s}$ for the secondary field are specified implicitly by the boundary condition (183).

1.4.3.4.3 High-Frequency Approximations

In the illuminated region A' on a perfectly conducting obstacle away from surface singularities (such as edges, tips, or corners) and from strongly curved regions (where the radius of curvature is not large compared to wavelength), one may approximate the induced surface currents by their "physical optics" value. The physical optics currents \vec{J}^p are based on the local behavior of high-frequency fields described in Sec. 1.4.3.1 and are taken at any point P on A' to have the same value as on an infinite perfectly conducting plane tangent to A' at P . Thus

$$\vec{J}^p(\vec{r}) = 2 \vec{\hat{n}} \times \vec{H}^i(\vec{r}), \quad \vec{r} \text{ on } A' \quad (187)$$

where \vec{H}^i is the incident vector magnetic field. In the shadow region one assumes $\vec{J}^p = 0$. When \vec{J}^p is substituted into (182), one obtains the physical optics approximation of the secondary field. This approximate field, when evaluated by the asymptotic method of Sec. 1.4.3.3.2, is found to give correctly the geometric-optical reflected field and the diffracted field near the shadow boundaries. It does not provide, however, good results for the diffracted field away from the shadow boundaries.

Even on a smoothly curved convex object with large radius of curvature, the physical optics currents become invalid near the shadow boundaries. One may therefore attempt to add to \vec{J}^p a correction \vec{J}^f , named "fringe current" by Ufimtsev [43], so that the sum equals the exact current value. Because of the validity of the physical optics currents well inside the illuminated region, and away from edges or corners, the fringe currents are confined to the vicinity of those portions on A' that lie near shadow boundaries or surface singularities.

The method of fringe currents has been exploited to correct the physical optics fields for scatterers with edges. However, as employed by Ufimtsev, the method has limitations because it does not yield the currents \vec{J}^f per se, but only the far fields produced by them. An alternative procedure approximates the fringe currents by equivalent edge currents \vec{J}^e flowing along an edge (Fig. 21), their value being selected so that they give the correct GTD (Geometrical Theory of Diffraction) field in its regions of validity. This approximation causes certain difficulties which have been discussed in a paper by Knott and Senior [44].

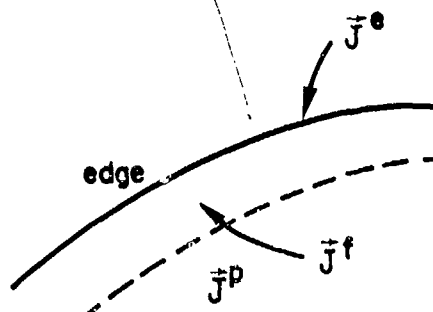


Fig. 21. Various current distributions on the illuminated side of a conducting obstacle bounded by an edge.

1.4.3.5 The GTD Vector Fields [45]

In this and subsequent sections the emphasis will be placed on the electromagnetic vector problem at the high-frequency, early-time limit whereas the previous sections, namely, Secs. 1.4.3.1 through 1.4.3.3, treat exclusively the scalar fields.

Let the total distance along the ray path from the reference point to the field point P be ξ ; the reference point O is commonly chosen to be the point at which the GTD field is excited. In free space the GTD electric field can be given the general form

$$\vec{E}(\xi, s) \sim \vec{F}(0, s) \cdot \vec{C}(s) f_s(\xi) e^{-s\xi/c} \quad (188)$$

in which

$\vec{F}(0, s)$ = forcing function (the incident field, source or reference field) at 0,

$f_s(\xi)$ = spreading factor expressing the power conservation in a tube or strip of rays,

$e^{-s\xi/c}$ = delay factor between 0 and P along the ray path,

$\vec{C}(s)$ = dyadic coefficient, which is the remaining part of the radiating system function and, in the case of scattering, depends on the local geometry of the body at the point of reflection or diffraction and perhaps the local behavior of the incident field.

The corresponding expression for the magnetic field, except at a convex surface, is

$$\vec{H}(\xi, s) \sim \vec{I}_\xi \times \vec{E}(\xi, s) / Z_0 \quad (189)$$

where, as before, ξ is a unit vector in the direction of the ray path. In the following "asymptotically equal to" \sim is replaced by "equal to" =, with the understanding that the expressions are high-frequency approximations.

Eq.(188) can be inverse Laplace transformed to give the following time-dependent field

$$\vec{E}(\xi, t) = f_s(\xi) \vec{S}(\xi, t) \quad (190)$$

where

$$\vec{S}(\xi, t) = \frac{1}{2\pi j} \int_{\Omega_0 - j\infty}^{\Omega_0 + j\infty} \vec{F}(0, s) \cdot \vec{C}(s) e^{s(t - \xi/c)} ds \quad (191)$$

or employing convolution,

$$\begin{aligned}\vec{J}(\xi, t) &= \int_{t_0}^{t-\xi/c} \vec{F}(0, t') \cdot \vec{C}(t-t') dt', \quad t - \xi/c > t_0 \\ &= 0, \quad t - \xi/c < t_0\end{aligned}\quad (192)$$

where t_0 is the time at 0 when the forcing function is turned on. The electric field $\vec{E}(\xi, t)$ as obtained from (190) is usually valid only for early times, more precisely, when t is close to $t_0 + \xi/c$.

If a caustic occurs on the ray path at P_1 between 0 and P, the expression for $\vec{E}(\xi, s)$ contains an additional factor of $\exp(j\pi/2)$, but (188) is still valid within a wavelength or so of P_1 . The presence of a caustic at P_1 is more serious for the calculation of $\vec{E}(\xi, t)$, because it leads to a noncausal result. We exclude this case from the present treatment.

The GTD representations of the electric and magnetic fields can be written as

$$\vec{E}(\vec{r}, s) = \vec{E}^i(\vec{r}, s) + \vec{E}^r(\vec{r}, s) + \vec{E}^d(\vec{r}, s) \quad (193)$$

$$\vec{H}(\vec{r}, s) = \vec{H}^i(\vec{r}, s) + \vec{H}^r(\vec{r}, s) + \vec{H}^d(\vec{r}, s) \quad (194)$$

where the first two terms in the above expressions are the incident and reflected components of the geometrical-optics field, and the last term is the diffracted field.

The surface current and charge densities induced on perfectly conducting surfaces are of interest. At the point \vec{r} on such a surface

$$\vec{J}(\vec{r}, s) = \vec{1}_n \times \vec{H}(\vec{r}, s) \quad (195)$$

$$\rho(\vec{r}, s) = \epsilon \vec{1}_n \cdot \vec{E}(\vec{r}, s) \quad (196)$$

where \vec{J} and ρ are related by the continuity equation (7). The geometrical-optics current and charge densities are

$$\vec{J}_0(\vec{r}, s) = 2 \vec{I}_n \times \vec{H}^1(\vec{r}, s) \quad (197)$$

$$\rho_0(\vec{r}, s) = 2 \epsilon \vec{I}_n \cdot \vec{E}^1(\vec{r}, s) \quad (198)$$

in the illuminated region, and zero in the shadow region. Deep in the illuminated region, well away from shadow boundaries, edges and vertices, the high-frequency surface current and charge densities may be adequately approximated by \vec{J}_0 and ρ_0 .

In the case of propagation away from the radiating source or structure we have for $\vec{E}(\xi, s)$ as given by (188)

$$\vec{F}(0, s) = \vec{E}(0, s) \quad (199)$$

$$\vec{C}(s) = \vec{I} \quad (200)$$

$$f_s(\xi) = \sqrt{\frac{R_1 R_2}{(R_1 + \xi)(R_2 + \xi)}} \quad (201)$$

in which R_1, R_2 are the principal radii of curvature of the wavefront at 0. For two-dimensional configurations we may let $R_2 \rightarrow \infty$ and obtain

$$f_s(\xi) = \sqrt{\frac{R_1}{R_1 + \xi}} \quad (202)$$

and in the case of plane waves, where R_1 as well as R_2 approaches ∞ , $f_s(\xi) = 1$.

Fields of this type are of interest here, because the field inducing a surface current or charge may have been initially reflected or diffracted by, for example, a fin, wing or fuselage of an aircraft before reaching the surface point in question.

1.4.3.5.1 Reflection

The GTD field contains the incident and reflected fields of geometrical optics as its leading terms. Let a high-frequency wave be incident on a smooth, perfectly conducting surface S as shown in Fig. 22.

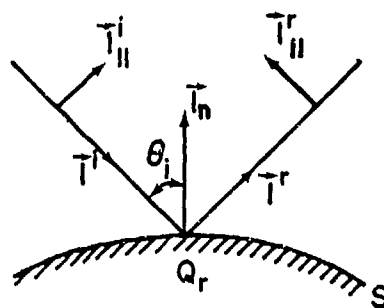


Fig. 22. Reflection at a curved surface.

For the field $\vec{E}^r(\xi, s)$ reflected from the point Q_r we have for (188)

$$\vec{F}(0, s) = \vec{E}^i(Q_r, s) \quad (203)$$

$$\vec{C}(s) = \vec{R} \text{ (dyadic reflection coefficient)} \quad (204)$$

and $f_g(\xi)$ has the same form as in the preceding case except that R_1, R_2 are replaced by R_1^r, R_2^r , the principal radii of curvature of the reflected wavefront at Q_r . Here, ξ is the distance between Q_r and the observation point P , and

$$\vec{R} = \vec{T}_{\parallel}^i \vec{T}_{\parallel}^r - \vec{T}_\perp^i \vec{T}_\perp^r \quad (205)$$

is clearly independent of ψ for a perfectly conducting surface. The unit vector \vec{T}_\perp is perpendicular to the plane of incidence, and the unit vectors \vec{T}_{\parallel}^i and \vec{T}_{\parallel}^r are parallel to the plane of incidence as shown in Fig. 22. Expressions for R_1^r, R_2^r are given in the appendix of [46].

The geometrical optics approximation can be improved by including higher-order frequency-dependent terms obtained from the Luneberg-Kline expansion. Luneberg-Kline expansions for fields reflected from cylinders, spheres and other curved surfaces with simple geometries are given in [47]. These higher-order terms improve the high-frequency approximation if the specular point Q_r is well away from a shadow boundary. Although they do provide some useful information in the early-time period, these higher-order terms are, in general, not useful in extending the early-time solutions to intermediate times.

1.4.3.5.2 Edge Diffraction

A UTD (Uniform Theory of Diffraction) solution for a high-frequency electromagnetic wave incident on a curved edge (Fig. 23) has been given in [46].

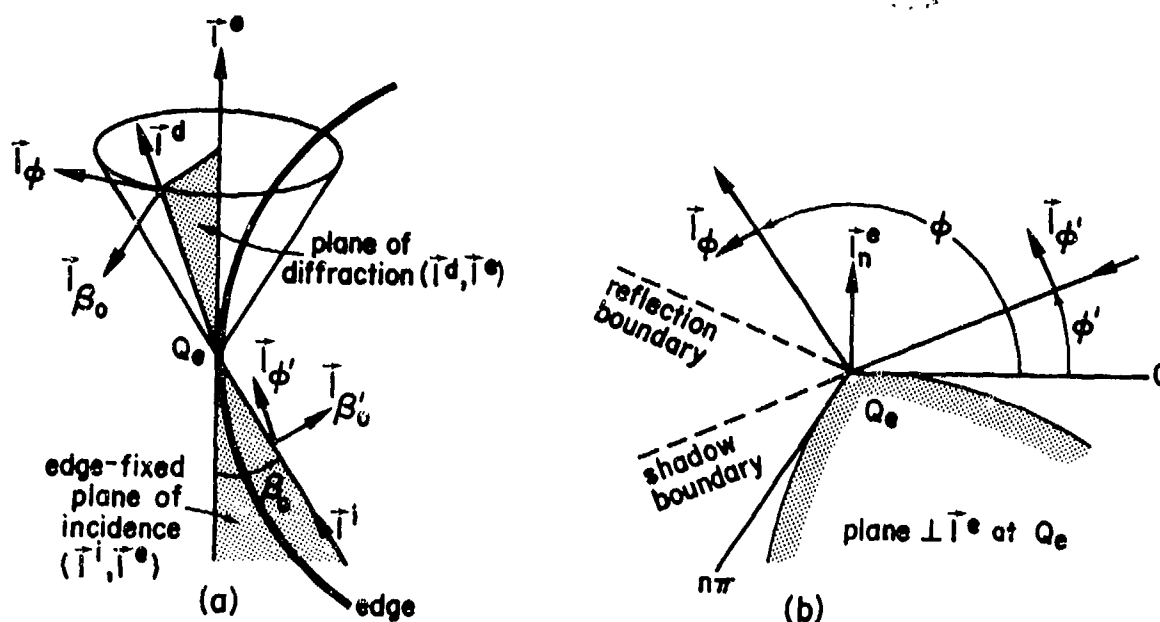


Fig. 23. Diffraction at a curved edge.

In the case of the field $\vec{E}^1(\xi, s)$ diffracted from the point Q_e on the edge of a curved wedge, we have for (188)

$$\vec{F}(0, s) = \vec{E}^1(Q_e, s) \quad (206)$$

$$\vec{C}(s) = \vec{D}(\vec{I}^1, \vec{I}^d, L^1, L^{ro}, L^{rn}, s)$$

(dyadic diffraction coefficient
for curved wedge)

(207)

$$f_s(\xi) = \sqrt{\frac{\rho_c}{\xi(\rho_c + \xi)}} \quad (208)$$

in which

- \vec{I}^1 = unit vector in the direction of incidence at Q_e
- \vec{I}^d = unit vector in the direction of diffraction at Q_e
- L^1 = distance parameter for the incident wave
- L^{ro} = distance parameter for the wave reflected from the 0 surface of the wedge (Fig. 23b)
- L^{rn} = distance parameter for the wave reflected from the n surface of the wedge (Fig. 23b)
- ξ = distance between Q_e and P
- ρ_c = distance between Q_e and the caustic on the diffracted ray and is given by

$$\frac{1}{\rho_c} = \frac{1}{\rho_e^1} - \frac{\vec{I}_n^e \cdot (\vec{I}^1 - \vec{I}^d)}{a \sin^2 \beta_0} \quad (209)$$

where ρ_e^1 is the radius of curvature of the incident wavefront at Q_e taken in the plane of \vec{I}^1 and \vec{I}^e (the unit vector tangent to the edge at Q_e), \vec{I}_n^e is the associated unit normal vector to the edge directed away from

the center of curvature, $a > 0$ is the radius of curvature at Q_e , and β_0 the angle between \hat{i}^i and \hat{i}^e as shown in Fig. 23. The dyadic diffraction coefficient \vec{D} is given by

$$\vec{D} = -\hat{i}_{\beta_0} \hat{i}_{\beta_0} D_s(\hat{i}^i, \hat{i}^d, \chi, s) - \hat{i}_{\phi} \hat{i}_{\phi} D_h(\hat{i}^i, \hat{i}^d, \chi, s) \quad (210)$$

in which

$\hat{i}_{\phi} =$ unit vector perpendicular to the edge-fixed plane of incidence

$\hat{i}_{\phi} =$ unit vector perpendicular to the edge-fixed plane of diffraction

$$\hat{i}_{\beta_0} = \hat{i}^i \times \hat{i}_{\phi}$$

$$\hat{i}_{\beta_0} = \hat{i}^d \times \hat{i}_{\phi}$$

and χ represents the parameters L^i , L^{ro} and L^{rn} collectively. The edge-fixed plane of incidence contains \hat{i}^i and \hat{i}^e , and the edge-fixed plane of diffraction contains \hat{i}^d and \hat{i}^e .

The soft and hard scalar diffraction coefficients D_s and D_h can be factored to yield

$$D_{s,h}(\hat{i}^i, \hat{i}^d, \chi, s) = -\frac{1}{2n\sqrt{2\pi}} \sum_{m=1}^4 d_m^{s,h}(\hat{i}^i, \hat{i}^d) f_t(x_m, s) \quad (211)$$

where $n\pi$ is wedge angle (Fig. 23b). Expressions for $d_m^{s,h}(\hat{i}^i, \hat{i}^d)$ and $f_t(x_m, s)$ are given elsewhere [46]. Outside the transition regions the frequency dependence of the edge diffraction coefficient simplifies to

$$f_t(x_m, s) = \frac{1}{\sqrt{s}} \quad (212)$$

If the incident field at Q_e has a rapid spatial variation or $\vec{E}^i(Q_e, s) = 0$, a second term must be added to $\vec{E}^d(\xi, s)$. This second term can be put into the ray optical form of (188) with

$$\vec{F}(0,s) = \frac{\partial}{\partial n} \vec{E}^i(Q_e, s) \quad (213)$$

$$\vec{C}(s) = \frac{c}{s \sin \beta_0} \frac{\partial}{\partial \phi'} \vec{D}(\vec{l}^i, \vec{l}^d, L^i, L^{ro}, L^{rn}, s) \quad (214)$$

(dyadic slope diffraction coefficient
for wedge)

and $f_s(\xi)$ given by (208). Here, the partial derivative with respect to n is taken in the direction normal to the edge-fixed plane of incidence, whose angular position with respect to the illuminated surface of the wedge is ϕ' (see Fig. 23).

If the edge diffraction problem is two-dimensional in nature, then $\rho_c \rightarrow \infty$ and the spreading factor in (208) reduces to

$$f_s(\xi) = 1/\sqrt{\xi} \quad (215)$$

Explicit edge diffraction coefficients for certain geometries can be found in [46].

1.4.3.5.3 Vertex Diffraction

For the field $\vec{E}^d(\xi, s)$ diffracted from the vertex Q_v of a cone, a plane angular sector, a rectangular parallelepiped, or a pyramid, we have

$$\vec{F}(0,s) = \vec{E}^i(Q_v, s) \quad (216)$$

$$\vec{C}(s) = \vec{D}^v(\vec{l}^i, \vec{l}^d, L^i, L^{rm}, s) \quad (217)$$

(dyadic diffraction coefficient for vertex)

$$f_s(\xi) = \frac{1}{\xi} \quad (218)$$

In contrast to edge diffraction, expressions for the vertex diffraction coefficients are scarce. They are available principally for wide angle and narrow angle circular cones, where the field point is away from

shadow boundaries, reflection boundaries, and the surface of the cone. Thus, the dependence of the vertex diffraction coefficients on the distance parameters L^1, L^m ($m=0,1,\dots$) is unknown at present. However, it is apparent from dimensional considerations that outside the transition regions the vertex diffraction coefficient must vary with complex frequency as s^{-1} .

Some frequency-domain results for diffraction by a circular semi-infinite cone are given in [47]. Diffraction by a blunt tip is given in [48], and the transient diffraction of a scalar wave by a narrow-angle, semi-infinite cone can be found in [49].

1.4.3.5.4 Surface Diffraction

Diffraction at a convex surface is a less local phenomenon than that at an edge or vertex, and for this reason its physical description is more complex. A portion of the ray trajectory ξ_s follows a geodesic between the points Q_1 and Q_2 on the surface, as depicted in Fig. 24. Thus, $\xi = \xi_s + \xi_o$, where ξ_o is the straight line portion between Q_2 and the field point P. In the paragraphs to follow high-frequency expressions for the field and current are given at observation points in the shadow region away from the shadow boundary. The accuracy of these expressions increases as the observation point moves further into the shadow region. If the observation point is in the illuminated region and away from the shadow boundary, the geometrical optics term dominates whose accuracy can be improved somewhat by including higher-order terms from the appropriate Luneberg-Kline series. The GTD description of electromagnetic diffraction at a perfectly-conducting convex surface has been given in [50,51].

In discussing the diffraction at a convex surface, it is convenient to introduce the factor

$$T_p(\xi_s, s) = \exp \left\{ - \int_0^{\xi_s} \alpha_p(x, s) dx \right\} \quad (219)$$

which describes in part the amplitude variation and phase shift of the p th surface-ray modal field between Q_1 and Q_2 . Here, α_p is the complex

attenuation constant of the p th surface-ray mode. Later, the superscripts s and h are added to denote the soft and hard boundary conditions. The total field vanishes at the surface in the former case, whereas the normal derivative of the total field vanishes in the latter. Expressions for α_p and the other GTD parameters for the convex surface can be found in Part 2.

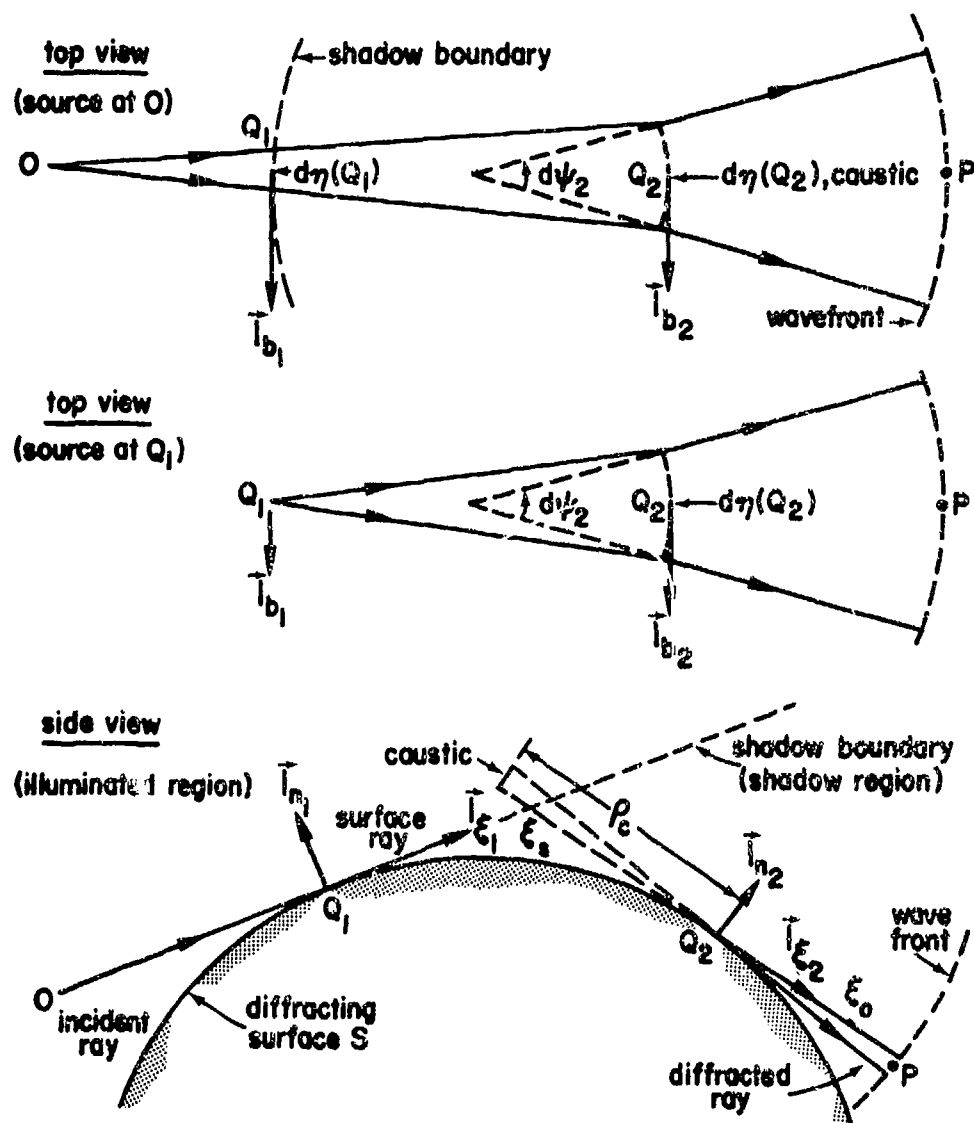


Fig. 24. Diffraction at a convex surface.

Diffraction where both the source point 0 and the field point P are away from the convex surface will be considered first. The geometry is shown in Fig. 24. Referring to (188) one has

$$\vec{F}(0,s) = \vec{E}^1(Q_1,s) \quad (220)$$

$$\vec{C}(s) = \vec{I}_{n_1} \vec{I}_{n_2} F(\xi_s, s) + \vec{I}_{b_1} \vec{I}_{b_2} G(\xi_s, s) \quad (221)$$

and

$$f_s(\xi) = \sqrt{\frac{d\eta_1}{d\eta_2}} \sqrt{\frac{\rho_c}{\xi_o(\rho_c + \xi_o)}} \quad (222)$$

is the net spreading factor for the surface ray and the diffracted ray Q_2P . The tangential, binormal, and normal unit vectors to the ray at the point Q_i ($i=1,2$) are denoted by $\vec{I}_{\xi_i}, \vec{I}_{b_i}, \vec{I}_{n_i}$, respectively. Also in (221)

$$F(\xi_s, s) = \sum_{p=1}^{\infty} D_p^h(1,s) T_p^h(\xi_s, s) D_p^h(2,s) \quad (223)$$

$$G(\xi_s, s) = \sum_{p=1}^{\infty} D_p^s(1,s) T_p^s(\xi_s, s) D_p^s(2,s) \quad (224)$$

where $D_p(i,s)$ is the surface diffraction coefficient at the point Q_i , and again the hard or soft boundary condition is identified by an additional superscript h or s.

Next, let the observation point be on the surface at Q_2 . Now, the surface current and charge are of interest; they are determined from (195) and (196). The current can be put into the form of (188), i.e.,

$$\vec{J}(\xi_s, s) = \vec{I}_{\xi_2} J_{\xi}(\xi_s, s) + \vec{I}_{b_2} J_b(\xi_s, s) \quad (225)$$

$$\sim \vec{F}(0,s) \cdot \vec{C}(s) f_s(\xi_s) e^{-s\xi_s/c}$$

Furthermore, at high frequencies the continuity equation may be approximated by

$$\rho(\xi_s, s) = -\frac{1}{s} \frac{\partial}{\partial \xi_s} J_\xi(\xi_s, s) \quad (226)$$

Referring to (225) with the source point at 0 away from the surface one has

$$\vec{E}(0, s) = \vec{E}^1(Q_1, s) \quad (227)$$

$$\vec{C}(s) = \vec{I}_{n_1} \vec{I}_{\xi_2} \mathcal{V}(\xi_s, s) - \vec{I}_{b_1} \vec{I}_{b_2} \mathcal{K}(\xi_s, s) \quad (228)$$

$$f_s(\xi_s) = \sqrt{\frac{d\eta_1}{d\eta_2}} \quad (229)$$

where

$$\mathcal{V}(\xi_s, s) = Y_0 \sum_{p=1}^{\infty} D_p^h(1, s) T_p^h(\xi_s, s) A_p^h(2, s) \quad (230)$$

and $\mathcal{K}(\xi_s, s)$ has the same form as $\mathcal{V}(\xi_s, s)$, except that the superscript h is replaced by s . In the above expression the $A_p^h(2, s)$ are the attachment coefficients required to convert the surface ray modal fields to their actual magnetic field strengths at the surface, and $Y_0 = 1/Z_0$.

From (226) the surface charge density ρ is given by

$$\begin{aligned} \rho(\xi_s, s) = & \vec{I}_{n_1} \cdot \vec{E}^1(Q_1, s) Y_0 \sqrt{\frac{d\eta_1}{d\eta_2}} e^{-\xi_s s/c} \times \\ & \times \sum_{p=1}^{\infty} \left[\frac{1}{c} + \frac{\alpha_p^h(\xi_s, s)}{s} \right] D_p^h(1, s) T_p^h(\xi_s, s) A_p^h(2, s) \end{aligned} \quad (231)$$

where the approximation

$$\frac{1}{s} \frac{\partial}{\partial \xi_s} \left[T_p^h(\xi_s, s) A_p^h(2, s) \sqrt{\frac{d\eta_1}{d\eta_2}} e^{-\xi_s s/c} \right] \sim$$

$$- \left[\frac{1}{c} + \frac{\alpha_p^h(\xi_s, s)}{s} \right] T_p^h(\xi_s, s) A_p^h(2, s) \sqrt{\frac{d\eta_1}{d\eta_2}} e^{-\xi_s s/c} \quad (232)$$

has been used. Note that $A_p^h(2, s)$ and $d\eta_2$ are functions of ξ_s , but in general they are slowly varying in comparison with $T_p^h(\xi_s, s)$ and $\exp(-\xi_s s/c)$.

It is convenient to treat the radiation from a slot or aperture in a perfectly conducting convex surface by introducing an equivalent source at each point Q_1 in the aperture. The equivalent source is the infinitesimal magnetic current $d\vec{J}_m$ or the magnetic dipole moment $d\vec{m}$ defined by

$$d\vec{J}_m(Q_1, s) = sv d\vec{m}(Q_1, s) = \vec{E}(Q_1, s) \times \vec{l}_{n_1} da, \quad (233)$$

where $\vec{E}(Q_1, s)$ is the aperture electric field and da is an infinitesimal area element at Q_1 . The electric field at P may be put into the form of (188) with

$$\vec{F}(0, s) = \int d\vec{J}_m(Q_1, s)$$

(integration over aperture) (234)

$$\vec{C}(s) = \vec{l}_{b_1 n_2} \vec{l}_{s_2} F_s(\xi_s, s) + \vec{l}_{\xi_1 b_2 s} \vec{l}_{s_2} G_s(\xi_s, s) \quad (235)$$

$$f_s(\xi) = \sqrt{\frac{1}{\rho_c} \frac{d\psi_1}{d\psi_2}} \sqrt{\frac{\rho_c}{\xi_o(\rho_c + \xi_o)}} \quad (236)$$

in which $d\psi_1$ is the angle between the tangents to a pair of infinitesimally displaced surface rays at Q_1 and $d\psi_2 = d\eta_2/\rho_c$ is the angle between the tangents to the same two rays at Q_2 . In (235)

$$F_s(\xi_s, s) = -\frac{s}{4\pi c} \sum_{p=1}^{\infty} L_p^h(1, s) T_p^h(\xi_s, s) D_p^h(2, s) \quad (237)$$

and $G_s(\xi_s, s)$ has the same form as $F_s(\xi_s, s)$, except that the superscript h is replaced by s . In the above expression the $L_p^h(1, s)$ are the launching coefficients for the surface-ray modes. Using reciprocity it can be shown that

$$L_p^h = A_p^h, \quad L_p^s = -A_p^s \quad (238)$$

When the observation point is on the surface at Q_2 , the surface current is given by (225) with

$$\vec{F}(0, s) = \int d\vec{J}_m(Q_1, s) \quad (239)$$

$$\vec{C}(s) = \vec{I}_{b_1} \vec{I}_{\xi_2} \vartheta_s(\xi_s, s) - \vec{I}_{\xi_1} \vec{I}_{b_2} \mathcal{C}_s(\xi_s, s) \quad (240)$$

$$f_s(\xi_s) = \sqrt{\frac{1}{\rho_c} \frac{d\psi_1}{d\psi_2}} \quad (241)$$

where

$$\vartheta_s(\xi_s, s) = \frac{s}{4\pi c} Y_0 \sum_{p=1}^{\infty} L_p^h(1, s) T_p^h(\xi_s, s) A_p^h(2, s) \quad (242)$$

and $\mathcal{C}_s(\xi_s, s)$ has the same form as $\vartheta_s(\xi_s, s)$, except that the superscript h is replaced by s . Employing (226) one finds the associated surface charge density to be

$$\rho(\xi_s, s) = - \int \vec{I}_{b_1} \cdot d\vec{J}_m(Q_1, s) Y_0 \sqrt{\frac{1}{\rho_c} \frac{d\psi_1}{d\psi_2}} \times$$

$$\frac{s}{4\pi c} \sum_{p=1}^{\infty} \left[\frac{1}{c} + \frac{\alpha_p^h(\xi_s, s)}{s} \right] L_p^h(1, s) T_p^h(\xi_s, s) A_p^h(2, s) \quad (243)$$

For an infinitesimal electric current element $\vec{I}_{n_1} I(Q_1, s) d\ell$ at Q_1 the diffracted electric field at P away from the surface is

$$\vec{E}(\xi, s) = \vec{I}_{n_2} z_0 I(Q_1, s) d\ell F_s(\xi_s, s) f_s(\xi) e^{-s\xi/c} \quad (244)$$

with

$$f_s(\xi) = \sqrt{\frac{1}{\rho_c} \frac{d\psi_1}{d\psi_2}} \sqrt{\frac{\rho_c}{\xi_0(\rho_c + \xi_0)}} \quad (245)$$

and the surface current and charge at Q_2 are

$$J(\xi_s, s) = \vec{I}_{\xi_2} I(Q_1, s) d\ell \vartheta_s(\xi_s, s) \sqrt{\frac{1}{\rho_c} \frac{d\psi_1}{d\psi_2}} e^{-s\xi_s/c} \quad (246)$$

$$\rho(\xi_s, s) = - \frac{I(Q_1, s) d\ell}{4\pi} \frac{s}{c} \sqrt{\frac{1}{\rho_c} \frac{d\psi_1}{d\psi_2}} e^{-s\xi_s/c} \times$$

$$\sum_{p=1}^{\infty} \left[\frac{1}{c} + \frac{\alpha_p^h(\xi_s, s)}{s} \right] L_p^h(1, s) T_p^h(\xi_s, s) A_p^h(2, s) \quad (247)$$

REFERENCES

- [1] R.E. Kleinman, "The Rayleigh region," Proc. IEEE, vol. 53, August 1965, pp. 848 - 856.
- [2] P. Werner, "On the exterior boundary-value problem of perfect reflection for stationary electromagnetic wave fields," J. Math. Anal. and Appl., vol. 7, December 1963, pp. 348 - 391.
- [3] A.F. Stevenson, "Solution of electromagnetic scattering problems as power series in the ratio (dimension of scatterer)/wavelength," J. Appl. Phys., vol. 24, September 1953, pp. 1134 - 1142.
- [4] J. Van Bladel, Electromagnetic Fields, McGraw-Hill, New York, 1964.
- [5] B. Noble, "Integral equation perturbation methods in low-frequency diffraction," Electromagnetic Waves, R. Langer, Ed., The University of Wisconsin Press, Madison, 1962.
- [6] R.E. Kleinman, "Far field scattering at low frequencies," Appl. Sci. Res., vol. 18, August 1967, pp. 1 - 8, and also "Dipole moments and near field potentials," Appl. Sci. Res., vol. 27, April 1973, pp. 335 - 340.
- [7] K.S.H. Lee and L. Marin, "Interaction of external system-generated EMP with space systems," IN 179, August 1973, and also AP-22, September 1974, pp. 683 - 689.
- [8] D.S. Jones, The Theory of Electromagnetism, Pergamon Press, New York, 1964, p. 55.
- [9] M.I. Sancer, R.W. Latham, and A.D. Varvatsis, "Relationship between total currents and surface current densities induced on aircraft and cylinders," IN 194, August 1974.
- [10] K.S.H. Lee, "Balanced transmission lines in external fields," IN 115, July 1972.
- [11] T.T. Taylor, "Magnetic polarizability of a short right circular conducting cylinder," J. Res. NBS 64B4, 1960, p. 199.

- [12] R.W. Latham and K.S.H. Lee, "Magnetic-field distortion by a specific, axisymmetric, semi-infinite, perfectly conducting body," SSN 102, April 1970.
- [13] C.H. Papas, Theory of Electromagnetic Wave Propagation, McGraw-Hill, New York, 1965.
- [14] C.E. Baum, "Emerging technology for transient and broad-band analysis and synthesis of antennas and scatterers," IN 300, November 1976, and also Proc. IEEE, vol. 64, No. 11, November 1976, pp. 1598 - 1616.
- [15] C.T. Tai, Dyadic Green's Functions in Electromagnetic Theory, Intext Educational Publishers, San Francisco, 1971.
- [16] L.D. Landau and E.M. Lifshitz, Statistical Physics, Pergamon Press Ltd., London, 1958, p. 124.
- [17] J.B. Keller, R.E. Kleinman, and T.B.A. Senior, "Dipole moments in Rayleigh scattering," J. Inst. Maths. Appl. 9, 1972, pp. 14 - 22.
- [18] R.E. Kleinman and T.B.A. Senior, "Rayleigh scattering cross sections," Radio Science, 7, 1972, pp. 937 - 942.
- [19] K.S.H. Lee, "Electrically small ellipsoidal antennas," SSN 103, February 1974.
- [20] K.S.H. Lee and C.E. Baum, "Application of modal analysis to braided-shield cables," IN 132, January 1973, and also EMC-17, August 1975, pp. 159 - 169.
- [21] C.E. Baum, "Dipole moment and polarizability conventions and some related matters," AFWL EMP Interaction Handbook Memo 1, part B, July 1976.
- [22] J. Lam, "Exact solution of the problem of quasi-static electric field penetration into a hemispherical indentation in an infinite conducting plane," IN 175, April 1974; "Quasi-static magnetic field penetration into a hemispherical indentation in an infinite conducting plane," IN 179, May 1974.

- [23] C.E. Baum, "Electromagnetic reciprocity and energy theorems for free space including sources generalized to numerous theorems, to combine fields, and to complex frequency domain," *MaN* 33, December 1973.
- [24] T.B.A. Senior, "Low-frequency scattering by a dielectric body," *Radio Science*, 11, 1976, pp. 477-482.
- [25] C.E. Baum, "On the singularity expansion method for the solution of electromagnetic interaction problems," *IN* 88, December 1971.
- [26] C.E. Baum, "The singularity expansion method," in L.B. Felsen (ed.), Transient Electromagnetic Fields, Springer-Verlag, New York, 1975.
- [27] C.E. Baum, "Introduction to SEM," presented at 1973 G-AP International Symposium and USNC/URSI Meeting, August 1973.
- [28] B. van der Pol and H. Bremmer, Operational Calculus, Cambridge University Press, Cambridge, 1964.
- [29] J.P. Martinez, Z.L. Pine and F.M. Tesche, "Numerical results of the singularity expansion method as applied to a plane wave incident on a perfectly conducting sphere," *IN* 112, May 1972.
- [30] L. Marin and R.W. Latham, "Analytical properties of the field scattered by a perfectly conducting finite body," *IN* 92, January 1972.
- [31] L. Marin, "Natural-mode representation of transient scattering from rotationally symmetric perfectly conducting bodies and numerical results for a prolate spheroid," *IN* 119, September 1972.
- [32] L. Marin and T.K. Liu, "A simple way of solving transient thin-wire problems," *Radio Science* 11, 1976, pp. 149-155.
- [33] G. Bedrosian, "Stick-model characterization of the total axial current and linear charge density on the surface of an aircraft subjected to an EMP; frequency-domain external-interaction current and charge transfer functions," *IN* 327, September 1977.
- [34] R.F. Harrington, Field Computation by Moment Methods, Macmillan Co., New York, 1968.

- [35] F.M. Tesche, "On the singularity expansion method as applied to electromagnetic scattering from thin wires," IN 102, April 1972.
- [36] J.B. Keller, "Geometrical theory of diffraction," J. Opt. Soc. Am. 52, 1962, pp. 116 - 130.
- [37] G. Deschamps, "Ray techniques in electromagnetics," Proc. IEEE 60, 1972, pp. 1022 - 1035.
- [38] L.B. Felsen and N. Marcuvitz, Radiation and Scattering of Waves, Prentice-Hall, Inc., Englewood Cliffs, New Jersey, 1973, Chap. 1, Sec. 1.7.
- [39] G.L. James, Geometrical Theory of Diffraction for Electromagnetic Waves, Peter Peregrinus, Ltd., Southgate House, Stevenage, Herts, England, 1976, Chap. 4 - 6.
- [40] S. Choudhary and L.B. Felsen, "Asymptotic theory for inhomogeneous waves," AP-21, No. 6, November 1973.
- [41] L.B. Felsen, "Evanescent waves," J. Opt. Soc. Am., 66, No. 8, August 1976, pp. 751 - 760.
- [42] H. Jeffreys, Asymptotic Expansions, Oxford University Press, London, 1962.
- [43] P. Ya. Ufimtsev, "Approximate computation of diffraction of plane electromagnetic waves at certain metal objects - I. Diffraction patterns at a wedge and ribbon," Sov. Phys. - Tech. Phys. 27, 1957, pp. 1708 - 1718, and "II. Diffraction by a disk and by a finite cylinder," Sov. Phys. - Tech. Phys. 3, 1958, pp. 2386 - 2396.
- [44] E.F. Knott and T.B.A. Senior, "Comparison of three high-frequency diffraction techniques," Proc. IEEE 62, 1974, pp. 1468 - 1474.
- [45] R.G. Kouyoumjian, "The geometrical theory of diffraction and its application," Topics in Applied Physics, vol. 3, edited by R. Mittra, Berlin, Heidelberg, New York: Springer Verlag, 1975, pp. 165 - 215.

- [46] R.G. Kouyoumjian and P.H. Pathak, "A uniform geometrical theory of diffraction for an edge in a perfectly conducting surface," Proc. IEEE, vol. 62, 1974, pp. 1448 - 1461.
- [47] J.J. Bowman, T.B.A. Senior and P.L.E. Uslenghi, Electromagnetic and Acoustic Scattering by Simple Shapes, Amsterdam, The Netherlands, North-Holland Pub., 1969.
- [48] L. Kaminetsky and J.B. Keller, "Diffraction coefficients for higher-order edges and vertices," SIAM J. Appl. Math., vol. 22, 1972, pp. 109 - 134.
- [49] K.K. Chan and L.B. Felsen, "Transient and time-harmonic diffraction by a semi-infinite cone," AP-25, 1977, pp. 802 - 807.
- [50] R.G. Kouyoumjian, "Asymptotic high-frequency methods," Proc. IEEE, vol. 53, August 1965, pp. 864 - 876.
- [51] P.H. Pathak and R.G. Kouyoumjian, "An analysis of the radiation from apertures in curved surfaces by the geometrical theory of diffraction," Proc. IEEE, vol. 62, 1974, pp. 1438 - 1447.

CHAPTER 1.5

SCALE MODELING

1.5.1 THEORETICAL BACKGROUND

In any study of electromagnetic phenomena it is ultimately necessary to determine the field quantities involved. If the system is at all complex, an analytical solution of the problem may be impossible to obtain and a computer solution based on the use of differential and/or integral equations prohibitively expensive. It is then necessary to resort to measurements, and these may also be desirable to validate any (approximate) theoretical and numerical results that have been found. However, even an experimental study of a full-scale EMP problem may be difficult and costly to perform because of the size of the system, and it is therefore natural to look to small-scale simulation or modeling as a means of facilitating the measurements. This technique has been widely used, particularly in scattering and antenna work where it is often convenient to perform the measurements on a small-scale version of the original system, but it can also be used to provide information about many other properties of the system.

The modeling of electromagnetic systems is an important tool both theoretically and experimentally. The method of conformal mapping is an example in which a given system is modeled by another whose solution is easier to find, and the desired solution is then obtained from the model solution via the mapping function. The application of transform techniques can also be viewed as a form of modeling, and such modelings are often non-linear in the sense that the solution of the original problem is not linearly related to that of the model. The concept and feasibility of non-linear modeling in general is discussed in [1], and though it would appear to offer some advantages over linear modeling, the procedures have not yet been adequately developed. We shall therefore confine our attention to the simpler case of linear modeling (or scaling), whose value is primarily in connection with experimental measurements.

The possibility of constructing a scale model of an electromagnetic system is based on the linearity of the field equations and the principle of electrodynamic similitude [2,3]. Within the confines of linear modeling, it is necessary to exclude systems having any non-linear component in the form of a non-linear impedance or medium (e.g., ferromagnetic material), or a component which is time-dependent. In such cases, non-linear modeling is necessary to provide a precise simulation.

It is a relatively simple matter to determine the conditions for a scale model to simulate the system. Consider a system in which $\vec{E}(\vec{r}, t)$ and $\vec{H}(\vec{r}, t)$ are the electric and magnetic field vectors, where \vec{r} denotes the position vector of an arbitrary point and t is the time. If, in the model, all variables are represented by primed quantities, we write, following [4]

$$\begin{aligned}\vec{r} &= p \vec{r}', & t &= \tau t' \\ \vec{E} &= g \vec{E}', & \vec{H} &= h \vec{H}'\end{aligned}\tag{1}$$

where p , τ , g and h are respectively the mechanical, temporal, electric and magnetic scale factors. We remark that four factors are all that are needed, since only four fundamental units (mass, length, time and charge) are required to describe an electromagnetic quantity. In both systems the fields are required to satisfy Maxwell's equations and the constitutive relations, and if $\epsilon(\vec{r})$ and $\mu(\vec{r})$ are the (complex) permittivity and permeability respectively, then at corresponding points of the systems

$$\epsilon' = \frac{pg}{\tau h} \epsilon, \quad \mu' = \frac{ph}{\tau g} \mu\tag{2}$$

In a similar manner the relations between the other electromagnetic quantities in the two systems can be derived.

For any arbitrary choices of the scale factors p , g , h and τ it is theoretically possible to construct a model to simulate a full-scale

system exactly. In practice, however, there are certain restrictions on the factors due to the limited ranges of variation of ϵ and μ in actual media which can be used in the model. One of the media in the full-scale system is often free space (air) and it is generally desirable to simulate this using free space in the scaled model, not only for convenience but also because of the higher attenuation in most other media. This is certainly customary in scattering and antenna measurements, and it now follows that for these regions of the model

$$\epsilon' = \epsilon, \quad \mu' = \mu \quad (3)$$

Since (2) must be satisfied everywhere, (3) must be true for all media, implying

$$\frac{p_g}{\tau_h} = 1 = \frac{p_h}{\tau_g} \quad (4)$$

from which we have

$$\tau = p, \quad g = h \quad (5)$$

The temporal and mechanical scale factors are therefore identical, as are the magnetic and electric ones. Thus, for a system and its model in a common medium, there are only two factors, p and h , which can be arbitrarily chosen.

The restriction $h = g$ imposed by (5) can be understood by noting that h/g is the ratio of the wave impedance at a point in the model to that at the corresponding point in the full-scale system. Since the same medium is used in both, the impedances must be the same. Note also that the restriction fixes only the ratio of g to h and does not restrict the choice of either. If h is left arbitrary, the model has been termed [4] a *geometrical* one in which the geometrical configurations of the lines of force are simulated but not the power levels of the full-scale system. On the other hand, if a specific value is assigned to $h = g$ the model is an *absolute* one in which the power levels are also simulated and quantitative data are obtained immediately.

In spite of the fact that the power level used in a geometrical model is unknown, it is still possible to obtain quantitative results. The most common method is to employ a standard whose performance is known. To illustrate the method let us consider the problem of determining the radar cross section of a target. If the model is simply a geometric one, the scattered power is compared with that scattered by another body such as a sphere, plate or corner reflector when placed at the same position as the target and illuminated by the same field. Provided the scattering cross section of the calibrating body is known (usually from computations) the cross section of the target can be found. This is the customary procedure, but note that if in the model experiment the incident power is tapped and measured directly, h can be determined and the model becomes an absolute one.

Let us consider now a geometrical model in which only the mechanical scale factor p is assigned. The ratio of any full-scale length to the corresponding model length is thus given by p , which is usually chosen to yield a model of convenient size for the measurements. The relations between some of the more important electrical (and other) quantities are listed in table 1.

Linear (or scale) modeling is an important tool. It can make possible the study of a large system in free space using a small scale version in, for example, the controlled conditions that an anechoic chamber provides, but it is not without its limitations. If one of the media is lossy it may be very difficult to find a material which simulates this at the scale frequency and, in practice, it is generally impossible to scale precisely the non-zero impedances associated with any circuits, antennas, etc. The extent to which this is a major shortcoming depends on the quantities to be measured.

1.5.2 SCALE-MODEL MEASUREMENTS

The scale model actually used in measurements may be plastic (assembled from a hobby-shop kit), a manufacturer's table display model, or one specially constructed from wood or metal in a machine shop. Non-metallic models are given several coats of silver conducting paint, and

TABLE 1. RELATIONS FOR A PRACTICAL GEOMETRICAL MODEL

Quantity	Full-Scale System	Model System
length	l	$l' = l/p$
time	t	$t' = t/p$
frequency	f	$f' = pf$
wavelength	λ	$\lambda' = \lambda/p$
propagation constant	k	$k' = pk$
phase velocity	v	$v' = v$
permittivity (complex)	ϵ	$\epsilon' = \epsilon$
conductivity	σ	$\sigma' = p\sigma$
permeability	μ	$\mu' = \mu$
resistance	R	$R' = R$
reactance	X	$X' = X$
impedance	Z	$Z' = Z$
capacitance	C	$C' = C/p$
inductance	L	$L' = L/p$
scattering area	A	$A' = A/p^2$
magnetic field	\vec{H}	$\vec{H}' = \vec{H}/h$
electric field	\vec{E}	$\vec{E}' = \vec{E}/h$
current (surface) density	\vec{J}	$\vec{J}' = \vec{J}/h$
current (volume) density	\vec{J}_v	$\vec{J}'_v = \vec{J}_v p/h$
current	I	$I' = I/hp$
charge (surface) density	ρ	$\rho' = \rho/h$
charge (volume) density	ρ_v	$\rho'_v = \rho_v p/h$
charge	Q	$Q' = Q/hp^2$

mounting holes are cut as necessary for the accommodation of surface field sensors. It is important to note that it may be impractical to model, in the case of aircraft, its finer details such as wing flaps, windows, or other airframe discontinuities. Even if this were possible, the sensors used may not be small enough to detect the local field perturbations produced by these discontinuities. Thus scale-model measurements are best suited to the determination of "large-scale" currents and charges on conducting bodies.

The configuration of the scale-model measurement facility at the University of Michigan is shown in Fig. 1. Its major components are

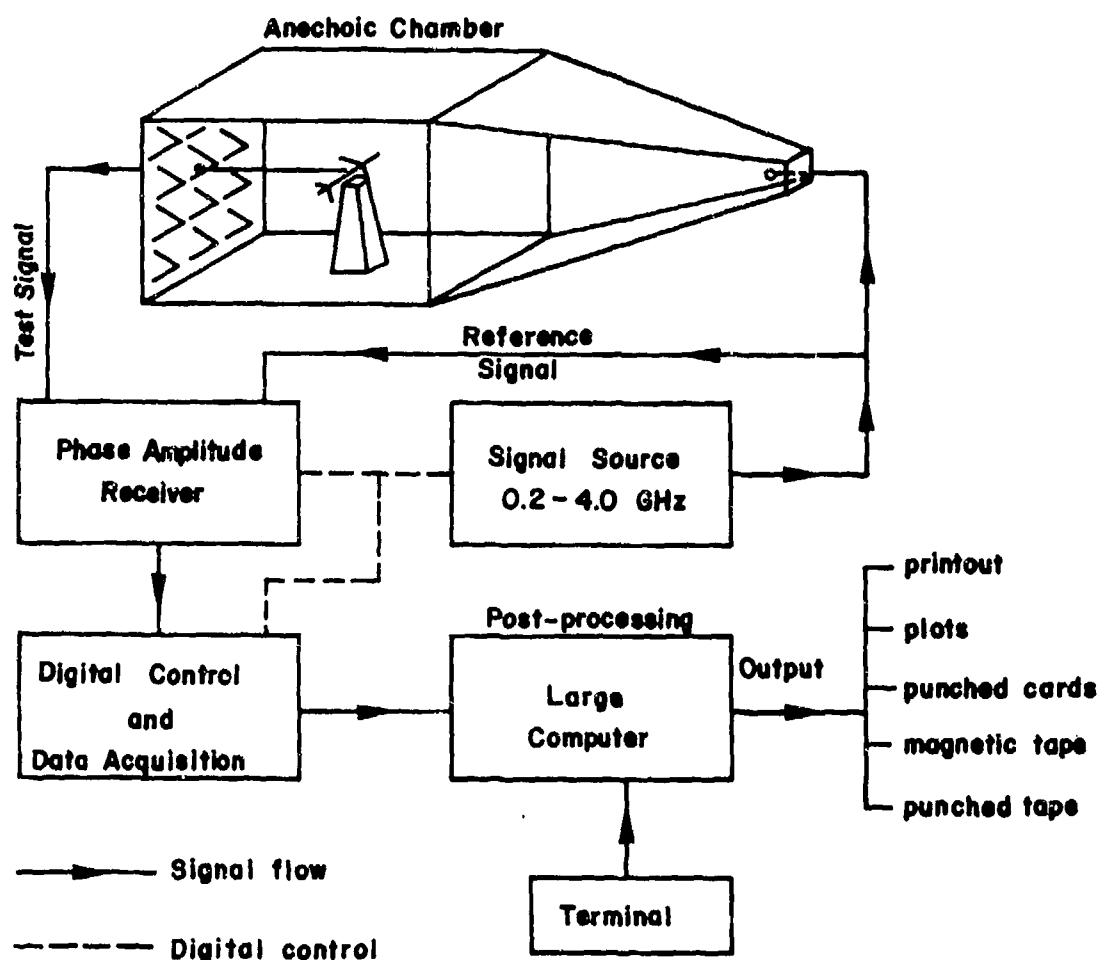


Fig. 1. Surface-field measurement facility at the University of Michigan.

the tapered anechoic chamber 50 feet in length, the signal source, the receiver, and the control and recording equipment. This system is linked to a large computer where the data are processed. The operating frequency range of this facility is presently 0.45-4.25 GHz. In practice, the maximum useful frequency range for scale-model measurements is 0.1-10 GHz. Below 0.1 GHz standard absorbing materials no longer provide a good simulation of the free-space environment, and above 10 GHz it is difficult to make sensors which are small in comparison to wavelength and yet have adequate sensitivity.

Some typical probes and sensors used in measurements are shown in Fig. 2. The AFWL-designed sensor series MGL-8 and ACD-1 [5] are useful on larger models (linear dimensions ≥ 50 cm), but on smaller models it is usually necessary to rely on miniaturized sensors which are specially fabricated. These typically take the form of loops, half loops, and monopoles made of 0.52 mm diameter coaxial cable. These small sensors may be individually calibrated; or it may be more convenient to calibrate the entire system of which the sensor is a part [6].

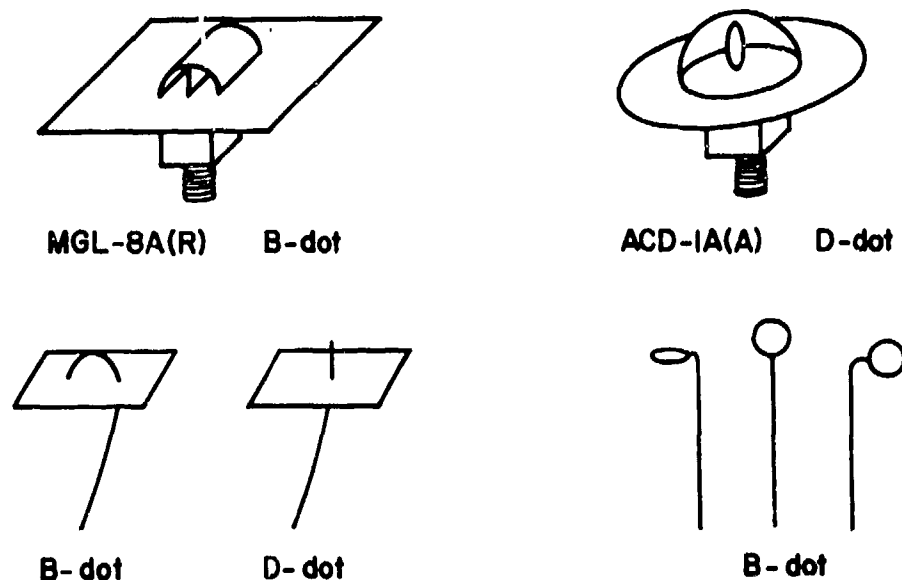


Fig. 2. Types of laboratory-made sensors used in scale-model measurements. The top ones were developed by AFWL and those at the bottom were made in the Radiation Laboratory at the University of Michigan.

The accuracy of scale-model measurement data can be determined, at least for simple test objects, by comparison of the data with theoretical predictions. In the Michigan facility, the measured data agree with theoretical predictions within ± 0.5 dB in amplitude and $\pm 2.5^\circ$ in phase for a spherical test object. The sphere is probably too simple a test object to adequately determine model measurement errors. However, the following sources of error can be identified from experience at the University of Michigan [7,8]:

- (a) Background noise as evidenced by a measured signal in such cases when, from symmetry, the true field component must be zero. This encompasses the effect of equipment (thermal) noise, the impurity of the field in the chamber, errors in the alignment of a sensor on the model, signal and gain instabilities of the equipment, and possible interactions of the sensor lead with the model. Such noise can be pictured as a circle of uncertainty about the measured value in the complex plane. When all quantities are normalized to the incident field value, the magnitude of the noise signal is typically of order 0.2, and the signal itself can be written as $0.2 \exp(j\psi)$, where ψ is arbitrary. The error due to the noise is therefore only 2 percent for measured fields of magnitude 10, but can be as much as 20 percent (or larger) at stations in shadow regions where the field amplitudes are unity or less.
- (b) Phase errors due to errors in positioning of a model with respect to the incident field reference plane. With adequate care it is possible to position models to within ± 1.5 mm of the desired location, which translates to an average phase error of ± 4 degrees. In many instances, however, the models themselves are not accurate to this extent, leading to an additional phase error.
- (c) Errors produced by sensor integration when measurements are made near edges and small-radius surfaces that create fields

which are non-uniform over the dimensions of the sensors. Although the sensors used are only 2 to 3 mm in size, the averaging effect can produce as much as 20 percent reduction in amplitude with models as small as a 1/383 scale E-4 [8]. Fortunately, the trend is to the use of lower measurement frequencies and larger models for which the integration error should be no more than about 5 percent.

The probable error resulting from these effects differs from case to case, but from comparisons of data using different scale models it would appear that in most circumstances results can be obtained which are accurate to 1 dB in amplitude and 10 degrees in phase, provided good models are available.

REFERENCES

- [1] R.K. Ritt, "The modeling of physical systems," AP-4, No. 3, July 1956, pp. 216 - 218.
- [2] J.A. Stratton, Electromagnetic Theory, McGraw-Hill Book Company, New York, N.Y., 1941, pp. 488 - 490.
- [3] R.W.P. King, Fundamental Electromagnetic Theory, Dover Publications, Inc., New York, N.Y., 1963, pp. 316 - 320.
- [4] G. Sinclair, "Theory of models of electromagnetic systems," Proc. IRE, Vol. 36, No. 11, November 1948, pp. 1364 - 1370.
- [5] S.L. Olson, Electromagnetic Pulse Sensor Handbook, Vol. 1, Sensors MGL-S8(R) and ACD-S1A(R) (1975), AFWL, 1971.
- [6] V.V. Liepa, "Sweep frequency surface field measurements," University of Michigan Radiation Laboratory Report No. 013378-1-F, AFWL-TR-75-217, 1975.
- [7] V.V. Liepa, "Surface field measurements on scale model EC-135 aircraft," University of Michigan Radiation Laboratory Report No. 014182-1-F, AFWL-TR-77-101, 1977.
- [8] V.V. Liepa, "Surface field measurements on scale model E-4 aircraft," University of Michigan Radiation Laboratory Report No. 014182-2-F, AFWL-TR-77-111, 1977.

CHAPTER 1.6

ERROR ESTIMATION

The application of theoretically or empirically derived formulas to the prediction of the behavior of a given system necessarily involves some degree of inaccuracy, since a mathematical model of a given physical system can never take all of the features of that system into account. The essence of mathematical or scale modeling is to treat those aspects of the system that are judged to be of the greatest importance and to ignore the remainder. Thus, given judicious choices of models and accurate mathematical analyses, one can predict the behavior of the modeled system with a certain degree of accuracy, but never with exactitude. It is therefore desirable that the accuracy of a given theoretical model be estimated and that this estimate be used in conjunction with the application of the model to a specific system [1,2].

Since the systems considered in this document (e.g., aircraft and missiles) are so complicated, they are broken down for modeling purposes into simpler subsystems which are amenable to analysis. The basis for this decomposition is the topological concept described in Chap. 1.2. Given the error estimates for the individual subsystem analyses, the problem of error analysis for the system itself becomes that of properly combining the error estimates for the subsystem analyses. It is the objective of this chapter to present a formalism by means of which this error-combination process can be accomplished.

Since the error in a given subsystem analysis is not precisely known, a probabilistic approach to the problem of error description will be useful. This approach and its method of application are described in the following sections of this chapter. We begin in Sec. 1.6.1 with a general discussion of linear EMP interaction models and of the probabilistic description of the system response functions in the frequency and time domains. Then in Sec. 1.6.2 are considered the input quantities required for the error description of the stimulus and transfer functions. The error description of an elementary (single-path) response function is developed in Sec. 1.6.3. In Sec. 1.6.4 we

discuss the problem of error analysis for series and parallel interaction paths. Confidence bounds are considered in Sec. 1.6.5.

1.6.1 GENERAL CONSIDERATIONS

The EMP interaction problem is assumed to be linear and describable by frequency-domain relations of the form*

$$\tilde{R}_{ij}(\omega, [V_n]; \ell) = \tilde{T}_{ij}(\omega, [V_n]; \ell) \tilde{S}_j(\omega; \ell) \quad (1)$$

in which

ω = electromagnetic field frequency in radians/sec; ω
 $= 2\pi f$, where f is the frequency in Hz.

$[V_n]$ = vector describing the electrical state of the
system; $n = 1, 2, \dots, N$.

ℓ = ℓ th topological layer or shell of shielding in the
interaction problem; $\ell = 1, 2, \dots, L$.

$\tilde{R}_{ij}(\omega, [V_n]; \ell)$ = frequency-domain response at the i th
response point in the ℓ th layer, due to a stimulus
at the j th point of entry (POE) of the ℓ th layer
 $i = 1, 2, \dots, I(\ell)$; $j = 1, 2, \dots, J(\ell)$.

$\tilde{S}_j(\omega; \ell)$ = frequency-domain stimulus applied at the j th POE
of the ℓ th layer.

$\tilde{T}_{ij}(\omega, [V_n]; \ell)$ = transfer function which produces
 $\tilde{R}_{ij}(\omega, [V_n]; \ell)$ from $\tilde{S}_j(\omega; \ell)$.

The total response $\tilde{R}_i(\omega, [V_n]; \ell)$ at the i th response point to the
 J stimuli is given by the sum of the individual responses, viz.,

$$\tilde{R}_i(\omega, [V_n]; \ell) = \sum_{j=1}^{J(\ell)} \tilde{R}_{ij}(\omega, [V_n]; \ell)$$

* In this chapter, frequency-domain relations are expressed in terms of
real radian frequency ω (i.e., $s = j\omega$).

which gives, in view of (1),

$$\tilde{R}_1(\omega, [V_n]; \ell) = \sum_{j=1}^{J(\ell)} \tilde{T}_{1j}(\omega, [V_n]; \ell) \tilde{S}_j(\omega; \ell) \quad (2)$$

The transfer functions \tilde{T}_{1j} may themselves represent several series and/or parallel interaction subpaths, and are then expressed in terms of elementary transfer functions \tilde{T}_{1jp}^m as

$$\tilde{T}_{1j}(\omega, [V_n]; \ell) = \sum_{p=1}^{P(i,j)} \prod_{m=1}^{M(p,i,j)} \tilde{T}_{1jp}^m(\omega, [V_n]; \ell) \quad (3)$$

in which \tilde{T}_{1jp}^m denotes the transfer function of the m th series portion of the p th parallel subpath. $P(i,j)$ denotes the number of parallel subpaths linking the j th POE or stimulus point to the i th response point, and $M(p,i,j)$ is the number of series segments of the p th parallel subpath. These transfer-function relations are shown in Fig. 1. The time-domain response function $R_{1j}(t, [V_n]; \ell)$ is the Fourier integral of the frequency-domain response $\tilde{R}_{1j}(\omega, [V_n]; \ell)$, namely

$$R_{1j}(t, [V_n]; \ell) = \frac{1}{2\pi} \int_{-\infty}^{\infty} \tilde{R}_{1j}(\omega, [V_n]; \ell) e^{j\omega t} d\omega \quad (4)$$

The error estimation problem for the linear interaction model which has been described above is that of combining errors in the transfer functions \tilde{T}_{1jp}^m and the stimulus functions \tilde{S}_j to obtain the resulting error in the frequency-domain response \tilde{R}_1 . From the error in the frequency-domain response, one may calculate the error in the time-domain response by evaluating a Fourier integral.

We shall assume in the remainder of this chapter that \tilde{R}_{1j} , \tilde{T}_{1j} (or \tilde{T}_{1jp}^m), and \tilde{S}_j represent the true values of the response, transfer, and stimulus functions respectively, and that the predicted values of these quantities are respectively $\hat{\tilde{R}}_{1j}$, $\hat{\tilde{T}}_{1j}$ (or $\hat{\tilde{T}}_{1jp}^m$), and $\hat{\tilde{S}}_j$. We may then treat the \tilde{R}_{1j} ,

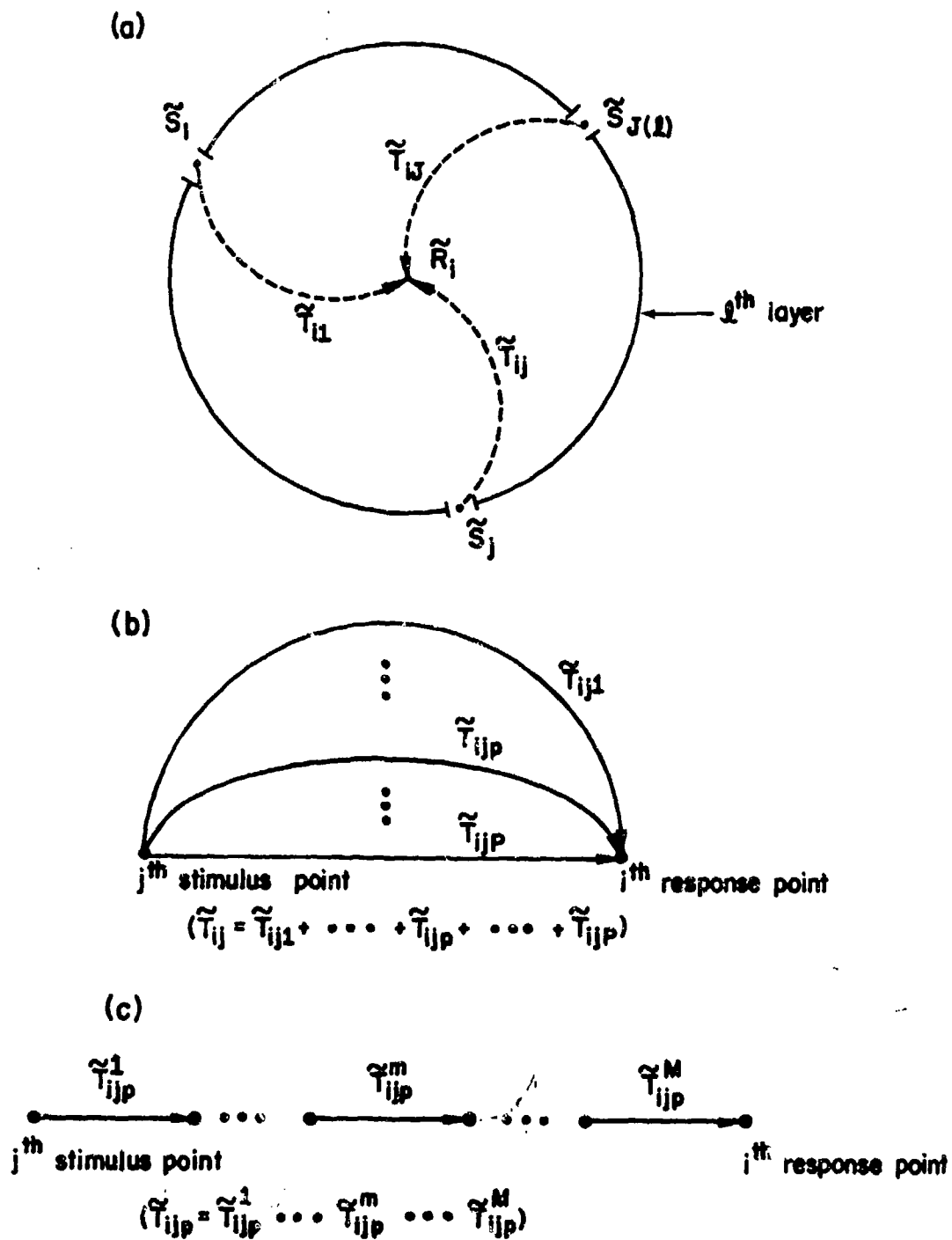


Fig. 1. Illustrating transfer-function relations for linear interaction model. (a) Interaction paths; (b) parallel interaction subpaths; (c) series interaction subpaths.

\tilde{T}_{1j} , and \tilde{S}_j as confidence-error random variables distributed around the predicted values \hat{R}_{1j} , \hat{T}_{1j} , and \hat{S}_j . More precisely, \tilde{R}_{1j} , \tilde{T}_{1j} , and \tilde{S}_j are stochastic processes with parameter ω , whose sample functions are distributed around the functions \hat{R}_{1j} , \hat{T}_{1j} , and \hat{S}_j . If it were possible to obtain a complete probabilistic description of the random processes $\tilde{T}_{1j}(\omega)$ and $\tilde{S}_j(\omega)$ in terms of their joint probability density functions, one could derive a complete description of the response process $\tilde{R}_{1j}(\omega)$ and thus of its Fourier integral $R_{1j}(t)$ [3,4]. Such an endeavor is far too complicated to be pursued here; rather, we shall focus our attention on a partial probabilistic description of the time-domain response process $R_{1j}(t)$ and determine what frequency-domain information is required for such a partial description.

We shall describe $R_{1j}(t)$ in terms of its mean (or expected value) and its variance. These are defined as [4, pp.138 ff.].

$$\begin{aligned}\mathcal{E}\{R_{1j}(t)\} &= \overline{R_{1j}(t)} = \text{expected value of } R_{1j}(t) \\ \text{var}\{R_{1j}(t)\} &= \overline{[R_{1j}(t) - \overline{R_{1j}(t)}]^2} \\ &= \overline{R_{1j}^2(t)} - \overline{R_{1j}(t)}^2\end{aligned}\quad (5)$$

\mathcal{E} denotes the expectation operator. The mean function $\overline{R_{1j}(t)}$ exhibits the central trend of the sample functions of the process $R_{1j}(t)$; the variance function measures the amount of spread of the sample functions around the mean. A closely related quantity which we shall also consider is the expected value of the energy in the response

$$\begin{aligned}\mathcal{E}(E_{1j}) &= \overline{E_{1j}} = \int_{-\infty}^{\infty} \overline{[R_{1j}(t)]^2} dt \\ &= \int_{-\infty}^{\infty} \text{var}\{R_{1j}(t)\} dt + \int_{-\infty}^{\infty} \overline{R_{1j}(t)}^2 dt\end{aligned}\quad (6)$$

The frequency-domain quantities necessary for the determination of the mean and variance of $R_{1j}(t)$ and the expected value of the energy in the response are the mean and covariance functions

$$\begin{aligned} \mathcal{E}\{\tilde{R}_{1j}(\omega)\} &= \overline{\tilde{R}_{1j}(\omega)} \\ \text{cov}\{\tilde{R}_{1j}(\omega), \tilde{R}_{1j}(\omega')\} &= \overline{\tilde{R}_{1j}(\omega)\tilde{R}_{1j}^*(\omega')} - \overline{\tilde{R}_{1j}(\omega)} \overline{\tilde{R}_{1j}^*(\omega')} \end{aligned} \quad (7)$$

since, as is easy to show,

$$\overline{R_{1j}(t)} = \frac{1}{2\pi} \int_{-\infty}^{\infty} \overline{\tilde{R}_{1j}(\omega)} e^{j\omega t} d\omega \quad (8)$$

$$\text{var}\{R_{1j}(t)\} = \left(\frac{1}{2\pi}\right)^2 \int_{-\infty}^{\infty} \int_{-\infty}^{\infty} \text{cov}\{\tilde{R}_{1j}(\omega), \tilde{R}_{1j}(\omega')\} e^{j(\omega - \omega')t} d\omega d\omega'$$

Equivalently, we may consider $\overline{\tilde{R}_{1j}(\omega)}$ and the correlation function

$$\begin{aligned} \text{cor}\{\tilde{R}_{1j}(\omega), \tilde{R}_{1j}(\omega')\} &= \overline{\tilde{R}_{1j}(\omega)\tilde{R}_{1j}^*(\omega')} \\ &= \text{cov}\{\tilde{R}_{1j}(\omega), \tilde{R}_{1j}(\omega')\} + \overline{\tilde{R}_{1j}(\omega)} \overline{\tilde{R}_{1j}^*(\omega')} \end{aligned} \quad (9)$$

The error-analysis problem therefore reduces to that of determining the mean and correlation (or covariance) functions of the frequency-domain response process $\tilde{R}_{1j}(\omega)$. These are expressed in terms of the stimulus and transfer functions as

$$\begin{aligned} \overline{\tilde{R}(\omega)} &= \overline{\tilde{T}(\omega)\tilde{S}(\omega)} \\ \overline{\tilde{R}(\omega)\tilde{R}^*(\omega')} &= \overline{\tilde{T}(\omega)\tilde{T}^*(\omega')\tilde{S}(\omega)\tilde{S}^*(\omega')} \end{aligned} \quad (10)$$

in which the subscripts have been dropped.

We shall assume that the frequency-domain processes $\tilde{T}(\omega)$ and $\tilde{S}(\omega)$ are uncorrelated; this assumption is reasonable in view of the linear model under consideration. Thus (10) simplifies to

$$\overline{\tilde{R}(\omega)} = \overline{\tilde{T}(\omega)} \overline{\tilde{S}(\omega)} \quad (11)$$

$$\overline{\tilde{R}(\omega)\tilde{R}^*(\omega')} = \overline{\tilde{T}(\omega)\tilde{T}^*(\omega')} \overline{\tilde{S}(\omega)\tilde{S}^*(\omega')}$$

and the mean and correlation functions of $\tilde{R}(\omega)$ are simply the products of the corresponding functions for $\tilde{T}(\omega)$ and $\tilde{S}(\omega)$. In the next section we will turn to the problem of evaluating the mean and correlation functions of $\tilde{T}(\omega)$ and $\tilde{S}(\omega)$ in terms of an assumed error model.

1.6.2 ERROR SPECIFICATION FOR STIMULUS AND TRANSFER FUNCTIONS

The transfer function $\tilde{T}(\omega)$ and the stimulus $\tilde{S}(\omega)$ can be expressed as the sums of the predicted values of these quantities, $\hat{T}(\omega)$ and $\hat{S}(\omega)$ respectively, and error random variables $\tilde{e}_t(\omega)$ and $\tilde{e}_s(\omega)$

$$\tilde{T}(\omega) = \hat{T}(\omega) + \tilde{e}_t(\omega) \quad (12)$$

$$\tilde{S}(\omega) = \hat{S}(\omega) + \tilde{e}_s(\omega)$$

Expressing the mean and correlation functions of $\tilde{T}(\omega)$ and $\tilde{S}(\omega)$ in terms of this representation, we find that

$$\begin{aligned} \overline{\tilde{T}(\omega)} &= \overline{\hat{T}(\omega)} + \overline{\tilde{e}_t(\omega)} \\ \overline{\tilde{S}(\omega)} &= \overline{\hat{S}(\omega)} + \overline{\tilde{e}_s(\omega)} \\ \overline{\tilde{T}(\omega)\tilde{T}^*(\omega')} &= \overline{\hat{T}(\omega)\hat{T}^*(\omega')} + \overline{\hat{T}(\omega)\tilde{e}_t^*(\omega')} \\ &\quad + \overline{\hat{T}^*(\omega')\tilde{e}_t(\omega)} + \overline{\tilde{e}_t(\omega)\tilde{e}_t^*(\omega')} \end{aligned} \quad (13)$$

$$\begin{aligned} \overline{\tilde{S}(\omega) \tilde{S}^*(\omega')} &= \hat{S}(\omega) \hat{S}^*(\omega') + \hat{S}(\omega) \overline{\tilde{e}_s^*(\omega')} \\ &+ \hat{S}^*(\omega') \overline{\tilde{e}_s(\omega)} + \overline{\tilde{e}_s(\omega) \tilde{e}_s^*(\omega')} \end{aligned} \quad (13)$$

The quantities necessary for the error specification of $\tilde{T}(\omega)$ and $\tilde{S}(\omega)$ are therefore the mean and correlation functions of the error random variables $\tilde{e}_t(\omega)$ and $\tilde{e}_s(\omega)$.

Now we introduce certain assumptions concerning the error random variables $\tilde{e}_t(\omega)$ and $\tilde{e}_s(\omega)$. The fundamental assumptions are that

- (a) the magnitudes and phases of $\tilde{e}_t(\omega)$ and $\tilde{e}_s(\omega)$ are independent
- (b) the phases are uniformly distributed on intervals of width 2π .

These assumptions imply that at a given frequency ω , the point $\hat{T}(\omega)$ in the complex \tilde{T} -plane is surrounded by a "circle of uncertainty" whose radius is measured by $|\tilde{e}_t(\omega)|$. The probability that $\tilde{T}(\omega)$ lies within a distance $|t_0|$ of the point $\hat{T}(\omega)$ is therefore given by [4, p. 94]

$$P \left\{ |\tilde{e}_t(\omega)| \leq |t_0| \right\} = \int_0^{|t_0|} f_{|\tilde{e}_t(\omega)|}(\tau) d\tau \quad (14)$$

where

$$f_{|\tilde{e}_t(\omega)|} = \text{probability density function of the random variable } |\tilde{e}_t(\omega)|$$

Similar statements also hold for $\tilde{S}(\omega)$. As an example, if $|\tilde{e}_t(\omega)|$ has a Rayleigh density and a mean-square value $|\tilde{e}_t(\omega)|^2 = \langle \tilde{e}_t^2(\omega) \rangle$, then

$$f_{|\tilde{e}_t(\omega)|}(\tau) = \frac{2\tau}{\langle \tilde{e}_t^2(\omega) \rangle} e^{-\tau^2 / \langle \tilde{e}_t^2(\omega) \rangle} \quad (15)$$

for $\tau \geq 0$, and zero otherwise; and (14) gives

$$P \left\{ |\tilde{e}_t(\omega)| \leq |t_0| \right\} = 1 - \exp(-|t_0|^2 / \langle \tilde{e}_t^2(\omega) \rangle) \quad (16)$$

The above two assumptions also imply that $\overline{\tilde{e}_t(\omega)} = \overline{\tilde{e}_s(\omega)} = 0$, so that there is no systematic bias in the predicted values $\hat{T}(\omega)$ and $\hat{S}(\omega)$; if such a bias were known (or suspected) to be present, it would be incorporated into the predicted values. Thus the zero means of $\tilde{e}_t(\omega)$ and $\tilde{e}_s(\omega)$ can be considered to reflect a maximum degree of ignorance concerning these errors.

It is also convenient to express $\tilde{e}_t(\omega)$ and $\tilde{e}_s(\omega)$ as being proportional to $\hat{T}(\omega)$ and $\hat{S}(\omega)$, respectively,

$$\begin{aligned}\tilde{e}_t(\omega) &= \tilde{x}_t(\omega)\hat{T}(\omega) \\ \tilde{e}_s(\omega) &= \tilde{x}_s(\omega)\hat{S}(\omega)\end{aligned}\tag{17}$$

in which the constants of proportionality are the random variables $\tilde{x}_t(\omega)$ and $\tilde{x}_s(\omega)$. These random variables have phases which are independent of their amplitudes and which are uniformly distributed on intervals of width 2π . Their mean-square magnitudes are respectively $\langle \tilde{x}_t^2(\omega) \rangle$ and $\langle \tilde{x}_s^2(\omega) \rangle$. The expressions (17) are useful for dealing with frequency-domain error estimates expressed on a fractional or percentage basis.

The above two assumptions permit us to write

$$\begin{aligned}\overline{\tilde{T}(\omega)} &= \hat{T}(\omega) \\ \overline{\tilde{S}(\omega)} &= \hat{S}(\omega) \\ \overline{\tilde{T}(\omega)\tilde{T}^*(\omega')} &= \hat{T}(\omega)\hat{T}^*(\omega') \left[1 + \overline{\tilde{x}_t(\omega)\tilde{x}_t^*(\omega')} \right] \\ \overline{\tilde{S}(\omega)\tilde{S}^*(\omega')} &= \hat{S}(\omega)\hat{S}^*(\omega') \left[1 + \overline{\tilde{x}_s(\omega)\tilde{x}_s^*(\omega')} \right]\end{aligned}\tag{18}$$

from which it is easily shown that

$$\begin{aligned}
\text{cov}\{\tilde{T}(\omega), \tilde{T}(\omega')\} &= \hat{T}(\omega) \hat{T}^*(\omega') \overline{\tilde{x}_t(\omega) \tilde{x}_t^*(\omega')} \\
\text{cov}\{\tilde{S}(\omega), \tilde{S}(\omega')\} &= \hat{S}(\omega) \hat{S}^*(\omega') \overline{\tilde{x}_s(\omega) \tilde{x}_s^*(\omega')} \\
\text{var}\{\tilde{T}(\omega)\} &= \langle \tilde{x}_t^2(\omega) \rangle |\hat{T}(\omega)|^2 \\
\text{var}\{\tilde{S}(\omega)\} &= \langle \tilde{x}_s^2(\omega) \rangle |\hat{S}(\omega)|^2
\end{aligned} \tag{19}$$

It is apparent that the correlation functions of the error random variables $\tilde{x}_t(\omega)$ and $\tilde{x}_s(\omega)$ are the quantities which are necessary for the determination of the mean and variance of the time-domain response. These correlations could be readily evaluated if the joint probability densities of $\tilde{x}_t(\omega)$ and $\tilde{x}_t^*(\omega')$, or $\tilde{x}_s(\omega)$ and $\tilde{x}_s^*(\omega')$, were known. It is, however, unlikely that such information would be available in a practical situation. Thus we must either be provided with the actual or estimated error correlation functions themselves, or be satisfied with such information concerning the time-domain response as can be gleaned from a knowledge of the mean-square values $\langle \tilde{x}_t^2(\omega) \rangle$ and $\langle \tilde{x}_s^2(\omega) \rangle$ alone.

In the next section we consider the combination of these error specifications into error measures for an elementary or single-path response function.

1.6.3 ERROR ANALYSIS FOR AN ELEMENTARY RESPONSE

When the input-output relation in the frequency domain is of the form $\tilde{R}(\omega) = \tilde{T}(\omega)\tilde{S}(\omega)$, we say that the response is elementary. The mean and variance of the frequency-domain elementary response are

$$\begin{aligned}
\overline{\tilde{R}(\omega)} &= \hat{T}(\omega) \hat{S}(\omega) \equiv \hat{R}(\omega) \\
\text{var}\{\tilde{R}(\omega)\} &= |\hat{R}(\omega)|^2 \left[(1 + \langle \tilde{x}_t^2(\omega) \rangle)(1 + \langle \tilde{x}_s^2(\omega) \rangle) - 1 \right]
\end{aligned} \tag{20}$$

and the mean-square value of $\tilde{R}(\omega)$ is

$$\begin{aligned}
|\tilde{R}(\omega)|^2 &= \text{var}\{\tilde{R}(\omega)\} + |\hat{R}(\omega)|^2 \\
&= |\hat{R}(\omega)|^2 (1 + \langle \tilde{x}_t^2(\omega) \rangle) (1 + \langle \tilde{x}_s^2(\omega) \rangle)
\end{aligned}
\tag{21}$$

From (4) and (20), the expected value of the time-domain elementary response is

$$\overline{R(t)} = \frac{1}{2\pi} \int_{-\infty}^{\infty} \hat{R}(\omega) e^{j\omega t} d\omega \equiv \hat{R}(t) \tag{22}$$

Thus, the expected value of the response in either domain is identical to its predicted value.

The variance of the time-domain elementary response is

$$\begin{aligned}
\text{var}\{R(t)\} &= \left(\frac{1}{2\pi}\right)^2 \int_{-\infty}^{\infty} \int_{-\infty}^{\infty} \hat{R}(\omega) \hat{R}^*(\omega') \left\{ \overline{\tilde{x}_s(\omega) \tilde{x}_s^*(\omega')} + \overline{\tilde{x}_t(\omega) \tilde{x}_t^*(\omega')} \right. \\
&\quad \left. + \overline{\tilde{x}_s(\omega) \tilde{x}_s^*(\omega')} \overline{\tilde{x}_t(\omega) \tilde{x}_t^*(\omega')} \right\} e^{j(\omega - \omega')t} d\omega d\omega'
\end{aligned}
\tag{23}$$

It is apparent that $\text{var}\{R(t)\}$ will be difficult (or at least tedious) to evaluate, except perhaps under very special circumstances. Furthermore, it is probably unreasonable to expect that the correlation functions $\overline{\tilde{x}_s(\omega) \tilde{x}_s^*(\omega')}$ and $\overline{\tilde{x}_t(\omega) \tilde{x}_t^*(\omega')}$ would even be available for use in (23). Therefore, although (23) is a correct expression for $\text{var}\{R(t)\}$, it may not be practically useful. Thus we must seek an alternate measure of the variance of the time-domain response.

It is not difficult to show that the integral of $\text{var}\{R(t)\}$ over time is

$$\begin{aligned}
\int_{-\infty}^{\infty} \text{var}\{R(t)\} dt &= \frac{1}{2\pi} \int_{-\infty}^{\infty} \text{var}\{\tilde{R}(\omega)\} d\omega \\
&= \frac{1}{2\pi} \int_{-\infty}^{\infty} |\hat{R}(\omega)|^2 \left[\langle \tilde{x}_s^2(\omega) \rangle + \langle \tilde{x}_t^2(\omega) \rangle + \langle \tilde{x}_s^2(\omega) \rangle \langle \tilde{x}_t^2(\omega) \rangle \right] d\omega \\
&= \bar{E} - E^0 \geq 0
\end{aligned}
\tag{24}$$

in which \bar{E} denotes the expected value of the energy in the response and E^0 denotes the predicted value of this quantity, namely,

$$\begin{aligned}\bar{E} &= \frac{1}{2\pi} \int_{-\infty}^{\infty} |\hat{R}(\omega)|^2 [1 + \langle \tilde{x}_s^2(\omega) \rangle] [1 + \langle \tilde{x}_t^2(\omega) \rangle] d\omega \\ E^0 &= \frac{1}{2\pi} \int_{-\infty}^{\infty} |\hat{R}(\omega)|^2 d\omega = \int_{-\infty}^{\infty} [\hat{R}(t)]^2 dt\end{aligned}\quad (25)$$

Thus if $\hat{R}(t)$ has a reasonably well defined duration, say τ , then the variance of $R(t)$ can be estimated by

$$\text{var}\{R(t)\} \sim \frac{1}{\tau} (\bar{E} - E^0) = \frac{E^0}{\tau} \left(\frac{\bar{E}}{E^0} - 1 \right) \quad (26)$$

An estimate of the relative fluctuation f_r of $R(t)$ around its expected or predicted value is then given by the quantity

$$f_r \equiv (\bar{E}/E^0 - 1)^{1/2} \geq 0 \quad (27)$$

If the mean-square errors $\langle \tilde{x}_s^2(\omega) \rangle$ and $\langle \tilde{x}_t^2(\omega) \rangle$ are independent of ω , then

$$\begin{aligned}\text{var}\{R(t)\} &\sim \frac{E^0}{\tau} (\langle \tilde{x}_s^2 \rangle + \langle \tilde{x}_t^2 \rangle + \langle \tilde{x}_s^2 \rangle \langle \tilde{x}_t^2 \rangle) \\ f_r &= (\langle \tilde{x}_s^2 \rangle + \langle \tilde{x}_t^2 \rangle + \langle \tilde{x}_s^2 \rangle \langle \tilde{x}_t^2 \rangle)^{1/2}\end{aligned}\quad (28)$$

In the next section we discuss error measures for non-elementary response functions, i.e., those arising from series and/or parallel interaction paths.

1.6.4 ERROR ANALYSIS FOR NON-ELEMENTARY RESPONSES

In this section we will discuss the development of error measures for response functions resulting from series and/or parallel interaction

paths. The series case will be treated in Sec. 1.6.4.1, and the parallel case in Sec. 1.6.4.2.

1.6.4.1 Series Interaction Paths

The transfer function $\tilde{T}_{ijp}(\omega, [V_n]; L)$ which represents a series connection of interaction subpaths is represented as a product of individual transfer functions:

$$\tilde{T}_{ijp}(\omega, [V_n]; L) = \prod_{m=1}^{M(p, i, j)} \tilde{T}_{ijp}^m(\omega, [V_n]; L) \quad (29)$$

in which $\tilde{T}_{ijp}^m(\omega)$ represents the transfer function of the m th series portion of the p th parallel interaction path. There are M such portions comprising the p th parallel path. We assume that the errors in the series subpath transfer functions are uncorrelated, i.e.,

$$\begin{aligned} \overline{\tilde{e}_{tp}^m(\omega) \tilde{e}_{tp}^{m'}(\omega)} &= \overline{\tilde{e}_{tp}^m(\omega)} \overline{\tilde{e}_{tp}^{m'}(\omega)} = 0 \quad (m \neq m') \\ &= \langle \tilde{e}_{tp}^m(\omega)^2 \rangle \quad (m = m') \end{aligned} \quad (30)$$

where

$$\tilde{T}_{ijp}^m(\omega) = \hat{T}_{ijp}^m(\omega) + \tilde{e}_{tijp}^m(\omega) = \hat{T}_{ijp}^m(\omega) [1 + \tilde{x}_{tijp}^m(\omega)] \quad (31)$$

Under this assumption, we readily obtain the following results (the i, j subscripts are dropped)

$$\overline{\tilde{T}_p(\omega)} = \hat{T}_p(\omega) = \prod_{m=1}^M \hat{T}_p^m(\omega) \quad (32)$$

$$\overline{\tilde{T}_p(\omega) \tilde{T}_p^*(\omega')} = \hat{T}_p(\omega) \hat{T}_p^*(\omega') \prod_{m=1}^M \left[1 + \overline{\tilde{x}_{tp}^m(\omega) \tilde{x}_{tp}^{m*}(\omega')} \right]$$

in which

$$\hat{T}_p(\omega) \hat{T}_p^*(\omega') = \prod_{m=1}^M \hat{T}_p^m(\omega) \hat{T}_p^{m*}(\omega') \quad (33)$$

Now by incorporating these results in the analysis of the previous section, we obtain the following error measures for the response R_p

$$\overline{\tilde{R}_p(\omega)} = \hat{R}_p(\omega) = \hat{S}(\omega)\hat{T}_p(\omega) \quad (34)$$

$$\begin{aligned} \text{var}\{\tilde{R}_p(\omega)\} &= |\hat{R}_p(\omega)|^2 \left\{ [1 + \langle \tilde{x}_s^2(\omega) \rangle] \prod_{m=1}^M [1 + \langle \tilde{x}_{tp}^m(\omega)^2 \rangle] - 1 \right\} \\ &= \overline{|\tilde{R}_p(\omega)|^2} - |\hat{R}_p(\omega)|^2 \end{aligned} \quad (35)$$

$$\overline{R_p(t)} = \hat{R}_p(t) \quad (36)$$

$$\begin{aligned} \text{var}\{R_p(t)\} &= \left(\frac{1}{2\pi}\right)^2 \int_{-\infty}^{\infty} \int_{-\infty}^{\infty} \hat{R}_p(\omega) \hat{R}_p^*(\omega') e^{j(\omega - \omega')t} d\omega d\omega' \\ &\quad \left\{ \left[1 + \overline{\tilde{x}_s(\omega) \tilde{x}_s^*(\omega')} \right] \prod_{m=1}^M \left[1 + \overline{\tilde{x}_{tp}^m(\omega) \tilde{x}_{tp}^{m*}(\omega')} \right] - 1 \right\} \end{aligned} \quad (37)$$

$$\overline{E}_p = \frac{1}{2\pi} \int_{-\infty}^{\infty} |\hat{R}_p(\omega)|^2 [1 + \langle \tilde{x}_s^2(\omega) \rangle] \prod_{m=1}^M [1 + \langle \tilde{x}_{tp}^m(\omega)^2 \rangle] d\omega \quad (38)$$

In the special case where $\langle \tilde{x}_s^2(\omega) \rangle$ and $\langle \tilde{x}_{tp}^m(\omega)^2 \rangle$ ($m = 1, 2, 3, \dots, M$) are independent of ω , we have

$$\overline{E}_p = E_p^0 (1 + \langle \tilde{x}_s^2 \rangle) \prod_{m=1}^M [1 + \langle \tilde{x}_{tp}^m \rangle^2] \quad (39)$$

$$\text{var}\{R(t)\} \sim \frac{E_p^0}{t} \left\{ (1 + \langle \tilde{x}_s^2 \rangle) \prod_{m=1}^M [1 + \langle \tilde{x}_{tp}^m \rangle^2] - 1 \right\} \quad (40)$$

$$f_r \sim \left\{ (1 + \langle \tilde{x}_s^2 \rangle) \prod_{m=1}^M [1 + \langle \tilde{x}_{tp}^m \rangle^2] - 1 \right\}^{\frac{1}{2}} \quad (41)$$

1.6.4.2 Parallel Interaction Paths

The frequency-domain response $\tilde{R}(\omega)$ resulting from the presence of parallel interaction paths is represented as the sum of the responses due to each of the parallel paths, namely,

$$\tilde{R}(\omega) = \sum_{p=1}^P \tilde{R}_p(\omega) \quad (42)$$

If we assume that the errors arising from each of the P parallel paths are uncorrelated, then we obtain

$$\overline{\tilde{R}(\omega)} = \sum_{p=1}^P \overline{\tilde{R}_p(\omega)} = \sum_{p=1}^P \hat{\tilde{R}}_p(\omega) \quad (43)$$

$$\text{var}\{\tilde{R}(\omega)\} = \sum_{p=1}^P \text{var}\{\tilde{R}_p(\omega)\} \quad (44)$$

$$\text{cov}\{\tilde{R}(\omega), \tilde{R}(\omega')\} = \sum_{p=1}^P \text{cov}\{\tilde{R}_p(\omega), \tilde{R}_p(\omega')\} \quad (45)$$

in the frequency domain, and

$$\overline{R(t)} = \sum_{p=1}^P \overline{R_p(t)} = \sum_{p=1}^P \hat{R}_p(t) \quad (46)$$

$$\text{var}\{R(t)\} = \sum_{p=1}^P \text{var}\{R_p(t)\} \quad (47)$$

in the time domain.

Denoting by \bar{E} and E^0 the expected and predicted values of the energy in the total response respectively, and by E_p and E_p^0 the expected and predicted values of the energy in each of the P response functions $\tilde{R}_p(\omega)$ or $R_p(t)$, we can show that

$$\bar{E} - E^0 = \sum_{p=1}^P (\bar{E}_p - E_p^0) \geq 0 \quad (48)$$

It is important to emphasize that in general

$$\bar{E} \neq \sum_{p=1}^P \bar{E}_p$$

$$E^0 \neq \sum_{p=1}^P E_p^0$$

since, e.g.,

$$\int_{-\infty}^{\infty} [\hat{R}_1(t) + \hat{R}_2(t)]^2 dt \neq \int_{-\infty}^{\infty} [\hat{R}_1^2(t) + \hat{R}_2^2(t)] dt$$

In the following section of this chapter we will discuss confidence bounds on the errors in the response functions.

1.6.5 CONFIDENCE BOUNDS

A confidence bound on the error in a given quantity of interest is the probability that the error is greater than, or less than, some specified value. For example, consider a random variable v which is the sum of a "true" value v_0 and an error random variable e_v

$$v = v_0 + e_v \quad (49)$$

A confidence bound on the error in the quantity v would be expressed as

$$P\{|e_v| \geq e_0\} \leq b(e_0) \quad (50)$$

in which $b(e_0)$ is a function of the real, positive variable e_0 .

Consider as a specific example the case for which $|e_v|$ is a Rayleigh-distributed random variable with mean-square value $\langle e_v^2 \rangle$. Then it is easy to show that

$$P\{|e_v| \geq e_0\} = \exp(-e_0^2 / \langle e_v^2 \rangle) \quad (51)$$

and therefore that, e.g.,

$$\begin{aligned} P\{|e_v| \geq 2\langle e_v^2 \rangle^{1/2}\} &= 0.018 \\ P\{|e_v| \geq \langle e_v^2 \rangle^{1/2}\} &= 0.368 \\ P\{|e_v| \geq \frac{1}{2}\langle e_v^2 \rangle^{1/2}\} &= 0.779 \end{aligned} \quad (52)$$

If the probability density of the random variable of interest is not known, it is possible to obtain general (but not necessarily tight) confidence bounds. A useful starting point for such confidence bounds is the inequality of Bienaymé [4]

$$P\{|x-a| \geq \alpha\} \leq \alpha^{-n} \mathcal{E}\{|x-a|^n\} \quad (53)$$

in which x is a random variable and a , α and n are parameters. In this chapter we have assumed that mean-square values of the error random variables of interest will be available; so let us choose $a=0$, $x=e_v$, $\alpha=e_0$, and $n=2$. Then (53) becomes

$$P\{|e_v| \geq e_0\} \leq \langle e_v^2 \rangle / e_0^2 \quad (54)$$

which is a confidence bound expressed in terms of the mean-square value of the random variable e_v . To demonstrate that this bound, because of its generality, may not be a tight one, compare (52) with similar results from (54)

$$\begin{aligned} P\{|e_v| \geq 2\langle e_v^2 \rangle^{1/2}\} &\leq 0.25 \\ P\{|e_v| \geq \langle e_v^2 \rangle^{1/2}\} &\leq 1.0 \end{aligned} \quad (55)$$

Since the probability of any event is less than or equal to unity, the bound (54) is useful only when $\langle e_v^2 \rangle \leq e_0^2$.

As a simple example of the application of a bound of the form of (54), consider an elementary frequency-domain response

$$\begin{aligned}\tilde{R}(\omega) &= \hat{R}(\omega) + \tilde{e}_r(\omega) \\ &= \hat{R}(\omega) [1 + \tilde{x}_r(\omega)] \\ &= \hat{R}(\omega) [1 + \tilde{x}_t(\omega) + \tilde{x}_s(\omega) + \tilde{x}_t(\omega)\tilde{x}_s(\omega)]\end{aligned}\tag{56}$$

The mean-square value of the relative error $\tilde{x}_r(\omega)$ is

$$\langle \tilde{x}_r^2(\omega) \rangle = \langle \tilde{x}_t^2(\omega) \rangle + \langle \tilde{x}_s^2(\omega) \rangle + \langle \tilde{x}_t^2(\omega) \rangle \langle \tilde{x}_s^2(\omega) \rangle\tag{57}$$

Thus, from (54)

$$P\{|\tilde{x}_r(\omega)| \geq x_0\} \leq \frac{1}{2} \left[\langle \tilde{x}_t^2(\omega) \rangle + \langle \tilde{x}_s^2(\omega) \rangle + \langle \tilde{x}_t^2(\omega) \rangle \langle \tilde{x}_s^2(\omega) \rangle \right]\tag{58}$$

where x_0 is a real, positive parameter. If

$$\langle \tilde{x}_t^2(\omega) \rangle^{1/2} = \langle \tilde{x}_s^2(\omega) \rangle^{1/2} = 0.10\tag{59}$$

then, for example,

$$P\{|\tilde{x}_r(\omega)| \geq 0.25\} \leq 0.32\tag{60}$$

implying that the probability that the magnitude of the relative error in the response exceeds 25% is less than 32%.

Examples of the application of the material in this chapter to specific problems will be found in Sec. 3.2.5.

REFERENCES

- [1] Charles T.C. Mo, "Statistical relationship between testing and predictions of EMP interaction," IN 331, January 1977.
- [2] C. Ashley and W.R. Graham, "Estimation of errors in calculating transfer functions from pulsed data," MN 19, September 1973.
- [3] S. Karlin, A First Course in Stochastic Processes, Academic Press, New York, 1969.
- [4] Athanasios Papoulis, Probability, Random Variables, and Stochastic Processes, McGraw-Hill, New York, 1965.

PART 2

FORMULAS AND DATA

CHAPTER 2.1

EXTERNAL INTERACTION

EMP interaction with electrical systems inside structures such as aircraft, missiles, satellites and buildings depends upon many factors. To make the interaction analysis tractable the entire process is separated into three approximately independent parts which account for the external interaction, the mode of penetration to the interior of the structure, and the excitation of the elements of the electrical system within the structure. The approximations involved in this procedure are that the electromagnetic field external to the structure is independent of the interior system (i.e., the system must be at least partially shielded from the electromagnetic field) and that the mode of penetration is insensitive to the components of the system interior to the structure. This chapter deals with EMP interaction with the outer surface of the outermost layer of a system in the topological model, for example, the exterior surface of the aircraft skin.

Systems such as aircraft and missiles generally have a complete or nearly complete metallic covering that serves as a shield against external electromagnetic fields. The modes of field penetration are, for example, (a) the penetration through windows and holes in the metal covering, through joints in the metal skin, through cracks around access doors and through exhaust ports; (b) the direct excitation of electrical cabling, power lines or other conductors that run outside the metallic covering over a portion of their length and then run inside to some internal subsystem; (c) the direct excitation of system antennas; and (d) diffusion through the metal skin. Engineering data and formulas pertinent to each of these penetration modes are presented in this chapter.

2.1.1 COUPLING

The EMP generated by a nuclear detonation depends upon the height of the burst, the specific device, the distance from the burst, the

height of the observation, and other factors. Instead of considering every possible example of EMP environment, only two canonical environments are presented followed by two convenient approximations. A more general treatment would require canonical environments to be constructed using averages, extreme values (upper and lower bounds), and perhaps statistical distributions of pertinent EMP environmental parameters [1].

A case of particular interest is the so-called high-altitude EMP resulting from an exoatmospheric nuclear detonation. Beneath the source region in the upper atmosphere the EMP is generally approximated as a spherical wave, while over a small portion of the wave front the EMP may be considered a plane wave with linear polarization (or more accurately, circular polarization with a very slow precession rate). The electric and magnetic fields of the plane-wave EMP can be expressed as

$$\begin{aligned}\vec{E}(\vec{r}, t) &= \vec{f}(t - \vec{1}_Y \cdot \vec{r}/c) \\ \vec{H}(\vec{r}, t) &= \frac{1}{Z_0} \vec{1}_Y \times \vec{f}(t - \vec{1}_Y \cdot \vec{r}/c)\end{aligned}\tag{1}$$

where \vec{f} is the waveform, $\vec{1}_Y$ is the unit vector in the direction of propagation, Z_0 is the free-space wave impedance and c is the vacuum speed of light. At points in the vicinity of the earth's surface, plane wave reflection can be used to obtain the total electromagnetic field. Throughout this chapter the plane-wave fields as given by (1) are used.

2.1.1.1 Difference of Two Exponentials

One commonly used EMP waveform is given by the difference of two exponentials multiplied by a unit-step function $u(t)$, viz.

$$f(t) = E_0 \left(e^{-t/\tau_f} - e^{-t/\tau_r} \right) u(t)\tag{2}$$

with the Laplace transform

$$F(s) \equiv \mathcal{L}\{f(t)\} = \frac{E_0}{s + 1/\tau_f} - \frac{E_0}{s + 1/\tau_r}\tag{3}$$

where, typically, the rise time $\tau_r = 2$ ns and the fall time $\tau_f = 250$ ns. A plot of (2) is shown in Fig. 1. This waveform turns on at $t = 0+$ with a finite slope, reaches a peak value in a few nanoseconds, and decays slowly to zero. Its important time-domain characteristics are summarized in table 1 and its frequency-domain characteristics in table 2.

2.1.1.2 Reciprocal of the Sum of Two Exponentials

Another canonical waveform coming into common usage is the reciprocal of the sum of two exponentials given by

$$f(t) = \frac{E_0}{e^{-(t-t_0)/\tau_r} + e^{(t-t_0)/\tau_f}} \quad (4)$$

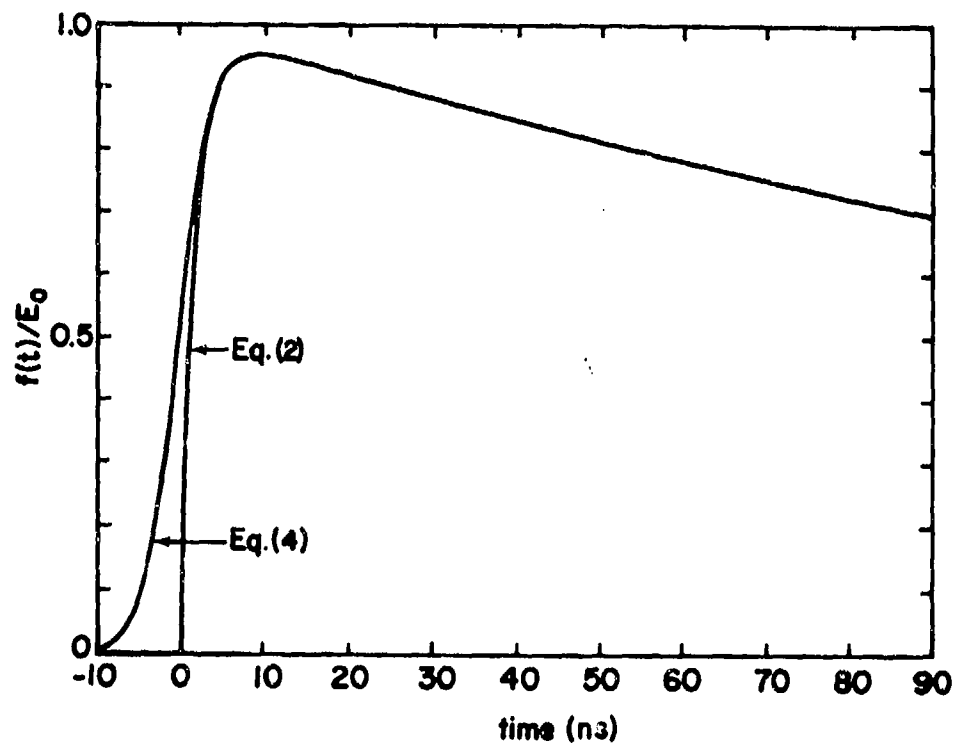


Fig. 1. Two canonical EMP waveforms: $\tau_r = 2$ ns, $\tau_f = 250$ ns, $t_0 = 0$.

TABLE 1. TIME-DOMAIN CHARACTERISTICS OF TWO CANONICAL EMP WAVEFORMS

	$f_1(t) = E_0(e^{-t/\tau_f} - e^{-t/\tau_r})u(t)$	$f_2(t) = E_0 \left[e^{-\frac{-(t-t_0)/\tau_r}{\tau_r + e^{(t-t_0)/\tau_f}}} \right]^{-1}$
Rise Times (10% - 90%)	$2.2 \tau_r$	$4.4 \tau_r$
Peak Values	$E_0 [1 + (\tau_r/\tau_f)(\ln\{\tau_r/\tau_f\} - 1)]$	$E_0 [1 + (\tau_r/\tau_f)(\ln\{\tau_r/\tau_f\} - 1)]$
Duration of Pulse (for Decay to 10% of Peak)	$2.3 \tau_f$	$t_0 + 2.3 \tau_f$
$\int_{-\infty}^{\infty} f(t)dt$	$E_0 \tau_f$	$E_0 \tau_f$

TABLE 2. FREQUENCY-DOMAIN CHARACTERISTICS OF TWO CANONICAL EMP WAVEFORMS

	$\mathcal{L}\{f_1(t)\}$	$\mathcal{L}\{f_2(t)\}$
Low-Frequency Approx. $\tau_f s \ll 1$	$E_0 \tau_f$	$E_0 \tau_f e^{-st_0}$
Mid-Frequency Approx. $1/\tau_f \ll s \ll 1/\tau_r$	E_0/s	$(E_0/s)e^{-st_0}$
High-Frequency Approx. $\tau_r s \gg 1$	$E_0/(\tau_r s^2)$	$\pm E_0 \tau_r^2 j e^{-\tau_r s } e^{-st_0}$
Zeros	None	None
Poles	$s = -1/\tau_r, -1/\tau_f$	$s = -n(1/\tau_r + 1/\tau_f) - 1/\tau_f, n = 0, 1, 2, 3, \dots$

with the two-sided Laplace transform

$$F(s) \equiv \mathcal{L}\{f(t)\} = \frac{E_0 \pi \tau_r \tau_f}{\tau_r + \tau_f} \operatorname{csc} \left[\frac{\pi \tau_r}{\tau_r + \tau_f} (\tau_f s + 1) \right] e^{-st_0} \quad (5)$$

This type of waveform, shown in Fig. 1, is similar to the waveform (2) except that the rise is of an exponential form with no discontinuity in the function or its derivatives. Consequently, the waveform (2) has much more high-frequency content and a correspondingly faster (10% - 90%) rise time for the same parameters τ_r and τ_f . The waveform (4) is of interest because it is more consistent with the exponential growth of the nuclear radiation emanating initially from a burst. Its important time- and frequency-domain characteristics are given in tables 1 and 2.

2.1.1.3 Unit-Step Pulse

Many interaction applications depend primarily on the mid-frequency content of the EMP, i.e., $1 \text{ MHz} \leq f \leq 20 \text{ MHz}$. In this case the frequency-domain representation

$$F(s) = E_0/s \quad (6)$$

approximates the mid-frequency content very well. The inverse Laplace transform of (6) yields the unit-step waveform representation for the EMP

$$f(t) = E_0 u(t) \quad (7)$$

which is mathematically more convenient than either of the canonical waveforms (2) and (4), and yet its interaction is essentially the same as the "actual" EMP interaction over an appropriate frequency range.

2.1.1.4 Unit-Step With Exponential Decay

Another mathematically simple waveform approximation to the EMP is the unit step with exponential decay

$$f(t) = E_0 e^{-t/\tau_f} u(t) \quad (8)$$

with Laplace transform given by

$$F(s) = \frac{E_0}{s + 1/\tau_f}$$

which accurately represents the low- and mid-frequency content of the two canonical pulses (2) and (4).

2.1.2 PROPAGATION

2.1.2.1 Low and Intermediate Frequencies

In the study of EMP interaction with the metallic or other highly conducting covering of electrical systems it is expedient to idealize the actual surface configuration of the covering. Results for such idealized configurations should be, to a suitable degree of approximation, appropriate for the actual configurations. In this section, both frequency-domain and time-domain results for the external surface current and charge densities are presented for a few generic configurations -- the prolate spheroid, the right circular cylinder, and perpendicularly crossed cylinders. More complex structures such as the intersecting cylinder model and the body-of-revolution model of an aircraft are also treated. In each case the incident wave is a plane-wave EMP. Questions of modeling procedures and accuracy are also addressed. Sample calculations are provided to illustrate the applications of the formulas, tables and parametric data curves.

2.1.2.1.1 Prolate Spheroid

A common idealized configuration is the prolate spheroid (Fig. 2). As $h \rightarrow a$ the spheroid becomes a sphere, and for $h \gg a$ it approaches a slender rod. Hence this configuration has a wide range of application.

The transformations between the cylindrical coordinates (z, r, ϕ) and the prolate spheroid coordinates (ξ, ζ, ϕ) are (Fig. 2)

$$\begin{aligned} z &= h \xi \zeta \\ r &= h \sqrt{(\xi^2 - 1)(1 - \zeta^2)} \\ \phi &= \phi \end{aligned} \tag{9}$$

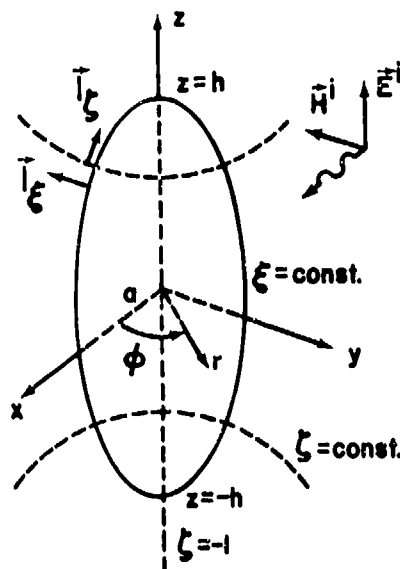


Fig. 2. Plane wave broadside incident on a prolate spheroid.

where the eccentricity e is given by

$$e = \sqrt{1 - (a/h)^2} \quad (10)$$

a. Quasi-Static Surface Current and Charge Densities

At low frequencies for which the wavelength $\lambda \gg h$, the quasi-static approximation may be used to obtain the induced surface current and charge densities $\vec{J}(\zeta, \phi, s)$ and $\rho(\zeta, \phi, s)$ on the spheroid. When the incident electric and magnetic fields are directed parallel to the z -axis and the negative y -axis, respectively (Fig. 2), one has [2,3]

$$J_{\phi}(\zeta, \phi, s) = \frac{2H^1(s)}{2 - \alpha_0} \sqrt{\frac{1 - e^2}{1 - e^2 \zeta^2}} \zeta \sin \phi \quad (11)$$

$$J_{\zeta}(\zeta, \phi, s) = \frac{2H^1(s)}{2 - \alpha_0} \cos \phi + s \epsilon_0 a \frac{E^1(s)}{2(1 - \alpha_0)} \sqrt{1 - \zeta^2} \quad (12)$$

$$\rho(\zeta, s) = \frac{\epsilon_0 E^1(s)}{1 - \alpha_0} \sqrt{\frac{1 - e^2}{1 - e^2 \zeta^2}} \zeta \quad (13)$$

where

$$\alpha_0 = \frac{1}{e^2} \left[1 + \frac{1}{2} \frac{1-e^2}{e} \ln \left(\frac{1-e}{1+e} \right) \right] \quad (14)$$

Note that on the surface of the spheroid

$$\xi = 1/e, \quad \zeta = z/h \quad (15)$$

Eqs. (11) - (13) are derived from exact solutions of a magnetostatic and an electrostatic boundary-value problem.

b. Intermediate-Frequency Surface Current and Charge Densities

In the mid-frequency range where $\lambda \sim h$, the total surface current density on an electrically thin spheroid ($\lambda \gg a$) may be obtained by combining the quasi-static current distributions, (11) and (12), and the total axial current $I(\zeta, s)$, namely [4]

$$\vec{J}(\zeta, \phi, s) = \frac{I(\zeta, s)}{2\pi r} \vec{I}_\zeta + \frac{2H^1(s)}{2-\alpha_0} \left\{ \sqrt{\frac{1-e^2}{1-e^2\zeta^2}} \zeta \sin \phi \vec{I}_\phi + \cos \phi \vec{I}_\zeta \right\} \quad (16)$$

where $r = a\sqrt{1-\zeta^2}$, and the first term on the right-hand side reduces to the second term on the right-hand side of (12) at low frequencies.

The singularity-expansion representations of the total axial current $I(\zeta, s)$ and the corresponding surface charge density $\rho(\zeta, s)$ are [5]

$$I(\zeta, s) = \sum_{\alpha=1}^{\infty} \left[\frac{s}{s_\alpha(s-s_\alpha)} + \frac{s}{s_\alpha^*(s-s_\alpha^*)} \right] \eta_\alpha(s) i_\alpha(\zeta) \quad (17)$$

$$\rho(\zeta, s) = \sum_{\alpha=1}^{\infty} \left[\frac{1}{s_\alpha(s-s_\alpha)} + \frac{1}{s_\alpha^*(s-s_\alpha^*)} \right] \eta_\alpha(s) \rho_\alpha(\zeta) \quad (18)$$

where the class-2 coupling coefficient $\eta_\alpha(s)$, the natural modes $i_\alpha(\zeta)$ and $\rho_\alpha(\zeta)$, and the natural frequency s_α are given by [6]

$$\eta_{\alpha}(s) = \frac{2\pi c}{Z_0 \psi_a} \int_{-1}^1 i_{\alpha}(\zeta) E_{\zeta}^1(\zeta, s) d\zeta \quad (19)$$

$$i_{\alpha}(\zeta) = \sin[\alpha\pi(1+\zeta)/2] \quad (20)$$

$$\rho_{\alpha}(\zeta) = -\frac{\alpha}{4ah} \frac{\cos[\alpha\pi(1+\zeta)/2]}{\sqrt{1-e^2\zeta^2}} \quad (21)$$

$$s_{\alpha} = \frac{c}{2h\psi_a} [j\alpha\pi\psi_a - E(2\alpha\pi)] \quad (22)$$

Here, the antenna parameter ψ_a and the function E are defined by

$$\psi_a = 2 \ln(2h/a) - 0.614 \quad (23)$$

$$E(2\alpha\pi) = 0.577 + \ln(2\alpha\pi) - Ci(2\alpha\pi) + j Si(2\alpha\pi) \quad (24)$$

and Ci and Si denote the cosine and sine integrals [7].

In the case of an incident plane wave propagating parallel to the x -axis with \vec{E}^1 parallel to the z -axis (Fig. 2), the coupling coefficient η_{α} defined by (19) is found to be

$$\eta_{\alpha}(s) = \frac{8c}{\alpha Z_0 \psi_a} E^1(s) e^{\gamma_a}, \quad \alpha = 1, 3, 5, \dots \quad (25)$$

for slender spheroids ($a \ll h$). Formulas (22) and (25) are tabulated in tables 3 and 4, along with the solutions obtained by some elaborate numerical methods.

The frequency-domain current $I(0, j\omega)$ at the mid-points of several thin prolate spheroids and the frequency-domain charge density $\rho(1, j\omega)$ at their tips are tabulated in tables 5 and 6 for a broadside incident plane wave (Fig. 2). Although only two modes from (17) and (18) are used in the computation, the computed results differ from the exact results for

TABLE 3. COMPLEX NATURAL FREQUENCIES ($2s h/c$) FOR A CYLINDER-LIKE OBJECT ($a/h = 0.1$)

α	Formula (22)	Prolate Spheroid (Numerical) [8]	Cylinder (Exact Kernel- Numerical)	Cylinder (Approx. Kernel- Numerical)
1	$-0.4534 + j2.8778$	$-0.530 + j2.916$	$-0.4380 + j2.5849$	$-0.4279 + j2.5377$
2	$-0.5770 + j6.0057$	$-0.800 + j5.954$	$-0.6879 + j5.5098$	$-0.6815 + j5.3829$
3	$-0.6540 + j9.1425$	$-0.994 + j9.020$	$-0.7866 + j8.4120$	$-0.8167 + j8.1833$
4	$-0.7073 + j12.282$	$-1.164 + j12.102$		
5	$-0.7487 + j15.422$	$-1.316 + j15.196$		

TABLE 4. COMPLEX COUPLING COEFFICIENTS, $\{\eta_\alpha(s)/[c E^1(s)]\} \times 10^3$, FOR A THIN CYLINDER ($a/h = 0.1$) WITH BROADSIDE ILLUMINATION

α	Formula (25)	Numerical Solution
1	$3.617 + j1.070$	$3.901 + j2.180$
2	0.0	0.0
3	$0.7521 + j0.9760$	$1.596 + j1.471$
4	0.0	0.0
5	$0.02094 + j0.73206$	$1.093 + j1.4290$
6	0.0	0.0

TABLE 5. AXIAL CURRENT AT THE CENTER OF A PROLATE SPHEROID AND A CYLINDER
WITH BROADSIDE ILLUMINATION ($k = \omega/c$), $kI(0, j\omega)/E^1(j\omega)$

kh	a/h	Formula (17)*	Prolate Spheroid- Exact Calculation	Cylinder-Approx. Numerical Calculation
1.2	0.01417	2.96 + j7.39	1.662 + j7.306	3.852 + j10.45
1.571	0.01417	20.33 - j12.69	27.37 - j0.043	17.96 - j12.20
2.0	0.01417	2.18 - j9.37	7.200 - j10.86	5.431 - j9.754
3.0	0.01417	0.18 - j4.96	3.640 - j8.278	3.469 - j8.279
1.212	0.1406	10.11 + j10.32	8.136 + j14.39	27.72 + j2.128
1.586	0.1406	20.79 - j10.15	27.37 - j0.2501	16.60 - j10.95
2.02	0.1406	7.54 - j13.15	18.23 - j10.08	12.82 - j10.91
3.03	0.1406	2.07 - j8.87	13.99 - j11.22	12.23 - j14.01

TABLE 6. SURFACE CHARGE DENSITY AT THE TIP OF A PROLATE SPHEROID WITH BROADSIDE
ILLUMINATION ($k = \omega/c$), $\rho(1, j\omega)/[E_0^1(j\omega)]$

kh	a/h	Formula (18)*	Exact Solution
1.571	0.01417	-2.444 - j38.75	-8.167 - j52.16
1.586	0.1406	-17.73 - j39.22	-0.4746 - j51.94

*Only two modes are used for the numerical data.

the induced axial current by less than 50%, and at the first resonance the difference is less than 16%. It is expected, however, that the accuracy of (16) is considerably greater than that of (17) because (16) involves an accurate determination of the contribution of the quasi-static current. The accuracy of the formula (16) should be within about 15% of the actual value induced on a prolate spheroid.

As mentioned in Sec. 2.1.1.3, the intermediate-frequency representation of the nuclear EMP is given by

$$E^1(s) = E_0/s \quad (26)$$

which is the spectrum of a unit-step pulse. When this expression is substituted in (17) and (18) and inverse Laplace transforms are performed one obtains the following time-domain results

$$I(\zeta, t) = 2\text{Re} \left[\sum_{\alpha=1}^{\infty} \eta_{\alpha}(s_{\alpha}) i_{\alpha}(\zeta) e^{s_{\alpha}(t - \zeta h/c \cos \theta)} \right] u(t - \zeta h/c \cos \theta) \quad (27)$$

$$\rho(\zeta, t) = 2\text{Re} \left[\sum_{\alpha=1}^{\infty} \eta_{\alpha}(s_{\alpha}) \rho_{\alpha}(\zeta) \frac{e^{s_{\alpha}(t - \zeta h/c \cos \theta)} - 1}{s_{\alpha}} \right] u(t - \zeta h/c \cos \theta) \quad (28)$$

where Re denotes the real part of the expression, and θ is the angle between the z-axis and the direction of propagation (Fig. 2). Expression (27) is plotted in Fig. 3 for $\theta = 90^\circ$ along with some accurate numerical result for a right circular cylinder [9].

c. Simple Estimate of the Time-Domain Current

For the class of slender cylinder-like objects it is possible to derive a simple formula for estimating the time-domain response of the axial current to a unit-step incident pulse. First, the object is represented by an equivalent right circular cylinder (thus the object must at least be similar to a cylinder) with an equivalent radius a_{eq} defined as

$$a_{eq} \equiv P/2\pi \quad (29)$$

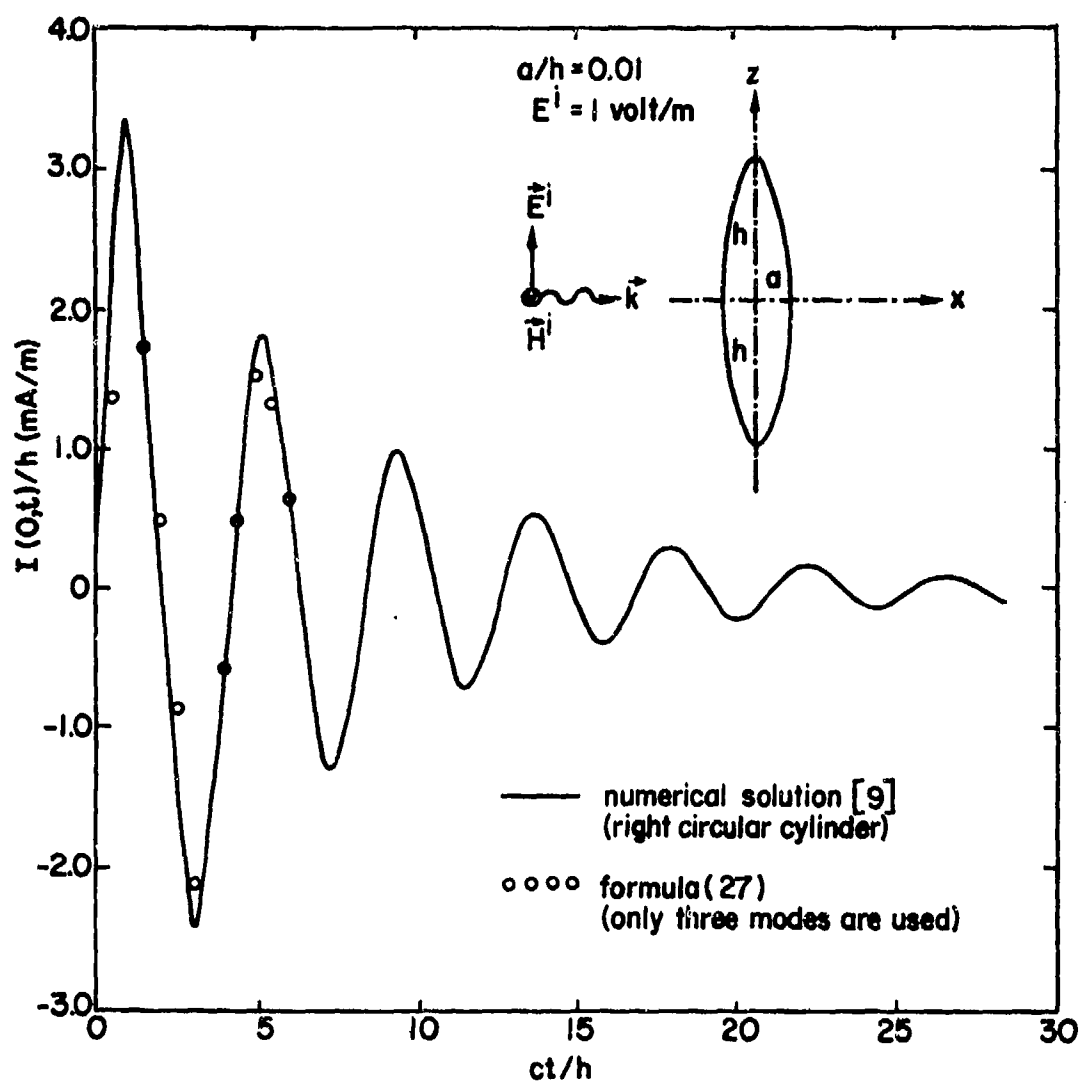


Fig. 3. Total axial current at $z=0$ induced by a unit-step pulse.

where P is the perimeter of the cross section of the object. Note that this procedure for estimating the current is valid only when

$$L \gg a_{eq} \quad (30)$$

where L is the total axial length of the object.

Second, the axial current is obtained by using [10]

$$I(z,t) = \frac{LH^1}{\ln(L/4a_{eq})} f_I(z/L, ct/L) \quad (31)$$

where $I(z,t)$ is the current through the cross section at z at time t and H^1 is the amplitude of the incident magnetic field. The function f_I is presented in Fig. 4 for $z/L = 0, 1/4$, and broadside incidence.

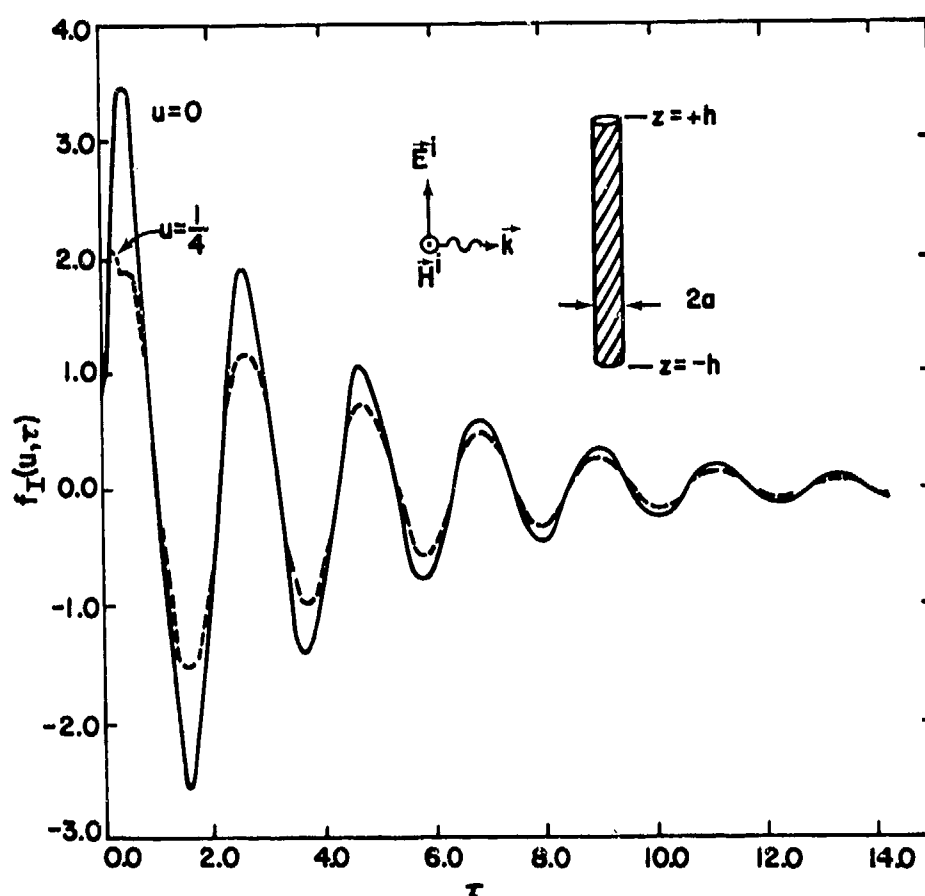


Fig. 4. Normalized axial current for a unit-step incident pulse.
 $u = z/L$, $\tau = ct/L$; $L = 2h$.

d. Ground Plane Effects

If the ground is highly conducting, i.e., if $\sigma_g \gg \omega \epsilon_g$, where σ_g and ϵ_g are the ground conductivity and permittivity, then the interaction of the object near the ground can be treated by image theory (Fig. 5). In this case the ground plane can be replaced by the image of the object over the ground. Both the object and its image are then considered to be illuminated by the direct plane wave and the ground-reflected plane wave (the plane wave from the image source). For a poorly conducting ground, however, a much more complicated analysis is required (see, for example, [11]).

Two specific orientations are of primary interest, $\theta_o = 0$ (horizontal wires) and $\theta_o = \pi/2$ (vertical wires). For the vertical configuration the interaction between the wire and its image can be neglected if $h - L/2 \gg a$, where the wire length is L , the wire radius is a and the height above ground of the center of the wire is h . In this case the current and charge induced on the vertical wire can be obtained as described above except that now there are two plane waves incident on the wire (direct- and ground- reflected).

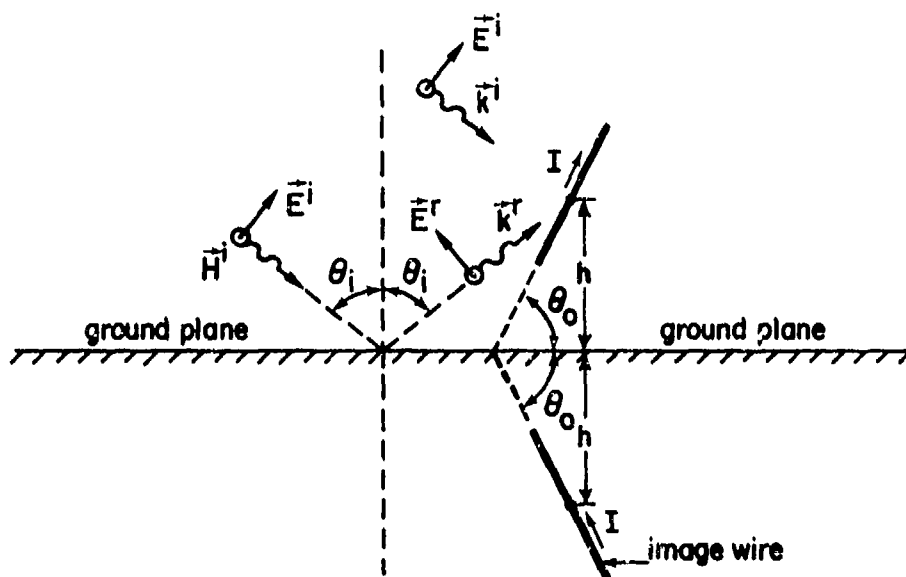


Fig. 5. Arbitrarily oriented wire close to a ground plane with image wire shown.

In the case where the vertical wire is in contact with a perfectly conducting ground plane, the wire together with its image should be considered as a single wire of length $4h$. Detailed information on a single wire in free space can be found in [12].

The interaction of a horizontal wire with the ground plane is considerably more significant than that of a vertical wire. When the horizontal wire is close to the ground, it and its image form a two-wire transmission line, which is a very high-Q resonant structure. Results in terms of SEM parameters can be found in [13].

For a horizontal slender spheroid over a perfectly conducting ground immersed in a plane wave shown in Fig. 6, the induced surface current is approximately given by

$$J_{\zeta}(\zeta, \phi, s) \approx \frac{I(\zeta, s)}{2\pi r} g_I(\zeta, \phi) + 2(H_{\phi}^I + H_{\phi}^T) \quad (32)$$

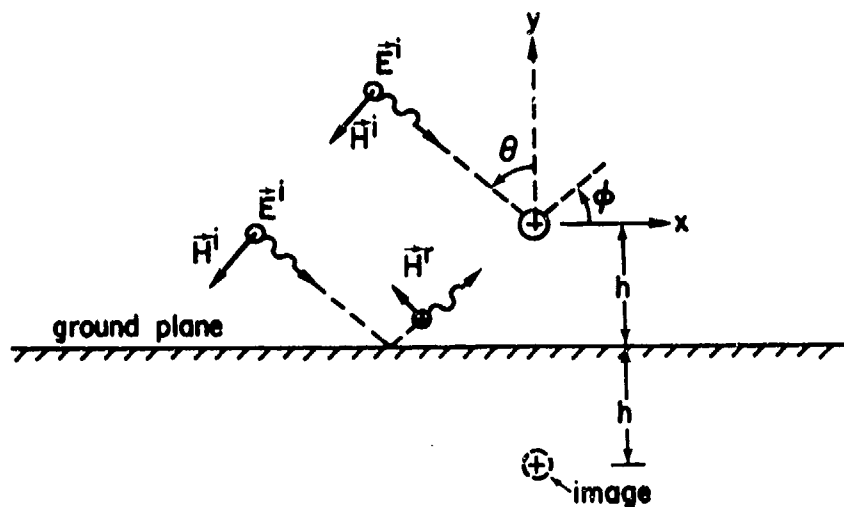


Fig. 6. Cross-sectional view of a horizontal slender prolate spheroid over a ground plane with plane wave illumination. E^i is parallel to the axis of the prolate spheroid.

where (see Fig. 2)

$$g_I = \frac{\sqrt{1 - (r/h)^2}}{1 + r/h \cos \phi} \quad (33)$$

$$r = a\sqrt{1 - \zeta^2} \quad (34)$$

$$I(\zeta, s) = \sum_{\alpha=1}^{\infty} \left[\frac{s}{s_{\alpha}(s - s_{\alpha})} + \frac{s}{s_{\alpha}^*(s - s_{\alpha}^*)} \right] \eta_{\alpha}(s) i_{\alpha}(\zeta) [1 - e^{-\gamma \Delta}] \quad (35)$$

with $\Delta = 2h \tan \theta \sin \theta$, and η_{α} and i_{α} respectively given by (19) and (20). Typical results for the natural frequencies and coupling coefficients for a unit-step incident wave ($E^i = 1$ V/m) are given in table 7.

TABLE 7. NATURAL FREQUENCIES AND COUPLING COEFFICIENTS FOR A HORIZONTAL WIRE (OR SLENDER PROLATE SPHEROID) OF LENGTH L AND RADIUS a ABOVE A GROUND PLANE ($2h/L = 0.4$, $\theta = 0^\circ$, $L/a = 20$)

α	$s_{\alpha} L/c$	$\eta_{\alpha} \times 10^3/c$
1	$-0.08985 + j2.5918$	$4.675 - j0.9449$
2	----	0.0
3	$-0.64293 + j8.0338$	$1.390 + j1.110$
4	----	0.0

2.1.2.1.2 Right Circular Cylinder

The geometry is shown in Fig. 7, where an E-polarized or H-polarized wave is normally incident upon an open-ended tubular cylinder of radius a extending from $z = -h$ to $z = h$. When the electric vector of the incident wave is parallel to the cylinder axis, the wave is said to be E-polarized.

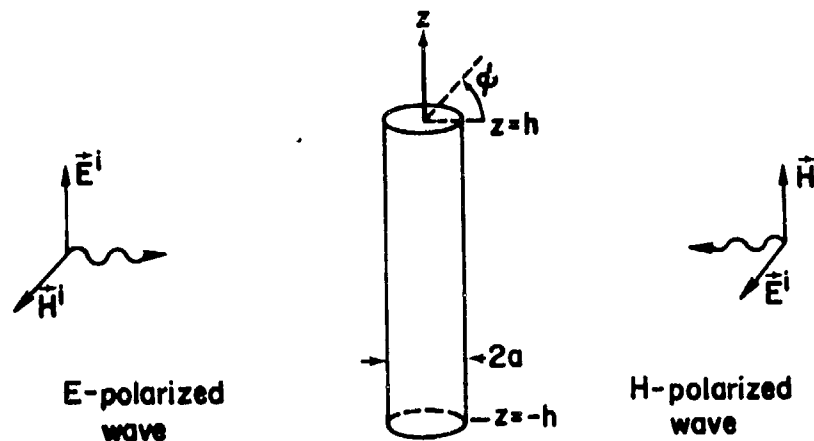


Fig. 7. An E-polarized or H-polarized wave incident on an open-ended cylindrical tube.

When the magnetic vector of the incident wave is parallel to the cylinder axis, the wave is H-polarized. The surface current and charge densities to be presented below are the sums of those on the inner and outer surfaces of the tube. When $ka < 1$, the inside of the tube is well below cutoff for waveguide modes, so that the interior surface current and charge densities are very small except within a distance $d \sim a$ from the open ends.

Experiments indicate that the exterior current density on an open-ended tube differs little from that on a similar tube whose ends are closed by flat conducting disks [14].

The axial and circumferential components of the induced surface current density are of the following form [15], in which k is used instead of γ and the dependence of \vec{J} and ρ on k should be understood.

E-polarized field

$$J_z(\phi, z) = A(kz) + B(kz)\cos \phi + C(kz)\cos 2\phi + D(kz)\cos 3\phi + \dots \quad (36)$$

$$J_\phi(\phi, z) = -j[B'(kz)\sin \phi + C'(kz)\sin 2\phi + D'(kz)\sin 3\phi + \dots] \quad (37)$$

H-polarized field

$$J_{\phi}(\phi, z) = A_H(kz) + B_H(kz)\cos \phi + C_H(kz)\cos 2\phi + D_H(kz)\cos 3\phi + \dots \quad (38)$$

$$J_z(\phi, z) = -j[B'_H(kz)\sin \phi + C'_H(kz)\sin 2\phi + D'_H(kz)\sin 3\phi + \dots] \quad (39)$$

in which the coefficient functions $A(kz), \dots$ also depend upon ka and kh . The infinite series implied by (36) - (39) converge rapidly when $ka \leq 1$. When $ka \approx 1$, the expressions given explicitly above are adequate to represent accurately the surface current density components. When $ka \leq 0.1$, only the terms through $\sin \phi$ and $\cos \phi$ are required.

As $kh \rightarrow \infty$, the coefficient functions $A(kz), \dots$ cease to depend on kz and approach the constant values for an infinitely long cylinder which are given in table 8. In what follows, A, \dots denotes the constant value approached by $A(kz), \dots$ as $kh \rightarrow \infty$.

The induced surface charge density is given for either polarization by

$$\rho(\phi, z) = (j/c) \left(\frac{1}{k} \frac{\partial J_z}{\partial z} + \frac{1}{ka} \frac{\partial J_{\phi}}{\partial \phi} \right) \quad (40)$$

a. Cylinder of Finite Length ($kh \geq 1$)

E-polarization

Convenient approximate expressions for the coefficient functions $A(kz), \dots$ in (36) are as follows

$$A(kz) \approx (A + A_1 \cos kh)e(kz) + A_1(\cos kz - \cos kh) \quad (41)$$

$$B(kz) \approx (B + B_1 \cos kh)e(kz) + B_1(\cos kz - \cos kh) \quad (42)$$

$$C(kz) \approx C_1 e(kz) \quad (43)$$

$$D(kz) \approx D_R e(kz) \quad (44)$$

TABLE 8. FOURIER COEFFICIENTS IN mA/V FOR INFINITELY LONG CYLINDER

E-Polarization: $E_z^i = 1 \text{ V/m}$

$$J_z(\phi) = A + B \cos \phi + C \cos 2\phi + D \cos 3\phi + E \cos 4\phi + \dots$$

ka	$A = A_R + jA_I$	$B = B_R + jB_I$	$C = C_R + jC_I$	$D = D_R + jD_I$	$E = E_R + jE_I$
0.01	16.83 - j50.59	-5.30 - j0.00	0.00 + j0.03	0.00 - j0.00	0.00 - j0.00
0.05	6.86 - j13.60	-5.28 - j0.01	0.00 + j0.13	0.00 - j0.00	0.00 - j0.00
0.10	5.03 - j7.74	-5.23 - j0.04	0.00 + j0.26	0.01 - j0.00	0.00 - j0.00
0.50	2.94 - j1.39	-4.47 - j0.74	-0.01 + j1.24	0.16 - j0.00	0.00 - j0.01
1.00	2.18 - j0.25	-3.28 - j1.85	-0.14 + j2.04	0.58 - j0.00	0.00 - j0.10

H-Polarization: $H_z^i = 2.65 \text{ mA/m}$

$$J_\phi(\phi) = A_H + B_H \cos \phi + C_H \cos 2\phi + D_H \cos 3\phi + E_H \cos 4\phi + \dots$$

ka	$A_H = A_{HR} + jA_{HI}$	$B_H = B_{HR} + jB_{HI}$	$C_H = C_{HR} + jC_{HI}$	$D_H = D_{HR} + jD_{HI}$	$E_H = E_{HR} + jE_{HI}$
0.01	-2.65 - j0.00	0.00 + j0.05	0.00 - j0.00	0.00 - j0.00	0.00 - j0.00
0.05	-2.64 - j0.01	0.00 + j0.27	0.00 - j0.00	0.00 - j0.00	0.00 - j0.00
0.10	-2.61 - j0.02	0.00 + j0.54	0.01 - j0.00	0.00 - j0.00	0.00 - j0.00
0.50	-2.23 - j0.37	0.48 + j2.62	0.33 - j0.00	0.00 - j0.03	0.00 - j0.00
1.00	-1.64 - j0.92	1.27 + j3.41	1.33 - j0.11	0.00 - j0.21	-0.03 - j0.00

in which $A_1 = (1/2)[A(0) - A(\pi)]$, $B_1 = (1/2)[B(0) - B(\pi)]$, and

$$e(kz) = \begin{cases} 1, & 0 \leq |z| \leq (h-d) \\ \sin[\pi(h-|z|)/2d], & h-d \leq |z| \leq h \end{cases} \quad (45)$$

d is a characteristic distance which is usually set equal to a . The approximate formulas (41) - (44) are valid when $kh \geq \pi/2$. The constant coefficients A , B , C_1 and D_R are tabulated in table 8, whereas A_1 and B_1 can be found from Figs. 8 and 9.

H-polarization

The component $J_\phi(\phi, z)$ on tubular conductors of finite length differs little from that on an infinitely long cylinder, except near the open ends where it rises sharply. The coefficients given in table 8 are good approximations to the functions $A_H(kz)$, ... for finite-length cylinders for all values of $|kz| \leq k(h-d)$, where d is of the order of a .

b. Electrically Short, Thin Cylinder ($kh < 1$)

E-polarization

When $ka < 0.1$, the axial current density $J_z(\phi, z)$ is accurately approximated by

$$J_z(\phi, z) \approx A(kz) + B_R(kz) \cos \phi \quad (46)$$

The coefficients A and B_R at $z=0$ are shown in Fig. 10 as functions of kh , for $ka=0.01$ and 0.05 . $A(kz)$ and $B_R(kz)$ are shown in Fig. 11 for $ka=0.05$ as functions of z/h with kh as the parameter. When $kh \leq \pi/2$, we have

$$A(kz) \approx A(0) \frac{\cos kz - \cos kh}{1 - \cos kh} \quad (47)$$

$$B_R(kz) \approx B_R e(kz) \quad (48)$$

in which $A(0) = A + A_1$, where A and A_1 have been defined before.

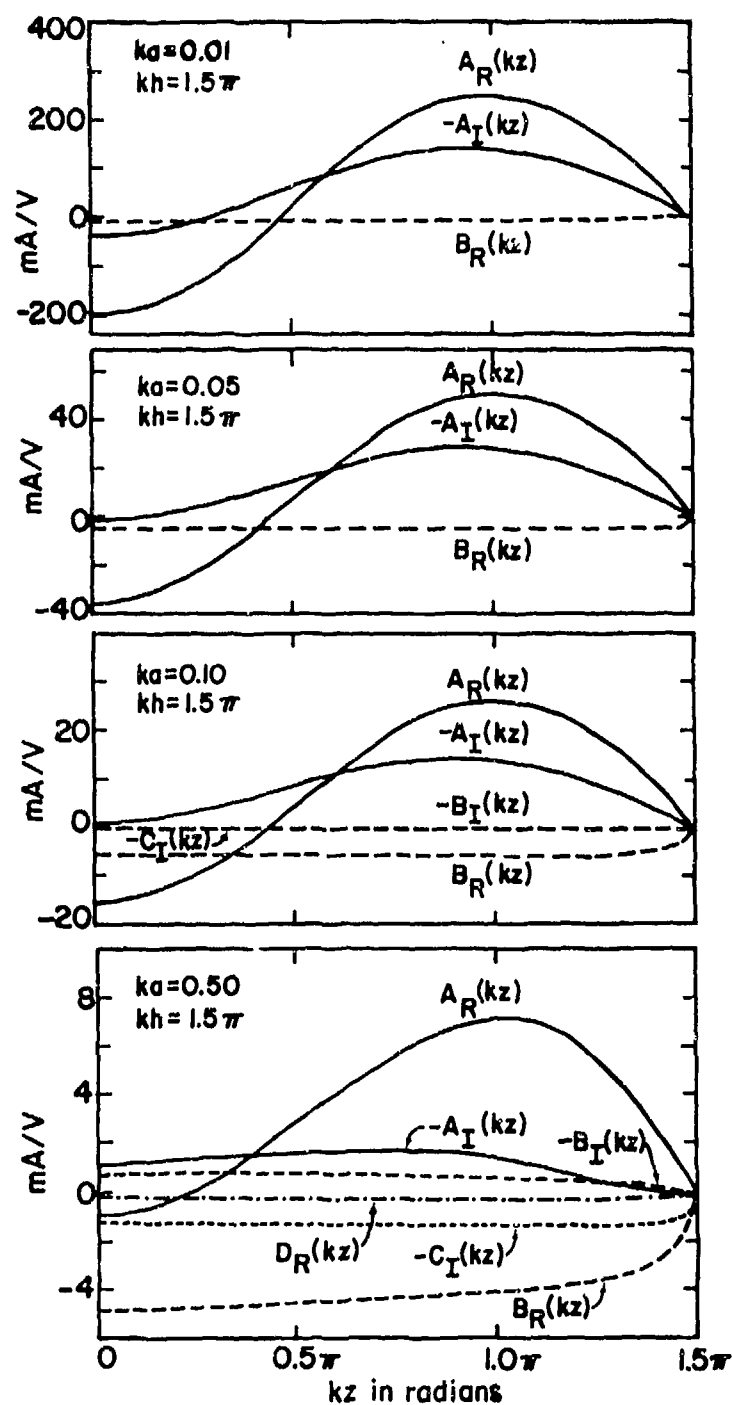


Fig. 8. Complex Fourier coefficients of the axial surface current density $J_z(\phi, z) = A(kz) + B(kz)\cos \phi + C(kz)\cos 2\phi + D(kz)\cos 3\phi$ on a tubular cylinder in an E-polarized field ($E_z^i = 1$ V/m).

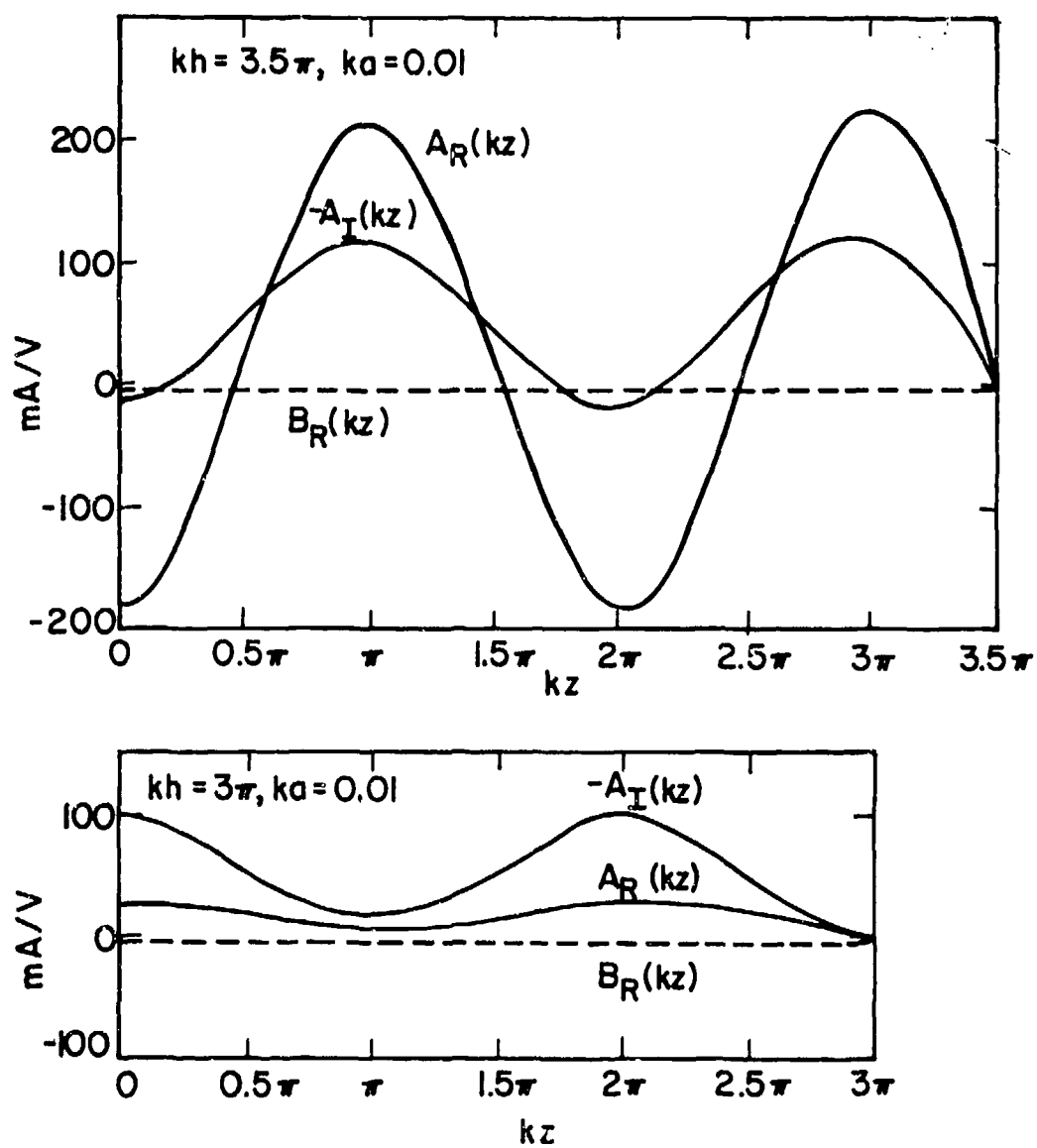


Fig. 9. Complex Fourier coefficients in $J_z(\phi, z) = A(kz) + B(kz)\cos \phi$ for a tubular cylinder in an E-polarized field ($E_z^1 = 1$ V/m).

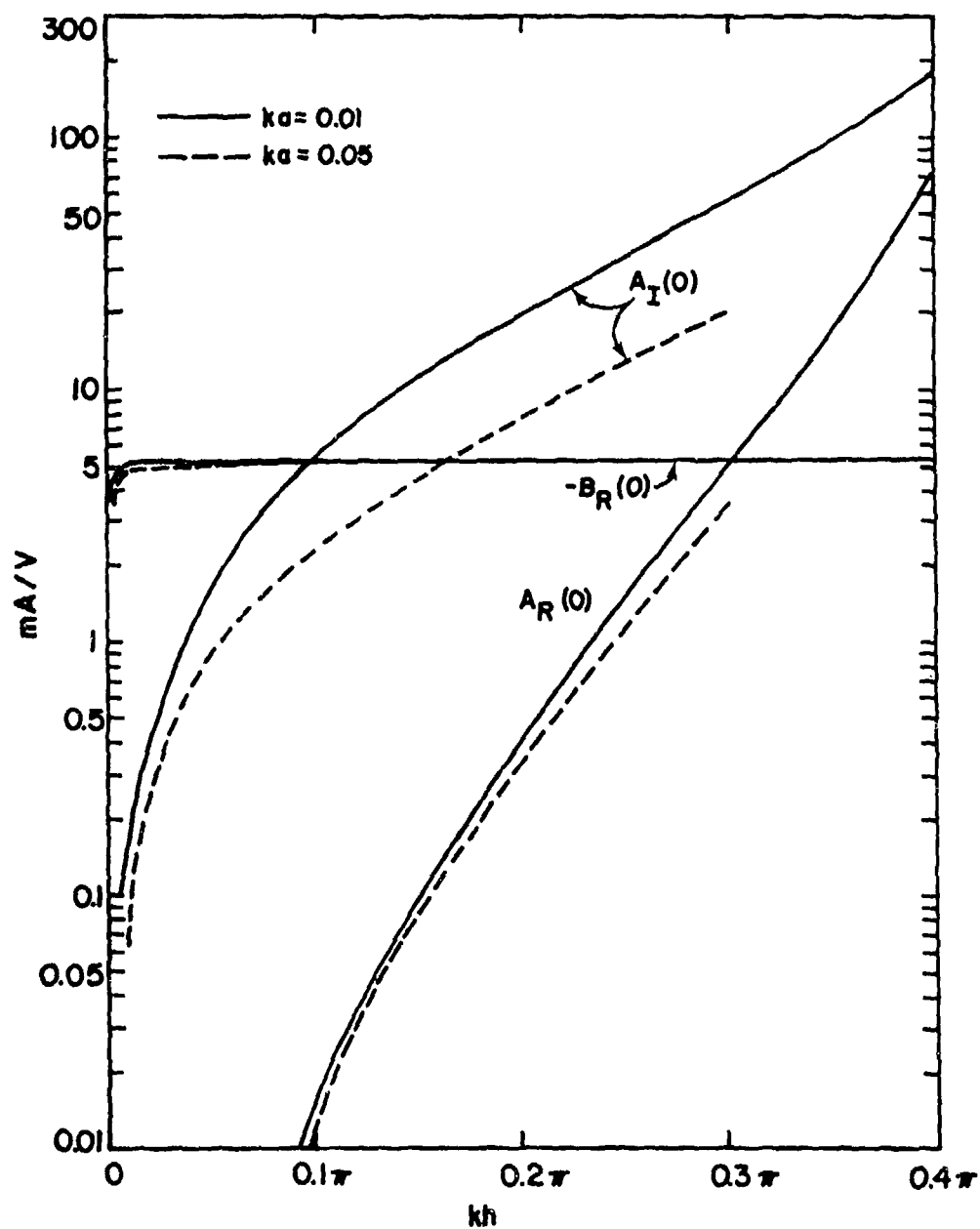


Fig. 10. Complex Fourier coefficients of surface density of axial current $J_z(\phi, 0) \approx A_R(0) + jA_I(0) + B_R(0)\cos\phi$ at $z=0$ on a tubular cylinder in an E-polarized field ($E_z^1 = 1$ V/m).

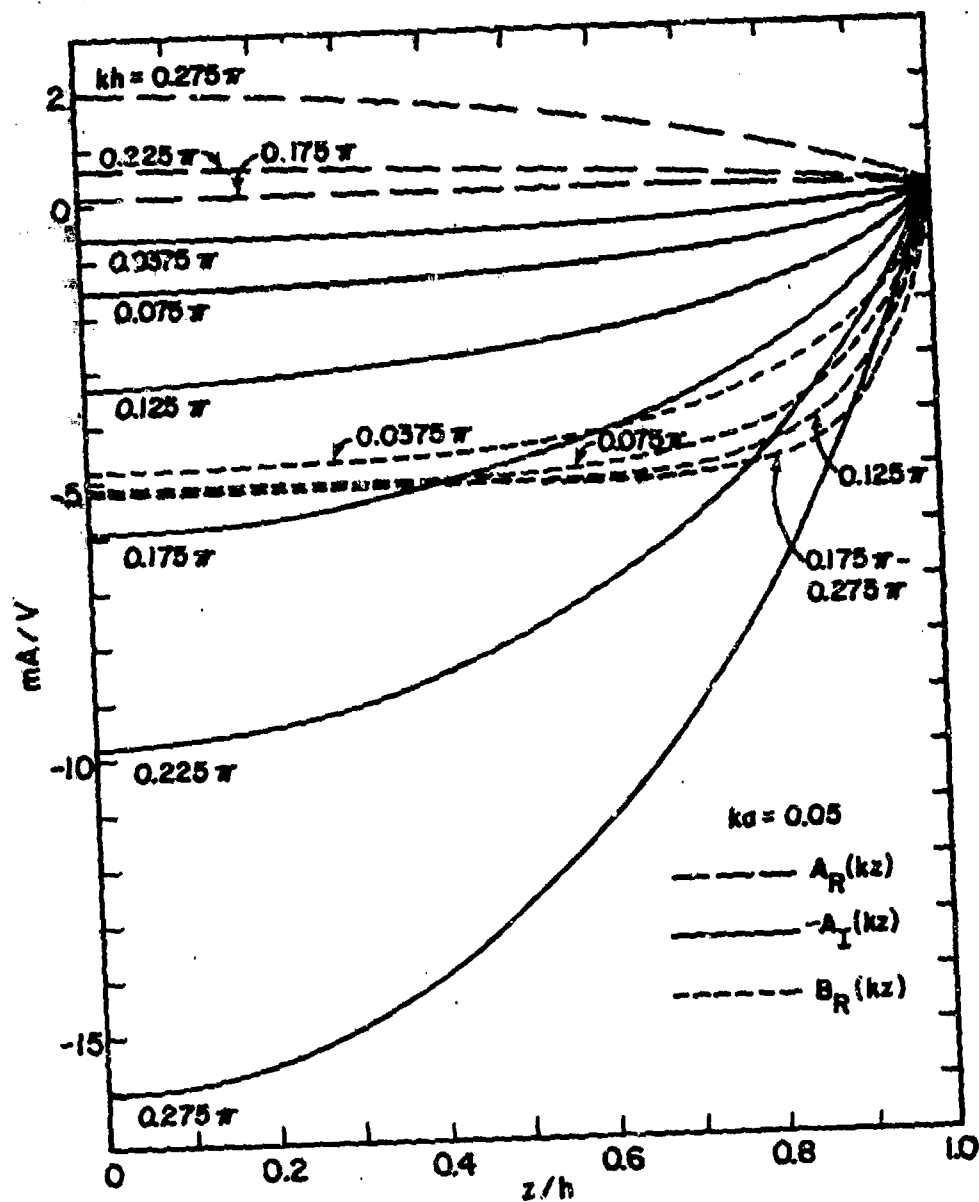


Fig. 11. Complex Fourier coefficients of surface density of axial current $J_z(\phi, z) = A_R(kz) + jA_I(kz) + B_R(kz)\cos\phi$ on a tubular cylinder in an E-polarized field ($E_z^1 = 1$ V/m).

The circumferential surface current density $J_\phi(\phi, z)$ on an electrically thin cylinder is given approximately by

$$J_\phi(\phi, z) \approx -B'_I(kz) \sin \phi \quad (49)$$

The function $B'_I(kz)$ is shown plotted as a function of z/h in Fig. 12 with $ka = 0.05$ and kh as the parameter. $J_\phi(\phi, z)$ is quite small everywhere except near the open ends, where it rises steeply to values comparable to those of the associated axial component, $J_z(\phi, z) \approx B'_R(kz) \cos \phi$. In effect, the axial current density approaches an open end on the illuminated half of the cylinder ($90^\circ < \phi < 270^\circ$), circulates around the cylinder as a transverse current with maxima at $\phi = 90^\circ$ and 270° near the end, and then continues as an oppositely directed axial current on the shadowed side.

H-polarization

When $ka \leq 0.1$, the circumferential surface current density $J_\phi(\phi, z)$ is well approximated by

$$J_\phi(\phi, z) \approx -H_z^I + 2jH_z^I ka \cos \phi \quad (50)$$

except within distances $d \sim a$ from the open ends.

The axial current density $J_z(\phi, z)$ is approximately given by

$$J_z(\phi, z) \approx -jB'_H(kz) \sin \phi \quad (51)$$

When $ka \leq 0.1$, $|B'_H(kz)| \ll |A_H(kz)|$, so that the axial current density is very small on thin cylinders excited by an H-polarized field.

c. Comparison with Measurements

Experimental results reported in [15,16] show excellent agreement with the theoretical results described above. Some typical results are shown in Fig. 13 for a tube with $ka = 0.05$ and $kh = 0.175\pi$. In Fig. 14 are shown the scale-model measurements of the induced current density versus frequency on a right circular cylinder of length 47m and radius 2m [17].

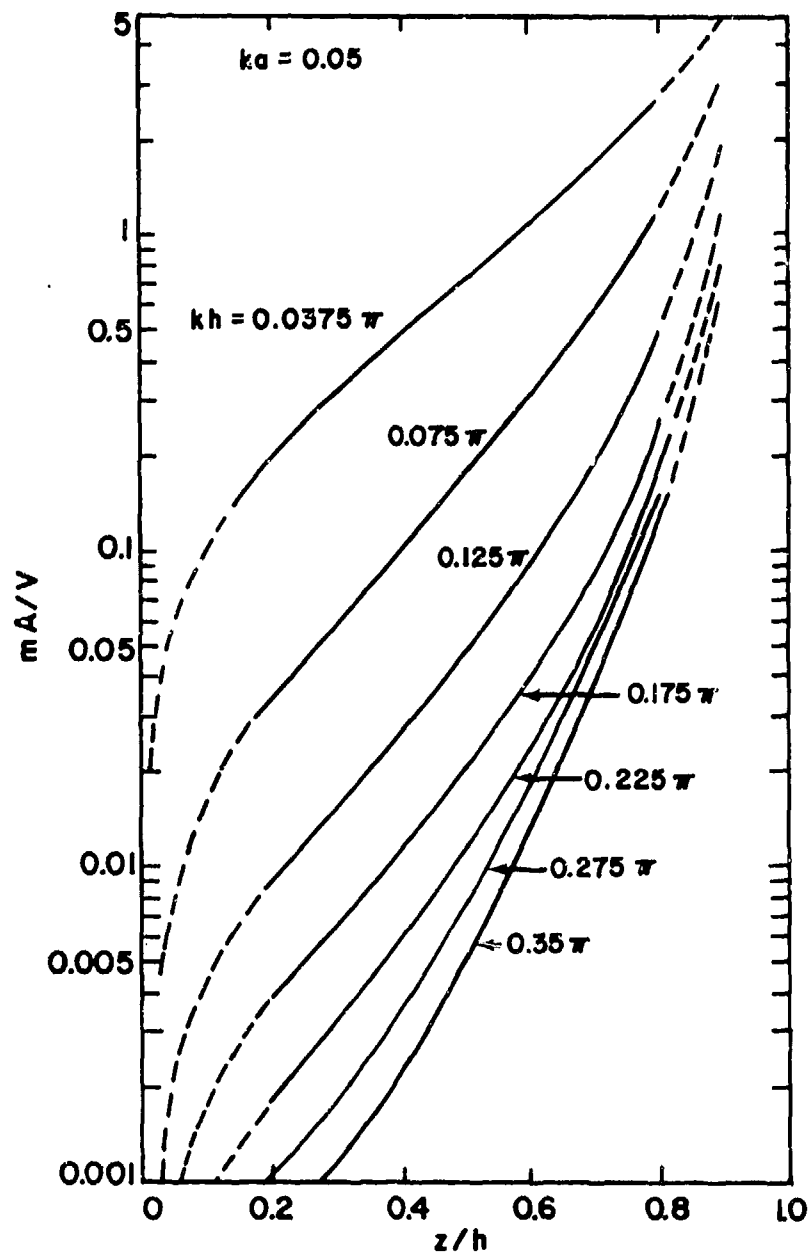


Fig. 12. Fourier coefficient $B_I^1(kz)$ of surface density of transverse current $J_\phi(\phi, z) \approx -B_I^1(kz)\sin\phi$ on a tubular cylinder in an E-polarized field ($E_z^i = 1$ V/m).

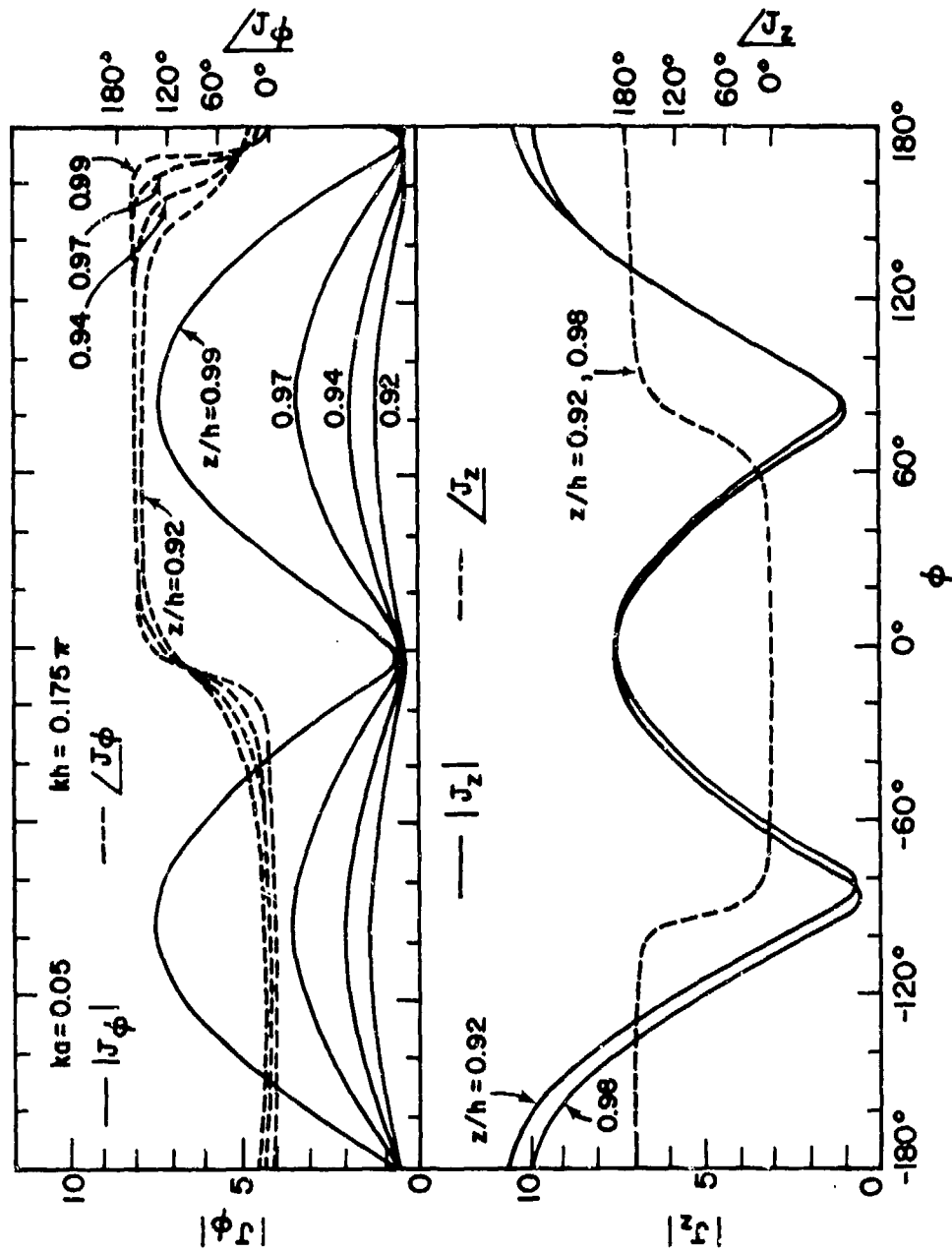


Fig. 13. Measured axial and transverse current densities (in arbitrary units) on a tubular cylinder in an E-polarized field. The illuminated side of the cylinder is the portion of the surface

$|\phi| > 90^\circ$.

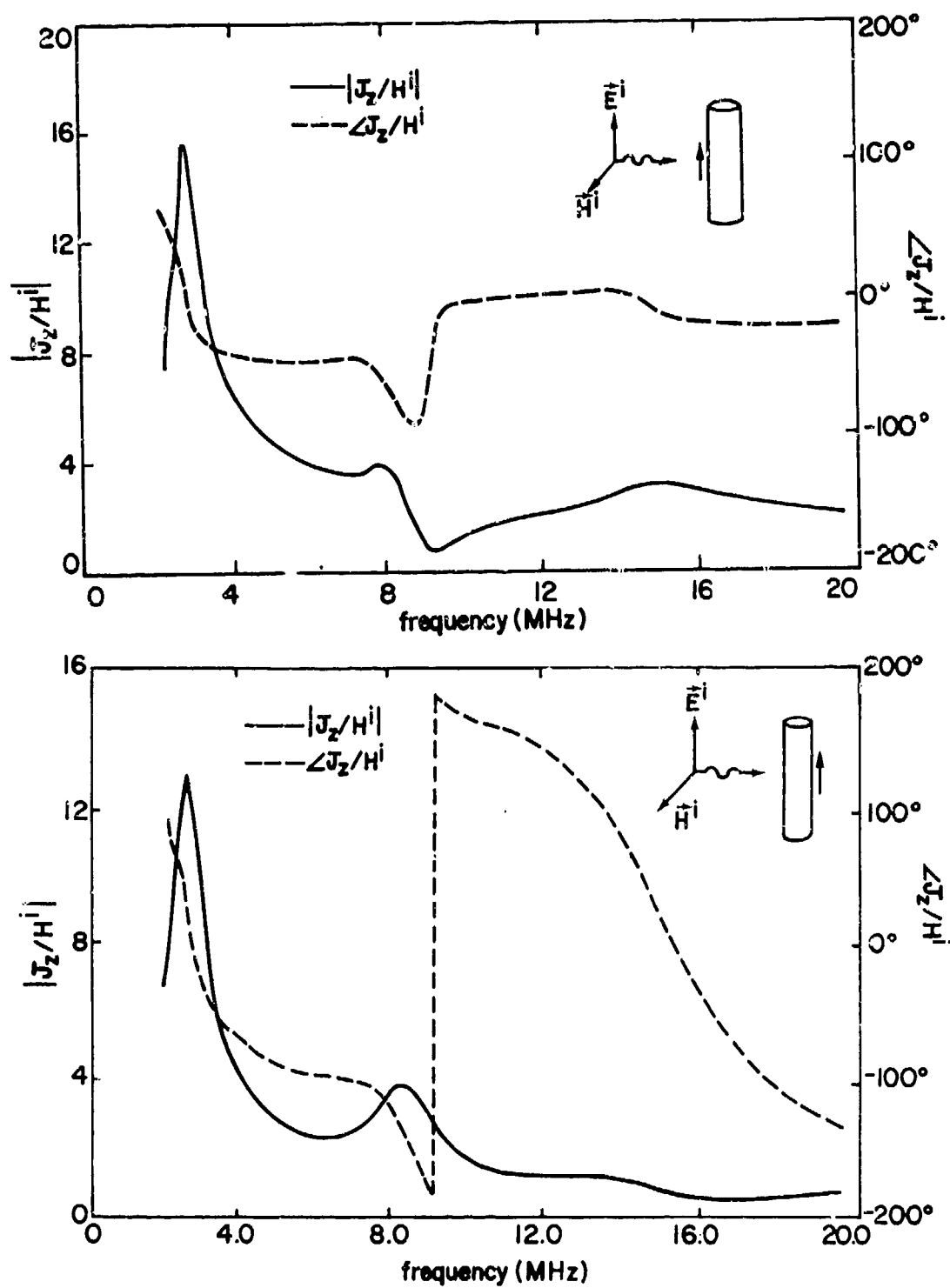


Fig. 14. Measured current density at the center front and rear of a right circular cylinder with length 47m and radius 2m.

2.1.2.1.3 Crossed Slender Spheroids or Cylinders

In the study of EMP interaction with aircraft-like configurations it is found that the interaction among the elements (wings, fuselage, etc.) has a significant effect on the natural frequencies of the entire structure. This effect is clearly seen in the case of two perpendicular crossed slender spheroids or cylinders. Fig. 15 illustrates the intersecting spheroid configuration.

a. Surface Current Density on Crossed Slender Structures

The current density induced on the surface of an intersecting slender spheroid configuration can be expressed efficiently and simply in the SEM formulation. For a given element or arm the surface current density may be approximated by [18]

$$\vec{J}(z, \phi, s) = \left[\frac{I(z, s)}{2\pi r(z)} + 2H_z^1 \right] \vec{I}_z + H_z^1 (1 - \gamma a \cos \phi) \vec{I}_\phi \quad (52)$$

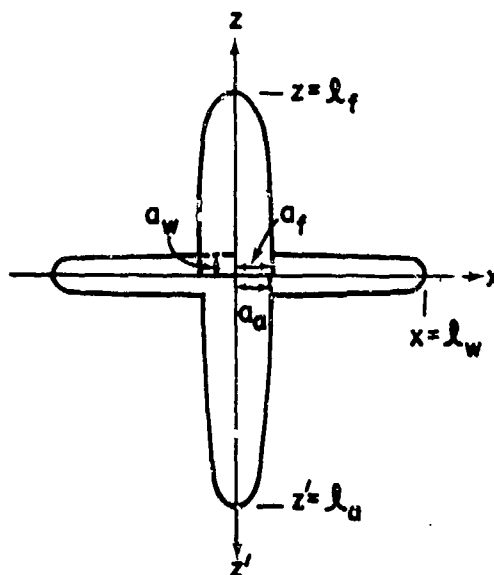


Fig. 15. Parameters of intersecting spheroids.

where $I(z, s)$ is the total axial current and, as before, $r(z) = a\sqrt{1 - (z/h)^2}$ (see Fig. 2).

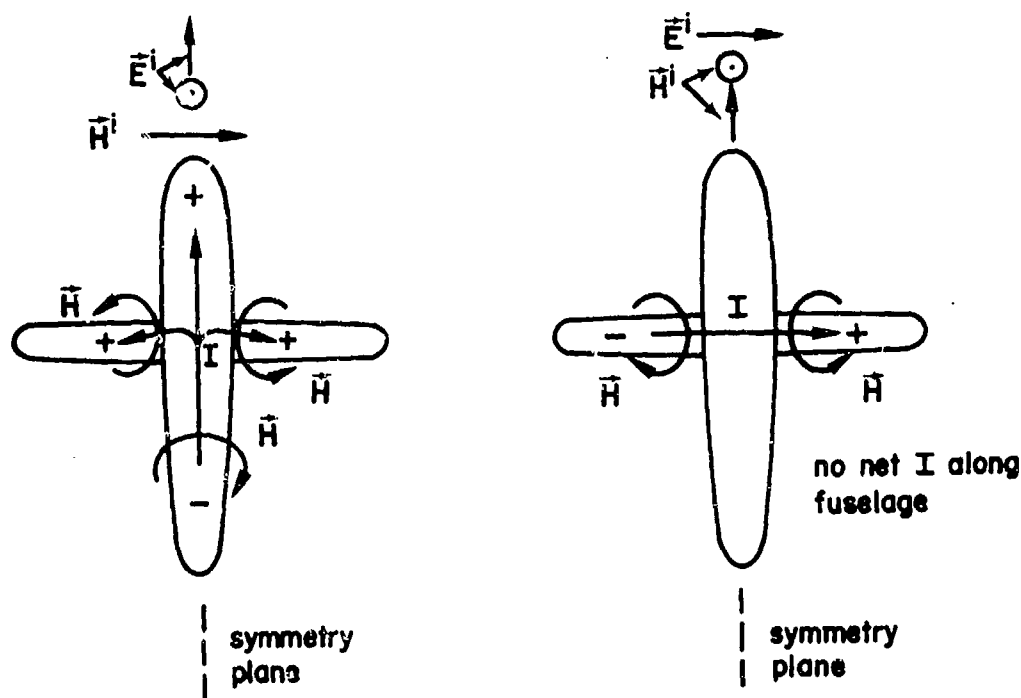
In order to express the axial current on the structure it is convenient to use 1×3 matrices for the currents and the current modes, namely

$$\begin{bmatrix} I_f(z, s) \\ I_a(z', s) \\ I_w(x, s) \end{bmatrix} = \sum_{\alpha=1}^{\infty} \left[\left(\frac{s}{s_{\alpha}(s - s_{\alpha})} + \frac{s}{s_{\alpha}^*(s - s_{\alpha}^*)} \right) \right] \eta_{\alpha}(s) \begin{bmatrix} i_{\alpha}^f(z) \\ i_{\alpha}^a(z') \\ i_{\alpha}^w(x) \end{bmatrix} \quad (53)$$

Here z , z' and x are element coordinates defined in Fig. 15, η_{α} is the coupling coefficient defined by (19), and the elements of the current mode matrix are

$$\begin{aligned} i_{\alpha}^f(z) &= C_{\alpha}^f \frac{\sin k_{\alpha}(\ell_f - z)}{\sin k_{\alpha} \ell_f} \\ i_{\alpha}^a(z') &= C_{\alpha}^a \frac{\sin k_{\alpha}(\ell_a - z')}{\sin k_{\alpha} \ell_a} \\ i_{\alpha}^w(x) &= C_{\alpha}^w \frac{\sin k_{\alpha}(\ell_w - x)}{\sin k_{\alpha} \ell_w} \end{aligned} \quad (54)$$

where $k_{\alpha} = \text{Re}(-j\gamma_{\alpha})$ and C_{α}^f , etc. are current mode amplitudes. It may be noted that only one ℓ_w element current is considered, since the currents on the ℓ_w elements can be separated into symmetric and antisymmetric parts with respect to the ℓ_a and ℓ_f elements (Fig. 16). The antisymmetric part does not couple to the ℓ_a and ℓ_f elements and can therefore be obtained from the analysis of an isolated spheroid. For the symmetric part (ℓ_w element currents being antiparallel), however, coupling does occur and the foregoing expressions apply specifically. For a more detailed discussion of the component separation see [19].



(a) symmetric part: top view

(b) antisymmetric part: top view

Fig. 16. Decomposition of current into symmetric and antisymmetric parts.

Values for the natural frequencies, coupling coefficients and current mode amplitudes are given in tables 9 and 10 for aircraft-like parameters and topside incidence in which \vec{E}^i is parallel to the ℓ_a and ℓ_f elements and \vec{k} is perpendicular to the plane of Fig. 15. An extensive study of the SEM parameters as a function of the system configuration can be found in [19].

The accuracy of (53) should be within 10 to 20%, while (52) should be much more accurate, with less than 10% error.

TABLE 9. NATURAL FREQUENCIES, CURRENT MODES AND COUPLING COEFFICIENTS FOR PERPENDICULAR CROSSED WIRES
IN FREE SPACE WITH TOPSIDE INCIDENCE ($\vec{E}^1 || \ell_a$ and ℓ_f ELEMENTS,
 $L = 2\ell_w = \ell_a + \ell_f$, $L/a = 20$, $\ell_a = \ell_f$)

α	$s_\alpha L/c$	$\eta_\alpha \times 10^3 / [c E^1(s_\alpha)]$	C_α^a	C_α^f	C_α^w
1	-0.4203 + j2.508	-4.464 - j2.068	1.00 + j0.00	-0.505 - j0.120	-0.246 + j0.0599
2	-0.1140 + j3.257	0.0	-0.942 + j0.181	+0.942 + j0.0181	-0.942 - j0.0181
3	-0.9173 + j6.709	0.0	-0.442 + j0.0538	-0.442 + j0.0538	+0.442 - j0.0538
4	-0.9528 + j8.294	-2.167 - j1.750	1.00 + j0.00	-0.227 - j0.0928	-0.387 + j0.0464
5	-2.699 + j12.49	0.0	-0.754 - j0.204	-0.754 - j0.204	+0.754 + j0.204

TABLE 10. NATURAL FREQUENCIES, CURRENT MODES AND COUPLING COEFFICIENTS FOR PERPENDICULAR CROSSED WIRES
IN FREE SPACE WITH TOPSIDE INCIDENCE ($\vec{E}^1 || \ell_a$ and ℓ_f ELEMENTS,
 $L = 2\ell_w = \ell_a + \ell_f$, $L/a = 20$, $\ell_f = \ell_a/2$)

α	$s_\alpha L/c$	$\eta_\alpha \times 10^3 / [c E^1(s_\alpha)]$	C_α^a	C_α^f	C_α^w
1	-0.2935 + j2.292	-4.556 - j1.763	1.00 + j0.00	-0.309 + j0.0712	-0.346 - j0.0356
2	-0.3356 + j3.839	+1.921 + j2.238	0.0439 + j0.156	0.972 + j0.00648	-0.464 + j0.0749
3	-0.6608 + j6.066	-0.9255 + j0.8373	-0.504 - j0.0154	+0.595 - j0.0378	-0.0453 + j0.0266
4	-1.006 + j8.156	+1.515 + j0.9595	0.921 + j0.0530	+0.652 + j0.0443	-0.786 - j0.0486
5	-1.867 + j14.01	+1.580 + j2.858			

b. Surface Charge Density on Crossed Slender Structures

From (53) one obtains, via the continuity equation, the charge densities

$$\begin{bmatrix} \rho_f(z, s) \\ \rho_a(z', s) \\ \rho_w(x, s) \end{bmatrix} = \sum_{\alpha=1}^{\infty} \left[\left(\frac{1}{s_{\alpha}(s - s_{\alpha})} + \frac{1}{s_{\alpha}^*(s - s_{\alpha}^*)} \right) \right] \eta_{\alpha}(s) \begin{bmatrix} \rho_{\alpha}^f(z) \\ \rho_{\alpha}^a(z') \\ \rho_{\alpha}^w(x) \end{bmatrix} \quad (55)$$

with the ρ_{α} given by

$$\begin{aligned} \rho_{\alpha}^f(z) &= - \frac{k_{\alpha}}{2\pi a_f} \frac{\cos[k_{\alpha} \ell_f (1 - z/\ell_f)]}{\sqrt{1 - e_f^2 (z/\ell_f)^2}} \frac{C_{\alpha}^f}{\sin k_{\alpha} \ell_f} \\ \rho_{\alpha}^a(z') &= - \frac{k_{\alpha}}{2\pi a_a} \frac{\cos[k_{\alpha} \ell_a (1 - z'/\ell_a)]}{\sqrt{1 - e_a^2 (z'/\ell_a)^2}} \frac{C_{\alpha}^a}{\sin k_{\alpha} \ell_a} \\ \rho_{\alpha}^w(x) &= - \frac{k_{\alpha}}{2\pi a_w} \frac{\cos[k_{\alpha} \ell_w (1 - x/\ell_w)]}{\sqrt{1 - e_w^2 (x/\ell_w)^2}} \frac{C_{\alpha}^w}{\sin k_{\alpha} \ell_w} \end{aligned} \quad (56)$$

where

$$\begin{aligned} e_f &= [1 - (a_f/\ell_f)^2]^{\frac{1}{2}}, & e_a &= [1 - (a_a/\ell_a)^2]^{\frac{1}{2}}, \\ e_w &= [1 - (a_w/\ell_w)^2]^{\frac{1}{2}} \end{aligned} \quad (57)$$

It is expected that (55) should be about as accurate as the corresponding current expression (53), i.e., 10-20% error may occur.

c. Intersecting Electrically Thick Cylinders

No analytical or numerical determinations of the surface currents and charges on intersecting electrically thick cylinders are available. However, extensive measurements of these quantities have been performed [20]. The

cases studied include three lengths of the horizontal cylinder and two locations along the vertical tube. Graphs of both the axial and transverse components of current density and of the charge density are available for $ka = 1$. The axial standing-wave patterns on the illuminated ($\phi = 180^\circ$) and shadowed ($\phi = 0^\circ$) sides are clearly shown in Fig. 17 for $k\ell = \pi$, $kh_1 = 2.5\pi$ and for $k\ell = 1.5\pi$, $kh_1 = 2\pi$. For purposes of comparison, the distribution along an isolated vertical cylinder is also shown.

The following general conclusions can be made regarding the surface current and charge densities on intersecting cylinders with $ka \geq 1$:

- (a) The distributions of current and charge densities are much less sensitive to changes in the lengths of the cylinders when they are electrically thick than when electrically thin.
- (b) The distribution of the charge density on an electrically thick cylinder is more sensitive to the nature of the incident field and the presence, dimensions, and location of an intersecting cylinder than is the distribution of current.
- (c) The charge density on the vertical member when excited by an incident E-polarized field (Fig. 7) has significantly different distributions when the incident field is not plane, when the horizontal member is absent, its location is changed, or when the arm lengths are varied. The current density is much less affected.
- (d) The distribution of the charge density on the horizontal cylinder in an H-polarized field (Fig. 7) is insensitive to the location of its intersection with the vertical member of the cross so long as the arms are equal in length. On the other hand, the amplitude of the axial standing-wave pattern as a function of ϕ is sensitive to the length of the arms.
- (e) As on the single cylinder, the axial current density on the vertical cylinder is substantially a superposition of forced and resonant components. The changes from the distribution along the single tube when an intersecting cylinder is present at different locations and with different arm lengths are due

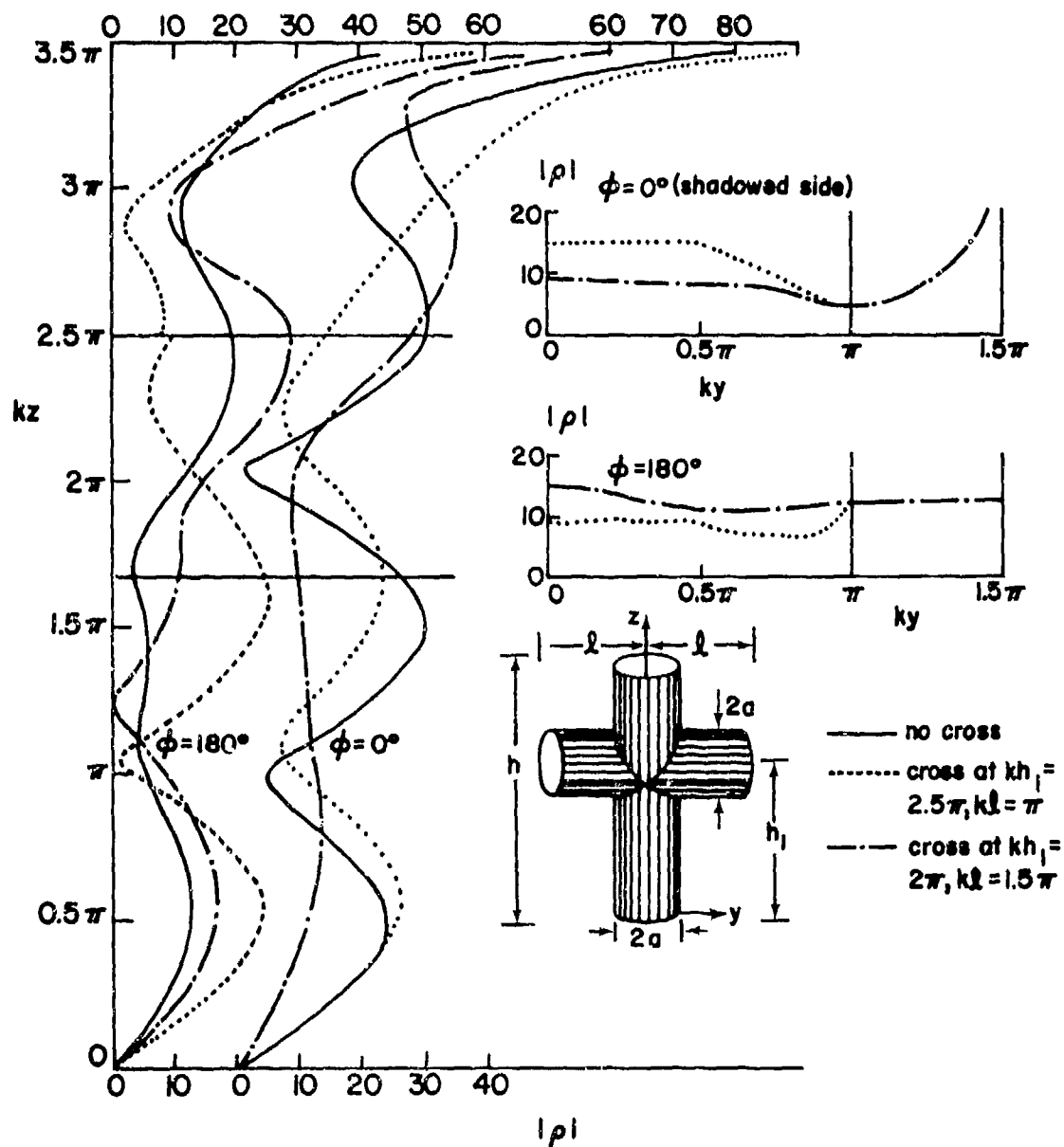


Fig. 17. Measured surface charge density on crossed cylinders with $kh = 3.5\pi$, $ka = 1$ for two locations of the junction and with no cross for normally (topside incidence) incident field, $\vec{E}^i = \vec{E}_z^i$. ($|\rho|$ in arbitrary units).

primarily to shifts in the relative phases of the forced and resonant components.

In general, the distributions of current and charge on the surface of intersecting electrically thick cylinders are quite similar to those on each of the individual cylinders alone in the same field. The relative amplitudes of the standing waves on the illuminated and shadowed sides of the vertical cylinder may differ considerably, but the standing-wave patterns are significantly changed only quite near the junction region. Thus, a knowledge of the distributions of current and charge density on single cylinders is of great value in the understanding and interpretation of these quantities on intersecting cylinders and in the rough approximation of their actual values.

d. Ground Plane Effects

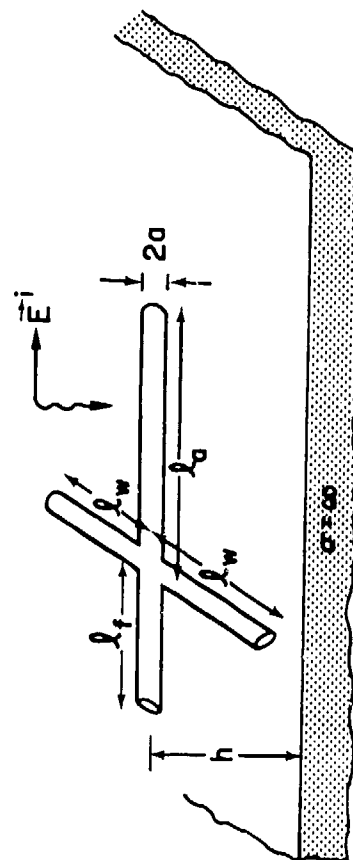
General observations regarding thin crossed cylinders or spheroids close to a ground plane are the same as those for an isolated cylinder or spheroid (see Sec. 2.1.2.1.1d). The surface current density is related to the axial current as given by (32) and the axial current may be expressed as given in (53), but the SEM parameters depend upon the height of the cylinders. For a typical aircraft-like configuration, the SEM parameters for the first 4 modes are given in table 11. A detailed study of the ground plane effects on the SEM parameters may be found in [13].

2.1.2.1.4 Aircraft Models

Complex structures such as aircraft are difficult to model for purposes of analytical and numerical studies. As of now, there exist several types of simplified models, the most notable of which are (a) the simple stick model [21], (b) the body-of-revolution model [22], (c) the surface-patch model [23], and (d) the wire-grid model [24]. Information on the computer codes for these models and other models can be found in [25]. The wire-grid model, although adequate for radar cross-section calculation, has many deficiencies in EMP interaction applications [26]. The surface-patch model, although much more accurate in nature, requires an inordinate amount

TABLE 11. NATURAL FREQUENCIES, CURRENT MODES AND COUPLING COEFFICIENTS FOR PERPENDICULAR CROSSED WIRES PARALLEL TO A PERFECT GROUND PLANE WITH TOPSIDE INCIDENCE AND PARALLEL POLARIZATION ($L = 2\ell_w = \ell_a + \ell_f$, $L/a = 20$, $\ell_a = 2\ell_f$, $h/L = 0.2$)

α	$s_\alpha L/c$	$\eta_\alpha \times 10^3 / [c E^1(s_\alpha)]$	C_α^a	C_α^f	C_α^w
1	$-0.0513 + j2.361$	$-5.072 - j0.4641$	$1.00 + j0.00$	$-0.290 + j0.017$	$-0.355 - j0.0086$
2	$-0.1021 + j3.769$	$2.599 + j0.9949$	$0.0862 - j0.804$	$1.00 + j0.00$	$-0.543 + j0.0402$
3	$-0.3909 + j5.740$	$-0.4523 - j0.3920$	$-0.730 + j0.0167$	$0.510 - j0.0035$	$0.110 - j0.0066$
4	$-0.6691 + j7.581$	$1.165 + j0.5860$	$0.988 - j0.0155$	$0.574 + j0.0435$	$-0.781 - j0.0140$



of computer time for any EMP time-domain data and, as of now, numerical data based on this model are lacking. Therefore, the data presented in this section are restricted to the simple stick model and the body-of-revolution model.

a. Simple Stick Models

"Simple" stick models are very useful for estimating the natural frequencies and natural axial current modes of an aircraft [21]. In a simple stick model, currents of the form

$$I(x) = I_{\text{ind}}(x) + A \sinh \gamma x + B \cosh \gamma x \quad (58)$$

are assumed on each of the elements or sticks (Fig. 18), where x denotes a distance coordinate along a given element and A and B are undetermined coefficients. The quantity I_{ind} denotes the current induced on a wire by an incident plane wave whose magnetic vector is perpendicular to the wire and is given by

$$I_{\text{ind}}(x) = \frac{-4\pi E^1}{\gamma Z_0 \Omega_a \sin \theta} e^{\gamma x \cos \theta} \quad (59)$$

in which $\Omega_a = 2 \ln[(\text{stick length})/(\text{stick radius})]$, $\vec{\gamma}$ is the propagation vector of the incident field, Z_0 is the intrinsic impedance of free space,

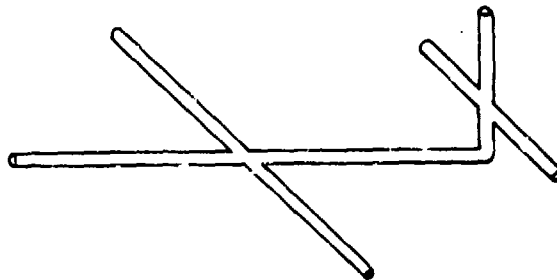


Fig. 18. A "simple" stick model.

E^i is the incident electric field strength, and θ is the angle between the propagation vector of the incident wave and the negative unit vector along the stick.

Enforcing appropriate end and junction conditions on the various stick currents leads to a system of linear equations for the unknown current coefficients A, B, etc. The resulting equations may be readily solved to yield the resonance frequencies and natural modes of the simple stick model. The damping constants of the natural modes are found by calculating the radiated power and the time-averaged stored energy of each of the natural modes (see Sec. 1.3.3.3).

This type of model has been used to calculate the first several natural frequencies and natural modes for the B-1, E-4, and EC-135 aircraft for symmetric excitation. The natural modes for the EC-135 model are shown in Fig. 19. The natural frequencies for all three aircraft are shown in the complex s-plane in Fig. 20.

b. Stick Models and Body-of-Revolution Models

The body-of-revolution model uses axial sections of spheroids and circular cylinders. A stick (intersecting cylinders) model of the B-1 aircraft is shown in Fig. 21a, while a body-of-revolution model of an EC-135 aircraft is given in Fig. 21b.

Integral-equation formulations and numerical techniques are generally required for these models. The numerical solutions based on these models must be augmented by the addition of an appropriate magnetostatic term in order to yield accurate solutions for induced surface current density [23,27]. Figs. 22 - 34 show some of the results obtained with these techniques [18].

In Figs. 22 - 24 are presented curves of the axial surface current density on models of the B-1 aircraft as a function of frequency for three cases: (a) stick model (numerical results), (b) a scale stick model (experimental results), and (c) a body-of-revolution model (numerical results).

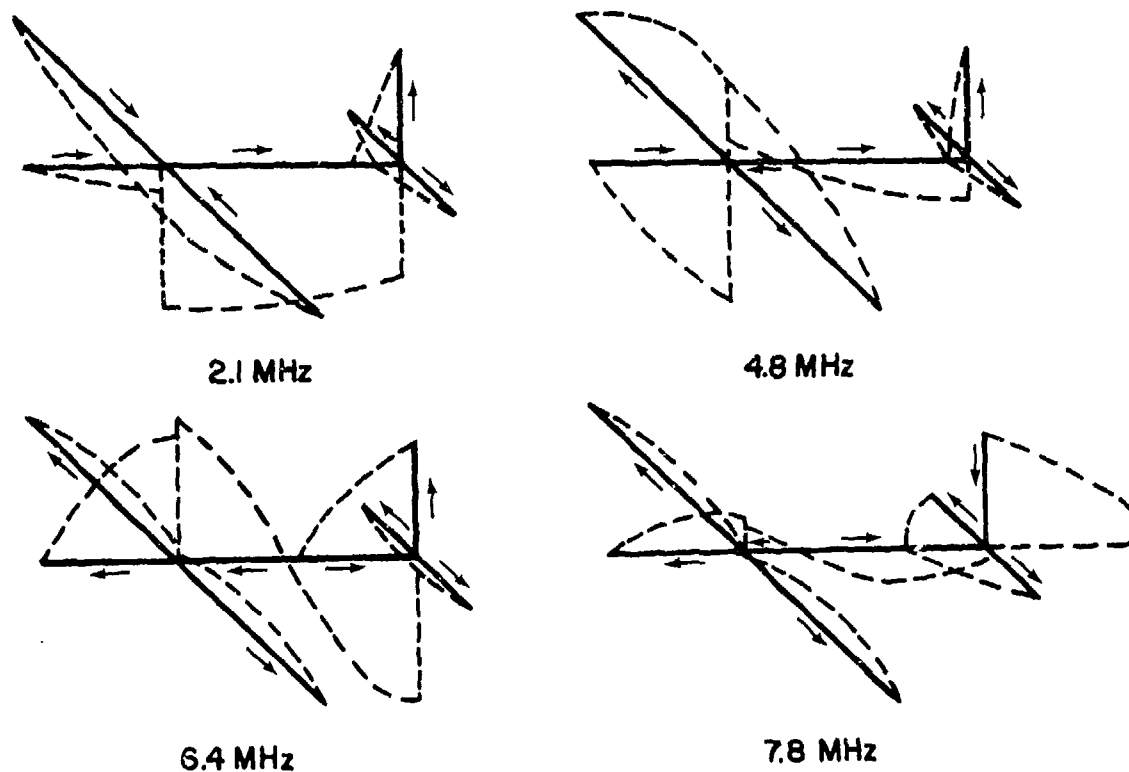


Fig. 19. EC-135 natural modes. The dashed lines represent the current distribution on the aircraft segments at resonance, while the arrows indicate directions of current flow.

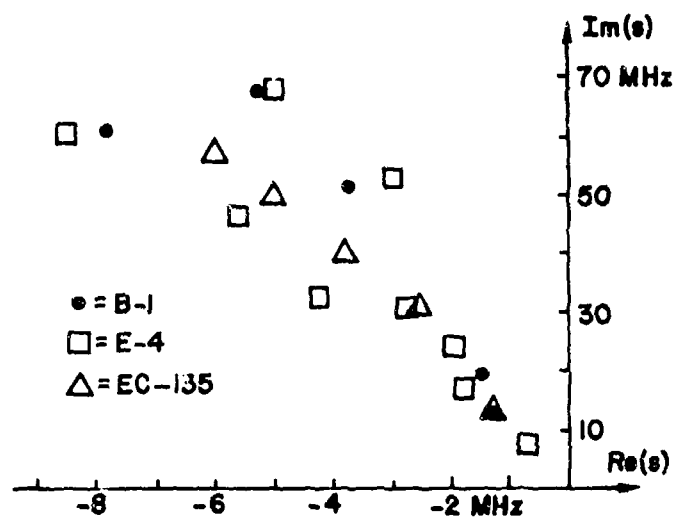


Fig. 20. Aircraft natural frequencies of B-1, E-4 and EC-135.

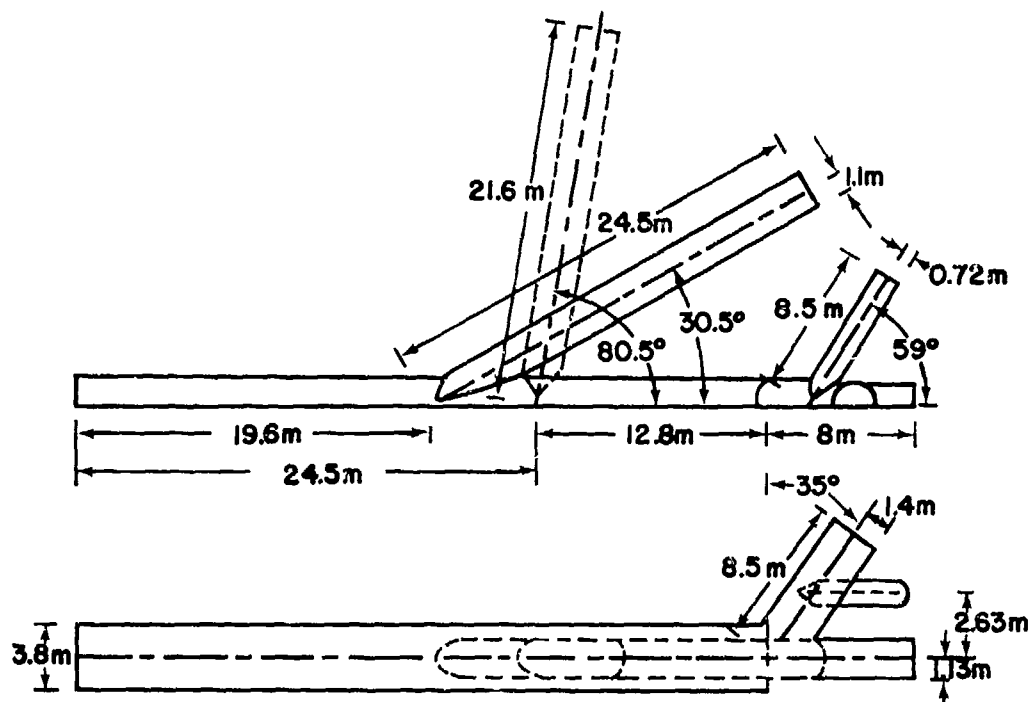


Fig. 21a. Stick (intersecting cylinders) model of the B-1 aircraft in the wings-forward and wings-swept configurations.

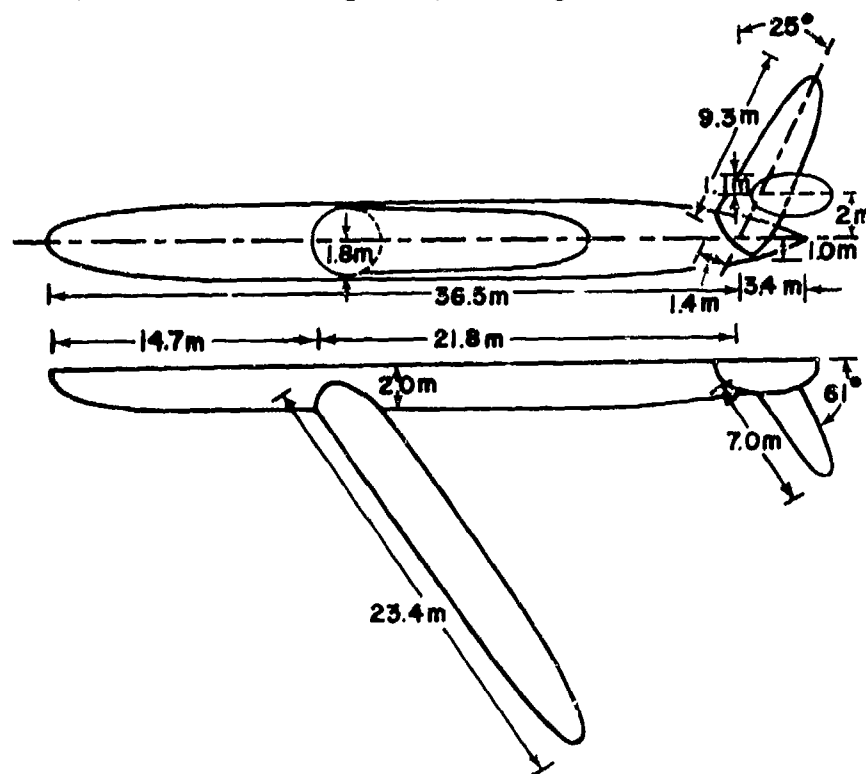


Fig. 21b. Body-of-revolution model of the EC-135 aircraft. Current zones are indicated with dotted lines.

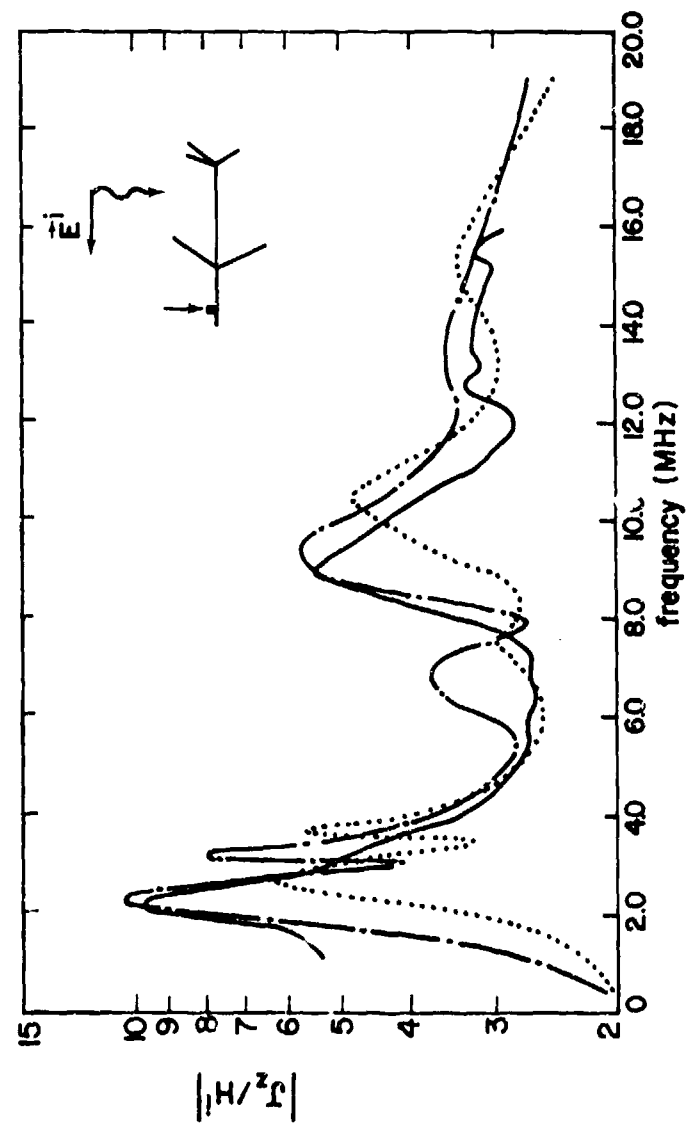


Fig. 22. Current density on the topside of the fuselage 5.0 meters from the nose of the B-1 with wings forward. — scaled stick model experimental data; - - - stick model numerical data; body-of-revolution code.

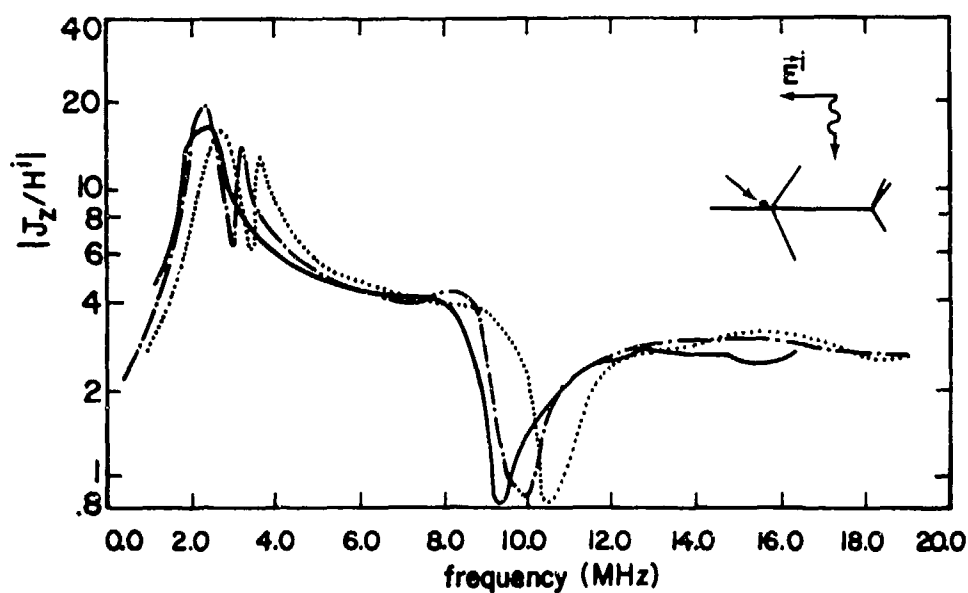


Fig. 23. Current density on the topside of the fuselage 22.5 meters from the nose of the B-1 with wings forward. — scaled stick model experimental data; — · — stick model numerical data; ···· body-of-revolution code.

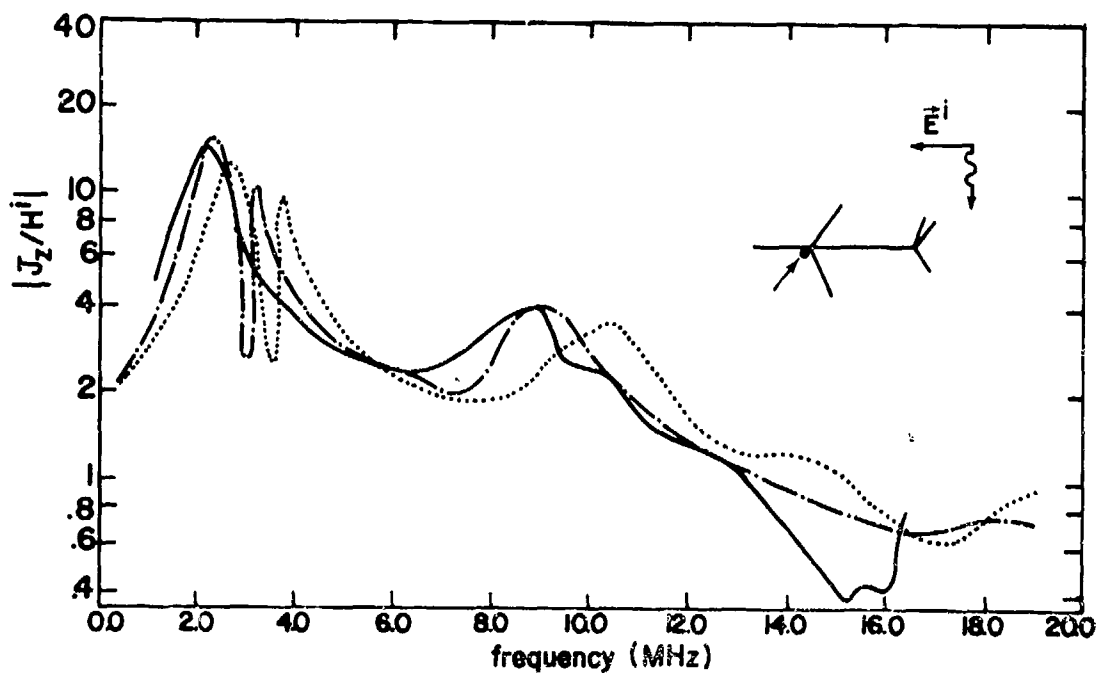


Fig. 24. Current density on the bottom of the fuselage 22.5 meters from the nose of the B-1 with wings forward. — scaled stick model experimental data; — · — stick model numerical data; ···· body-of-revolution code.

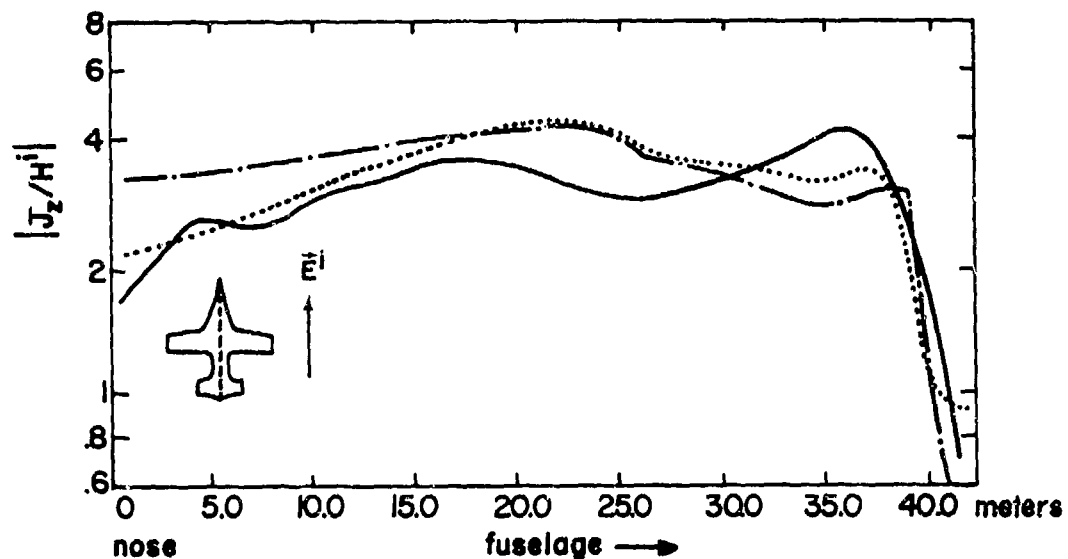


Fig. 25. Comparison of B-1 scale model measurements with numerical results for topside illumination and wings forward at $f = 6.4$ MHz. — experimental data; — · — stick model; · · · · body-of-revolution model.

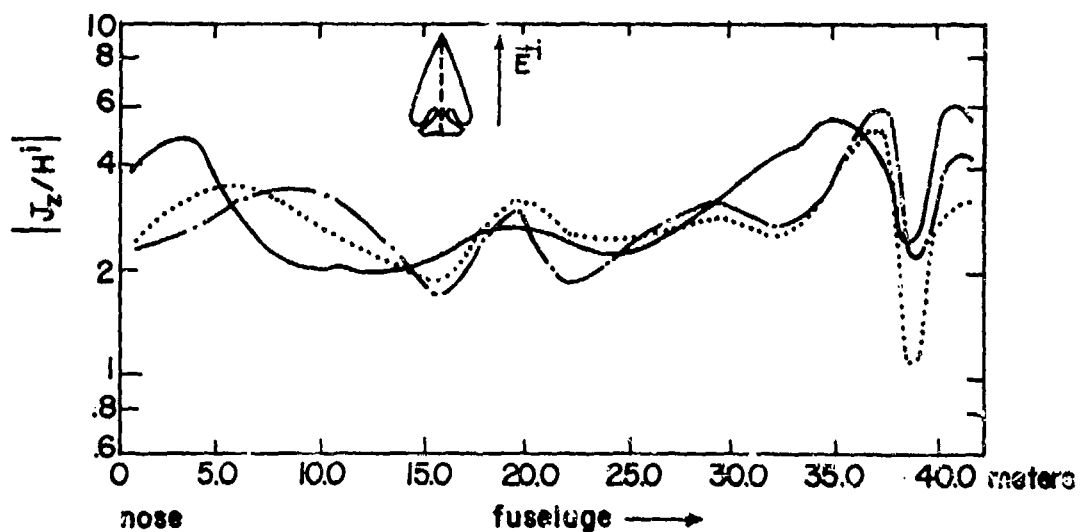


Fig. 26. Comparison of B-1 scale model measurements with numerical results for topside illumination and wings swept at $f = 18.16$ MHz. — experimental data; — · — stick model; · · · · body-of-revolution model.

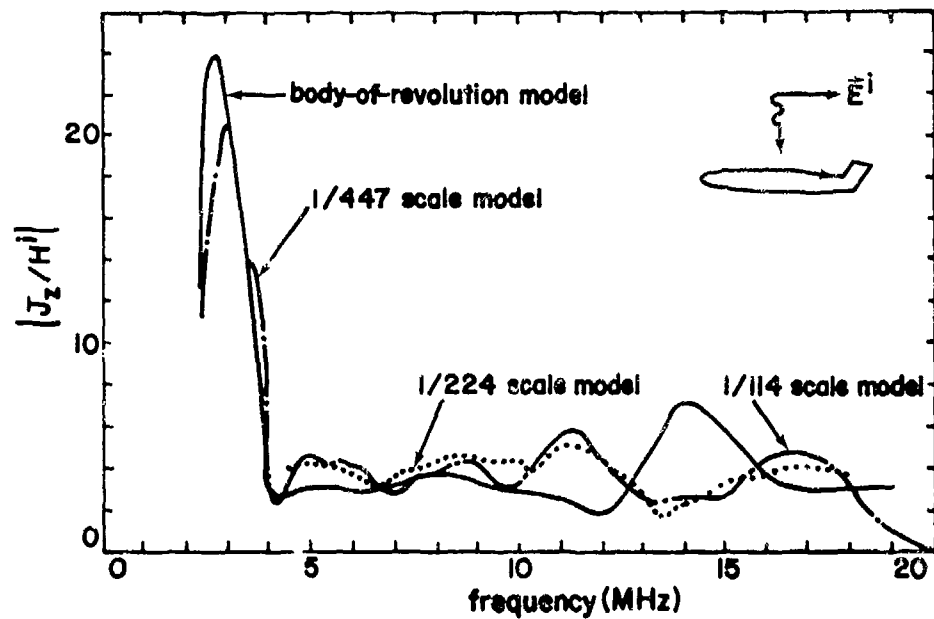


Fig. 27. Current density on the topside of the EC-135 fuselage 22.5 meters from the nose.

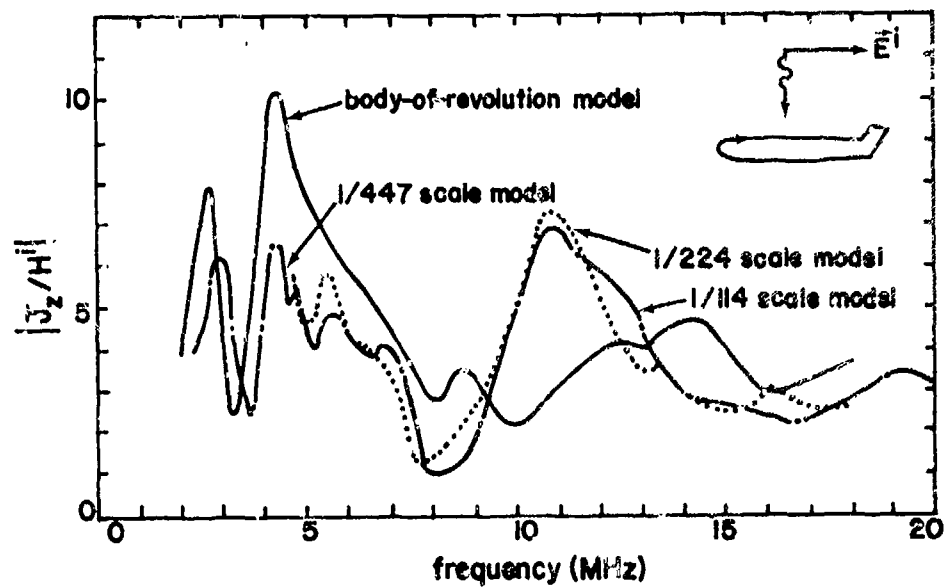


Fig. 28. Current density on the topside of the EC-135 fuselage 5.0 meters from the nose.

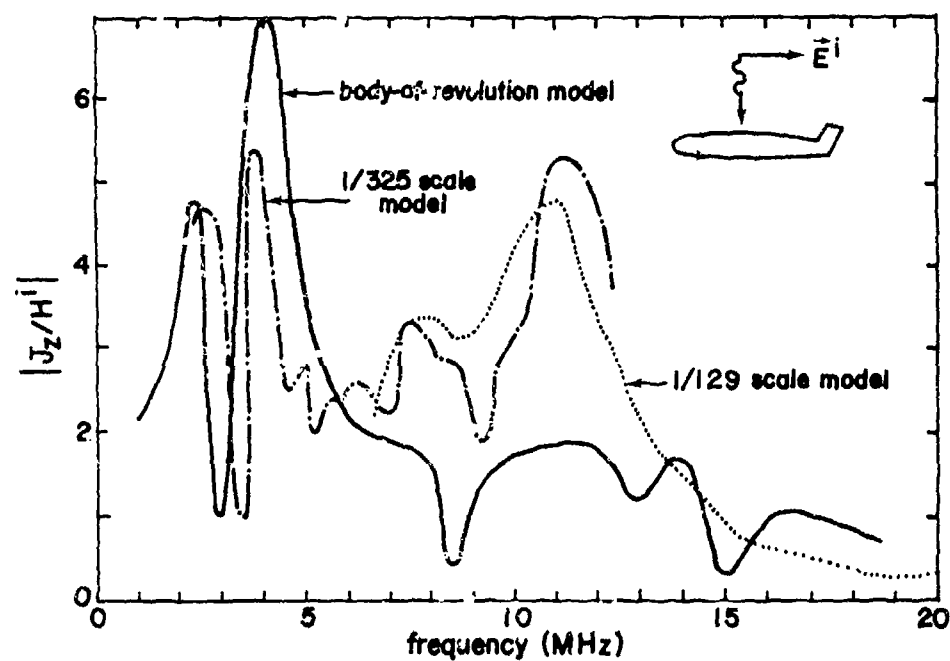


Fig. 29. Current density on the bottom side of the EC-135 fuselage 5.0 meters from the nose.

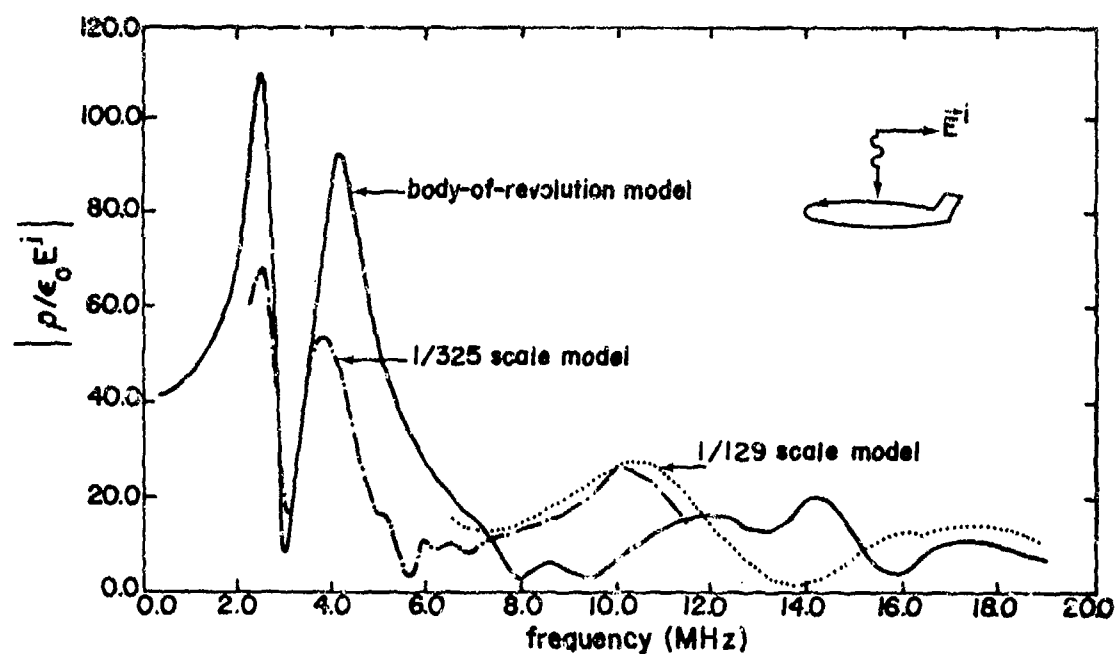


Fig. 30. Charge density on the nose of the EC-135 aircraft.

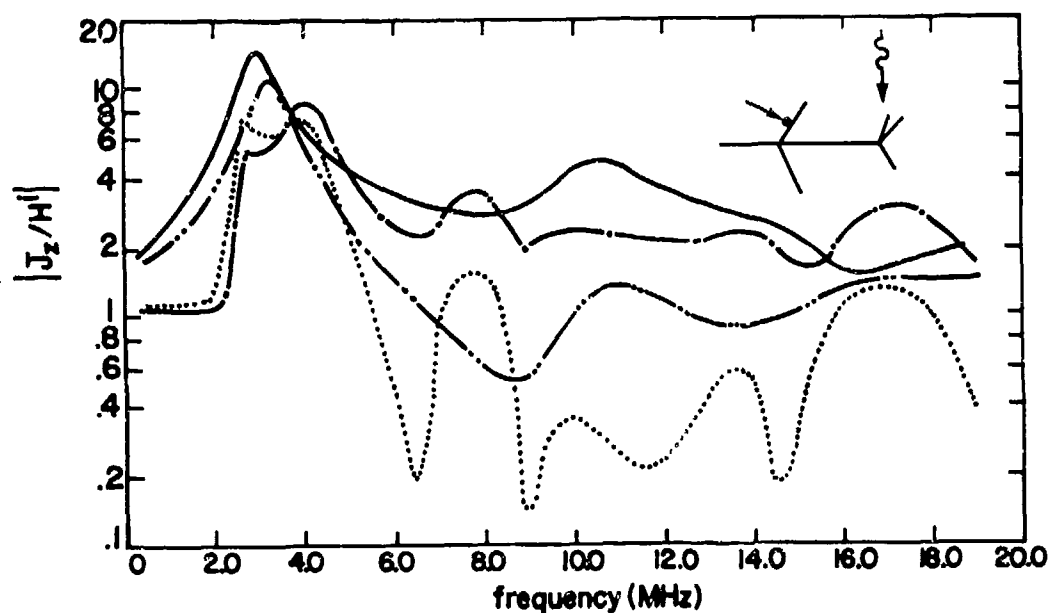


Fig. 31. Current density on the wing of EC-135. —, — at the top of aircraft with topside $\vec{E}^1 \parallel$ fuselage; at the bottom of aircraft with topside $\vec{E}^1 \parallel$ fuselage, — at the top of aircraft with topside $\vec{E}^1 \perp$ fuselage, — · — at the bottom of aircraft with topside $\vec{E}^1 \perp$ fuselage.

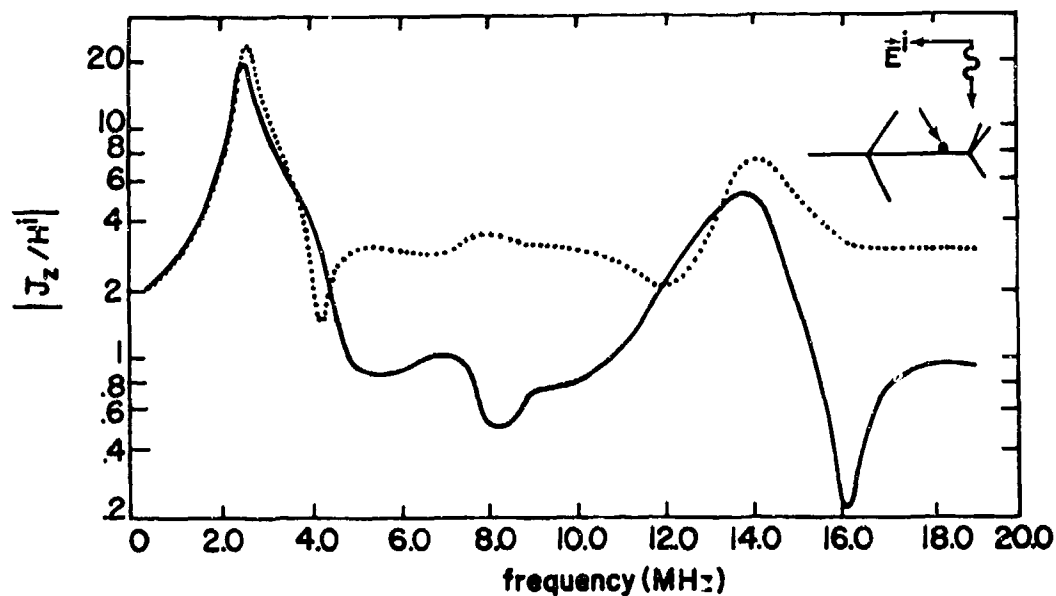


Fig. 32. Current density on the fuselage of EC-135. at the top of aircraft with topside $\vec{E}^1 \parallel$ fuselage; — at the bottom of aircraft with topside $\vec{E}^1 \parallel$ fuselage (stick model numerical data).

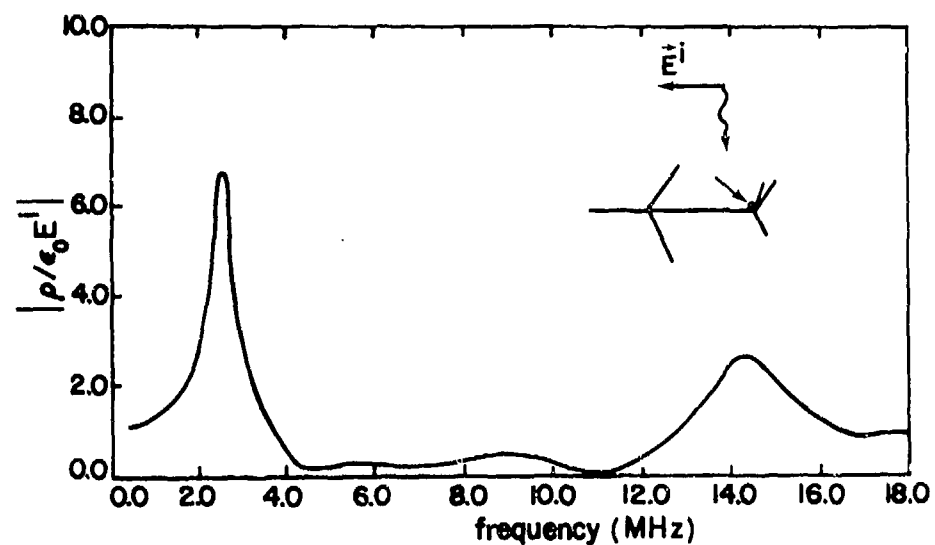


Fig. 33. Charge density on the vertical stabilizer section at the fuselage--vertical stabilizer junction of EC-135 (stick model numerical data).

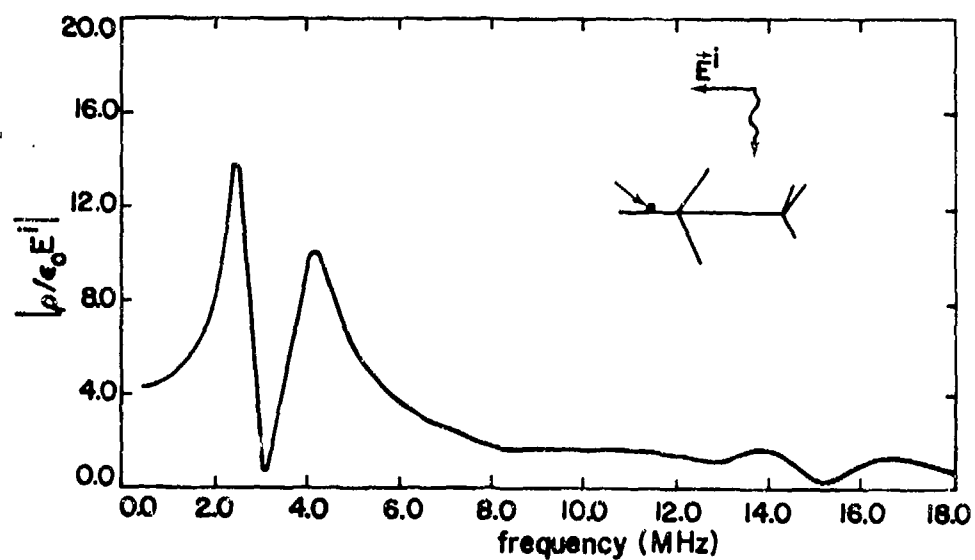


Fig. 34. Charge density on the fuselage of EC-135 (stick model numerical data).

In Figs. 25 and 26 are displayed fuselage surface current densities for the B-1 as functions of position along the fuselage for two different frequencies. Both the wings-forward and wings-swept configurations are shown. The measured data were obtained using a scale model.

Experimental data from scale-model measurements and numerical results from the body-of-revolution model of the EC-135 aircraft are compared in Figs. 27 - 30, in which are shown plots of the surface current density and surface charge density at various locations as functions of frequency. Further theoretical (numerical) results are presented in Figs. 31 - 34.

c. Thick Cylinder and Intersecting Flat Plate

Some experimental data are available for a more complicated model of an aircraft, an intersecting thick cylinder and flat plate [28]. The geometry is shown in Fig. 35. No analytical or numerical data are as yet available.

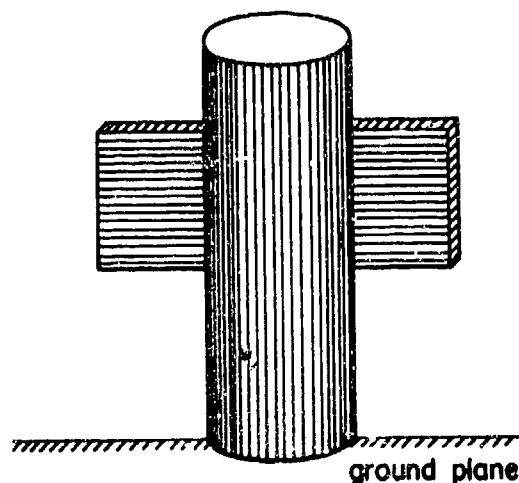


Fig. 35. Diagram of flat plate crossed with an electrically thick cylinder.

d. Ground-Plane Effects

The presence of a conducting ground plane beneath an aircraft causes the incident field to be reflected back onto the aircraft, with a phase shift of approximately 180° (for a highly conducting ground) for the component of the electric field parallel to the ground (and thus to the wings and fuselage of the aircraft). As a consequence of the reflection the total field illuminating the aircraft has less low-frequency spectral content than the incident EMP.

An additional effect of the ground is the formation of a high-Q transmission-line-like structure comprising the aircraft and its image in the ground plane. These structures resonate at about the same frequencies as the isolated aircraft but with a higher Q.

Some of the results for the induced currents and charges on an aircraft in the ground-alert configuration are summarized below [13].

- (a) The presence of the ground plane shifts the resonance frequencies by only a few percent, the lower-frequency resonances being shifted less than the higher-frequency resonances.
- (b) The resonant Q's are greatly increased when the ground plane is present.
- (c) For the same incident pulse, the peak current densities observed in the ground-alert configuration are comparable to those occurring in the in-flight configuration.
- (d) The presence of the ground plane reverses the importance of the first and second resonances in some cases.
- (e) The dc (late-time) component of the induced surface charge density is nonzero for the in-flight configuration and zero for the ground-alert configuration for \vec{E}^i parallel to the ground plane.
- (f) For the same incident pulse, the peak charge densities observed in the ground-alert configuration are comparable to those occurring in the in-flight configuration, except near the nose and the tip

of the vertical stabilizer. At those locations, the ground-alert peak charge density is about one-third the in-flight peak charge density for \vec{E}^1 parallel to the ground plane.

2.1.2.1.5 Modeling Accuracy

a. Model Selection

The features of the structure that should be included in the model depend upon their relative size and the accuracy desired. For example, should the engine nacelles be included in the model? If the current and/or charge is needed in the vicinity of the nacelle it is obvious that the nacelle is needed in the model. At distances from a surface protrusion (such as an engine nacelle) large in comparison with the dimensions of the protrusion, the effect of its presence may be neglected.

Fig. 36 is a crossed-wire model for the EC-135 aircraft which may be used to advantage in determining the interaction of the aircraft with the EMP because of the physical simplicity of the model.

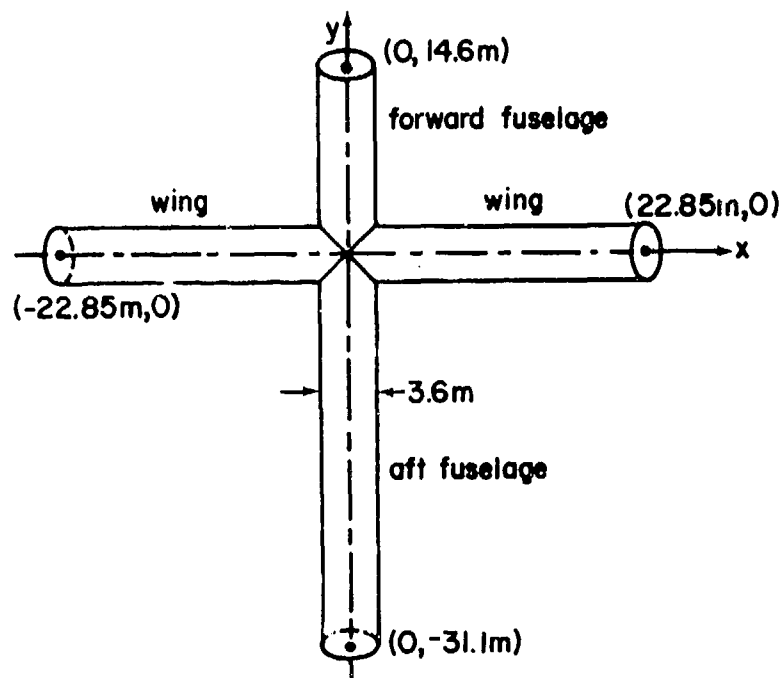


Fig. 36. Crossed-wire model of the EC-135 aircraft.

A comparison of time-domain peak currents I_{peak} and times t_c of the first zero crossing derived from the crossed-wire model and the body-of-revolution model are shown in table 12. The comparisons are quite favorable in view of the difference in complexity of the models. Although the current peak values compare quite well, only the currents on the forward fuselage and at the wing-fuselage junction have approximately the same time histories.

TABLE 12. COMPARISON OF RESULTS FROM THE CROSSED-WIRE MODEL WITH THE BODY-OF-REVOLUTION MODEL FOR THE EC-135 AND A TOPSIDE INCIDENT UNIT-STEP PULSE (See Fig. 36 for the definition of x,y coordinates)

Quantity	Location	Crossed-Wire Model	Body-of-Revolution Model
Resonant Freq.	----	2.4 MHz	2.6 MHz
I_{peak} t_c	y = 0-	0.16 A 204 ns	0.13 A 206 ns
I_{peak} t_c	y = 0+	0.108 A 138 ns	0.096 A 118 ns
I_{peak} (2nd peak) t_c	x = 0+	0.064 A 214 ns	0.0709 A 207 ns
$\rho_{\text{peak}}/(\epsilon_0 E^i)$ $\rho(t \rightarrow \infty)/(\epsilon_0 E^i)$	nose	12.9 9.9	27.6 19.8
ρ_{peak} $\rho(t \rightarrow \infty)$	wing tip	6.5 2.6	27.0 6.1
$\rho_{\text{peak}}/(\epsilon_0 E^i)$ $\rho(t \rightarrow \infty)/(\epsilon_0 E^i)$	vertical stabilizer tip	21.4 12.9	26.4 10.2

Also included in table 12 are comparisons of the charge densities. These are not as favorable as the current comparisons, since the charge densities are compared at the ends of the elements where the crossed-wire model has flat end-faces and the body-of-revolution model has ellipsoidal end-faces. The points selected for comparison represent points at which the charge density is largest. In table 12, ρ_{peak} is the peak value of the charge density and $\rho(t \rightarrow \infty)$ is the asymptotic value of the charge density.

b. Accuracy of the Results

It is difficult to quote an accuracy that can be achieved through theoretical analysis. Generally, when the physical structure is simple, errors of less than a few percent can be achieved in predicting the surface fields. However, if the structure is very complex, such as an aircraft, then error of a factor of two is probably the best that can be presently achieved.

2.1.2.2 High Frequencies

The transient surface current and charge densities are calculated in this section for certain simple-shaped geometries to demonstrate the utility and accuracy of the high-frequency expressions given in Sec. 1.4.3. The expressions can be used in several ways to obtain the transient response of an object. For example, they can be used in conjunction with intermediate-frequency spectral components to obtain the time-domain response by a numerical inversion, such as the FFT. Alternatively, the high-frequency solutions can be analytically transformed to the time domain and then smoothly joined to the intermediate-time results which may be obtained, for example, by the SEM or the solution of a time-domain integral equation.

2.1.2.2.1 Wedges

According to Sec. 1.4.3 the induced transient surface current and charge densities on the horizontal face of a wedge (Fig. 37) can be written as

$$\begin{aligned} \vec{J}(x,t) &= 2 \vec{I}_y \times \vec{H}^i(x,t) u(\pi - \phi') + \vec{J}^d(x,t) \\ \rho(x,t) &= 2 \epsilon \vec{I}_y \cdot \vec{E}^i(x,t) u(\pi - \phi') + \rho^d(x,t) \end{aligned} \quad (60)$$

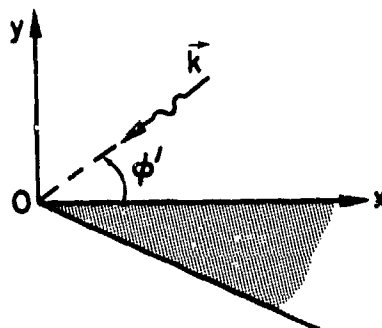


Fig. 37. Plane wave normally incident on a perfectly-conducting wedge.

in which $u(\pi - \phi')$ is the unit-step function. The first term on the right hand side is just the geometrical optics contribution.

In the TE case where \vec{H}^i is parallel to the z-axis (or edge) and given by

$$\vec{H}^i(x, y, t) = \vec{I}_z u[t + (x \cos \phi' + y \sin \phi')/c] \quad (61)$$

one has (cf. Sec. 1.4.3.5.2)

$$\vec{J}^d(x, s) = \vec{I}_x \frac{1}{s} D_h(\vec{I}^i, \vec{I}^d, \chi, s) \frac{e^{-sx/c}}{\sqrt{x}} \quad (62)$$

for the diffracted current density in the s-domain, and

$$\begin{aligned} \rho^d(T) = & \frac{1}{c} J_x^d(T) + \frac{1}{c} (T-1) J_x^d(T) \\ & - \frac{1}{c} \int_1^T J_x^d(T') dT', \quad T \geq 1 \end{aligned} \quad (63)$$

for the charge density in the t-domain, where $T = ct/x$. Eq.(63) shows that for very early times after the arrival of the diffracted wavefront ($t \approx x/c$, i.e., $T \approx 1$)

$$\rho^d(T) \approx \frac{1}{c} J_x^d(T) \quad (64)$$

The edge diffraction coefficient D_h in (62) is first introduced in (210) of Sec. 1.4.3.5.2; its explicit expressions for the half-plane and the ordinary wedge formed by two intersecting plane surfaces can be found in [29].

In the TM case the incident electric field \vec{E}^i is given by (61) with \vec{H}^i replaced by \vec{E}^i/Z_0 . Since $\vec{I}_y \cdot \vec{E}(x,t) = 0$ everywhere, one has

$$\rho(x,t) = 0 \quad (65)$$

$$J_z^d = -H_x^d(x,t)$$

Eq. (65) is obtained from $E_z^d(x,t)$ via Maxwell's equations and an integration with respect to time.

Calculations of the surface current and charge densities on the top face of a right-angle wedge and half-plane are presented in Figs. 38 and 39 for both TE and TM polarizations. The transient responses to a step-function pulse for various angles of incidence ϕ' are exhibited. The GTD (Geometrical Theory of Diffraction) curves in Fig. 38a are calculated using the edge diffraction coefficients given by Keller [30]; these diffraction coefficients are not valid at the shadow and reflection boundaries, where they become infinite. The UTD (Uniform Theory of Diffraction) curves are calculated from the uniform diffraction coefficients given in [29]. The exact curves are calculated from exact, closed-form time-domain solutions given in [31-33].

In Fig. 38a it is apparent that numerical results based on the GTD are valid only for very early times after the arrival of the diffracted wavefront at $ct/x = 1$, whereas those based on the UTD are seen to be in remarkable agreement with exact calculations for intermediate and even for late times; this is further confirmed by comparing the UTD curves in Fig. 38b with the exact curves in Fig. 38c. The numerical results for the half-plane shown in Fig. 39 reveal that there is essentially no difference between the UTD and exact values.

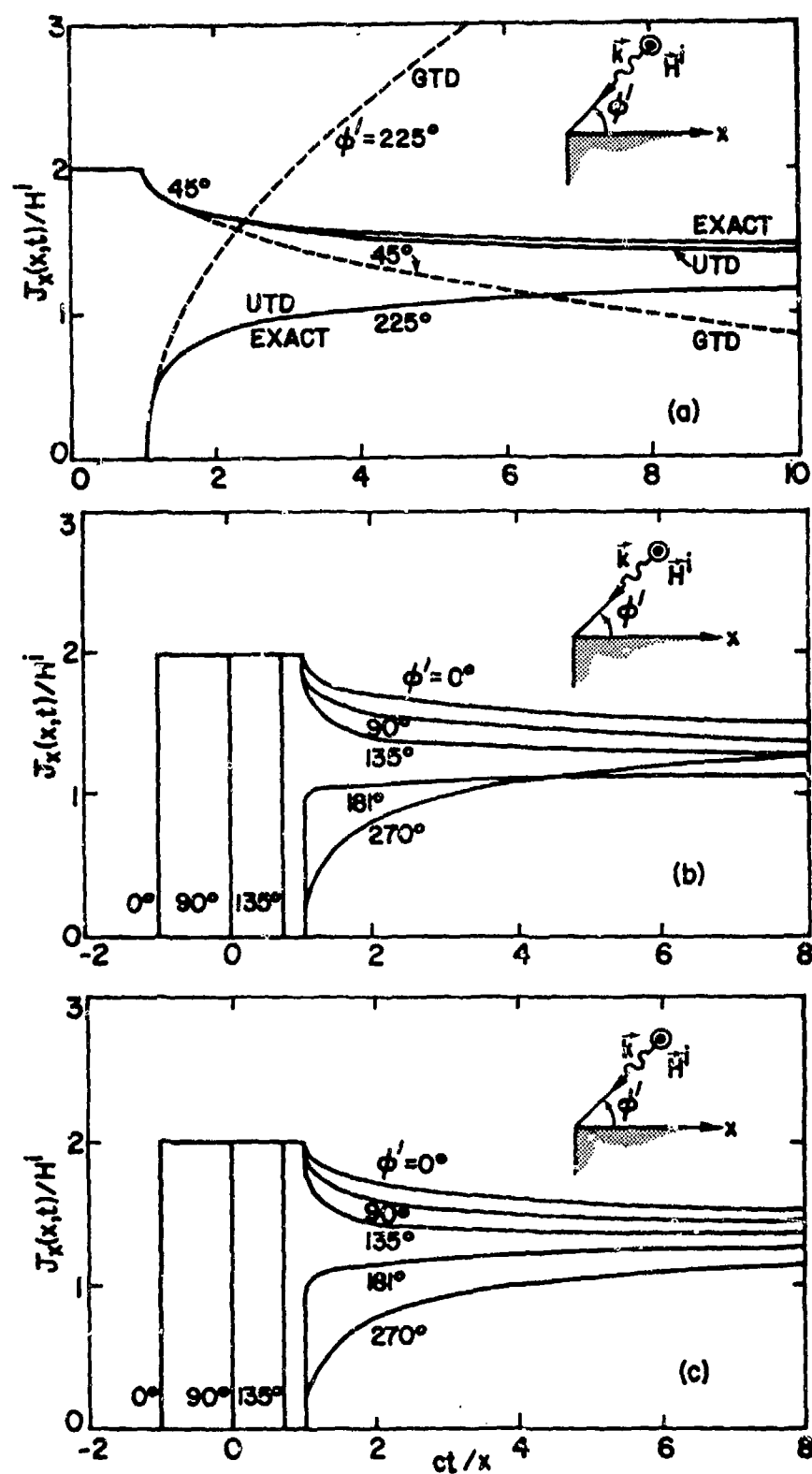


Fig. 38. Surface current densities on a right-angle wedge illuminated by a TE step-function plane wave calculated from (a) GTD, UTD, and exact solutions, (b) the UTD solution, and (c) the exact solution.

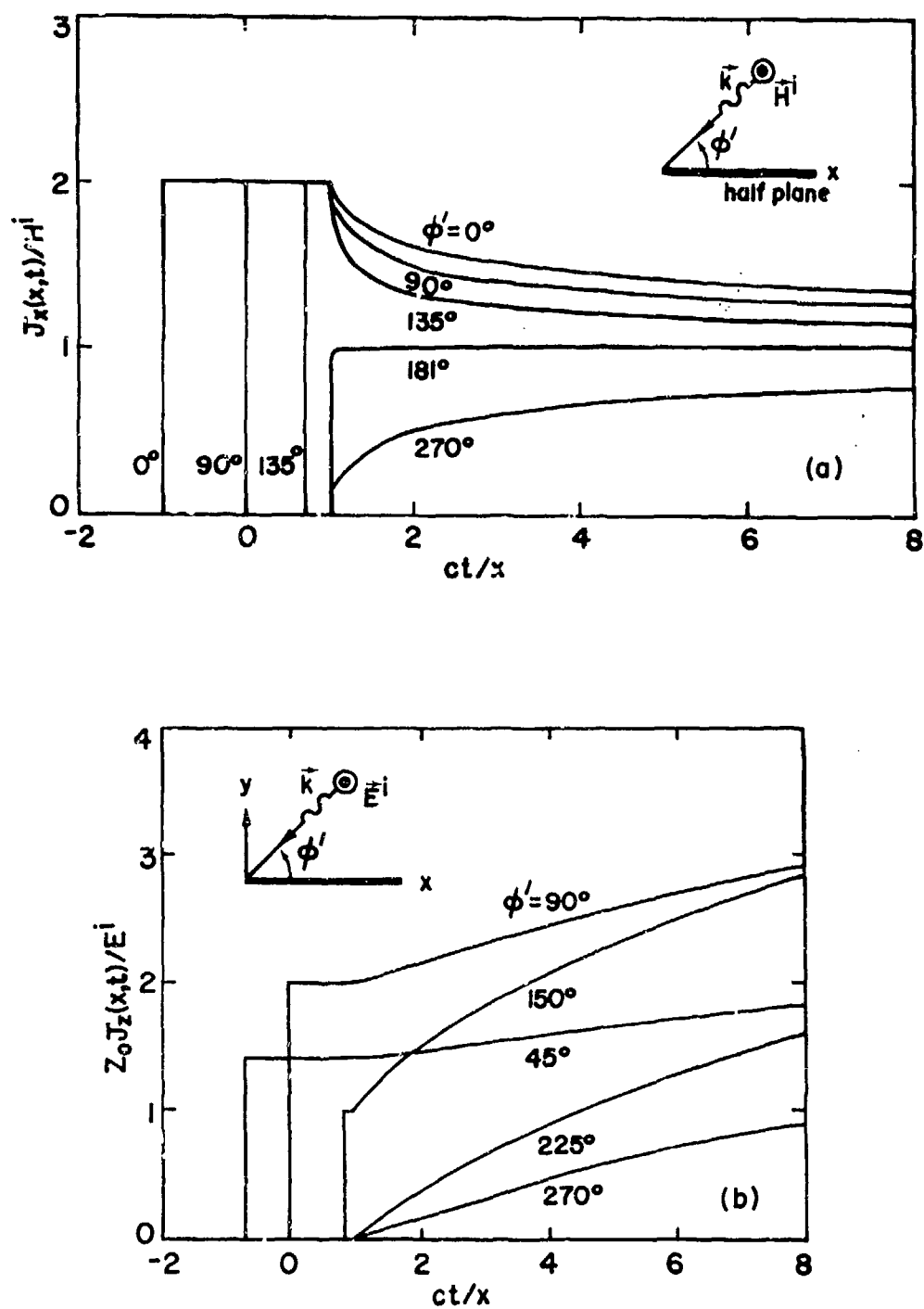


Fig. 39. Surface current densities on a half-plane illuminated by (a) a TE step-function plane wave, and (b) a TM step-function plane wave, calculated from the UTD and exact solutions.

When the top face is illuminated, the simple response predicted by geometrical optics for the interval $-\cos \phi' < T < 1$ is evident. The response curves for the right-angle wedge ($n=3/2$) and half-plane ($n=2$) are quite similar. For late times the response for the TE case approaches $2/n$, where $n\pi$ is the exterior angle of the wedge. Thus the response at intermediate and late times of the right-angle wedge is somewhat larger than that of the half plane.

Additional numerical results for the transient fields diffracted by perfectly conducting wedges illuminated by step-function plane waves can be found in [33-35]. It should be mentioned that an interesting closed-form result for the diffraction of the pulsed field from an electric (or magnetic) dipole in the presence of a perfectly conducting wedge has recently been obtained [36].

2.1.2.2.2 Cylinders

The transient current and charge densities induced on a perfectly conducting circular cylinder can be obtained analytically by inverse-transforming the high-frequency expressions given in Sec. 1.4.3.5.4 on the shadow side ($\pi/2 < \phi < 3\pi/2$) of the cylinder. The corresponding high-frequency expressions on the illuminated side ($0 < |\phi| < \pi/2$) can be obtained from the Luneberg-Kline series [37,38] and can easily be transformed to the time domain. The representation breaks down close to the shadow boundary.

Time-domain data for the surface current on a circular cylinder are given in Fig. 40 for TE and TM step-function incident plane waves. In the shadow region the early-time response for the TM case is much weaker than that for the TE case, which is expected because of the greater attenuation experienced by the TM surface ray modes. The curves in Fig. 40a appear to be approaching the late-time limit of unity, and so it is believed that they are reasonably accurate for intermediate times. It should be emphasized that the results in Fig. 40 were calculated from an exact inversion of the high-frequency solution.

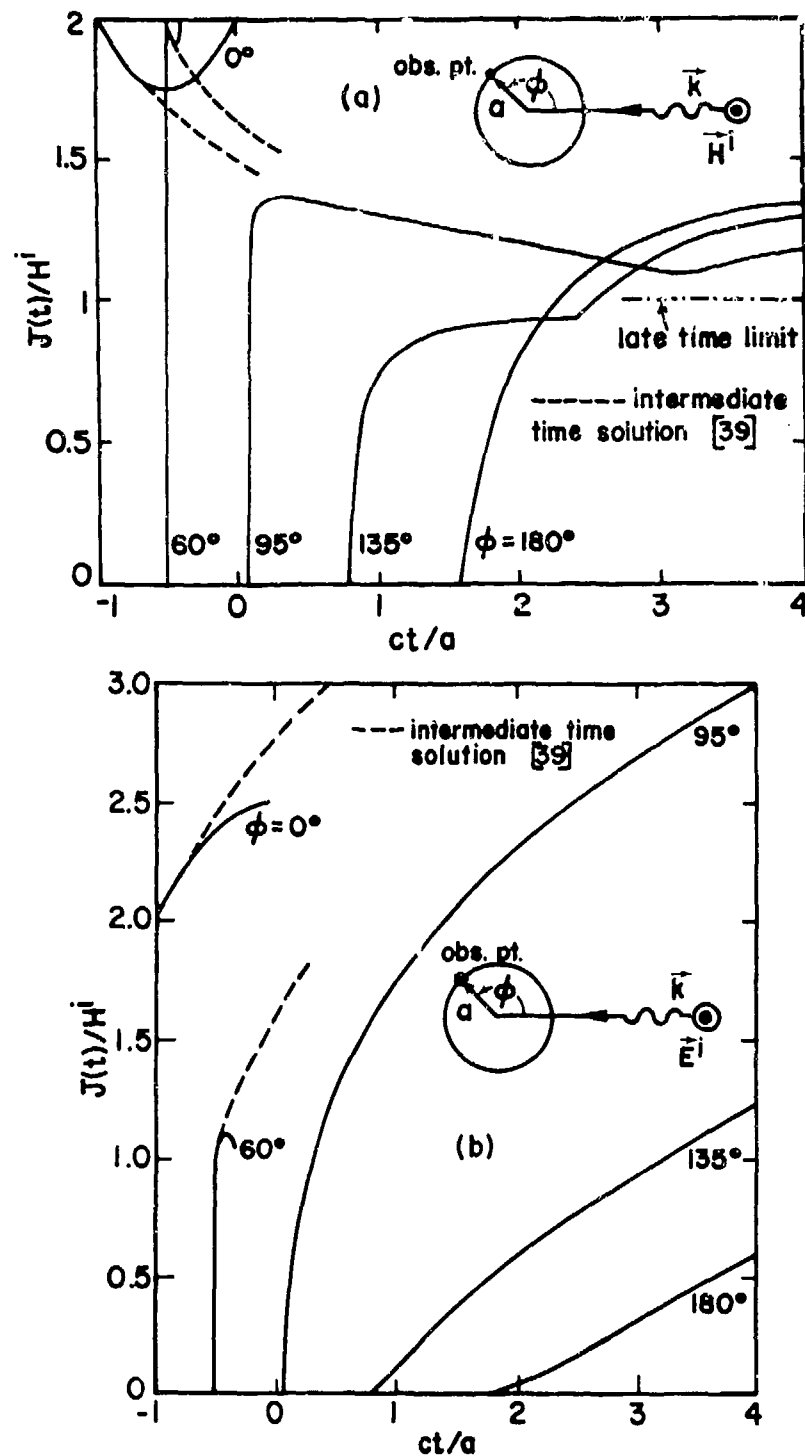


Fig. 40. Surface current densities on a circular cylinder illuminated by (a) a TE step-function plane wave, and (b) a TM step-function plane wave, calculated from the GTD solution.

The transient response in the shadow region begins at $ct/a = \phi - \pi/2$, and in Fig. 40 a second rise in the response at $3\pi/2 - \phi$ is evident for the 95° and 135° curves. This is due to the arrival of the wavefront from the shadow boundary at $3\pi/2$.

The early-time response curves in the illuminated region are seen to be useful only for relatively short times compared with the curves for the shadow region. This may be due to the fact that the high-frequency solution on the illuminated side, based on the Luneberg-Kline series, is not as accurate as that on the shadow side. The high-frequency solution on the shadow side can be used right up to the shadow boundary, whereas for the illuminated side it breaks down quickly as the boundary is approached. Perhaps this difficulty could be overcome by using solutions valid for the transition regions, which join smoothly with those for the shadow and illuminated regions, such as those described in [40].

As in the case of the wedge, there is no surface charge density in the TM case. In the TE case the surface charge density in the time domain can be found from the inversion of the expression given in Sec. 1.4.3.5.4. Additional numerical results for the transient surface currents on circular cylinders are given in [38].

2.1.2.2.3 Aircraft Model

The basic aircraft model that has been used extensively for GTD calculations is shown in Fig. 41, where the infinitely long, perfectly conducting elliptic cylinder models the fuselage while the flat, perfectly conducting plates model the aircraft wings. Also in Fig. 41 are shown the high-frequency surface current and charge densities for various incidence angles ϕ' of a TE incident plane wave [41]. The dimensions chosen ($a = b = 3.5$ meters) correspond to those of a 747 aircraft. The corresponding results for a TM-type incident wave are in general smaller.

2.1.2.3 Large Appendages

In this section data are presented for the effects of electrically large appendages on the induced currents and charges on aircraft, missiles

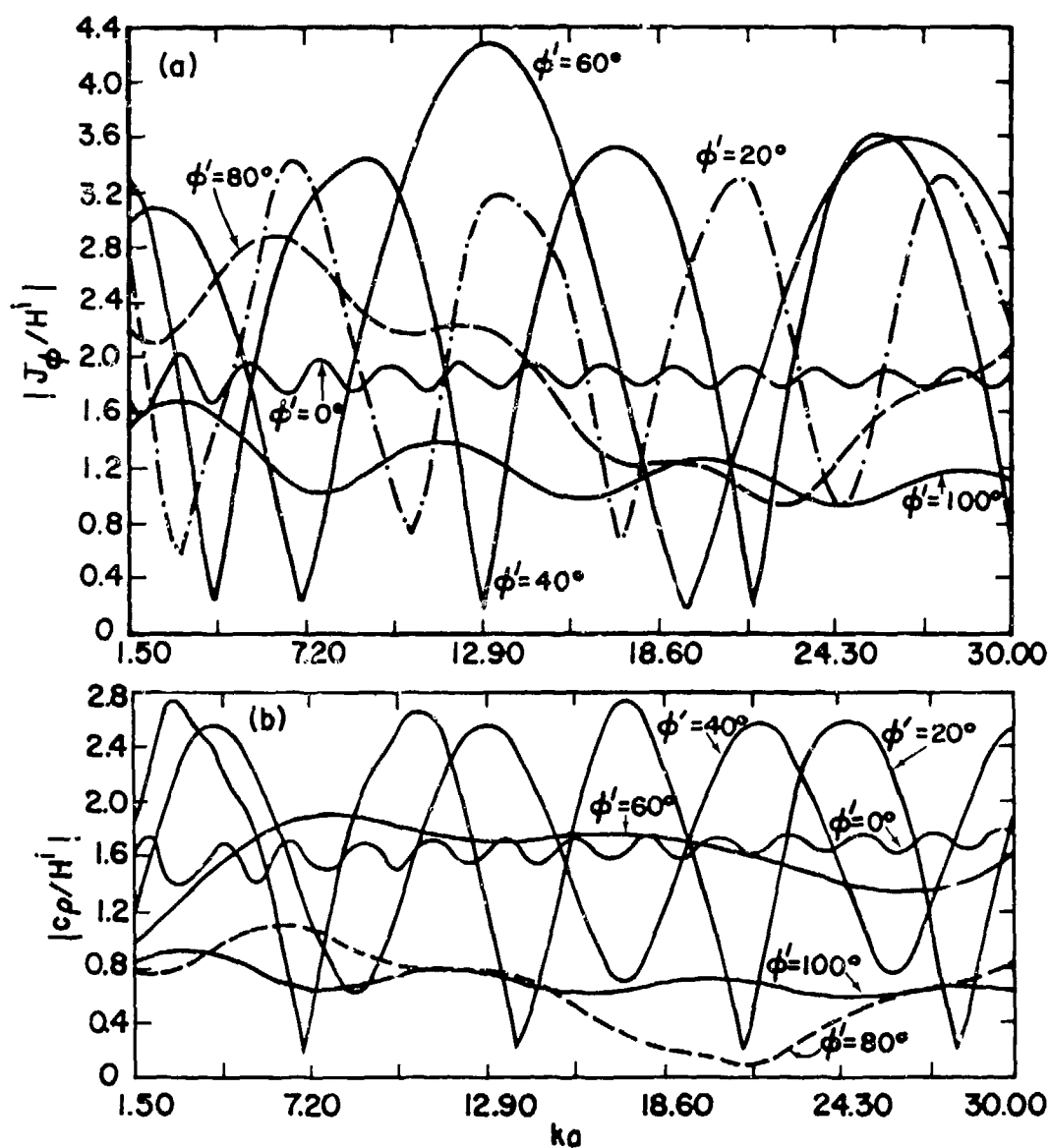
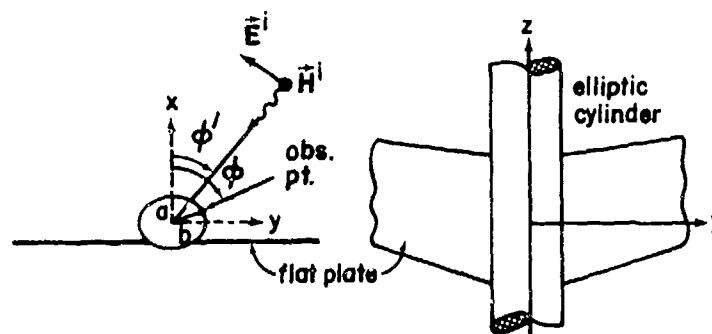


Fig. 41. (a) Surface current density and (b) surface charge density at $z=0$ and $\phi=60^\circ$ on a 747 ($a=b=3.5$ m) aircraft for a TE incident plane wave with various angles of incidence ϕ' .

and ground-based communications systems. The appendages considered include long trailing-wire antennas on aircraft, exhaust plumes associated with missiles in powered flight, and wires/cables external to ground facilities.

2.1.2.3.1 Trailing-Wire Aircraft Antennas

Two different VLF/LF transmitting antennas are shown in Fig. 42. These antennas operate in the frequency range 17 - 60 kHz, and are tuned by varying the wire lengths. The longer of the two wires in the counterpoise antenna or the single trailing wire can extend as much as 8.5 km behind the aircraft. Some data will be given in this section regarding the effect of the presence of this long wire on the currents and charges induced on the aircraft itself when the whole system is illuminated by an EMP, especially in the frequency range below the first resonance of the aircraft.

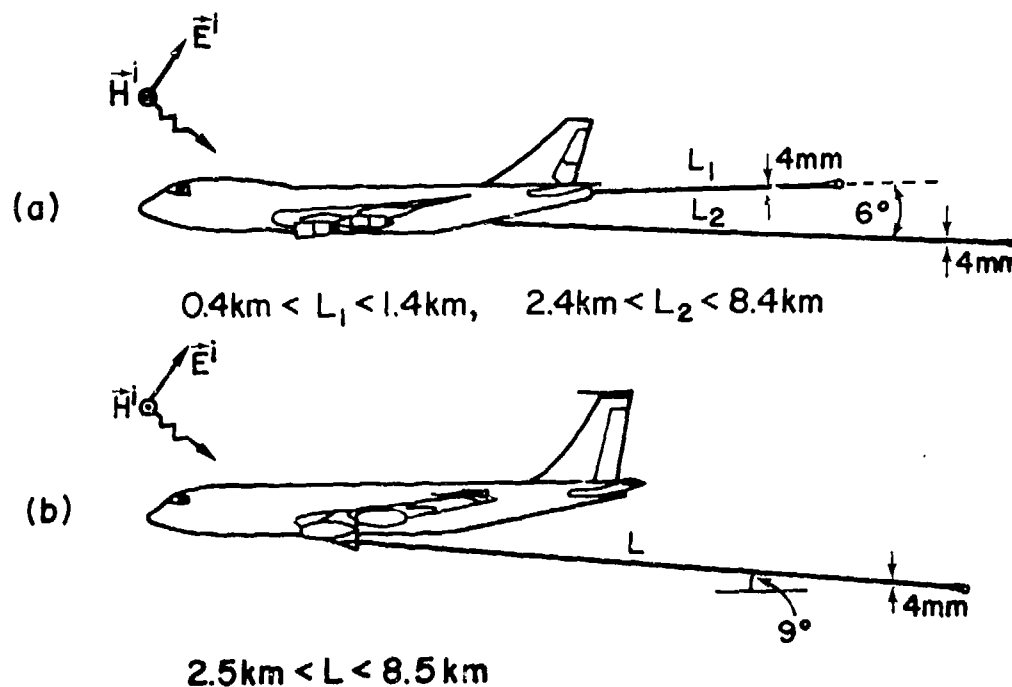


Fig. 42. (a) Dual-wire (counterpoise) and (b) trailing wire VLF/LF antennas.

A simplified model encompassing the salient features of the problem is shown in Fig. 43. The aircraft is modeled by a simple stick model (see Sec. 2.1.2.1.4a). The trailing wire is attached to the aircraft to the bottom of the fuselage under the wings. The current I_w injected from the long wire into the aircraft is given by [42]

$$I_w = \frac{4\pi E'_0(\omega)}{jkZ_0} \frac{\frac{1-F(L)}{1+F(L)} + \frac{\sec(k\ell_3) - \sec(k\ell_1)}{j[\tan(k\ell_1) + 2\tan(k\ell_2) + \tan(k\ell_3)]}}{\frac{1+F^2(L)}{1-F^2(L)} \psi_a + \frac{1}{j[\tan(k\ell_1) + 2\tan(k\ell_2) + \tan(k\ell_3)]}} \quad (66)$$

where $E'_0(\omega)$ is the spectrum of the incident EMP of the form of the difference of two exponentials as given by (2), i.e.,

$$E'_0(\omega) = E_0 \left(\frac{\tau_f}{1+j\omega\tau_f} - \frac{\tau_r}{1+j\omega\tau_r} \right) \quad (67)$$

with $\tau_f = 0.25 \mu s$, $\tau_r = 2 ns$, and the function $F(L)$ is given by

$$F(L) = \frac{\ln \left[1 - 2\pi j / \{ \ln(\Gamma k^2 a^2) - \ln[kL + (k^2 L^2 + \Gamma^{-2})^{1/2}] + 3\pi j/2 \} \right]}{\ln \{ 1 - 2\pi j / [2 \ln(\Gamma ka) + 3\pi j/2] \}} e^{-jkL} \quad (68)$$

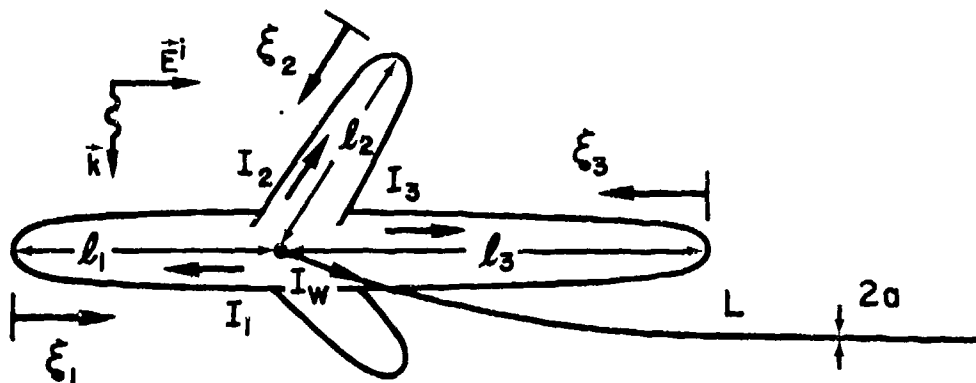


Fig. 43. Stick-model aircraft with attached trailing-wire antenna and topside incidence ($\ell_1 = 13 m$, $\ell_2 = 20 m$, $\ell_3 = 34 m$, $L = 8.473 km$, $a = 2 mm$).

with $\psi_a = -2 \ln(\Gamma ka) - j\pi$, and $\Gamma = 1.81072\dots$

The currents induced on the stick-model aircraft itself are

$$I_1(\xi_1) = \frac{4\pi E'_0}{Z_0 \Omega_a jk} f_1(\xi_1) - I_w g_1(\xi_1) \quad (69)$$

$$I_2(\xi_2) = \frac{4\pi E'_0}{Z_0 \Omega_a jk} h(\xi_2) - I_w g_2(\xi_2) \quad (70)$$

$$I_3(\xi_3) = \frac{-4\pi E'_0}{Z_0 \Omega_a jk} f_3(\xi_3) - I_w g_3(\xi_3) \quad (71)$$

where $\Omega_a = 2 \ln(L/a)$, with L being the length of the trailing wire and a its radius, and

$$f_n(\xi) = \cos(k\xi) - 1 + \sin(k\xi) \{ \tan(kl_n) + j^{n-1} \sec(kl_n) [\sec(kl_3) - \sec(kl_1)] \times [\tan(kl_1) + 2\tan(kl_2) + \tan(kl_3)]^{-1} \}, \quad n=1,3 \quad (72)$$

$$g_n(\xi) = \sin(k\xi) \sec(kl_n) / [\tan(kl_1) + 2\tan(kl_2) + \tan(kl_3)], \quad n=1,2,3, \quad (73)$$

$$h(\xi) = \sin(k\xi) \sec(kl_3) [\sec(kl_3) - \sec(kl_1)] / [\tan(kl_1) + 2\tan(kl_2) + \tan(kl_3)] \quad (74)$$

The coordinates ξ_1 , ξ_2 and ξ_3 are shown in Fig. 43. The expressions (66) - (74) have been derived by neglecting the damping of the aircraft resonances. This effect can be included by expanding each of the currents in Mittag-Leffler series and then introducing the damping for each resonance (cf. Sec. 2.1.2.1.4a).

The frequency variation of the total induced current at two points on the stick-model aircraft is shown in Figs. 44 and 45. The results shown are for a double exponential EMP with topside incidence (Fig. 43) and

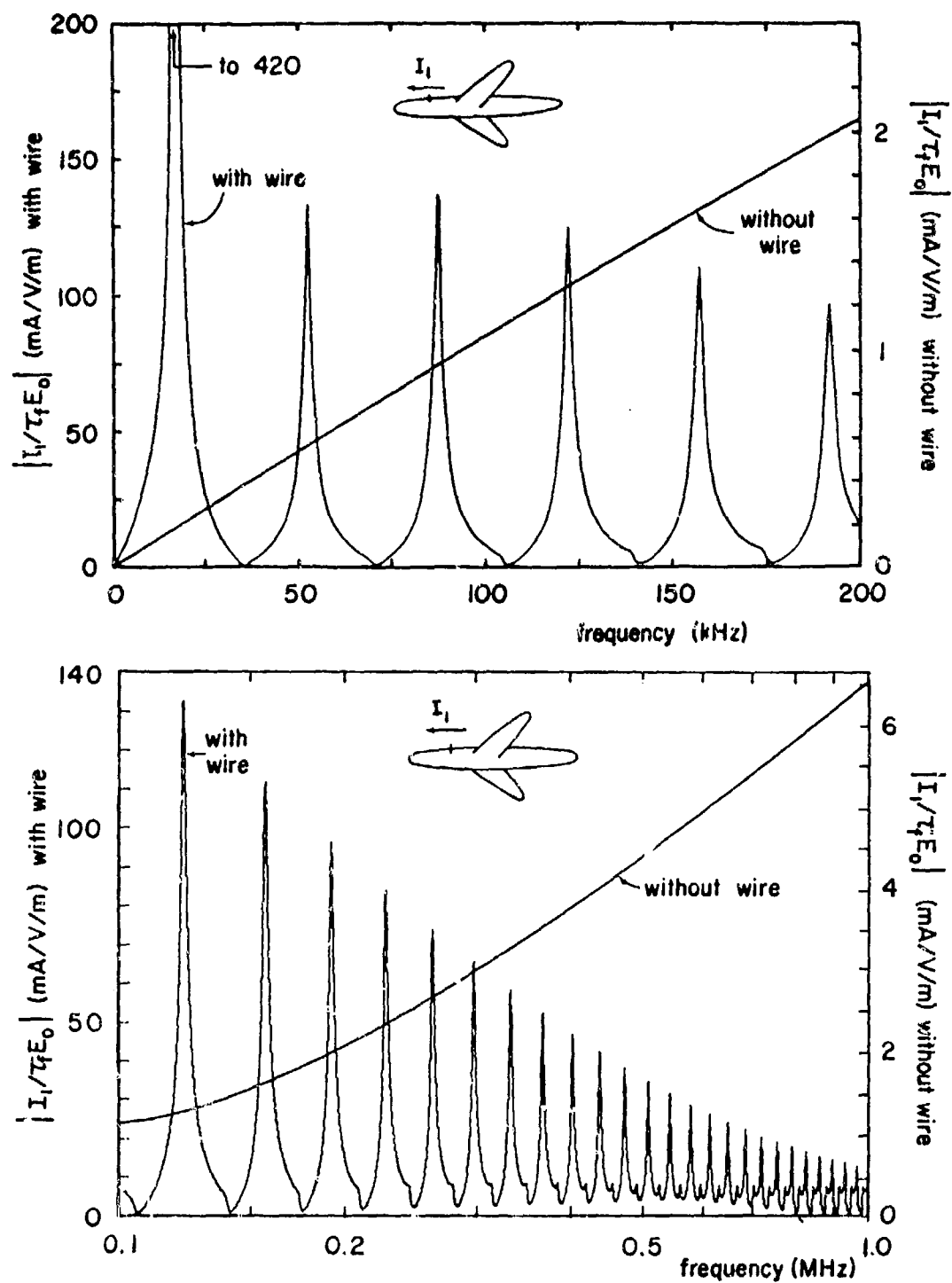


Fig. 44. Spectral density of the total induced fuselage current at the midpoint between the nose and the wing root.

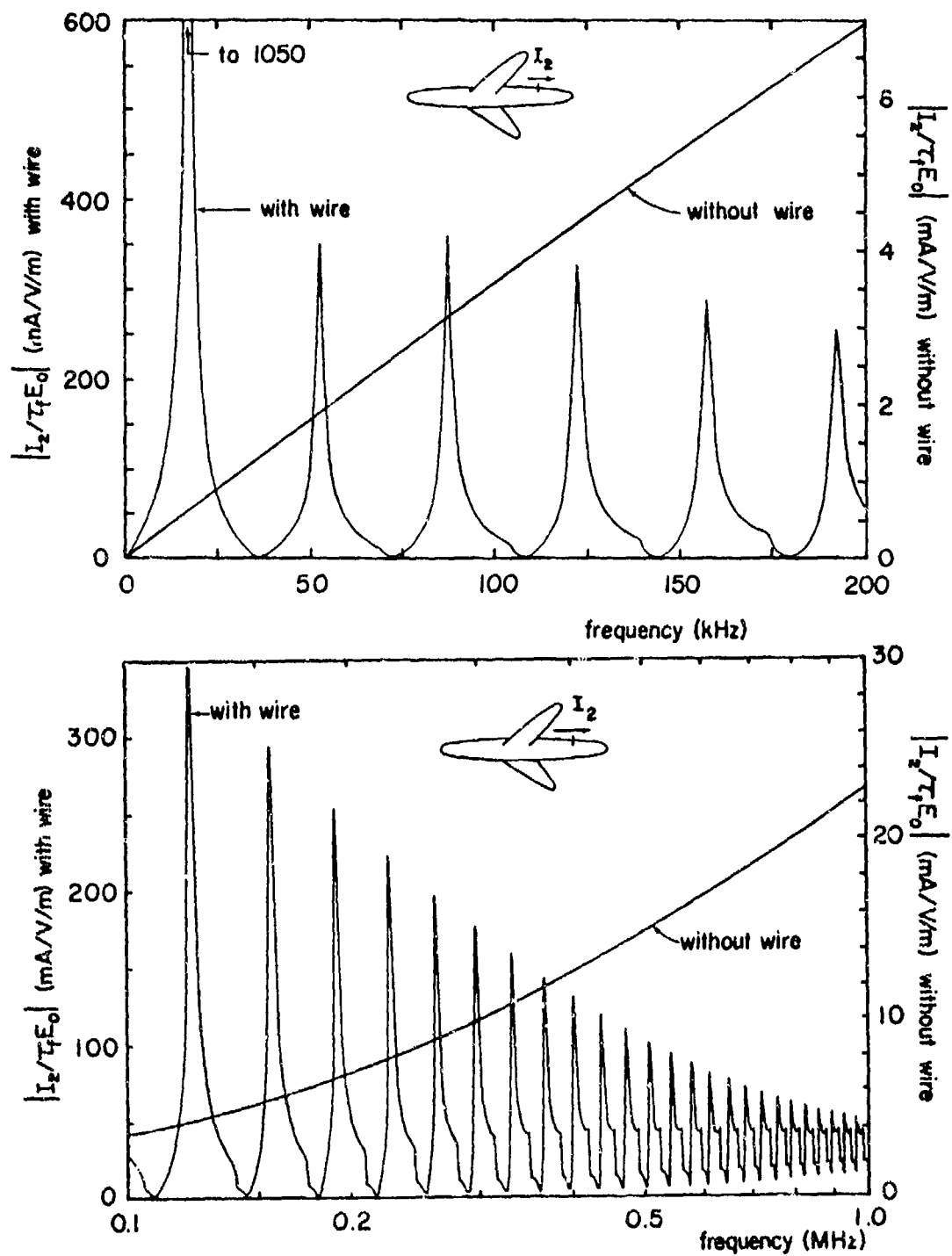


Fig. 45. Spectral density of the total induced fuselage current at the midpoint between the empennage and the wing root.

spectrum given by (67). Results are shown for frequencies below one MHz only, since the effect of the trailing wire on the aircraft currents is not so important in the resonance region of the aircraft [42]. It should be emphasized that the topside-incidence case does not give the maximum effect of the trailing wire on the induced currents and charges on the aircraft. The maximum effect seems to occur when the direction of incidence is nearly parallel to the wire and toward the aircraft.

2.1.2.3.2 Exhaust Plumes

The ionized exhaust gases ejected from a missile in powered flight behave like a conductive extension of the missile. The presence of this exhaust plume can affect the response of the missile to EMP excitation in at least two ways: (a) the conducting plume may significantly affect the surface currents induced on the missile body, and (b) the induced currents in the plume itself may couple directly to the interior of the missile through the nozzle assembly. Only the first effect will be discussed here, as the second is not at all well understood at present.

a. Missile-Plume Models

The simplest model for a missile-plume configuration is a thin cylinder of constant radius a and axially varying electrical properties. The geometry for such a model is shown in Fig. 46. The missile itself extends from $z = 0$ to $z = l_m$; the plume extends below the missile to $z = l_m + l_p$. The total axial current $I(z)$ at any point z , where $0 < z < l_m + l_p$, can be determined from the solution of an integral equation [43-46]. The limitations of this model and approach are that (a) only the axial current can be calculated; (b) it is necessary that $(l_m + l_p)/a \gg 1$; (c) the junction between the missile and the plume is assumed to be a simple electrical connection between two objects having different electrical conductivities. Recently, some limited results have been presented for a model in which the missile is treated as a conducting rod of conductivity σ_{em} and the plume is modeled as a homogeneous lossy dielectric body of revolution attached to the conducting rod [44]. However, we shall here restrict attention to the more completely developed thin-cylinder model for the missile and plume.

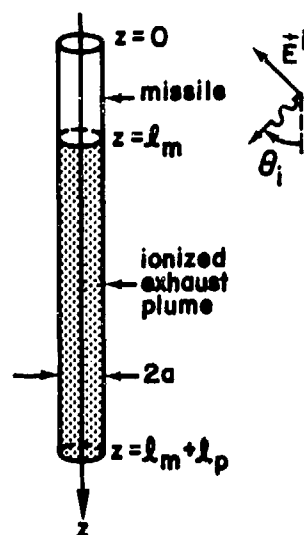


Fig. 46. The thin-cylinder model for a missile-plume configuration.

b. Electrical Plume Parameters

At low altitude a plume is usually modeled as a thin cylinder of radius a described by an equivalent internal impedance per unit length $Z_1'(z)$

$$Z_1'(z) = \hat{E}_z(z)/I(z) \quad (75)$$

in which $I(z)$ is the axial current at position z and $\hat{E}_z(z)$ is the average total axial electric field at the plume surface

$$\hat{E}_z(z) \equiv \frac{1}{2\pi} \int_0^{2\pi} E_z(a, \phi, z) d\phi \quad (76)$$

The principal contribution to the conductivity of the plume is the motion of free electrons under the influence of an applied field. The effective permittivity and conductivity of the plume in the cold-plasma model are

$$\epsilon_{ep} = \epsilon_0 \left[1 - \frac{\omega_p^2}{\omega^2 + \nu^2} \right] \quad (77)$$

$$\sigma_{ep} = \epsilon_0 \frac{\omega_p^2 \nu}{\omega^2 + \nu^2}$$

in which ν denotes the collision frequency and ω_p the plasma frequency

$$\omega_p^2 = n_e e^2 / (m_e \epsilon_0) \quad (78)$$

where n_e is the free-electron density in the plume, and e and m_e are respectively the electron charge and mass. In the frequency range of interest for EMP studies, $\omega \ll \nu$ and $\omega \ll \omega_p$, so that

$$\sigma_{ep} \approx \epsilon_0 \omega_p^2 / \nu \quad (79)$$

is a good approximation for the plume conductivity. Note that this approximate expression is independent of ω . In general, both ν and ω_p depend on the axial and radial spatial coordinates of the plume.

The equivalent internal impedance Z'_1 per unit length of the plume is calculated from a knowledge of, or assumptions concerning, the functional dependence of ω_p and ν on position in the plume. Results for three distinct plume models will be presented here. The simplest plume model is the *homogeneous-plume model* which is based on the assumption that the plume conductivity is constant everywhere within the plume. For this model the equivalent internal impedance Z'_1 per unit length is

$$Z'_1(z) = \frac{1}{2\pi a} (1+j) \sqrt{\frac{\omega \mu_0}{2\sigma_{ep}}} \quad (\text{homogeneous plume}) \quad (80)$$

Another plume model is the so-called *tapered-plume model* [45,46] which utilizes an assumed exponential variation for the plume conductivity, namely

$$\sigma_{ep}(z) = \sigma_{ep}(0)e^{-\alpha z}, \quad (\ell_m + \ell_p > z > \ell_m) \quad (81)$$

in which α is a constant. The internal impedance Z'_1 per unit length is identical to that given in (80) with σ_{ep} replaced by (81). The third model is the *inhomogeneous-plume model* whose plume conductivity σ_{ep} is allowed to vary as a function of radius and of axial position. The electron density n_e and the collision frequency ν may be calculated by the Aero Chem Low Altitude Plume Program (LAPP) [47] and then used to determine σ_{ep} using (77), but this procedure will cause considerable uncertainty in the results.

Smith, et al. [43] have considered two models of the inhomogeneous plume of finite length. In their first model, the conductivity and the plume radius are functions of axial position, and the conductivity at a given value of z is the maximum value predicted by the LAPP code at that axial position. The radius of the plume r_p is taken to be the radius at which this maximum conductivity occurs. In their second model, the plume radius r_p is assumed to be constant and equal to the missile radius, while the conductivity at each z is the maximum value predicted by the LAPP code at that z -value. For each of these two models, the equivalent internal impedance Z'_1 per unit length of the plume is of the form

$$Z'_1(z) = \frac{1}{2\pi r_p(z)} (1 + j) \sqrt{\frac{\omega \mu_0}{2\sigma_{ep}(z)}} \quad (82)$$

In summary, the various plume models use different approaches to the calculation of $Z'_1(z)$; but in each case the plume is modeled as a thin cylinder of radius a . Only the form of the axial variation in $Z'_1(z)$ differs among the models.

Fig. 47a shows frequency-domain results for a homogeneous-plume model for various conductivity values, while Fig. 47b exhibits similar data for a different angle of incidence [44]. In the case of broadside incidence, the presence of the plume tends to suppress the missile current, while at near grazing incidence, the plume tends to enhance the missile current.

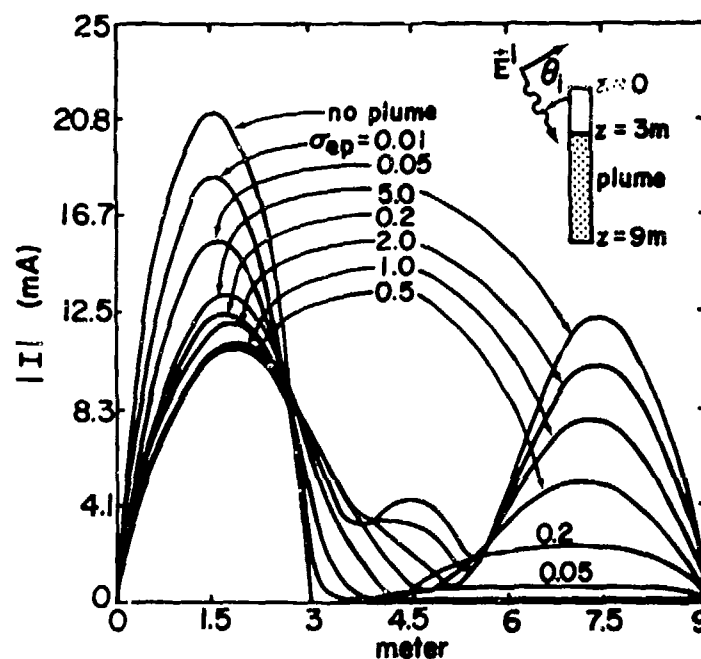


Fig. 47a. Current magnitude on a thin-cylinder model of 3-meter missile (6.4 cm radius) with 6-meter trailing plume ($f = 50$ MHz, broadside incidence $\theta_1 = 90^\circ$); homogeneous-plume model; $\sigma_{em} = \infty$, $\lambda E^1 = 1$ volt (λ is wavelength).

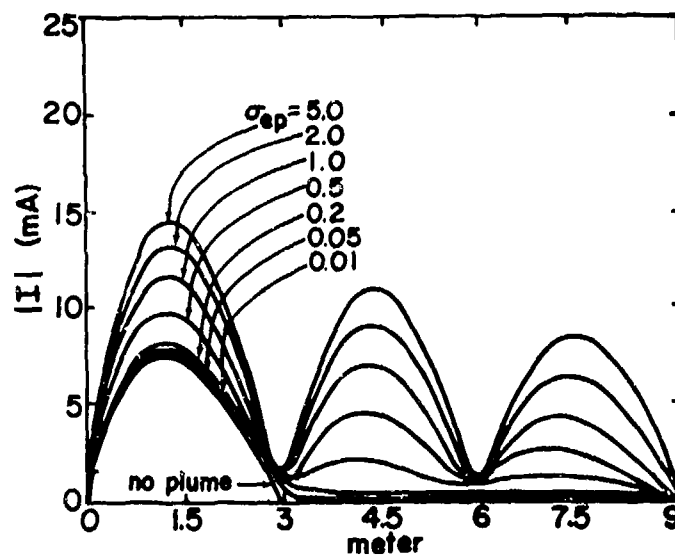


Fig. 47b. Current magnitude on a thin-cylinder model of 3-meter missile (6.4 cm radius) with 6-meter trailing plume ($\theta_1 = 30^\circ$, $f = 50$ MHz); homogeneous-plume model; $\sigma_{em} = \infty$, $\lambda E^1 = 1$ volt.

Fig. 48a shows the dependence of the missile current on wavelength for the homogeneous-plume model, while Fig. 48b shows this same dependence for an inhomogeneous plume whose conductivity profile is given in [43]. The unit-step transient response for a homogeneous plume and a tapered plume are shown respectively in Figs. 49a and 49b [48].

c. Validity of Approximations

Almost all the plume calculations presently employ the cold-plasma approximation. A plasma is considered to be "cold" when

$$\frac{v_t}{v_p} = \frac{\text{electron thermal velocity}}{\text{EM wave phase velocity}} \ll 1 \quad (83)$$

For EMP problems it can be shown that

$$\frac{v_t}{v_p(\omega)} \approx 5.2 \times 10^{-4} \sqrt{\frac{T_n}{\omega v}} \quad (84)$$

Fig. 50 presents curves of the ratio v_t/v_p versus frequency for $n_e = 10^{18} \text{ m}^{-3}$, $v = 10^9 \text{ sec}^{-1}$, and a temperature ranging from 500°K to 4000°K. From these curves one can find the frequency range in which the cold-plasma approximation is not violated.

2.1.2.3.3 External Wires and Cables

Long, thin conductors outside the first layer of shielding often occur in ground-based systems. Examples of such conductors are power lines, communication cables, metal piping, and similar appendages for station-keeping and communication. These conductors provide paths along which EMP-induced currents and charges may propagate toward the facility. Of primary interest is the Thévenin or Norton equivalent source representing the voltage or current delivered to the facility end of the conductor.

There are two categories of external conductors: above-ground conductors and those at or below the surface. The above-ground conductors are exposed to the incident EMP for the short time that elapses before the reflection from the ground arrives. Buried conductors are exposed only

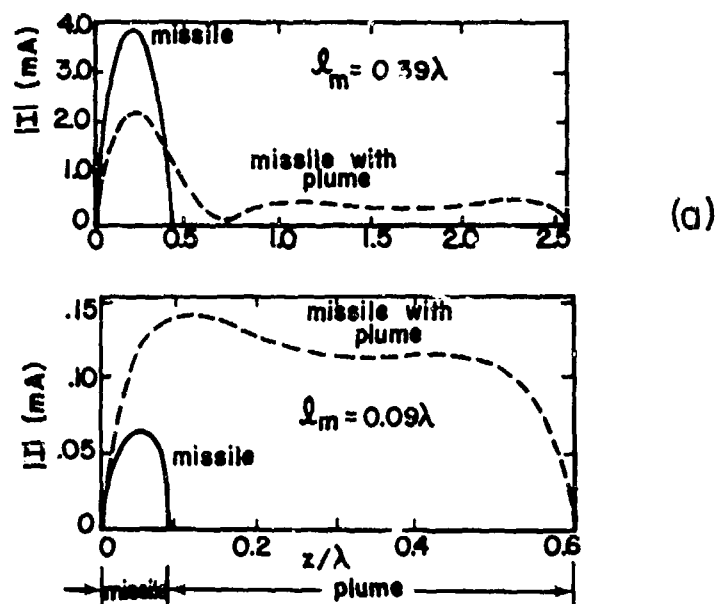


Fig. 48a. Comparison of magnitude of current on missile without a plume and missile with a homogeneous plume. Length of missile $l_m = 0.39\lambda$ (near resonance) and $l_m = 0.09\lambda$ (electrically short); $\sigma_{ep} = 0.25 \text{ mho/m}$, $\sigma_{em} = 3.54 \times 10^7 \text{ mho/m}$, $\lambda E^i = 1 \text{ volt}$, $\theta_i = 90^\circ$.

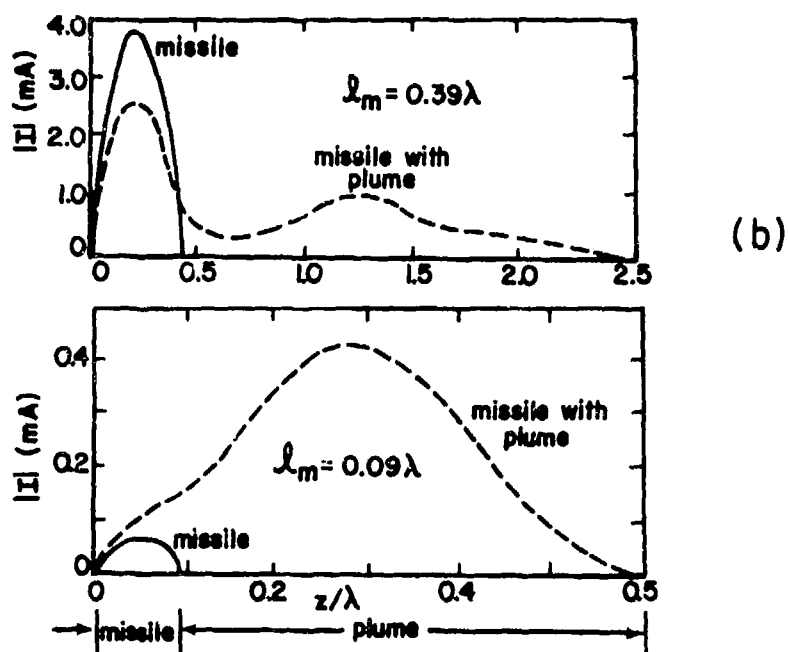


Fig. 48b. Comparison of magnitude of current on missile without a plume and missile with an inhomogeneous plume. Length of missile $l_m = 0.39\lambda$ (near resonance) and $l_m = 0.09\lambda$ (electrically short); $\sigma_{em} = 3.54 \times 10^7 \text{ mho/m}$, $\lambda E^i = 1 \text{ volt}$, $\theta_i = 90^\circ$.

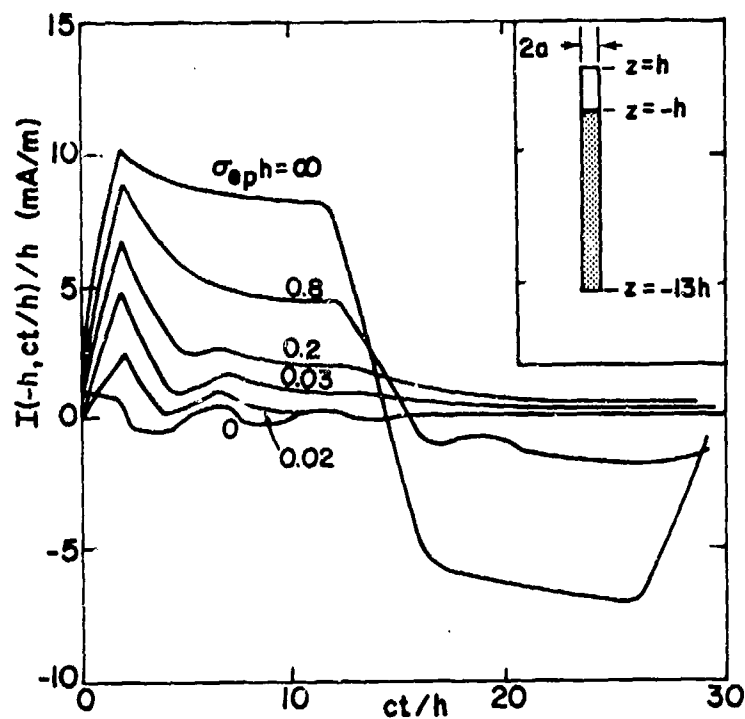


Fig. 49a. Unit-step response of missile nozzle current (broadside incidence, homogeneous-plume model, $\sigma_{em} = \infty$, $E^1 = 1$ V/m).

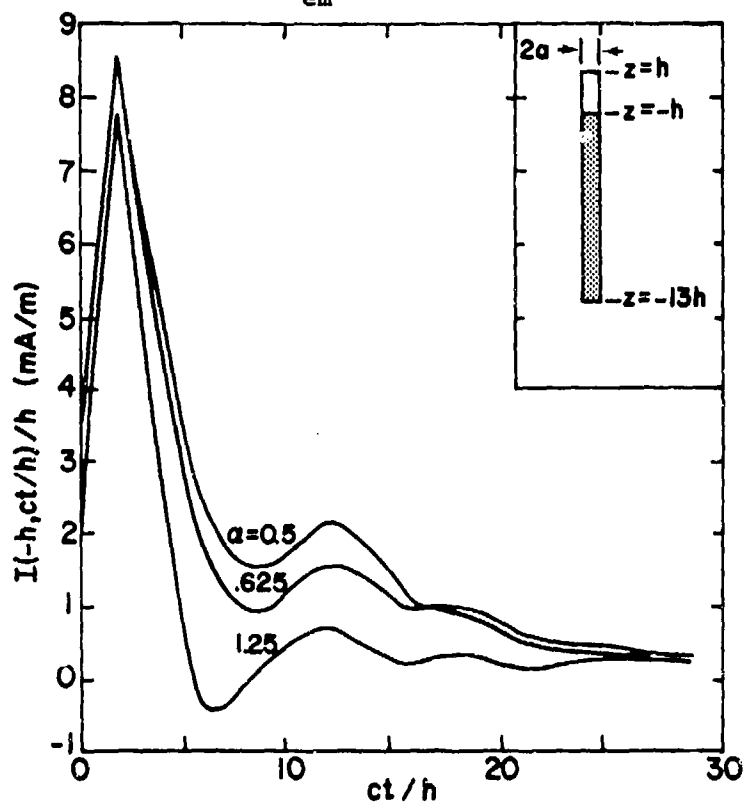


Fig. 49b. Unit-step response of missile nozzle current (broadside incidence, tapered-plume model, $\sigma_{ep} = 0.8e^{\alpha(1+z/h)}$ mhos, $\sigma_{em} = \infty$, $E^1 = 1$ V/m).

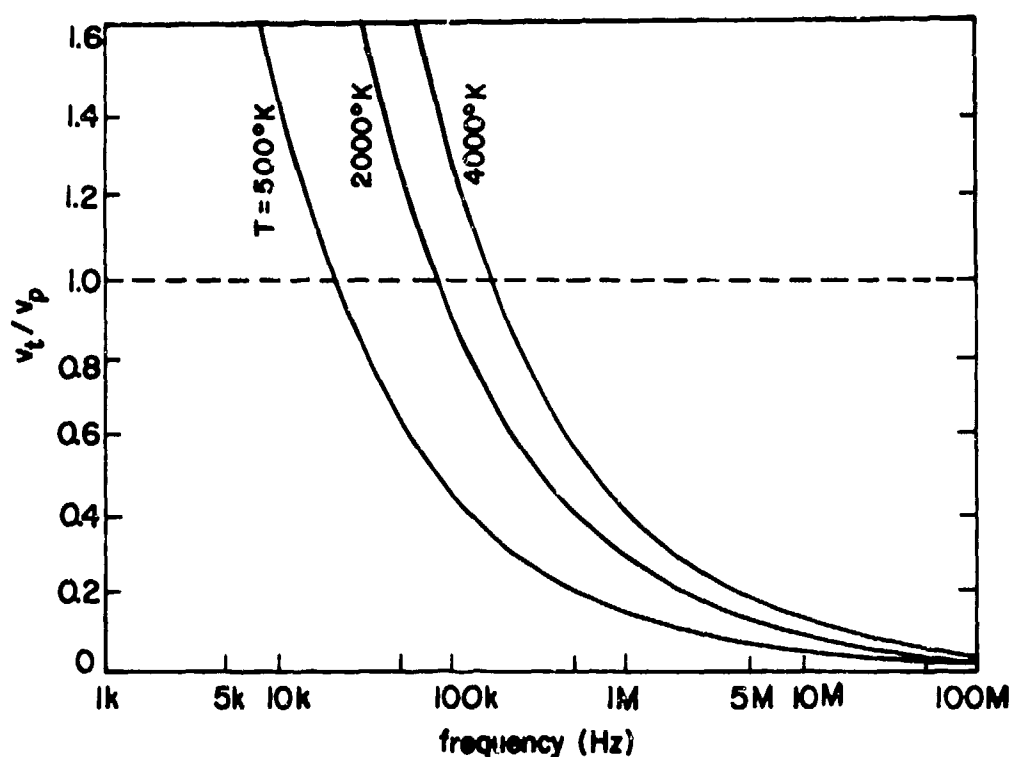


Fig. 50. v_t/v_p versus frequency ($n_e = 10^{18}/\text{m}^3$, $v = 10^9/\text{sec}$).

to that part of the EMP that propagates into the soil. Currents and charges on above-ground conductors are also distinguished by a velocity of propagation close to the speed of light, while their propagation on buried conductors is much slower and accompanied by appreciable attenuation. Because of these differences in propagation characteristics, an above-ground conductor is more sensitive to the direction of incidence of the EMP than a buried conductor.

a. Wire Above Ground

a.1 Early-Time Response

The response of an above-ground conductor before the arrival of ground reflection is the same as the response of an isolated conductor in space (without a ground plane). The current induced on an infinitely long conductor of radius a in free space is [49]

$$I(z,s) = \frac{4E^1}{k'Z_0} \frac{e^{-jkz \cos \theta}}{H_0^{(2)}(k'a)} \quad (85)$$

where $k = \omega/c = -js/c$, $k' = k \sin \theta$, $H_0^{(2)}$ is the Hankel function of the second kind and order zero, E^1 is the magnitude of the incident electric field, θ is the angle between the axis of the wire and the propagation vector of the incident wave, and the magnetic field of the incident wave is perpendicular to the wire. A plot of the current waveform induced by a step-function incident wave is shown in Fig. 51.

a.2 Complete Response for Perfectly Conducting Ground

The current induced on an infinitely long wire of radius a at a height h above a perfectly conducting ground plane by a plane wave whose magnetic vector is perpendicular to the axis of the wire is [50]

$$I(z,s) = \frac{4E^1}{k'Z_0} \frac{(1 - e^{-j2k'h \sin \theta})e^{-jkz \cos \theta}}{H_0^{(2)}(k'a) - H_0^{(2)}(2k'h)J_0(k'a)} \quad (86)$$

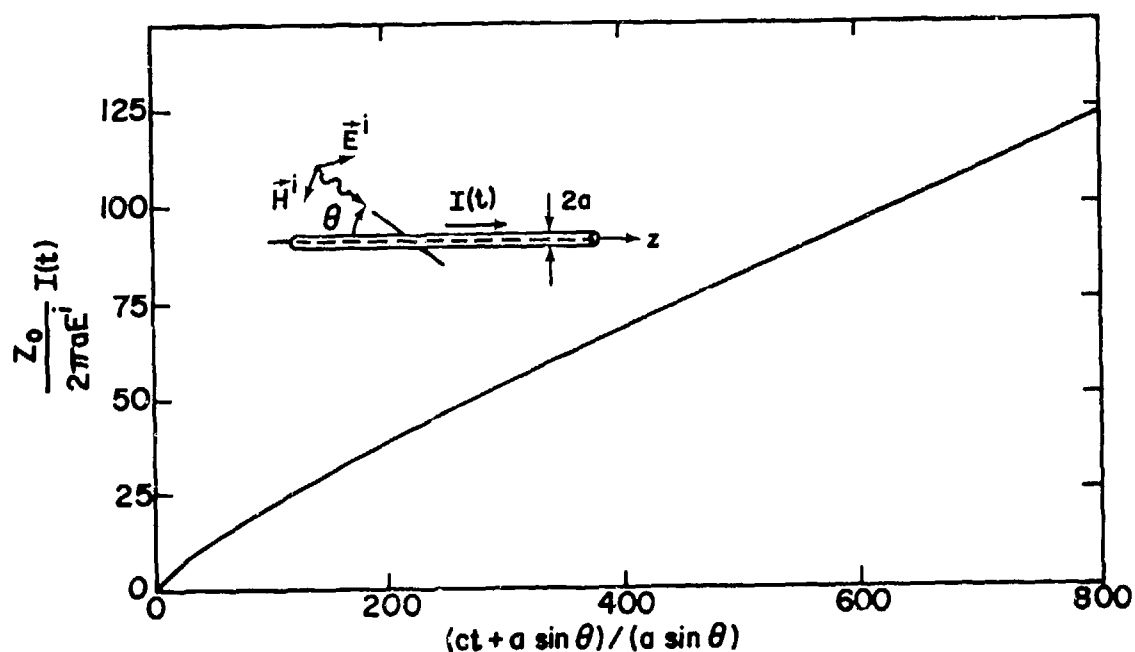


Fig. 51. Current induced on an infinite conductor by a step-function incident wave (transverse magnetic field).

where ϕ is the angle of rotation from the ground plane to the plane defined by the incident propagation vector and wire axis, and J_0 is the Bessel function of the first kind and order zero. The current induced by a step-function incident wave is shown in Fig. 52 for vertical polarization ($\phi = -90^\circ$). Also shown as a dashed curve is the transmission-line solution.

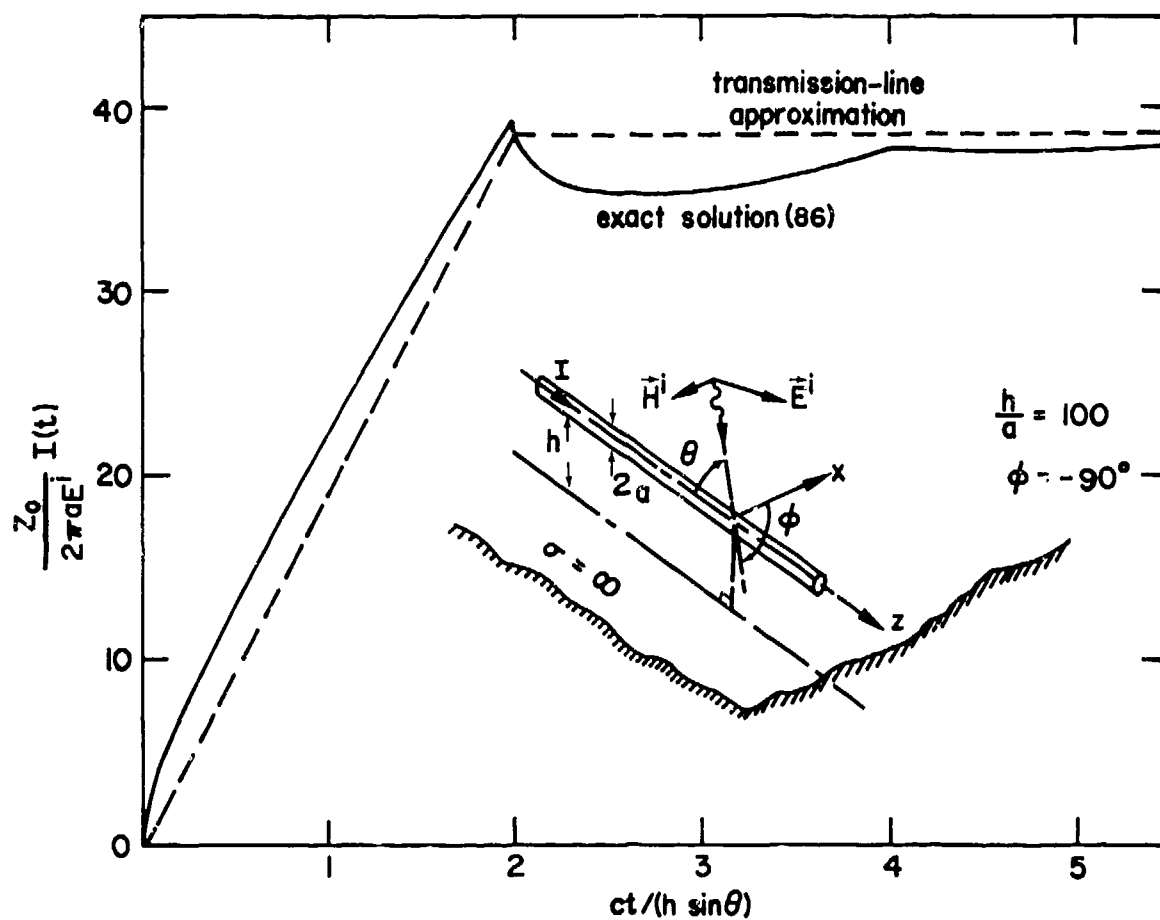


Fig. 52. Current induced on an infinite conductor over a perfectly conducting ground plane by a step-function incident wave (transverse magnetic field).

a.3 Late-Time Response (Imperfect Ground)

An approximation to the late-time current or voltage induced on a long, thin wire parallel to the surface of the earth has been obtained from transmission-line theory [51,52]. Although this approach is valid only when the wire height is small compared to a wavelength ($kh \ll 1$), the method gives surprisingly good results even when this condition is not satisfied (e.g., when $kh \approx 1$).

The current $I(z,s)$ and voltage $V(z,s)^*$ at any point z ($z_1 \leq z \leq z_2$) along the line is given by

$$I(z,s) = [K_1 + P(z)]e^{-\gamma z} + [K_2 + Q(z)]e^{\gamma z} \quad (87)$$

$$V(z,s) = Z_c \{ [K_1 + P(z)]e^{-\gamma z} - [K_2 + Q(z)]e^{\gamma z} \}$$

where K_1 and K_2 are determined from the terminal conditions at $z = z_1$ and $z = z_2$ by

$$K_1 = \rho_1 e^{\gamma z_1} \frac{\rho_2 P(z_2) e^{-\gamma z_2} - Q(z_1) e^{\gamma z_2}}{e^{\gamma(z_2 - z_1)} - \rho_1 \rho_2 e^{-\gamma(z_2 - z_1)}} \quad (88)$$

$$K_2 = \rho_2 e^{-\gamma z_2} \frac{\rho_1 Q(z_1) e^{\gamma z_1} - P(z_2) e^{-\gamma z_1}}{e^{\gamma(z_2 - z_1)} - \rho_1 \rho_2 e^{-\gamma(z_2 - z_1)}}$$

in which ρ_1, ρ_2 are the voltage reflection coefficients at z_1, z_2 respectively. The coupling functions $P(z)$ and $Q(z)$ are related to the total impressed field E_z by

* It is to be noted that V is the voltage of the TEM mode on the transmission line. The total voltage V^t is equal to $V + V^i$, where V^i is the potential directly related to the incident electric field. At the ends of the line, V^i must be taken into account.

$$\begin{aligned}
 P(z) &= \int_{z_1}^z e^{\gamma v} \frac{E_z(v)}{2Z_c} dv \\
 Q(z) &= \int_z^{z_2} e^{-\gamma v} \frac{E_z(v)}{2Z_c} dv
 \end{aligned}
 \tag{89}$$

The coefficients K_1 and K_2 account for the effects of the terminating impedances and the reflections therefrom, while P and Q account for the accumulation of the incremental coupled currents propagating in the positive and negative z directions.

The propagation factor γ and the line characteristic impedance Z_c in (87) for an imperfect ground are given approximately by [53]

$$\begin{aligned}
 \gamma &= jk H(s) \\
 Z_c &= Z_c^0 H(s)
 \end{aligned}
 \tag{90}$$

where Z_c^0 is the characteristic impedance of the line for perfectly conducting ground, and $H(s)$ is given by

$$H(s) = \left[1 + \left(\ln \frac{2h}{a} \right)^{-1} \left(\ln \frac{1 + \sqrt{s\tau_h}}{\sqrt{s\tau_h}} \right) + \frac{1}{\sqrt{s\tau_a}} \right]^{-\frac{1}{2}}
 \tag{91}$$

with $\tau_h = \mu_o g h^2$ and $\tau_a = \mu_w \sigma_w a^2$, σ being the ground conductivity, μ_w and σ_w being the permeability and conductivity of the wire. For typical wire conductivities and radii, the term containing τ_a is significant only at very low frequencies (at 1 MHz this term is only 1-2 percent of the term containing τ_h). Plots of $\text{Re}\{H(s)\}$ and $\text{Im}\{H(s)\}$ with the term containing τ_a neglected are given in Fig. 53 for frequencies between 10 kHz and 100 MHz and representative values of τ_h .

For above ground conductors, the impressed field E_z is related to the incident electric field amplitude E^i by

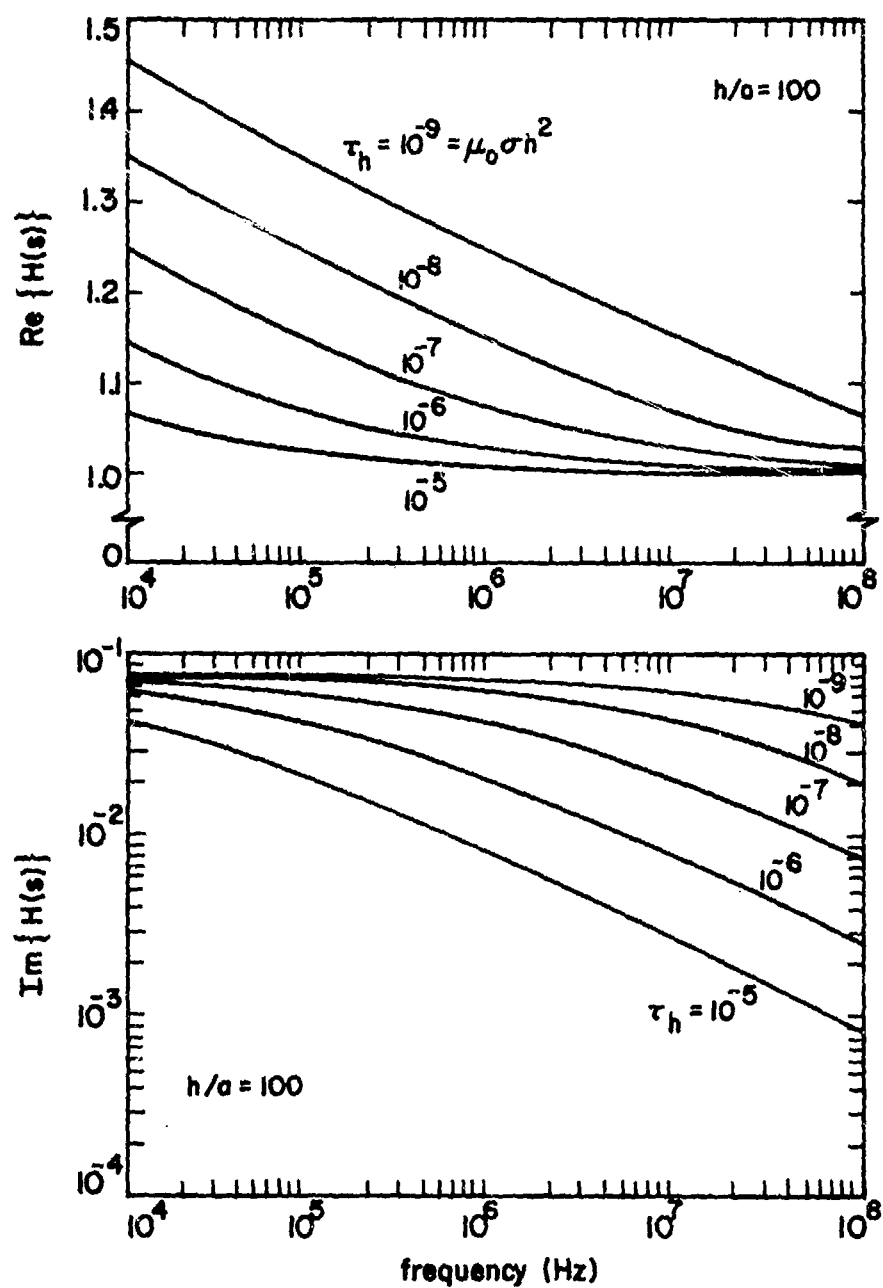


Fig. 53. Normalized propagation and attenuation constants as a function of frequency, line height h , and soil conductivity σ .

$$E_z = E^i (1 + R e^{-j2kh \sin \psi}) e^{-jkz \cos \psi \cos \phi}$$

$$\times \begin{cases} \sin \psi \cos \phi & \text{(vertical polarization)} \\ \sin \phi & \text{(horizontal polarization)} \end{cases}$$

where R is the reflection coefficient at the air/soil interface [54] and ψ and ϕ are the angles of incidence (see Fig. 54). The low-frequency approximation for the reflection coefficient gives

$$1 + R \approx 2 \sqrt{\frac{j\omega\epsilon_0}{\sigma}} (\sin \psi)^{\mp 1}, \quad \text{if } \begin{cases} \sigma \gg \omega\epsilon \\ \sigma \gg \omega\epsilon_0 / \sin^2 \psi \end{cases} \quad (92)$$

in which the upper sign is to be used for vertical polarization and the lower sign for horizontal polarization of the incident field. In the case of

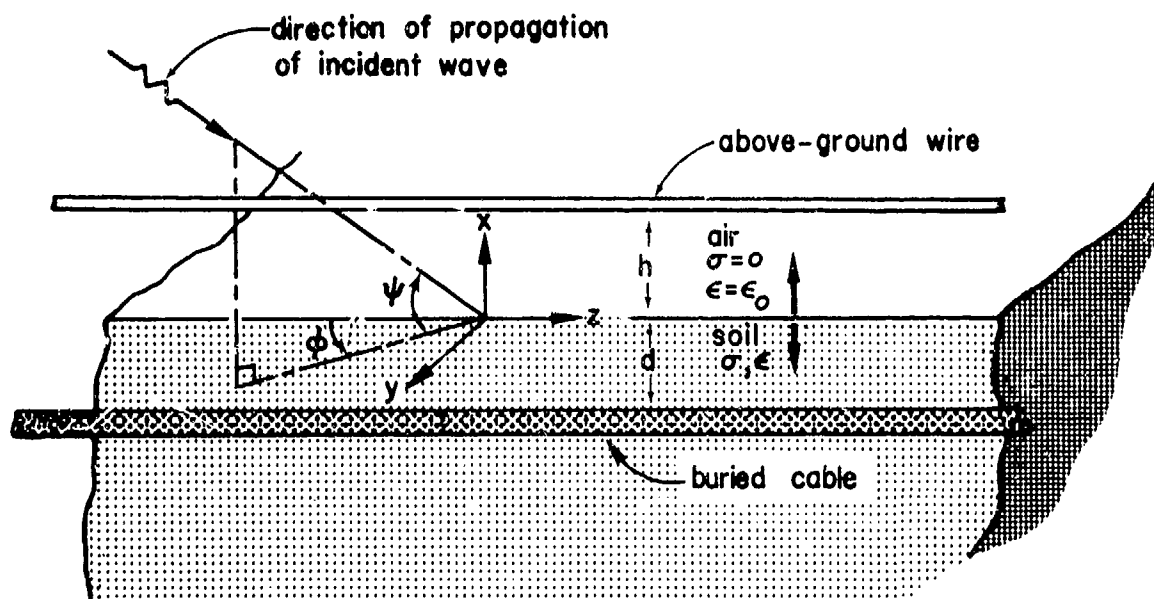


Fig. 54. Coordinates for angle of arrival of incident wave.

horizontal polarization the incident electric vector is parallel to the air/soil interface, whereas in the vertical polarization case the incident electric vector lies in the plane that contains the propagation vector and is perpendicular to the air/soil interface.

a.4 Semi-Infinite Wire (Short-Circuit Current)

With $z_1 = -\infty$ and $z_2 = 0$, the short-circuit current at $z = 0$ is

$$I_{sc}(0,s) \approx \frac{E_0 c D(\psi, \phi, s)}{Z_c} \left[\frac{1 - e^{-st_0}}{s} + 2\sqrt{\tau_e} \frac{e^{-st_0}}{\sqrt{s}} (\sin \psi)^{\mp 1} \right] \quad (93)$$

where $t_0 = (2h \sin \psi)/c$ and $\tau_e = \epsilon_0/\sigma$, and it has been assumed that $\gamma \approx s/c$. The function $D(\psi, \phi, s)$ is a directivity function given by

$$D(\psi, \phi, s) = \frac{1}{H(s) - \cos \psi \cos \phi} \begin{cases} \sin \psi \cos \phi \\ \sin \phi \end{cases} \quad (94)$$

where the upper term applies to vertical, and the lower term to horizontal, polarization, and $H(s)$ is given by (91).

The product $Z_c I_{sc}(0,s)$ calculated from (93) is shown in Fig. 55 as a function of normalized frequency with soil conductivity as a parameter for vertically polarized incident wave.

For a perfectly conducting ground ($\sigma = \infty$, $\tau_e = 0$) the second term inside the square bracket in (93) vanishes, and $D(\psi, \phi)$ and Z_c are then independent of frequency. This case is shown in Fig. 55 as a dashed curve.

For an impulse incident field $E_0 \delta(t)$, the time-domain current in the wire is

$$\frac{Z_c}{E_0 c D(\psi, \phi)} I_{sc}(0,t) = \begin{cases} 1 & 0 \leq t < t_0 \\ 2\sqrt{\frac{\tau_e}{\pi t_0}} (\sin \psi)^{\mp 1} \frac{1}{\sqrt{t/t_0 - 1}}, & t > t_0 \end{cases} \quad (95)$$

and for a step-function incident field, the time-domain current is

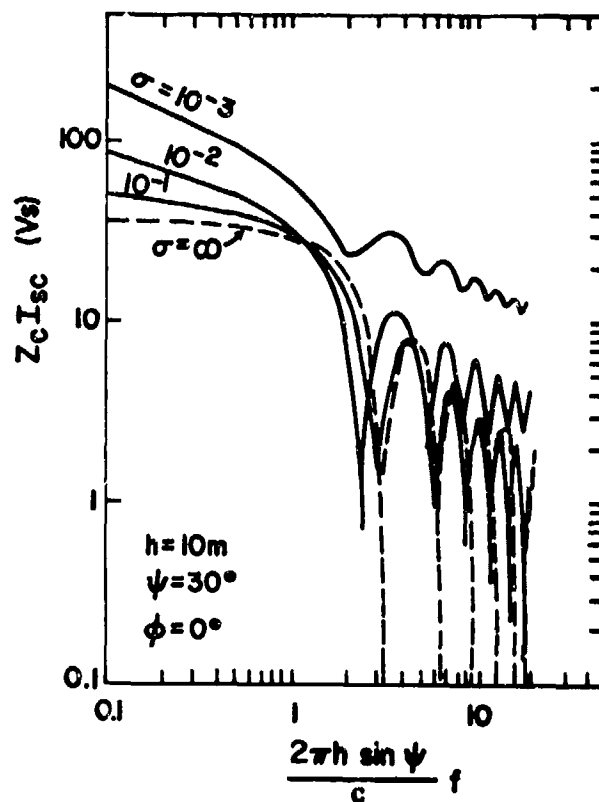


Fig. 55. Short-circuit current in above-ground wire for vertically polarized incident field.

$$\frac{Z_c}{E^1_{ct_0} D(\psi, \phi)} I_{sc}(0, t) = \begin{cases} t/t_0 & 0 \leq t \leq t_0 \\ 1 + 4 \sqrt{\frac{\tau_e}{\pi t_0}} (\sin \psi)^{\mp 1} \sqrt{t/t_0 - 1}, & t \geq t_0 \end{cases} \quad (96)$$

where Z_c and $D(\psi, \phi)$ are assumed to be independent of frequency. As before, the upper sign of the exponent of $\sin \psi$ applies to vertical, and the lower to horizontal polarization of the source field. Plots of the impulse and step function responses of the wire current are shown in Fig. 56 for nominal values of soil conductivity, wire height, and elevation angle ψ of incidence.

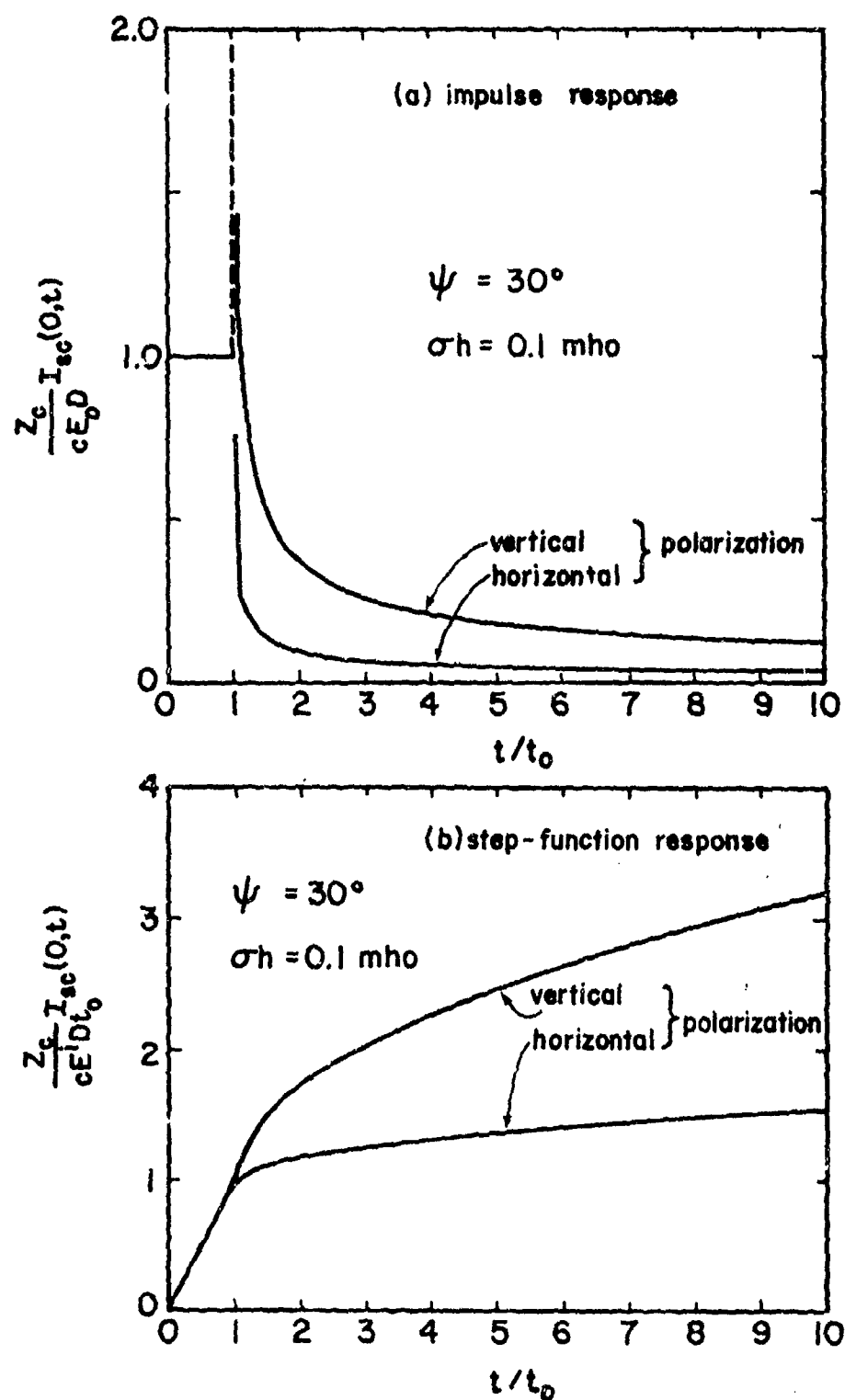


Fig. 56. Short-circuit current induced at the end of a semi-infinite above-ground wire by (a) an impulse and (b) by a step-function incident wave.

For an exponential incident pulse described by $E^1 \exp(-t/\tau)$, the short-circuit current I_{sc} is given by

$$\frac{Z_c}{E^1 c \tau D(\psi, \phi)} I_{sc}(0, t) = \begin{cases} 1 - e^{-t/\tau}, & (0 \leq t \leq t_0) \\ (e^{t_0/\tau} - 1) e^{-t/\tau} \\ + 2 \sqrt{\frac{\tau_e}{\tau}} (\sin \psi) \mp 1 e^{-t'/\tau} \frac{2}{\sqrt{\pi}} \int_0^{\sqrt{t'/\tau}} e^{u^2} du, & (t \geq t_0) \end{cases} \quad (97)$$

where $t' = t - t_0$. This waveform is shown in Fig. 57 for both polarizations of the incident field and representative values of $\sigma\tau$.

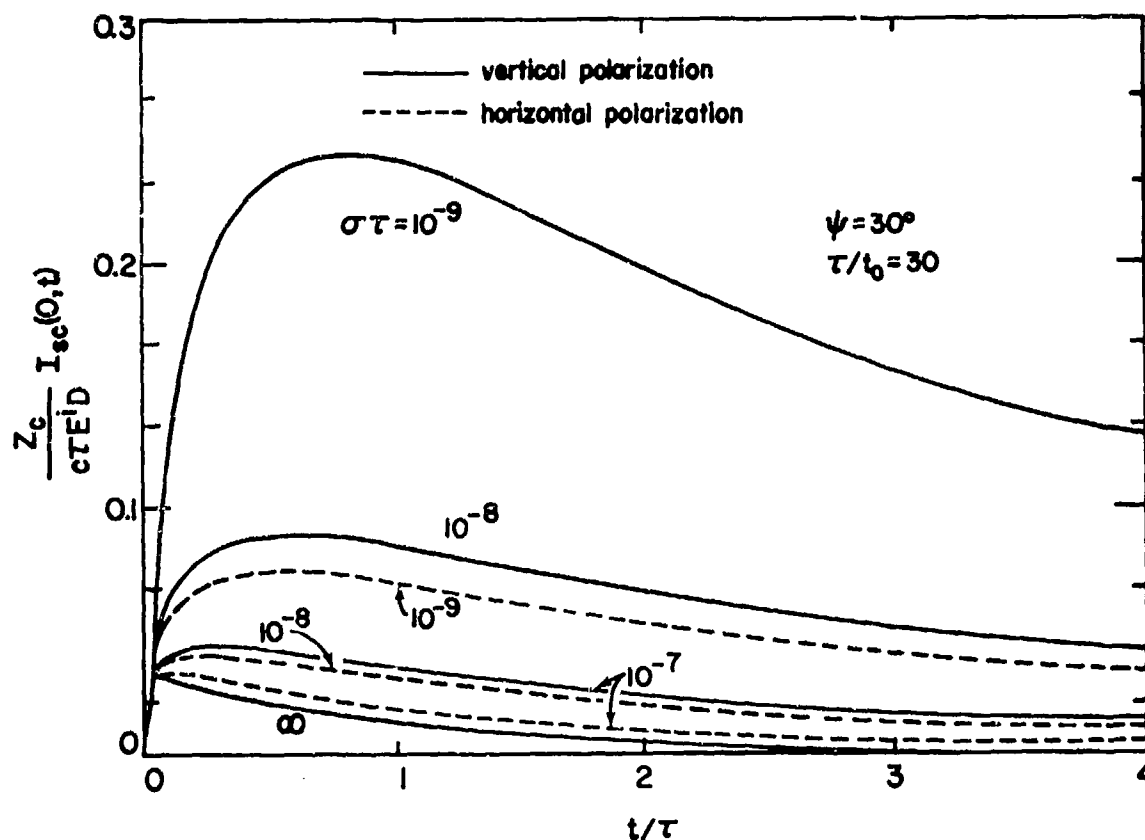


Fig. 57. Short-circuit current induced at the end of a semi-infinite above-ground wire by an exponential pulse $E^1 \exp(-t/\tau)$.

b. Buried Conductors

For buried cables the high frequencies are attenuated more severely by the soil than the low frequencies, and for cables with cylindrical shields the shield limits the high-frequency content of the energy penetrating into the internal conductors. Therefore, a low-frequency approach is often adequate for buried shielded cables and the transmission-line equations can be used as a starting point.

The impressed field at the buried cable is

$$E_z \approx 2E^i \sqrt{s\tau_e} e^{-\sqrt{s\tau_d}d} e^{-jk''z} D(\psi, \phi) \quad (98)$$

where $k'' = k \cos \psi \cos \phi$, $\tau_e = \epsilon_0/\sigma$, $\tau_d = \mu\sigma d^2$, d is the depth of burial and $D(\psi, \phi)$ is a function whose value depends on the polarization and angle of incidence of the incident field (Fig. 54)

$$D(\psi, \phi) = \begin{cases} \cos \phi \sin \psi & \text{(vertical polarization)} \\ \sin \phi & \text{(horizontal polarization)} \end{cases} \quad (99)$$

b.1 Current in Long Buried Cables

The current induced at any point z along an infinitely long buried cable is

$$I(z, s) \approx E_z / Z'_s \quad (100)$$

where $Z'_s = Z_c \gamma$. Eq.(100) is the classical form for the current induced in an infinitely long buried cable; it also applies to points far from the ends of a cable of finite length.

The impedance Z'_s in (100) is the soil impedance per unit length of the cable given by

$$Z'_s \approx \frac{\omega\mu}{8} + j\omega \frac{\mu}{2\pi} \ln \left(\frac{\sqrt{2}\delta}{\Gamma a} \right), \quad (|\gamma a| \ll 1) \quad (101)$$

when the soil is of infinite extent. In this expression, a is the cable radius, Γ is the exponential of Euler's constant ($\Gamma = 1.781 \dots$), and δ is the skin depth of the soil. The impedance of a conductor at the air-soil interface (the worst deviation from the form above) is approximately the same as the impedance at an infinite depth [53]. In addition, for most practical cases one has

$$\frac{\omega \mu}{8} \ll \omega L'_s = \omega \frac{\mu}{2\pi} \ln \left(\frac{\sqrt{2} \delta}{\Gamma a} \right) \quad (102)$$

so that the approximation $Z'_s \approx j\omega L'_s$ can be used.

The internal impedance of metal cables is usually very small compared to the soil impedance Z'_s except at very low frequencies (i.e., a few hundred hertz).

For an insulated cable the impedance per unit length is essentially the same as for a bare cable. However, the insulation has a major effect on the shunt admittance per unit length Y' and hence on the propagation factor $\gamma = \sqrt{Z'Y'}$.

Eq.(100) can be written in the form

$$I(z,s) \approx \frac{(\pi \delta^2) \sigma E_z}{j \ln[\sqrt{2} \delta / (\Gamma a)]} \quad (103)$$

The logarithm term is rather insensitive to frequency and soil conductivity. The product $\pi \delta^2$ is the cross-section area of a cylinder of radius δ , and σE_z is the current density in the soil in the absence of the cable. Eq.(103) therefore states that the current induced in the cable is roughly proportional to the current that would flow in a cylinder of soil one skin-depth in radius if the conductor were removed. For typical communication-cable sizes and poor soil conductivities, the \ln -term has a value of about 10.

In more conventional form, the current far from the ends of a long cable is approximately given by

$$\frac{L'_s}{\sqrt{\tau} E^i_D(\psi, \phi)} I(z, s) \approx \frac{e^{-\sqrt{s}\tau_d}}{\sqrt{s}} \quad (104)$$

If L'_s is assumed to be independent of frequency, the current induced by an impulse $E_0 \delta(t)$ is

$$\frac{L'_s}{\sqrt{\tau} E_0 D(\psi, \phi)} I(z, t) \approx \frac{1}{\sqrt{\pi t}} e^{-\tau_d/(4t)} \quad (105)$$

and the current induced by a step field $E^i_u(t)$ is

$$\frac{L'_s}{\sqrt{\tau} E^i_D(\psi, \phi)} I(z, t) \approx 2\sqrt{\frac{t}{\pi}} e^{-\tau_d/(4t)} \quad (106)$$

The normalized induced currents for the impulse and step function excitations are shown in Fig. 58.

The cable current induced by an exponential incident field of the form $E^i \exp(-t/\tau)$ is

$$\frac{L'_s}{\sqrt{\tau\tau} E^i_D(\psi, \phi)} I(z, s) \approx \frac{e^{-\sqrt{s}\tau_d}}{\sqrt{s\tau} (s + 1/\tau)} \quad (107)$$

The time-domain current waveform is then [55]

$$\frac{L'_s}{\sqrt{\tau\tau} E^i_D(\psi, \phi)} I(z, t) \approx e^{-t/\tau} \frac{2}{\sqrt{\pi}} \int_0^{\sqrt{t/\tau}} e^{-p/u^2} e^{u^2} du \quad (108)$$

where $p = \tau_d/(4\tau) = \mu\sigma d^2/(4\tau)$. The normalized current waveform is plotted in Fig. 59 for several values of the depth parameter p .

b.2 Parametric Dependence

It can be seen that, except for the logarithmic dependence in L'_s , the induced current in (108) is

$$I(t, z) \propto E^i \sqrt{\tau/\sigma} \quad (109)$$

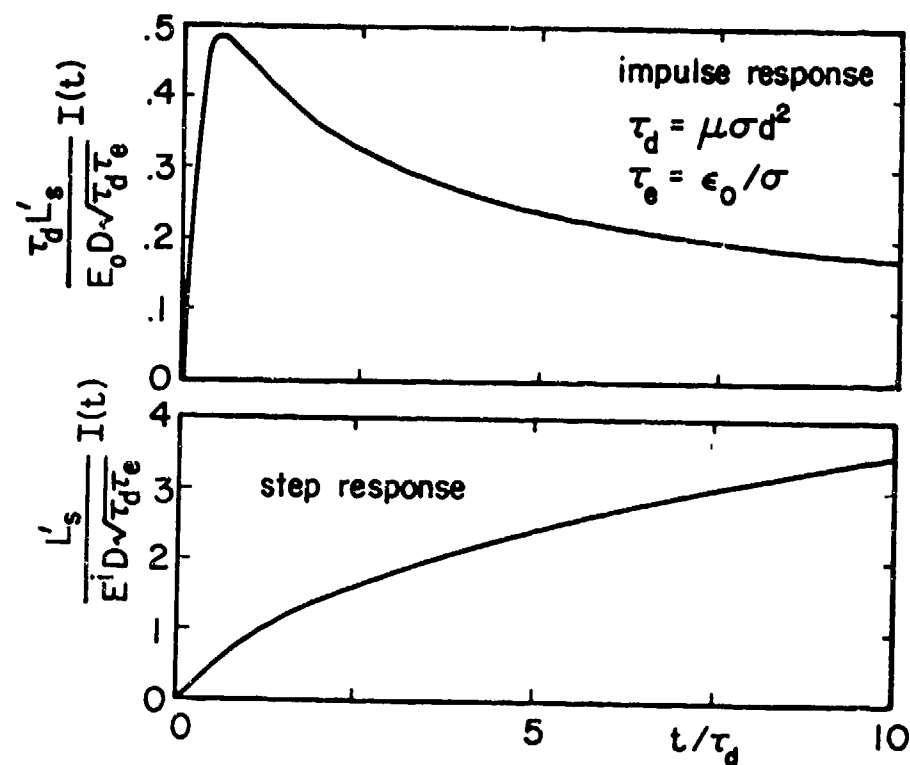


Fig. 58. Normalized current on long buried cable for impulse and step incident source fields.

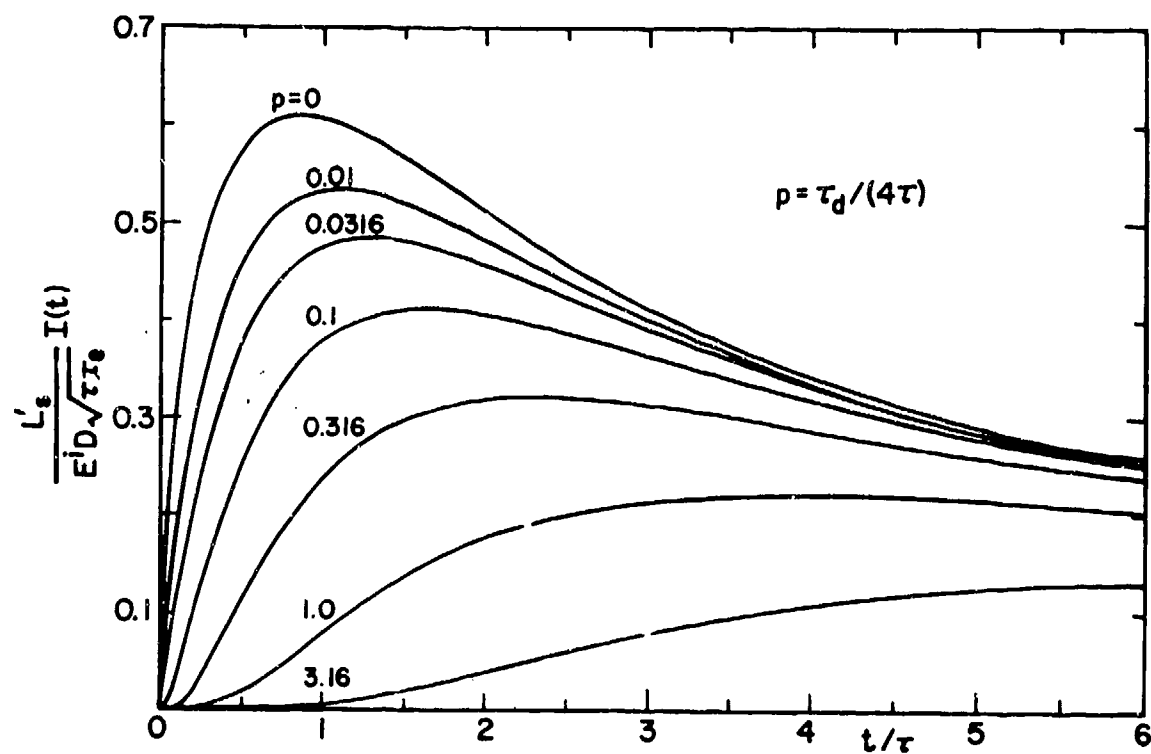


Fig. 59. Normalized current waveform on long buried cables for various values of the depth parameter p for exponential pulse excitation $E^1 \exp(-t/\tau)$.

A plot of the peak current as a function of soil conductivity with the exponential time constant τ as a parameter is given in Fig. 60. The peak current is normalized to the peak incident field E^i , and the value of $\ln(\sqrt{2} \delta/\Gamma a) = 10$ is used.

The induced current also depends on the angles of incidence of the wave through the directivity function $D(\psi, \phi)$ of (99).

b.3 Current Near the End of a Conductor

At the end of a semi-infinite cable the current is the same as the current far from the ends if the cable end is short circuited, half the current far from the ends if the cable end is terminated in its characteristic impedance, and zero if the cable end is open circuited.

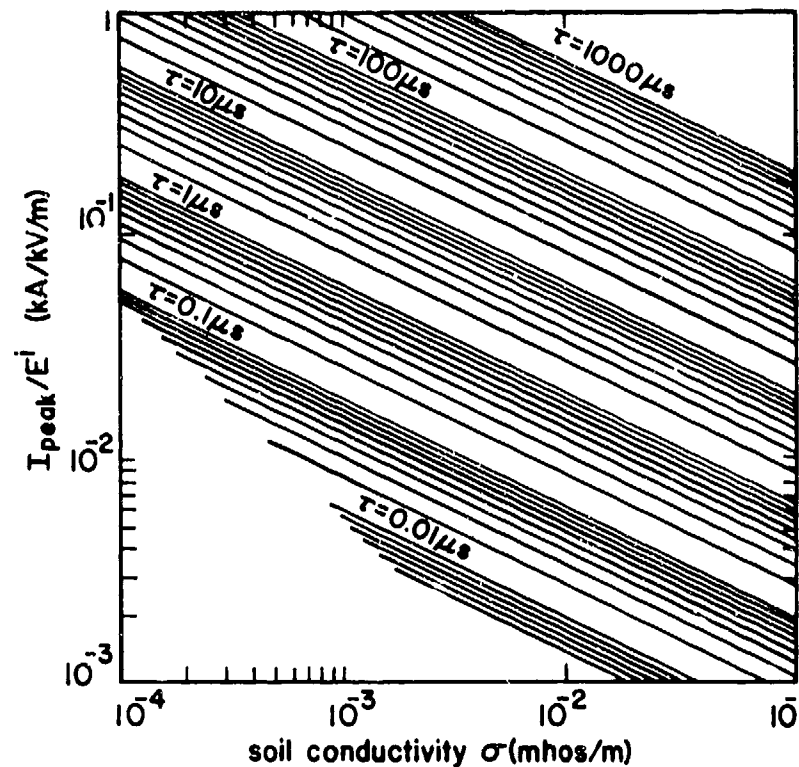


Fig. 60. Peak cable current as a function of soil conductivity for an incident exponential pulse, $E^i \exp(-t/\tau)$ and $D(\psi, \phi) = 1$.

The current near the end of an open-circuited cable is

$$I(z, s) \approx \frac{E_z}{Z_s} (1 - e^{-\gamma z}) \quad (110)$$

The current induced by an exponential pulse of incident field is

$$\frac{L'_s}{\sqrt{\tau\tau} e^{1D(\psi, \phi)}} I(z, s) \approx \frac{e^{-\sqrt{s\tau}d} - e^{-\sqrt{s\tau}dz}}{\sqrt{s\tau} (s + 1/\tau)} \quad (111)$$

where $\tau_{dz} = \mu\sigma(d+z)^2$. The current waveform is then

$$\frac{L'_s}{\sqrt{\tau\tau} e^{1D(\psi, \phi)}} I(z, t) \approx \mathfrak{J}(t/\tau, p_d) - \mathfrak{J}(t/\tau, p_{dz}) \quad (112)$$

where $p_d = \tau_d/(4\tau)$, $p_{dz} = \tau_{dz}/(4\tau)$ and

$$\mathfrak{J}(t/\tau, p) = e^{-t/\tau} \frac{2}{\sqrt{\pi}} \int_0^{\sqrt{t/\tau}} e^{-p/u^2} e^{u^2} du \quad (113)$$

which is plotted in Fig. 59. The waveform near the end of an open-circuited cable as calculated from (112) is shown in Fig. 61 for $p_d = 0$ (depth of burial $d = 0$) and several values of p_{dz} .

2.1.3 PENETRATION

In this section engineering formulas and data will be presented for three different electromagnetic penetration mechanisms: (a) penetration via deliberate antennas, (b) transmission through apertures, and (c) diffusion through imperfectly conducting walls. These penetration mechanisms also occur at other shielding layers of the topological model, and hence most data presented here apply to Chaps. 2.2 - 2.4.

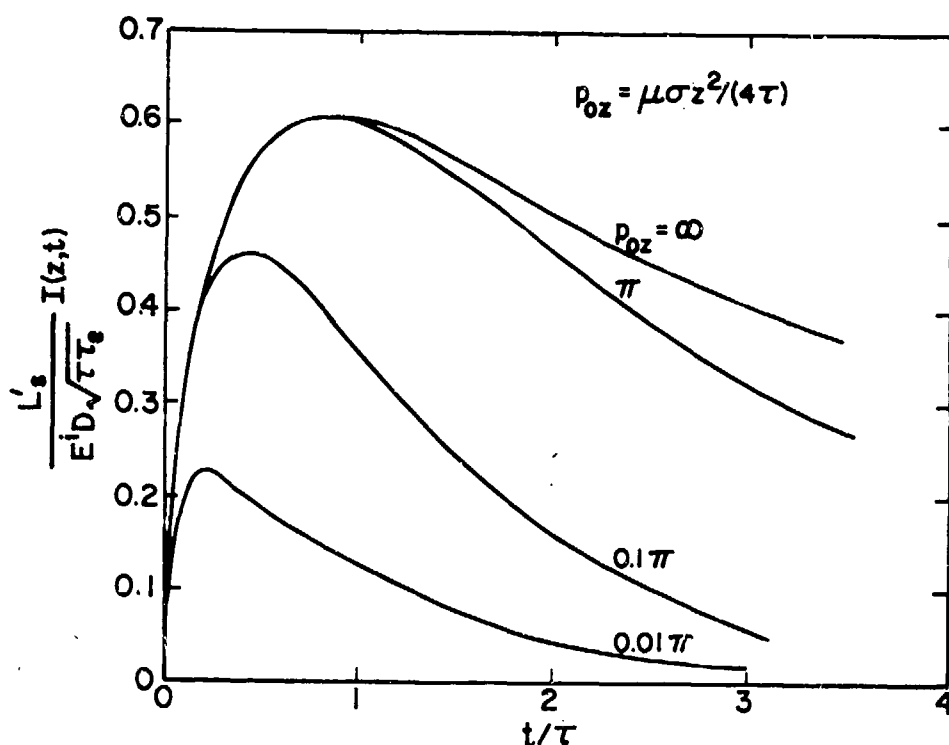


Fig. 61. Waveform of the cable current near the end when cable end is open-circuited for an exponential pulse excitation.

2.1.3.1 Antennas

Antennas are designed to transmit and receive electromagnetic energy within specified frequency bands, and aircraft antennas are no exception. Clearly, then, antennas are of major concern in the assessment of EMP vulnerability of a system such as an aircraft. The nuclear EMP is usually assumed to have a broad frequency spectrum as well as a high field strength. These characteristics of the EMP make it necessary to analyze the response of an antenna not only within its normal operating band but also outside this band, where the antenna's behavior is usually of no concern.

The response of an antenna is completely characterized by its Thévenin or Norton equivalent circuit at the antenna's input connector. Between the connector and the antenna gap there can exist many different kinds of matching or compensating networks to tune the antenna impedance to a desirable level.

at the connector. In Fig. 62a the internal network is a matching network which may comprise transmission lines, baluns, hybrid circuits, transformers or lumped elements. The external network consists only of the antenna's radiating element, which is characterized by the two parameters in the Thévenin or Norton equivalent circuit looking outward from the antenna gap. The aim is to calculate V_{oc} (or I_{sc}) and Z_{in} (or Y_{in}) of Fig. 62b, from the knowledge of which one can calculate the voltage and current at any linear or nonlinear load attached to the connector. For antennas whose maximum linear dimensions are small compared to the local radii or curvature, V_{oc} (or I_{sc}) can be factored into a product of effective height (or area) and the local charge (or current) density. The effective height or area is calculated by assuming an infinite ground plane, while the local charge or current density is to be obtained from the solution of the external interaction problem involving the aircraft in the absence of the antenna under consideration.

There are many ways of classifying antennas. One is to group them according to the function of the subsystem to which the antenna belongs.

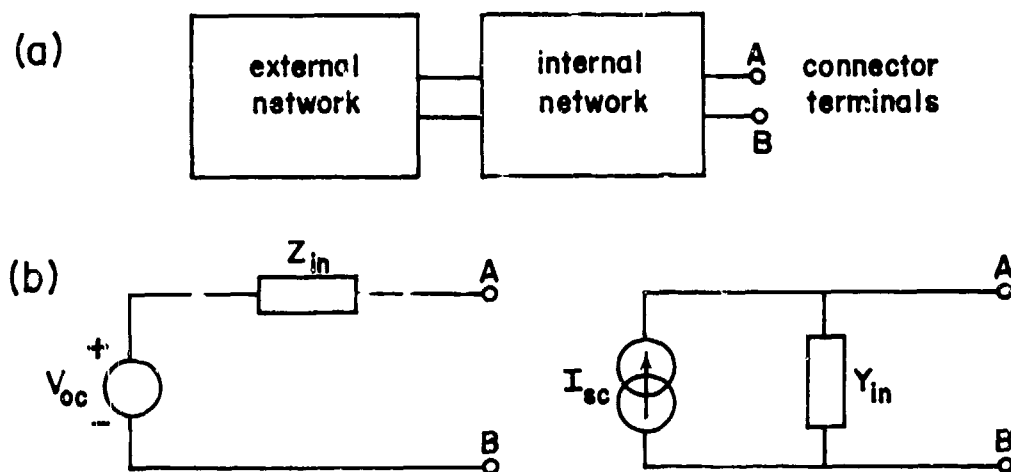


Fig. 62. Schematic diagram and equivalent circuits of an antenna.

This classification naturally leads to navigational, communication, ECM, radar antennas, and so on. This grouping of antennas is particularly useful when discussing antenna applications. Another widely used method of classification is based on the frequency band in which the antenna operates. This method leads to VLF, LF, HF, VHF, UHF, L-band, X-band antennas, and so on [56]. A third classification groups the antennas according to their physical structure, such as blades, loops, slots, wires, etc.; this latter classification will be adopted in this section.

This section deals only with aircraft communication and navigation antennas. Among the most notable omissions are the ECM and ECCM antennas. More detailed analyses of the antennas discussed in this section as well as other antennas can be found in [57,58].

2.1.2.1.1 Blade Antennas

This type of antenna is basically an antenna element built into a blade (Fig. 63) or aerodynamic vane mounted externally on the aircraft fuselage. The antenna height ranges from about 6 cm (L-band) to 45 cm (VHF). A mathematical model for this type of antenna is a half ellipsoid resting on a perfectly conducting ground plane [2].

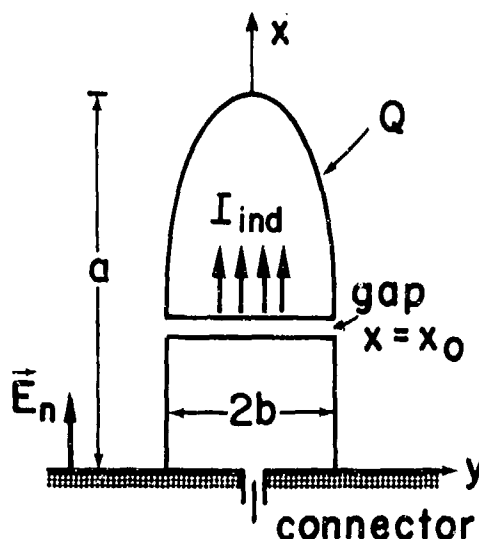


Fig. 63. Illustration of a typical blade antenna.

The two most convenient parameters for describing the external network of Fig. 62a are the induced short-circuit current I_{ind} and the antenna admittance Y_a at the gap (Fig. 63). From the continuity equation one has $I_{ind} = sQ(x_0)$, $Q(x_0)$ being the total charge collected by the portion of the antenna above $x = x_0$. For wavelengths greater than about four times the antenna height, Q can be obtained from the solution of the electrostatic problem of a perfectly conducting ellipsoid immersed in a uniform external field E_n , which is related to the surface charge density ρ on the conducting plane by $E_n = \rho/\epsilon_0$. If Q is expressed in terms of the displacement current density $s\epsilon_0 E_n$, the equivalent induction area A_{eq} may be introduced through the relation $I_{ind} = s\epsilon_0 E_n A_{eq}$. If one prefers to speak of the induced open-circuit voltage V_{ind} , the effective height h_e will appear through $V_{ind} = h_e E_n$. Since $I_{ind} = Y_a V_{ind}$ and since Y_a is basically given by sC_a one arrives at the relation

$$\epsilon_0 A_{eq} = h_e C_a \quad (114)$$

where C_a is the antenna capacitance.

For a half ellipsoid symmetrically resting on a perfectly conducting ground plane with semi-axes a, b, c (see Fig. 63 where c is the semi-axis along the z -direction), the equivalent area A_{eq} is given by [2]

$$A_{eq}(x_0) = \pi b c N_a (1 - x_0^2/a^2) \quad (115)$$

where $(a > b > c)$

$$N_a = \frac{(a^2 - b^2)\sqrt{a^2 - c^2}}{abc} \frac{1}{F(\varphi/\alpha) - E(\varphi/\alpha)} \quad (116)$$

F and E are respectively the incomplete elliptic integrals of the first and second kinds [7] and

$$\begin{aligned} \varphi &= \arcsin \sqrt{1 - c^2/a^2} \\ \alpha &= \arcsin \sqrt{(a^2 - b^2)/(a^2 - c^2)} \end{aligned} \quad (117)$$

When $c \ll b$, the ellipsoid degenerates into an elliptic disk or blade and consequently (115) is simplified to

$$A_{eq}(x_0) = \frac{\pi abm}{\sqrt{1-m}} \frac{1}{K(m) - E(m)} (1 - x_0^2/a^2) \quad (118)$$

where K and E are complete elliptic integrals of the first and second kinds, and $m = 1 - b^2/a^2$. Table 13 gives the values of the normalized equivalent area of a blade for various b/a ratios.

TABLE 13. NORMALIZED EQUIVALENT AREA OF AN ELLIPTIC DISK (BLADE ANTENNA)

$\frac{b}{a}$	$\frac{A_{eq}(0)}{\pi ab}$	$\frac{A_{eq}(0)}{\pi ab}$	$\frac{a}{b}$
10^{-3}	137.0980	1.0000	10^{-3}
10^{-2}	20.0328	1.0002	10^{-2}
0.1	3.6945	1.0112	0.1
0.2	2.4420	1.0324	0.2
0.3	1.9890	1.0581	0.3
0.4	1.7376	1.0864	0.4
0.5	1.5865	1.1162	0.5
0.6	1.4836	1.1469	0.6
0.7	1.4091	1.1782	0.7
0.8	1.3527	1.2100	0.8
0.9	1.3087	1.2413	0.9
1.0	1.2732	1.2732	1.0

For the calculation of Y_a in the Norton equivalent circuit across the antenna gap (Fig. 63), one considers a cylindrical antenna with equivalent radius equal to about one-fourth the averaged width of the blade [56]. Then the impedance sum formula for an asymmetrically driven antenna can be used, with proper account taken of the presence of the ground plane [59].

a. UHF Communication Antennas

A very common UHF antenna is shown in Fig. 64a, and Fig. 64b is the corresponding equivalent circuit in which L is the inductance of the short stub. This stub not only provides a dc path for lightning protection between the upper part of the antenna and the aircraft skin but also mechanically fastens the two parts of the antenna. The different sections of the transmission lines and the end capacitance C_e are for tuning purposes, so that within the operating frequency band (225 - 400 MHz) the VSWR is about 2:1 at the input connector. The capacitance C_p accounts for the two ends of the gap, and Y_a and I_{ind} are calculated as discussed above. Figs. 65a and 65b show the frequency variations of Z_{in} and h_e together with some measured data for Z_{in} .

b. UHF/L-Band Antennas

Figs. 66a and 66b depict all the electrical connections of a typical UHF/L-band antenna (operating in the frequency regimes of 225 - 400 MHz for the UHF-band and 0.95 - 1.22 GHz for the L-band). The total antenna height is about 20 cm, which is roughly equal to a quarter wavelength at the mid-frequency of the UHF-band. The equivalent circuit is given by Fig. 66c. The characteristic features of this antenna are the L-band choke and the two gaps. At frequencies below UHF the choke is ineffective, and hence the top and the mid-sections can be treated as one piece of metal. The external circuit elements Y_a and I_{ind} correspond to an antenna with a gap at about one-third the antenna's height from the base. Within the L-band the choke acts like a quarter-wavelength transmission line, and so the top section need not be considered. Within this frequency band Y_a and I_{ind} correspond to an antenna with a gap at one-half the antenna's height from the base, while other elements in Fig. 66c remain unchanged. What is not shown in Fig. 66a is the diplexer connected to terminals A,B via

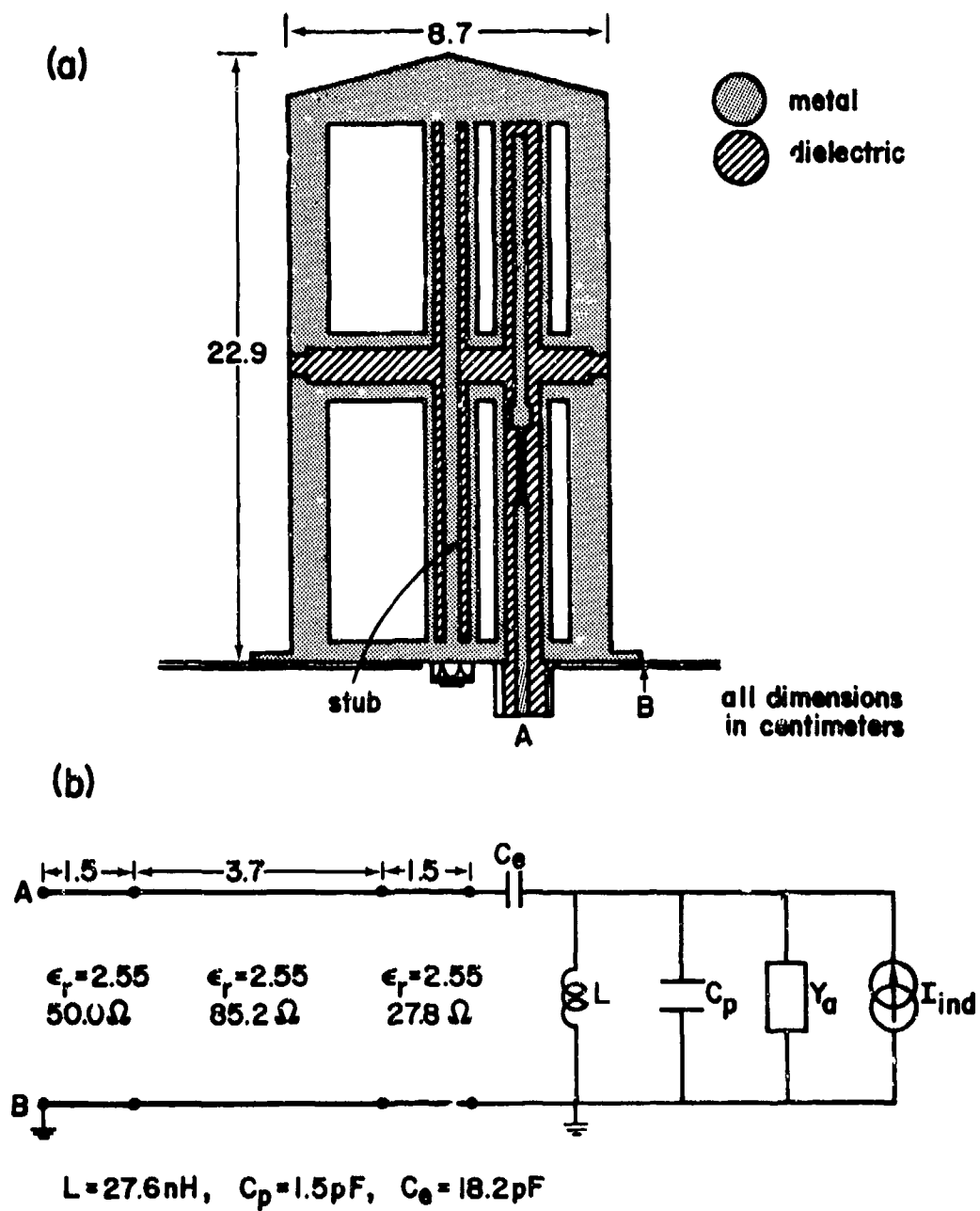


Fig. 64. Schematic diagram and equivalent circuit of the UHF Communication Antenna AT 1076.

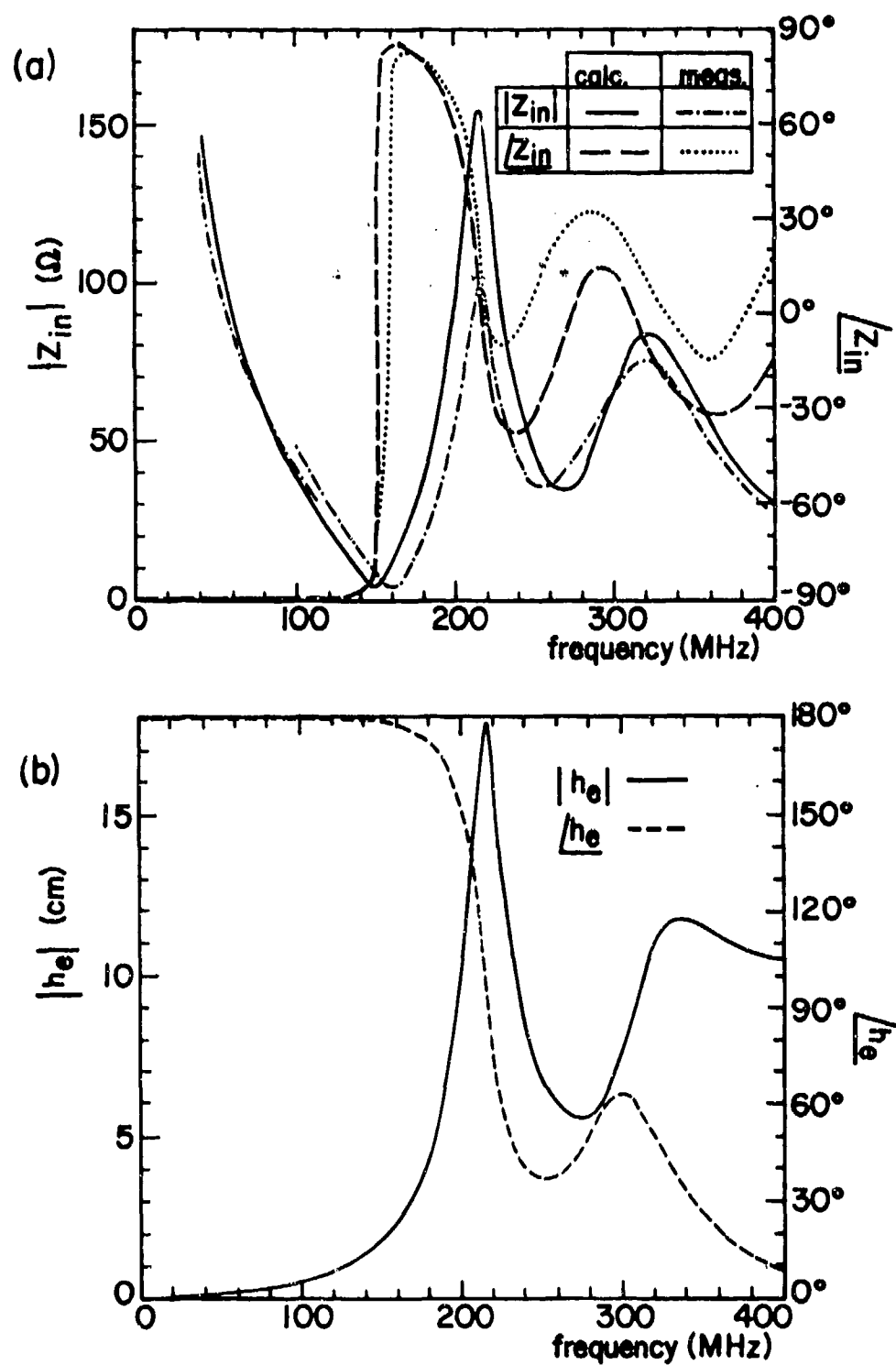


Fig. 65. Input impedance and effective height of the UHF Communication Antenna AT 1076 (225 - 400 MHz).

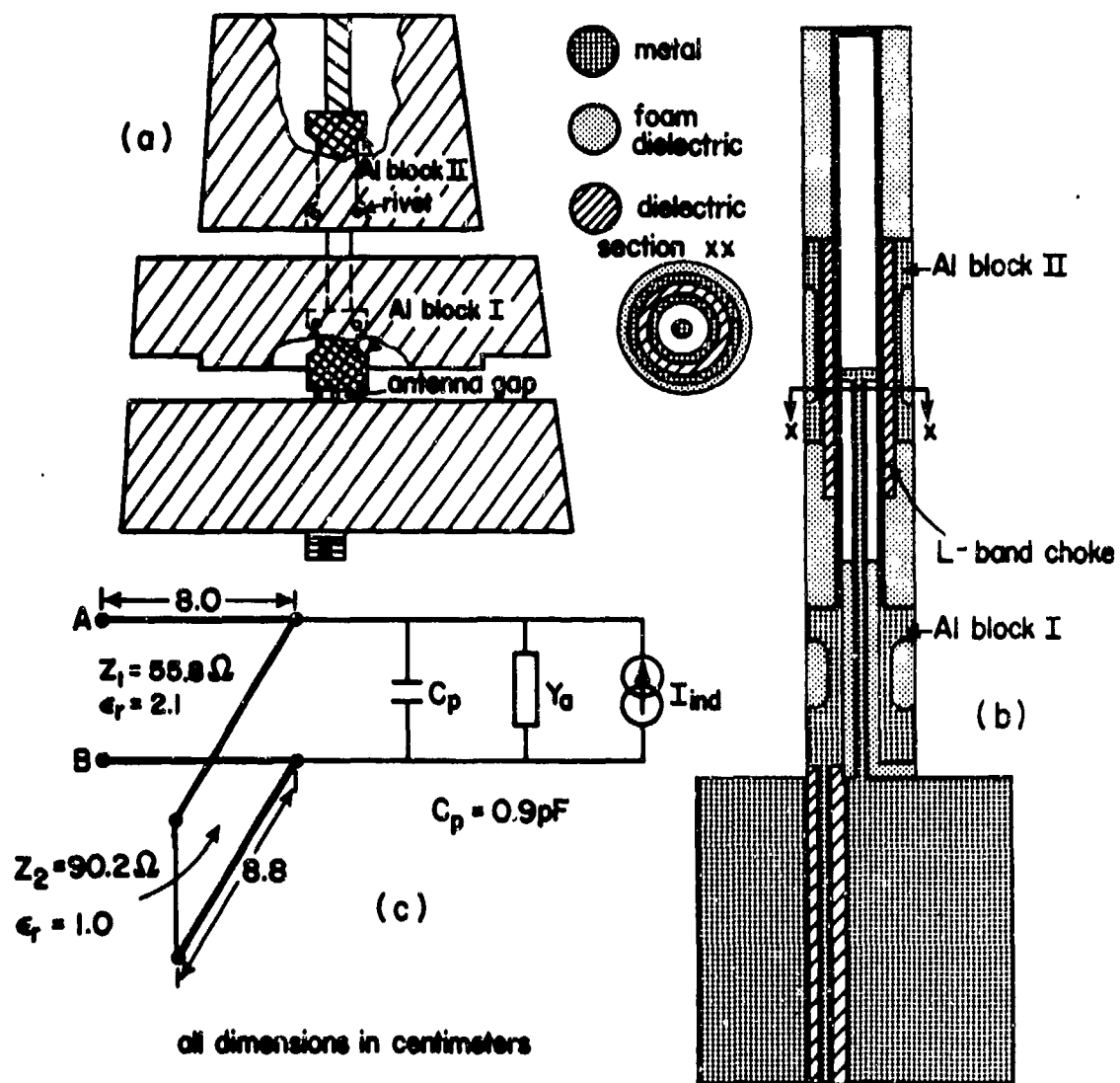


Fig. 66. Schematic diagram and equivalent circuit of the UHF/L-Band Antenna DM CNI8-1.

a coaxial cable. This diplexer has a low-pass filter and a high-pass filter to separate the UHF- and L-band channels. In Figs. 67a and 67b the frequency variation of the input impedance and the effective height are displayed together with some measured values for Z_{in} .

c. VHF Communication Antenna

A schematic diagram of a typical VHF communication antenna is shown in Figs. 68a and 68b. A careful examination of these figures reveals that Fig. 68c is the appropriate equivalent circuit for this antenna. The transmission lines with impedance $Z_c = 176 \Omega$ represent the empty portion of the slot, whereas the transmission line with impedance $Z_c/\sqrt{\epsilon_r} = 119 \Omega$ represents the dielectric-filled portion of the slot. The impedance Z_c can be estimated from the analysis of two coplanar strips of unequal width by the method of conformal mapping [60]. The positions of the tap points D, F, the length of the dielectric portion of the slot, and the three added coaxial cables act as a matching network, so that the VSWR is less than 1.75:1 at in-band frequencies (116 - 156 MHz). The ideal transformer in the equivalent circuit accounts for the fact that the short-circuit current between D and F is just a fraction of I_{ind} , which is the total induced current flowing through a cross section of the antenna (located at D or F and being parallel to the antenna base) when the slot is absent. The ideal transformer also accounts for the radiation effects on the antenna's input admittance, since Y_a in Fig. 68c is the admittance across a gap bisecting the entire antenna at the location of the cross section discussed above. For more details the reader is referred to [61]. The transformer ratio n can be estimated by examining the induced charge density on an ellipsoid immersed in a uniform static electric field. Fig. 69 shows the calculated input impedance together with some measured data.

d. VHF/UHF Communication Antenna

The antenna shown in Fig. 70a operates in two frequency ranges: 116 - 152 MHz (VHF) and 225 - 400 MHz (UHF). The elements shown with hatching and cross-hatching are metallic strips forming transmission lines and capacitances with the radiating metallic plate. The parallel piece of short-circuited

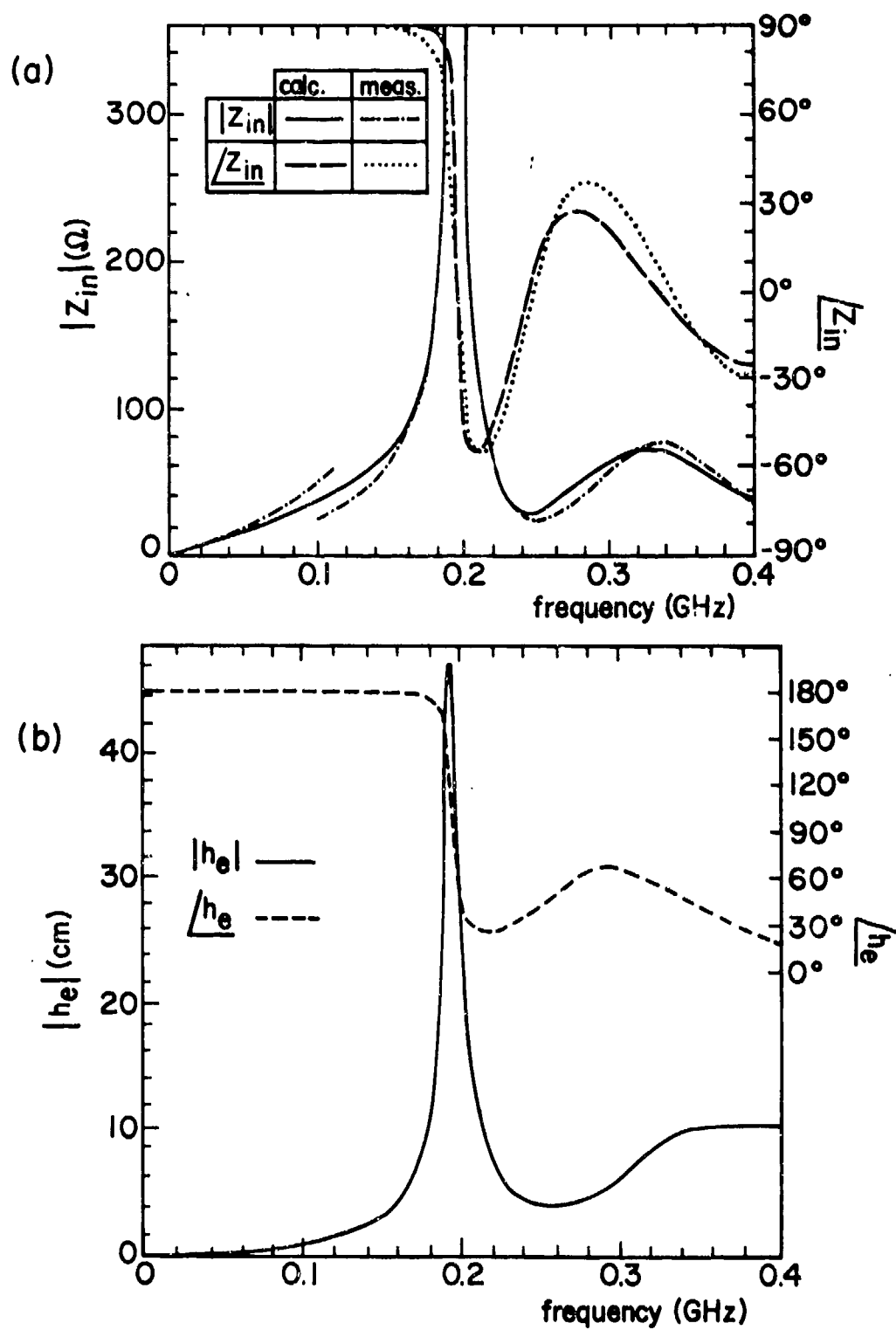


Fig. 67. Input impedance and effective height of the UHF/L-Band Antenna
DM CNI8-1 (UHF-band: 225 - 400 MHz. L-band: 0.95 - 1.22 GHz).

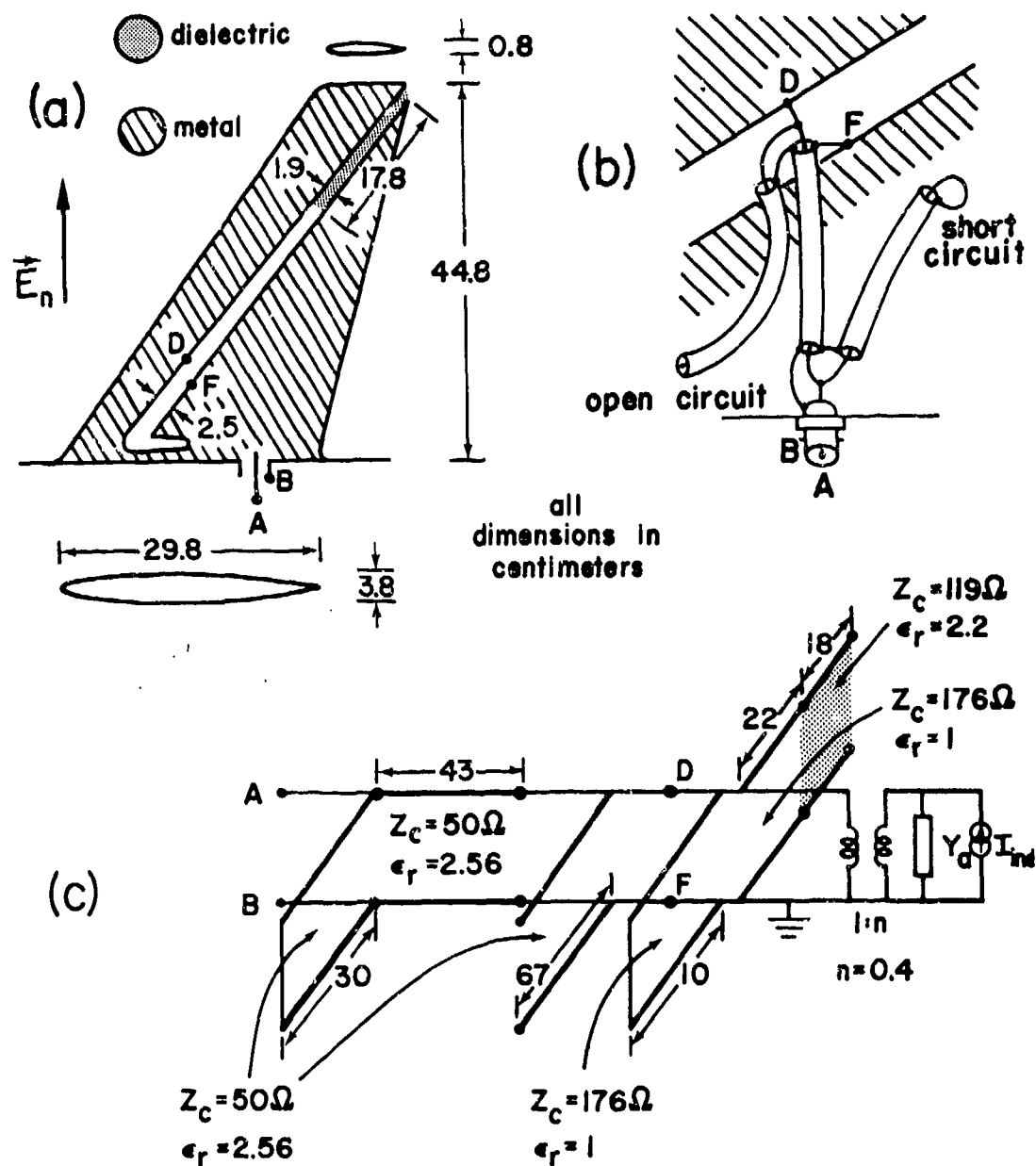


Fig. 68. Schematic diagram and equivalent circuit of the VHF Communication Antenna S65-8262-2.

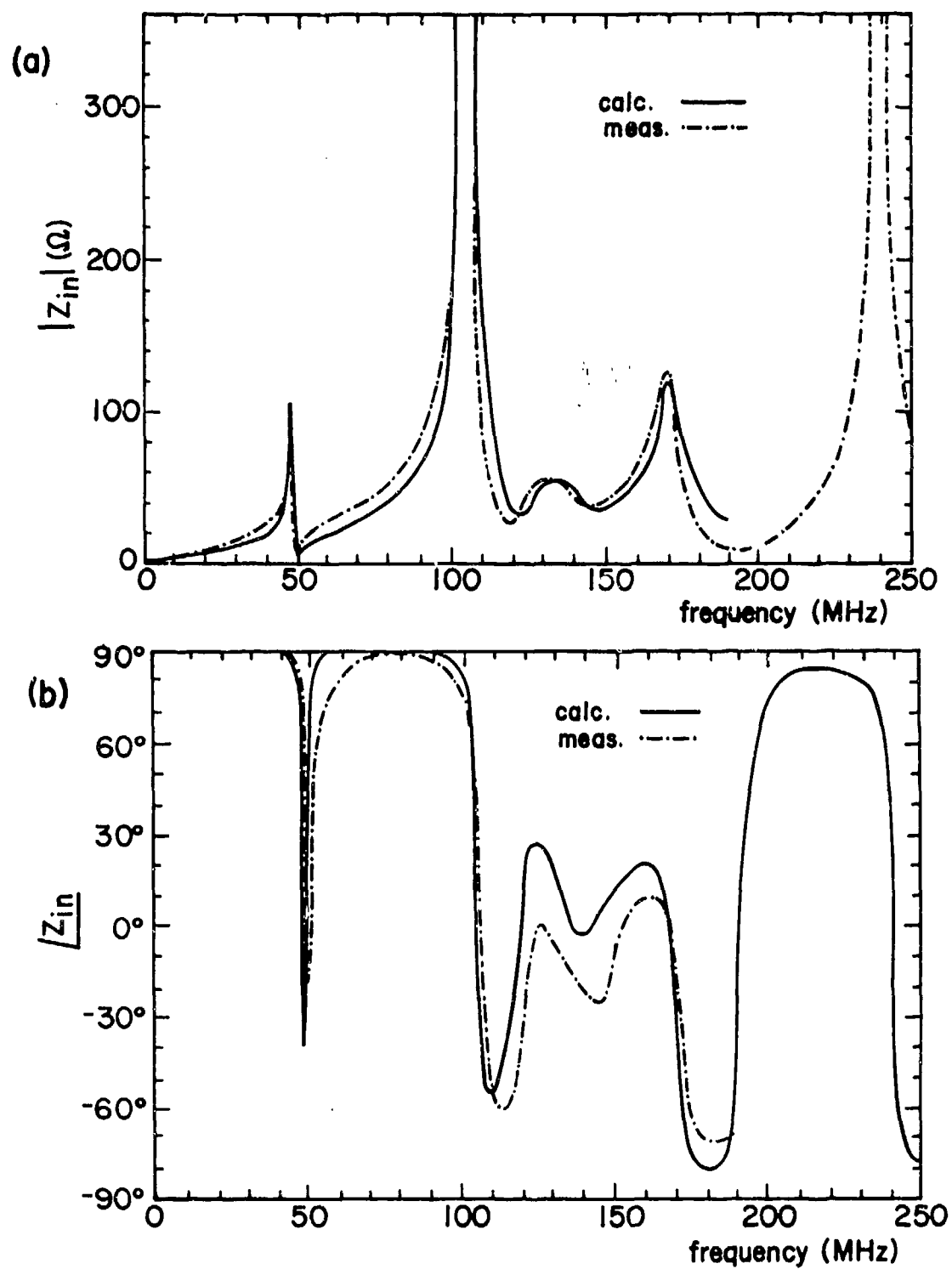


Fig. 69. Input impedance of the VHF Communication Antenna S65-8262-2 (116 - 156 MHz).

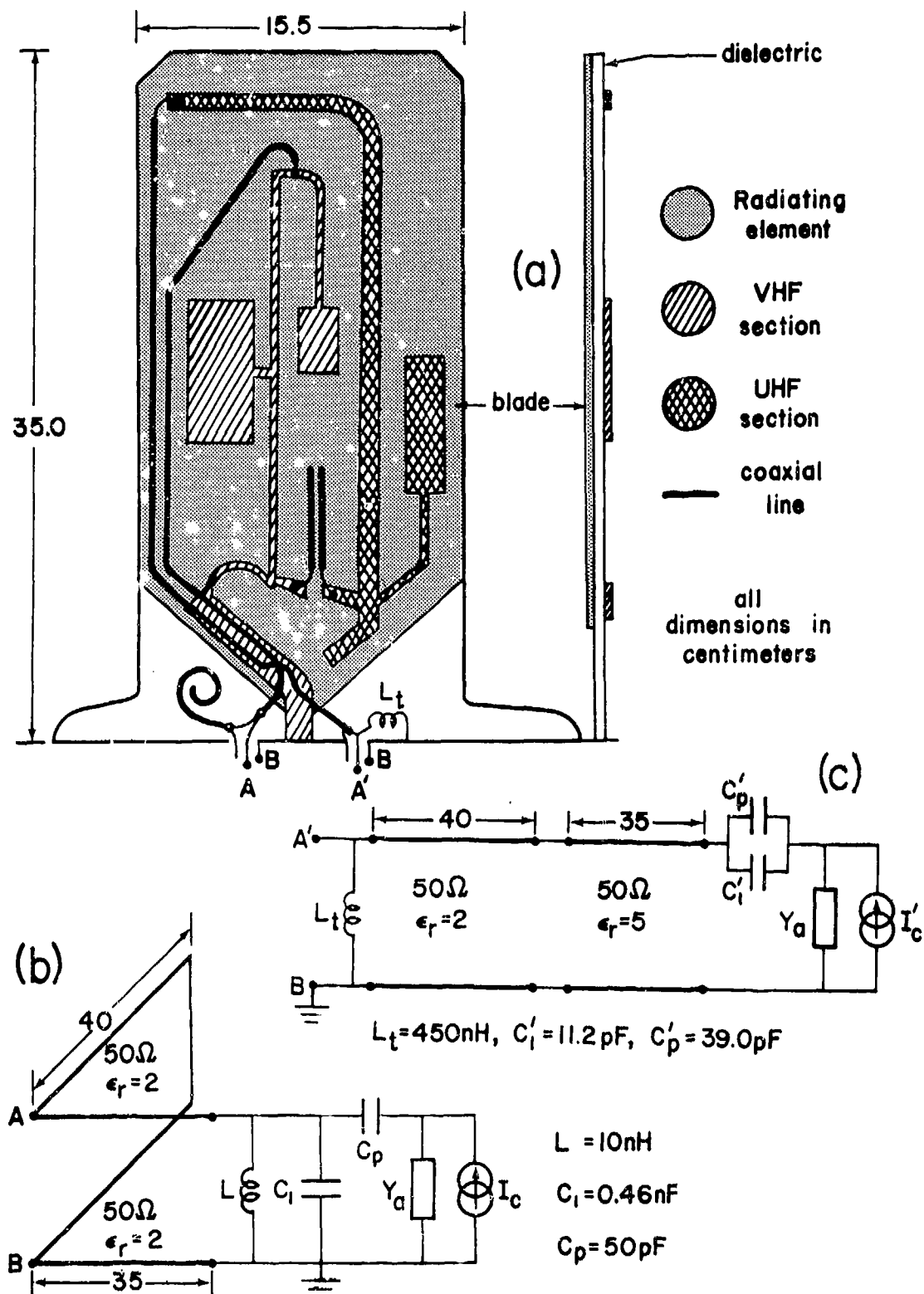


Fig. 70. Schematic diagram and equivalent circuits of the VHF/UHF Communication Antenna 37R-2U.

coaxial cable near the VHF terminal (A,B) acts as a quarter-wavelength choke in the UHF band and the lumped inductance near the UHF terminals (A',B) is intended to short circuit the VHF signal. Thus these two elements provide isolation between the two frequency bands. The equivalent circuits for the VHF and UHF sections are shown in Figs. 70b and 70c. The admittance Y_a is that of the base-fed blade antenna and the blade identified in Fig. 70a is the radiating element. The current generators $I_c (= sQ_c)$ and $I'_c (= sQ'_c)$ originate from the total charges Q_c and Q'_c induced on the two hatched plates and the cross-hatched plate, respectively, through capacitive coupling to the induced charge Q_{ind} on the radiating element. The ratio $n = Q_c/Q_{ind}$ (or $n' = Q'_c/Q_{ind}$) is approximately equal to the ratio of the total area of the two hatched plates (or the cross-hatched plate) to that of the radiating element. The circuit elements C_p (or C'_p) are the total capacitance between the hatched plates (or the cross-hatched plate) and the radiating metallic plate. The capacitances C_1 and C'_1 account for the capacitances of the hatched and cross-hatched strip lines together with the two open-ended pieces of coaxial cable located near the antenna center. The inductance L represents the aggregated effect of the hatched strip lines (including the fact that the strip line is grounded at the antenna base). The frequency variations of the input impedances at the two antenna terminals are shown in Figs. 71a and 71b.

e. L-Band Blade Antenna

Figs. 72a and 72b show two different antennas that both operate between 0.96 GHz and 1.21 GHz. Although their overall dimensions and in-band properties are similar, their out-of-band properties are quite different.

Fig. 72a shows a blade antenna with a slot (the slot often being referred to as a notch). The equivalent circuit is shown in Fig. 72c. The mode of operation and approach in analyzing this antenna are similar to those of the VHF communication antenna above. The induced current I_{ind} and antenna admittance Y_a in the equivalent circuit of Fig. 72c are the quantities referred to the same blade antenna having a feeding gap across the entire blade at D,F. The two transmission lines with characteristic impedances 147 Ω and 300 Ω are

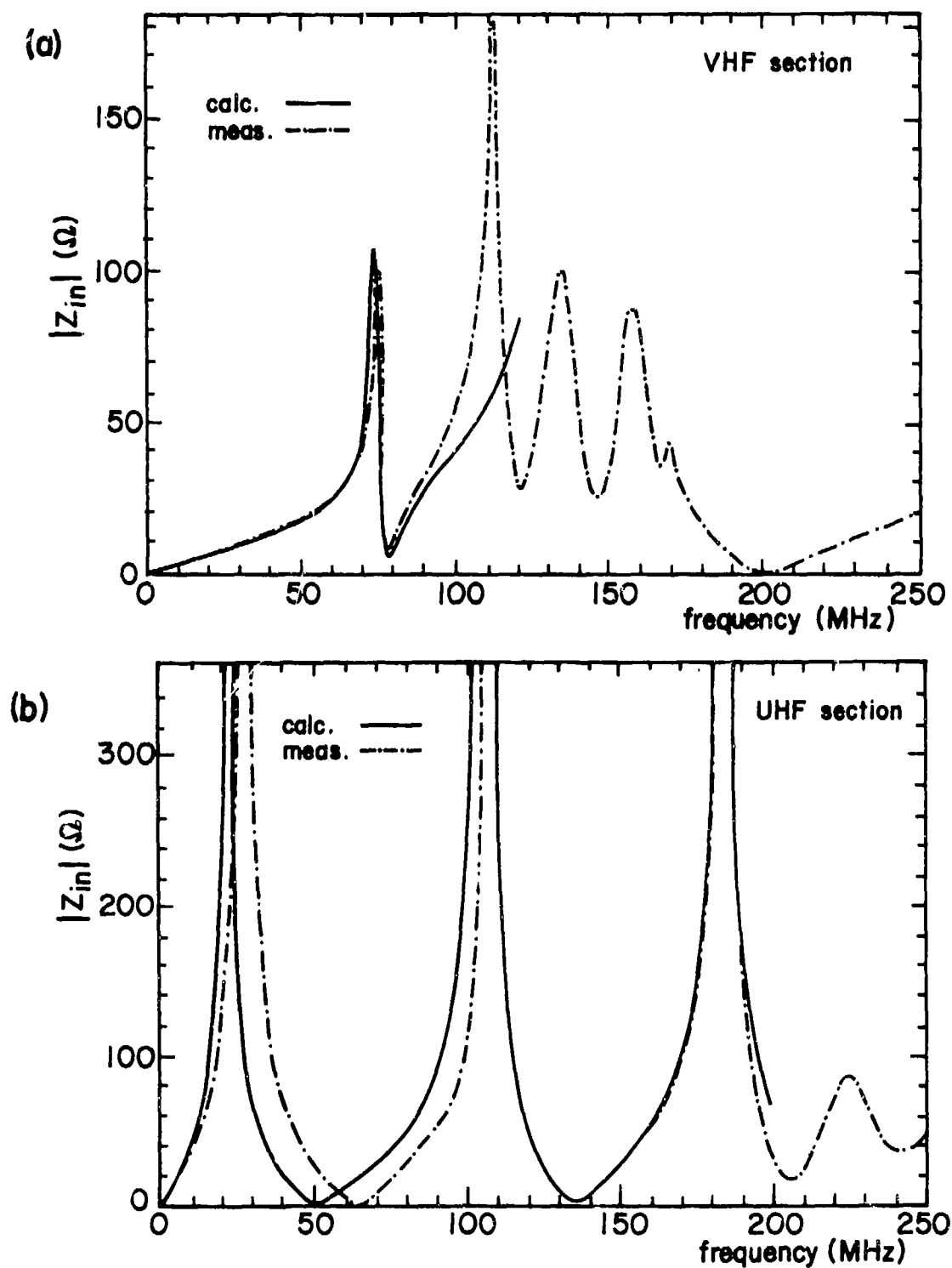


Fig. 71. Input impedances of (a) the VHF (116 - 152 MHz) section and (b) the UHF (225 - 400 MHz) section of the VHF/UHF Communication Antenna 37R-2U.

due to the slot, whereas the transmission line between D,F and A,B represents the coaxial cable with the characteristic impedance of 50Ω . The frequency variation of the antenna's input impedance is shown in Fig. 73a.

The interior structure of another L-band antenna is shown in Fig. 72b. The actual antenna element is a thin metal sheet cut out in a regular symmetric pattern. The holes cut out in the sheet have the effect of increasing the antenna inductance, since the current has to flow around the holes, thereby lengthening the current path. To find the input impedance, the antenna may be modeled as a conical monopole with height 7 cm. The cone angle is determined by equating the capacitances of the monopole model and actual antenna. The antenna capacitance was found to be about 7.8 nF using the variational principle, resulting in a cone angle of 82° [62]. The effective height is determined from the relationships

$$h_e E_n = V_{oc} = Z_a I_{sc} = s \epsilon_0 E_n A_{eq} Z_a \quad (119)$$

It is found in [2] that for a blade antenna, A_{eq} is slightly larger than twice the geometric area of the antenna element. The input impedance is displayed in Fig. 73b, while the effective heights of both antennas are given in Fig. 74.

Both L-band antennas have roughly the same input impedance and effective height at in-band frequencies. The notch antenna has an inductive input impedance and a very small effective height for low frequencies, whereas the other blade antenna has a capacitance input impedance and considerable effective height for low frequencies.

2.1.3.1.2 Loop Antennas

Loop antennas on aircraft are usually physically small and sometimes have ferrite cores. The frequency of operation ranges from tens of kilohertz (VLF) to hundreds of megahertz (VHF).

The theory of a circular loop is most extensive [63] and can be applied, for practically all engineering calculations, to loops of other

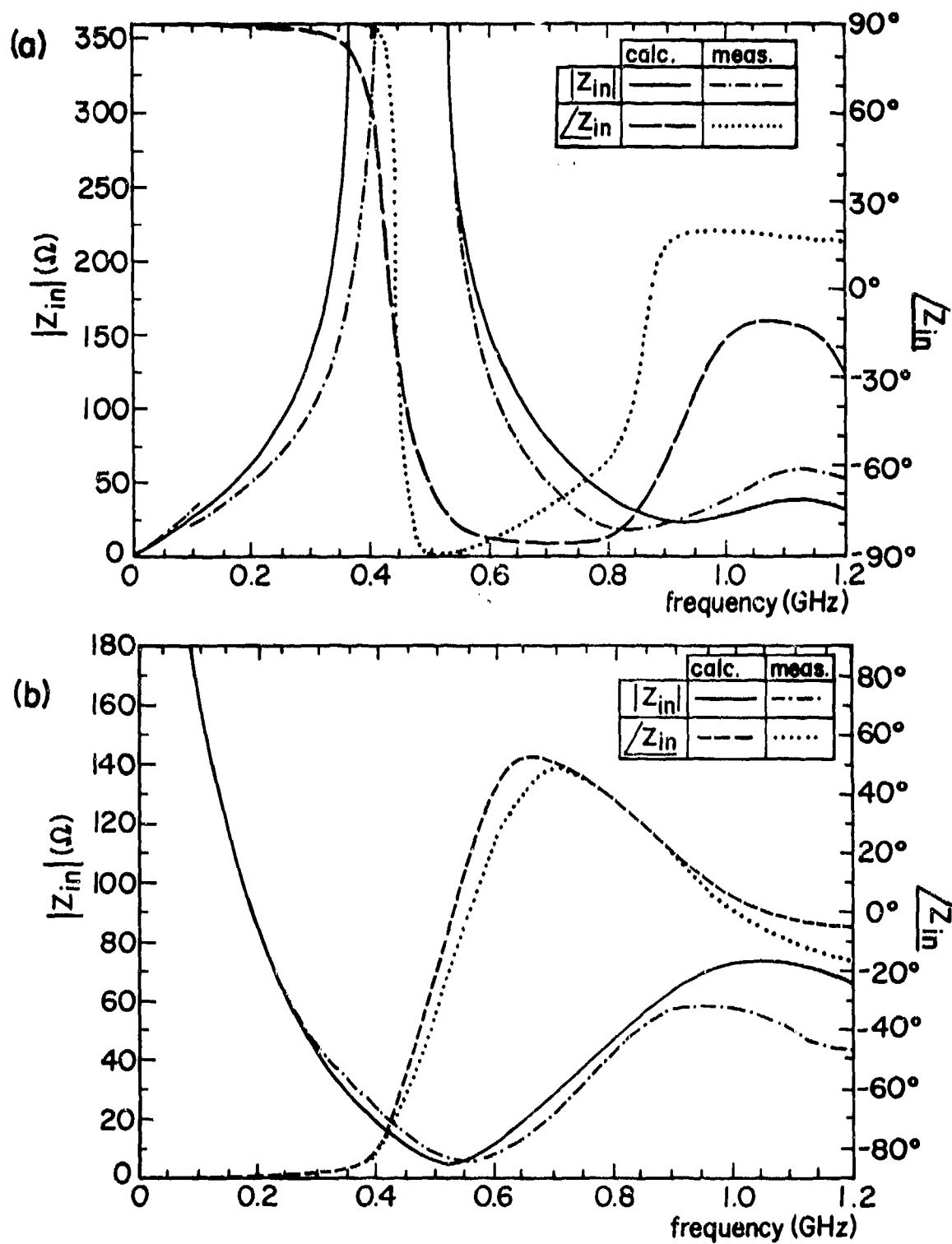


Fig. 73. Input impedances of two L-Band (0.96 - 1.21 GHz) Antennas:
 (a) S65-5366 and (b) AT-741.

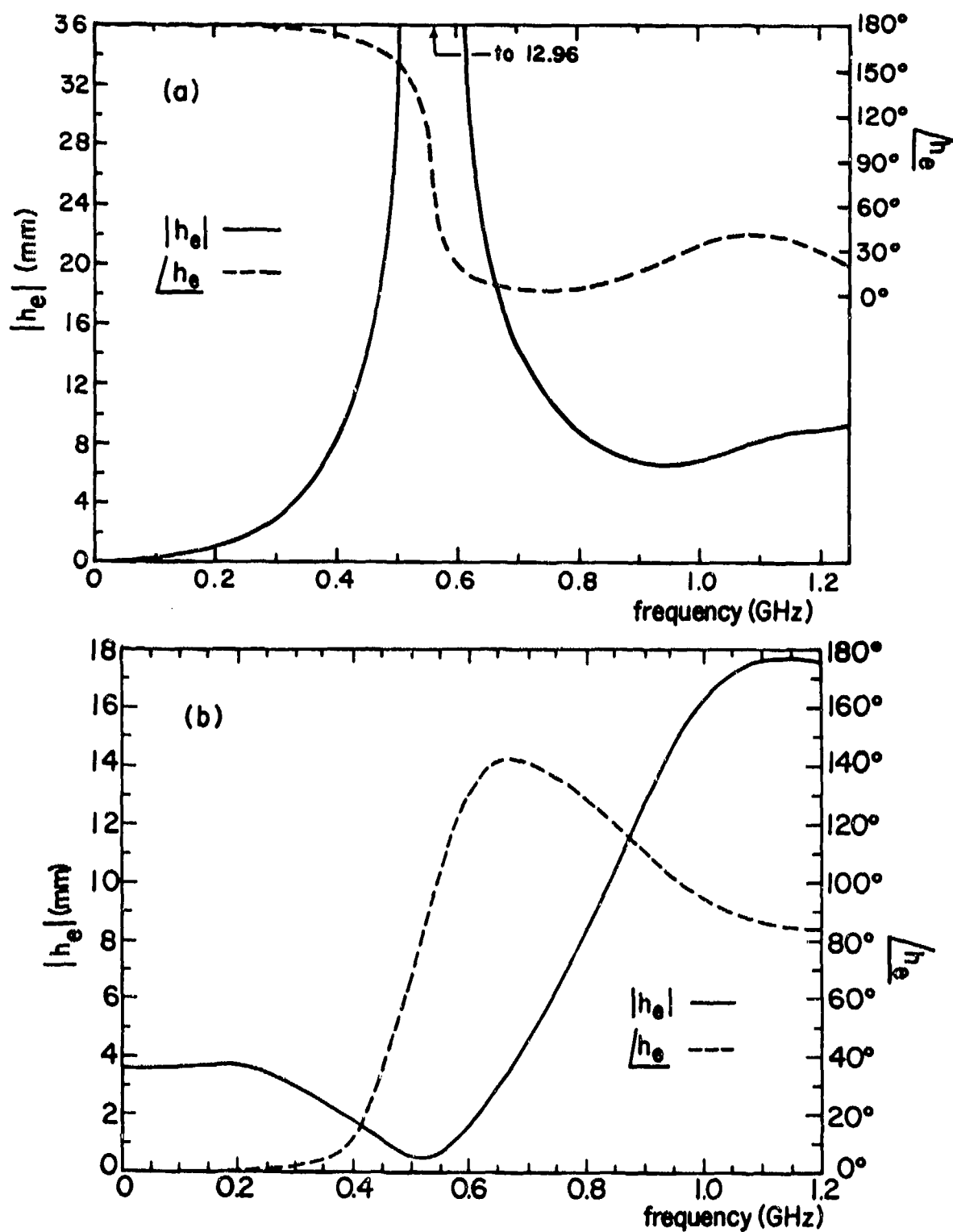


Fig. 74. Effective heights of two L-Band (0.96 - 1.21 GHz) Antennas:
(a) S65-5366 and (b) AT-741.

shapes provided that (a) the perimeter of the given loop is equated to that of a circular loop in the antenna-impedance (Z_a) calculation, and (b) the geometric areas are equated in the induced-voltage (V_{ind}) calculation. In certain cases where the ferrite core is a rectangular slab, such as the VLF magnetic-loop aircraft antenna, two magnetostatic boundary-value problems need to be solved for the determination of the external elements Z_a and V_{ind} [64].

a. Localizer Antenna

Figs. 75a and 75b show all the electrical elements of a localizer antenna and Fig. 75c is the equivalent circuit. The external elements Z_a and V_{ind} can be calculated as discussed above with due account for the factors of two resulting from the presence of the ground plane. The tuning capacitors at the ends of the loops (Fig. 75a) are represented by C in Fig. 75c. The coaxial cable wound around the center rods serves as a balun, converting a balanced signal into an unbalanced one for the terminals A,B and A',B within the in-band frequencies (108 - 112 MHz). The wires wrapped around the 100 Ω resistor can be identified as a hybrid circuit which splits an incoming signal into two equal parts for the two terminals A,B and A',B. Because of the close coupling between the wires, M can be taken equal to L. In Fig. 76a is plotted the input impedance Z_{in} referred to A,B with A',B open circuited or vice versa. Also shown in the figure are some measured data. In Fig. 76b is shown the frequency variation of V_{oc} across A,B or A',B for an incident plane wave with the electric field vector perpendicular to the ground plane and the magnetic field vector perpendicular to the plane of the loop.

b. VOR Antenna

Fig. 77a shows a VOR (VHF Omni-Range) antenna. This antenna is usually located inside a flush radome on the vertical stabilizer. The antenna proper consists of a rectangular loop containing three gaps. The capacitance C_1 in the equivalent circuit shown in Fig. 77b represents the combined capacitance of the two gaps on the long sides of the loop. This antenna has a very low VSWR (1.5:1) within in-band frequencies (108 - 118 MHz). This is

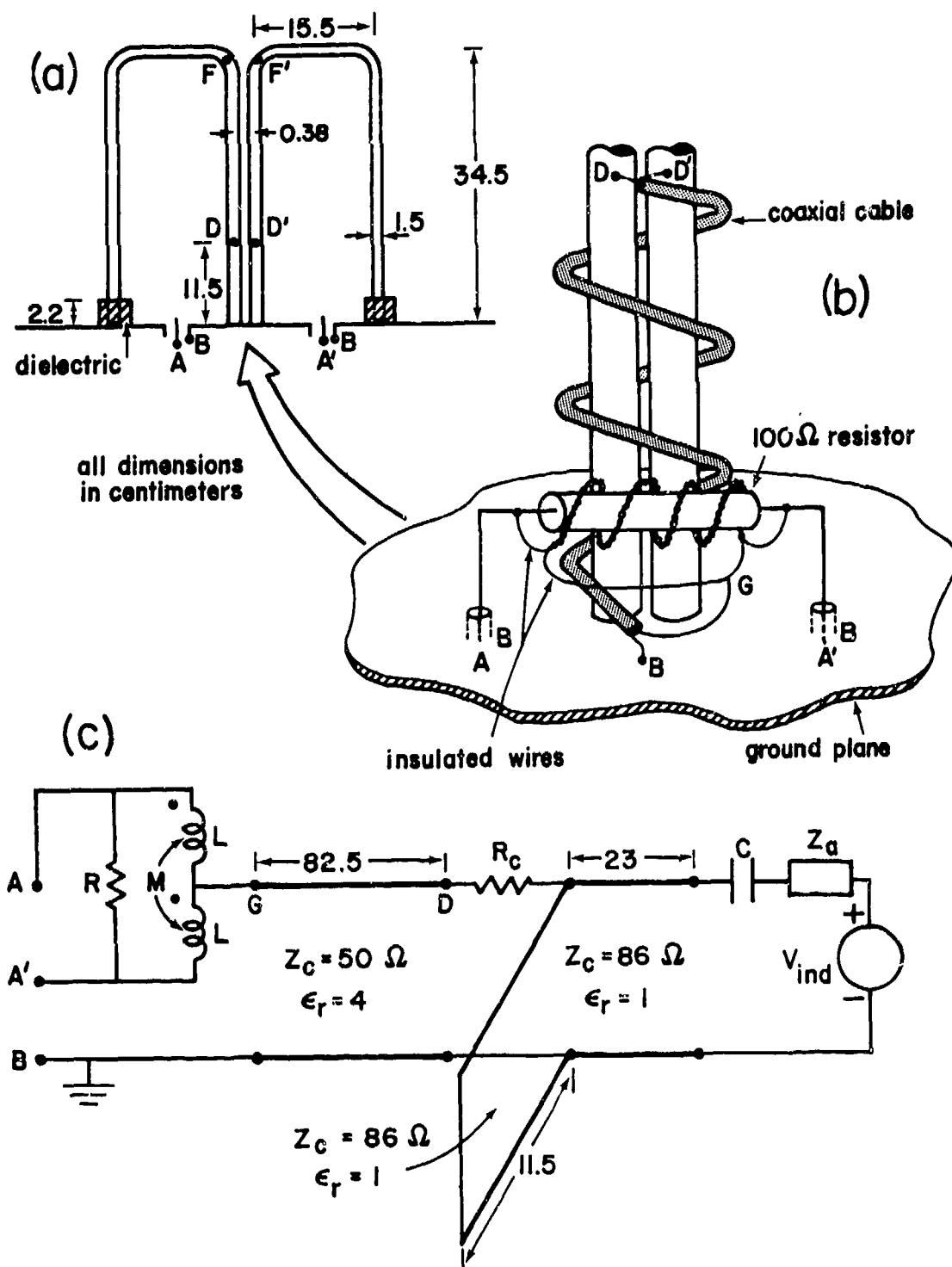


Fig. 75. Schematic drawing and equivalent circuit of the Localizer Antenna S65-147. R_c (contact resistance) = 1.5 Ω , L = 60.2 nH, M = 60.2 nH, R = 100 Ω , C = 2.8 nF.

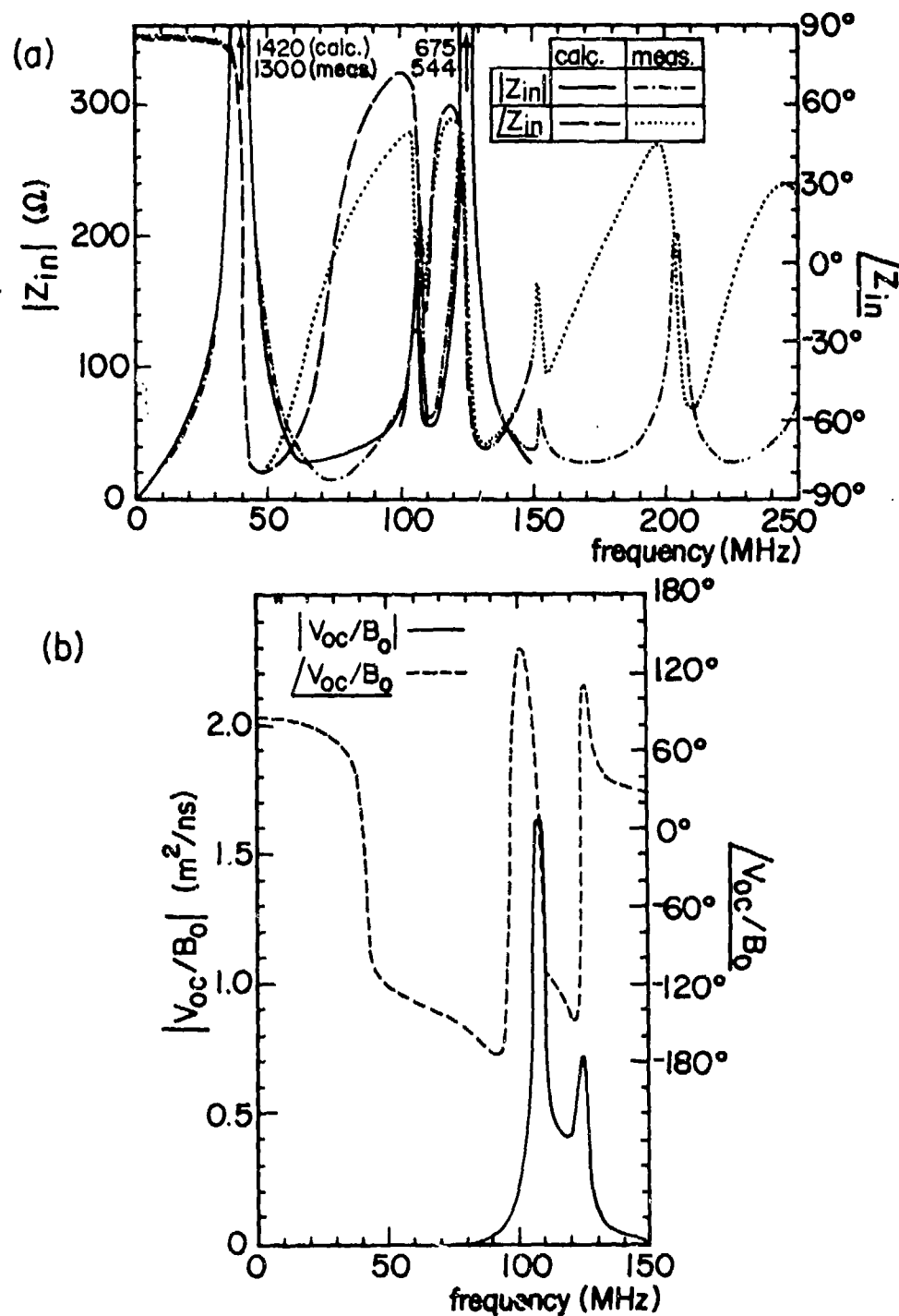
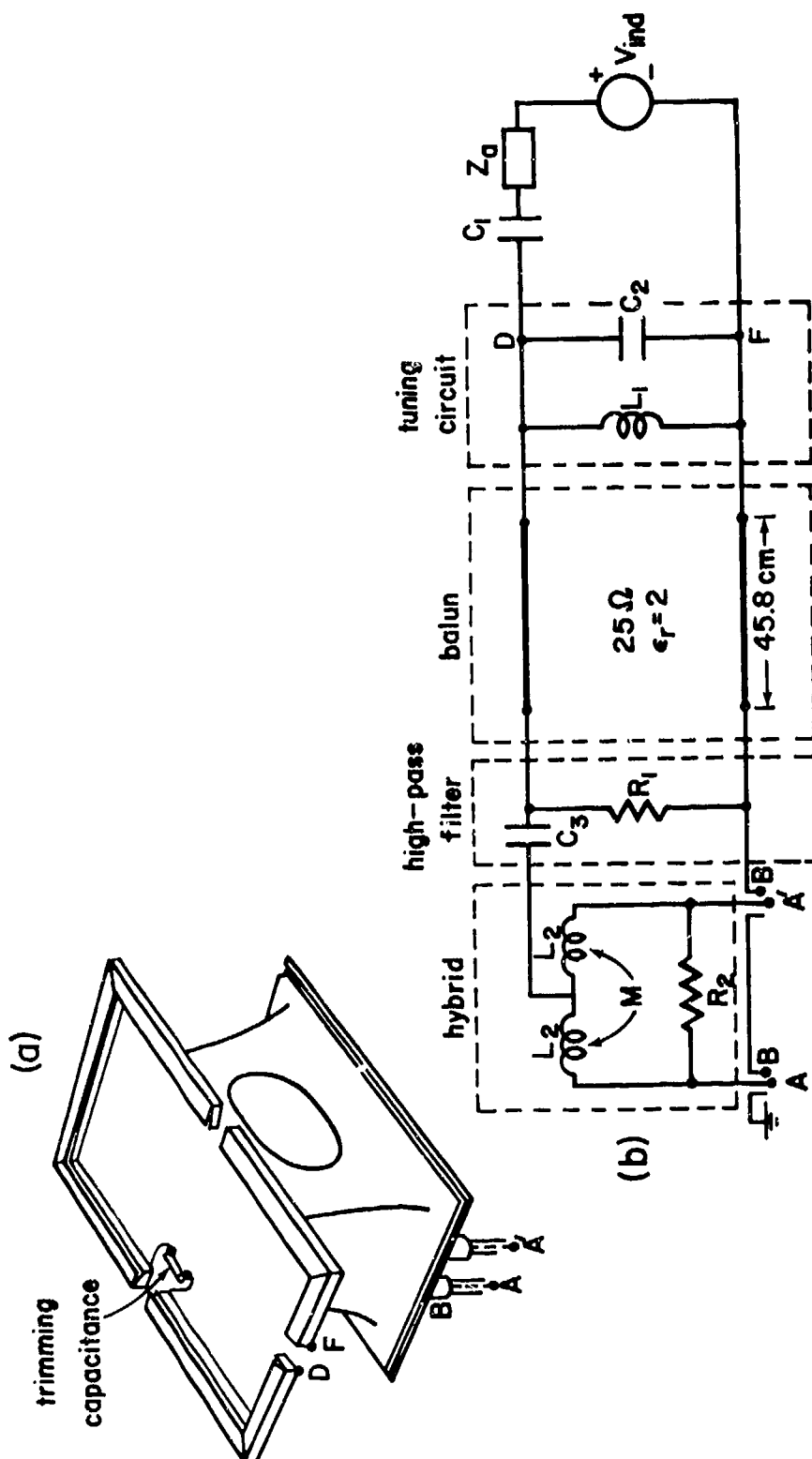


Fig. 76. Input impedance and open-circuit voltage of the Localizer Antenna S65-147 (108 - 112 MHz). (B_0 is the external magnetic field component perpendicular to the plane of the loops.)



$$L_1 = 12.6\text{ nH}, L_2 = 64.7\text{ nH}, M = -64.7\text{ nH}, R_1 = 260\Omega,$$

$$C_1 = 24\text{ pF}, C_2 = 382\text{ pF}, C_3 = 245\text{ pF}, R_2 = 100\Omega$$

Fig. 77. Schematic diagram and equivalent circuit of the VOR Antenna 60B00024 (108 - 118 MHz).

achieved by appropriately adjusting the tuning elements L_1 , C_1 and C_2 . The capacitance C_3 is used to block any low-frequency signals, while R_1 is used to dissipate these signals.

c. Magnetic-Loop Antenna

The magnetic-loop antenna is a VLF/LF (17 - 60 kHz) receiving antenna, usually mounted on the top of the fuselage and enclosed in a fiberglass radome. This antenna as shown in Fig. 78a has two sets of coils wound perpendicularly to each other on a matrix of ferrite rods. A schematic drawing depicting the winding arrangements of each coil and the tap points is shown in Fig. 78b. The equivalent circuit for the loop, the cable, and the junction box are presented in Fig. 78c. To determine the two external quantities Z_a and V_{ind} two independent magnetostatic boundary-value problems appropriate for a coil wound on a rectangular ferrite slab are solved by integral-equation techniques [64]. Fig. 79a shows the results of such calculations, where f_ϕ is the dimensionless flux enhancement factor due to the presence of the ferrite slab, and f_L is defined so that $f_L \mu_o a / 4\pi$ is the inductance of a single turn of wire wound on the ferrite slab, a being the wire radius. Thus, one has

$$\begin{aligned} V_{ind} &= -sNf_\phi B_o A, & Z_a &= R_a + sL_a \\ R_a &\approx 31.2 (NA/\lambda^2)^2, & L_a &= N^2 f_L \mu_o a / 4\pi \end{aligned} \quad (120)$$

and B_o is the magnetic field normal to the coil and A is the area of a single turn. The input impedance between A, A' is shown in Fig. 79b for frequencies below 1 MHz. Above 1 MHz the input impedance is dominated by the two shunt capacitances in the filter.

2.1.3.1.3 Slot Antennas

The theory of slot antennas is based on the Babinet principle, from which one can obtain results for a slot antenna directly from those of the complementary dipole antenna. Let the superscript s denote quantities of a slot antenna and the superscript d quantities of the complementary dipole antenna. Then

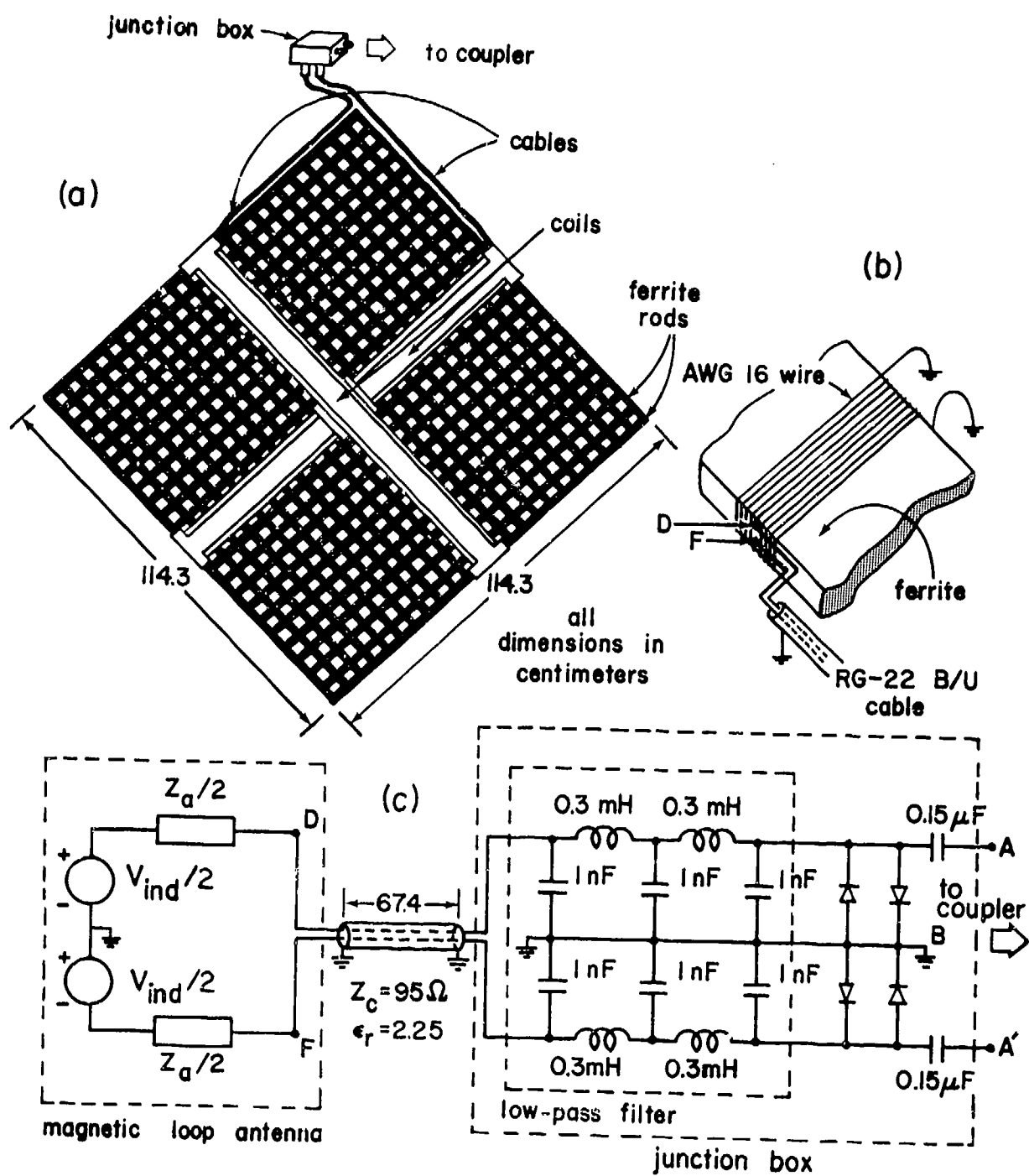


Fig. 78. Schematic diagrams and equivalent circuits of the Magnetic Loop Antenna AS-1909/ARC-96.

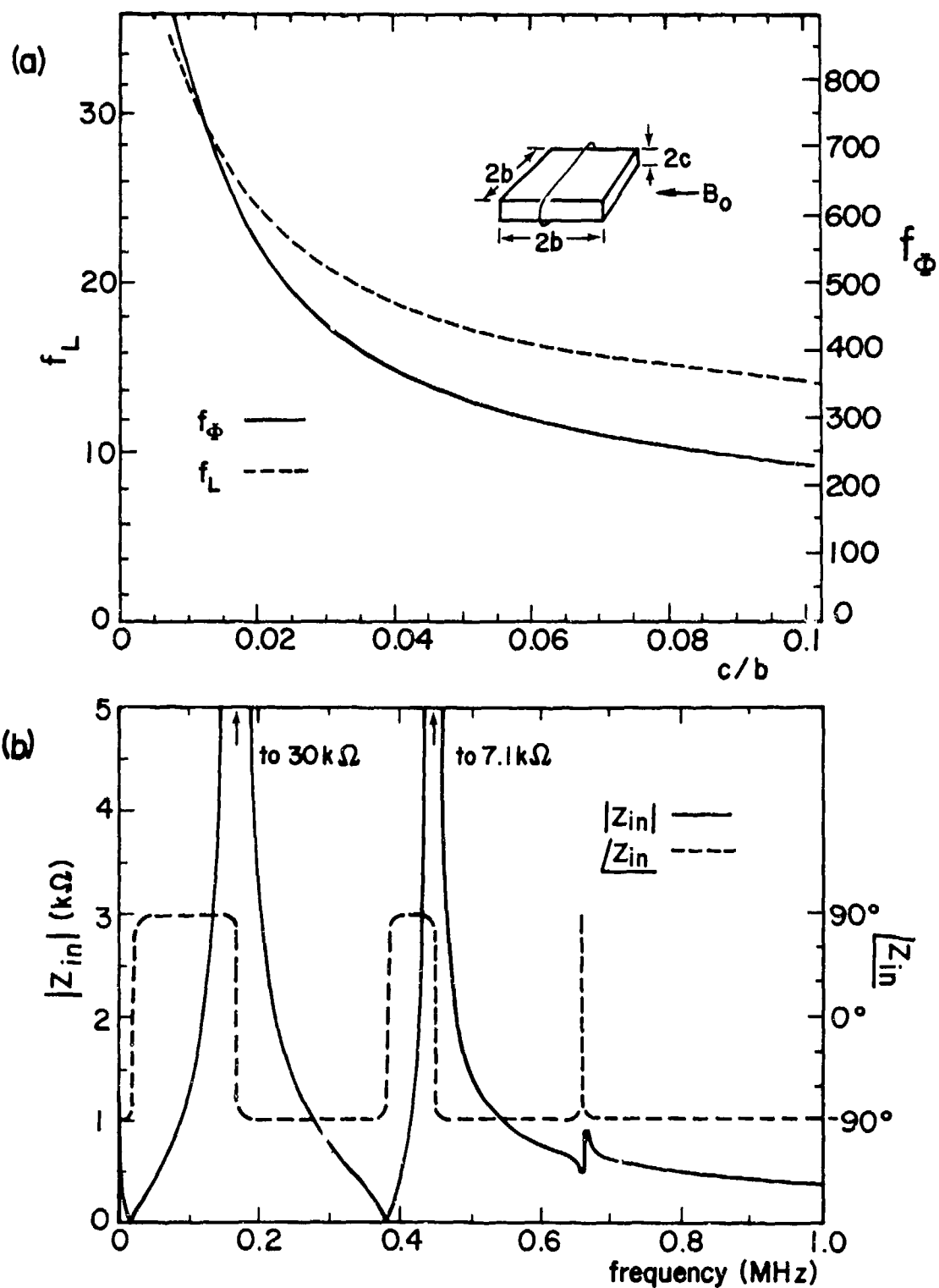


Fig. 79. (a) The flux enhancement factor f_Φ and the normalized inductance f_L of a single turn on a ferrite slab, and (b) the input impedance of the Magnetic Loop Antenna AS-1909/ARC-96 (17 - 60 kHz).

$$Z_{in}^{(s)} Z_{in}^{(d)} = \frac{1}{4} Z_0^2 \quad (121)$$

$$\vec{\gamma} \times \vec{h}_e^{(s)} = \frac{1}{2} \frac{Z_0}{Z_{in}^{(d)}} \gamma \vec{h}_e^{(d)} \quad (122)$$

where Z_0 is the free-space impedance and $\vec{\gamma}$ is the propagation vector of the incident plane wave. Eq.(121) relates the input impedances of the two antennas and is well-known to the antenna engineer. Eq.(122) is less familiar and expresses the relationship between the effective heights. In the case of a slot antenna, it is physically appealing to think of the short-circuit current $I_{sc}^{(s)}$ across, say, the mid-points of the slot. Then

$$\begin{aligned} I_{sc}^{(s)} &= \frac{1}{Z_{in}^{(s)}} V_{oc}^{(s)} = \frac{1}{Z_{in}^{(s)}} \vec{h}_e^{(s)} \cdot \vec{E}^i \\ &= 2\vec{H}^i \cdot \vec{h}_e^{(d)} \end{aligned} \quad (123)$$

where the last relation follows from (121) and (122) with $\vec{\gamma} \times \vec{E}^i = \gamma Z_0 \vec{H}^i$. Eq.(123) is dual to the equation $V_{oc}^{(d)} = \vec{E}^i \cdot \vec{h}_e^{(d)}$ for the complementary dipole antenna.

a. Glide-Slope Track Antenna

The glide-slope track antenna shown in Fig. 80a is a receiving antenna for the frequency range 329 - 335 MHz. It is the complement of a folded strip dipole with capacitive loading at both ends (Fig. 80b). The equivalent circuits of both antennas are shown in Figs. 80c and 80d. The element Z_a is the impedance of the common (or symmetric) mode, and the transmission line accounts for the differential (or antisymmetric) mode. The impedance Z_c is the characteristic impedance of the transmission line formed by the two parallel conductors of the folded dipole. More detailed analyses of the folded dipole are presented in [54, 56, 65, 66]. A derivation of the expression for the current generator in Fig. 80d is given in [67]. With

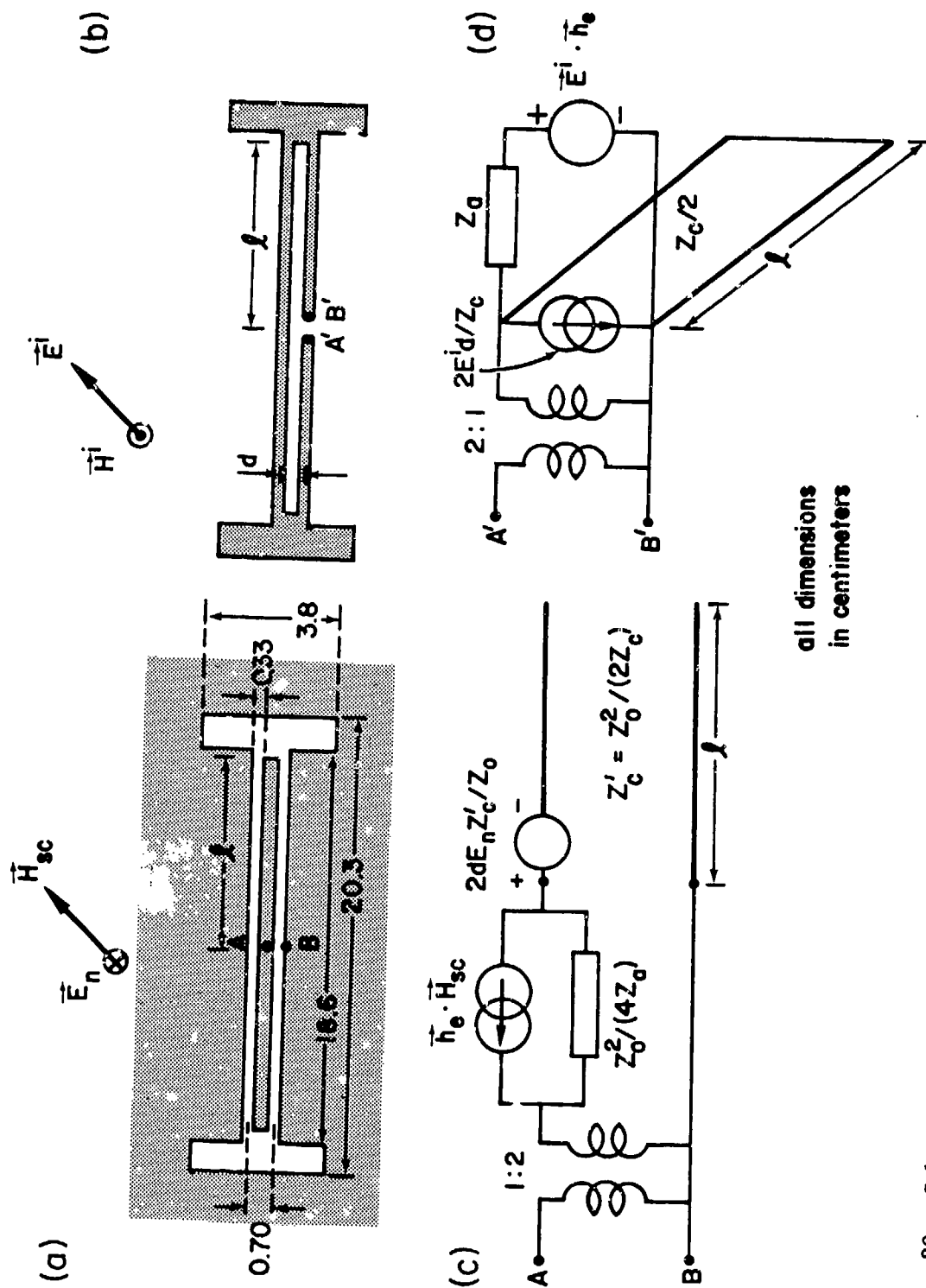


Fig. 80. Schematic diagrams and equivalent circuits of the B559 and B561 Glide Slope Track Antenna and its complementary strip antenna.

the aid of (121) - (123) one obtains the equivalent circuit shown in Fig. 80c for the slot antenna. The voltage generator with strength $2dE_n Z'_c / Z_0$ can be replaced by a current generator in parallel with the transmission line. Physically, this current generator can be understood as arising from the total net charge induced on the (short-circuited) center strip. The input impedance and effective height of the glide-slope track antenna are shown in Figs. 81a and 81b.

b. Glide-Slope Capture Antenna

The glide-slope capture antenna shown in Fig. 82a also makes use of a slot. This antenna is used to receive signals in the band 329 - 335 MHz. The equivalent circuit is presented in Fig. 82b, where C is the capacitance between the tuning stub and the strip line. The impedance Z_a can be determined by first finding the input impedance of the slot's equivalent dipole and then using (121). The strength of the voltage generator $V_{ind} = (Z_0 / Z_a) h_e E_n$, where h_e is approximately half the slot length for frequencies of interest. The input impedance and effective height are shown in Figs. 83a and 83b.

2.1.3.1.4 Bowl Antennas

Most aircraft antennas operating in the gigahertz frequency range are horn antennas. Sometimes the horns are quite shallow and in these cases the horns simply house the antennas. In other cases the horns are deeper, and the horn becomes an important part of the antenna proper. All these antennas are grouped here under one general heading -- the bowl antenna. For this type of antenna the calculation of field penetration into a bowl is an essential step, since the field picked up by the probe or loop inside is modified by the bowl. Usually the important wavelengths of the EMP are much larger than the dimensions of most of the bowls found on an aircraft; hence, techniques applicable to static boundary-value problems are adequate in the determination of field penetration. Analytical and numerical solutions have been found for a two-dimensional trough [68], a hemispherical indentation [69,70], and a semi-infinite circular pipe with an infinite

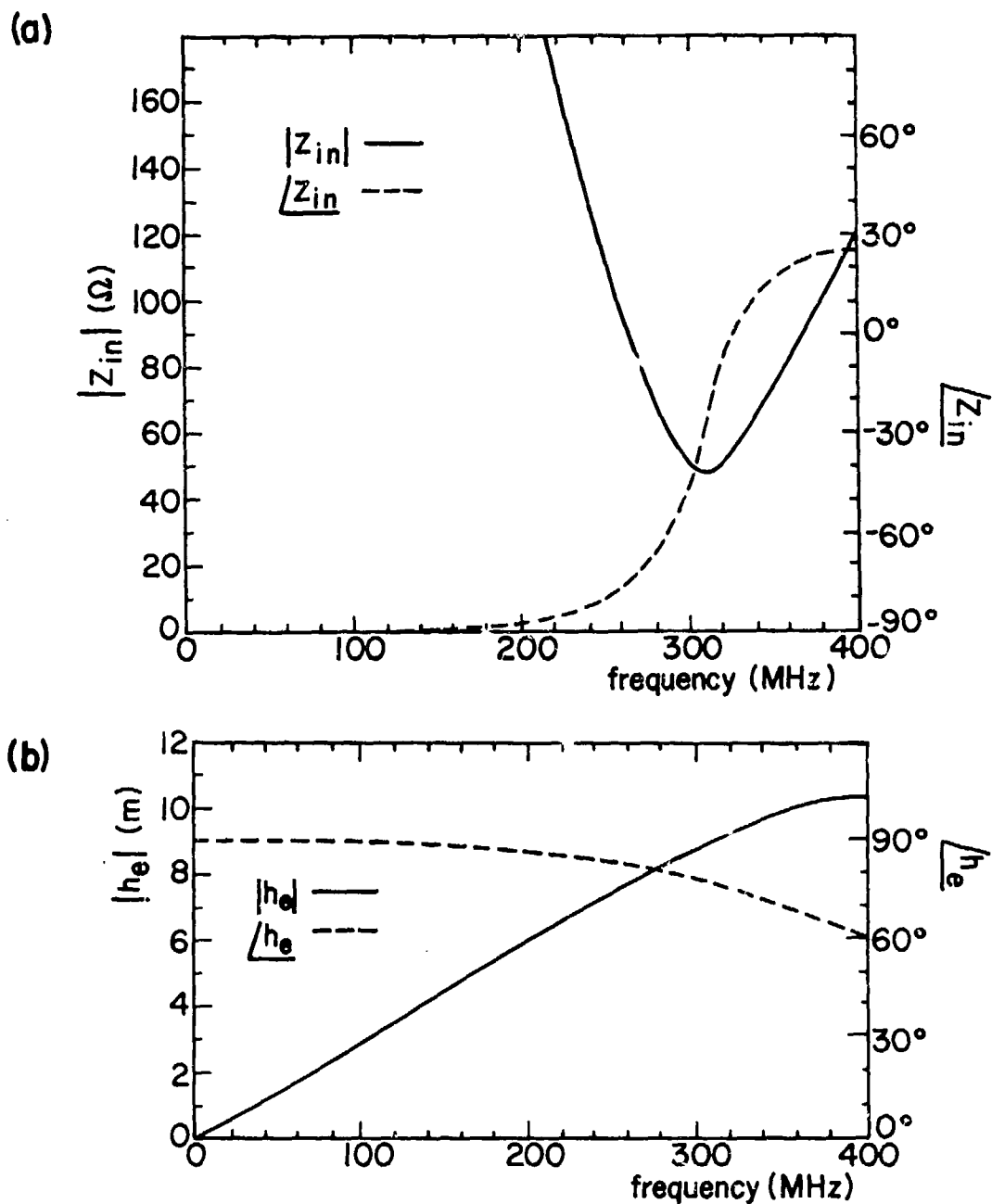


Fig. 81. Input impedance and effective height of the B559 and B561 Glide-Slope Track Antenna (329 - 335 MHz).

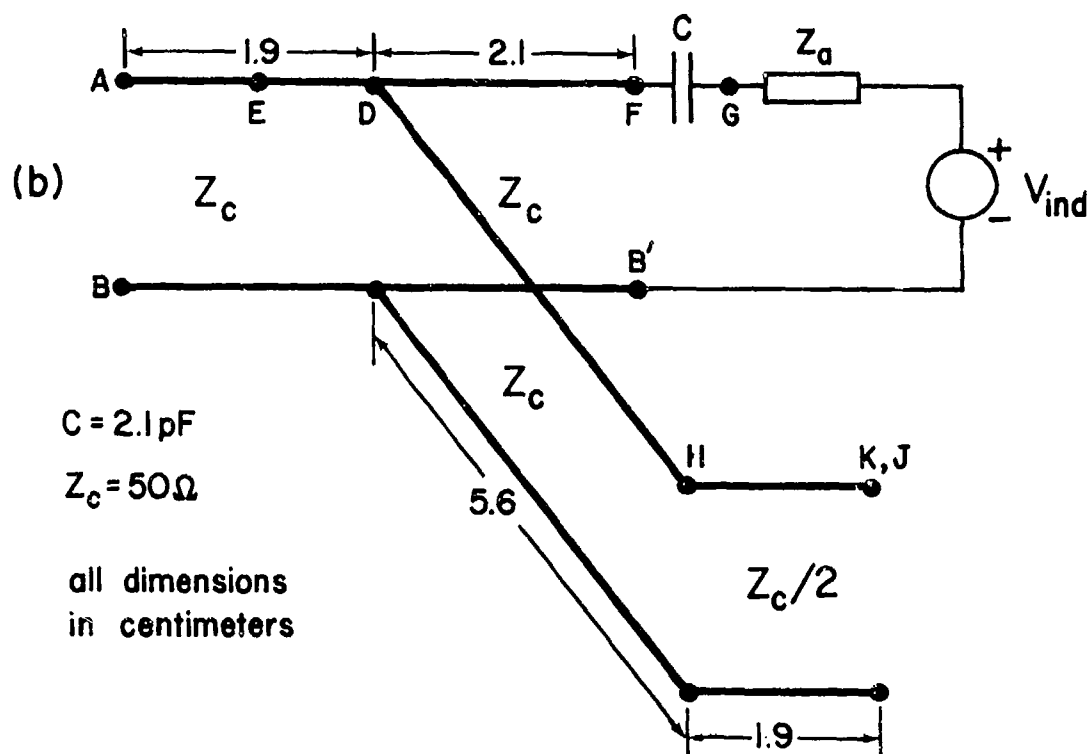
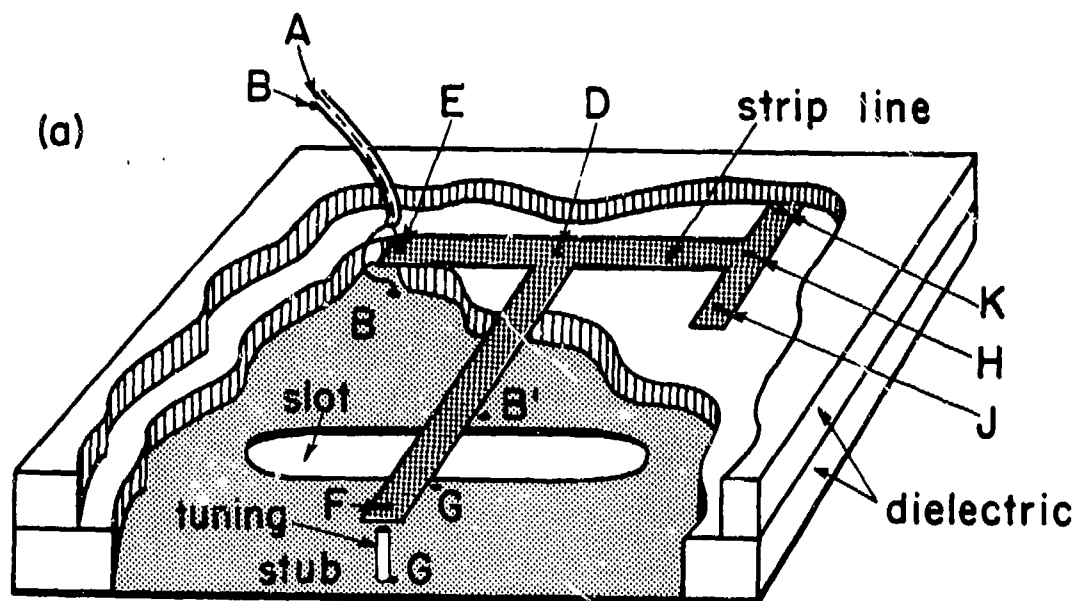


Fig. 82. Schematic diagram and equivalent circuit of the B558 Glide-Slope Capture Antenna.

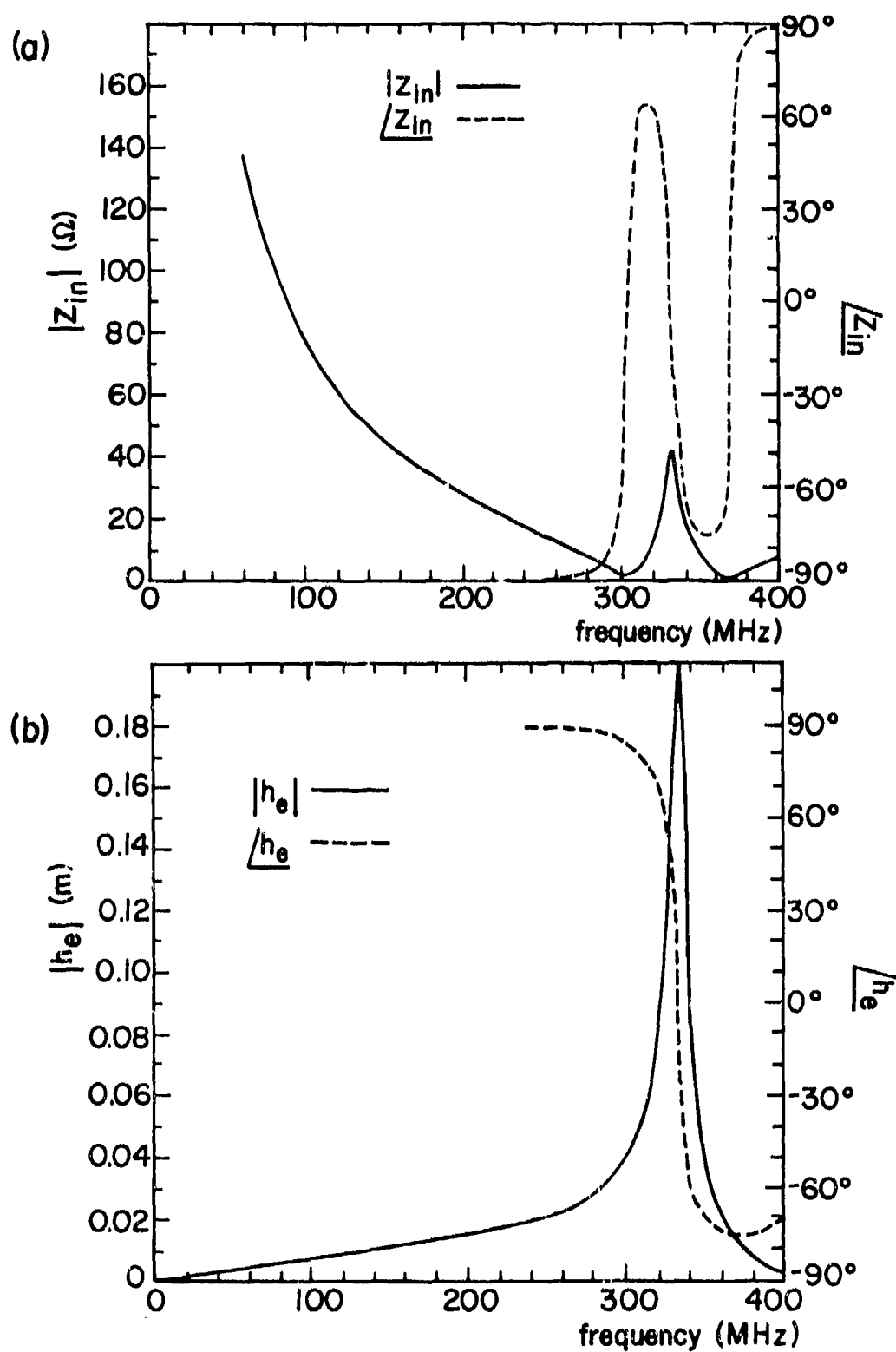


Fig. 83. Input impedance and effective height of the B558 Glide-Slope Capture Antenna (329 - 335 MHz).

flange [71,72]. For other bowl shapes one either idealizes the shape, so that a solution is already available, or resorts to some numerical scheme for the boundary-value problem appropriate for the bowl geometry at hand.

a. Marker Beacon Antenna

The marker beacon antenna shown in Fig. 84a is flush-mounted at the bottom of the fuselage and operates around 75 MHz. The bowl can be approximated by a hemispherical indentation. The equivalent circuit is given by Fig. 84b in which L_1 and L_2 are respectively the inductances of the small and large loops formed by the metal rod and the feed wire. Figs. 85a and 85b give the frequency variations of Z_{in} and V_{oc}/B_0 , where B_0 is the magnetic field tangential to the aircraft skin (with the bowl covered) and perpendicular to the plane of the large loop.

b. Low-Range-Radio-Altimeter Antenna

Figs. 86a and 86b show two typical low-range-radio-altimeter aircraft antennas, one with an electric probe and the other with a magnetic loop as the feeding element. These antennas operate between 4.2 - 4.4 GHz and are flush-mounted at the bottom of the fuselage. The equivalent circuits of these antennas are shown in Figs. 86c and 86d.

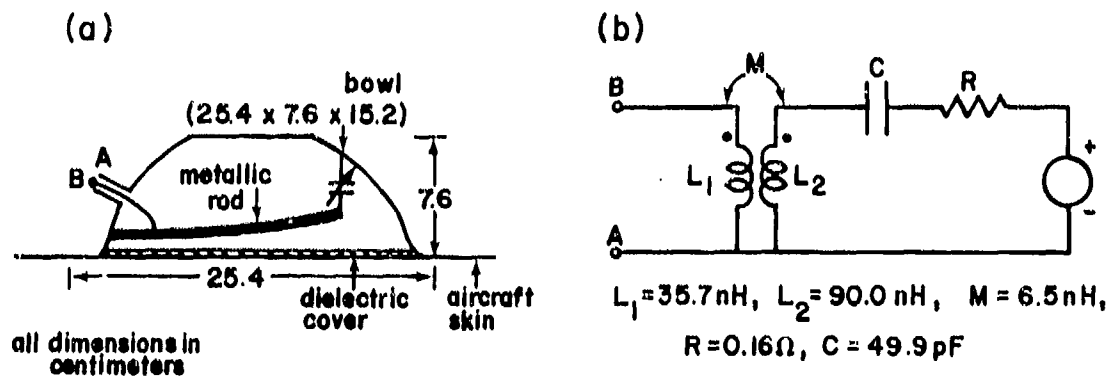


Fig. 84. Schematic diagram and equivalent circuit of the AT-536/ARN Marker Beacon Antenna.

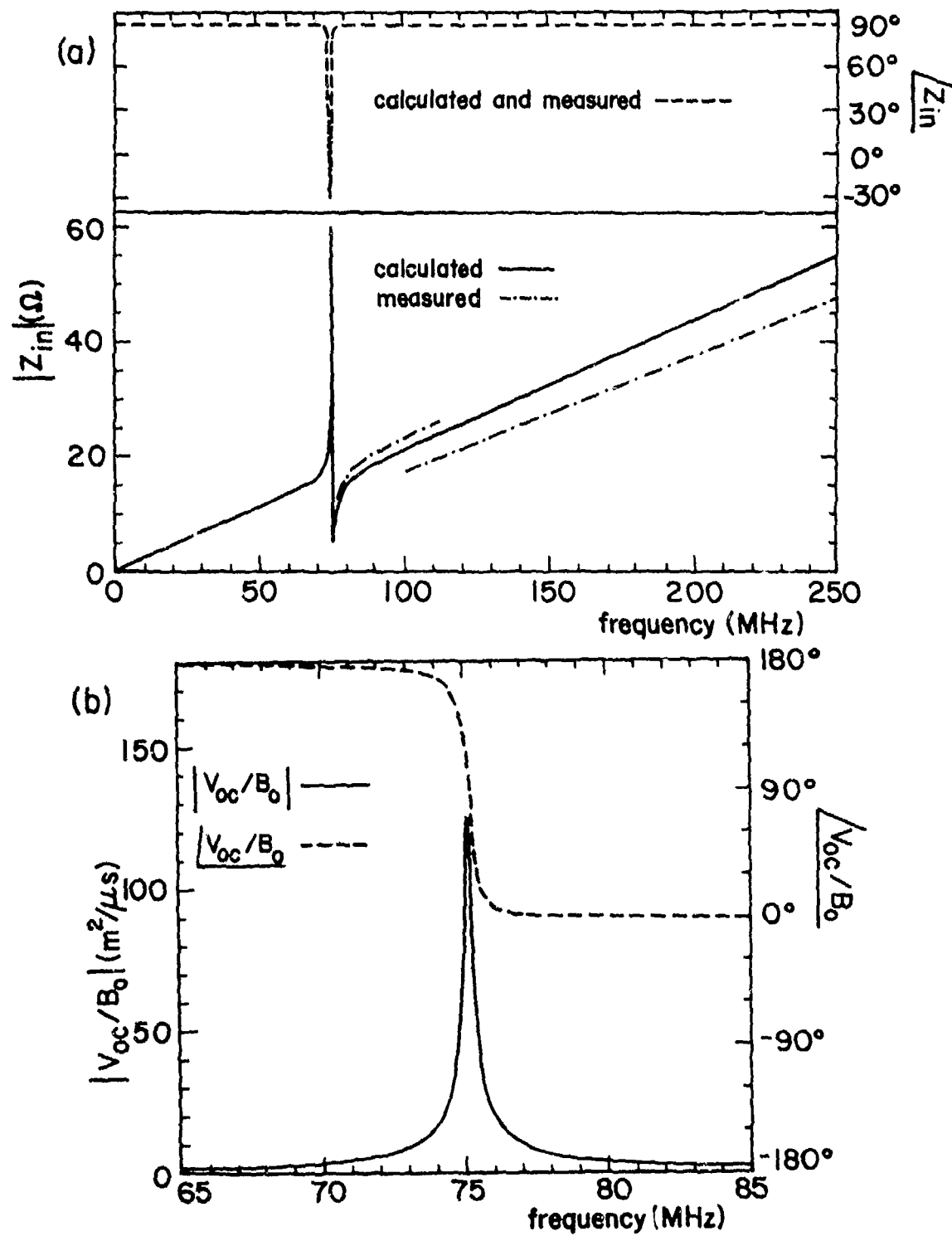


Fig. 85. Input impedance and open-circuit voltage of the AT-536/ARN Marker Beacon Antenna (75 MHz).

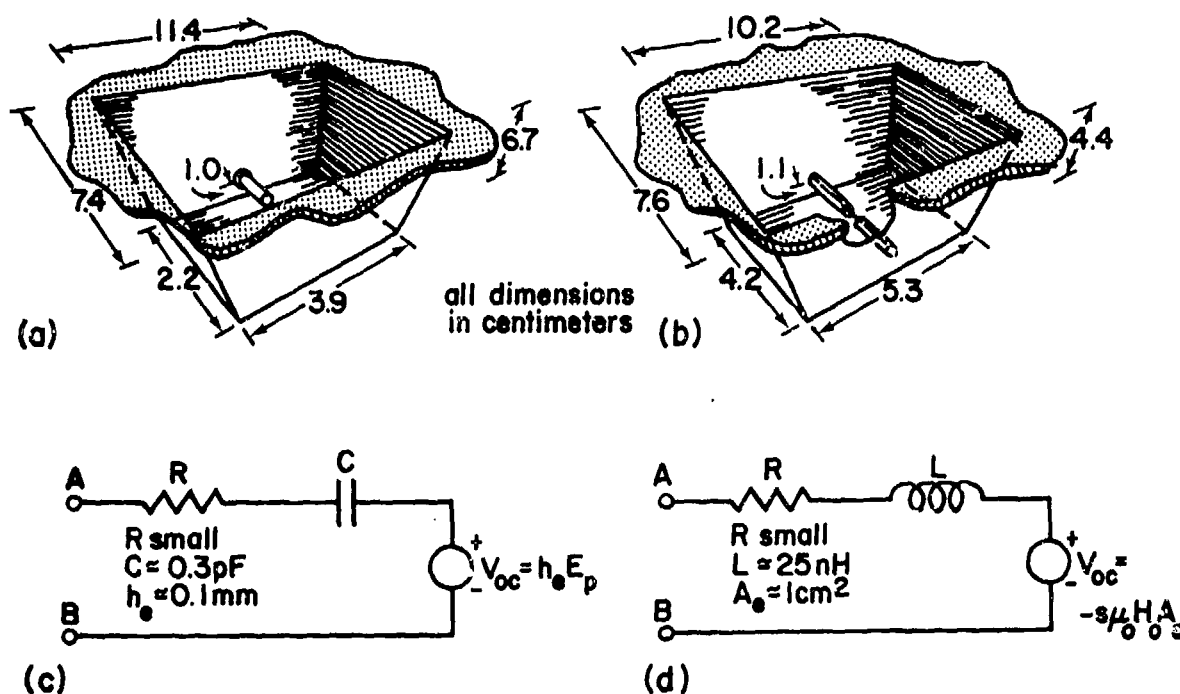


Fig. 86. Schematic diagrams and equivalent circuits of two typical low-range-radio-altimeter (LRRRA) antennas.

The two important problems to be considered are the field penetration into the horn and the effect of the horn on the impedance of the small stub or loop. From the viewpoint of mathematical tractability the geometries of Figs. 86a and 86b can be described as a quasi-pyramidal horn with an infinite flange. The boundary-value problem, either electrostatic or magnetostatic, is quite complicated to solve, since the solution requires solving a transcendental equation for the degree of the Legendre functions. Often an adequate engineering estimate can be obtained by studying the solutions for rectangular wells with different dimensions and then exercising one's judgment to choose the solution appropriate to the geometries of Figs. 86a and 86b.

2.1.3.1.5 Large Antennas

There exist antennas whose dimensions are comparable to or even greater than the dimensions of an aircraft. For these antennas the airframe is

either part of the antenna itself or appears simply as a capacitive loading on the antenna. The HF (2 - 30 MHz) fixed-wire antenna is a typical example of the former case, while the VLF/LF (17 - 60 kHz) trailing-wire antenna represents the latter. The method of analyzing these antennas is given in Sec. 2.1.2.3.1.

a. VLF/LF Trailing-Wire Antennas

Two common VLF/LF (17 - 60 kHz) transmitting wire antennas are shown in Fig. 42. The response of this type of antenna to EMP can be obtained using two different steps. In the first step, which is valid in the frequency range where the aircraft is electrically small, it is sufficient to use the capacitance C_a of the aircraft to characterize its influence on the antenna response. The interaction between the two wires in the case of the dual-wire antenna can be calculated expeditiously by decomposing the wire currents into common-mode (antenna-proper) currents and differential-mode (transmission-line) currents. In the second step, which is valid in the frequency region around the first few aircraft resonances, the aircraft is modeled by intersecting sticks, as given in Sec. 2.1.2.3.1.

Fig. 87b is the equivalent circuit appropriate for the situation depicted in Fig. 87a. Explicit approximate formulas for I'_{ind} , I''_{ind} , Z'_a , h , Z''_a , Z_c , α and β can be found in [73]. It should be noted that the response of the single trailing-wire antenna shown in Fig. 42 can be directly obtained from that of the dual-wire antenna by letting the length of the short wire go to zero.

The input admittance and the short-circuit induced current of the dual-wire antenna (Fig. 87) are given in Fig. 88 for frequencies below 0.5 MHz, and in Fig. 89 for the frequency range between 0.5 MHz and 6 MHz, which includes the first two resonant frequencies of the aircraft (E-4) under consideration. Notice that in Fig. 89 the frequency scale (1 MHz - 6 MHz) on the top is for the solid wiggly curve, whereas the bottom frequency scale (0.5 MHz - 1 MHz) is for the dotted curve. The loading effects of the antenna transmitter and coupler on the induced antenna-wire currents can be found in [74].

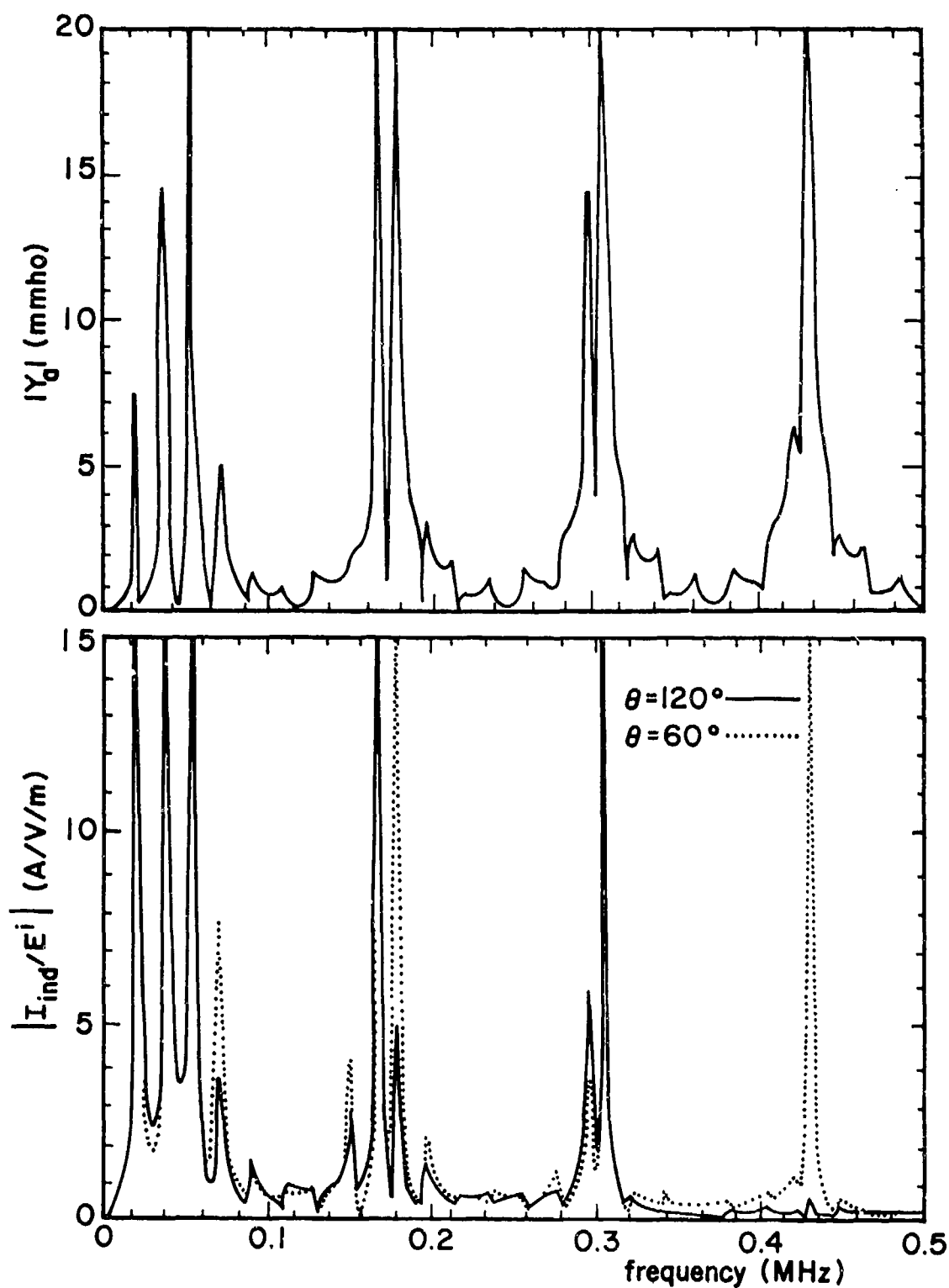


Fig. 88. Frequency variation below 0.5 MHz of input admittance Y_a and short-circuit induced current I_{ind} across A,B of Fig. 87. ($L_1 = 1.2$ km, $L_2 = 7.2$ km, $a = 2$ mm, $\theta_o = 3^\circ$, $h = 63$ m, $Z_c = 1.3$ k Ω , $C_a = 2.4$ nF.)

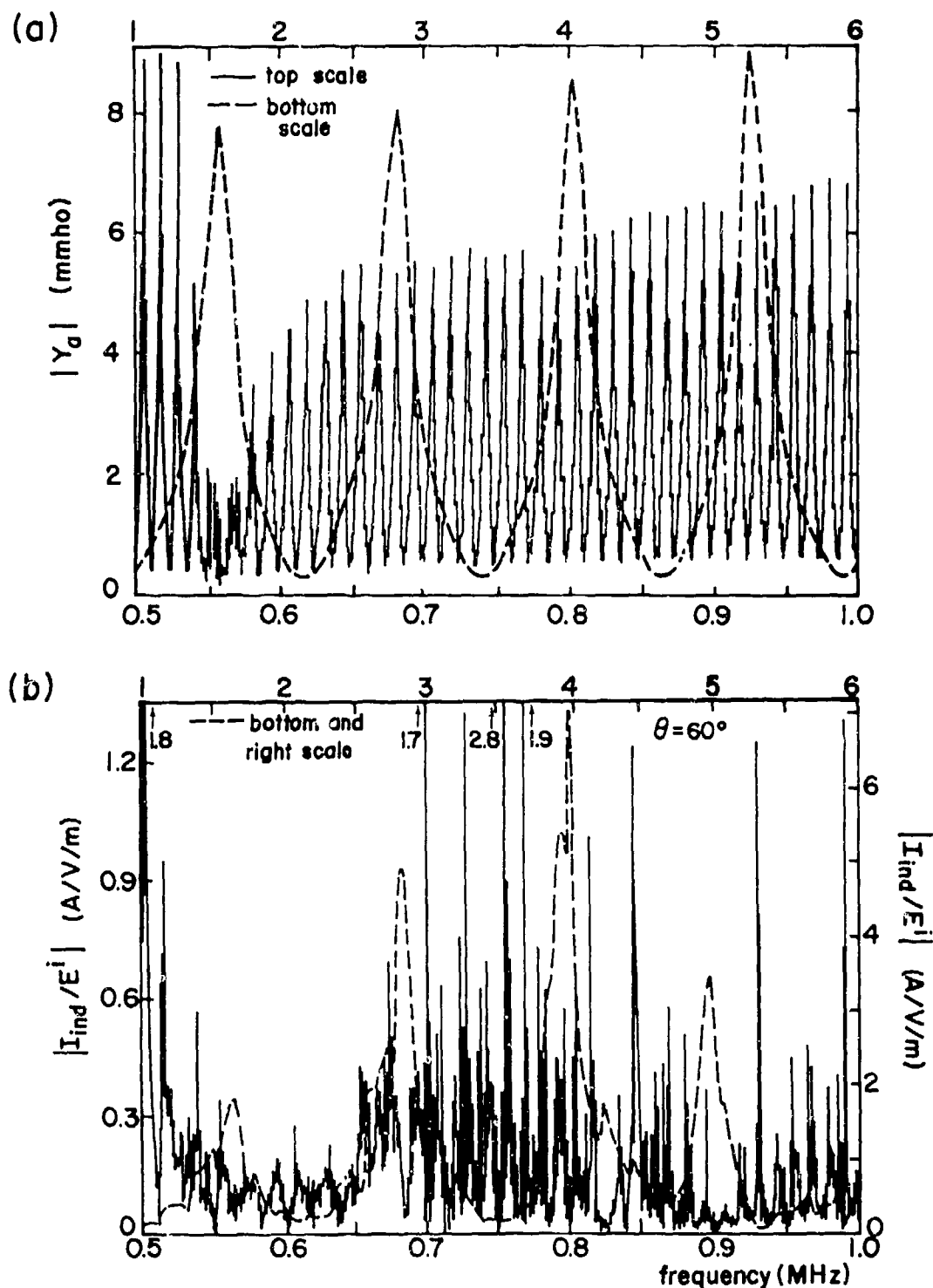


Fig. 89. Frequency variation (0.5 - 6 MHz) of input admittance Y_a and short-circuit induced current I_{ind} across A,B of Fig. 87. In (b) the bottom and right vertical scales are for the dotted line and the top and left vertical scales are for the solid line.

b. HF Fixed-Wire Antenna

The two HF fixed-wire antennas on the E-4 aircraft are shown in Fig. 90a. A schematic drawing of the stick-model aircraft used in the calculations is shown in Fig. 90b. To find the input impedance between A,B when the port A',B is terminated by the impedance Z_L , let the antenna be driven with the voltage V between A,B. The induced currents on the antenna wires and the aircraft can be decomposed into (a) radiating currents on the aircraft, (b) a TEM mode such that the wire currents are of equal magnitude and direction with the "return current" along the fuselage, and (c) a TEM mode such that the wire currents are of equal magnitudes but opposite directions (with no net current along the fuselage). The details of this decomposition can be found in [75]. An equivalent circuit of the antenna is shown in Fig. 90c. The admittance Y_a is defined at an imaginary gap across the fuselage at the location of the antenna feed-point, and can be obtained using a stick-model aircraft. The transmission line with the characteristic impedance Z_c' represents the first TEM mode described above, whereas the transmission line with impedance Z_c'' represents the second TEM mode. The ideal transformers account for the coupling between the TEM modes and the radiating currents. The current I_{ind} is induced on the fuselage by a plane wave at the location of the antenna feed gap and in the absence of the antenna wires (see Fig. 90b). The other current generators are found using the transmission-line theory of [2]. Fig. 91 shows the frequency variation of the input impedance and effective height. In this case, the effective height relates the open-circuit voltage to the incident electric field, and is a function of the angle of incidence and polarization of the incident plane wave. These quantities are defined in Fig. 90b. Furthermore, both the input impedance and effective height depend on the load impedance Z_L . In Fig. 91 the values $Z_L = 0$, $Z_L = \infty$ and $\theta = 120^\circ$ have been used. Quantities with superscript "sc" correspond to $Z_L = 0$, and quantities with superscript "oc" correspond to $Z_L = \infty$. The variation of h_e with θ can be found in [75]. The transient response of this antenna to an incident, double exponential plane wave is given in [76].

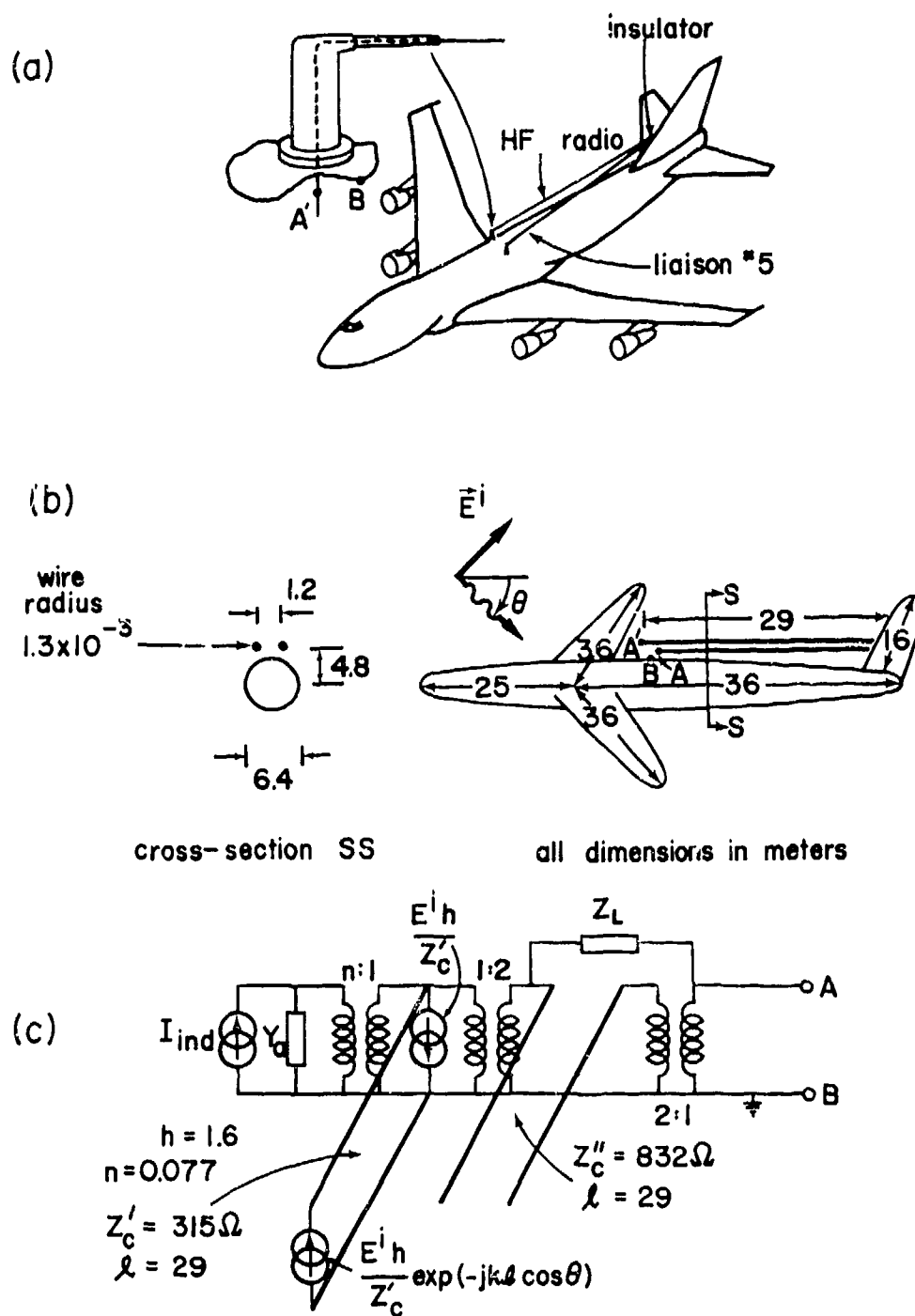


Fig. 90. Schematic diagrams and equivalent circuit of the two HF fixed-wire antennas on the E-4 aircraft. Z_L is the load impedance across A',B.

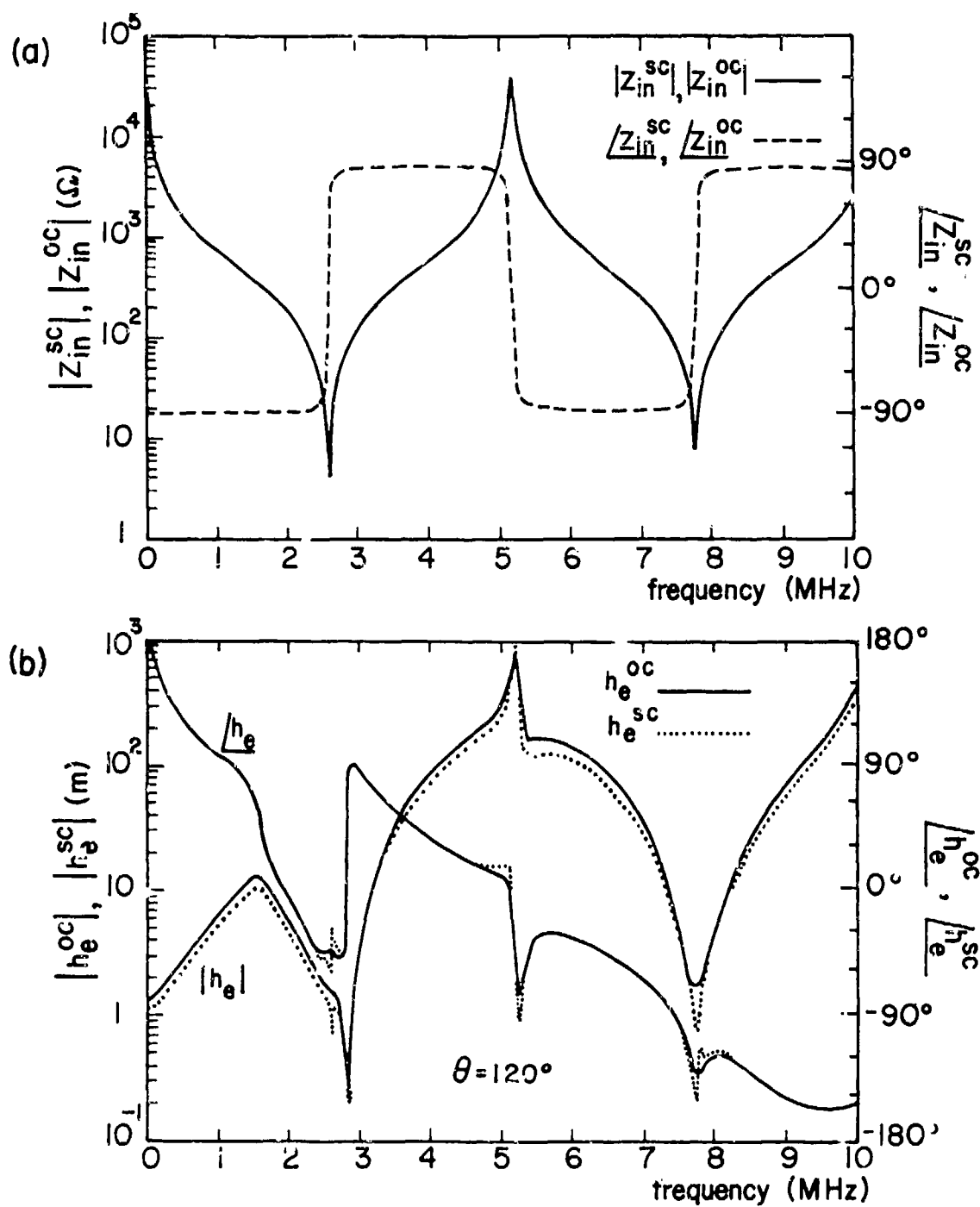


Fig. 91. Input impedance and effective height of the HF (2-30 MHz) fixed-wire antennas on the E-4 aircraft.

c. HF Notch Antenna

The HF notch antenna shown in Fig. 92b can be found on the B-1 aircraft. This antenna has a slot parallel to the leading edge of the vertical stabilizer and it is shunt fed at the base. The equivalent circuit is given in Fig. 92c. The circuit elements Y_a and I_{ind} refer to a horizontal gap across the entire vertical stabilizer at the junction between the fuselage and the stabilizer. These two quantities are obtained from stick-model calculations. The ideal transformer accounts for the fact that the induced short-circuit current flowing in the narrow strip of the leading edge of the vertical stabilizer is only a fraction of the total induced short-circuit current flowing in the entire vertical stabilizer. The transmission line with length 3.08 m accounts for the slot, and the voltage generator V_0 represents the magnetic field linking the slot at low frequencies. The input impedance and the equivalent height are shown in Fig. 93.

2.1.3.2 Apertures

The determination of EMP penetration through holes or apertures in the outer skin of a missile or an aircraft is an important first step in the overall assessment of induced voltages and currents at the connector pins of electronic boxes. Apertures of interest may be intentional (e.g., small windows, open access holes, etc.), or they may be inadvertent (as in the cases of cracks around doors and plates covering access ports and of poor electrical seams (riveted joints) in the outer skin of an aircraft or a missile).

In this section apertures of small and moderate electrical size in an infinite, perfectly conducting plane will be treated, whereas apertures backed by wires and cavities, and apertures on a curved surface will be dealt with in Chaps. 2.2 and 2.3.

2.1.3.2.1 Dipole-Moment Approximation and Polarizabilities

In many EMP-related applications, the apertures of interest are electrically small, a property which leads to very helpful simplification in computation. By electrically small it is meant that the maximum dimensions across the aperture are short relative to the wavelengths of

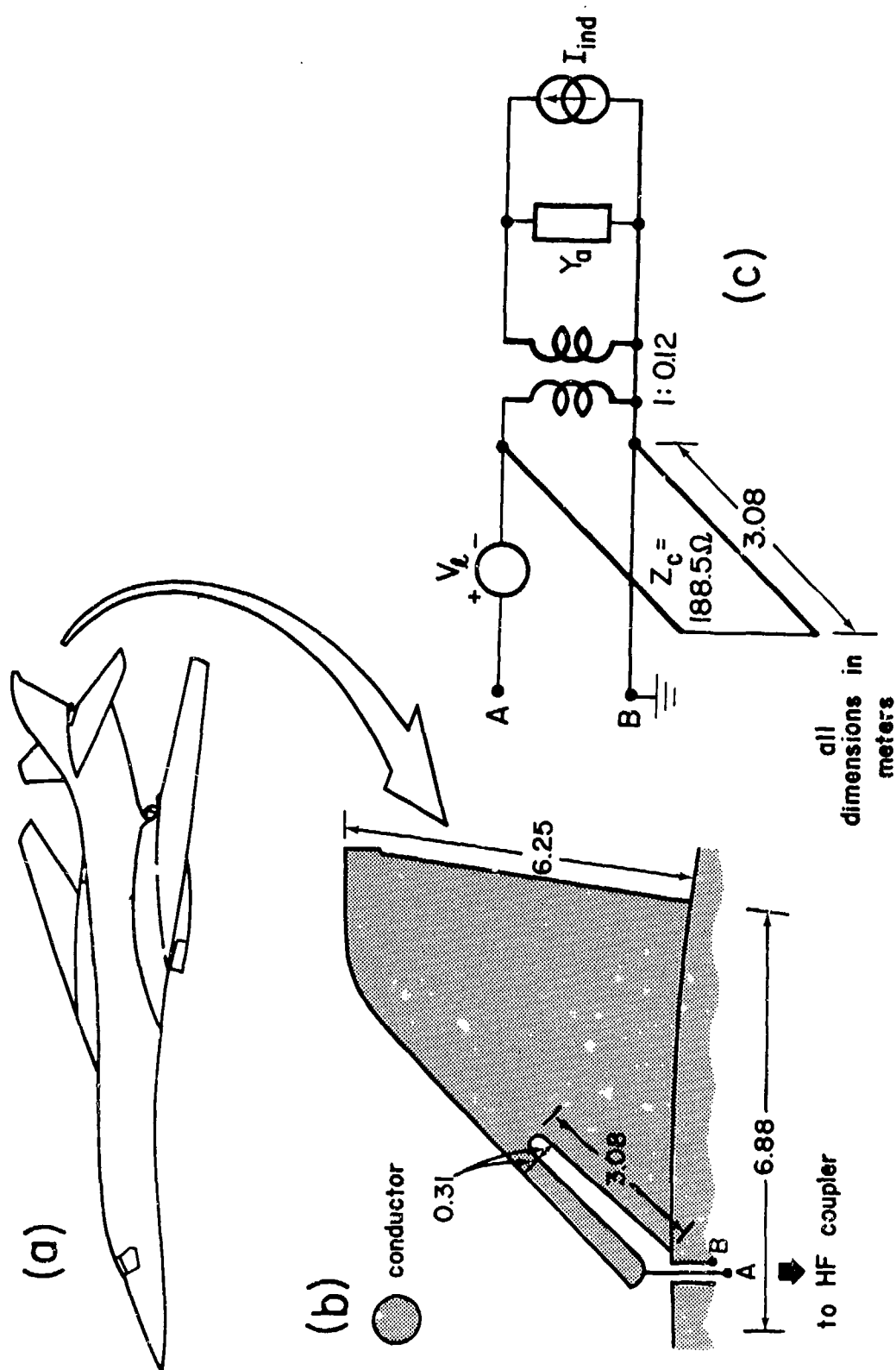


Fig. 92. Schematic diagrams and equivalent circuit for the HF notch antenna.

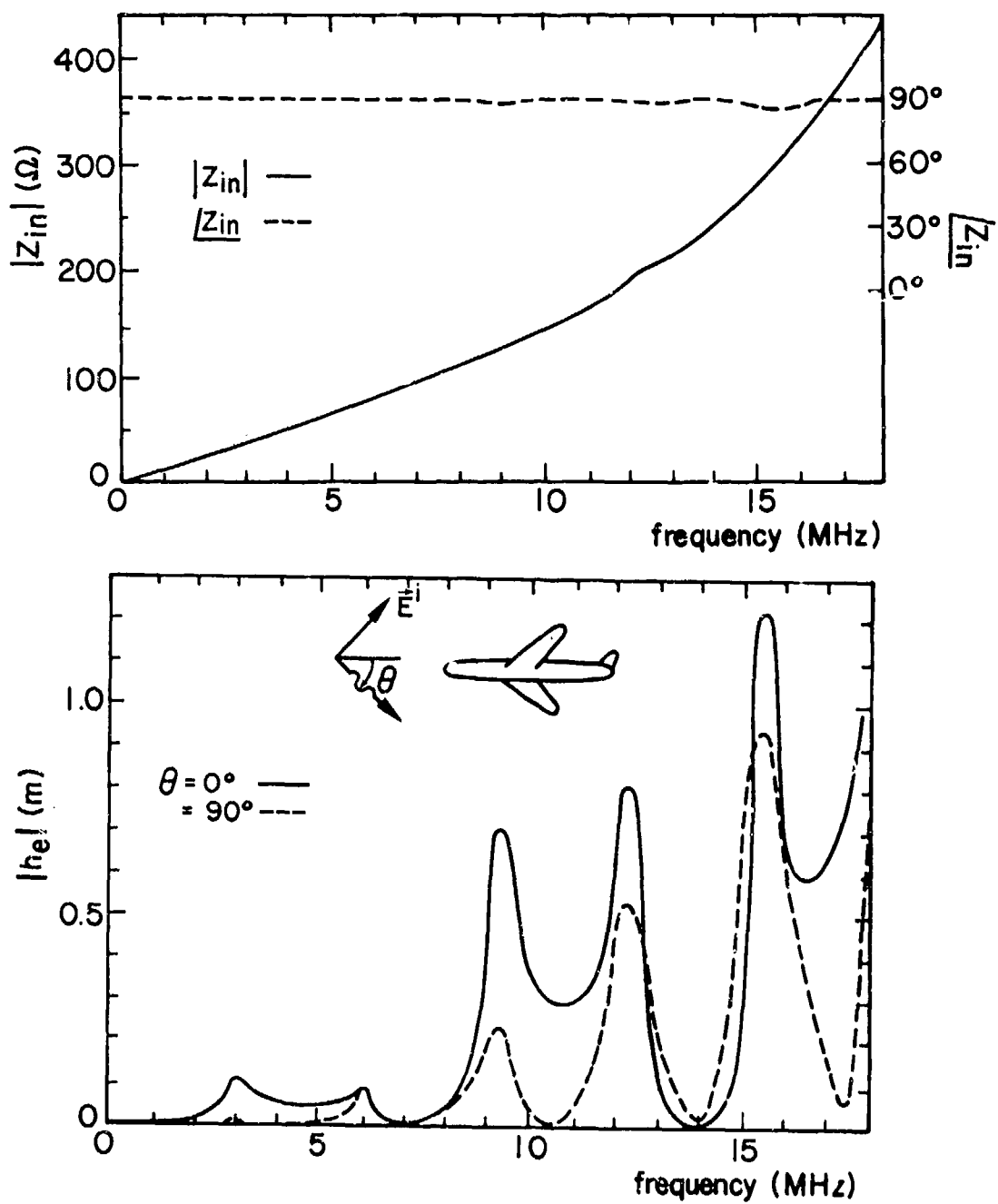


Fig. 93. Input impedance and effective height of the HF notch antenna.

interest. The electromagnetic field that penetrates an electrically small aperture in an infinite, perfectly conducting plane can be represented approximately by the radiation from equivalent electric and magnetic dipoles \vec{p}_a and \vec{m}_a of the aperture (cf. Sec. 1.4.1.4.2). The dipole fields \vec{E}^d , \vec{H}^d at \vec{r} radiated by \vec{p}_a and \vec{m}_a at the origin of the coordinate system in free space are given by

$$\begin{aligned}\vec{E}^d(\vec{r}, s) &= -\frac{1}{\epsilon} \nabla \times [\vec{p}_a(s) \times \nabla G(\vec{r}, s)] + s\mu \vec{m}_a(s) \times \nabla G(\vec{r}, s) \\ \vec{H}^d(\vec{r}, s) &= -s \vec{p}_a(s) \times \nabla G(\vec{r}, s) - \nabla \times [\vec{m}_a(s) \times \nabla G(\vec{r}, s)]\end{aligned}\quad (124)$$

where $G(\vec{r}, s) = e^{-\gamma r}/(4\pi r)$. In the time domain \vec{E}^d , \vec{H}^d are given by

$$\begin{aligned}\vec{E}^d(\vec{r}, t) &= \frac{1}{4\pi\epsilon} \nabla \times \left[\frac{1}{r^2} \dot{p}_a(t) \vec{i}_z \times \vec{i}_r \right] - \frac{1}{4\pi} \frac{1}{r^2} \dot{m}_a(t) \times \vec{i}_r \\ \vec{H}^d(\vec{r}, t) &= \frac{1}{4\pi} \frac{1}{r^2} \dot{p}_a(t) \vec{i}_z \times \vec{i}_r + \frac{1}{4\pi} \nabla \times \left[\frac{1}{r^2} \dot{m}_a(t) \times \vec{i}_r \right]\end{aligned}\quad (125)$$

where \vec{i}_z is the unit vector perpendicular to the plane of the aperture, and the dot represents time differentiation. Note that the radiated far field has been neglected in (125).

The aperture equivalent electric and magnetic dipole moments \vec{p}_a , \vec{m}_a are related to the electric and magnetic (imaged) polarizability tensors $\overleftrightarrow{\alpha}_e$ and $\overleftrightarrow{\alpha}_m$ of an aperture in an infinite ground plane by (cf. 1.4.1.4.2)

$$\vec{p}_a = 2\epsilon \overleftrightarrow{\alpha}_e \cdot \vec{E}_{sc}, \quad \vec{m}_a = -2\overleftrightarrow{\alpha}_m \cdot \vec{H}_{sc} \quad (126)$$

where \vec{E}_{sc} , \vec{H}_{sc} are the short-circuit fields at the aperture.

The representation of the effect of an aperture in a perfectly conducting surface by equivalent dipoles is suggested in Fig. 94. In Fig. 94a is seen

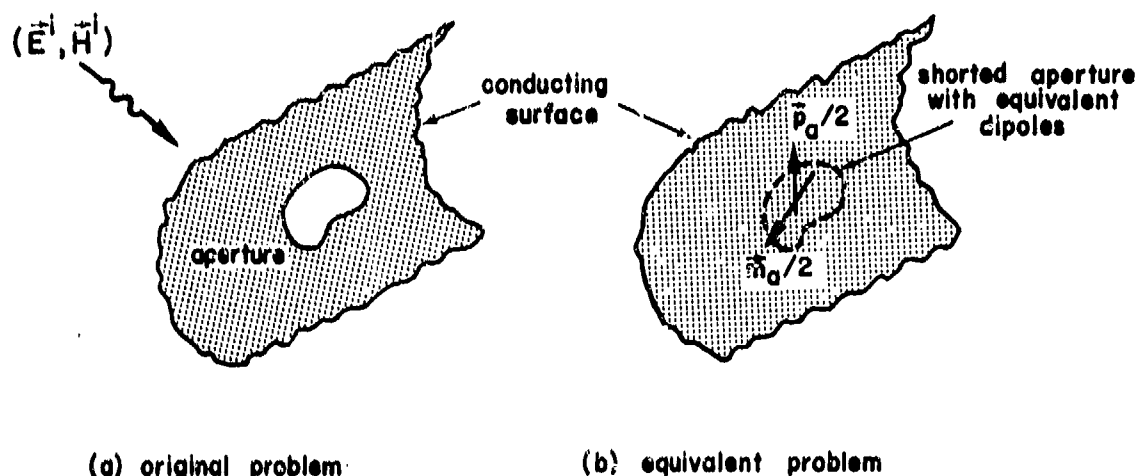


Fig. 94. (a) Portion of conducting surface with aperture; (b) shorted aperture with equivalent dipoles on shadow side of surface.

a portion of a conducting surface with an aperture illuminated by an incident field (\vec{E}^i, \vec{H}^i) , while in Fig. 94b is shown the equivalent problem. In the equivalent problem, the aperture is short-circuited, i.e., the conducting surface is made continuous, extending over the region where the aperture existed in the original problem, and the equivalent dipoles are placed at the shorted aperture on the shadow side of the surface — opposite from the so-called illuminated side of the surface in which the sources exist.

2.1.3.2.2 Simple Apertures

a. Simple Apertures of Small Electrical Size

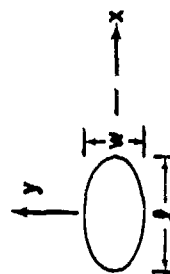
The imaged polarizabilities $\alpha_e^{\leftrightarrow}$ and $\alpha_m^{\leftrightarrow}$ for the circle, the ellipse, and the narrow slit have been computed theoretically [77-79] and their expressions are given in table 14.

Cohn [80,81] has experimentally confirmed the expressions in table 14 and has also experimentally determined the polarizabilities of apertures of several other shapes. His data, together with values based upon table 14, are presented in Figs. 95-98; Figs. 96-98 are taken from [82].

Table 14. APERTURE POLARIZABILITIES

Shape	$\alpha_{e,zz}$	$\alpha_{m,xx}$	$\alpha_{m,yy}$
Circle (d = Diameter)	$\frac{1}{12} d^3$	$\frac{1}{6} d^3$	$\frac{1}{6} d^3$
Ellipse* ($w < l$)	$\frac{\pi}{24} \frac{w^2 l}{E(m)}$	$\frac{\pi}{24} \frac{l^3}{K(m) - E(m)}$	$\frac{\pi}{24} \frac{l^3 m}{(l/w)^2 E(m) - K(m)}$
Narrow Ellipse ($w \ll l$)	$\frac{\pi}{24} w^2 l$	$\frac{\pi}{24} \frac{l^3}{\ln(4l/w) - 1}$	$\frac{\pi}{24} w^2 l$
Narrow Slit ($w \ll l$)	$\frac{\pi}{16} w^2 l$	$\frac{\pi}{24} \frac{l^3}{\ln(4l/w) - 1}$	$\frac{\pi}{16} w^2 l$

* Ellipse eccentricity $e = \sqrt{1 - (w/l)^2}$,



K and E are the complete elliptic integrals of the first and second kind, $m = e^2$.

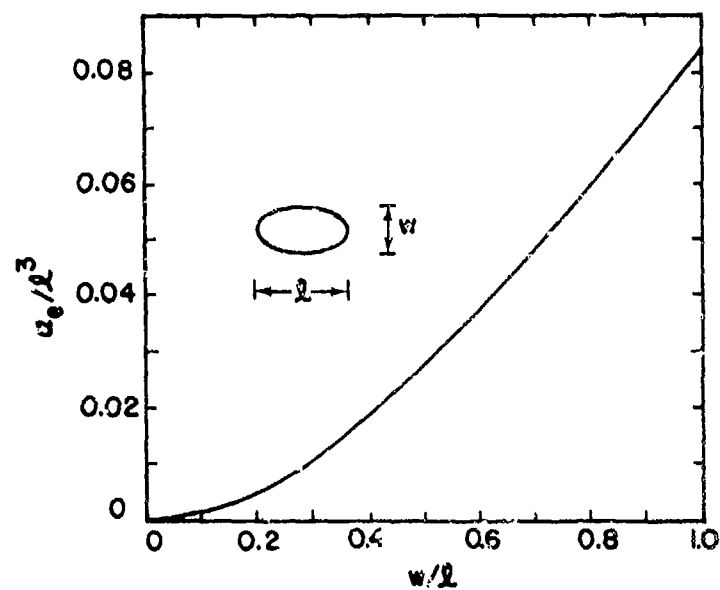


Fig. 95. Normalized electric (imaged) polarizability of an elliptical aperture.

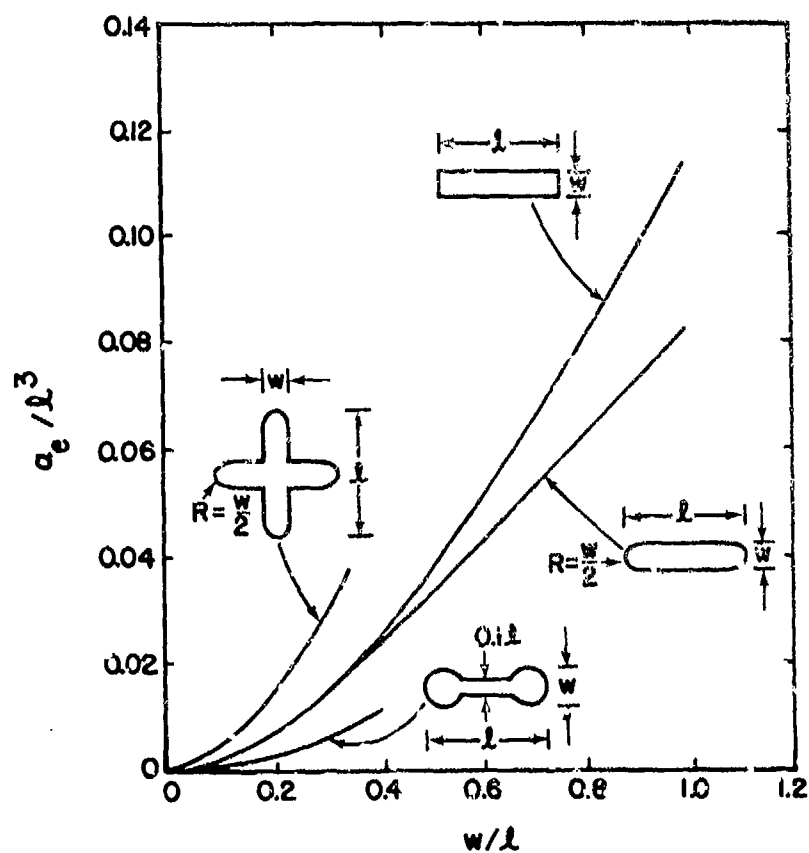


Fig. 96. Normalized electric (imaged) polarizabilities for four aperture shapes.

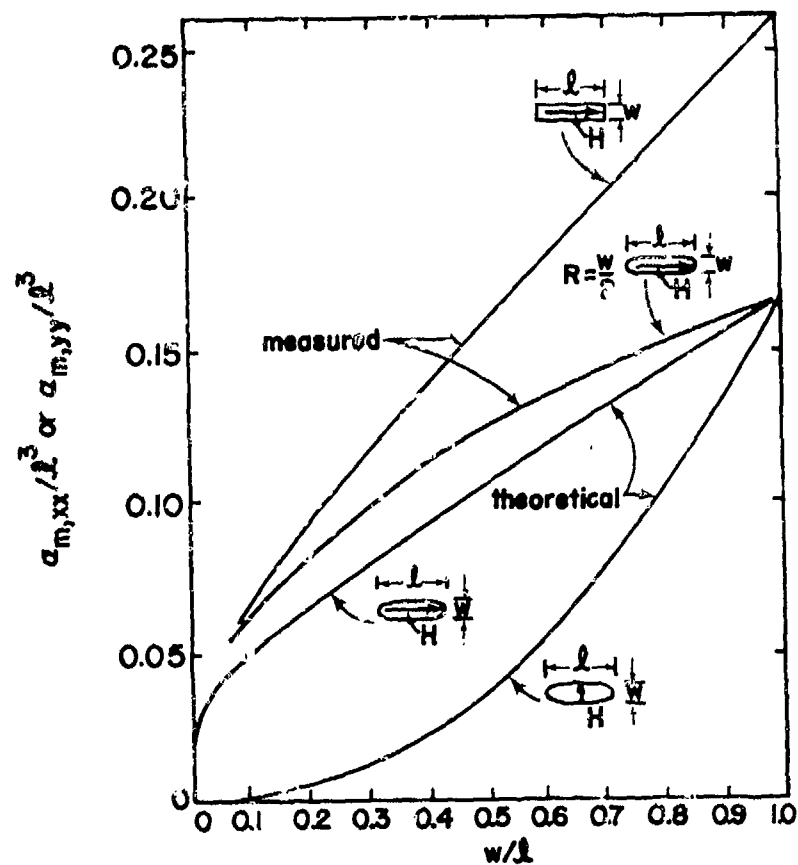


Fig. 97. Normalized magnetic (imaged) polarizabilities for elliptical, rectangular, and rounded rectangular apertures.

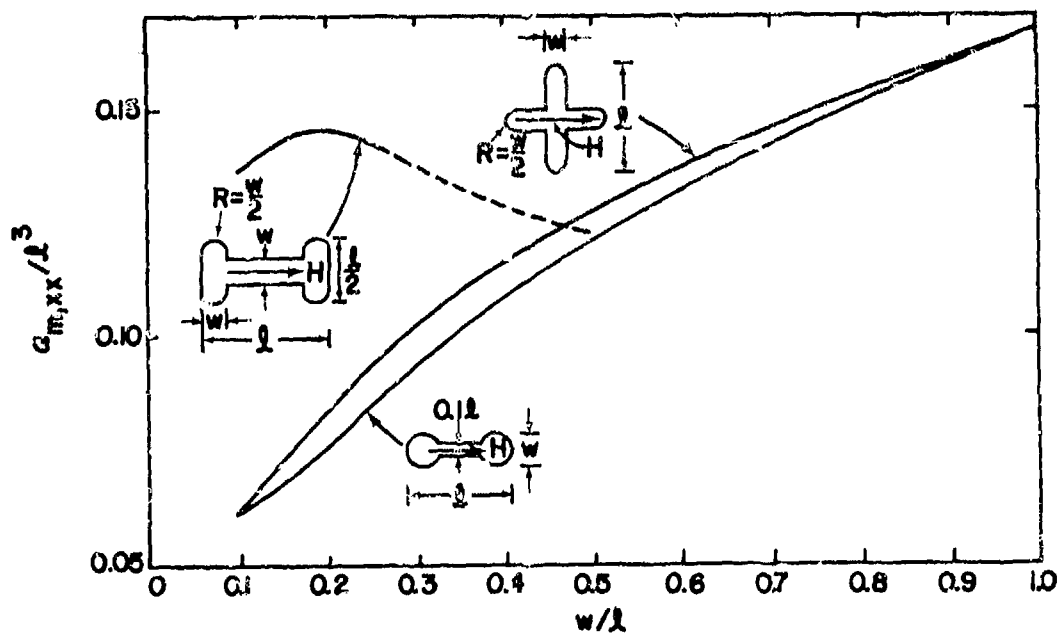


Fig. 98. Normalized magnetic (imaged) polarizabilities for three aperture shapes.

De Meulenaere and Van Bladel present polarizability data using a different normalization [79]. In Fig. 99 is plotted $\alpha_e A^{-3/2}$ versus w/ℓ , where A is the aperture area. As can be seen in Fig. 99, $\alpha_e A^{-3/2}$ is not very sensitive to aperture shape and depends almost entirely upon the width-to-length ratio w/ℓ . The normalized magnetic (imaged) polarizability components, $\alpha_{m,yy} A^{-3/2}$ and $A^{3/2} \alpha_{m,xx}^{-1}$, are presented in Figs. 100 and 101 [79]. Except for the cross, one sees very similar values for the various shapes. Since values for the ellipse are almost identical to those for the rounded-off rectangle, the curve for the ellipse is omitted.

The normalization factor $A^{3/2}$ used in Figs. 99-101 is very important in practical applications because of the fact that with the exception of $\alpha_{m,xx}$ for the cross, the normalized polarizabilities of various apertures are nearly the same as those for an ellipse. Hence, one may employ the simple formulas in table 14 for the ellipse to compute the polarizabilities of other shapes (except $\alpha_{m,xx}$ of the cross), if the normalization $A^{3/2}$ is used.

Latham [83] has noted that for an elliptical aperture, the electric (imaged) polarizability normalized by the ratio A^2/P , where A is the aperture area and P is its perimeter, is

$$\frac{P}{A^2} \alpha_e \approx \frac{4}{3\pi} \quad (127)$$

independent of the eccentricity of the ellipse. Latham also points out that a useful empirical formula for $\alpha_{m,yy}/(A^2/P)$ for a rectangular aperture is

$$\frac{P}{A^2} \alpha_{m,yy} \approx \frac{\pi}{8} (1 + 0.55 w/\ell) \quad (128)$$

When $w/\ell < 0.5$, (128) differs from an accurate numerical solution by less than 3%.

Jaggard and Papas [84] have proposed the following bounds for simple apertures with small eccentricity, which is defined to be $(1 - w^2/\ell^2)^{1/2}$,

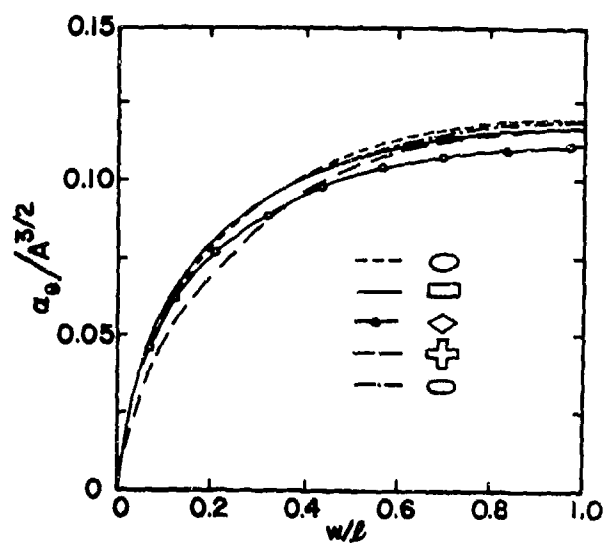


Fig. 99. Normalized electric (imaged) polarizabilities of various apertures.

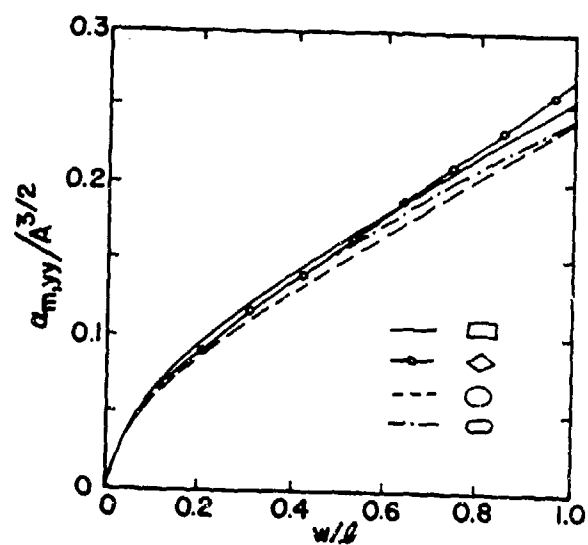


Fig. 100. Normalized magnetic (imaged) polarizabilities.

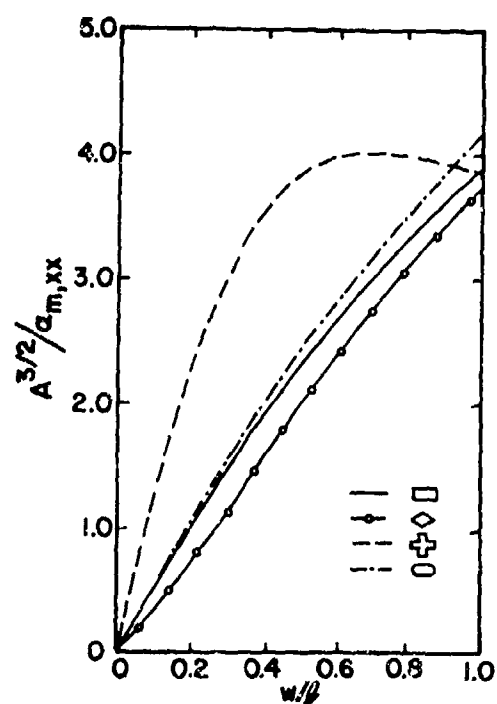
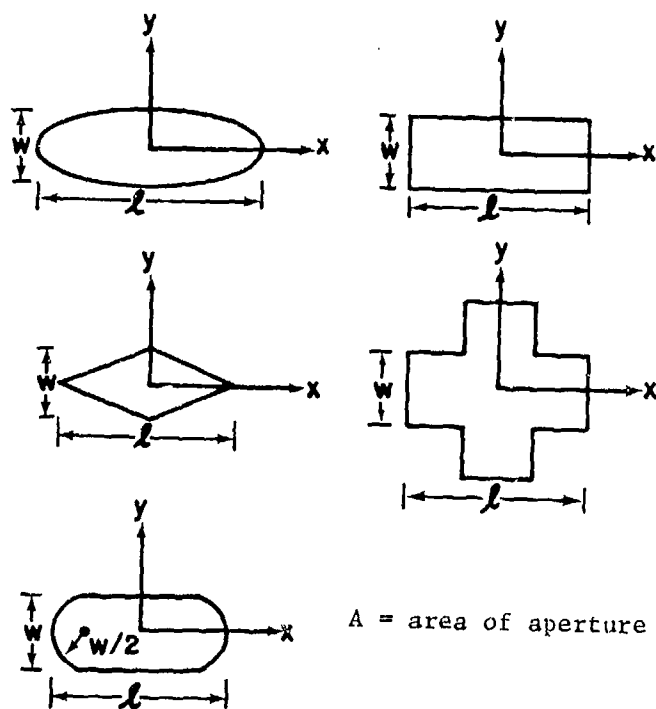


Fig. 101. Normalized reciprocal magnetic (imaged) polarizabilities.



$$\frac{16}{3\pi} \frac{A^2}{P} \leq \alpha_e \leq \frac{8}{3} \left(\frac{A}{\pi} \right)^{3/2} \quad (129)$$

$$\frac{16}{3} \left(\frac{A}{\pi} \right)^{3/2} \leq \langle \alpha_m \rangle \leq \frac{16}{3} \left(\frac{P}{2\pi} \right)^3 \quad (130)$$

where $\langle \alpha_m \rangle = (\alpha_{m,xx} + \alpha_{m,yy})/2$.

b. Simple Apertures of Moderate Electrical Size

If the frequency of interest is sufficiently high that the largest dimension of the aperture is no longer a small fraction of the wavelength, then the dipole-moment approximation is no longer valid. Fortunately, in most EMP applications this situation is relatively rare because of the band-limited nature of the EMP and the physical sizes of the systems of interest.

b.1 Circular Aperture

Fig. 102 shows the aperture electric field distribution for a circular aperture of radius 0.25λ for normal incidence [85]. Some comparisons with experimental results [86] are also given in the figure. Fig. 103 shows the penetrant electric and magnetic field along the axis of a circular aperture. The fields computed by the dipole-moment approximation are also displayed in the figure.

b.2 Slots

Long and narrow slots can be approximated in many EMP applications by infinitely long slots, if the observation point is not near the slot ends or near a point at which the slot field has a null. For TE illumination (which is more important than TM excitation) of an infinitely long, narrow slot in an infinite ground plane (Fig. 104) the electric field E_x in the slot is [87]

$$E_x(x,0) = \frac{1}{2\sqrt{(kw/2)^2 - (kx)^2}} \left[j \frac{Z_0 H_{sc,y}}{\ln(\Gamma kw/8) + j\pi/2} + kx E_{sc,z} \right] \quad (131)$$

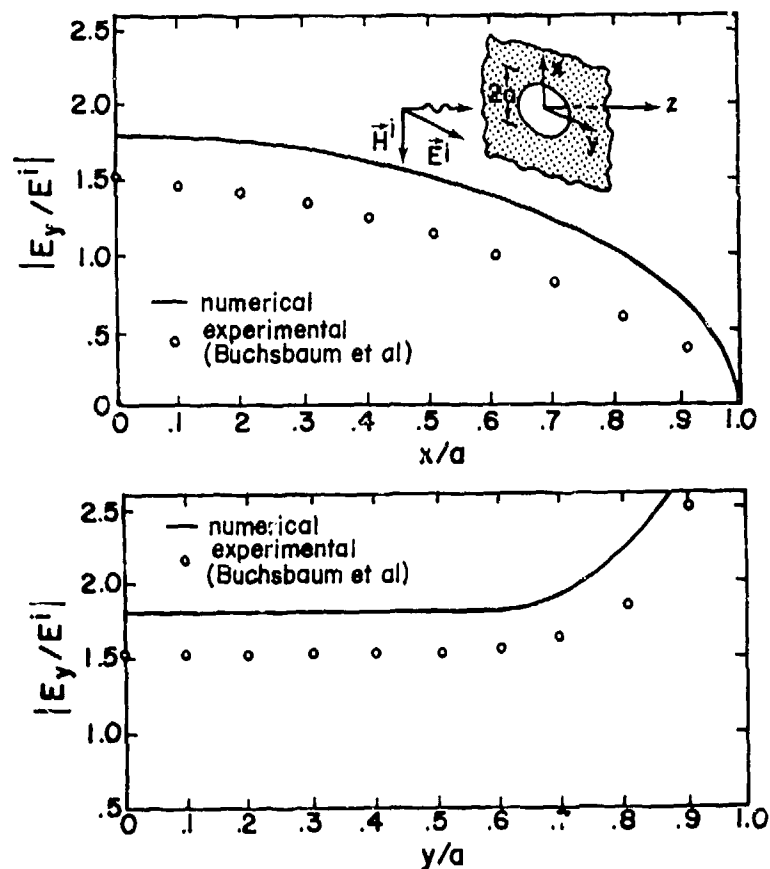


Fig. 102. Electric field distribution in the aperture of 0.5λ diameter for normal incidence.

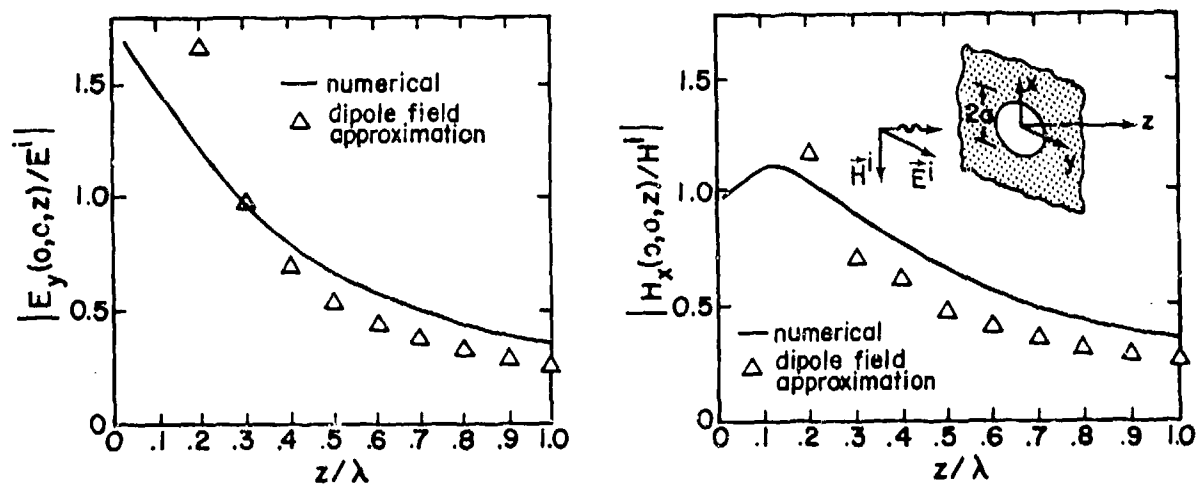


Fig. 103. Penetrant electric and magnetic field for an aperture of 0.5λ diameter and for normal incidence.

where $|kw| \ll 1$ and $\Gamma = 1.78107$ is Euler's constant and w is the slot width. At a distance ρ from the slot axis large relative to slot width w and small relative to wavelength λ , the magnetic field H_y is

$$H_y(\rho, \psi) = \frac{H_{sc,y}}{\ln(\Gamma kw/8) + j\pi/2} (f_e + j\pi/4) + j(kw/16)f_o E_{sc,z}/Z_o \quad (132)$$

where

$$f_e \approx \frac{1}{2} \ln\left(\frac{\Gamma k \rho}{2}\right) - \frac{1}{16} \left(\frac{w}{\rho} \sin \psi\right)^2 - \frac{3}{128} \left(\frac{w}{\rho} \sin \psi\right)^4$$

$$f_o \approx \frac{w}{\rho} \sin \psi + \frac{1}{4} \left(\frac{w}{\rho} \sin \psi\right)^3 \quad (133)$$

For a finite-length narrow slot maximum penetration occurs when the slot length is near $\lambda/2$ or an odd multiple thereof, and when the magnetic field of the excitation is directed parallel to the slot axis and is an

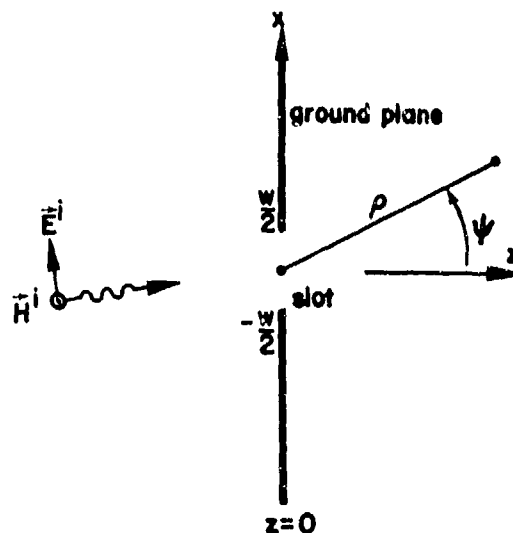


Fig. 104. Infinite slot in a ground plane subject to TE illumination (cross-sectional view).

even function relative to the slot center. Strong penetration also occurs through slots whose lengths are multiples of one wavelength when the axially directed magnetic field possesses a rich odd-function component. Such "worst case" data can be derived from the dual results available for thin wires.

As an example illustrative of the EMP field passing through a finite-length slot, $H_{sc,y}(t)$ is selected to be constant along the slot axis with the double exponential pulse time variation shown in Fig. 105a. Fig. 105b displays the time history of the electric field $E_x(t)$ at a point two meters behind the plane and passing through a $155 \text{ cm} \times 1.3 \text{ cm}$ slot.

2.1.3.2.3 Hatch Apertures

Examples of some hatch apertures of practical interest are shown in Fig. 106, each of which represents a narrow slot of width g cut in a thin, perfectly conducting plane. In all cases, $g \ll \lambda$, $g \ll w$, and $g \ll d$.

Figs. 106a and 106d might represent a "covered" access hole or doorway, while Fig. 106b might be a circular access hole with a cover hinged on one side (at $y = -d/2$) and latched on the other (at $y = d/2$). The example of Fig. 106e could be representative of a doorway closed by means of double doors, while Fig. 106c might represent the cover of a missile silo.

Polarizabilities for the hatch apertures of Fig. 106 are given in [88,89], and simple formulas for these polarizabilities are summarized in table 15. One should note that the presence of the hinge and latch in Fig. 106b has negligible effect on $\alpha_{m,yy}$, while it does modify $\alpha_{m,xx}$ and α_e , as is seen from a comparison of the polarizabilities of the apertures of Figs. 106a and 106b. Similarly, the presence of the center slot in Fig. 106e influences only $\alpha_{m,xx}$.

Closed doors and covered access holes often are sealed by means of conducting gaskets that can reduce the penetration of electromagnetic energy. The presence of the gasket can be accounted for in the determination of the polarizabilities [88,89], and the resulting polarizabilities of gasket-sealed hatch apertures are listed in table 16.

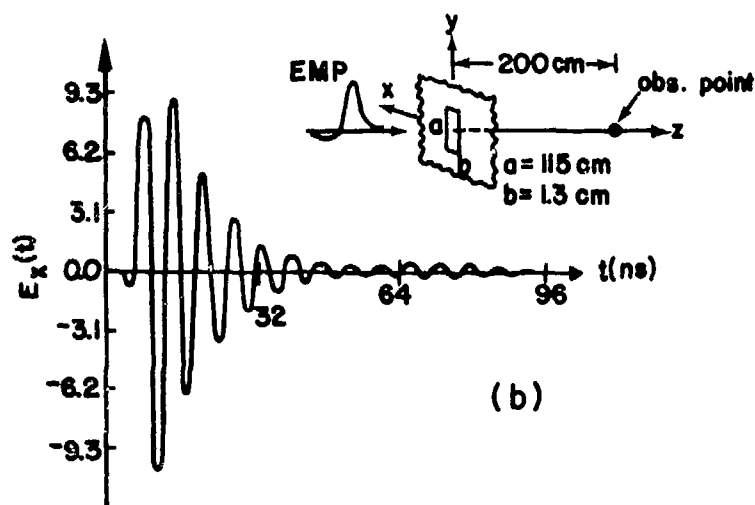
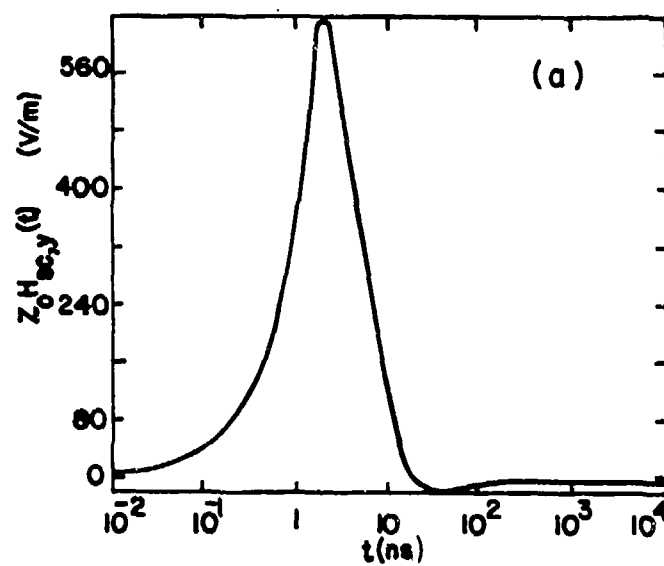


Fig. 105. (a) Waveform of the short-circuit field $H_{sc,y}(t)$ in the plane;
 (b) time-domain behavior of $E_x(t)$ at a point 2 meters behind
 the rectangular aperture.

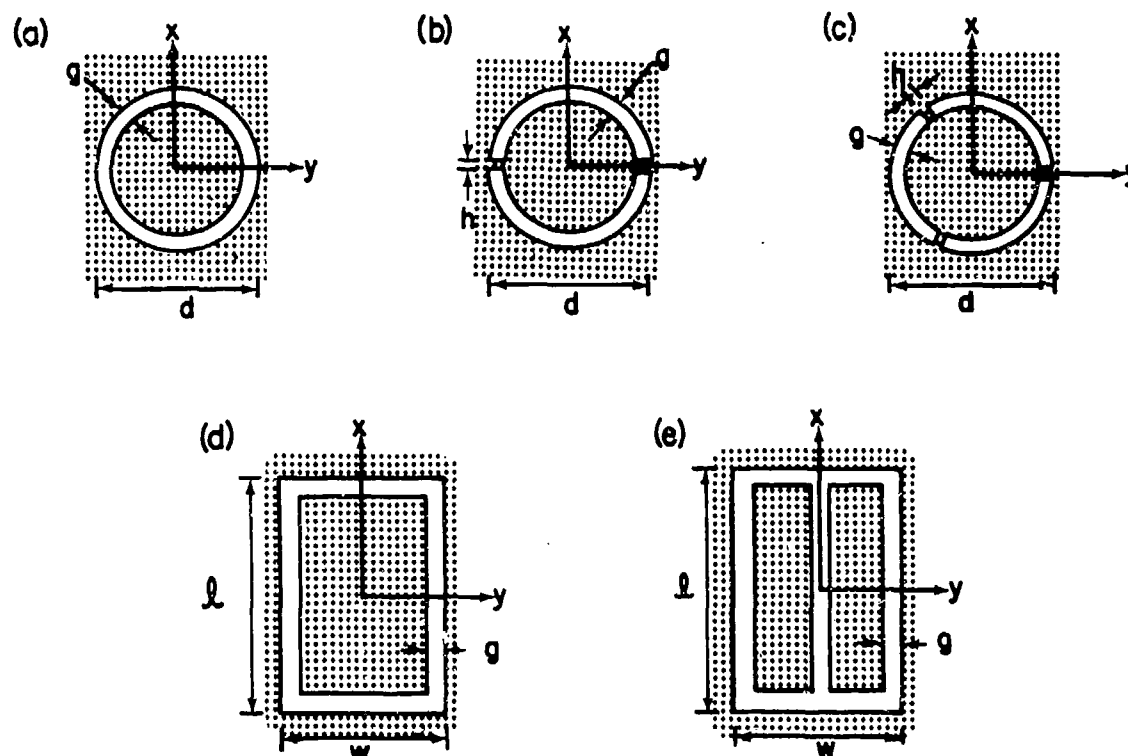


Fig. 106. Hatch apertures.

2.1.3.2.4 Array of Apertures

For a row of periodically spaced apertures as shown in Fig. 107 the normalized (imaged) polarizabilities $\bar{\alpha}_e$, $\bar{\alpha}_{m,xx}$ and $\bar{\alpha}_{m,yy}$ are given by [83,90], with the x,y -axes being the principal axes of the apertures,

$$\bar{\alpha}_e \equiv \frac{\alpha_e}{\alpha_{eo}} = \frac{1}{1 - \frac{2\zeta(3)}{\pi} \frac{\alpha_{eo}}{d^3}} \quad (134)$$

$$\bar{\alpha}_{m,xx} \equiv \frac{\alpha_{m,xx}}{(\alpha_{mo})_{xx}} = \frac{1}{1 + \frac{2\zeta(3)}{\pi} \frac{(\alpha_{mo})_{xx}}{d^3}} \quad (135)$$

Table 15. POLARIZABILITIES OF HATCH APERTURES

Aperture	α_e	$\alpha_{m,xx}$	$\alpha_{m,yy}$
Fig. 106a	$\frac{\pi^2}{32} \frac{d^3}{\ln(16 d/g) - 2}$	$\frac{\pi^2}{16} \frac{d^3}{\ln(16 d/g) - 2}$	$\frac{\pi^2}{16} \frac{d^3}{\ln(16 d/g) - 2}$
Fig. 106b	$\frac{\pi^2 d^3}{16 \Omega} \frac{2 s \mu \epsilon}{s \mu \epsilon + 128 k / (\pi \Omega d g^2)}$	$\frac{\pi^2 d^3}{8 \Omega} \left[1 - \frac{8/\pi^2}{1 + \Omega g^2 / (8 \pi d h)} \right]$	$\frac{\pi^2}{16} \frac{d^3}{\ln(16 d/g) - 2}$
Fig. 106c	$\frac{\pi^2 d^3}{16 \Omega} \frac{2 s \mu \epsilon}{s \mu \epsilon + 192 h / (\pi \Omega d g^2)}$	$\frac{\pi^2 d^3}{8 \Omega} \left[1 - \frac{27/(4 \pi^2)}{1 + 9 \Omega g^2 / (64 \pi d h)} \right]$	$\frac{\pi^2 d^3}{8 \Omega} \left[1 - \frac{27/(4 \pi^2)}{1 + 9 \Omega g^2 / (64 \pi d h)} \right]$
Fig. 106d	$\frac{\pi}{4} \frac{\ell^2 w}{(1 + \ell/w) \ln[4(\ell + w)/g]}$	$\frac{\pi}{12} \frac{\ell^3 [1 + 3(w/\ell)]}{\ln[4(\ell + w)/g]}$	$\frac{\pi}{12} \frac{w^3 [1 + 3(\ell/w)]}{\ln[4(\ell + w)/g]}$
Fig. 106e	$\frac{\pi}{4} \frac{\ell^2 w}{(1 + \ell/w) \ln[4(\ell + w)/g]}$	$\frac{\pi}{24} \frac{\ell^3 [8/3 + 7(w/\ell) + 2(w/\ell)^2]}{\ln[4(\ell + w)/g]}$	$\frac{\pi}{12} \frac{w^3 [1 + 3(\ell/w)]}{\ln[4(\ell + w)/g]}$

Note: $\Omega = 2[\ln(16d/g) - 2]$

Table 16. POLARIZABILITIES OF GASKET-SEALED HATCH APERTURES

Aperture	$\alpha_e(s)$	$\alpha_{m,xx}(s)$	$\alpha_{m,yy}(s)$
Fig. 106a	$\frac{2}{16} \frac{\pi s \epsilon}{2G_c + sC_c} \frac{d^4}{2G_c + sC_c}$	$\frac{2}{4\mu} \cdot \frac{d^2}{1/L_c + sG_c}$	$\frac{2}{4\mu} \cdot \frac{d^2}{1/L_c + sG_c}$
Fig. 106b	$\frac{2}{16} \frac{\pi s \epsilon}{2G_c + sC_c} \frac{d^4}{2G_c + sC_c + 2/sL_h}$		$\frac{2}{4\mu} \cdot \frac{d^2}{1/L_c + sG_c}$
Fig. 106c	$\frac{2}{16} \frac{\pi s \epsilon}{2G_c + sC_c} \frac{d^4}{2G_c + sC_c + 3/sL_h}$		
Fig. 106d	$\frac{s \epsilon l^2 w}{G + sC}$	$\frac{1}{1 + sL_x G_x} \alpha_{m,xx}^{(0)}$	$\frac{1}{1 + sL_y G_y} \alpha_{m,yy}^{(0)}$
Fig. 106e	$\frac{s \epsilon l^2 w}{G + sC}$	$\frac{1}{1 + s(L_x + L_a)G'_x} \alpha_{m,xx}^{(0)}$	$\frac{1}{1 + sL_y G_y} \alpha_{m,yy}^{(0)}$

Notes: (i) Δ = gasket thickness; σ = gasket conductivity.

(ii) The static polarizabilities $\alpha_{m,xx}^{(0)}$ and $\alpha_{m,yy}^{(0)}$ in the table entries are those of the corresponding hatch aperture without gasket found in table 15.

(iii) Constants: $G = 2\sigma\Delta(l+w)/g$; $C = 2\epsilon\Omega(l+w)/\pi$; $\Omega = 2\ln[4(l+w)/g]$; $L_x = \mu\pi l(1+2w/l)/8\Omega$;

$$L_y = \mu\pi w(1+2l/w)/8\Omega; \quad G'_x = \sigma\Delta l/g; \quad G'_y = G_x/(1+w/3l); \quad L_a = (\pi\mu l/24\Omega)w^2/l^2;$$

$$G_y = \sigma\Delta w/g; \quad G_c = \pi\sigma\Delta d/2g; \quad L_c = \mu d/[4\ln(16d/g) - 8]; \quad L_h = \mu\pi g^2/(64h);$$

$$C_c = 2\epsilon d[\ln(16d/g) - 2].$$

$$\bar{\alpha}_{m,yy} \equiv \frac{\alpha_{m,yy}}{(\alpha_{mo})_{yy}} = \frac{1}{1 - \frac{4\zeta(3)}{\pi} \frac{(\alpha_{mo})_{yy}}{d^3}} \quad (136)$$

Here α_{eo} , $(\alpha_{mo})_{xx}$ and $(\alpha_{mo})_{yy}$ are the polarizabilities of one isolated aperture in an infinite ground plane, and ζ is the Riemann zeta-function and $\zeta(3) = 1.202$. If there are only two apertures, one simply replaces $2\zeta(3)$ with unity in (134) - (136). A comparison of the simple formulas (134) - (136) with the numerical results of Fig. 108 [91] for the case of rectangular apertures shows that they are accurate to within 5% for (aperture-aperture separation) ≥ 2 times (aperture's maximum linear dimension).

2.1.3.2.5 Apertures With Impedance Loading

Loading an aperture with a sheet impedance or coating the conductor containing the aperture (Figs. 109a,b) will change the aperture's polarizabilities. The relation between the magnetic (imaged) polarizability α_m of a loaded aperture and that of the same aperture without impedance loading α_{mo} is approximately

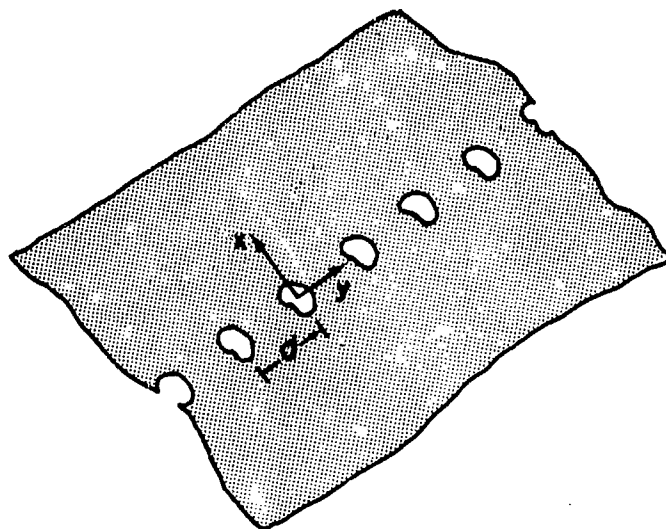


Fig. 107. A row of periodic small apertures.

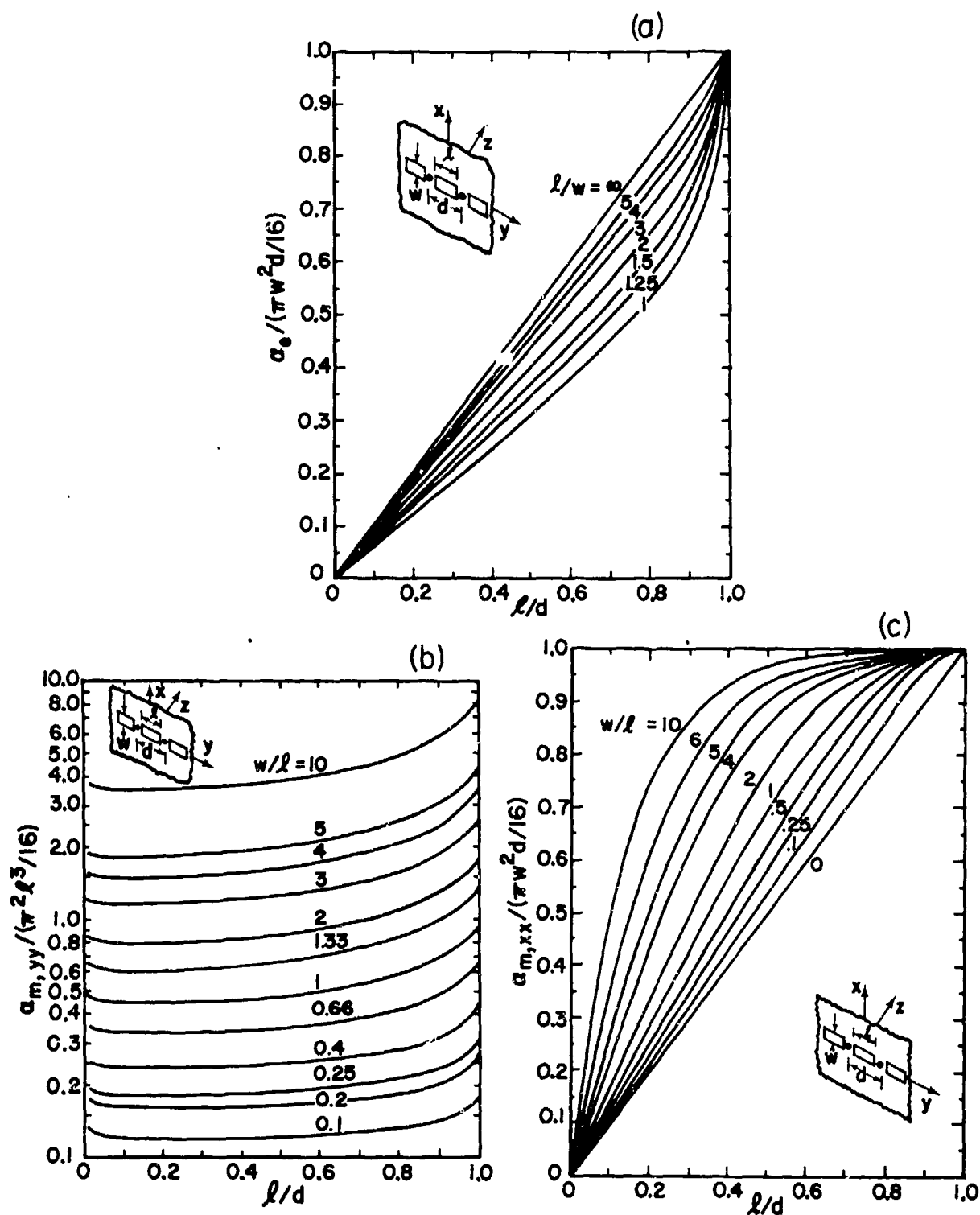


Fig. 108. (a) Normalized electric (imaged) polarizability; (b) and (c) normalized magnetic (imaged) polarizabilities for a single aperture in an infinite, linear array subject to uniform illumination.

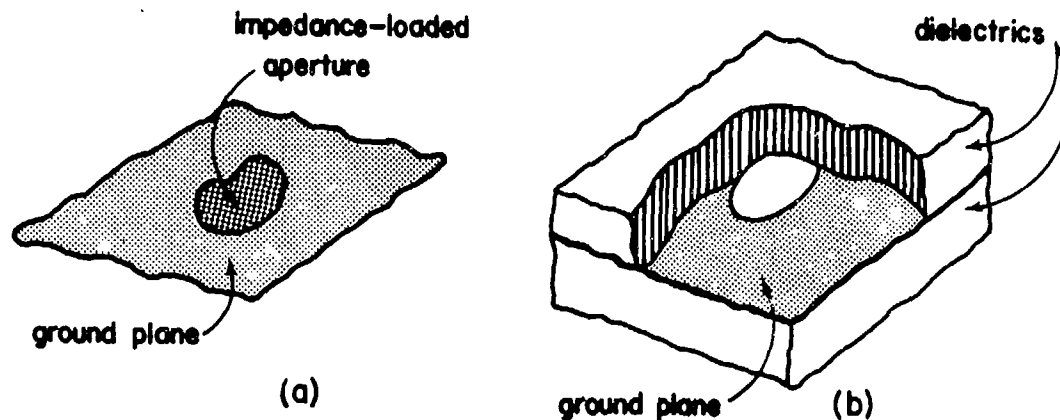


Fig. 109. (a) An impedance-loaded aperture in an infinite ground plane; (b) a hole in an infinite ground plane sandwiched by dielectric slabs.

$$\alpha_m \approx \left(1 + \frac{2}{3\pi} \frac{sL_a}{Z_s} \right)^{-1} \alpha_{m0} \quad (137)$$

in which Z_s denotes the sheet impedance of the aperture loading material, and L_a is the "equivalent" inductance of the unloaded aperture and given approximately by

$$L_a \approx \mu_0 \frac{A}{P} \quad (138)$$

for apertures of small eccentricity, where A = aperture area and P = aperture perimeter.

The factor by which the magnetic flux linking the aperture is reduced by the loading is the same as that given in (137) above, except that the factor $2/(3\pi)$ is replaced by $1/4$.

The geometry of a dielectric-backed and dielectric-coated conductor containing a circular aperture of radius a is shown in Fig. 110. The dielectric backing has relative permittivity ϵ_{r1} and the coating has relative

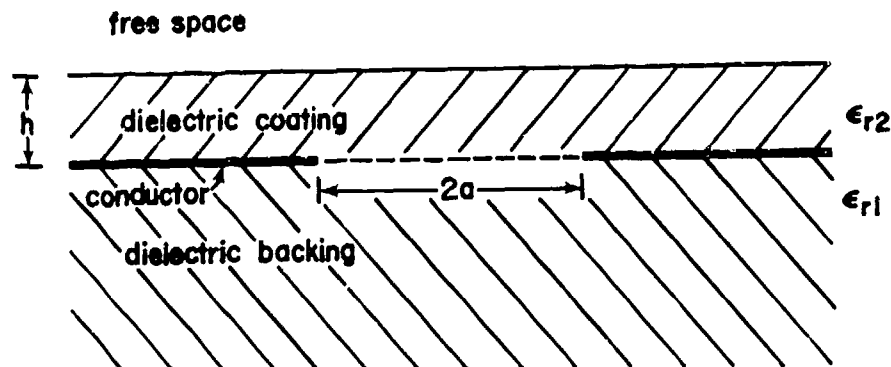


Fig. 110. A dielectric-coated and dielectric-backed circular aperture in a ground plane.

permittivity ϵ_{r2} and thickness h . The region above the coating is free space. The electric (imaged) polarizability of the aperture α_e is given by [92]

$$\alpha_e = \frac{2\epsilon_{r1}}{\epsilon_{r1} + \epsilon_{r2}} F(\epsilon_{r1}, \epsilon_{r2}, h/a) \alpha_{eo} \quad (139)$$

in which α_{eo} is the electric (imaged) polarizability of the aperture in the conducting plane when $\epsilon_{r1} = \epsilon_{r2} = 1$. In the limit as $h \rightarrow 0$, $F \rightarrow (\epsilon_{r1} + \epsilon_{r2}) / (\epsilon_{r1} + 1)$, so that

$$\lim_{h \rightarrow 0} \alpha_e = \left(\frac{2\epsilon_{r1}}{1 + \epsilon_{r1}} \right) \alpha_{eo} \quad (140)$$

and when $h \rightarrow \infty$, $F \rightarrow 1$, so that

$$\lim_{h \rightarrow \infty} \alpha_e = \left(\frac{2\epsilon_{r1}}{\epsilon_{r1} + \epsilon_{r2}} \right) \alpha_{eo} \quad (141)$$

The ratio α_e/α_{eo} is shown plotted as a function of h/a for various values of ϵ_{r1} and ϵ_{r2} in Fig. 111. It should be noted that when $(h/a) \geq 1$, the result given in (141) is quite accurate.

2.1.3.3 Metallic and Advanced Composite Walls

The transfer-function relationship between the tangential field components \vec{E}_{to} and \vec{H}_{to} on the outer surface of a metallic or advanced composite wall and the field components \vec{E}_{ti} and \vec{H}_{ti} on the inner surface of the wall is of the following form (Fig. 112)

$$\begin{bmatrix} \vec{E}_{ti} \\ \vec{H}_{ti} \end{bmatrix} = \begin{bmatrix} \overleftrightarrow{B}_{11} & \overleftrightarrow{B}_{12} \\ \overleftrightarrow{B}_{21} & \overleftrightarrow{B}_{22} \end{bmatrix} \cdot \begin{bmatrix} \vec{E}_{to} \\ \vec{H}_{to} \end{bmatrix} \quad (142)$$

The matrix of dyadics in (142) is a "boundary connection supermatrix" [93]. Its dyadic elements $\overleftrightarrow{B}_{ij}$ can be written as

$$\begin{aligned} \overleftrightarrow{B}_{11} &= B_{11} \vec{1} \\ \overleftrightarrow{B}_{12} &= -B_{12} \vec{1}_n \times \vec{1} \\ \overleftrightarrow{B}_{21} &= B_{21} \vec{1}_n \times \vec{1} \\ \overleftrightarrow{B}_{22} &= B_{22} \vec{1} \end{aligned} \quad (143)$$

in which the parameters B_{ij} depend upon the structure and composition of the wall and $\vec{1}_n$ is the unit vector normal to the wall and pointing into the "inside" region bounded by the wall.

Equivalent electric and magnetic surface current densities located on the inner surface of the wall are often useful in the calculation of the fields penetrating the wall. These source densities can be considered to radiate in free space, or the wall can be replaced by a perfect conductor with an impressed magnetic surface current density (in the latter case it is not necessary to consider the electric current density). The original problem and its equivalents are shown in Fig. 112. The equivalent surface densities \vec{J}_{eq} and $\vec{J}_{m,eq}$ are

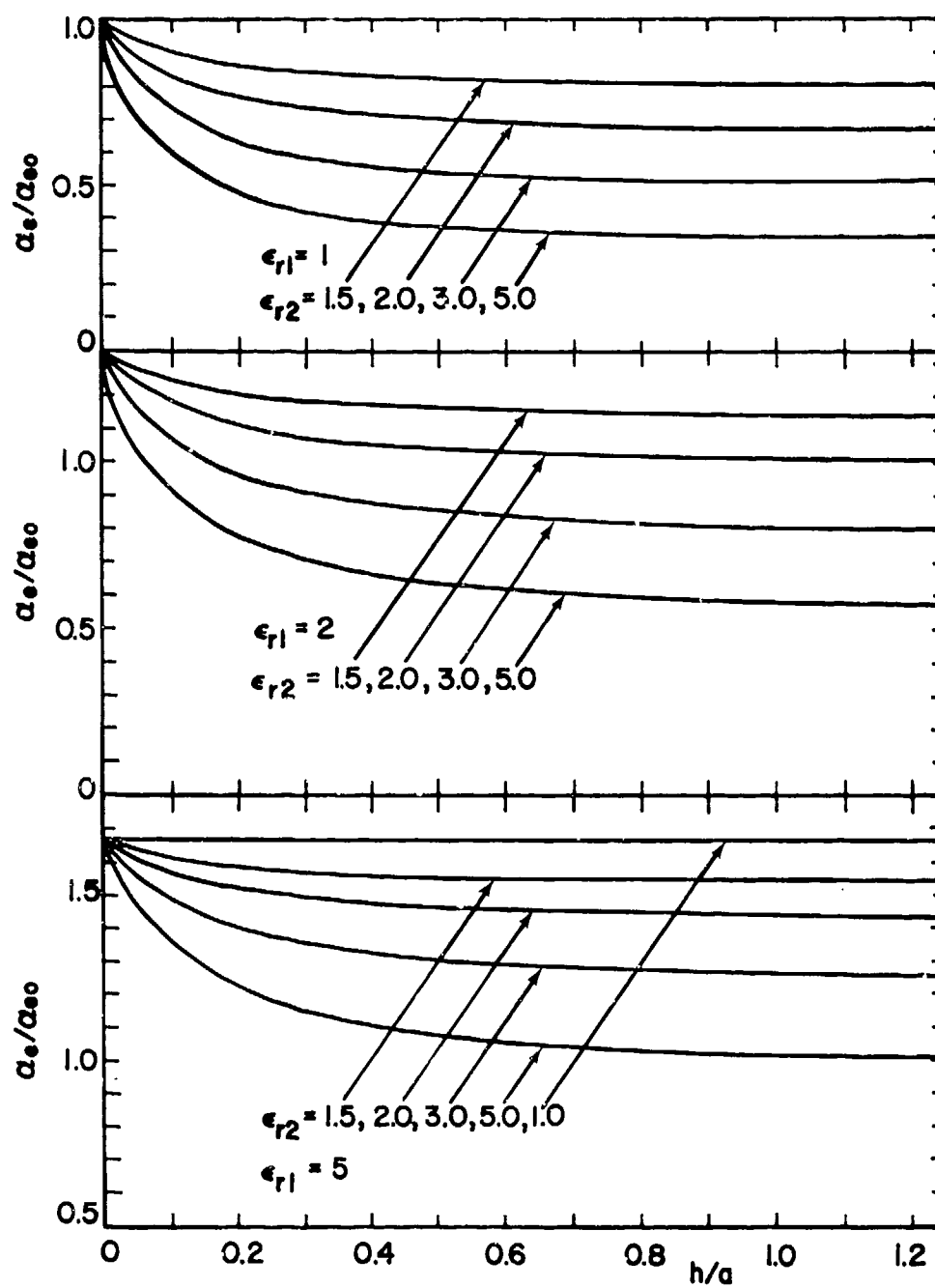
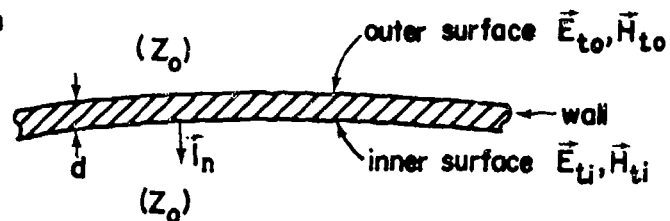


Fig. 111. Normalized electric (imaged) polarizability for various ϵ_{r1} and ϵ_{r2} values.

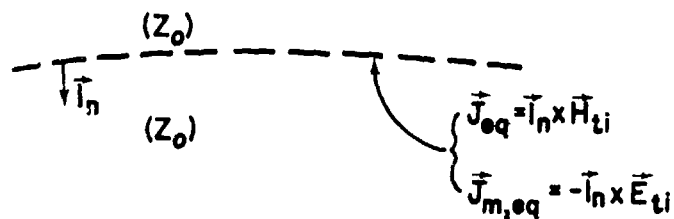
$$\begin{aligned}\vec{J}_{eq} &= \vec{I}_n \times \vec{H}_{ti} \\ &= -B_{21} \vec{E}_{to} + B_{22} \vec{I}_n \times \vec{H}_{to}\end{aligned}\quad (144)$$

$$\begin{aligned}\vec{J}_{m,eq} &= -\vec{I}_n \times \vec{E}_{ti} \\ &= -B_{11} \vec{I}_n \times \vec{E}_{to} - B_{12} \vec{H}_{to}\end{aligned}\quad (145)$$

original problem



equivalent problem: currents radiating in free space



equivalent problem: currents radiating in the presence of a perfect conductor

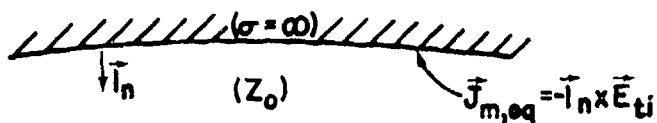


Fig. 112. The imperfect-wall penetration problem and its equivalent problems. The fields in the interior region are identical in each problem.

In most problems of interest, the wall is a good conductor, so that \vec{J}_{eq} , $\vec{J}_{m,eq}$ are related to \vec{H}_{sc} , \vec{H}_{sc} being the short-circuit field on the outside surface of the wall. In these cases, \vec{J}_{eq} and $\vec{J}_{m,eq}$ can be written in terms of the short-circuit surface current density $\vec{J}_{sc} = -\vec{I}_n \times \vec{H}_{sc}$ as

$$\vec{J}_{eq} = \vec{T}_{ce} \cdot \vec{J}_{sc} \quad (146)$$

$$\vec{J}_{m,eq} = \vec{T}_{cm} \cdot \vec{J}_{sc}$$

in which

$$\vec{T}_{ce} = -T_c(s) \vec{I} \quad (147)$$

$$\vec{T}_{cm} = -Z_o T_c(s) \vec{I}_n \times \vec{I}$$

and the transfer function $T_c(s)$ is

$$T_c(s) = (B_{11} - Z_o B_{21})^{-1} \quad (148)$$

The analysis and results presented here are based fundamentally on the assumption that the wall under consideration is physically thin in comparison to its local principal radii of curvature. Eqs.(146) and onward are valid for walls which act as "good" shields, so that the approximation $\vec{H}_{to} \approx \vec{H}_{sc}$ holds. This is the case in nearly all practical applications. It is also assumed that the medium on either side of the wall is free space.

2.1.3.3.1 Homogeneous Conducting Walls

The boundary-connection parameters B_{ij} for a solid conducting wall of thickness d , conductivity σ , and permittivity μ , are

$$\begin{aligned} B_{11} &= B_{22} = \cosh \sqrt{s\tau_d} \\ B_{12} &= -R \sqrt{s\tau_d} \sinh \sqrt{s\tau_d} \\ B_{21} &= -\frac{1}{R} \frac{\sinh \sqrt{s\tau_d}}{\sqrt{s\tau_d}} \end{aligned} \quad (149)$$

where $R = (\sigma d)^{-1}$ denotes the dc resistance of the wall material and $\tau_d = \mu \sigma d^2$ is the diffusion time constant. The transfer function $T_c(s)$ is then

$$T_c(s) = \left(\cosh \sqrt{s\tau_d} + \frac{Z_o}{R} \frac{\sinh \sqrt{s\tau_d}}{\sqrt{s\tau_d}} \right)^{-1} \quad (150)$$

A useful approximate expression for $T_c(s)$, valid with negligible error over the entire EMP frequency range, is

$$T_c(s) \approx \frac{R}{Z_o} \sqrt{s\tau_d} \operatorname{csch} \sqrt{s\tau_d} \quad (151)$$

The magnitude and phase of the function $(Z_o/R)T_c$ are shown plotted as a function of $f\tau_d$ (where f is the frequency) in Fig. 113a. When $2\pi f\tau_d \gg 1$,

$$\begin{aligned} (Z_o/R)|T_c| &\approx 2\sqrt{2\pi f\tau_d} e^{-\sqrt{\pi f\tau_d}} \\ \arg T_c &\approx \frac{\pi}{4} - \sqrt{\pi f\tau_d} \end{aligned} \quad (152)$$

The inverse Laplace transform of $T_c(s)$, from which the impulse responses of the equivalent surface current densities are readily obtained, is [94]

$$\begin{aligned} t_c(t) &\approx \frac{2\pi^2 R}{\tau_d Z_o} e^{-\pi^2 t/\tau_d} \quad (t \geq \tau_d) \\ &\approx \frac{2\pi^2 R}{\tau_d Z_o} \left(e^{-\pi^2 t/\tau_d} - 4e^{-4\pi^2 t/\tau_d} + 9e^{-9\pi^2 t/\tau_d} \right), \quad (\tau_d/20 \leq t \leq \tau_d) \quad (153) \\ &\approx \frac{R}{\sqrt{\pi} \tau_d Z_o} (t/\tau_d)^{-5/2} e^{-\tau_d/4t} \quad (t \leq \tau_d/20) \end{aligned}$$

A plot of $(Z_o\tau_d/R)t_c(t)$ as a function of t/τ_d is shown in Fig. 113b.

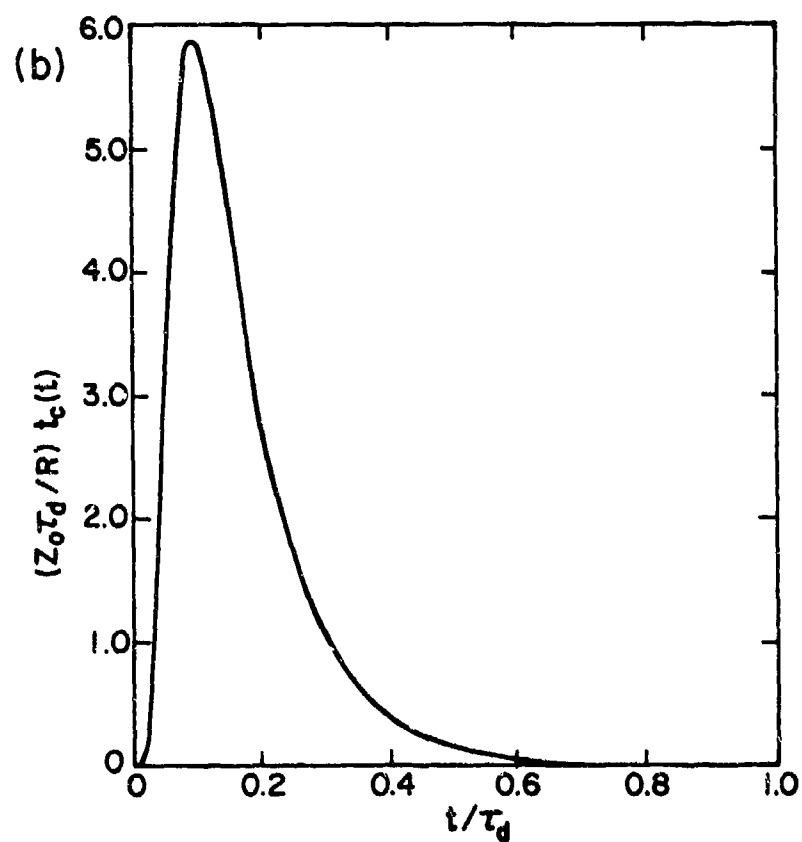
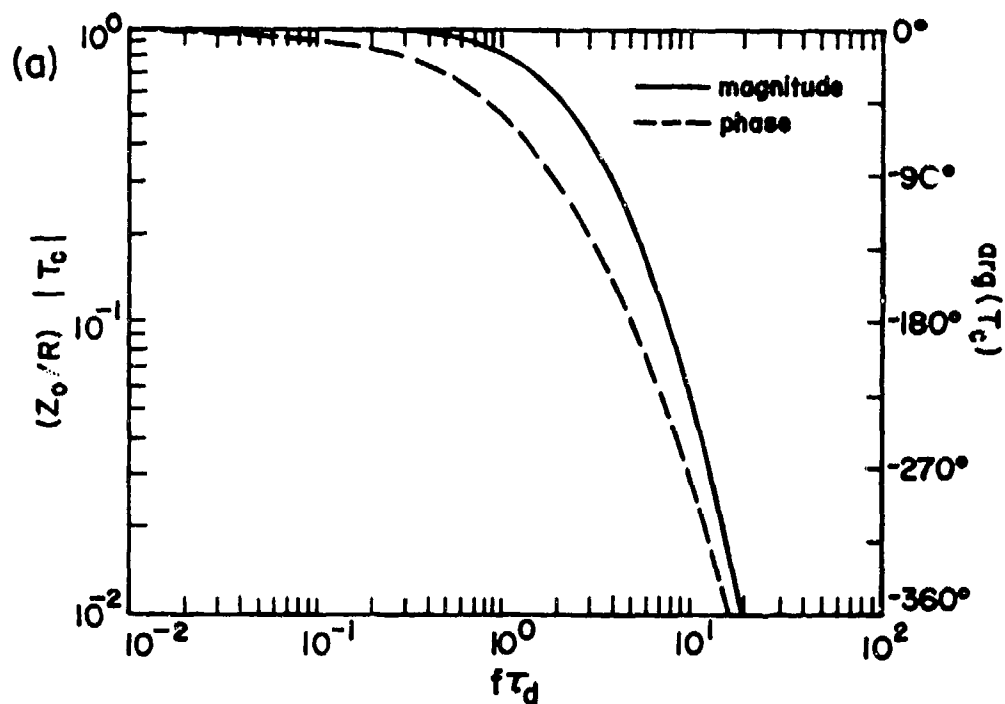


Fig. 113. (a) Magnitude and phase of $(Z_o/R)T_c$ versus $f\tau_d$ for imperfectly conducting solid walls, and (b) $(Z_o\tau_d/R)t_c(t)$ versus t/τ_d for imperfectly conducting solid walls — the impulse response.

Eq.(150) is valid whenever the wall material may be considered to be a good conductor, i.e., when the displacement current density can be neglected in comparison to the conduction current density: $2\pi f\epsilon_0/\sigma \ll 1$. Eq.(151) is valid if $Z_o \gg R$, $\sqrt{2\pi f\epsilon_0/\sigma} \ll 1$. The relative error in (151) is less than 0.25% when $f \leq 10^9$ Hz and $\sigma \geq 10^4$ mho/m; the relative error in (150) is completely negligible under these conditions.

Eq.(153) describes the time history of the impulse response of the equivalent surface current densities within a relative error of 0.1%.

2.1.3.3.2 Mesh-Shielded Nonconductive Walls

A mesh-shielded nonconductive wall (e.g., a boron-epoxy composite panel with a bonded-junction wire mesh embedded in one surface) is completely characterized for EMP shielding calculations by the following boundary-connection parameters B_{ij} :

$$\begin{aligned} B_{11} &= B_{22} = 1 \\ B_{12} &= 0 \\ B_{21} &= -1/Z_{sh} \end{aligned} \quad (154)$$

The impedance Z_{sh} is the equivalent sheet impedance of the mesh and is given by

$$\begin{aligned} Z_{sh} &= Z'_w a + \frac{\mu_0 a}{2\pi} \ln \left[(1 - e^{-2\pi r/a})^{-1} \right] \\ &\quad - \epsilon_p \frac{a}{2\pi s \epsilon_0 (1 + \epsilon_r)} \ln \left[(1 - e^{-2\pi r/a})^{-1} \right] v_s^2 \end{aligned} \quad (155)$$

where

a = mesh size

r = wire radius

ϵ_r = relative permittivity of the panel (typically $\epsilon_r \approx 5$)

Z'_w = impedance per unit length of wires

$= R'_w$ (dc resistance per unit length)

$$q_p = \begin{cases} 0, & \text{for perpendicular polarization (Fig. 114)} \\ 1, & \text{for parallel polarization (Fig. 114)} \end{cases}$$

$$\nabla_s^2 = \begin{cases} \text{surface Laplacian operator} \\ \frac{s^2}{c^2} \sin^2 \theta, & \text{for plane-wave fields (Fig. 114)} \end{cases}$$

In what follows, we consider locally plane-wave fields and write

$$Z_{sh} = R_{sh} + sL_{sh} \quad (156)$$

in which

$$R_{sh} = R'_w a, \quad L_{sh} = \frac{\mu_0 a}{2\pi} \left(1 - q_p \frac{\sin^2 \theta}{1 + \epsilon_r} \right) \ln \left[(1 - e^{-2\pi r/a})^{-1} \right] \quad (157)$$

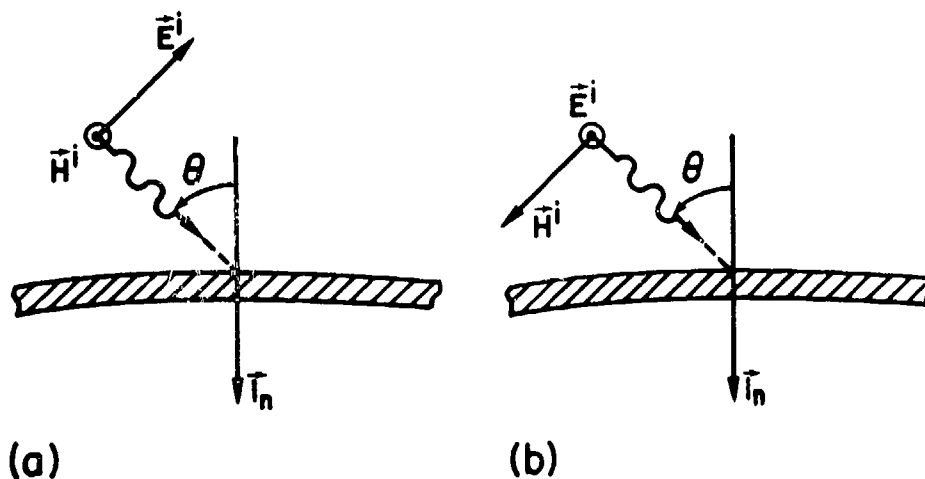


Fig. 114. (a) Parallel polarization; (b) perpendicular polarization.

The transfer function $T_c(s)$ is

$$T_c(s) = \frac{R_{sh} + sL_{sh}}{Z_o + R_{sh} + sL_{sh}} \quad (158)$$

Over the EMP spectrum $|R_{sh}/Z_o + sL_{sh}/Z_o| \ll 1$, and hence

$$T_c(s) \approx \frac{1}{Z_o} (R_{sh} + sL_{sh}) \quad (159)$$

Frequency-domain expressions for the magnitude and phase of T_c are

$$(Z_o/R_{sh}) |T_c| = \sqrt{1 + (2\pi f L_{sh}/R_{sh})^2} \quad (160)$$

$$\arg T_c = \arctan(2\pi f L_{sh}/R_{sh})$$

The inverse Laplace transform $t_c(t)$ of $T_c(s)$ is easily obtained from (159) and is given by

$$t_c(t) = \frac{R_{sh}}{Z_o} \delta(t) + \frac{L_{sh}}{Z_o} \delta'(t) \quad (161)$$

which clearly shows the "differentiating" character of a wall of this type.

Eq.(154) is valid when the mesh sheet admittance is large in comparison to the equivalent sheet admittance of the dielectric substrate. In typical cases, the relative error incurred by ignoring the admittance of the substrate is less than 0.1%.

Eq.(155) is derived under the assumption that the thin-wire approximation holds with respect to the mesh wires, i.e., that $r/a \ll 1$. The error incurred by the use of the thin-wire approximation is not precisely known. It is known, however, that the use of this approximation tends to underestimate the wire currents, so that the results presented here tend to overestimate the interior fields [93].

The assumption that Z'_w can be replaced by R'_w over the EMP frequency range is not correct at the upper end of the EMP spectrum. Precise error analyses are not yet available, but it is estimated that the relative error incurred by using this assumption is less than a few percent over the entire EMP spectrum.

Eq.(159) is valid when $R_{sh}/Z_o \ll 1$ and $2\pi f L_{sh}/Z_o \ll 1$. These conditions introduce negligible error over the entire EMP spectrum for practical cases.

2.1.3.3.3 Mesh-Shielded Conductive Walls

The transfer function $T_c(s)$ for a mesh-shielded conductive wall (e.g., a mesh-shielded graphite-epoxy composite panel) is

$$T_c(s) = \left[(1 + Z_o/Z_{sh}) \cosh \sqrt{s\tau_d} + \left(\frac{Z_o}{R} + \gamma u \frac{Z_o}{Z_{sh}} \right) \frac{\sinh \sqrt{s\tau_d}}{\sqrt{s\tau_d}} \right]^{-1} \quad (162)$$

In practice, $|Z_{sh}/Z_o| \ll 1$ and $|R\gamma d/Z_{sh}| \ll 1$, so that

$$T_c(s) \approx \left[\frac{Z_o}{Z_{sh}} \cosh \sqrt{s\tau_d} + \frac{Z_o}{R} \frac{\sinh \sqrt{s\tau_d}}{\sqrt{s\tau_d}} \right]^{-1} \quad (163)$$

which may also be expressed as

$$T_c(s) \approx T_c(0) \frac{1 + \rho + \alpha s\tau_d}{\cosh \sqrt{s\tau_d} + (\rho + \alpha s\tau_d) \frac{\sinh \sqrt{s\tau_d}}{\sqrt{s\tau_d}}} \quad (164)$$

in which

$$T_c(0) = \frac{R}{Z_o} \left(\frac{\rho}{1 + \rho} \right)$$

$$\rho = \frac{R'_w a}{R} \quad (165)$$

$$\alpha = \frac{a}{2\pi d} \ln \left[(1 - e^{-2\pi r/a})^{-1} \right]$$

Some representative curves of the magnitude of $T_c/T_c(0)$ as a function of $f\tau_d$ for various values of ρ and α are shown in Fig. 115. The larger values of α correspond to coarse meshes, thin panels, and/or fine wires; the larger values of ρ correspond to smaller values of wire conductivity and/or thick, highly conductive panels.

Relatively simple analytical expressions for the inverse Laplace transform of $T_c(s)$ for a mesh-shielded conductive panel do not exist, except in the limiting cases which have been described above. One may, however, construct a series expansion for $\tau_d t_c(t)$. One such representation is

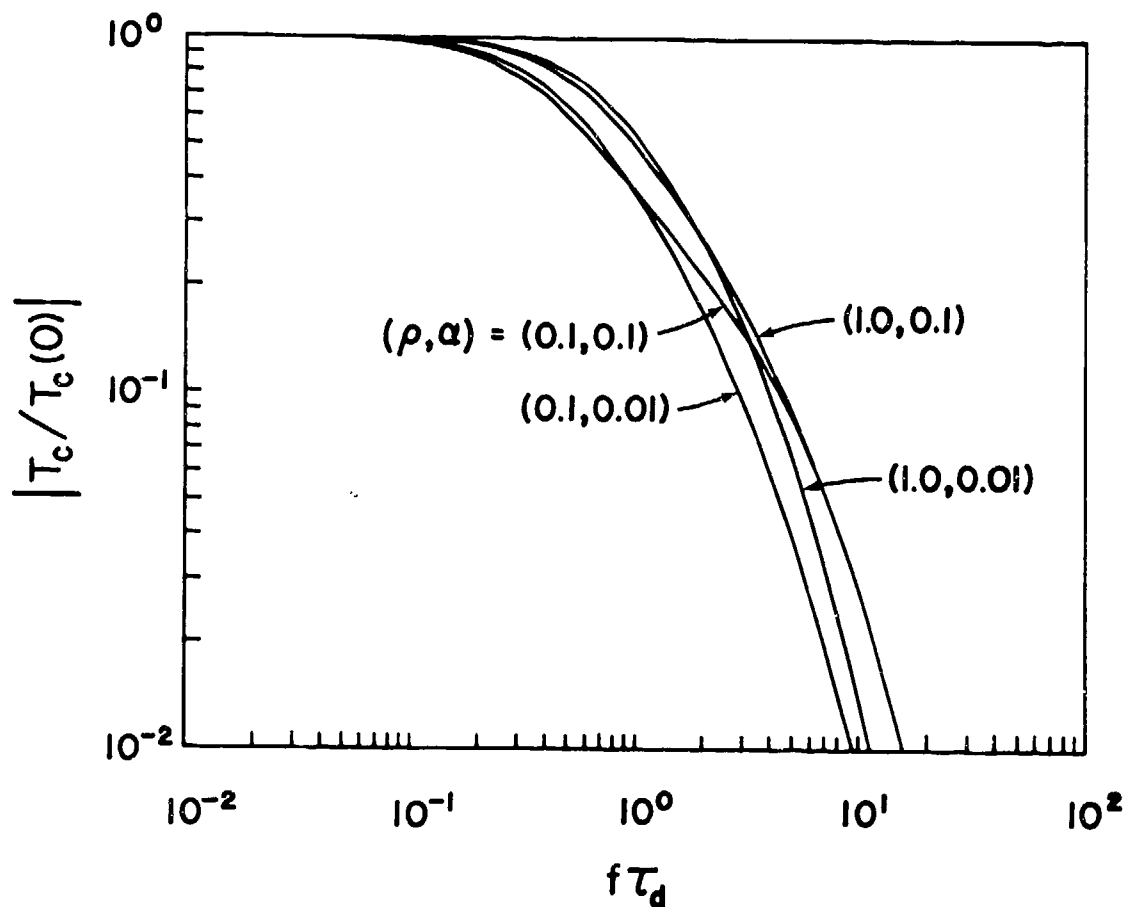


Fig. 115. Magnitude of $T_c/T_c(0)$ versus $f\tau_d$ for mesh-shielded conductive walls.

$$\tau_d t_c(t) = T_c(0) \sum_{n=1}^{\infty} \frac{-2u_n(1+\rho - \alpha u_n^2) \exp(-u_n^2 t/\tau_d)}{\frac{d}{du} \left[\cos u + (\rho - \alpha u^2) \frac{\sin u}{u} \right] \Big|_{u=u_n}} \quad (166)$$

in which the u_n are the positive real roots of

$$\cos u + (\rho - \alpha u^2) \frac{\sin u}{u} = 0, \quad u > 0 \quad (167)$$

The series in (166) converges for all $t > 0$, and for $t > \tau_d$ the first term is sufficient to represent $\tau_d t_c(t)$. When $t \ll \tau_d$, the following early-time representation is useful:

$$\begin{aligned} \tau_d t_c(t)/T_c(0) \approx & \frac{e^{-\tau_d/4t}}{\sqrt{\pi}} \left(\frac{\tau_d}{t} \right)^{5/2} \left\{ 1 - (1 + 1/\alpha) \frac{t}{\tau_d} \right. \\ & \left. + \frac{2(t/\tau_d)^2}{p-q} \left[\frac{p(1+p)}{1+2pt/\tau_d} - \frac{q(1+q)}{1+2qt/\tau_d} \right] \right\} \end{aligned} \quad (168)$$

in which

$$p, q = \frac{1}{2\alpha} (1 \pm \sqrt{1-4\rho\alpha}) \quad (169)$$

Representative plots of $\tau_d t_c(t)/T_c(0)$ versus t/τ_d are shown in Fig. 116.

Eq.(162) is analytically exact. Eqs.(163) and (164) are valid when the conditions $|Z_{sh}/Z_o| \ll 1$ and $|\gamma dR/Z_{sh}| \ll 1$ hold, and (164) is valid when (156) can be used to represent Z_{sh} . For typical meshes and conductive substrates, (164) is accurate to within a few percent.

Eq.(166) is the exact Laplace inverse of (164). When $t/\tau_d \geq 1$ the first term represents $\tau_d t_c(t)$ to within 0.1%, if the root is accurately calculated. The early-time expression of (168) is accurate to within 0.1%, for $t/\tau_d \leq 0.05$.

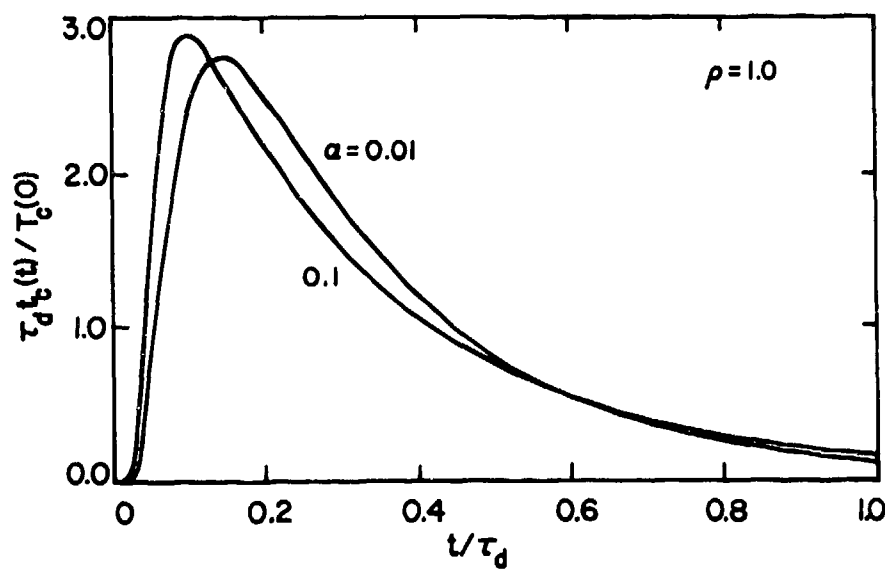
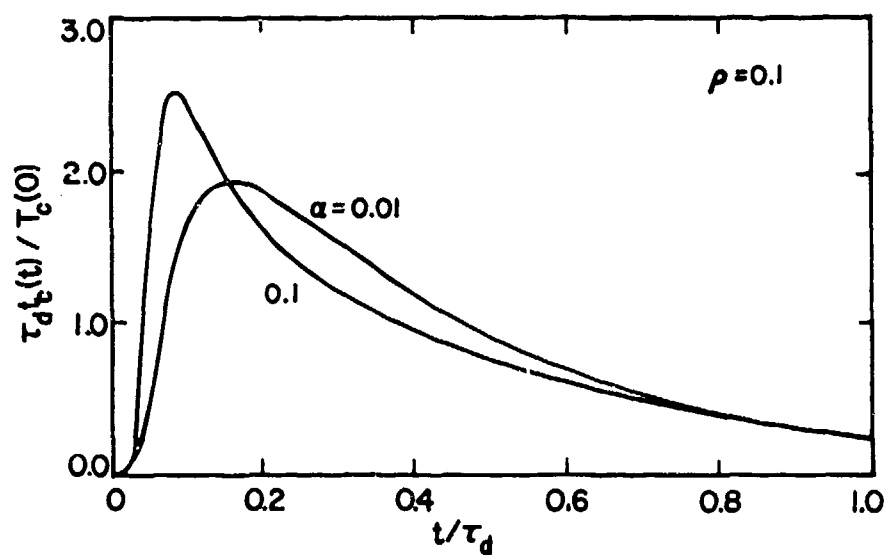


Fig. 116. $\tau_d t_c(t) / T_c(0)$ versus t/τ_d for mesh-shielded conductive walls.

REFERENCES

- [1] C.E. Baum, "Some considerations concerning analytic EMP criteria wave-forms," TN 285, October 1976.
- [2] K.S.H. Lee, "Electrically-small ellipsoidal antennas," SSN 193, February 1974.
- [3] M.I. Sancer, R.W. Latham, and A.D. Varvatsis, "Relationship between total currents and surface current densities," IN 194, August 1974.
- [4] C.D. Taylor and C.W. Harrison, Jr., "Current and charge densities induced on the surface of a prolate spheroid illuminated by a plane wave electromagnetic field," EMC-19, August 1977, pp.127 - 131.
- [5] C.E. Baum, "The singularity expansion method," Topics in Applied Physics, vol. 10, Transient Electromagnetic Fields (edited by L.B. Felsen), Springer-Verlag, New York, 1976.
- [6] L. Marin and T.K. Liu, "A simple way of solving transient thin-wire problems," IN 253, October 1975.
- [7] M. Abramowitz and I.A. Stegun, ed. Handbook of Mathematical Functions, AMS 55, National Bureau of Standards, 1964.
- [8] L. Marin, "Natural-mode representation of transient scattering from rotationally symmetric, perfectly conducting bodies and numerical results for a prolate spheroid," IN 119, September 1972.
- [9] R.W. Sassman, "The current induced on a finite, perfectly conducting, solid cylinder in free space by an electromagnetic pulse," IN 11, July 1967.
- [10] C.D. Taylor, "A simple procedure for estimating the current induced on cylinder-like conductors illuminated by a unit step electromagnetic pulse," IN 176, July 1973.
- [11] T.K. Sarkar and B.J. Strait, "Analysis of arbitrarily oriented thin wire antennas over a plane imperfect ground," Scientific Report No. 9 on Contract F19628-73-C-0047, AFCL-TR-75-0641, Syracuse, N.Y., December 1975.

- [12] F.M. Tesche, "On the singularity expansion method as applied to electromagnetic scattering from thin wires," IN 102, April 1972, and also AP-21, January 1973, pp.53 - 59.
- [13] T.T. Crow, C.D. Taylor and M. Kumbale, "The singularity expansion method applied to perpendicular crossed wires over a perfectly conducting ground plane," accepted for publication in IEEE Trans. Ant. Prop.
- [14] C.C. Kao, "Three-dimensional electromagnetic scattering from a circular tube of finite length," J. Appl. Phys., Vol. 40, November 1969, pp.4732 - 4740.
- [15] R.W. Burton, R.W.P. King, and D.J. Blejer, "Surface currents and charges on an electrically thick conducting tube in an E-polarized, normally incident, plane-wave field, 2, measurements," Radio Science, Vol. 11, August - September 1976, pp.701 - 711.
- [16] R.W. Burton, R.W.P. King, and D.J. Blejer, "Surface currents and charges on an electrically thick and long conducting tube in E- and H-polarized, normally incident, plane-wave fields," Radio Science, Vol. 13, January - February 1978, pp.75 - 91.
- [17] V.V. Liepa and T.B.A. Senior, "Some analyses of EC-135 aircraft model data," SSN 242, September 1977.
- [18] C.D. Taylor, "External interaction of the nuclear EMP with aircraft and missiles," AP-26, January 1978, pp.64 - 76.
- [19] T.T. Crow, B.D. Graves, and C.D. Taylor, "The singularity expansion method as applied to perpendicular crossed wires," IN 161, October 1973, and also AP-23, July 1975, pp.540 - 546.
- [20] R.W.P. King, D.J. Blejer, S.K. Wang, and R.W. Burton, "Currents and charges induced by normally incident plane wave on single and crossed tubular cylinders with $ka = 2.0$," Radio Science, Vol. 13, January - February 1978, pp.107 - 119.
- [21] G. Bedrosian, "Stick-model characterization of the natural frequencies and natural modes of aircraft," IN 326, September 1977.

- [22] C.D. Taylor, K.T. Chen, and T. Crow, "An improvement on wire modeling for determining the EMP interaction with aircraft," IN 241, October 1974.
- [23] M.I. Sancer, S. Siegel, and A.D. Varvatsis, "Foundation of the magnetic field integral equation code for the calculation of electromagnetic pulse external interaction with aircraft," IN 320, December 1976.
- [24] Y.T. Lin and J.H. Richmond, "EM modeling of aircraft at low frequencies," AP-23, January 1975, pp.53 - 57.
- [25] C.E. Baum and J.P. Castillo, "Numerical EMP codes (NEC)," Interaction Application Memos, Memo 12, August 1977.
- [26] K.S.H. Lee, L. Marin, and J.P. Castillo, "Limitations of wire-grid modeling of a closed surface," IN 231, May 1975, and EMC-18, August 1976, pp.161 - 175.
- [27] M.I. Sancer, "Fundamental errors associated with the gross modeling of the physical features of metallic enclosures," IN 298, December 1976.
- [28] R.W.P. King, D.J. Blejer, and R.W. Burton, "Surface currents and charges induced on a cross formed by an electrically thick cylinder and a flat plate in a normally incident plane wave field," submitted for publication.
- [29] R.G. Kouyoumjian and P.H. Pathak, "A uniform geometrical theory of diffraction for an edge in a perfectly conducting surface," Proc. IEEE, Vol. 62, November 1974, pp.1448 - 1461.
- [30] J.B. Keller, "Geometrical theory of diffraction," J. Opt. Soc. Amer., Vol. 52, 1962, pp.116 - 130.
- [31] J.B. Keller and A. Blank, "Diffraction and reflection of pulses by wedges and corners," Commun. Pure Appl. Math., Vol. 4, 1954, pp.75 - 94.
- [32] F.G. Freidlander, Sound Pulses, London, New York: Cambridge University Press, 1958, pp.120 - 124.
- [33] J.I. Makhoul, "Contour plots for the diffraction of a pulse by a wedge," Radio Science, Vol. 1, 1966, pp.609 - 613.
- [34] C.E. Baum, "The diffraction of an electromagnetic plane wave at a bend in a perfectly-conducting planar sheet," SSN 47, August 1967.

- [35] D.F. Higgins, "The diffraction of an electromagnetic plane wave by interior and exterior bends in a perfectly-conducting sheet," SSN 128, January 1971.
- [36] L.B. Felsen, "Diffraction of the pulsed field from an arbitrarily oriented electric or magnetic dipole by a perfectly conducting wedge," SIAM J. Appl. Math., Vol. 26, 1974, pp.306 - 314.
- [37] J.J. Bowman, T.B.A. Senior, and P.L.E. Uslenghi, Electromagnetic and Acoustic Scattering by Simple Shapes, Amsterdam, The Netherlands, North-Holland Pub., 1969.
- [38] R.H. Schafer and R.G. Kouyoumjian, "Transient currents on a cylinder illuminated by an impulsive plane wave," AP-23, 1975, pp. 627 - 638.
- [39] S.W. Lee, V. Jamnejad, and R. Mittra, "An asymptotic series for early time response in transient problems," IN 128, October 1972, and also AP-21, November 1973, pp.895 - 899.
- [40] R.G. Kouyoumjian, "The geometrical theory of diffraction and its application," Topics in Applied Physics, Vol. 3, edited by R. Mittra, Berlin, Heidelberg, New York: Springer-Verlag, 1975, pp.165 - 215.
- [41] Y. Hwang, W.D. Burnside, and L. Peters, Jr., "High frequency surface charge and current density induced on the B1 and 747 aircrafts," Interaction Application Memos, Memo 7, January 1975.
- [42] L. Marin and K.S.H. Lee, "Deliberate aircraft antenna model development, vol. II: theoretical studies of the VLF/LF antennas on the E-4 and EC-135 aircraft and their effects on the other antennas," AFWL-TR-76-218, May 1977.
- [43] G.S. Smith, J.D. Norgard, J. Edwards, "Alteration of the surface current on a missile by the presence of an exhaust plume," EMC-19, November 1977, pp.383 - 394.
- [44] L.L. Tsai, T.K. Wu, R.D. Darone, G.L. Brown, "Some aspects of valid EMC testing of missiles," EMC-20, May 1978, pp.306 - 313.
- [45] C.D. Taylor, "Electromagnetic scattering by thin inhomogeneous circular cylinders," IN 17, July 1967, and also Radio Science, Vol. 2, No. 7, July 1967, pp.729 - 738.

- [46] C.W. Harrison, Jr., E.A. Arouson, "On the response of a missile with exhaust trail of tapered conductivity to a plane wave electromagnetic field," IN 22, December 1968, and also EMC-11, May 1969, pp.40-49.
- [47] R.R. Mikatarian, C.J. Kau, H.S. Pergament, "A fast computer program for nonequilibrium rocket plume predictions," AFRPL-TR-72-94, August 1972.
- [48] "Missile plume effects," Electromagnetic Pulse Handbook for Missiles and Aircraft in Flight, AFWL-TR-73-68, September 1972.
- [49] P.R. Barnes, "The axial current induced on an infinitely long, perfectly conducting, circular cylinder in free space by a transient electromagnetic wave," IN 64, March 1971.
- [50] C. Flammer and H.E. Singhaus, "The interaction of electromagnetic pulses with an infinitely long conducting cylinder above a perfectly conducting ground," IN 144, July 1973.
- [51] W.E. Scharfman and E.F. Vance, "EMP coupling and propagation to power lines: theory and experiment," Technical Report 8, SRI Project 7995, Contract F29601-69-C-0127, Stanford Research Institute, Menlo Park, California, May 1973.
- [52] E.F. Vance, Electromagnetic Pulse Handbook for Electric Power Systems, DNA 3466F, Defense Nuclear Agency, Washington D.C., December 1974.
- [53] E.D. Sunde, Earth Conduction Effects in Transmission Systems, Dover Publications, New York, 1968.
- [54] S.A. Schelkunoff and H.T. Friis, Antennas: Theory and Practice, John Wiley & Sons, New York, 1952, p.204.
- [55] E.F. Vance, "Coupling to cables," Chapter 11, DNA 2114, Defense Nuclear Agency, Washington, D.C., December 1974.
- [56] H. Jaski, Editor, Antenna Engineering Handbook, McGraw-Hill, New York, 1961.
- [57] T.K. Liu, K.S.H. Lee, and L. Marin, "Broadband responses of deliberate aircraft antennas, Part I," IN 228, May 1975.

- [58] K.S.H. Lee and L. Marin, "Deliberate aircraft antenna model development," AFWL-TR-76-218 (2 volumes), Air Force Weapons Laboratory, Kirtland AFB, New Mexico, May 1977.
- [59] R.W.P. King, "Asymmetrically driven antennas and the sleeve dipole," Proc. IRE, Vol. 38, 1950, pp.1154 - 1164.
- [60] T.K. Liu, "Impedances and field distributions of two coplanar parallel perfectly conducting strips with arbitrary widths," IN 182, July 1974.
- [61] R.L. Tanner, "Shunt and notch-fed HF aircraft antennas," AP-6, 1958, pp.35 - 43.
- [62] G.H. Brown and O.M. Woodward, Jr., "Experimentally determined radiation characteristics of conical and triangular antennas," RCA Rev., Vol. 13, December 1952.
- [63] R.E. Collin and F.J. Zucker, Editors, Antenna Theory, McGraw-Hill, New York, 1969.
- [64] J. Lam, "Interaction of a rectangular ferrite slab with magnetic fields," IN 250, September 1975.
- [65] W.B. Roberts, "Input impedance of folded dipole," RCA Rev., Vol. 8, 1947.
- [66] S. Uda and Y. Mushiake, Yagi-Uda Antennas, Maruzen Co., Ltd., Tokyo, 1954, p.19.
- [67] K.S.H. Lee, "Balanced transmission lines in external fields," IN 115, July 1972.
- [68] L. Marin, "Quasi-static field penetration into a two-dimensional rectangular well in a ground plane," IN 171, March 1974.
- [69] J. Lam, "Exact solution of the problem of quasi-static electric-field penetration into a hemispherical indentation in an infinite conducting plane," IN 175, April 1974.
- [70] J. Lam, "Quasi-static magnetic-field penetration into a hemispherical indentation in an infinite conducting plane," IN 179, May 1974.
- [71] R.W. Latham and K.S.H. Lee, "Magnetic-field leakage into a semi-infinite pipe," IN 10, August 1967, and also Canadian Journal of Physics, Vol. 46, 1968, pp.1455 - 1462.

- [72] H. Kaden, Wirbelströme und Schirmung in der Nachrichtentechnik, Springer-Verlag, Berlin, 1959.
- [73] L. Marin, K.S.H. Lee, and J.P. Castillo, "Broadband analysis of VLF/LF aircraft wire antennas," AP-26, January 1978, pp.141 - 145.
- [74] L. Marin and K.S.H. Lee, "Response of the VLF/LF dual-wire (counterpoise) antenna system on the E-4 (AABNCP)," AFWL-TR-78-36, February 1979.
- [75] L. Marin, "Response of the HF fixed-wire antennas on the E-4," AFWL-TR-78-42, February 1979.
- [76] G. Bedrosian and L. Marin, "Transient response of the HF fixed-wire antennas on the E-4," AFWL-TR-78-43, February 1979.
- [77] R.E. Collin, Field Theory of Guided Waves, McGraw-Hill, New York, 1960, pp.294 - 298.
- [78] C.G. Montgomery, R.H. Dicke, and E.M. Purcell (eds.), Principles of Microwave Circuits, McGraw-Hill, New York, 1948, p.178.
- [79] F. De Meulenaere and J. Van Bladel, "Polarizability of some small apertures," AP-25, No. 2, March 1977, pp.198 - 205.
- [80] S.B. Cohn, "Determination of aperture parameters by electrolytic-tank measurements," Proc. IRE, Vol. 39, November 1951, pp.1416 - 1421.
(See correction: Vol. 40, January 1952, p.33).
- [81] S.B. Cohn, "The electric polarizability of apertures of arbitrary shape," Proc. IRE, Vol. 40, September 1952, pp.1069 - 1071.
- [82] G.L. Matthaei, L. Young, and E.M.T. Jones, Microwave Filters, Impedance-Matching Networks, and Coupling Structures, McGraw-Hill, New York, 1964, pp.233 - 235.
- [83] R.W. Latham, "Small holes in cable shields," IN 118, September 1972.
- [84] D.L. Jaggard and C.H. Papas, "On the application of symmetrization to the transmission of electromagnetic waves through small convex apertures of arbitrary shape," IN 324, October 1977.

- [85] B.D. Graves, T.T. Crow, and C.D. Taylor, "On the electromagnetic field penetration through apertures," IN 199, 1974.
- [86] S.J. Buchsbaum, A.R. Milne, D.C. Hogg, G. Berkefi, and G.A. Woonton, "Microwave diffraction by apertures of various shapes," Journal of Applied Physics, Vol. 26, No. 6, June 1955, pp.706 - 715.
- [87] C.M. Butler, "Penetration through a narrow slot in a screen separating different media," in preparation.
- [88] F.C. Yang, K.S.H. Lee, and L. Marin, "Analysis of EMP penetration into a weapons bay," AFWL-TR-77-133, December 1977.
- [89] K.C. Chen, "Electric polarizabilities of some simple hatch apertures," AFWL-TR-76-137, July 1976.
- [90] D.L. Jaggard, "Transmission through one or more small apertures of arbitrary shape," IN 323, September 1977.
- [91] A.D. Varvatsis and M.I. Sancer, "EMP penetration through dielectric skin panels on the leading edge of aircraft wings," IN 325, May 1977.
- [92] L. Marin, "Effects of a dielectric jacket of a braided-shield cable on EMP coupling calculations," IN 178, May 1974.
- [93] K.F. Casey, "Electromagnetic shielding by advanced composite materials," IN 341, June 1977.
- [94] G. Bedrosian and K.S.H. Lee, "EMP penetration through metal skin panels and into aircraft cavities," IN 314, August 1976.

CHAPTER 2.2

INTERMEDIATE INTERNAL INTERACTION, I: LINE CONDUCTORS

Between the first layer of shield (e.g., the aircraft's skin) and the connector pins of equipment boxes is a region where intermediate internal interaction takes place. Within this region there may be cable shields and other conduits such as hydraulic lines, control cables, pneumatic ducts, etc. Generically, these may all be referred to as line conductors. In this chapter engineering formulas and data will be presented to describe the interaction of these conductors.

2.2.1 COUPLING

The line conductors in the intermediate internal interaction region may be excited locally by nearby apertures or in a distributed sense by the field that diffuses through conducting walls. We will first present formulas and data to describe the voltage and current sources appropriate for local excitation by nearby apertures and then the voltage source for distributed excitation by diffused fields.

2.2.1.1 Line Conductors Near Apertures

Many EMP problems have to do with coupling through apertures to line conductors (wires) passing near them. For the low-frequency portion of the EMP spectrum, the usual approach is to represent the aperture by equivalent dipole sources. In a rigorous analysis, these dipole sources would be computed taking into consideration the scattering from the line conductor back into the aperture. In practice, it is usually possible to neglect the scattering from the conductor into the aperture. In this section results are presented for a line conductor coupled to a single aperture in an infinite ground plane and to an array of periodically spaced apertures.

2.2.1.1.1 Line Conductors Near a Single Aperture

In Fig. 1 is shown a line conductor (wire) parallel to a conducting sheet with an aperture. The wire and the conducting sheet form a trans-

mission line. When the aperture is electrically small, its effects on the transmission-line mode can be represented by the equivalent circuit shown in Fig. 2, where the equivalent voltage and current sources, V_{eq} and I_{eq} , are given by [1]

$$\begin{aligned} V_{eq} &= j\omega\mu_0 \left(\frac{h}{\pi R_0^2} \right) \vec{I}_x \cdot \vec{\alpha}_m \cdot \vec{H}_{sc} \\ I_{eq} &= j\omega\epsilon_0 \left(\frac{h}{\pi R_0^2} \right) \frac{\alpha_e Z_0}{Z_c} E_{sc} \end{aligned} \quad (1)$$

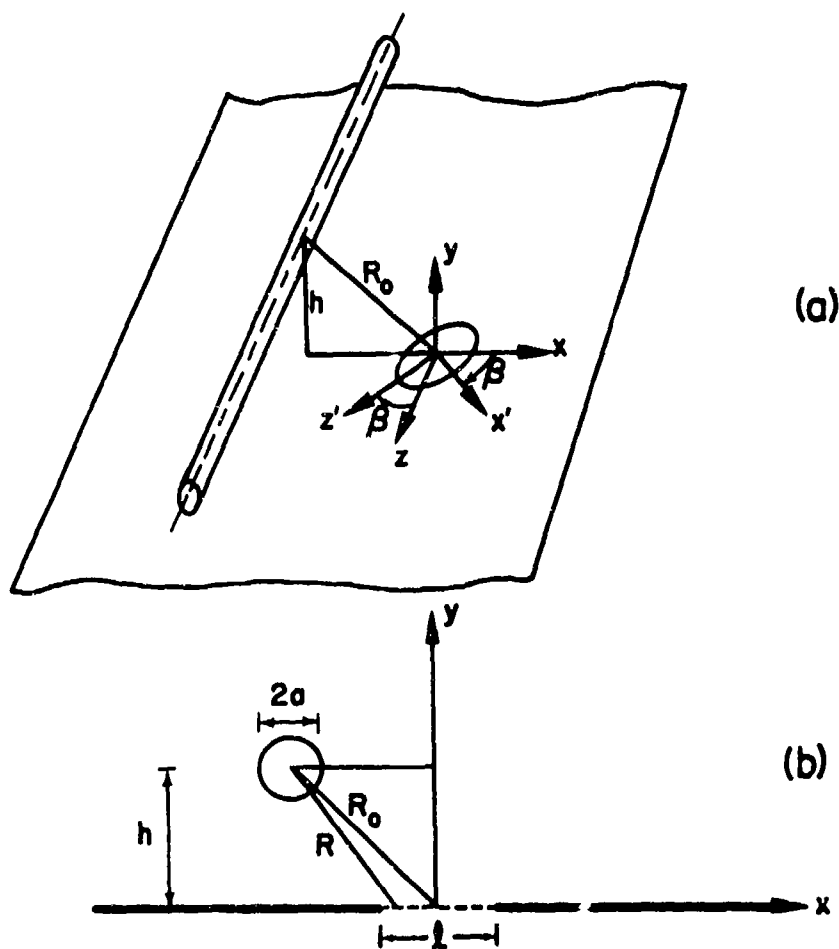


Fig. 1. (a) Coordinate system for a line conductor above a ground plane with an aperture, (b) cross-sectional view.

and the inductance and capacitance, L_a and C_a , of the hole by

$$\begin{aligned} L_a &= \mu_0 \alpha_{a,xx} \left(\frac{h}{\pi R_0^2} \right)^2 \\ C_a &= -\mu_0 \frac{\alpha_e}{Z_c^2} \left(\frac{h}{\pi R_0^2} \right)^2 \end{aligned} \quad (2)$$

Here, the characteristic impedance Z_c of the transmission line and the wave impedance Z_0 are

$$\begin{aligned} Z_c &= \frac{1}{2\pi} Z_0 \operatorname{arccosh}(h/a) \approx \frac{1}{2\pi} Z_0 \ln(2h/a) \\ Z_0 &= \sqrt{\mu_0/\epsilon_0} \end{aligned} \quad (3)$$

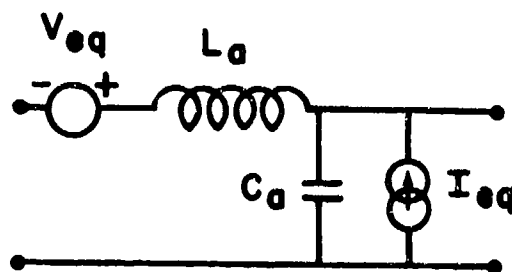
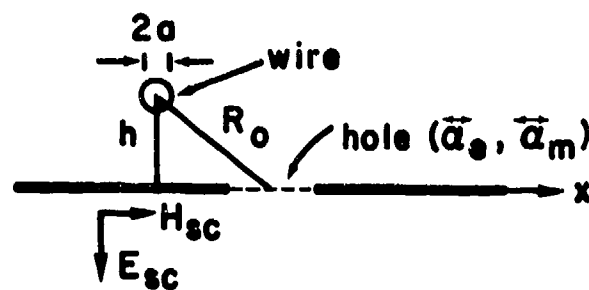


Fig. 2. Equivalent circuit of a small hole ($R_0 \gg$ hole's dimensions).

and the polarizabilities $\alpha_e^{\leftrightarrow}, \alpha_m^{\leftrightarrow}$ for a variety of aperture shapes are given in Sec. 2.1.3.2.1.

If the principal axes x' and z' of the aperture are not parallel to the x - and z -axes as defined in Fig. 1, then the aperture magnetic dipole moments \vec{m}_a must be transformed to the x, y, z coordinate system according to

$$\begin{aligned} m_{a,x} &= m_{a,x'} \cos \beta - m_{a,z'} \sin \beta \\ m_{a,z} &= m_{a,x'} \sin \beta + m_{a,z'} \cos \beta \end{aligned} \quad (4)$$

where β is the angle between the x - and x' -axes (Fig. 1). Hence, the quantity $\vec{l}_x \cdot \alpha_m^{\leftrightarrow} \cdot \vec{H}_{sc}$ contained in V_{eq} in (1), expressed in both primed and unprimed coordinates, is given by

$$\begin{aligned} \vec{l}_x \cdot \alpha_m^{\leftrightarrow} \cdot \vec{H}_{sc} &= (\alpha_{m,x'x'} \cos^2 \beta + \alpha_{m,z'z'} \sin^2 \beta) (\vec{l}_x \cdot \vec{H}_{sc}) \\ &+ (\alpha_{m,x'x'} - \alpha_{m,z'z'}) \cos \beta \sin \beta (\vec{l}_z \cdot \vec{H}_{sc}) \end{aligned} \quad (5)$$

and the quantity $\alpha_{m,xx}$ contained in L_a in (2) by

$$\alpha_{m,xx} = \alpha_{m,x'x'} \cos^2 \beta + \alpha_{m,z'z'} \sin^2 \beta \quad (6)$$

For most combinations of the parameters ω , R_0 and a , the lumped circuit elements L_a and C_a of the aperture may be neglected. It is useful to observe that the negative capacitance element represents the lumped effect of the decrease in the line capacitance per unit length which, in turn, results from the decreased charging surface available because of the presence of the aperture. The additional magnetic flux paths which penetrate the aperture increase the line inductance per unit length near the aperture; this effect is accounted for by adding a positive lumped inductance.

If the wire is so close to the aperture that the effect of the aperture can no longer be represented by dipole sources, then a correction factor for the equivalent sources may be used. For a circular aperture, the corrected equivalent sources are given by [1]

$$V_{eq} = f_s V_{eq, \text{small hole}} \quad (7)$$

$$I_{eq} = f_s I_{eq, \text{small hole}}$$

where the factor f_s , plotted in Fig. 3, merely multiplies the small-hole source terms defined in (1). It should be noted that in deriving the factor f_s in (7), the influence of the wire on the aperture field has been neglected, an assumption which becomes less valid as the wire approaches the aperture. The factor $[\ell/(2R_0)]^3$ is a reasonable estimate of the relative error involved in this assumption.

2.2.1.1.2 Line Conductor Near Periodic Arrays of Apertures

In many cases wires are situated near an array of identical periodically-spaced apertures. In such situations the influence of the wire on the apertures may often be neglected, as mentioned in the previous section, but it is often impossible to neglect the coupling of adjacent apertures in computing aperture equivalent sources. However, if there is a sufficiently large number of elements it can often be assumed that the central elements in the array have the same aperture fields (and, consequently, the same dipole moments, etc.) as they would have in an infinite array. While it is common to treat more than seven or eight elements in an array as approximating an infinite array, there are no simple rules regarding the errors involved in such approximations, since the errors depend critically on such widely varying parameters as array spacing, aperture geometry, excitation, and frequency.

For a wire behind and parallel to a linear array of apertures, an equivalent circuit representing the coupling of each individual aperture to the transmission line takes the form shown in Fig. 4a where the equivalent sources and circuit elements are defined in Fig. 2. The polarizabilities α_e , α_m to be used in (1) and (2) must be those of each aperture in an infinite array environment, and are given in Sec. 2.1.3.2.1.

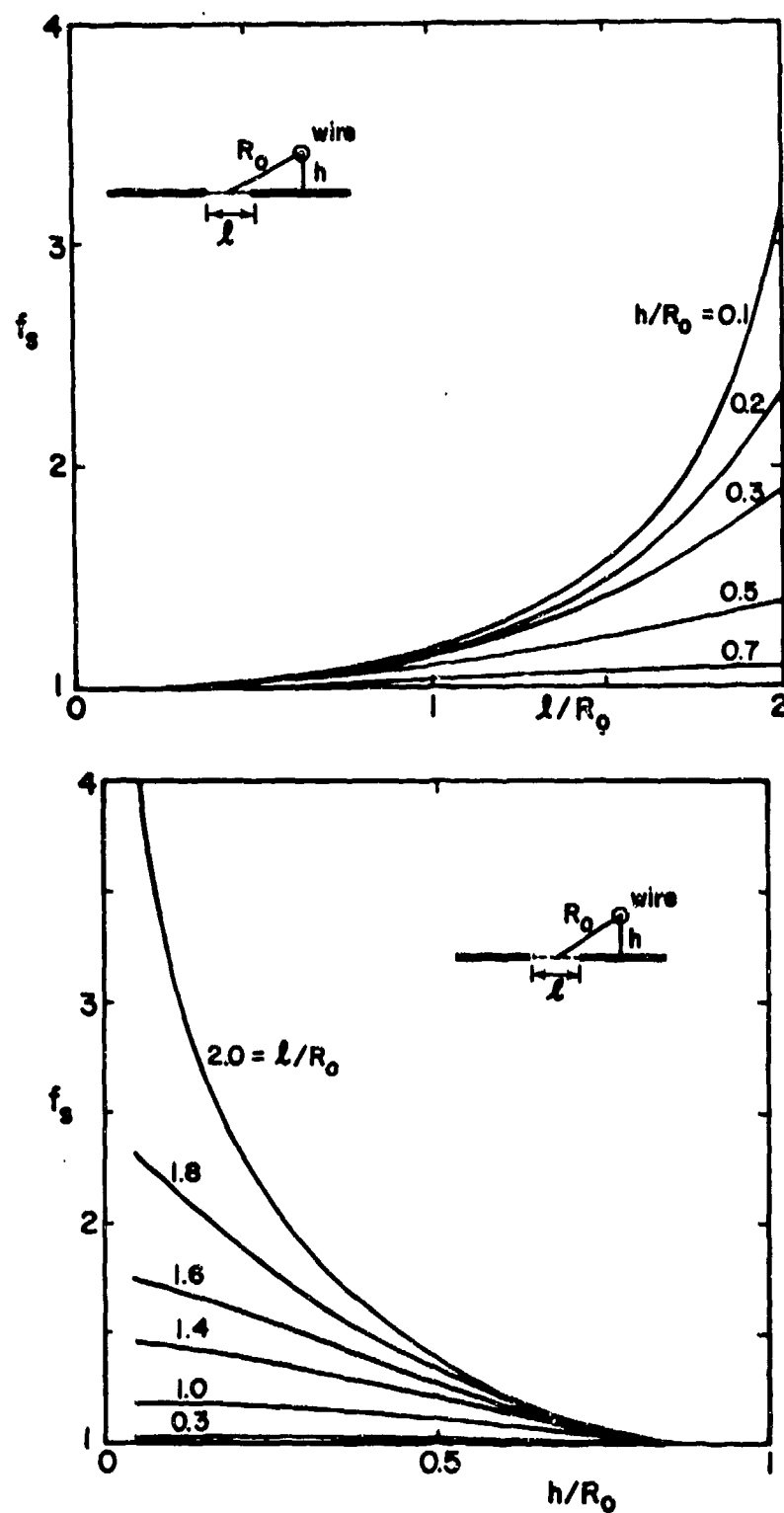


Fig. 3. Effects of diameter l of a circular aperture and height h of wire above a ground plane on the source factor f_s .

If the apertures of an array are closely spaced in terms of wavelengths, the analysis of EMP coupling may often be made simpler by averaging over a period the lumped elements (sources and impedances) modeling the apertures and treating these elements as distributed quantities. Hence the array of lumped elements separated by sections of transmission line as shown in Fig. 4a may be replaced by a continuous transmission line with distributed parameters as shown in Fig. 4b, where

$$\begin{aligned} L' &= L'_0 + L_a/d, & C' &= C'_0 - C_a/d \\ V'_{eq} &= V_{eq}/d, & I'_{eq} &= I_{eq}/d \end{aligned} \quad (8)$$

in which d is the period between apertures and the quantities L_a , C_a , V_{eq} and I_{eq} are defined in (1) and (2) with the polarizabilities taken to be those of an array environment, and L'_0 and C'_0 are the line inductance and capacitance per unit length with shorted apertures.

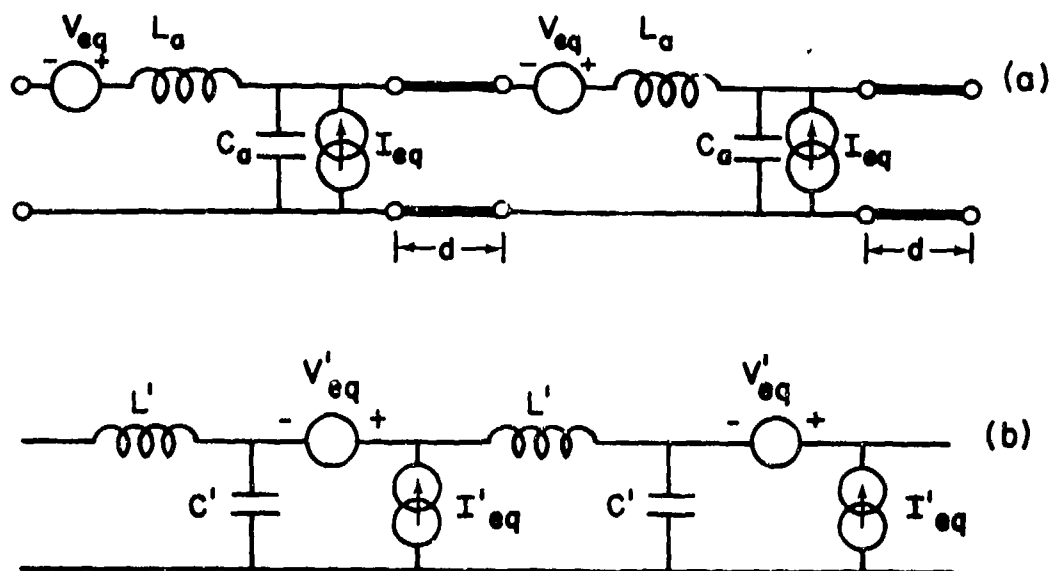


Fig. 4. (a) Transmission line with lumped elements for widely-spaced apertures; (b) equivalent circuit per section of line for closely-spaced apertures.

2.2.1.1.3 Line Conductors Inside a Triangular Waveguide With Periodic Apertures

A special but important EMP penetration is the leading edge of an aircraft wing covered by an array of dielectric skin panels which approximates a periodic array of apertures. The section of wing exposed to EMP penetration via the panels contains a pneumatic duct and some unshielded cables inside an approximately triangular waveguide region as shown in Fig. 5. The interior problem may be modeled as a triangular waveguide with a center conductor, as far as the penetrant fields are concerned. An array of apertures is used to model the skin panels, whose dielectric constant has been assumed to be that of free space. The exterior problem of determining the short-circuit charge density ρ and current density \vec{J} can be treated by the techniques in Chap. 2.1.

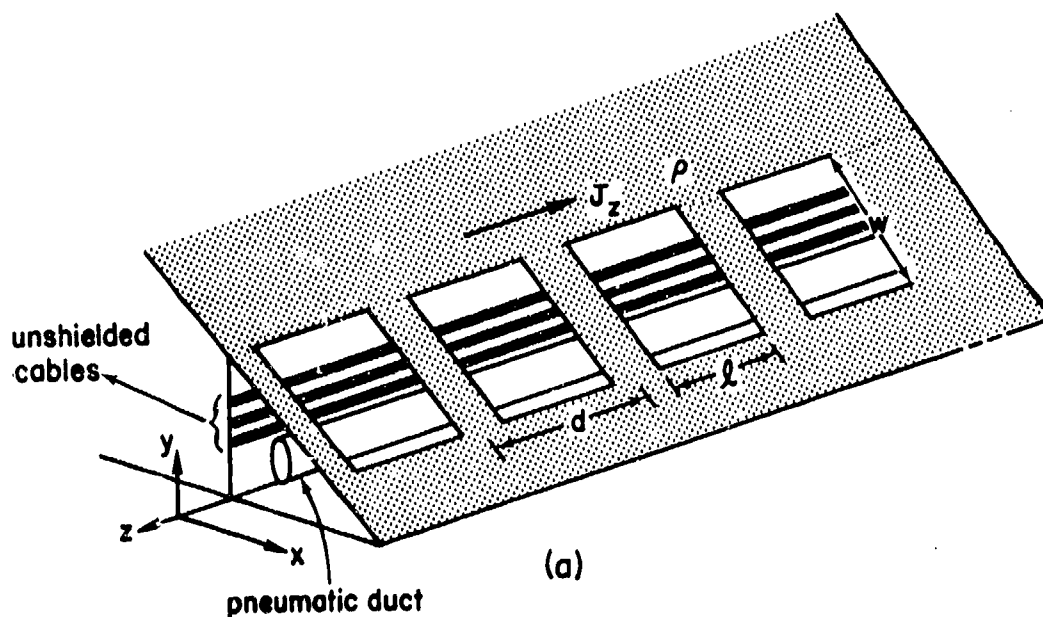


Fig. 5. The edge of the wing modeled as a cylindrical tube with a triangular cross section and a periodic array of rectangular apertures.

The equivalent circuit of Fig. 4b is most appropriate to describe the interaction problem of Fig. 5. The distributed parameters are given by [2]

$$\begin{aligned} L' &= L'_0 + L_a/d, & C' &= C'_0 - C_a/d \\ V'_{eq} &= \frac{j\omega\mu_0\alpha_m}{d} \frac{Z_c}{Z_0} \frac{\partial\phi}{\partial n} J_z(z) \\ I'_{eq} &= - \frac{j\omega\alpha_e}{d} \frac{\partial\phi}{\partial n} \rho(z) \end{aligned} \quad (9)$$

where L'_0 and C'_0 are the inductance and capacitance per unit length of the transmission line formed by the duct and triangular waveguide, $Z_c = \sqrt{L'_0/C'_0}$, and L_a and C_a are the corresponding lumped element quantities representing the effect of the apertures on the transmission-line mode. The scalar potential function ϕ describes the TEM mode in the closed-aperture transmission line. The polarizabilities α_e , α_m are given in Fig. 108 of Sec. 2.1.3.2.

The quantities L'_0 , C'_0 and $(\partial/\partial n)\phi$ in (9) have the following approximate form

$$\begin{aligned} L'_0 &= \frac{\mu_0\epsilon_0}{C'_0} = \frac{\mu_0}{2\pi} \ln\left(\frac{D_0}{N_0}\right) \\ \frac{\partial\phi}{\partial n} &= \frac{2}{\ln(N_0/D_0)} \left[\frac{\cos\theta_{1a}}{R_{1a}} - \frac{\cos\theta_{2a}}{R_{2a}} + \frac{\cos\theta_{3a}}{R_{3a}} - \frac{\cos\theta_{4a}}{R_{4a}} \right] \end{aligned} \quad (10)$$

where (see Fig. 6)

$$N_0 = R_{10}R_{20}R_{30}R_{40}$$

$$D_0 = R_{50}R_{60}R_{70}R_{80}$$

$$R_{ij} = \text{distance between point } i \text{ and point } j, \text{ where } i, j = 0, 1, \dots, 8, a.$$

θ_{ia} = angle between the outward normal vector at point a and the vector from point i to point a.

Note that the point a has to be chosen such that $(\partial/\partial n)\phi$ at a is approximately the average value of $(\partial/\partial n)\phi$ over the aperture.

2.2.1.2 Line Conductors Near a Conducting Surface

When there is a time-varying surface current flowing on one side of a finitely conducting sheet (such as the metallic skin of an aircraft or the raceway of a missile), the magnetic field associated with this current can diffuse through the sheet material and appear on the other side of the sheet. This diffusive field can couple to conductors lying behind the sheet by electromagnetic induction. In the following, formulas are given which describe this magnetic-field coupling through a conducting sheet to a line conductor.

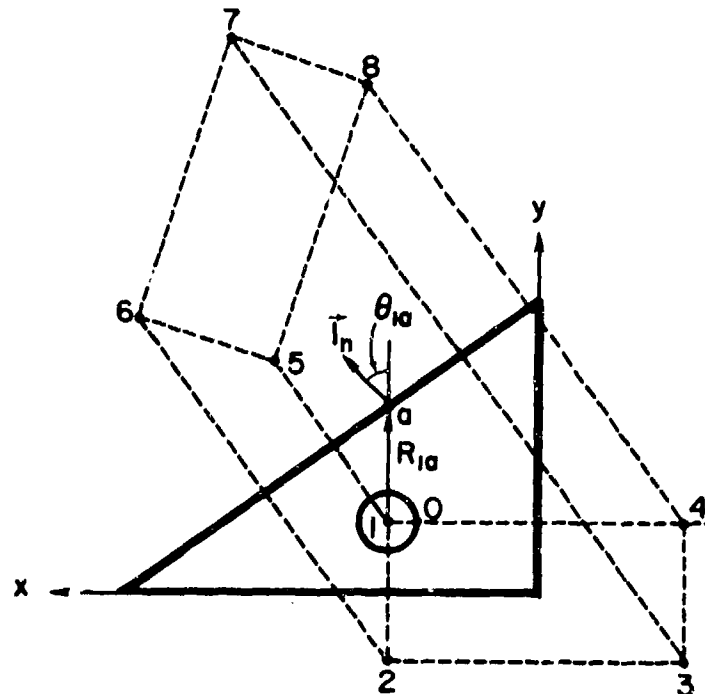


Fig. 6. Geometry for the definitions of R_{1j} and θ_{1a} .

Fig. 7a shows a conductor passing over a plane sheet at a uniform height h . The sheet has thickness d , conductivity σ , and permeability μ . It is assumed that both σ and μ are frequency-independent. Let a time-harmonic current be induced on the under-surface of the conducting sheet, and the associated magnetic field be \vec{H}_{sc} , as shown in Fig. 7a. The effect of this magnetic field on the transmission line above the sheet can be represented by a distributed voltage source $V'(s)$ in the transmission-line equations, viz.,

$$\frac{dV}{dz} + Z'I = V'(s), \quad \frac{dI}{dz} + Y'V = 0 \quad (11)$$

The equivalent circuit representation of the transmission line is shown in Fig. 7b. The source term $V'(s)$ is calculated from Faraday's law to be

$$V'(s) = -j\omega\mu_0 h T_m \vec{I}_x \cdot \vec{H}_{sc} \quad (12)$$

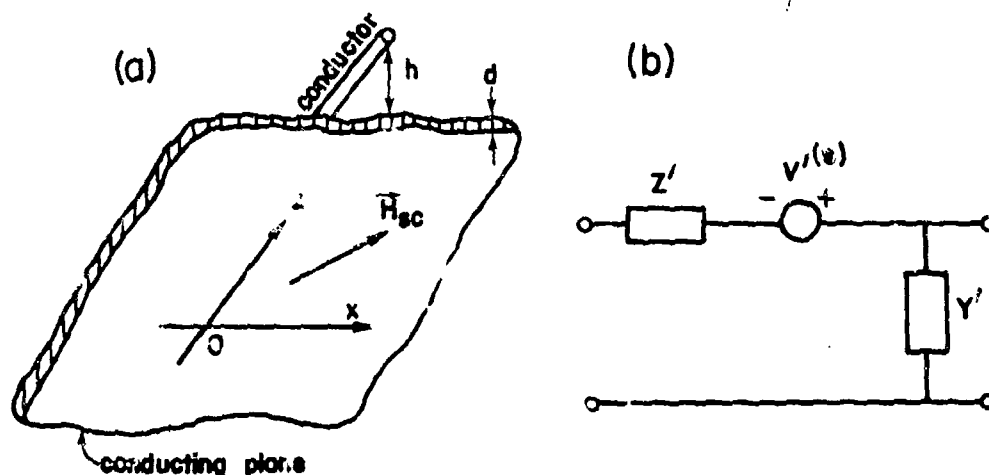


Fig. 7. Coupling of a magnetic field \vec{H}_{sc} through a conducting sheet to a conductor. The effects of this coupling can be represented by a distributed voltage source $V'(s)$ in the transmission-line equation for the conductor-plane configuration.

where T_m is the tangential magnetic field transfer function across the conducting sheet. It is given by

$$T_m = \frac{1}{\cosh \gamma d + Z_0 \sqrt{\epsilon/\mu} \sinh \gamma d} \quad (13)$$

where

$$\epsilon = \epsilon_0 + \sigma/j\omega, \quad \gamma = j\omega\sqrt{\mu\epsilon} \quad (14)$$

At EMP frequencies, one always has $\sigma \gg \omega\epsilon_0$. In this case the following expressions apply

$$\epsilon \approx \sigma/j\omega, \quad \gamma \approx \frac{1+j}{\delta}, \quad \delta = \sqrt{\frac{2}{\omega\mu\sigma}} \quad (15)$$

where δ is the skin depth of the sheet material.

Fig. 8 shows a plot of the transfer function T_m for a conducting sheet of thickness 1.5 mm, taken from [3].

2.2.2 PROPAGATION

One idealized model of a transmission line which has found wide application in the EMP interaction analysis consists of a perfectly conducting straight wire running at a constant distance over the surface of an infinite, perfectly conducting ground plane. Electric signals can be transmitted freely along this line in the form of current and voltage waves. Their propagation is governed by a pair of transmission-line equations. The propagation characteristics are determined by the uniform, distributed impedance and admittance per unit length of the line.

This section deals with the treatment of certain deviations from this idealized transmission-line model that are relevant to EMP interaction analysis. The discussions here are limited to those deviations that can be represented by changes in the impedance and the admittance of the line. Deviations that are equivalent to current and voltage

sources are treated in Sec. 2.2.1 and Chap. 2.4. The deviations discussed here fall under the two headings of (1) local discontinuities, or nonuniformities, in the otherwise uniform transmission-line geometry, when all the conductors are considered perfectly conducting, and (2) distributed corrections in the impedance and admittance parameters arising from finite conductivity.

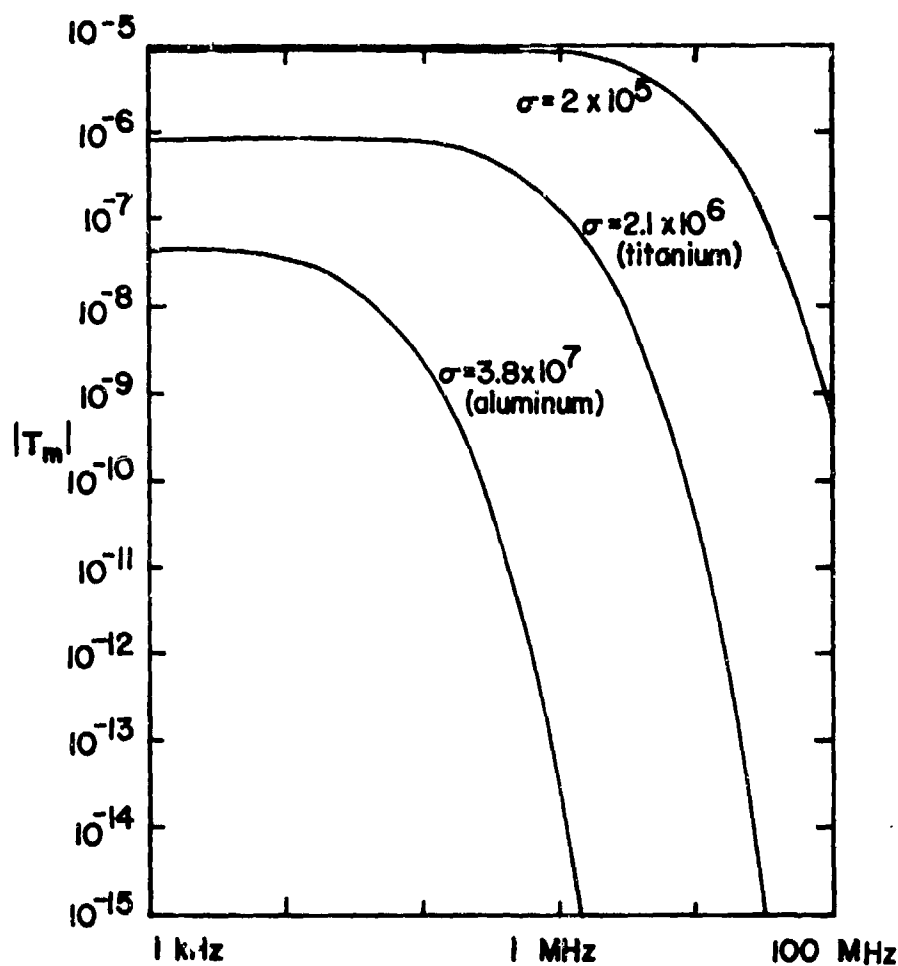


Fig. 8. Magnitude of the tangential magnetic field transfer function T_m for a conducting sheet as a function of frequency. The sheet has thickness 1.5 mm, permeability μ_0 , and conductivity σ which is in units of mhos per meter.

2.2.2.1 Lumped Circuit Elements of Discontinuities

A strictly uniform transmission line is not often found in practice. Instead, localized geometrical nonuniformities frequently occur along the length of a line. Examples of such nonuniformities are cable bends, cable clamps, shield apertures, and nearby conductors. These produce local deviations of the distributed line impedance and admittance from their uniform values, resulting in a scattering of the waves on the line. If the dimensions of the nonuniformities are small compared to a wavelength, the scattering effects can be represented by loading onto the uniform line an appropriate equivalent lumped network circuit. Fig. 9 shows one example of a nonuniformity and its modeling by a symmetrical T section. The network is assumed to have zero spatial extension, and is to be inserted into the uniform line at the location of the nonuniformity. The lumped impedance and admittance elements Z_d and Y_d , characterizing the nonuniformity, are to be calculated from appropriate quasi-static electromagnetic boundary-value problems. The calculated results for some common cable discontinuities, applicable to the EMP interaction problem, are summarized below.

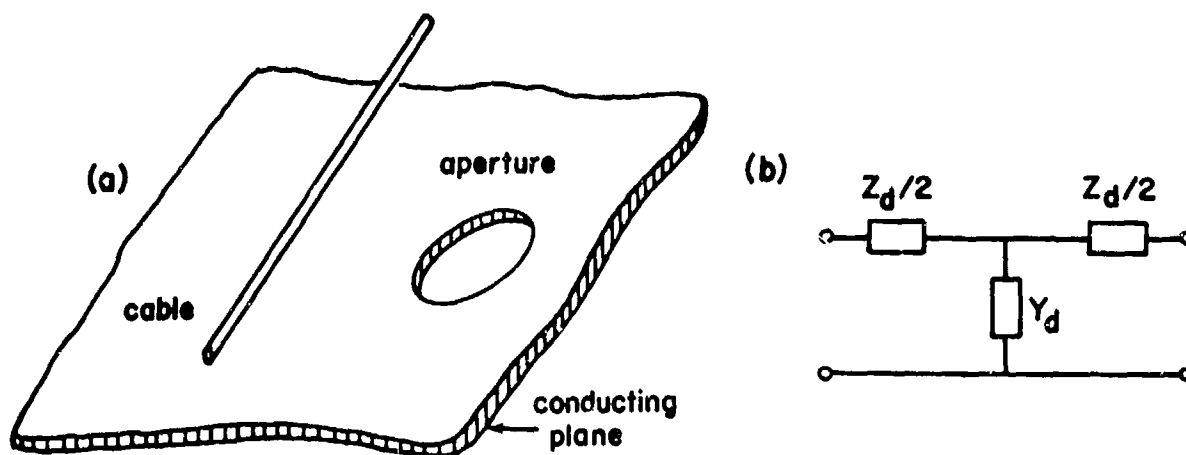


Fig. 9. An example of discontinuity in the cable geometry and its equivalent lumped network.

2.2.2.1.1 Abrupt Cable Bend [4,5]

Fig. 10a shows a cable modeled by a wire of radius a passing over a conducting plane at a constant height h . The wire is assumed thin ($a \ll h$). The cable has an abrupt bend through an angle α . Fig. 10b is an equivalent lumped network circuit representation of the bend. The parameter L_d is the difference between the total inductance of the bend cable and that of a straight cable. The parameter C_d is the corresponding difference in the total capacitance. The normalized values of these parameters are calculated to be

$$\frac{L_d}{hL'} = \frac{4}{\ln(2h/a)} (\alpha \cot \alpha - 1), \quad \frac{C_d}{hC'} = \frac{1}{\ln(2h/a)} (1 - \alpha \csc \alpha) \quad (16)$$

where L' and C' are the inductance and capacitance per unit length of the uniform line and are given by

$$L' = \mu_0 \epsilon_0 / C' = \frac{\mu_0}{2\pi} \ln(2h/a) \quad (17)$$

The expression for L_d is exact within the thin-wire assumption; that for C_d is obtained by a variational method and is accurate to within a few percent.

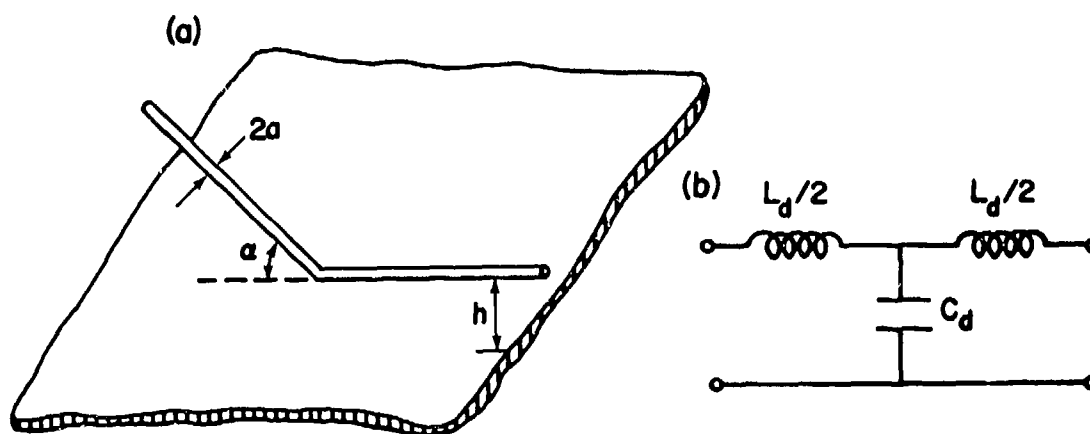


Fig. 10. An abrupt cable bend and its equivalent lumped network circuit.

2.2.2.1.2 Circular Cable Bend [4,5]

Fig. 11a shows a cable with a smooth bend modeled by a circular arc of radius R and angle β . The cable is of radius a and passes over a conducting plane at a constant height h . It is assumed that $a \ll h$. This configuration is a generalization of the abrupt bend, and the latter is recovered in the limit $R \rightarrow 0$. The circular bend, however, is the more realistic cable bend geometry.

The circular bend is again characterized by the bend inductance L_d and the bend capacitance C_d , as shown in Fig. 11b. The two quantities are functions of the four geometrical parameters R , β , a and h . In [4,5] L_d and C_d are calculated and expressed in terms of a number of rather complicated one-dimensional integrals to be computed numerically. The computed results are shown in Fig. 12.

The results for L_d are exact within the thin-wire assumption. Those for C_d are obtained from a variational principle and are accurate to within a few percent.

2.2.2.1.3 Cable Clamp [6]

Fig. 13a shows a model of a common type of cable clamp. It consists of a thin metallic tube of length l and radius b , concentric with the

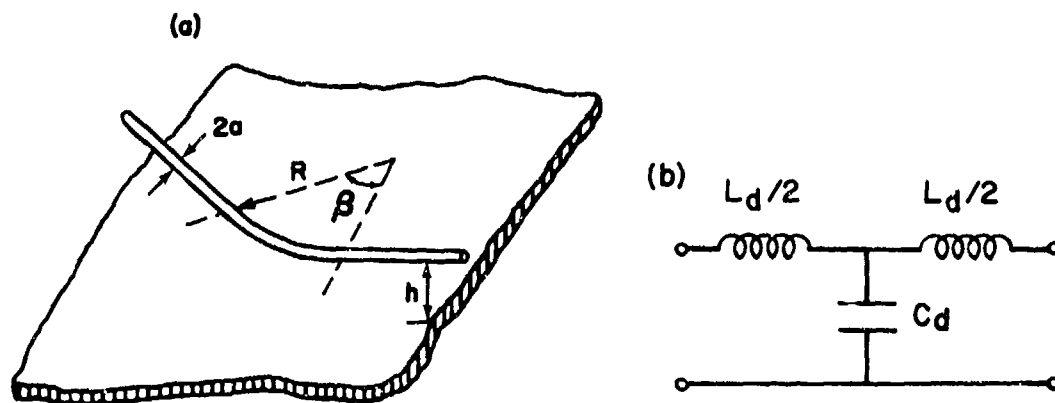


Fig. 11. A circular cable bend and its equivalent lumped network circuit.

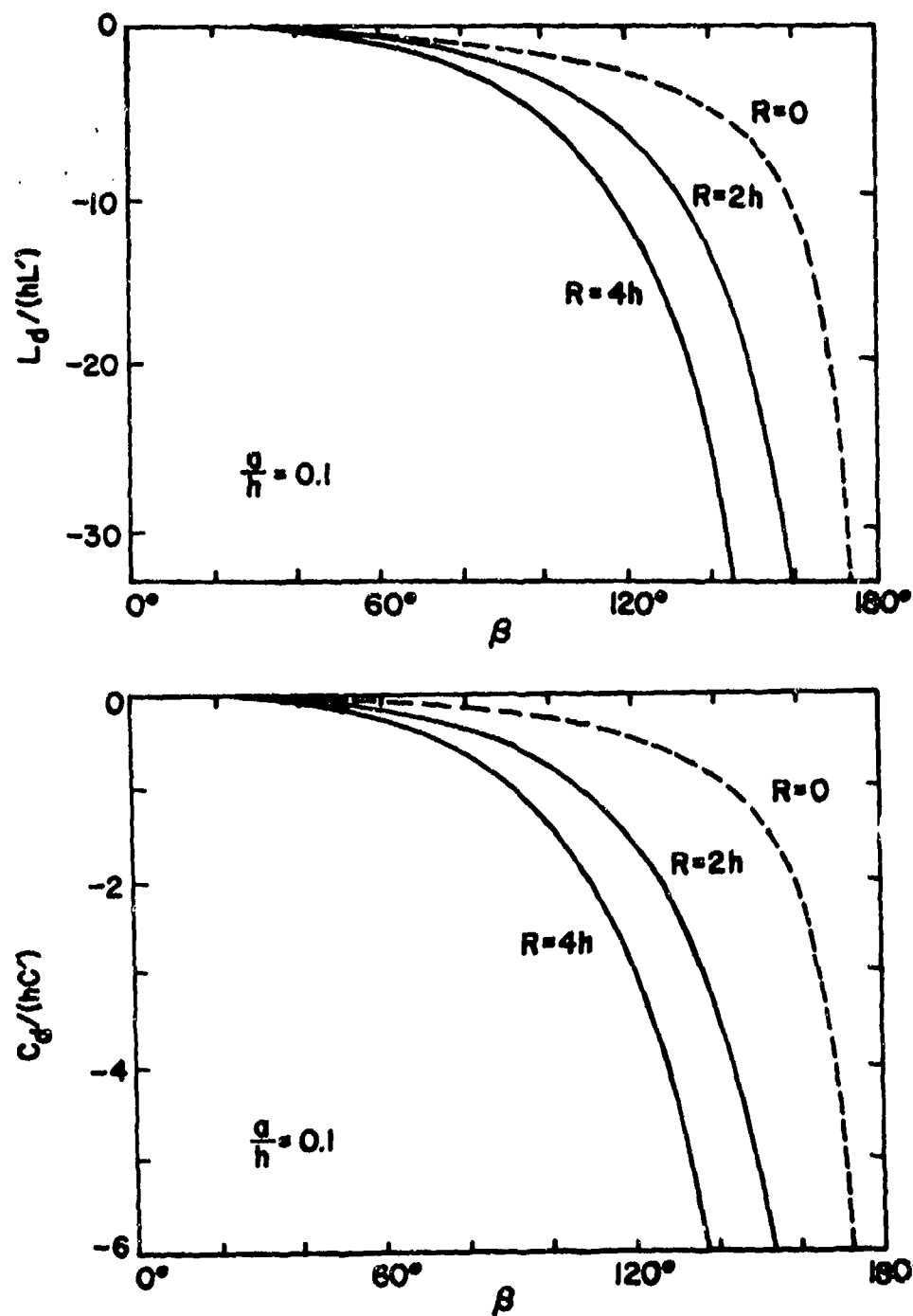


Fig. 12. Equivalent inductance L_d and capacitance C_d of a circular cable bend of radius R and angle β of Fig. 11. The broken line is for the case of an abrupt bend ($R=0$).

cable. The space between the cable and the tube is filled with a dielectric of permittivity ϵ . The tube is connected at the middle to the conducting plane by a thin, vertical, metallic strip of width d .

An equivalent lumped circuit representation of the cable clamp is shown in Fig. 13b. The inductances and capacitances therein are given by

$$\begin{aligned} L_1 &= \frac{\mu_0 l}{4\pi} \ln\left(\frac{b}{a}\right), & C_2 &= \frac{2\pi\epsilon l}{\ln(b/a)} \\ L_3 &= \frac{\mu_0 l}{8\pi} \operatorname{arccosh}\left(\frac{h}{b}\right), & C_4 &= \frac{\pi\epsilon_0 l}{\operatorname{arccosh}(h/b)} \\ L_5 &= \frac{\mu_0}{4\pi} \left[(h-b) \operatorname{arcsinh}\left(\frac{h-b}{d/4}\right) - \sqrt{(h-b)^2 + \left(\frac{d}{4}\right)^2} + \frac{d}{4} \right] \end{aligned} \quad (18)$$

In practice, the effects of the elements C_4 and L_5 are often negligible. The circuit in Fig. 13b can then be simplified to the common form shown in Fig. 11b, with $L_d = 2L_1 + 4L_3$ and $C_d = C_2$.

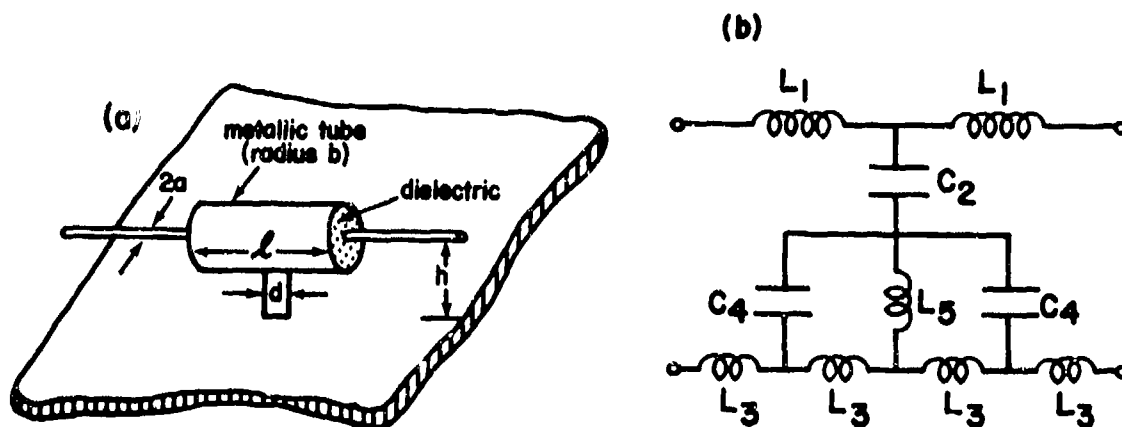


Fig. 13. A model of a cable clamp and its equivalent lumped network circuit.

2.2.2.1.4 Circular Aperture on Ground Plane [1]

Fig. 14a shows a cable passing by a circular aperture on the ground plane. The cable has radius a , and is at a uniform height h above the plane. The radius of the hole is R , and the shortest distance between its center and the cable is D . It is assumed that the hole is small ($R \ll D$), and that it opens onto an empty, semi-infinite, free space below the ground plane.

The equivalent lumped circuit for this discontinuity is shown in Fig. 14b. The elements L_d and C_d are given by

$$\frac{L_d}{hL'} = \alpha_m \frac{2h}{\pi D^4 \ln(2h/a)}, \quad \frac{C_d}{hC'} = -\alpha_e \frac{2h}{\pi D^4 \ln(2h/a)} \quad (19)$$

where α_m and α_e are, respectively, the absolute values of the magnetic and electric polarizabilities of the circular aperture of radius R and are given by

$$\alpha_m = \frac{4}{3} R^3, \quad \alpha_e = \frac{2}{3} R^3 \quad (20)$$

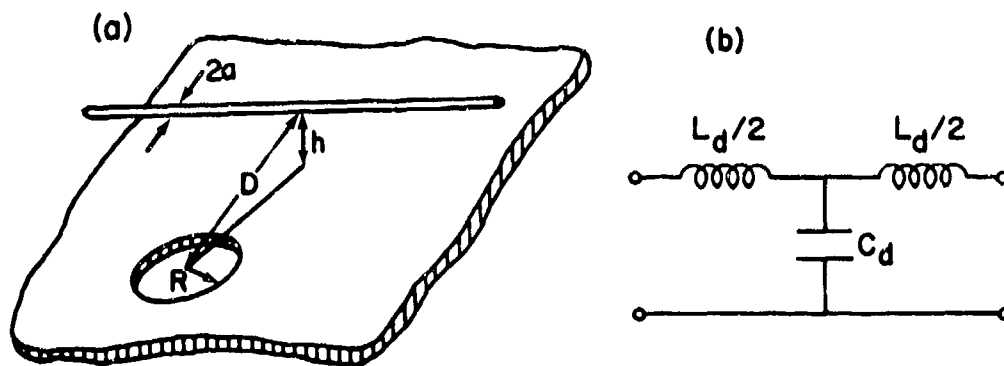


Fig. 14. A circular aperture on the ground plane and its equivalent lumped network circuit.

The formulas (19) for L_d and C_d apply also to small apertures of other shapes. One need only substitute for α_m and α_e the values appropriate to the apertures of concern. It should be kept in mind that α_m is the aperture magnetic polarizability in the direction perpendicular to the wire. The polarizabilities of specific apertures are given in Sec. 2.1.3.2.

2.2.2.1.5 Thin Rib on Ground Plane [7]

Fig. 15a shows a cable passing over a conducting plane. The cable is modeled by a single straight wire of radius a , and at a constant height h above the plane. A rib in the form of a thin metallic strip of breadth b juts out vertically from the plane, at right angle to the direction of the wire. The rib greatly alters the electric field in its vicinity, but leaves the magnetic field relatively unperturbed. The effect of this discontinuity is therefore mainly capacitive. The equivalent lumped circuit consists of a shunt capacitance C_d (Fig. 15b) and its normalized value, obtained by numerically solving a pair of coupled integral equations, is shown in Fig. 16.

2.2.2.1.6 Periodic Discontinuities [8]

Very often, identical discontinuities recur at regular intervals along the length of a transmission line. Examples of such periodic

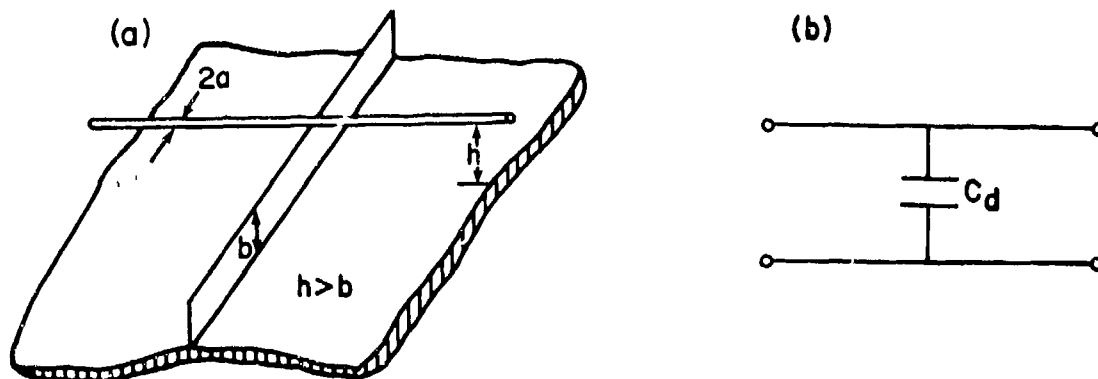


Fig. 15. A thin rib on the ground plane and its equivalent lumped network circuit.

structures along aircraft cables are periodically applied cable clamps and periodic airframe ribs over which the cable runs are anchored. These cables are equivalent to periodically loaded transmission lines.

Fig. 17a shows a uniform transmission line loaded at regular intervals with identical two-port lumped-element networks. Each load is taken to have the structure of a symmetrical T section, as shown in Fig. 17b. It is made up of a discontinuity series impedance Z_d and a discontinuity shunt admittance Y_d . The loading interval is denoted by d .

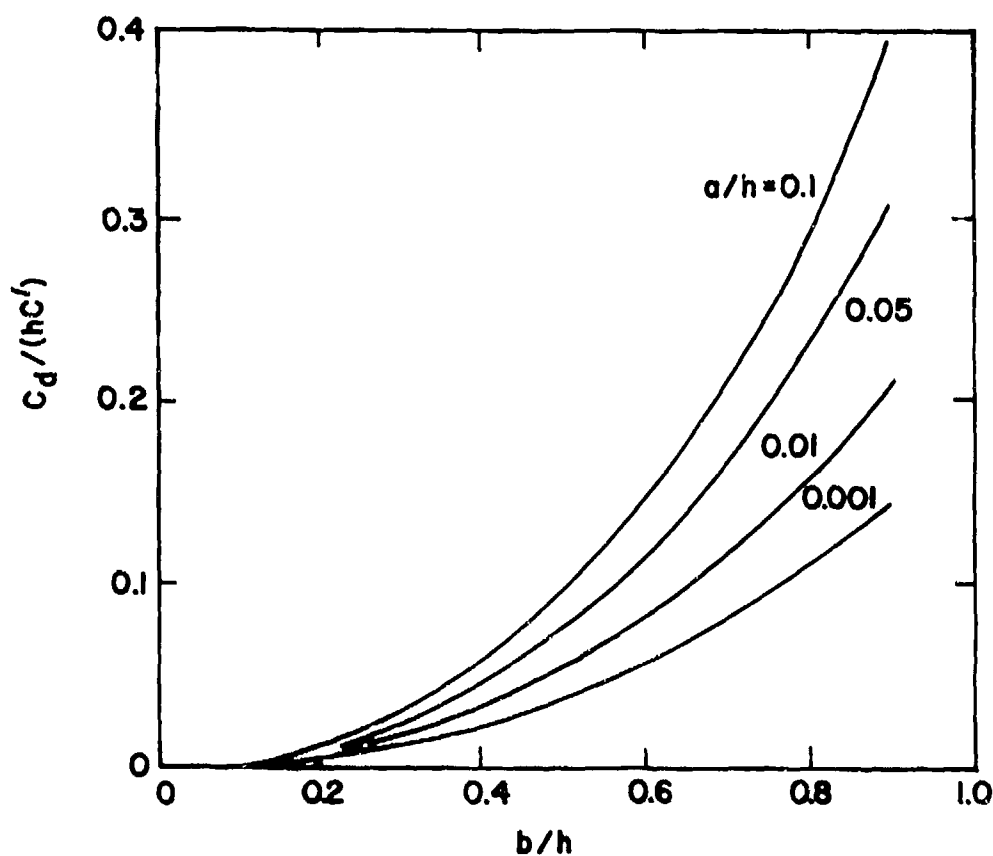


Fig. 16. Normalized equivalent capacitance C_d of a thin vertical rib on the ground plane of Fig. 15.

On a uniform transmission line, electric signals can propagate by means of simple-harmonic current and voltage waves. On a periodically loaded line, these waves become modulated by the periodicity of the loading. They then have the general form

$$\psi(z,t) = u_k(z)e^{-jkz + j\omega t} \quad (21)$$

The wave number k is determined by the detailed structure of the line, and $u_k(z)$ is periodic in z with the loading period d .

The properties of these waves are contained in the so-called dispersion relation which expresses k as a function of ω . For the periodically loaded line of Fig. 17, the dispersion relation is obtained in the following form

$$\begin{aligned} \cos kd = & \left(1 + \frac{1}{2} Y_d Z_d\right) \cosh(d\sqrt{Y'Z'}) \\ & + \frac{1}{2} \sqrt{\frac{Y'}{Z'}} \left(Z_d + \frac{1}{4} Y_d Z_d^2 + Y_d \frac{Z'}{Y'}\right) \sinh(d\sqrt{Y'Z'}) \end{aligned} \quad (22)$$

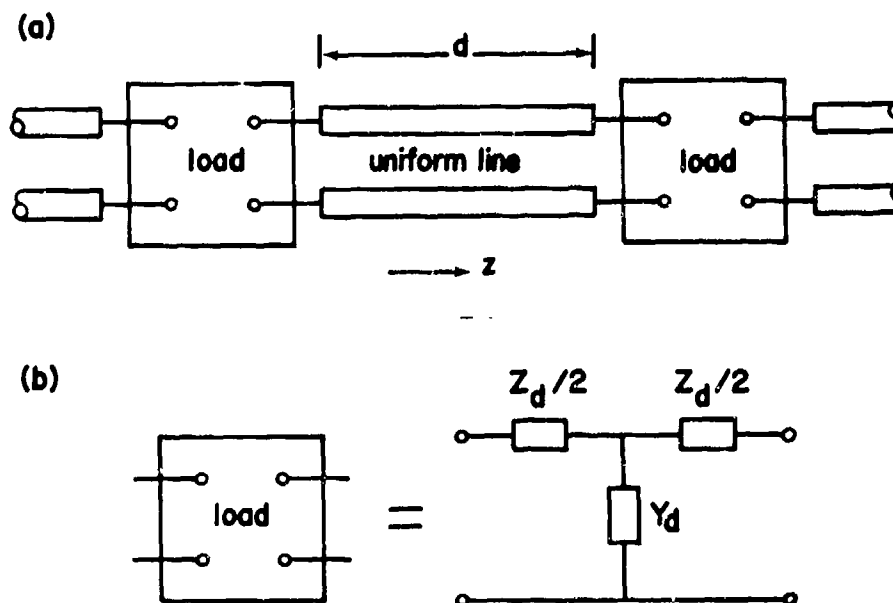


Fig. 17. A periodically-loaded transmission line with loading period d .

where Z' and Y' are, respectively, the series impedance and the shunt admittance per unit length of the uniform line. Note that k appears only in the function $\cos kd$.

The graphical method is a powerful procedure for analyzing the dispersion relation. For the discontinuities shown in Figs. 10 through 15, one may take

$$\begin{aligned} Y' &= j\omega C', & Z' &= j\omega L' \\ Y_d &= j\omega C_d, & Z_d &= j\omega L_d \end{aligned} \quad (23)$$

Then the dispersion relation becomes

$$\cos kd = \left(1 - \frac{1}{2} \alpha \theta^2\right) \cos \theta - \frac{\theta}{2} \sqrt{\frac{\alpha}{\beta}} \left(1 + \beta - \frac{1}{4} \alpha \theta^2\right) \sin \theta \quad (24)$$

where

$$\theta = \omega d \sqrt{L' C'}, \quad \alpha = \frac{L_d C_d}{d^2 L' C'}, \quad \beta = \frac{C_d L'}{L_d C'}$$

Fig. 18a shows a plot of the dispersion relation in the $(\omega, \cos kd)$ plane for $\alpha = 0.2$ and $\beta = 0.5$. The frequency ranges over which the curve lies between the horizontal lines -1 and 1 are the passbands, since they correspond to real values of k . The frequency ranges over which the curve lies beyond -1 and 1 are the stopbands, since they correspond to complex values of k .

Fig. 18b shows a plot of the dispersion relation in the (k, ω) plane. One sees readily that ω is a periodic function of k . Each continuous curve corresponds to a passband. Each point on a curve is a possible mode of propagation. The phase velocity v_p and the group velocity v_g of a mode are given by

$$v_p = \frac{\omega}{k}, \quad v_g = \frac{\partial \omega}{\partial k} \quad (25)$$

Thus v_p is proportional to the slope of a straight line drawn from the origin to the point (k, ω) , while v_g is proportional to the slope of the curve at the latter point. It is seen that at a given ω there exists an infinite sequence of phase velocities, while the group velocity is unique up to a sign.

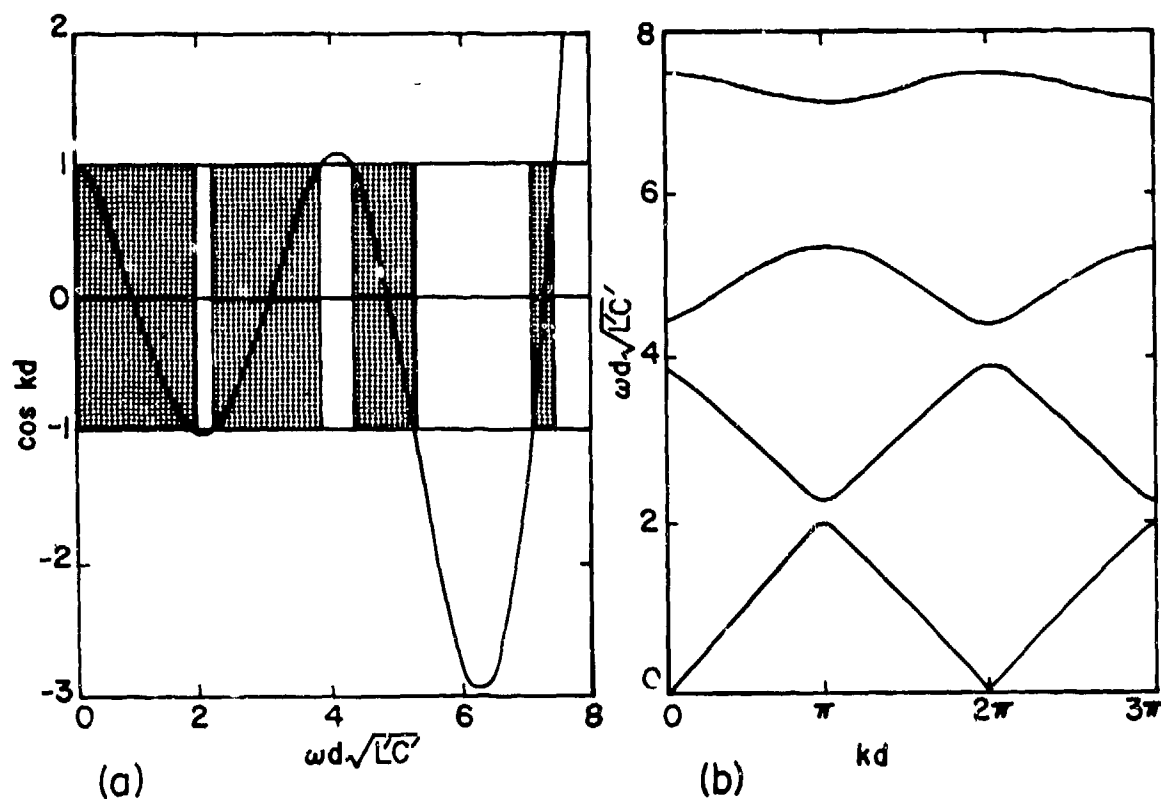


Fig. 18. A plot of the dispersion relation of a periodically-loaded transmission line of period d on the $(\omega, \cos kd)$ plane in Fig. 18a and on the (k, ω) plane in Fig. 18b. The shaded areas in Fig. 18a are the passbands and each continuous curve in Fig. 18b represents a passband.

2.2.2.2 Distributed Impedances of a Wire Over a Finitely Conducting Surface

Many cable runs in the interior of an aircraft, a missile, or a large communication system are routed over flat conducting sheets, of which the aircraft skin, the metallic floors, ceilings, and bulkheads are examples. When all the conductors can be assumed perfectly conducting, the determination of the propagation characteristics of such cable systems is the subject of standard transmission-line analysis. This section deals with the correction to the propagation parameters when the metallic sheets are no longer assumed perfectly conducting.

In Fig. 19 is shown the configuration of a single straight wire over an infinite, flat, nonmagnetic, metallic sheet. The wire is perfectly conducting, of radius a , and located at a height h above the sheet. The sheet is of thickness d , conductivity σ , and permeability μ_0 . It is assumed that σ is both uniform and frequency-independent.

In the limit of infinite sheet conductivity ($\sigma = \infty$), the series impedance Z' and the shunt admittance Y' per unit length of the

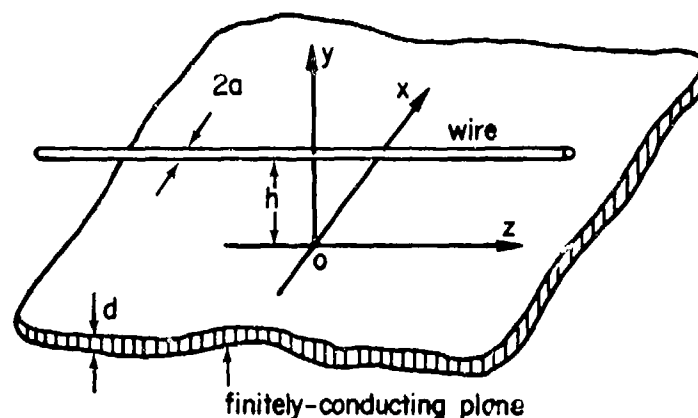


Fig. 19. A cable passing over a finitely-conducting plane sheet of conductivity σ and thickness d .

transmission line, as depicted by the configuration of Fig. 19, are

$$Z' = \frac{j\omega\mu_0}{2\pi} \ln\left(\frac{2h}{a}\right), \quad Y' = 2\pi j\omega\epsilon_0 / \ln\left(\frac{2h}{a}\right), \quad (h \gg a) \quad (26)$$

When the sheet conductivity σ is finite, the electromagnetic fields can penetrate into the sheet material as well as leak into the space below the sheet. These effects bring about a distortion of the fields, so that a longitudinal electric field component appears. As a consequence the fields above the sheet are no longer purely TEM. The wave propagation is damped to a certain extent, since electromagnetic energy is irreversibly lost through heat dissipation in the sheet material. In this case the variation of current and voltage along the line is still described by the source-free transmission-line equations (11); but the impedance and admittance parameters Z' and Y' must be corrected for finite sheet conductivity. It is found that from the solution of an appropriate boundary-value problem, Z' and Y' are given by [9,10]

$$Z' = R'_s + j\omega L'_{\text{eff}}, \quad \frac{1}{Y'} = R'_p + \frac{1}{j\omega C'_{\text{eff}}} \quad (27)$$

where

$$L'_{\text{eff}} = \frac{\mu_0}{4\pi} \left[2 \ln\left(\frac{2h}{a}\right) + \Lambda \right]$$

$$C'_{\text{eff}} = \frac{4\pi\epsilon_0}{2 \ln\left(\frac{2h}{a}\right) - \Lambda} \quad (28)$$

$$R'_s = \frac{\mu_0}{4\pi} \omega \Lambda, \quad R'_p = \frac{\Lambda}{4\pi\epsilon_0 \omega} \quad (29)$$

The dimensionless quantity Λ is given by

$$\Lambda = \frac{\delta}{h} = \frac{1}{h} \sqrt{\frac{2}{\omega\mu_0\sigma}} \quad (30)$$

which completely contains the effects of the finite sheet conductivity.

The results in (27) - (30) are valid down to frequencies at which the skin depth δ becomes comparable to the sheet thickness d . For the aluminum aircraft skin, d is typically of the order of 1 millimeter. The results are therefore applicable down to about 10 kHz.

To investigate the behavior of Z' and Y' below 10 kHz, one has to take into account the finite sheet thickness d . The boundary-value problem becomes considerably more complicated, and no quantitative results are as yet available in the literature.

2.2.3 PENETRATION

In this section EMP penetration through an imperfect tubular shield is treated. The penetration can proceed by way of two physical mechanisms: (1) diffusion through the imperfectly conducting shield material, and (2) leakage through the shield apertures. The determination of these two penetration effects for the tubular geometry is of major concern to the analysis of cable shields. In this connection it is dealt with fully in Chap. 2.4, which discusses cable interaction. The present treatment is therefore limited to consideration of (1) EMP diffusion through cable conduits (distributed penetration), and (2) aperture penetration at conduit junctions (local penetration).

2.2.3.1 Cable Conduit

Important cable runs in certain aircraft are shielded electromagnetically in special conduits. The conduits are essentially metallic tubes with diameters ranging from 1 to 3 cm. The conduit material is commonly a type of ferrous alloy or aluminum. The electrical conductivity of ferrous alloy is about that of steel ($\sim 10^7$ mhos/meter) and its permeability has a high value, of the order of $10^4 \mu_0$. The electrical conductivity of aluminum is 3.54×10^7 mhos/meter and its permeability is μ_0 .

A cable conduit is usually modeled by an infinitely long and apertureless cylindrical shell as shown in Fig. 20. The shell material

is characterized electromagnetically by the constant and uniform conductivity σ and permeability μ . The inner radius of the shell is denoted by b , and the outer radius by c . The cable shielded within the conduit is modeled by a single conductor and represented in Fig. 20 by an infinitely long, perfectly conducting, and nonmagnetic cylinder of radius a , concentric with the cylindrical shell.

Let the total EMP-induced current in the entire conductor system (shield and cable) be denoted by I_t . This current is assumed to have only a z -component and to be axially symmetric. It consists of a core current I flowing in the inner conductor and a shield current I_s flowing in the shell

$$I_t = I + I_s \quad (31)$$

Let V be the potential of the inner conductor relative to the shield. Then, for harmonic time variation $e^{j\omega t}$ the propagation of V and I is governed by the pair of transmission-line equations (11), namely

$$\begin{aligned} \frac{dV}{dz} + Z'I &= E_z(b) \\ \frac{dI}{dz} + Y'V &= 0 \end{aligned} \quad (32)$$

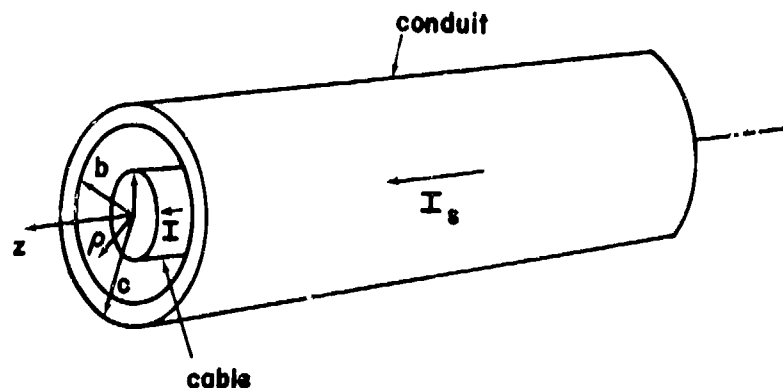


Fig. 20. Model of a cable conduit as a tubular shell.

where Z' and Y' are given by (26) with $2h$ replaced by b . The term $E_z(b)$ on the right-hand side of (32) is the z -component of the electric field on the inner surface of the shell ($\rho = b$). Its presence in the equation is due to the finite conductivity of the shield, and is given by [11-13]

$$E_z(b) = -Z'_1 I + Z'_T I_t \quad (33)$$

where

$$Z'_1 = \frac{k}{2\pi b \sigma} \frac{Y_0(kb)J_1(kc) - J_0(kb)Y_1(kc)}{J_1(kb)Y_1(kc) - Y_1(kb)J_1(kc)} \quad (34)$$

$$Z'_T = \frac{k}{2\pi c \sigma} \frac{J_1(kb)Y_0(kb) - Y_1(kb)J_0(kb)}{J_1(kb)Y_1(kc) - Y_1(kb)J_1(kc)} \quad (35)$$

with $k = \sqrt{-j\omega\mu\sigma}$, and J_0 , Y_0 , etc. denoting Bessel functions of the first and second kinds. Z'_1 is referred to as the internal impedance per unit length and Z'_T as the shield transfer impedance per unit length.

Substituting (33) into the first equation of (32) one obtains

$$\frac{dV}{dz} + (Z' + Z'_1)I = Z'_T I_t \quad (36)$$

The effects on the transmission-line equation due to the finite conductivity of the conduit shield consist of a correction to the series impedance Z' and the appearance of a distributed voltage source term $Z'_T I_t$. The transfer impedance Z'_T is completely determined by the frequency and the shield material and dimensions. For a highly conducting shield the total current I_t is, to a good approximation, given by the EMP-induced current on the outer surface of a perfectly conducting cylinder. Eq.(36) and the second equation of (32) jointly describe the excitation and propagation of voltage and current disturbances within the conduit as a result of EMP diffusion through the conduit.

The transfer impedance Z_T' is completely defined by (35); but for EMP shielding analysis a simpler asymptotic formula suffices. This formula obtains when the skin depth δ , defined in (15), of the shield material is much smaller than the shield radius. When $\delta \ll b < c$, (35) reduces to

$$Z_T' \approx R_{dc}' \frac{\gamma d}{\sinh \gamma d} \quad (37)$$

$$R_{dc}' = \frac{1}{2\pi\omega d\sqrt{\mu c}}$$

where R_{dc}' is the dc shield resistance per unit length, γ is defined in (14), and $d = c - b$ is the shield thickness. For a tubular shield of high permeability and radius of the order of 1 centimeter, the formula (37) is valid down to about 1 kHz; for a nonmagnetic shield it holds down to about 10 kHz.

Defining the amplitude A and the phase β such that

$$\frac{Z_T'}{R_{dc}'} = \frac{\gamma d}{\sinh \gamma d} = A e^{j\beta} \quad (38)$$

one finds that

$$A = \frac{2d/\delta}{\sqrt{\cosh(2d/\delta) - \cos(2d/\delta)}} \quad (39)$$

$$\beta = \frac{\pi}{4} - \frac{d}{\delta} - \arctan \frac{\sin(2d/\delta)}{e^{2d/\delta} - \cos(2d/\delta)} \quad (40)$$

Thus the transfer impedance is a function of the ratio d/δ . The dependences on ω and μ are absorbed into that on δ . Fig. 21 is a plot of A and β as functions of d/δ . It is seen that for $d/\delta \gg 1$, as when the frequency becomes high, the amplitude A of the transfer impedance is vanishingly small, and one has

$$A \rightarrow 2\sqrt{2} \frac{d}{\delta} e^{-d/\delta}$$

(41)

$$\beta \rightarrow \frac{\pi}{4} - \frac{d}{\delta}$$

The magnetic permeability μ of the conduit material enters the shielding formulas only through the skin depth δ . A high value of μ decreases δ and hence enhances the shielding effectiveness. Materials possessing high permeabilities are the ferromagnets and their alloys.

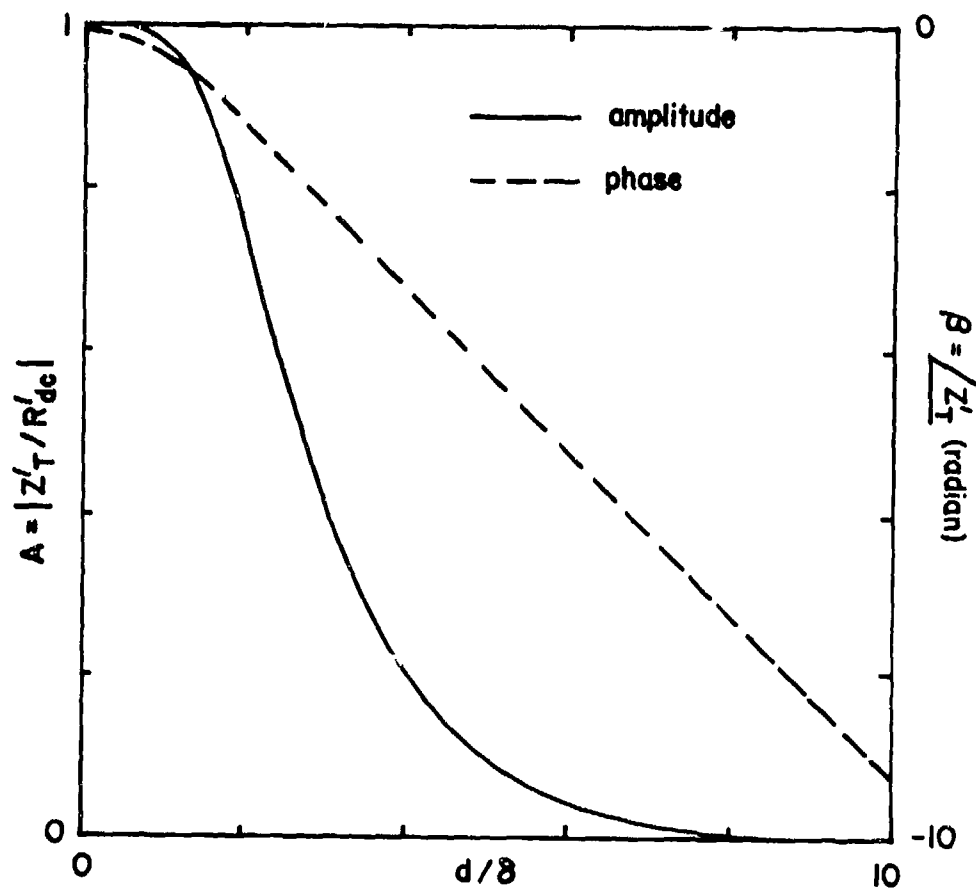


Fig. 21. Normalized transfer impedance Z'_T per unit length of a tubular shield.

They are increasingly being used in electromagnetic shielding technology. The high permeability of a ferromagnetic material is due to the existence of large numbers of microscopic ferromagnetic domains in it that can easily be aligned in an applied field. However, when the applied field approaches a certain large value, practically all the ferromagnetic domains are fully aligned. A further increase in the applied field strength cannot bring about any more alignment. The ferromagnetic material is then said to be saturated. Therefore, in a weak applied field, the permeability of a ferromagnetic material is constant and large. As the material approaches saturation in a strong field, μ begins to drop towards μ_0 . Thus saturation, or even partial saturation, renders a ferromagnetic conduit less effective in shielding external electromagnetic fields.

The shielding analysis carried out in this section is valid only for an unsaturated shield. Its extension to include the nonlinear effects of saturation consists in accounting for the dependence of μ on the magnetic field. This analysis is a nonlinear boundary-value problem, and involves considerable mathematical difficulty. The problem is further complicated by the occurrence of hysteresis, making μ a double-value function of \vec{H} . As a consequence, the theory of ferromagnetic shields is not yet fully developed. Some early attempts on the problem can be found in the recent literature [14,15].

2.2.3.2 Conduit Junction

A typical cable conduit is made up of several segments. In some cases, two adjacent segments are joined together end-to-end by means of a connector. In other cases, the segments are simply welded together or mated together through screw threads. These different kinds of connections have a certain degree of imperfection which gives rise to local EMP penetration. In this section the discussion will be limited to penetration through conduit connectors. Fig. 22 illustrates the principal components of a conduit connector. In the connector the matching ends of two adjacent conduit segments are joined together

inside a coupler. The coupler is a broad metallic ring which fits snugly over the ends of the conduits to be joined. When the two outer rings of the connector are tightened, two coils of fine flexible spring are pressed against the ends of the coupler and the conduits, thereby sealing the narrow apertures between the ends of the two conduits.

At EMP frequencies, penetrations through the apertures at the two ends of the coupler by the electric field and the longitudinal component of the magnetic field (directed along the axis of the conduit) are entirely negligible. These two field components are severely attenuated as they enter the coaxial region between the coupler ring and the outer surfaces of the two conduit segments. The distance of significant penetration is of the order of the clearance between the coupler and the conduit. By making the clearance small and the width of the coupler large, these two field components can be effectively blocked. However, the penetration by a transverse external magnetic field is a different matter. An example of such a magnetic field is

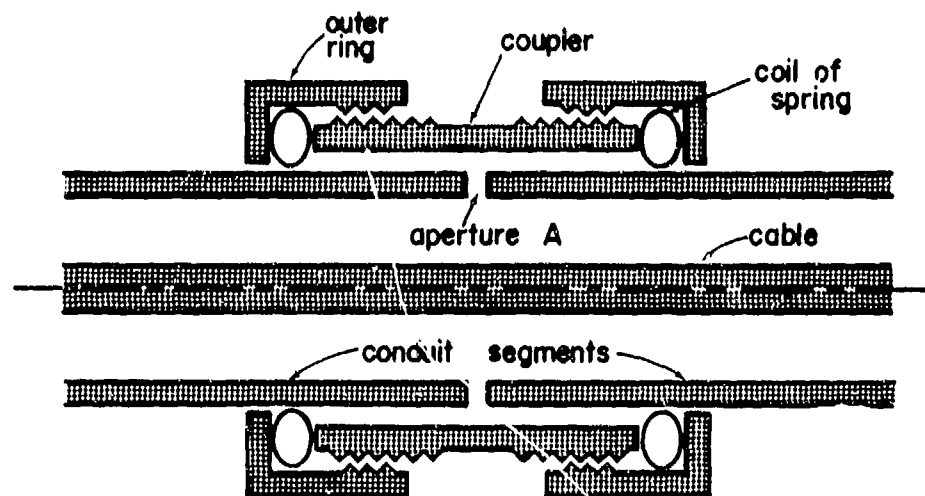


Fig. 22. Principal structural elements of the cable conduit connector.

that generated by EMP-induced axial skin currents flowing on the outer surface of the conduit. This transverse magnetic field couples into the conduit interior through the circumferential slot A (Fig. 22) and induces currents on the cables inside the conduit.

An electromagnetic equivalent of the conduit connector shown in Fig. 22 is given in Fig. 23. It incorporates the essential electromagnetic shielding features in the connector design. The two spring coils, which are made up of extremely fine and closely packed turns of wire, are here modeled by two equivalent imperfectly conducting annular gaskets. They plug the two openings at the ends of the coupler ring. Most of the minor aspects of the actual connector geometry, notably the two outer rings, have been eliminated.

At EMP frequencies the magnetic field at the internal aperture A in Fig. 23 can be expressed in terms of three admittances Y_s , Y_{int} and Y_{ext}

$$H_{\phi}(A) = J_{sc} \frac{Y_{int}}{Y_s + Y_{int} + Y_{ext}} \quad (42)$$

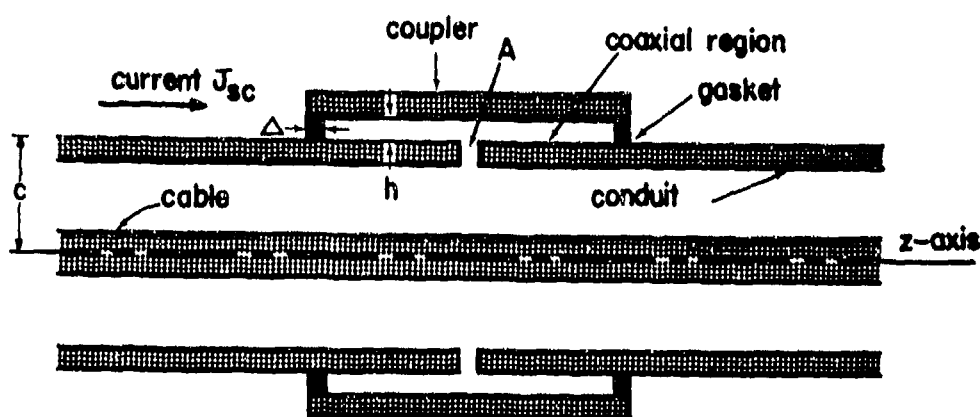


Fig. 23. Geometry of an electromagnetic equivalent of the cable conduit of Fig. 22.

The admittance Y_g is the sheet admittance characterizing each of the two gaskets. It is given by the product of the gasket conductivity and the gasket thickness Δ

$$Y_g = \sigma \Delta \quad (43)$$

The admittance Y_{int} is the internal admittance characterizing the small coaxial region between the coupler and the conduit, while the admittance Y_{ext} is the external admittance characterizing the free space outside the conduit.

The admittances Y_{int} and Y_{ext} are found to be [16]

$$Y_{int} \approx \frac{1}{2Z_o}, \quad Y_{ext} \approx j\omega \frac{\epsilon_o h}{\pi} \ln \left(\frac{1}{kh} \right) \quad (44)$$

The magnetic field $H_\phi(A)$ given by (42) can penetrate into the conduit interior and excite the cable within. The open-circuit voltage V_{oc} induced by this field across the aperture gap A is approximately given by

$$V_{oc} = Z_T I_t \quad (45)$$

$$Z_T = \frac{h}{\pi c} \frac{1}{Y_g + Y_{int} + Y_{ext}} \quad (46)$$

where h is the separation between the coupler and the conduit (Fig. 23), c is the outer radius of the conduit, and $I_t = 2\pi c J_{sc}$.

The effects of the aperture field $H_\phi(A)$ on the cable within the conduit can be represented by taking the source term in the transmission-line equations (11) to be

$$V'(s) = Z_T I_t \delta(z - z_o) \quad (47)$$

where z_o is the z -coordinate of the center of the aperture A .

REFERENCES

- [1] K.S.H. Lee and F.C. Yang, "A wire passing by a circular aperture in an infinite ground plane," IN 317, February 1977.
- [2] A.D. Varvatsis and M.I. Sancer, "EMP penetration through dielectric skin panels on the leading edge of aircraft wings," IN 325, May 1977.
- [3] G. Bedrosian and K.S.H. Lee, "EMP penetration through metal skin panels and into aircraft cavities," IN 314, August 1976.
- [4] J. Lam, "Equivalent lumped parameters for a bend in a two-wire transmission line: part I. inductance," IN 303, December 1976.
- [5] J. Lam, "Equivalent lumped parameters for a bend in a two-wire transmission line: part II. capacitance," IN 304, January 1977.
- [6] F.M. Tesche and T.K. Liu, "An electric model for a cable clamp on a single-wire transmission line," IN 307, December 1976.
- [7] S. Coen, T.K. Liu and F.M. Tesche, "Calculation of the equivalent capacitance of a rib near a single-wire transmission line," IN 310, February 1977.
- [8] J. Lam, "Propagation characteristics of a periodically loaded transmission line," IN 302, November 1976.
- [9] H. Kaden, Wirbelströme und Schirmung in der Nachrichtentechnik, Springer-Verlag, Berlin, 1959, pp. 56 - 61.
- [10] C. Flammer, "On the scattering of electromagnetic waves by a perfectly conducting cylinder over a finitely conducting ground," IN 145, August 1973.
- [11] S.A. Schelkunoff, "Electromagnetic theory of coaxial transmission lines and cylindrical shields," Bell Sys. Tech. J. 13, 1934, pp. 532 - 579.
- [12] H. Kaden, Wirbelströme und Schirmung in der Nachrichtentechnik, Springer-Verlag, Berlin, 1959, pp. 292 - 295.

- [13] E.F. Vance, "Internal voltages and currents in complex cables," IN 8, June 1967.
- [14] R.R. Ferber and F.J. Young, "Enhancement of EMP shielding by ferromagnetic saturation," IEEE Trans. Nuclear Sci., NS-17, pt. 3, 1970, pp. 354 - 359.
- [15] D.E. Merewether, "Analysis of the shielding characteristics of saturable ferromagnetic cable shields," EMC-12, 1970, pp. 134 - 137.
- [16] J. Lam, "Analysis of EMP penetration through the B-1 cable conduit connector," AFWL-TR-77-91, July 1976.

CHAPTER 2.3

INTERMEDIATE INTERNAL INTERACTION, II: CAVITIES

Within the intermediate internal interaction region, which is defined to be the region between the outermost layer of the system's shield topology and the next inward shield — usually the equipment boxes —, there exist line conductors and cavities. Examples of line conductors are hydraulic lines, control cables, pneumatic ducts, electrical cables, etc. Data and formulas for their interaction properties have been given in the preceding chapter. This chapter is devoted to data presentation for cavities, typical examples of which are aircraft cockpits, avionics bays, wheel wells, and weapons bays.

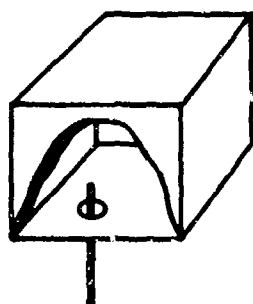
2.3.1 COUPLING

The sources that excite the cavities behind the surface $S_{m-1,m}$ which separates the volumes V_{m-1} and V_m arise from various kinds of penetration on $S_{m-1,m}$, as described in Chap. 1.2. Examples of these sources are shown in Fig. 1. If the sources such as those depicted in Figs. 1a - c can be approximated by point dipoles, they are called localized sources; otherwise, they are referred to as distributed sources (see Figs. 1d - f). These sources have been treated in Sec. 2.1.3 under the assumptions that the surface $S_{m-1,m}$ is flat and the cavity behind it is an infinite half-space. In practice, these assumptions will be violated to a certain extent. In this section various modifications of the results of Sec. 2.1.3 will be given when these two assumptions are removed.

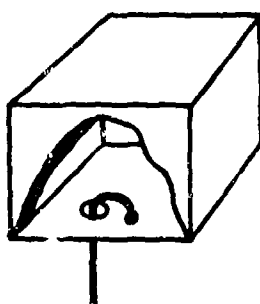
2.3.1.1 Coupling via Apertures

There are various factors that would affect the penetration sources based on the planar approximation [1]. The most common factors are the curvature itself, nearby conductors or apertures, a backup cavity, an impedance cover or a dielectric coating. Each of these factors will be discussed in this section.

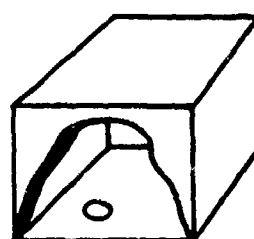
LOCALIZED SOURCES



(a) stub

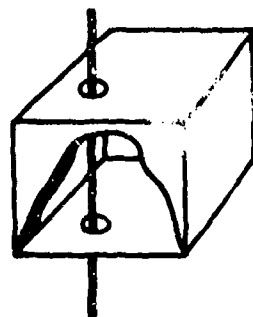


(b) loop

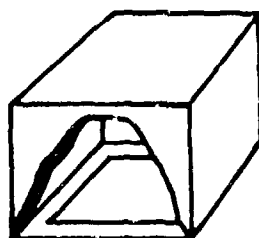


(c) hole

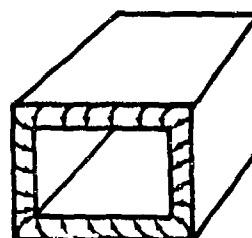
DISTRIBUTED SOURCES



(d) wire



(e) rectangular hatch



(f) diffusion through walls

Fig. 1. Typical sources exciting a cavity.

2.3.1.1.1 Aperture in a Curved Surface

The only problem that has been solved rigourously regarding the effect of curvature on polarizabilities is that of an infinitely long slot in an infinite hollow circular cylindrical shell [2]. Let

α'_e, α'_m = electric, magnetic polarizability per unit length of an infinite slot of width $a\theta_0$ in an infinite cylindrical shell (see Fig. 2)

$\alpha'_{eo}, \alpha'_{mo}$ = electric, magnetic polarizability per unit length of an infinite slot of width $a\theta_0$ in an infinite ground plane

$$= (a\theta_0)^2/4$$

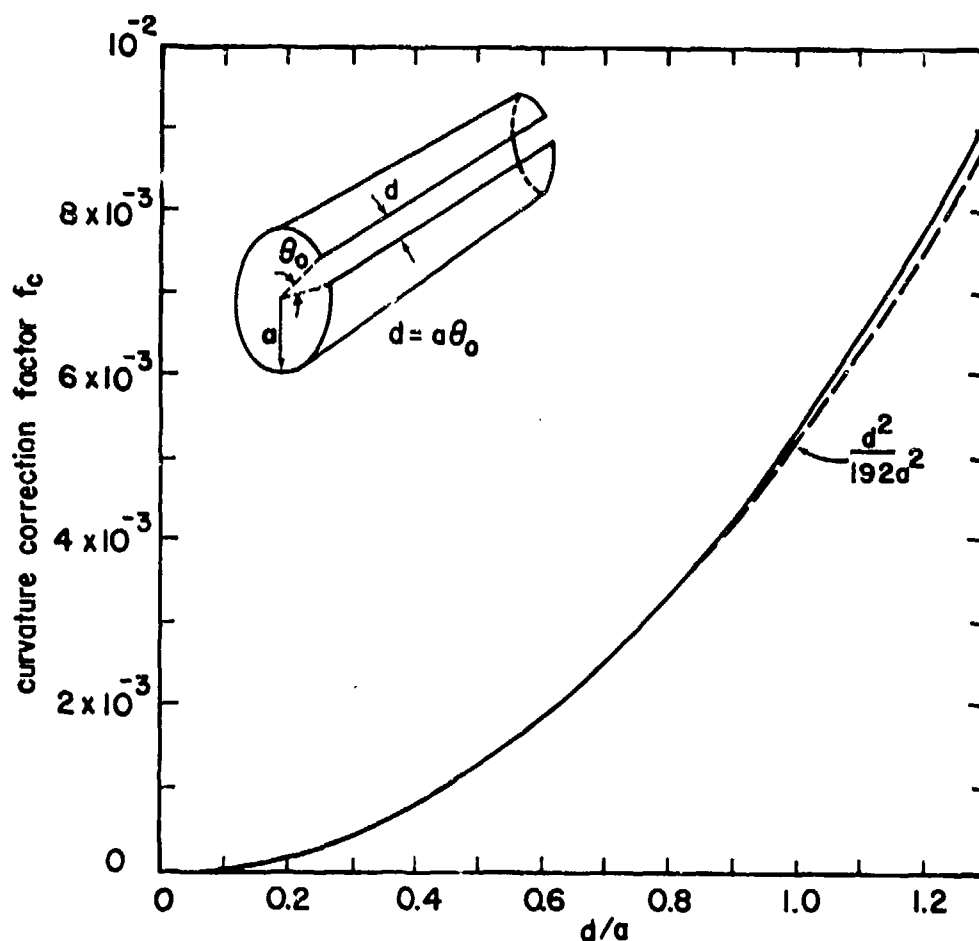


Fig. 2. Curvature effect on the polarizabilities of a two-dimensional slot.

Then, the normalized polarizabilities $\bar{\alpha}_e$ and $\bar{\alpha}_m$ defined by

$$\bar{\alpha}_e = \alpha'_e / \alpha'_{eo}, \quad \bar{\alpha}_m = \alpha'_m / \alpha'_{mo}$$

are given by

$$\bar{\alpha}_e = \bar{\alpha}_m = 1 - f_c(d/a) \quad (1)$$

$$f_c(x) = 1 + 64 \frac{\cos(x/4) \ln[\cos(x/4)]}{x^2 [1 + \cos(x/4)]} \quad (2)$$

$$\approx \frac{x^2}{192}, \quad \text{for } x < 1 \quad (3)$$

The geometry of the problem and the curvature correction factor f_c given by (2) and (3) are shown in Fig. 2. The simple approximate formula (3) is accurate to within 1.5% for $d/a \leq 1$ (or the angular opening $\theta_0 \leq 57.3^\circ$), and the correction required is less than 0.6%.

2.3.1.1.2 Aperture With a Backup Ground Plane

A particular static boundary-value problem is solved in [2] to study the effect of a nearby conductor on the polarizabilities of an aperture in an infinite ground plane. The aperture is taken to be a circular hole of radius a and the nearby conductor an infinite perfectly conducting plane parallel to the plane of the hole and at a distance h away (see Fig. 3). The normalized polarizabilities $\bar{\alpha}_e$ and $\bar{\alpha}_m$ can be written as

$$\bar{\alpha}_e = \bar{\alpha}_m = 1 - f_p(h/a) \quad (4)$$

where the correction factor f_p is a positive function of h/a and the normalizing polarizabilities α_{eo} and α_{mo} of a circular hole in an infinite ground plane are given by

$$\alpha_{eo} = \frac{2}{3} a^3, \quad \alpha_{mo} = \frac{4}{3} a^3 \quad (5)$$

The curve in Fig. 3 is obtained via a dual integral-equation formulation followed by numerical computation. If the variational principle is employed, an explicit expression for f_p is obtained, namely

$$\bar{\alpha}_e = \bar{\alpha}_m = \frac{1}{1 + (2/\pi) \sum_{n=1}^{\infty} F(nh/a)} \quad (6)$$

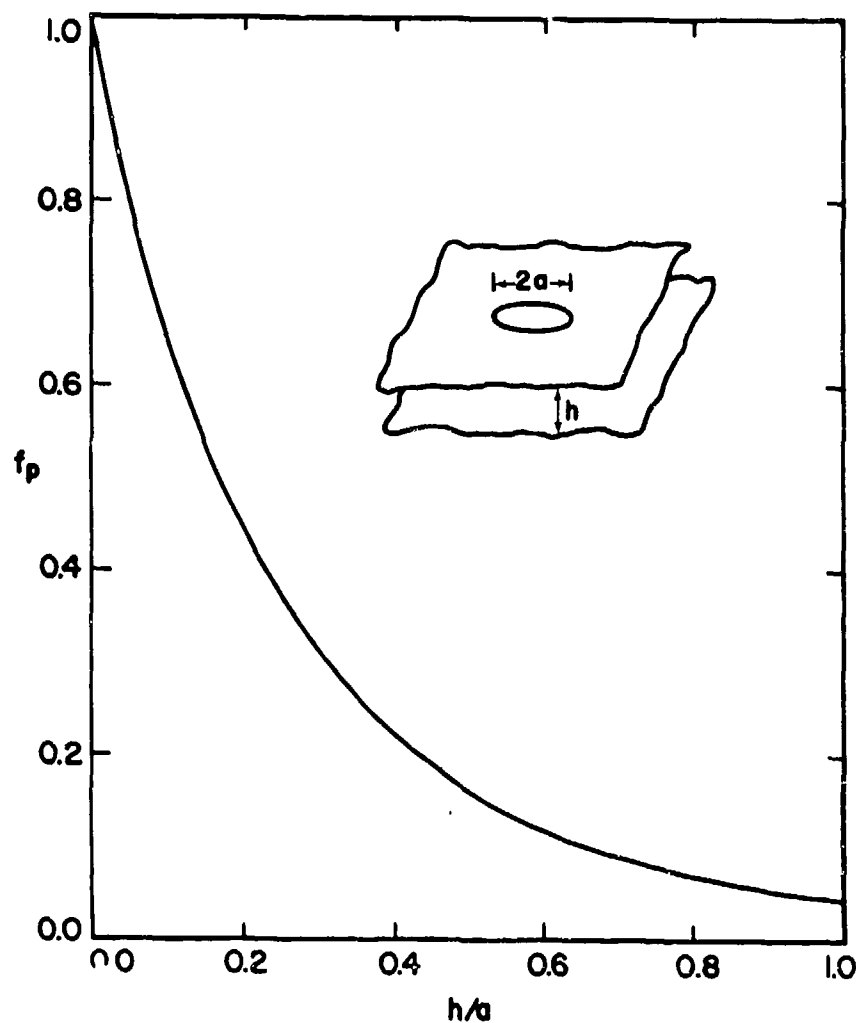


Fig. 3. Effect of a nearby infinite plate on the polarizabilities of a circular hole.

where

$$F(x) = \arctan(1/x) + x - (x^3 + 3x/2)\ln(1 + 1/x^2) \quad (7)$$

The expression (6) differs from the correct value by less than 0.03% for $h \geq a/2$ and less than 11% for $h < a/2$. From Fig. 3 it may be concluded that if the backup plane is at least one aperture radius away, the correction required is less than 5%.

2.3.1.1.3 Aperture With a Backup Cavity

The effect of a backup cavity on the polarizabilities of an aperture has not been treated to the extent where quantitatively useful information is available. In the case where the cavity is a long cylinder with a circular opening in the plane of its flange as shown in Fig. 4, the effect of the long cylinder on the magnetic polarizability of the opening can be obtained by a simple manipulation of the results in [3]. With α_{mo} given in (5) as the normalizing factor, the normalized magnetic polarizability $\bar{\alpha}_m$ is given by

$$\begin{aligned} \bar{\alpha}_m &= 1 - f_b \\ f_b &= 1 - \frac{3\pi}{4} \sum_r C_r J_2(\zeta_r) / \zeta_r \\ &\approx 0.33 \end{aligned} \quad (8)$$

where ζ_r denotes the roots of $J_1'(\zeta_r) = 0$, J_1 and J_2 are Bessel functions of the first kind of order 1 and 2, the prime denotes differentiation with respect to the argument, and the C_r 's satisfy a matrix equation [3]. The first two values are $\zeta_1 = 1.84$, $\zeta_2 = 5.33$ and $C_1 = 1.68$, $C_2 = -0.84$. The value $f_b = 0.33$ is accurate to within 5%. Thus, for the geometry shown in Fig. 4 the effect of a deep cylindrical cavity on the aperture's magnetic polarizability is $33\% \pm 5\%$.

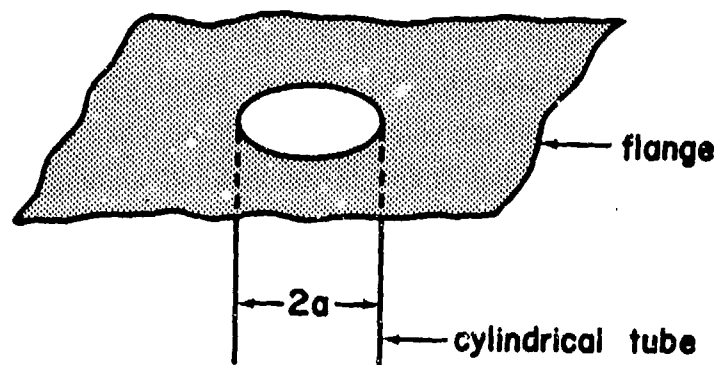


Fig. 4. A circular hole backed up by an infinite cylindrical tube.

2.3.1.1.4 Aperture With Other Modifications

There are other effects, such as nearby apertures (Fig. 5a), impedance loading (Fig. 5b) and dielectric coating (Fig. 5c), that may change the aperture's polarizabilities. Formulas for these effects can be found in Sec. 2.1.3.2.1.

2.3.1.2 Coupling via Diffusion

In EMP shielding problems involving closed conducting shells, displacement currents may be neglected throughout. Hence, for the regions outside and inside the enclosure (Fig. 6a) one may write

$$\begin{aligned}\vec{H}^{\text{ex}} &= -\nabla\phi_m^{\text{ex}}, & \nabla^2\phi_m^{\text{ex}} &= 0 \\ \vec{H}^{\text{in}} &= -\nabla\phi_m^{\text{in}}, & \nabla^2\phi_m^{\text{in}} &= 0\end{aligned}\tag{9}$$

and within the enclosure's wall one has, in the s -domain,

$$\begin{aligned}\nabla \times \vec{H} &= \sigma \vec{E} \\ \nabla \times \vec{E} &= -\mu_s \vec{H}\end{aligned}\tag{10}$$

The quantity of interest is the cavity field \vec{H}^{in} or the interior magnetic scalar potential ϕ_m^{in} . The source term for ϕ_m^{in} is either the normal derivative $(\partial/\partial n)\phi_m^{in}$ or ϕ_m^{in} itself on the inner surface S_1 of the cavity wall (Fig. 6a). These boundary values are related to the boundary values $(\partial/\partial n)\phi_m^{ex}$ and ϕ_m^{ex} on the outer surface S_0 of the cavity; the relationship can be obtained by integrating (10) across the enclosure's

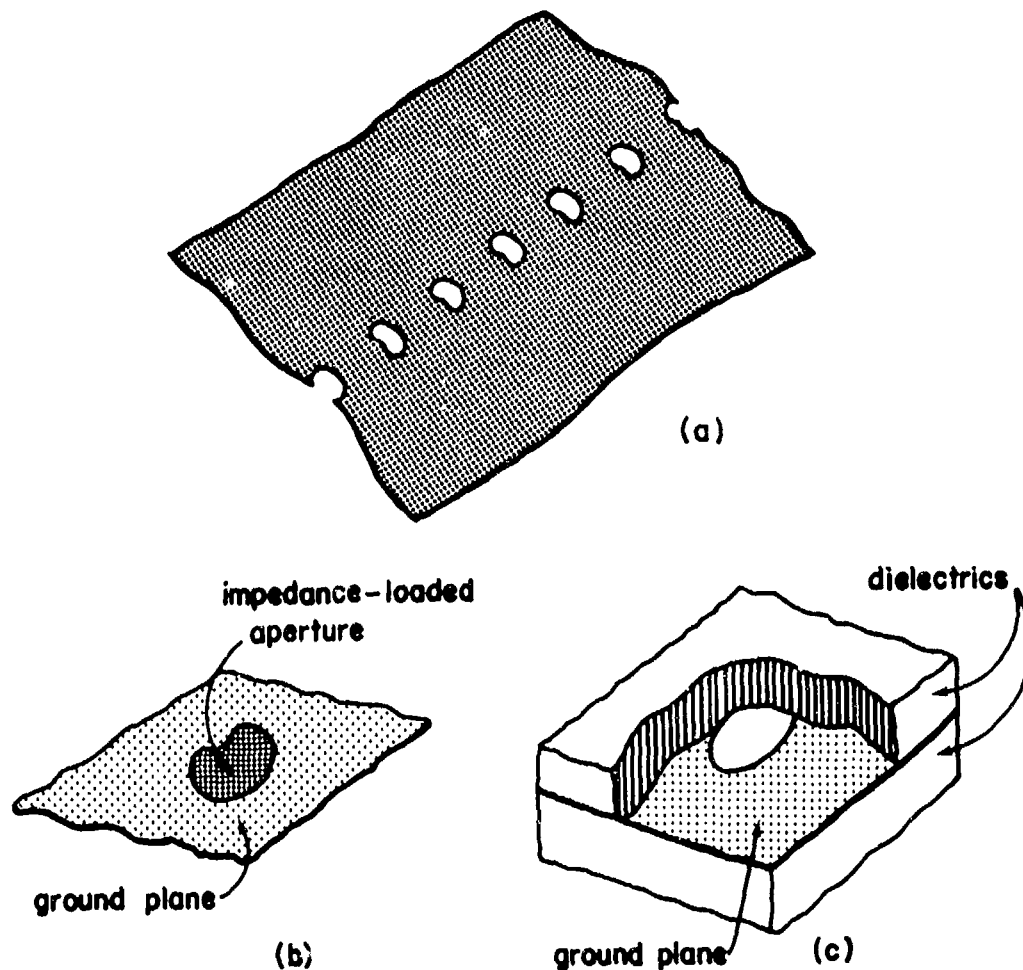


Fig. 5. (a) A row of periodic small apertures, (b) an impedance-loaded aperture in an infinite ground plane, and (c) a circular hole in an infinite ground plane sandwiched by dielectric slabs.

wall. A knowledge of this boundary relationship greatly simplifies the original two-surface boundary-value problem (Fig. 6a) to the one-surface boundary-value problem (Fig. 6b). For the more general case where displacement currents need to be taken into account, the boundary conditions between the two sides of the cavity wall are of the form of a "boundary connection supermatrix," presented in Sec. 2.1.3.3.

For metallic enclosures whose wall conductivity is usually very high, the true source for the penetrant cavity field is the normal component of the magnetic field H_n^{in} (which is equal to the magnetic surface charge density ρ_m^{in} divided by μ_0) on the inner surface S_i of the cavity wall. This source can be calculated by a perturbation technique by first assuming the wall to be perfectly conducting [4,5]. It turns out that H_n^{in} on S_i is inversely proportional to the wall conductivity and directly proportional to the spatial variations of the induced surface currents on S_o .

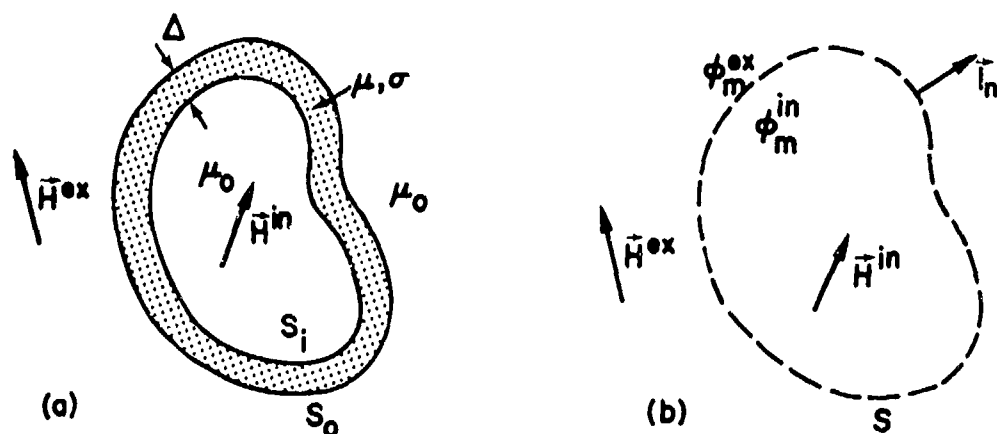


Fig. 6. (a) An enclosure with conducting walls, (b) a mathematical configuration in which the volume enclosed by S is equal to the interior volume of Fig. 6a and the surface S is similar to either S_i or S_o of Fig. 6a.

2.3.1.2.1 Cavities With Electrically Thin Walls

For cavities whose wall thickness is less than the wall's skin depth the boundary conditions across S (Fig. 6b) are given by [4]

$$\frac{\partial}{\partial n} \phi_m^{\text{ex}} = \frac{\partial}{\partial n} \phi_m^{\text{in}} = \frac{1}{s\mu_0\sigma\Delta} \nabla_s^2 (\phi_m^{\text{in}} - \phi_m^{\text{ex}}) \quad (11)$$

where σ and Δ are the wall's conductivity and thickness, and ∇_s^2 is a surface Laplacian operator. In practice, one may neglect $\nabla_s^2 \phi_m^{\text{in}}$ in comparison to $\nabla_s^2 \phi_m^{\text{ex}}$ and obtain from (11) for the surface magnetic charge density ρ_m^{in}

$$\rho_m^{\text{in}} = \mu_0 H_n^{\text{in}} \approx \frac{R}{s} \nabla_s^2 \phi_m^{\text{ex}} \quad (12)$$

where $R = (\sigma\Delta)^{-1}$ is the resistance of the wall. If ϕ_m^{ex} is eliminated in favor of the surface current density \vec{J} , (12) becomes

$$\rho_m^{\text{in}} \approx \frac{1}{s} R \vec{l}_n \cdot \nabla_s \times \vec{J} \quad (13)$$

where \vec{J} is obtained by solving an external interaction problem for the case of infinite wall conductivity (see Sec. 2.1.2).

2.3.1.2.2 Shells of Arbitrary Electrical Thickness

For cavities whose wall thickness is comparable to or greater than the wall's skin depth the boundary conditions are much more complicated and are given by [4]

$$\begin{aligned} \frac{\partial}{\partial n} (\phi_m^{\text{in}} + \phi_m^{\text{ex}}) &= \alpha \nabla_s^2 (\phi_m^{\text{in}} - \phi_m^{\text{ex}}) \\ \frac{\partial}{\partial n} (\phi_m^{\text{in}} - \phi_m^{\text{ex}}) &= \beta \nabla_s^2 (\phi_m^{\text{in}} + \phi_m^{\text{ex}}) \end{aligned} \quad (14)$$

where

$$\alpha = \frac{2}{s\mu_o\sigma\Delta} \frac{\sqrt{s\tau_d}/2}{\tanh(\sqrt{s\tau_d}/2)} \quad (15)$$

$$\beta = \frac{\mu_r\Delta}{2} \frac{\tanh(\sqrt{s\tau_d}/2)}{\sqrt{s\tau_d}/2}$$

and $\tau_d = \mu\sigma\Delta^2$ and $\mu_r = \mu/\mu_o$. In practice, $\nabla_s^2 \phi_m^{in}$ may be neglected in comparison to $\nabla_s^2 \phi_m^{ex}$, and (14) and (15) give

$$\rho_m^{in} \approx \frac{1}{s} Z_T \vec{I}_n \cdot \nabla_s \times \vec{J} \quad (16)$$

where the transfer impedance Z_T is

$$Z_T = R \frac{\sqrt{s\tau_d}}{\sinh\sqrt{s\tau_d}} \quad (17)$$

and is plotted in Fig. 21 of Sec. 2.2.3 and Fig. 1 of Sec. 2.4.1.

2.3.2 PROPAGATION

Electromagnetic energy can penetrate into a cavity either through apertures in the cavity surface or by means of diffusion through cavity walls. Engineering formulas and data for excitation of cavity fields by apertures are given in Sec. 2.3.2.1 and by diffusion in Sec. 2.3.2.2.

2.3.2.1 Cavity Excitation via Apertures

Although electromagnetic penetration through an aperture into a cavity is a problem of great practical interest, quantitatively useful results exist only for a few simple cavity-aperture geometries because the general problem of calculating the interaction between aperture and cavity is very difficult, if not impossible, to solve. However, if the cavity-aperture problem can be separated into two independent problems,

namely, (a) the aperture problem in an infinite ground plane and (b) the cavity problem with given aperture field, then the amount of information on the cavity excitation via apertures can be greatly increased. Under this decoupling approximation the results of Sec. 2.1.3.2 on the aperture problem in an infinite ground plane serve as input to the cavity problem which is relatively easy to solve, since methods to calculate the cavity field distribution with known aperture field are well developed [6-10].

In the following, results derived under this approximation are presented as well as results obtained without this approximation.

2.3.2.1.1 Parallel-Plate Cavities

a. Small Apertures in the Front Plate

Electromagnetic penetration into a parallel-plate region through an electrically small elliptic aperture has been investigated in [11,12], in which the aperture is replaced by point dipoles with polarizabilities $\alpha_e^{\leftrightarrow}$ and $\alpha_m^{\leftrightarrow}$ appropriate to an elliptical hole (see Sec. 2.1.3.2.1). The geometry is shown in Fig. 7 where the x-axis is parallel to the major axis of the elliptic aperture. Figs. 8a-d show some typical normalized time-harmonic data indicative of the behavior of the penetrant field. The data are applicable under the following conditions:

- (a) linear dimension of aperture \ll plate separation h , wavelength λ , and the distance between the aperture and the field point;
- (b) $|h - n\lambda/2| > \lambda/20$, $n = 1, 3, 5, 7, \dots$

Although the results presented are for the elliptic aperture case, the curves shown in Figs. 8a-d also apply to small apertures of any shape, provided that suitable polarizabilities are used.

b. Long Slot in the Front Plate

A slot with length much greater than its uniform width may be approximated by an infinitely long uniform slot. The problem of an

infinitely long uniform slot in the front plate of a parallel-plate cavity excited by an EMP has been treated in [13,14].

The geometry of the problem considered in [13] is shown in Fig. 9, in which the incident fields are assumed to be uniform and $h \ll w \ll \lambda$ (wavelength). The following results are obtained for the region between the plates and $|x| > w/2$

$$\begin{pmatrix} E_x \\ H_z \end{pmatrix} \approx \frac{x}{|x|} \begin{pmatrix} E_{sc} \\ -H_{sc} \end{pmatrix} e^{-\pi(|x| - w/2)/h} \sin(\pi z/h)$$

$$\begin{pmatrix} E_z \\ H_x \end{pmatrix} \approx - \begin{pmatrix} E_{sc} \\ H_{sc} \end{pmatrix} e^{-\pi(|x| - w/2)/h} \cos(\pi z/h)$$
(18)

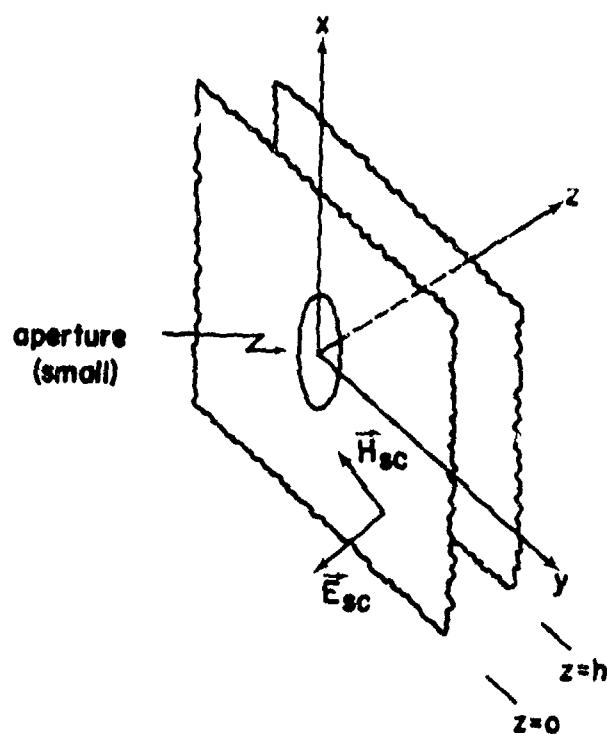


Fig. 7. Parallel plates with aperture in front plate.

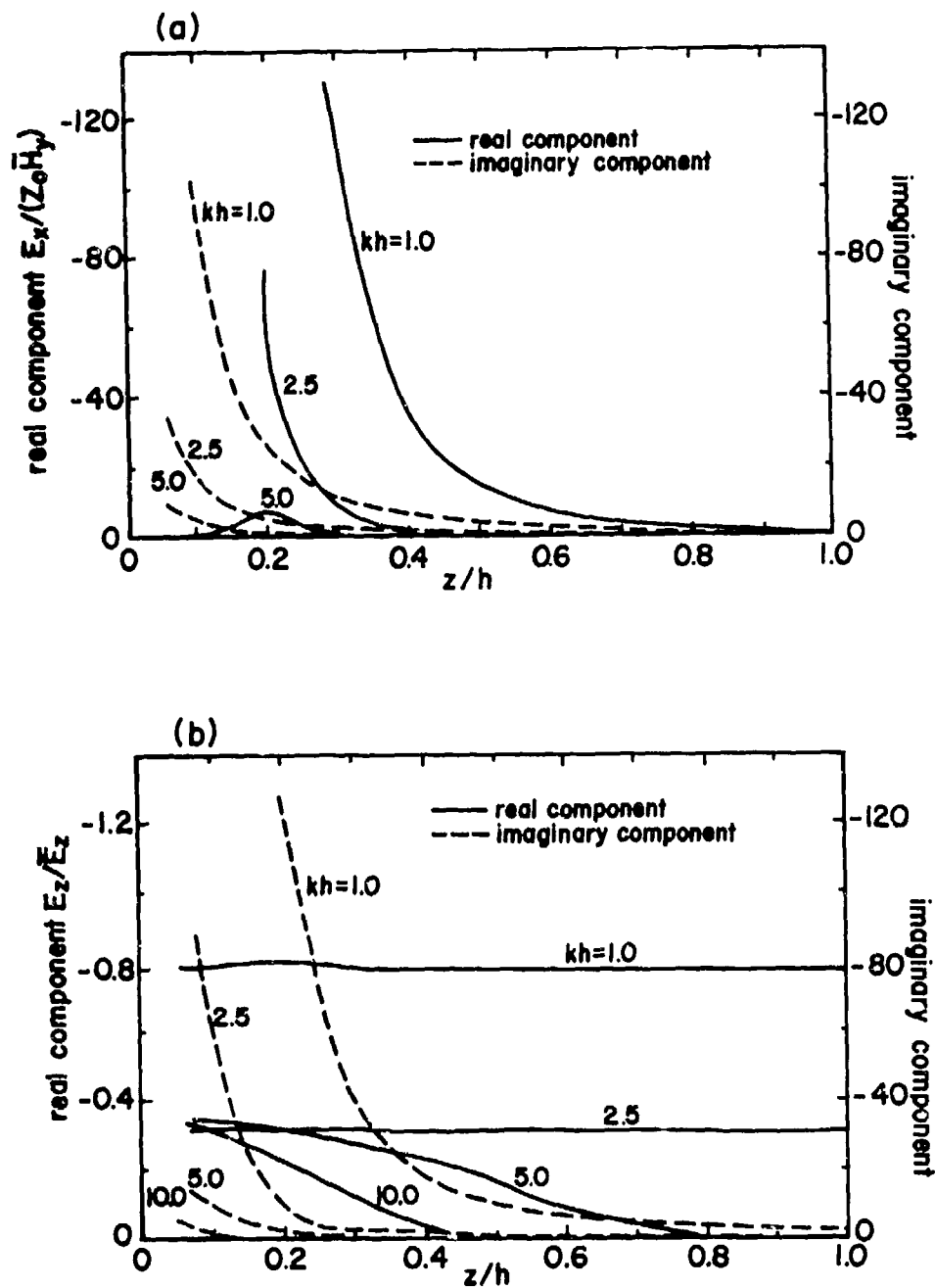


Fig. 8. Real and imaginary parts of (a) $E_x(0,0,z)/(Z_0 \bar{H}_y)$ and (b) $E_z(0,0,z)/\bar{E}_z$, where $\bar{H}_y = k^3 \alpha_{m,yy} H_{sc,y}/(2\pi)$ and $\bar{E}_z = k^3 \alpha_{e,zz} E_{sc,z}/\pi$.

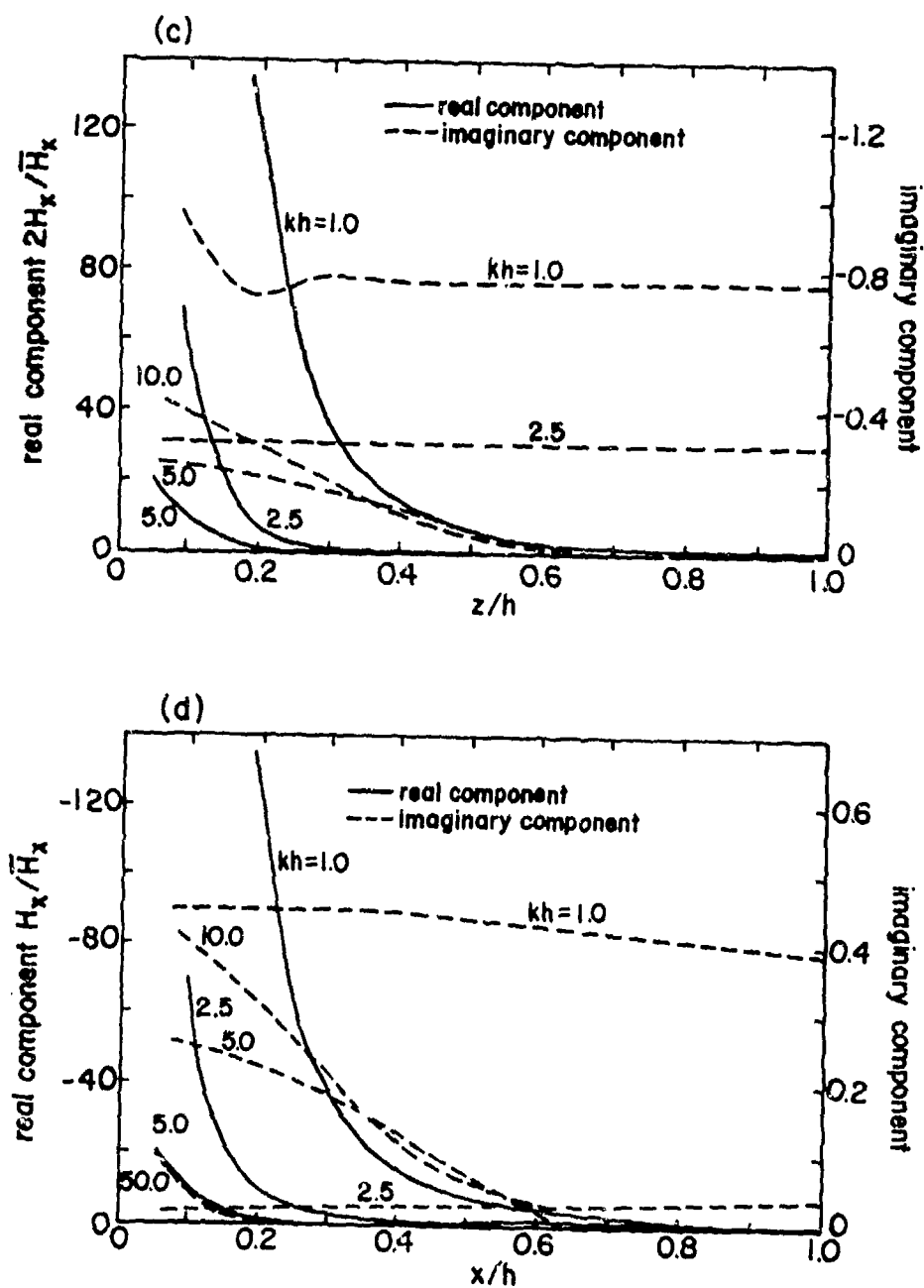


Fig. 8. Real and imaginary parts of (c) $2H_x(0,0,z)/\bar{H}_x$ and (d) $H_x(x,0,0)/\bar{H}_x$, where $\bar{H}_x = k^3 \alpha_{m,xx} H_{sc,x} / \pi$.

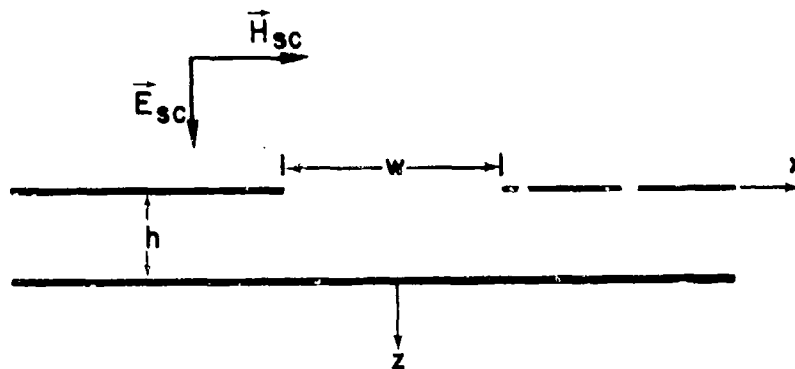


Fig. 9. Parallel plates with uniform slot in the front plate.

It is seen that in this special case the characteristic length for EMP penetration is h . Eqs.(18) are found to be useful for an estimation of the low-frequency EMP penetration through joints of aircraft skin panels.

The geometry of the problem considered in [14] is shown in Fig. 10. The slot is excited by a normally incident plane wave whose electric field is parallel to the x -axis. It is found that the strength of the field component E_x at the slot's center generally differs from that in an isolated, slotted plate. The difference, however, is small if $w < h < \lambda/2$. The TEM field in the region between the plates is plotted in Fig. 11 as function of plate separation h , where $h < \lambda/2$ in which case only the TEM mode can propagate.

c. Periodic Array of Rectangular Apertures in the Front Plate

In Fig. 12 is shown the geometry of the problem of low-frequency magnetic field penetration into the parallel-plate region through a periodic array of rectangular apertures.

The problem is solved in [13] in which an integral equation for the normal component of the aperture magnetic field is first formulated and solved subsequently by introducing a suitable trial function with an adjustable constant. The normal component of the aperture magnetic field is, for $p \gg 2h$,

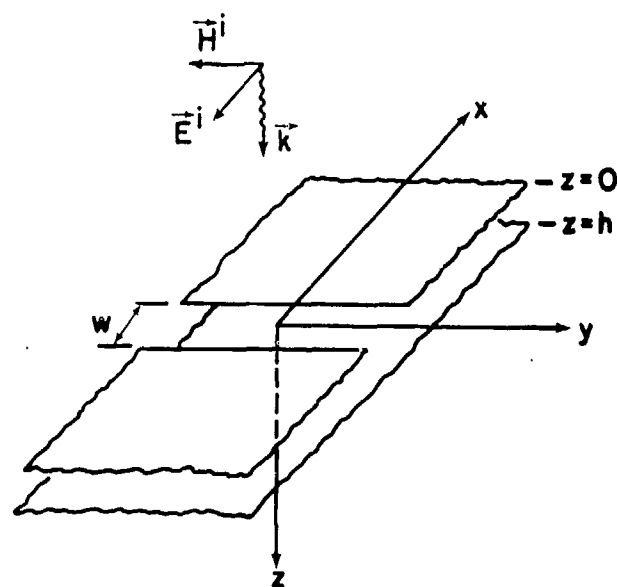


Fig. 10. Slotted parallel-plate waveguide.

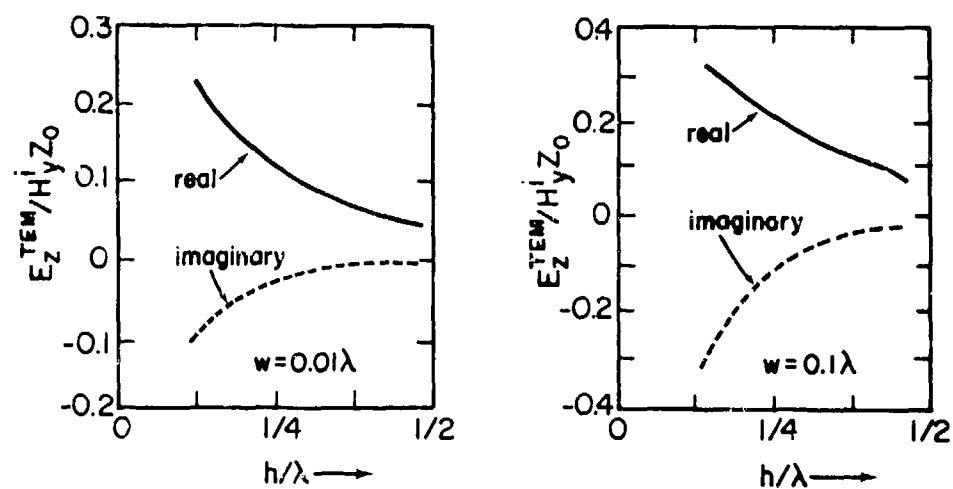


Fig. 11. TEM electric field in a slotted parallel-plate guide due normally incident wave with E-field transverse to the slot axis.

$$H_z(x, y, 0) = \frac{-Ky}{\sqrt{(w^2/4 - x^2)(\ell^2/4 - y^2)}} \quad (19)$$

where

$$K = \frac{2h H_{sc}}{p \sum_{n=1}^{\infty} \frac{1}{n^2} J_1(n\pi\ell/p) [1 - \cos(n\pi\ell/p)] \frac{1 - \exp(-n\pi w/p) I_0(n\pi w/p)}{n\pi w/p}} \quad (20)$$

which simplifies to

$$K \approx \frac{h H_{sc}}{2J_1(\pi)} \approx 1.3 h H_{sc} \quad (21)$$

for $p \gg w$ and $p \approx \ell$. Here, J_1 and I_0 are Bessel functions.

From the aperture field (19) one finds that the maximum penetrant field strength inside the parallel-plate region is given by

$$\max |H(x)| \approx H_{sc} \exp(-2\pi|x|/p) \quad (22)$$

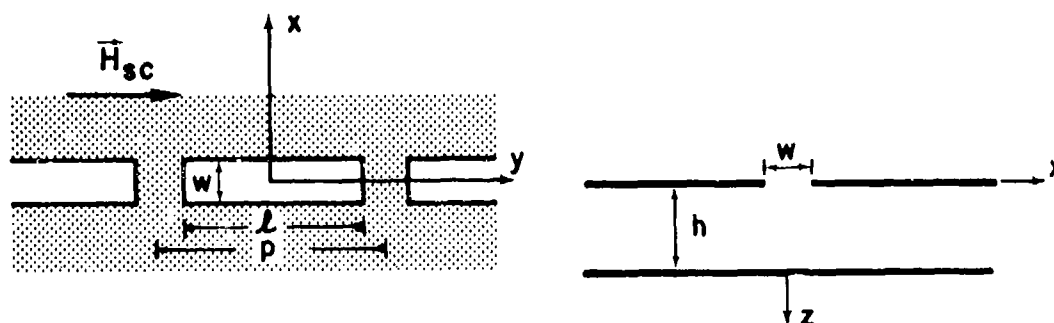


Fig. 12. Parallel plates with a periodic array of rectangular apertures in the front plate.

for $|x| > w$ (Fig. 12), and the maximum penetrant magnetic flux density ϕ' per unit length is given by

$$\max |\phi'(x)| \approx \frac{\pi^2}{4} h H_{sc} \exp(-2\pi|x|/p) \quad (23)$$

2.3.2.1.2 Infinite Circular Cylindrical Cavities

a. Magnetic-Field Penetration via an Aperture

The degradation in magnetic-field shielding due to the presence of an aperture in a long hollow conducting tube (Fig. 13) is studied in

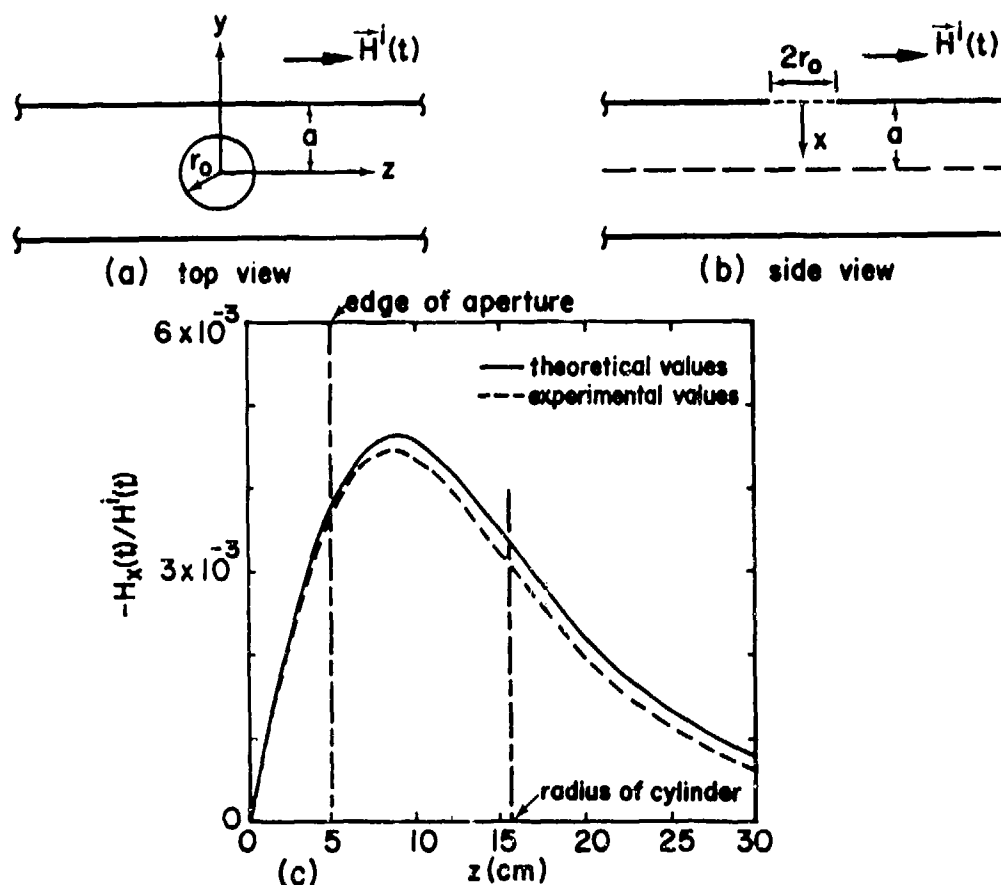


Fig. 13. (a) and (b) Small aperture in a long cylindrical shell immersed in uniform axial magnetic field $\vec{H}^1(t)$, and (c) peak-to-peak ratio of $-H_x(a,0,z,t)$ to $\vec{H}^1(t)$ along the cylinder's axis for $a = 16.5$ cm, $r_0 = 5$ cm, and $H^1(t) \propto t \exp(-\alpha t)$ with $\alpha = 10^6$.

[15,16] which contain a comparison of experimental data with theoretical data, the latter being obtained from the solution for an infinite plane with a circular aperture. The excellent agreement can be attributed to the fact that the dimensions of the aperture are small compared to the tube's radius and the distance between the aperture and the field point, and that the tube's radius is only a small fraction of the important spectral wavelength of the incident field.

b. Long Slot in a Long Circular Cylinder

The geometry depicted in the inset of Figs. 14a,c is the cross section of an infinitely long circular cylinder with an angular opening of $2\phi_0$. The electric field vector of the incident plane wave is parallel to the cylinder's axis and the incident wave has a zero phase at the cylinder's center. Figs. 14a,b show the angular variations of the aperture field for half-angles $\phi_0 = 10^\circ$ and 30° and for various values of ka . The field at the aperture center is plotted in Fig. 14c as a function of ka for two opening angles, $\phi_0 = 10^\circ$ and $\phi_0 = 30^\circ$. Note the dramatic effects of the interior resonance near $ka = 2.4$ [17].

Figs. 15a,b show the electric field variation along the cylinder's radius from the aperture's center to the cylinder's center for various frequencies [17]. The dramatic increase in interior fields can be seen for the wider aperture and for frequencies near the interior resonance. Fig. 15c is a plot of the cavity field magnitude at the center of the cavity as a function of frequency. Again, the effect of resonance is seen to be quite dramatic.

A plot of the first interior complex resonance frequency as a function of the aperture half-angle ϕ_0 can be found in Fig. 16. Although any opening of the cavity will shift the resonance frequency, the effect is quite small for $\phi_0 \leq 10^\circ$ but increases rapidly with increasing ϕ_0 .

In the case where the wavelength of the incident wave is much greater than the diameter of the cylinder, one may use an electrostatic boundary-value problem to find the low-frequency penetrant field. For the field polarization shown in Fig. 17, the penetrant electric and magnetic fields at the center of the cavity take the simple form

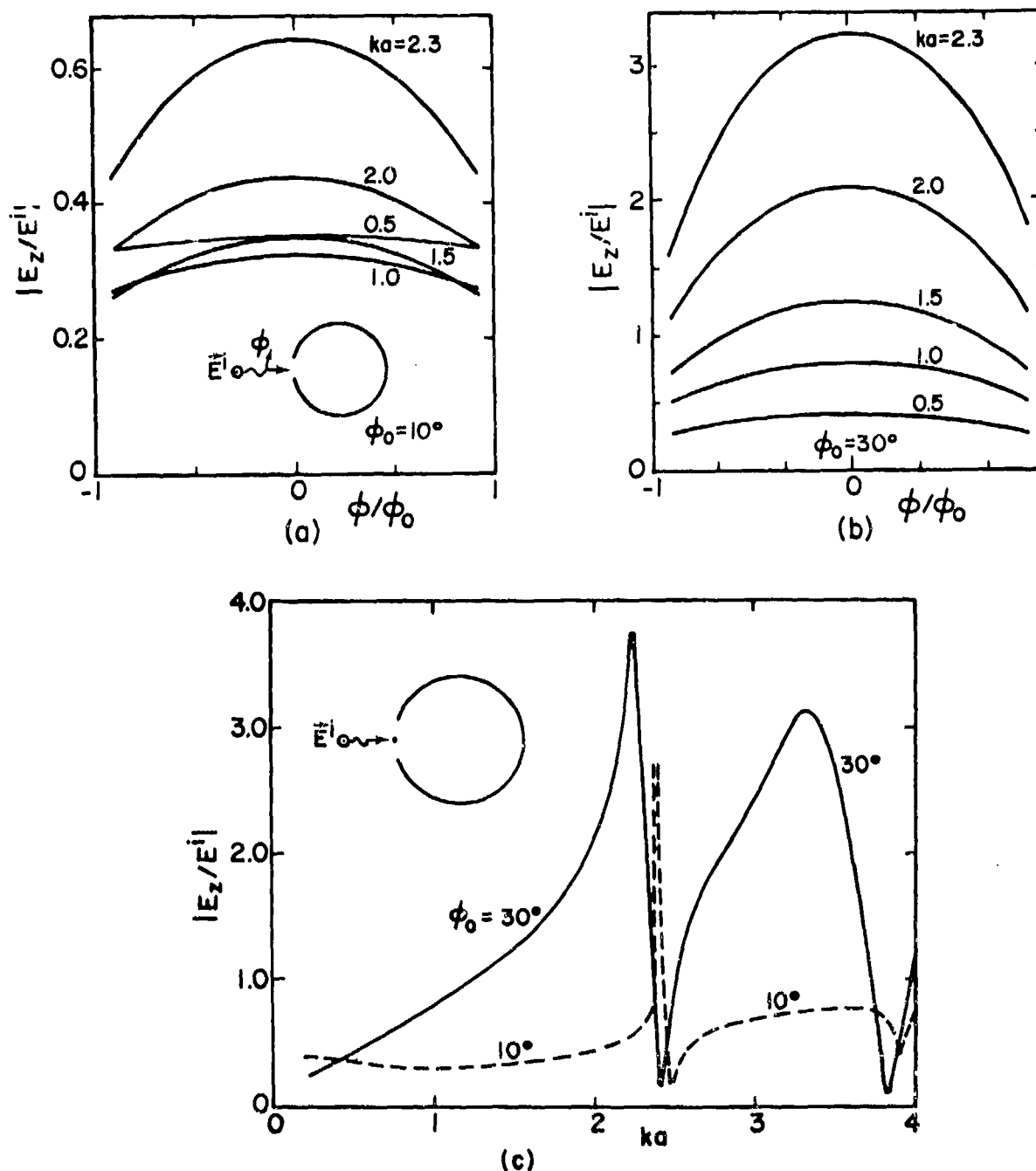


Fig. 14. (a) Aperture field magnitude for $\phi_0 = 10^\circ$ and various values of ka , where a is the radius of the cylinder, (b) aperture field for $\phi_0 = 30^\circ$ and various values of ka , and (c) field amplitude at the center of the aperture for half-angle $\phi_0 = 10^\circ$ and 30° . The axis of the cylindrical shell is parallel to the z -axis.

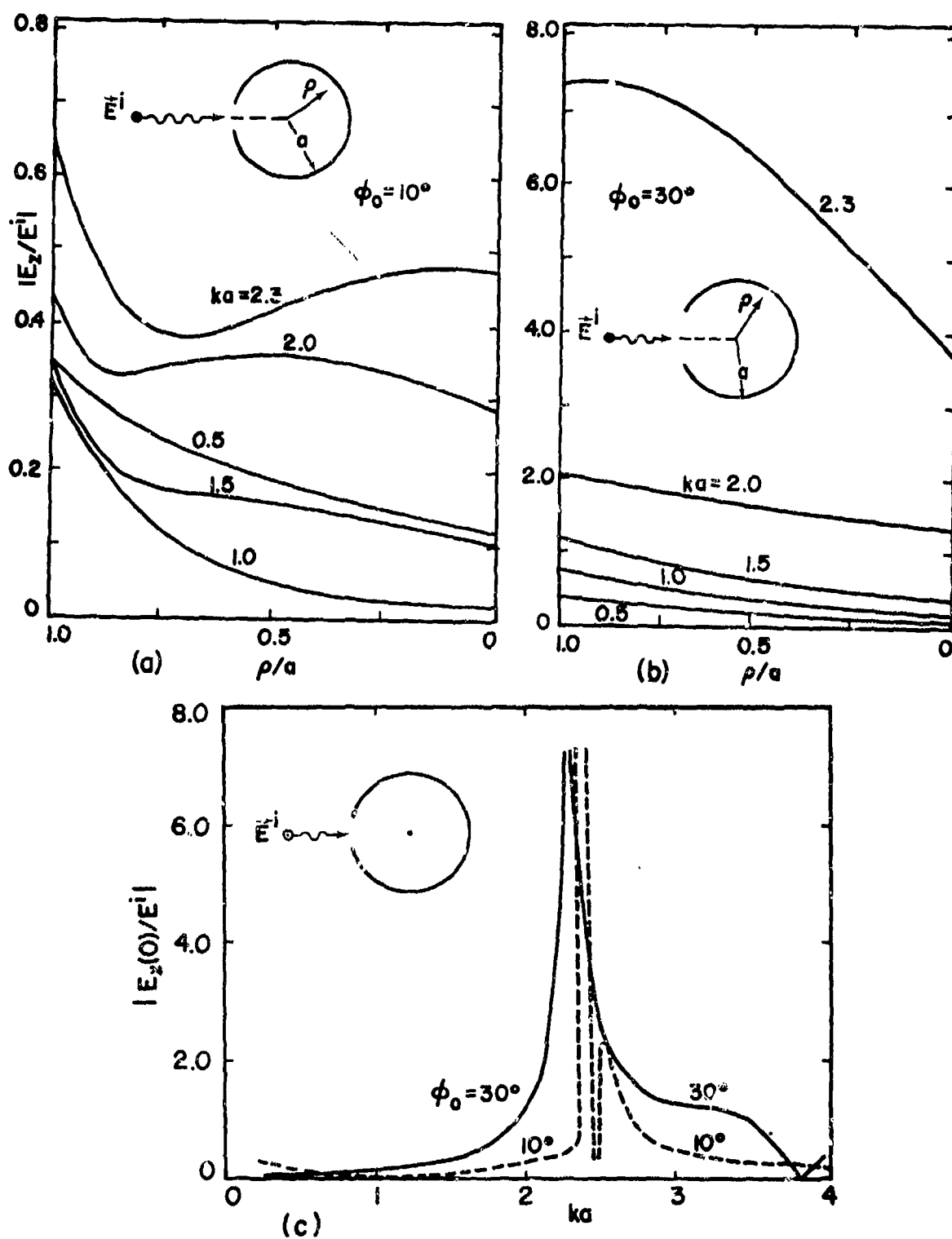


Fig. 15. Variation of interior field along $\phi = 0^\circ$ with ka as parameter for (a) $\phi_0 = 10^\circ$, and (b) $\phi_0 = 30^\circ$, and (c) field at the center of the cavity versus ka for $\phi_0 = 10^\circ$ and 30° .

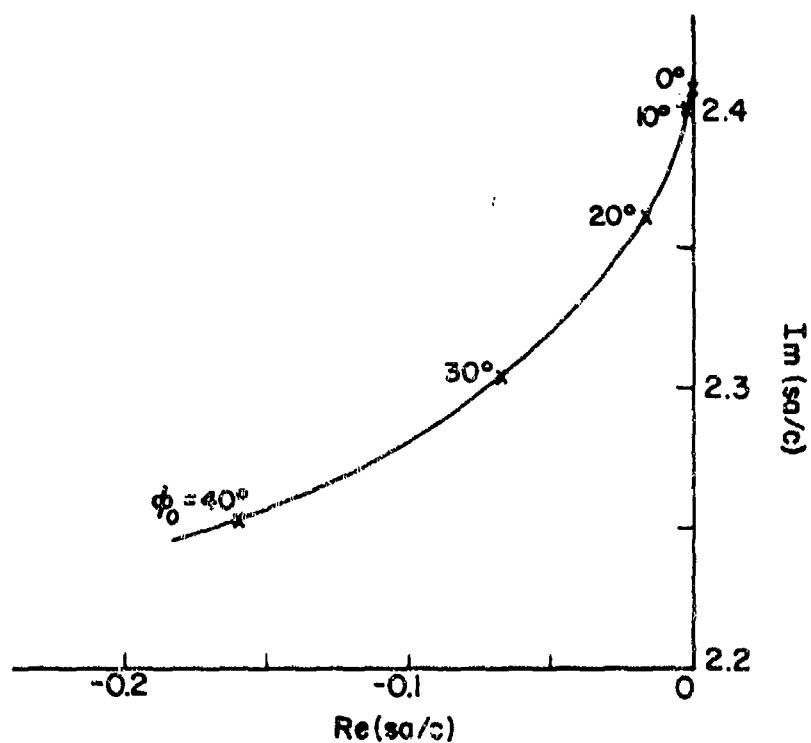


Fig. 16. First interior complex resonance frequency for $0 \leq \phi_0 \leq 40^\circ$, where a is the radius of the cylinder, c is the vacuum speed of light, and $2\phi_0$ is the angle of the opening.

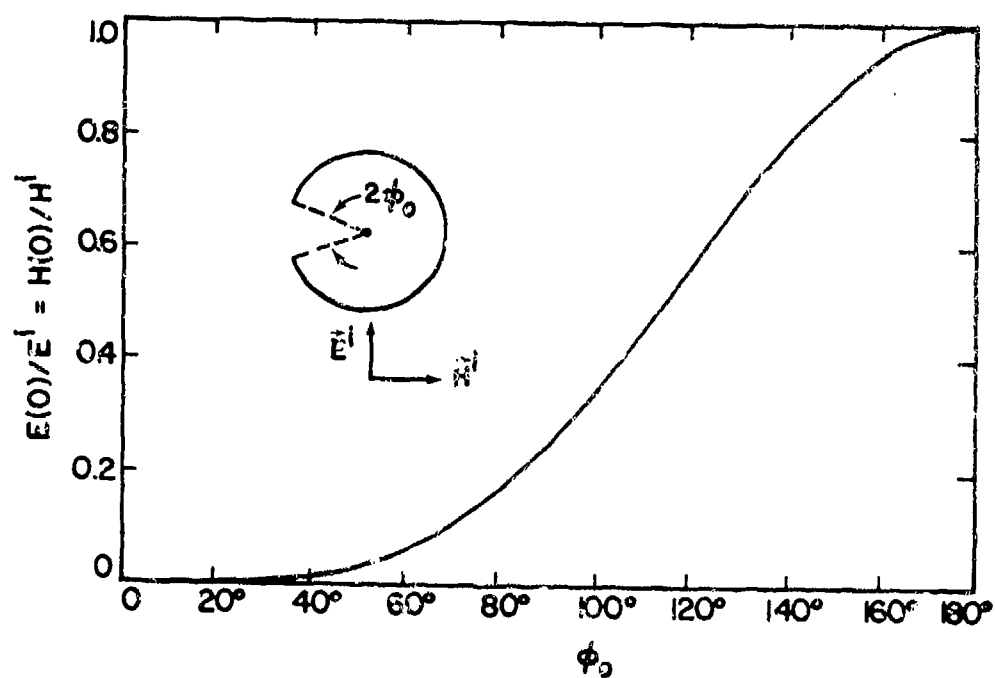


Fig. 17. Static penetrant fields at the center of the cylinder versus aperture opening.

$$\frac{E(0)}{E^i} = \frac{H(0)}{H^i} = \sin^4(\phi_0/2) \quad (24)$$

which is plotted in Fig. 17.

In the case where the cylindrical shell has N slots periodically distributed around its periphery (Fig. 18), the low-frequency penetrant field at the center of the cavity is given by [18]

$$\frac{E_z(0)}{E^i} = \frac{F}{N \ln(1/ka)} \quad (25)$$

where F is a function only of $N\phi_0/\pi$, ϕ_0 being the half angular opening of one slot. In Fig. 18, F is plotted versus $N\phi_0/\pi$.

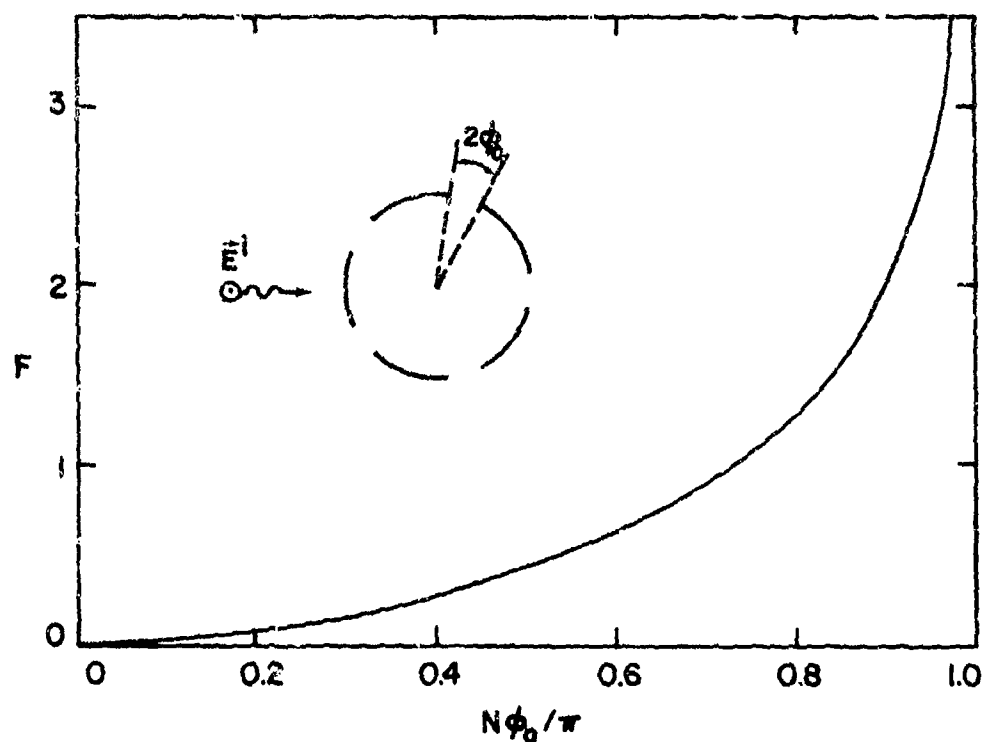


Fig. 18. The function F versus $N\phi_0/\pi$, N being the number of apertures or strips.

2.3.2.1.3 Simply-Connected Cavities

a. Circular Aperture in the Wall of a Spherical Cavity

The geometry is shown in the inset of Fig. 19 where the circular aperture is centered about the polar axis and the angle $2\theta_0$ specifies the angular opening of the aperture. A time-harmonic plane wave is traveling along the negative z-axis and polarized with its electric vector along the x-axis.

In Figs. 19 - 22 the variations of the total electric and magnetic fields are shown along the sphere's diameter from the center of the aperture to the back of the cavity [19]. In addition to the solution obtained by solving the exact equations numerically, three different approximate solutions are given. In the approximate solution A, the aperture electric field distribution is assumed to be that of the incident field but with an adjustable amplitude. The interior fields are then represented in terms of cavity modes whose coefficients are computed from mode matching. The adjustable amplitude is determined from the continuity of the magnetic field at a chosen point on the aperture. In the approximate solution B, the Kirchhoff approximation is used and the interior fields are computed from Huygens' principle. In the approximate solution C, the aperture is represented by equivalent dipole moments which are computed as if the aperture were in an infinite planar sheet. The approximate solutions B and C, of course, do not take into account the presence of the cavity and hence, as Figs. 19 - 22 show, they exhibit no resonance effects.

The energy density, $|\vec{E}|^2 + |Z_0 \vec{H}|^2$, at the center of the cavity as a function of ka is shown in Fig. 23 for two aperture openings, $\theta_0 = 10^\circ$ and $\theta_0 = 30^\circ$. The resonances at $ka \approx 2.75$ and 4.49 are clearly seen and are more pronounced for the smaller aperture. At non-resonant frequencies, the density for $\theta_0 = 30^\circ$ exceeds that for $\theta_0 = 10^\circ$ by as much as 10^6 .

At low frequencies where ka is much less than unity, the penetrant field at the center of the cavity takes an extremely simple form, namely

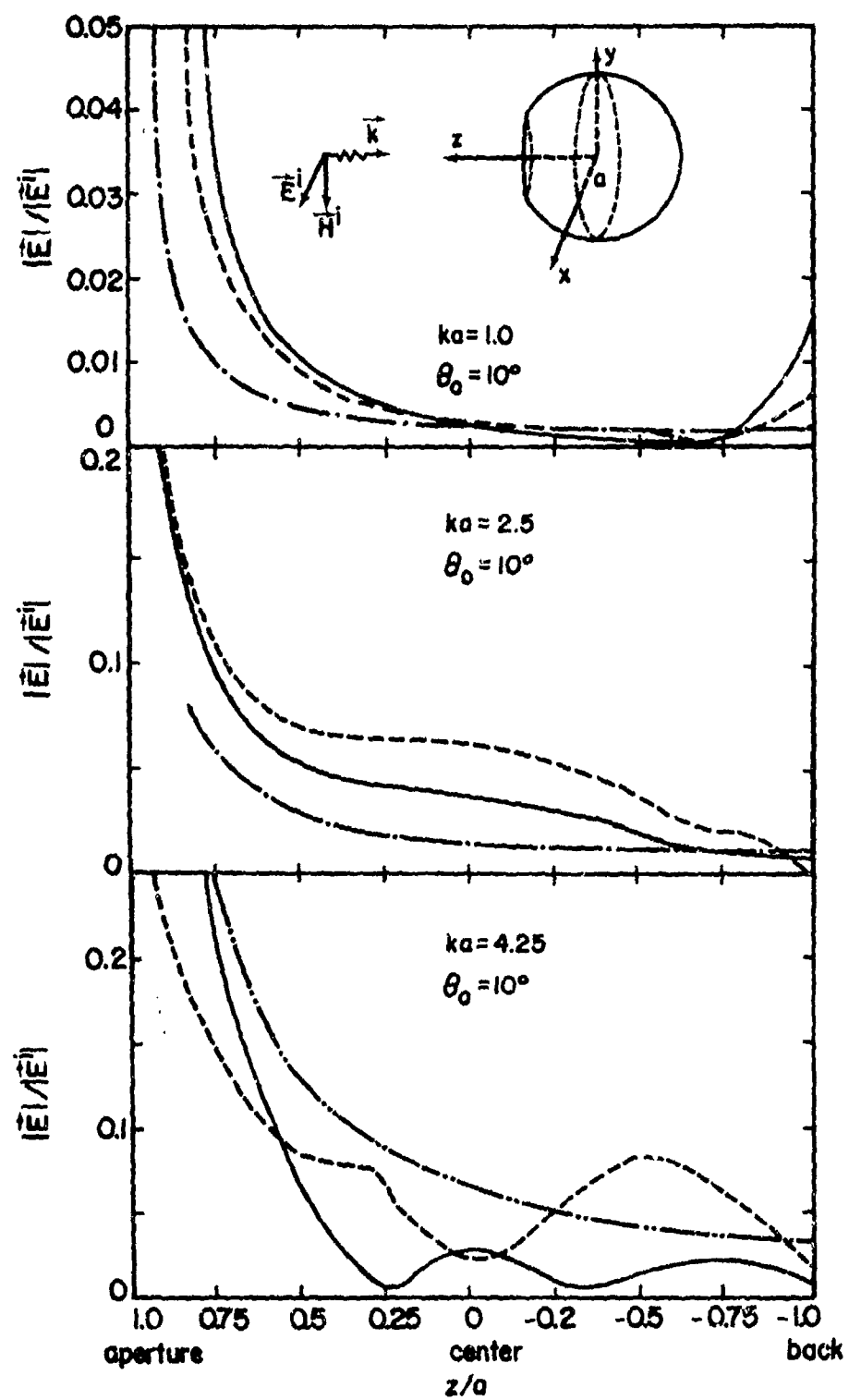


Fig. 19. Normalized total electric field along the z -axis for half opening angle $\theta_0 = 10^\circ$; exact (—), approximation A (---), approximation B (— · —), approximation C (— · —).

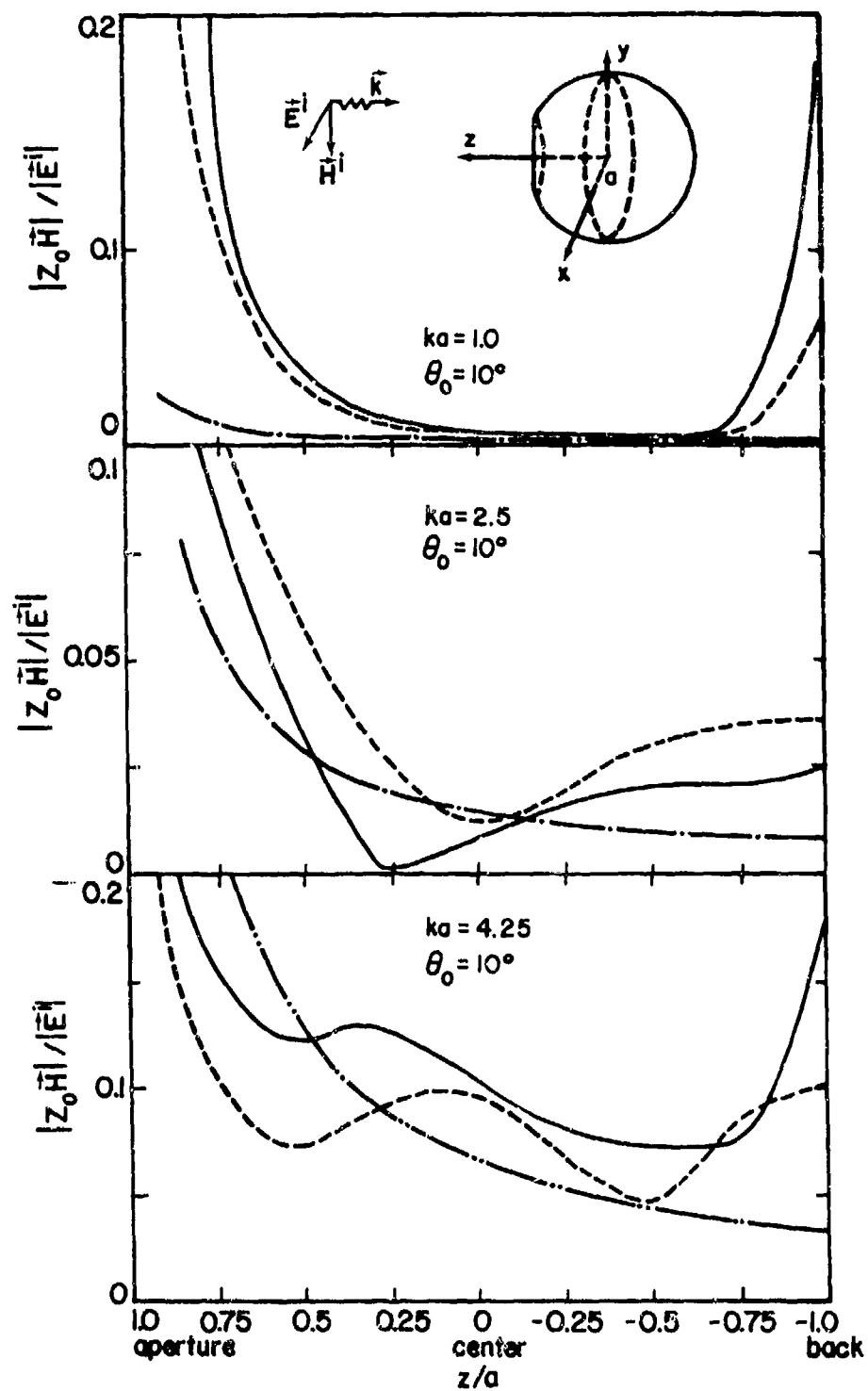


Fig. 20. Normalized total magnetic field along the z -axis for half opening angle $\theta_0 = 10^\circ$; exact (—), approximation A (---), approximation B (-·-·-), approximation C (- - -).

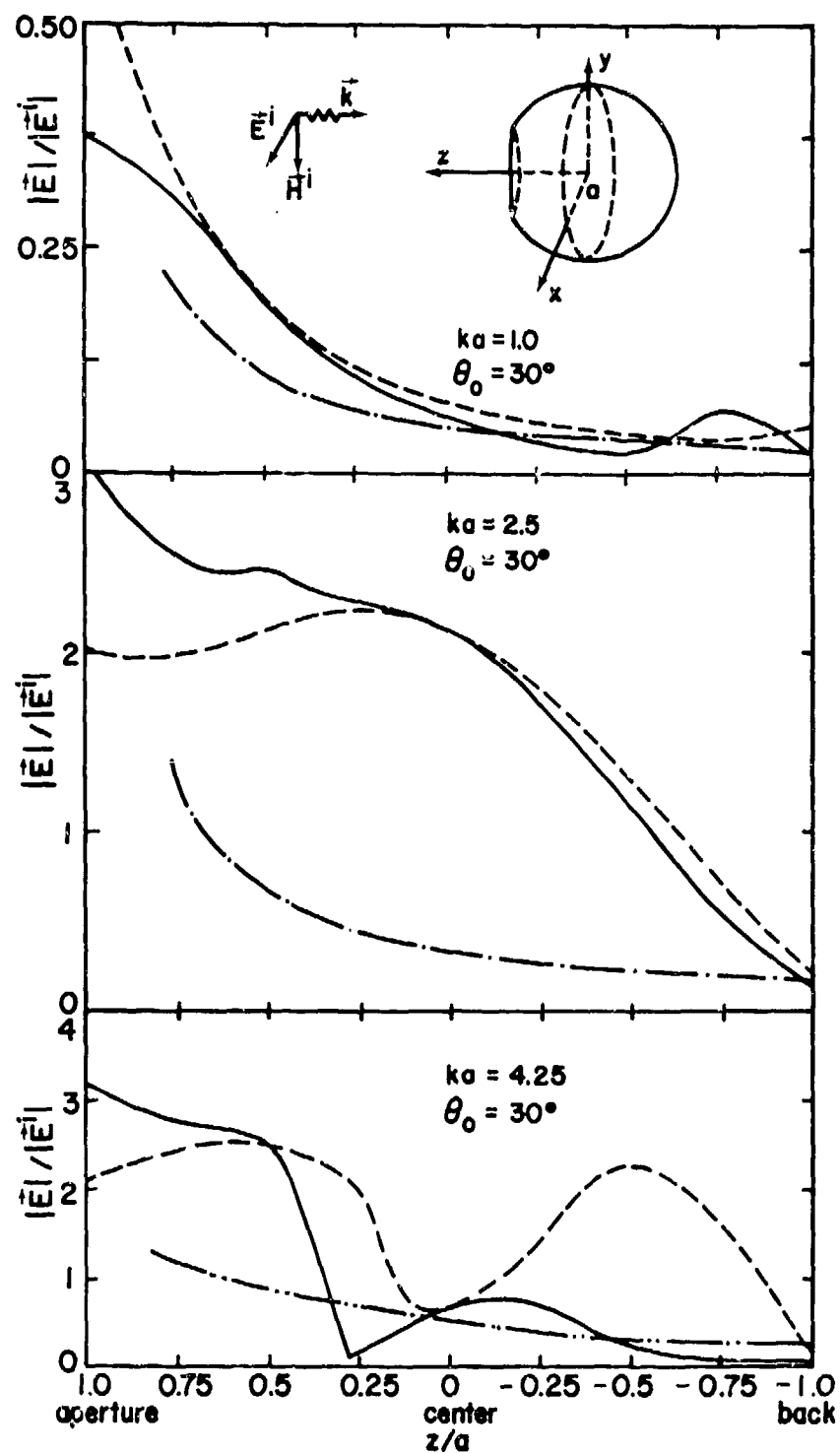


Fig. 21. Normalized total electric field along the z -axis for half opening angle $\theta_0 = 30^\circ$; exact (---), approximation A (---), approximation B (---), approximation C (---).

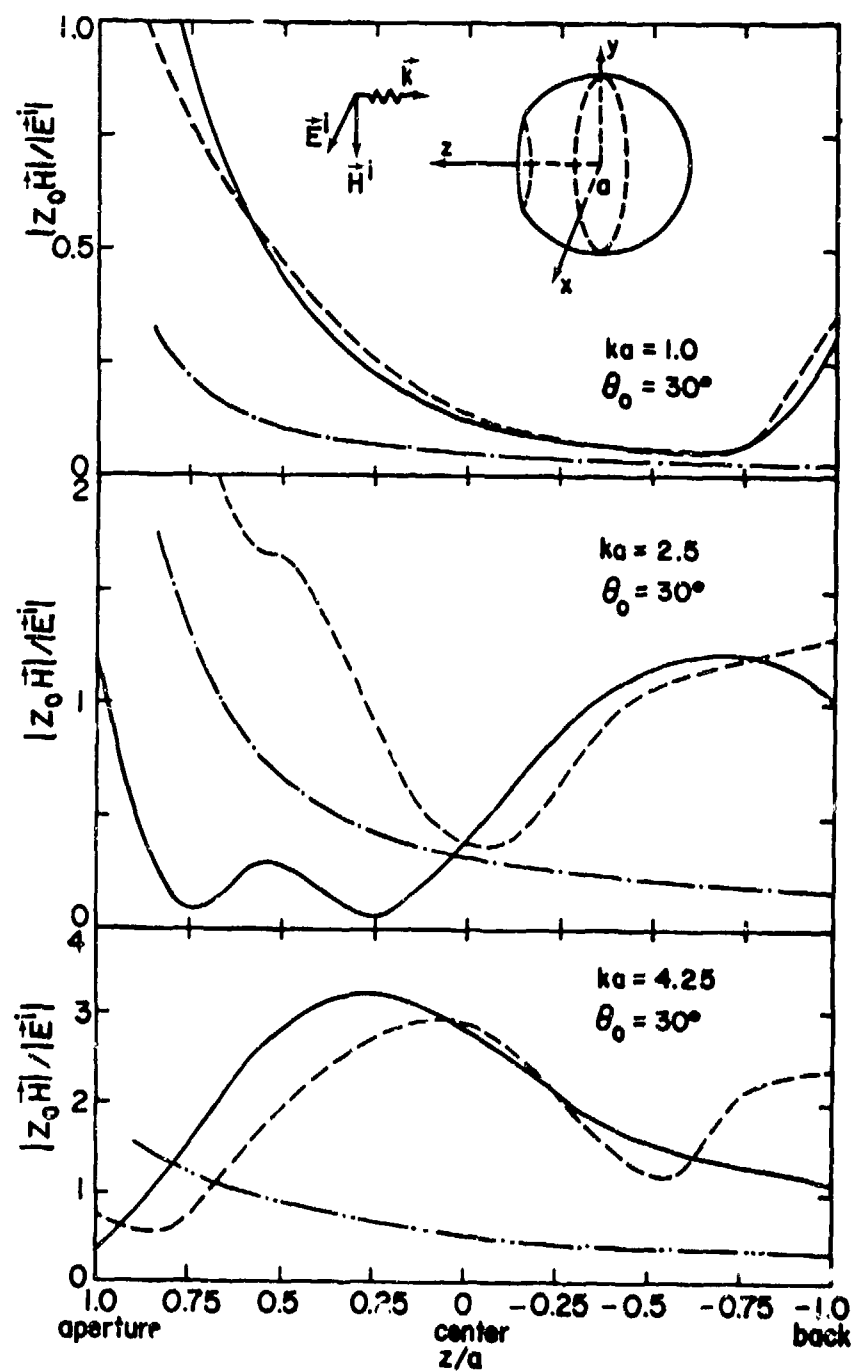


Fig. 22. Normalized total magnetic field along the z -axis for half opening angle $\theta_0 = 30^\circ$; exact (—), approximation A (---), approximation B (-·-·-), approximation C (- - -).

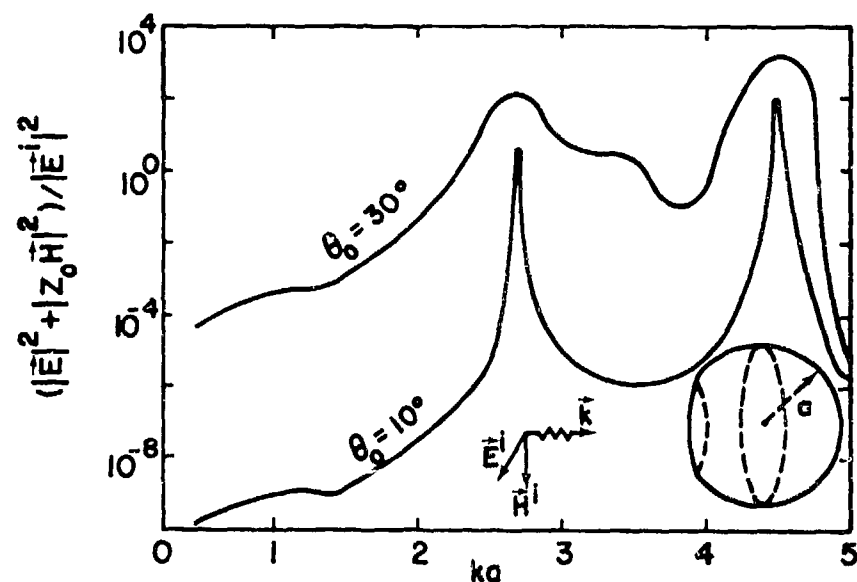


Fig. 23. Normalized energy density $(|\vec{E}|^2 + |z_0 \vec{H}|^2) / |\vec{E}^1|^2$ as a function of ka .

$$\frac{E_z(0)}{E^1} = \frac{1}{\pi} \left(\theta_0 - \frac{1}{3} \sin 3\theta_0 \right) \quad (26)$$

for \vec{E}^1 parallel to z -axis (Fig. 24a), and

$$\frac{E_y(0)}{E^1} = \frac{H_z(0)}{H^1} = \frac{1}{\pi} \left(\theta_0 - \frac{1}{2} \sin \theta_0 - \frac{1}{2} \sin 2\theta_0 + \frac{1}{6} \sin 3\theta_0 \right) \quad (27)$$

for \vec{E}^1 and \vec{H}^1 respectively transverse and parallel to the z -axis (Fig. 24b), where θ_0 is the half angle of the aperture opening. Eqs.(26) and (27) are plotted in Figs. 24a,b as functions of θ_0 .

b. Small Apertures in the Wall of Cylindrical Cavity

Two different aperture locations in the wall of a cylindrical cavity are shown in Figs. 25a,b. With the technique discussed in [10] simple formulas can be obtained for the penetrant quasi-static magnetic field at the center of the cavity.

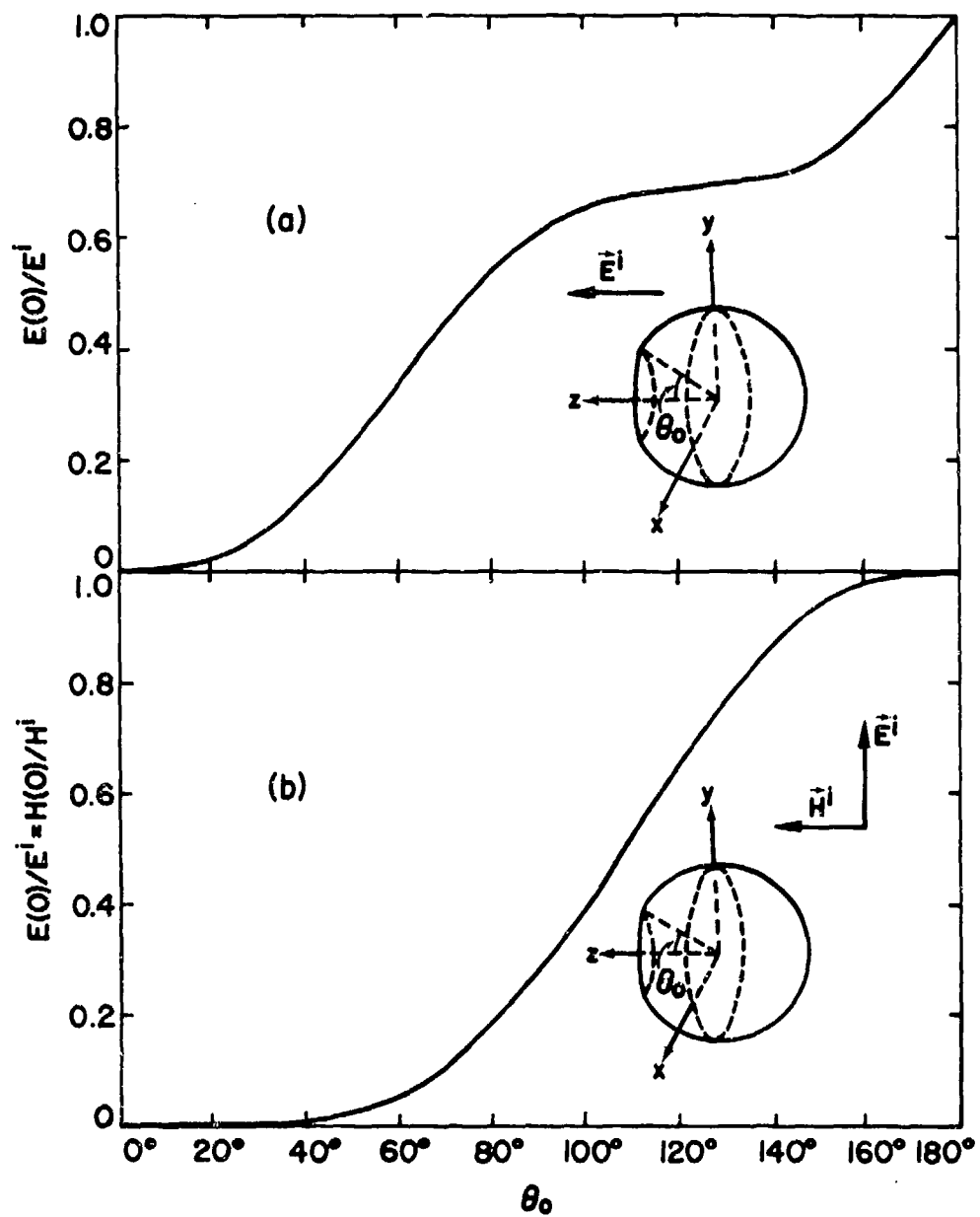


Fig. 24. Normalized static penetrant field at the center of a spherical cavity with a circular aperture for (a) \vec{E}^i parallel to the polar axis, and (b) \vec{E}^i transverse and \vec{H}^i parallel to the polar axis.

- (a) For $l \gg a$ (Fig. 25a) the low-frequency penetrant magnetic field at the center of the cavity for an aperture at $(\rho_0, 0, 0)$ is given by

$$\vec{H} = \frac{1.33}{2a\rho_0} e^{-\zeta_{11}l/(2a)} (A\vec{I}_x + B\vec{I}_y) + \vec{I}_z \frac{7.52}{a^3} e^{-\zeta_{02}l/(2a)} J_1(\zeta_{02}\rho_0/a) \vec{I}_x \cdot \vec{\alpha}_m \cdot \vec{H}_{sc} \quad (23)$$

where

$$A = \frac{\zeta_{11}\rho_0}{a} J_1'(\zeta_{11}\rho_0/a) \vec{I}_x \cdot \vec{\alpha}_m \cdot \vec{H}_{sc}$$

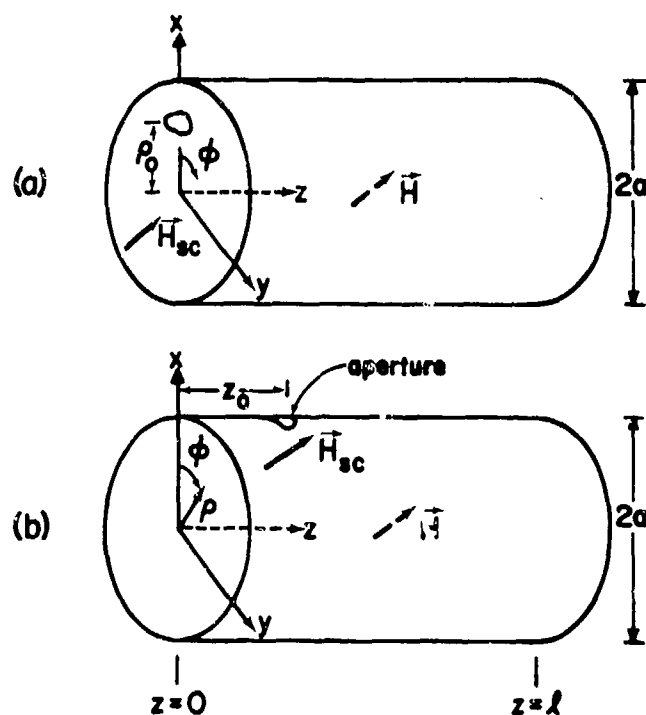


Fig. 25. A cylindrical cavity with a small aperture in the wall: (a) aperture at $(\rho_0, 0, 0)$; (b) aperture at $(a, 0, z_0)$ where a is the radius of the cylinder.

$$B = J_1(\zeta_{11}\rho_0/a)\vec{l}_y \cdot \vec{\alpha}_m^{\leftrightarrow} \cdot \vec{H}_{sc}$$

$$\zeta_{11} \approx 1.84, \quad \zeta_{02} \approx 3.83$$

- (b) For $|z_0 - \ell/2| \gg a$ (Fig. 25b) the low-frequency penetrant magnetic field at the center of the cavity for an aperture at $(a, 0, z_0)$ is given by

$$\begin{aligned} \vec{H} \approx & \frac{0.776}{a^3} e^{-\zeta_{11}|z_0 - \ell/2|/a} (C\vec{l}_x + D\vec{l}_y) \\ & + \vec{l}_z \frac{3.03}{a^3} e^{-\zeta_{02}|z_0 - \ell/2|/a} \vec{l}_z \cdot \vec{\alpha}_m^{\leftrightarrow} \cdot \vec{H}_{sc} \end{aligned} \quad (29)$$

where

$$C = \zeta_{11} \vec{l}_z \cdot \vec{\alpha}_m^{\leftrightarrow} \cdot \vec{H}_{sc}, \quad D = \vec{l}_y \cdot \vec{\alpha}_m^{\leftrightarrow} \cdot \vec{H}_{sc}$$

- (c) For $a \gg \ell$ (Fig. 25b) the low-frequency penetrant magnetic field at the center of the cavity for an aperture at $(a, 0, z_0)$ is given by

$$\begin{aligned} \vec{H} \approx & \frac{1}{\pi \ell a^2} \vec{l}_y \cdot \vec{\alpha}_m^{\leftrightarrow} \cdot \vec{H}_{sc} \vec{l}_y \\ & + \vec{l}_z \frac{4.44}{a \ell^2} \sqrt{\frac{a}{\ell}} e^{-\pi a/\ell} \sin(\pi z_0/\ell) \vec{l}_z \cdot \vec{\alpha}_m^{\leftrightarrow} \cdot \vec{H}_{sc} \end{aligned} \quad (30)$$

In the above formulas, $\vec{\alpha}_m^{\leftrightarrow}$ is the magnetic polarizability of the aperture in an infinite plane (see Sec. 2.1.3.2.1), \vec{H}_{sc} is the field at the aperture with the aperture covered. The validity of the above formula lies in the assumption that the aperture is smaller than all other relevant dimensions of the problem, in addition to being electrically small.

c. Apertures Backed by a Rectangular Cavity

Figs. 26a, b show two different kinds of apertures in the wall of a rectangular cavity. For the problem depicted in Fig. 26a simple formulas for the quasi-static penetrant magnetic field at the center of the cavity are summarized below [10].

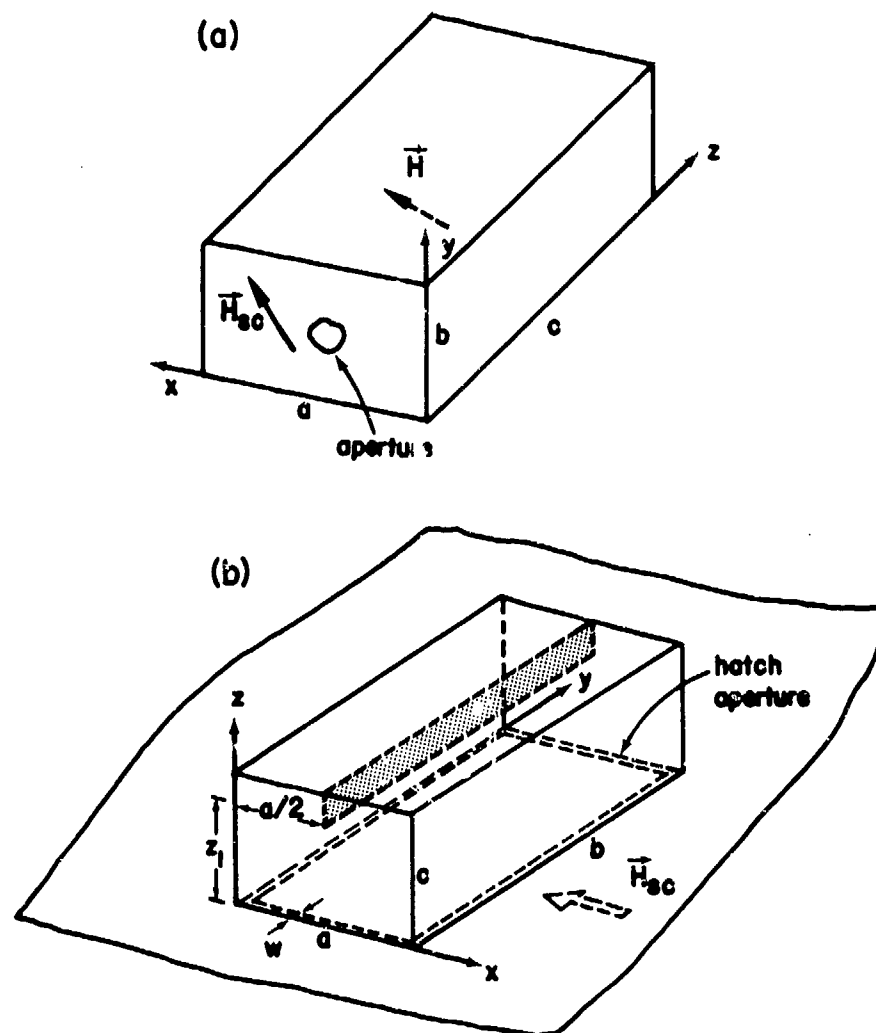


Fig. 26. (a) A rectangular cavity with a small aperture in one of its walls, (b) a hatch aperture with gasket in an infinite planar plate backed by a rectangular cavity.

(a) $c \gg a > b$ (deep cavity)

$$\begin{aligned} \vec{H}(a/2, b/2, c/2) \approx & \vec{1}_x \frac{2\pi}{ab} e^{-\pi c/(2a)} \sin(\pi x_0/a) m_x \\ & + \vec{1}_y \frac{2\pi}{ab^2} e^{-\pi c/(2b)} \sin(\pi y_0/b) m_y \end{aligned} \quad (31)$$

(b) $a > b \gg c$, $|x_0 - a/2| \geq b$ (shallow cavity)

$$\begin{aligned} \vec{H}(a/2, b/2, c/2) \approx & \vec{1}_y \frac{\pi}{b^2 c} e^{-\pi |x_0 - a/2|/b} [m_y \sin(\pi y_0/b) - m_x \cos(\pi y_0/b)] \\ & + \vec{1}_x \frac{4\pi}{b^2 c} e^{-2\pi |x_0 - a/2|/b} [m_x \cos(2\pi y_0/b) - m_y \sin(2\pi y_0/b)] \end{aligned} \quad (32)$$

where (x_0, y_0) is the center of the aperture and

$$m_x = \vec{1}_x \cdot \vec{\alpha}_m \cdot \vec{H}_{sc}, \quad m_y = \vec{1}_y \cdot \vec{\alpha}_m \cdot \vec{H}_{sc} \quad (33)$$

In each case the aperture is assumed to be small compared to all relevant length parameters of the problem.

For the problem of Fig. 26b, an expression for the magnetic flux linking a rectangular loop (see the shaded area of Fig. 26b) formed by a line located at $z = z_1$, $x = a/2$ and the cavity walls is given by [20]

$$\Phi = \frac{RL}{R + sL} f(a, b, c, z_1) H_{sc} \quad (34)$$

where

$$\begin{aligned} f(a, b, c, z_1) = & \frac{8a}{\pi(a+2b)} (b + 4a/\pi^2) \frac{\sinh[\pi(c - z_1)/a]}{\sinh(\pi c/a)}, \quad \text{if } c > a \\ f(a, b, c, z_1) = & \frac{4a}{a+2b} \left\{ \frac{c - z_1}{ac} \left[\frac{a(a+2b)}{4} - \frac{z_1(2c - z_1)}{3} \right] \right. \\ & \left. - \frac{1}{\pi} (b - 4c^2/\pi^2 a) \operatorname{sech}^2(\pi a/2c) \sin(\pi z_1/c) \right\}, \quad \text{if } a > c \end{aligned}$$

$$R = 2w/(\sigma\Delta a), \quad L = \pi\mu_0(a+2b)/(4\Omega),$$

$$\Omega = 2 \ln[4(a+b)/w],$$

σ = conductivity of gasket

Δ = thickness of gasket

2.3.2.1.4 Coaxial Cavities

a. Coaxial Cavity With a Small Aperture in the Outer Conductor

The geometry of the problem is shown in Fig. 27. An approximate expression for the magnetic field of the dominant mode excited through an electrically small aperture A by a quasi-static external short-circuit magnetic field \vec{H}_{sc} is given by [10]

$$\vec{H} \approx \vec{1}_\phi \frac{-1}{2\pi a l \ln(a/b)} \frac{1}{\rho} \vec{1}_{\phi_0} \cdot \vec{\alpha}_m \cdot \vec{H}_{sc} \quad (35)$$

where $\vec{\alpha}_m$ is the magnetic polarizability of the aperture in an infinite plane (see Sec. 2.1.3.2.1), $\vec{1}_\phi$ and $\vec{1}_{\phi_0}$ are respectively the unit vectors along the ϕ -direction at the field point and the aperture. The dimension of the aperture is small compared to all other relevant dimensions of the problem.

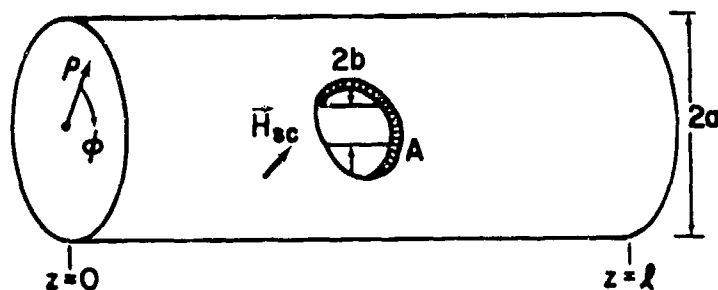


Fig. 27. A coaxial cavity with an aperture in the outer conductor.

b. Coaxial Cavity With a Hatch Aperture in the Outer Conductor

For the geometry shown in Fig. 28 the magnetic field of the dominant mode excited through a hatch aperture by a quasi-static short-circuit magnetic field $\vec{H}_{sc} = \vec{I}_{\phi} \vec{H}_{sc}$ is given by [21]

$$\vec{H} \approx \vec{I}_{\phi} \frac{1}{\rho} \frac{2a\phi_o^2}{2\pi} \frac{H_{sc}}{2\ln(a/b)} \frac{2+3\ell/(a\phi_o)}{3+3\ell/(a\phi_o)} \frac{RL}{\mu_o(R+sL)} \quad (36)$$

where

$$R = w/(\sigma\Delta a\phi_o)$$

$$L = \frac{\pi\mu_o a\phi_o}{4 \ln[4(\ell+2a\phi_o)/w]} [1 + \ell/(a\phi_o)]$$

and σ and Δ are respectively the conductivity and thickness of the gasket.

2.3.2.1.5 Depressions

a. Infinitely Long Rectangular Trough in a Ground Plane

The cross section of a two-dimensional rectangular trough in a ground plane is shown in Fig. 29a, where the dimensions h and w are assumed

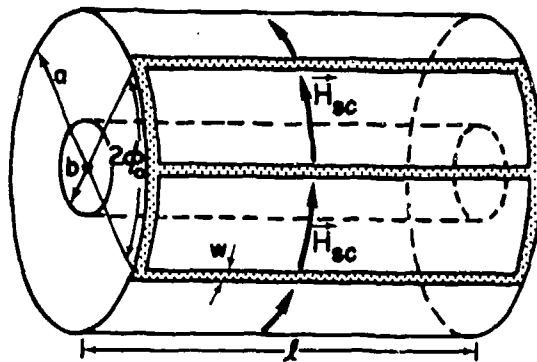


Fig. 28. A coaxial cavity with a hatch aperture loaded by a gasket in the outer conductor.

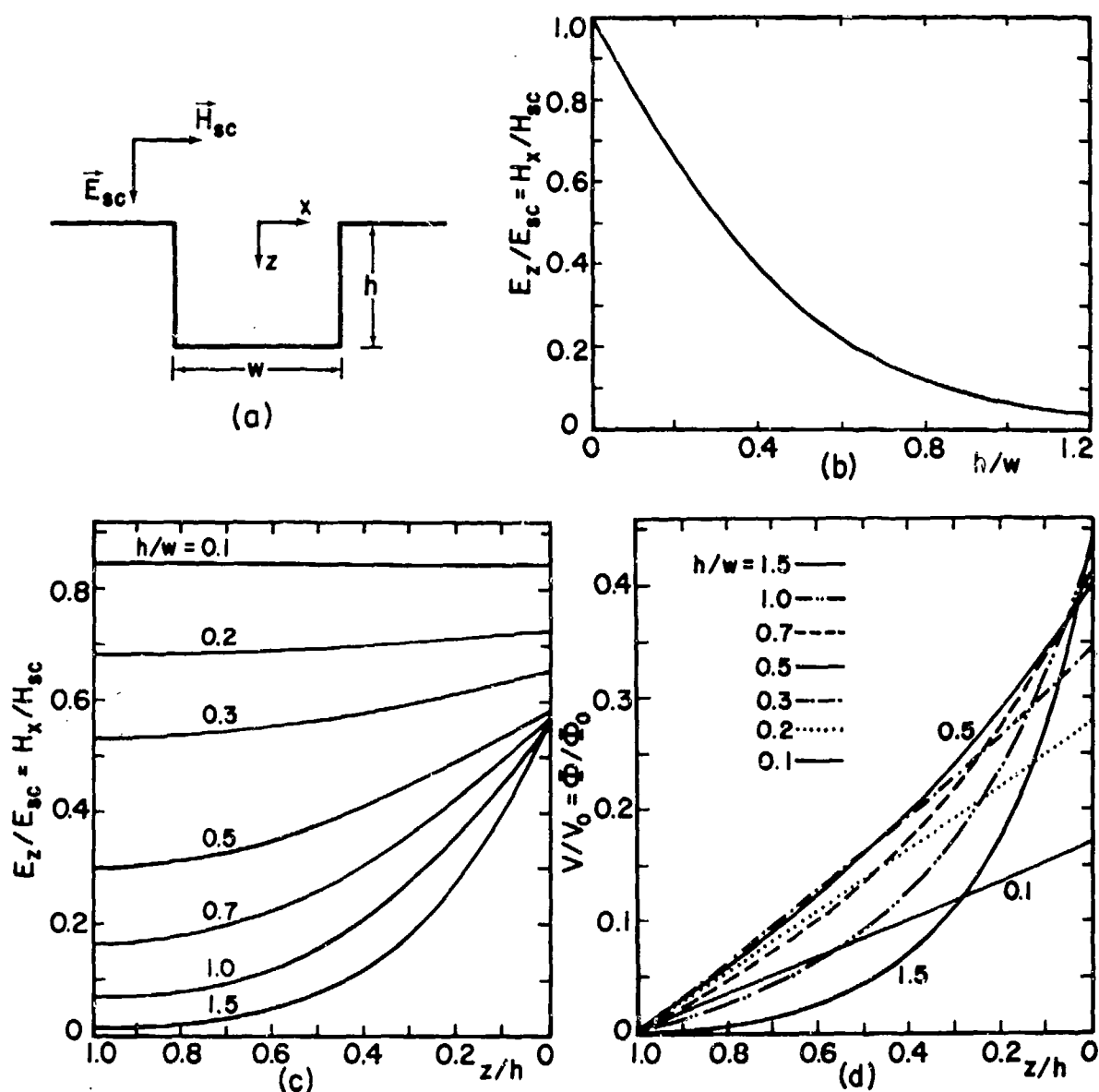


Fig. 29. (a) Cross section of an infinitely long rectangular trough in a ground plane, (b) the normalized magnetic and electric fields at the center of the trough's bottom, (c) the normalized magnetic and electric fields along the center line of the trough, and (d) the normalized magnetic flux and the normalized electrostatic potential along the center line of the trough, where $V_0 = E_{sc} w/2$ and $\Phi_0 = \mu_0 H_{sc} w/2$.

to be small compared to the wavelengths of the incident wave. Thus, the quasi-static approximation can be used, and the field inside the trough can be obtained by the method of conformal mapping [22,23]. Fig. 29b shows the field strength at the center of the trough's bottom. Fig. 29c gives the field variation along the center line of the trough. Fig. 29d shows the variation along the center line of the trough of the normalized magnetic flux between $z = z$ and $z = h$ and the normalized electrostatic potential relative to the bottom of the trough.

b. Infinitely Long Rectangular Trough Flanked by Two Dikes in a Ground Plane

The field penetration into a rectangular trough flanked by two dikes in a ground plane has been analyzed in [23] in connection with EMP penetration into an open nose wheel well of an aircraft. The geometry of the problem is shown in Fig. 30a. Under the quasi-static approximation, the two-dimensional boundary-value problem is solved by the method of conformal mapping. Fig. 30b shows the field strength along the center line of the trough. Fig. 30c gives the normalized magnetic flux and electrostatic potential along the center line of the trough.

For $h \geq w/2$, the field strength at the center of the trough's bottom is given by the simple formula

$$\frac{E_z}{E_{sc}} = \frac{H_x}{H_{sc}} \approx 0.4789 e^{-\pi h/w} \quad (37)$$

c. Magnetic-Field Penetration Into a Semi-Infinite Pipe

The penetration of a quasi-static magnetic field into a perfectly conducting, semi-infinite circular pipe under four different end conditions has been analyzed in [3] (see Figs. 31a-d). The magnetic field of the dominant mode along the axis of the pipe is found to be

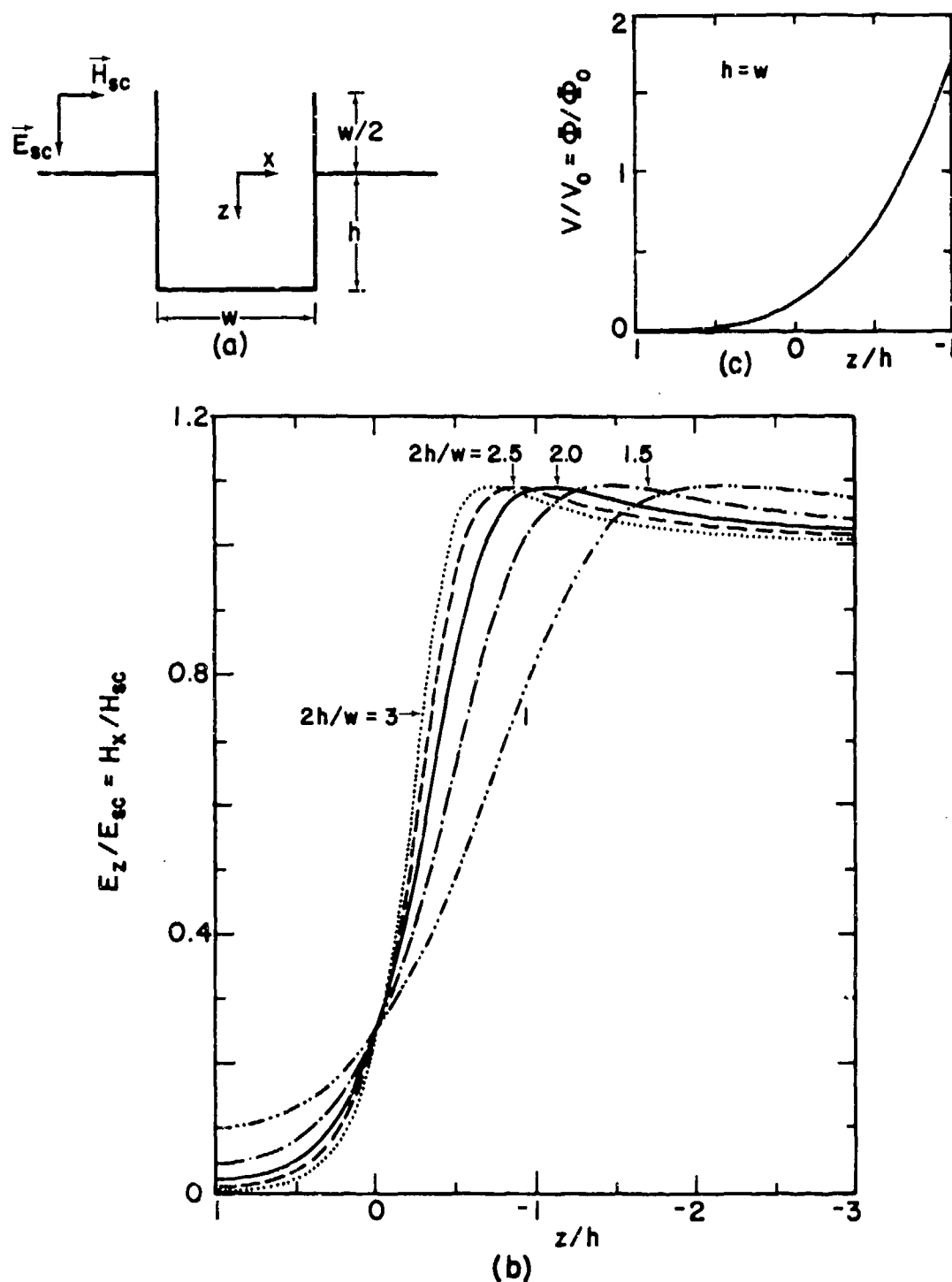


Fig. 30. (a) Cross section of an infinitely long rectangular trough flanked by two dikes in a ground plane, (b) normalized field components along the center line of the trough, (c) normalized magnetic flux and electric potential along the center line of the trough for $h = w$, where $V_0 = E_{sc} w/2$ and $\Phi_0 = \mu_0 H_{sc} w/2$.

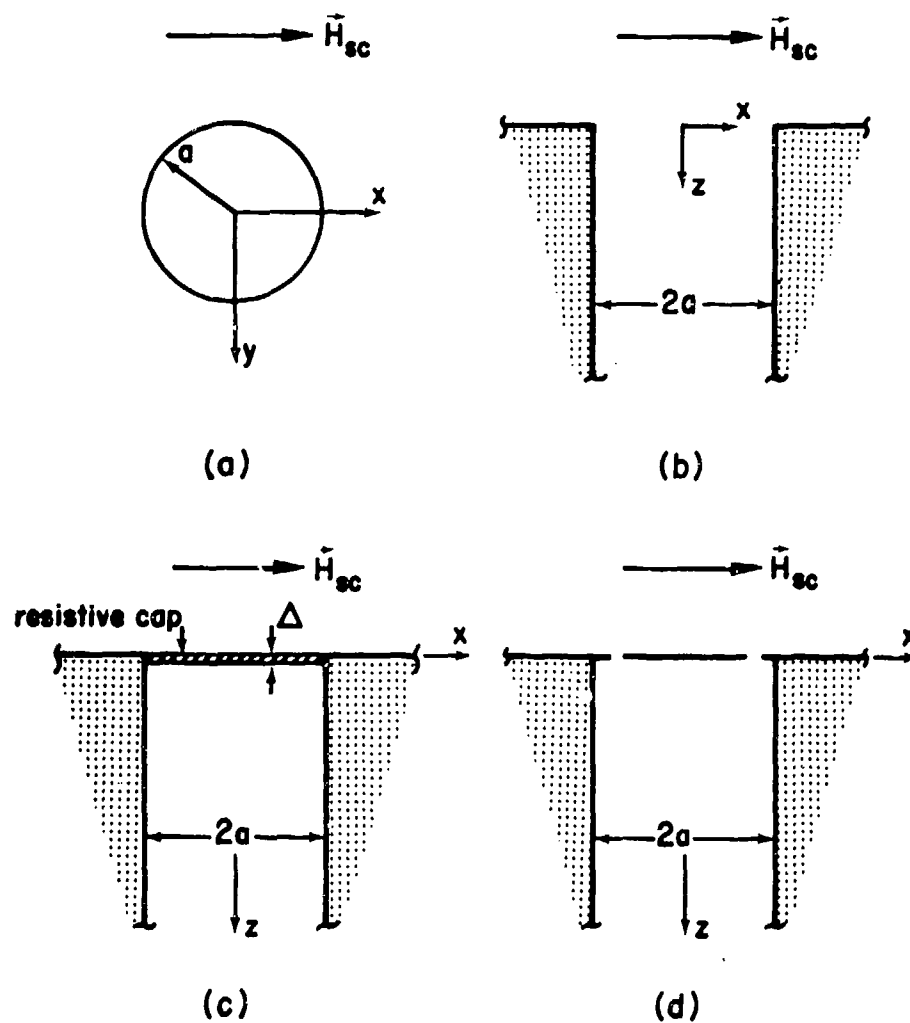


Fig. 31. A semi-infinite pipe immersed in an external magnetic field:
 (a) without flange, top view, (b) with flange, side view,
 (c) with flange and resistive cap, side view, and (d) with
 flange and annular slot, side view.

$$H_x = \frac{1}{2} C_1 H_{sc} \exp(-\zeta_1 z/a), \quad z > 0 \quad (38)$$

where $\zeta_1 = 1.84118$ and $C_1/2$ is given in table 1.

TABLE 1. THE COEFFICIENT $C_1/2$

Perfectly Conducting, Semi-Infinite Pipe	$C_1/2$
With a perfectly conducting flange	0.838
Without a flange	1.120
With a perfectly conducting flange and a resistive cap	$\frac{0.838}{1 + 0.349 s \mu_0 a \sigma \Delta}$
With a perfectly conducting flange and a cap having an annular slot of width $a/2000$ at a distance $a/10$ from the pipe's wall	0.30

From the table it is observed that (1) the effect of removing the flange is about 34%, (2) the effect of inserting a resistance cap is to yield a "shielding ratio" similar to that in other low-frequency shielding problems, and (3) a perfectly conducting cap with an annular slot, even though the slot is extremely narrow, seems to have little effectiveness in shielding against the external magnetic field.

d. Hemispherical Depression in an Infinite Conducting Plane

A hemispherical depression in an infinite conducting plane is shown in Fig. 32. The quasi-static electric field penetration into such a depression has been solved exactly by the method of inversion in [24], whereas the quasi-static magnetic field problem has been treated by an integral-equation formulation solved numerically to a high degree of accuracy [25]. It is found that in the illuminated side, the circular aperture backed by the hemispherical cavity has the following polarizabilities

$$\alpha_e \approx 0.55 a^3, \quad \alpha_m \approx 0.87 a^3 \quad (39)$$

which are smaller than those given by (5) of a circular aperture in an infinite plane without cavity backing. Fig. 32a shows the normalized magnetic flux Φ linking a loop. Fig. 32b gives the averaged electric field $\bar{E}_z(z)$ along the axis defined by

$$\bar{E}_z(z) = \frac{1}{a-z} \int_z^a E_z(0,0,z) dz \quad (40)$$

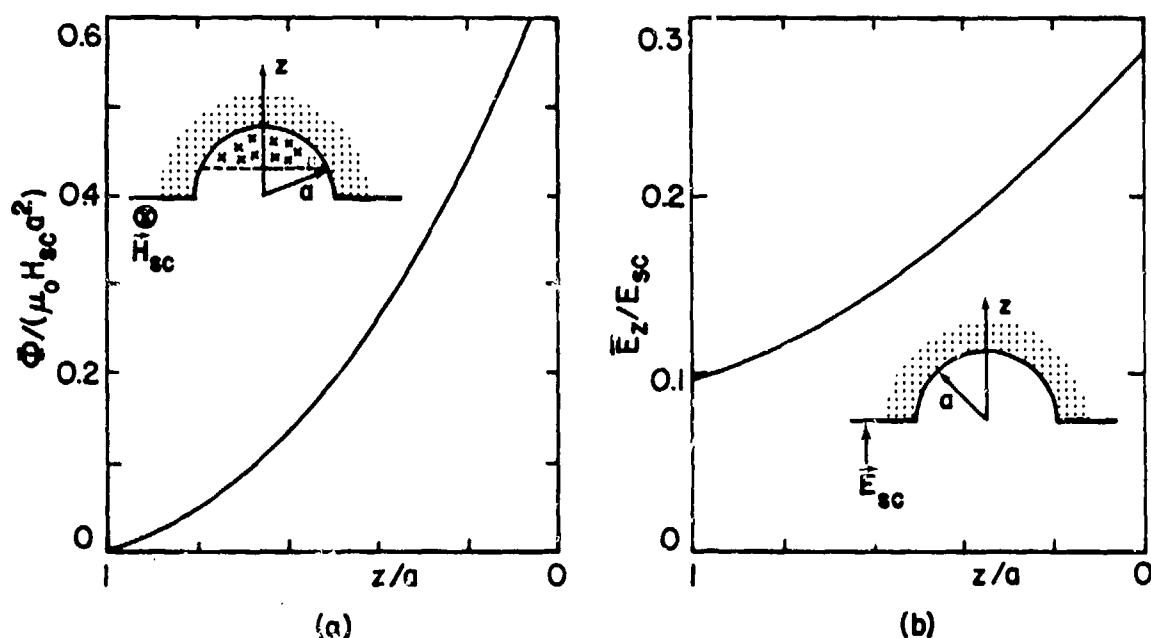


Fig. 32. (a) Normalized magnetic flux versus z/a for a loop making an angle $\phi = \pi/2$ with respect to \vec{H}_{sc} ; for other values of ϕ , Φ is diminished by a factor $\sin \phi$. (b) Averaged electric field along the symmetry axis in the cavity.

2.3.2.2 Diffusive Penetration Into Cavities

The diffusive penetration comes about because the conductivity of the walls, albeit high, is not infinite. At low frequencies for which the wall thickness is less than the skin depth, the diffusion mechanism is known to be an effective means for penetration by the magnetic field, while penetration by the electric field is negligibly small by comparison. At higher frequencies for which the wall thickness is larger than the skin depth, most of the incoming electromagnetic energy is shielded out by reflection and attenuation losses due to the cavity walls. Thus, diffusion penetration is of concern to the EMP system analyst mainly for the low-frequency magnetic field.

In this section simple working formulas are given, both in frequency and time domain, to calculate the cavity fields for certain simple-shaped enclosures. These simple formulas are then generalized so as to be applicable to general-shaped enclosures.

2.3.2.2.1 Physical Considerations of Shielding

Fig. 33 shows an electromagnetic pulse $H^{ex}(t)$ of width τ_0 impinging on a closed metallic shell of conductivity σ , permeability μ , and wall

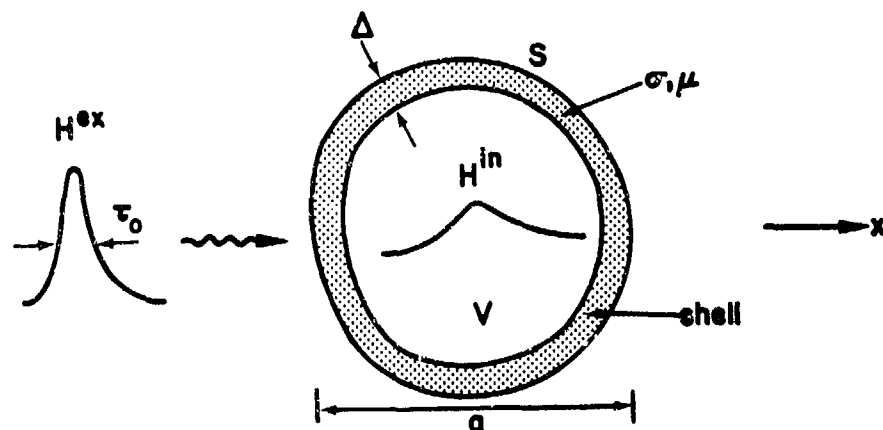


Fig. 33. An external electromagnetic pulse impinging on a closed cavity with finitely conducting walls. V = interior volume of enclosure; S = surface of enclosure.

thickness Δ . The qualitative features of the penetrant pulse $H^{in}(t)$ can be obtained by first identifying the important time parameters involved in the problem and then studying their relative magnitudes for enclosures used in practice [26]. These parameters are the pulse width τ_0 of the incident wave, the transit time $\tau_a (= a/c)$ for a signal traveling across the enclosure, the diffusion time $\tau_d (= \mu\sigma\Delta^2)$ of the enclosure's wall, and the fall time τ_f of the interior pulse $H^{in}(t)$. The fall time τ_f can be understood as the time constant of an LR circuit which describes the decay of the induced eddy-current loops in the shell. Clearly, these current loops have a resistance $R \propto 1/(\sigma\Delta)$ and an inductance $L \propto \mu_0 a$. Hence, $\tau_f = L/R \propto \mu_0 \sigma \Delta a$. In terms of the volume V and surface S of the enclosure one then expects $\tau_f \propto \mu_0 \sigma \Delta V/S$. For a typical high-altitude EMP and a typical enclosure of several meters in diameter and a few millimeters in wall thickness made of aluminum, $\tau_a \approx$ tens of nanoseconds, $\tau_0 \approx$ hundreds of nanoseconds, $\tau_d \approx$ tens of microseconds, while $\tau_f \approx$ tens of milliseconds. It is thus seen that these time parameters are well separated by orders of magnitude. The great separation in value between τ_a and τ_0 is not crucial in order to have a simple description of the diffusion and decay processes that are involved in the physics of shielding by an enclosure. Suppose the external pulse H^{ex} strikes the enclosure surface at $t=0$ (see Fig. 33). Then for $t < \tau_d$, the interior pulse H^{in} is insignificant, since τ_d is the time for the pulse to "ooze" through the wall. For t of the order of τ_d , H^{in} reaches its peak and by this time the external pulse has long passed the enclosure. For $t > \tau_d$, the enclosure is left alone to decay through energy dissipation in the walls according to the decay law of eddy currents [27], implying that the fall time τ_f of H^{in} is given by L/R and the peak value of H^{in} is proportional to R/L . Furthermore, H^{ex} is effectively an impulse compared to H^{in} because $\tau_0 \ll \tau_d$. Thus the total time integral of H^{ex} is expected to play an important role, and so one can introduce an effective impulse strength H_0 as

$$H_0 = \int_{-\infty}^{\infty} H^{ex}(t) dt \quad (41)$$

In terms of H_0 the peak value of H^{in} is expected to be proportional to $H_0 R/L$ with a dimensionless proportionality constant of order unity.

In the frequency domain, the important length parameters are the wall thickness Δ , the enclosure maximum linear dimension a , the wall skin depth δ ($= \sqrt{2/(\omega\sigma\mu)}$), and the characteristic wavelength λ_0 ($= c\tau_0$) of the incident pulse. Typically, $\Delta \approx$ a few millimeters, $a \approx$ several meters, $\lambda_0 \approx$ hundreds of meters, and $\delta \approx 5 \times 10^{-3} \sqrt{\lambda}$ millimeters for an aluminum shell with λ being the wavelength variable of H^{in} and measured in meters. For $\delta < \Delta$ the wall is said to be electrically thick and the attenuation and reflection losses in the wall account for a great deal of shielding. For $\delta > \Delta$ the wall is electrically thin and the shielding comes entirely from the eddy-current distribution in the wall, while the attenuation and reflection losses become irrelevant. This implies that for an electrically thin shell the geometrical shape of the enclosure is critical [4]. If one uses the above typical values, the dividing point $\delta = \Delta$ corresponds to $\lambda \approx$ tens of kilometers (or $f \approx$ tens of kHz); that is to say, for $\lambda >$ tens of km (or $f <$ tens of kHz) diffusive penetration will become important and if the planar-shield approximation to enclosure geometry is used, shielding effectiveness can be overestimated by as much as 5 orders of magnitude or 100 dB [28].

2.3.2.2.2 Simple-Shaped Enclosures

There are three canonical shapes of enclosure that have engaged the attention of many investigators in the past, namely, two parallel plates [5,29], an infinite circular cylindrical shell [5,30,31], and a spherical shell [5,31-33]. For these geometries the penetrant cavity field takes an extremely simple analytical form under the assumption that displacement currents are neglected throughout. This assumption has been shown to be sufficiently adequate for treating EMP shielding problems [34]. Other cavity shapes such as a prolate spheroidal shell [35] and a finite hollow cylinder [36] have also been studied but with no simple useful results.

The basic equations to be solved are

$$\nabla \times \vec{E}(\vec{r}, s) = -s\vec{B}(\vec{r}, s) \quad (42)$$

$$\nabla \times \vec{H}(\vec{r}, s) = \begin{cases} \sigma \vec{E}(\vec{r}, s), & \text{inside shell} \\ 0, & \text{outside shell} \end{cases} \quad (43)$$

with the usual boundary conditions that tangential \vec{E} and \vec{H} be continuous across the air-shell interfaces (see Fig. 33). The constitutive relation between \vec{H} and \vec{B} is

$$\vec{B} = \begin{cases} \mu \vec{H}, & \text{inside shell} \\ \mu_0 \vec{H}, & \text{outside shell} \end{cases} \quad (44)$$

a. Frequency-Domain Solution

Define the transfer function T_m as

$$T_m(s) = \frac{H^{in}(s)}{H^{ex}(s)} = \frac{\text{magnetic field inside cavity}}{\text{magnetic field in the absence of shield}} \quad (45)$$

In what follows, H^{ex} is taken to be uniform. We will use T_p for two parallel plates (Fig. 34a), $T_c^{(l)}$ for a cylindrical shell with a longitudinal H^{ex} (Fig. 34b), $T_c^{(t)}$ for a cylindrical shell with a transverse H^{ex} (Fig. 34c) and, finally, T_s for a spherical shell (Fig. 34d). Solving (42) and (43) for these geometries one obtains [28]

$$T_p(p) = \frac{1}{\cosh p + Kp \sinh p} \quad (46)$$

$$T_c^{(l)}(p) = \frac{1}{\cosh p + \frac{1}{2} Kp \sinh p} \quad (47)$$

$$T_c^{(t)}(p) = \frac{1}{\cosh p + \frac{1}{2} \left(Kp + \frac{1}{Kp} \right) \sinh p} \quad (48)$$

$$T_s(p) = \frac{1}{\cosh p + \frac{1}{3} \left(Kp + \frac{2}{Kp} \right) \sinh p} \quad (49)$$

where

$$\begin{aligned} K &= \frac{\mu_o a}{\mu \Delta}, & p &= \sqrt{s \tau_d} \\ \tau_d &= \mu \sigma \Delta^2, & s &= j\omega = j2\pi f \end{aligned} \quad (50)$$

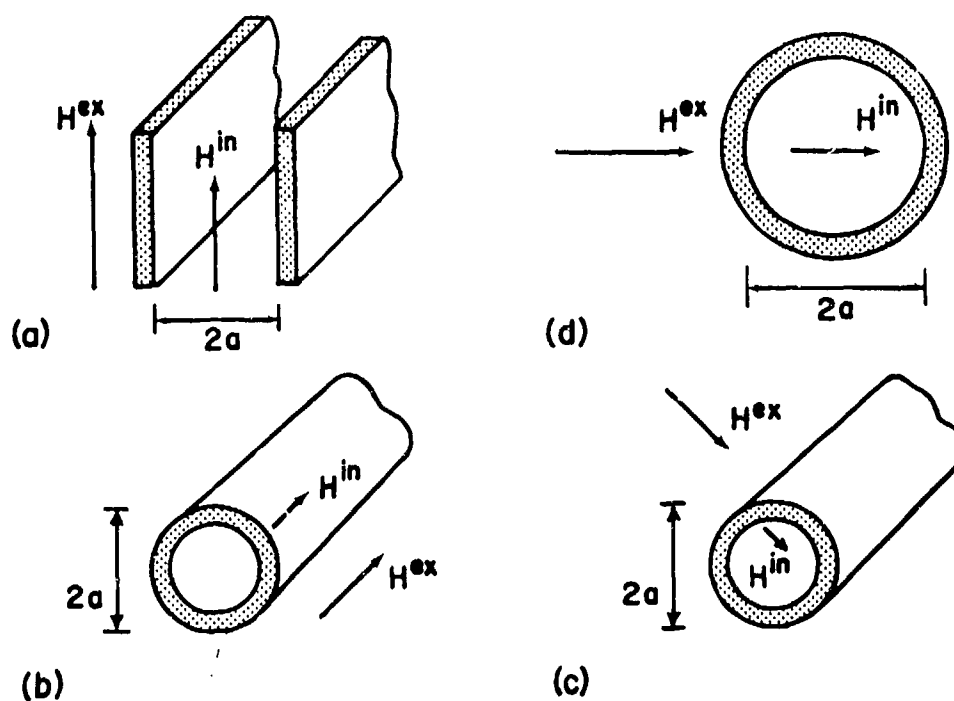


Fig. 34. (a) Two parallel plates, (b) a cylindrical shell with longitudinal H^{ex} , (c) a cylindrical shell with transverse H^{ex} , and (d) a spherical shell. All cavity walls have thickness Δ , conductivity σ , and permeability μ .

For non-ferrous shells, such as aluminum or titanium shells, $K \gg 1$ since the linear dimension of a typical cavity is several orders of magnitude larger than the wall thickness. In this case, (48) and (49) are simplified to

$$T_c \equiv T_c^{(t)} \approx T_c^{(l)} = \frac{1}{\cosh p + \frac{1}{2} Kp \sinh p} \quad (51)$$

$$T_s \approx \frac{1}{\cosh p + \frac{1}{3} Kp \sinh p} \quad (52)$$

The transfer functions T_p , T_c and T_s as given by (46), (51) and (52) are plotted in Fig. 35a for several values of K . They are again plotted in Fig. 35b in units of decibels in order to exhibit their "break points" and asymptotes.

For electrically thin shells ($\delta \gg \Delta$), (46), (51) and (52) are reduced to the simple forms

$$T_p(s) \rightarrow \frac{1}{1 + s\mu_0 \sigma \Delta a} \quad (53)$$

$$T_c(s) \rightarrow \frac{1}{1 + s\mu_0 \sigma \Delta a/2} \quad (54)$$

$$T_s(s) \rightarrow \frac{1}{1 + s\mu_0 \sigma \Delta a/3} \quad (55)$$

each of which has only one break point, i.e., the first break point in Fig. 35b. This break point is directly related to the decay constant of the late-time behavior of the interior pulse.

For electrically thick shells, i.e., $\delta \ll \Delta$, (46), (51) and (52) give

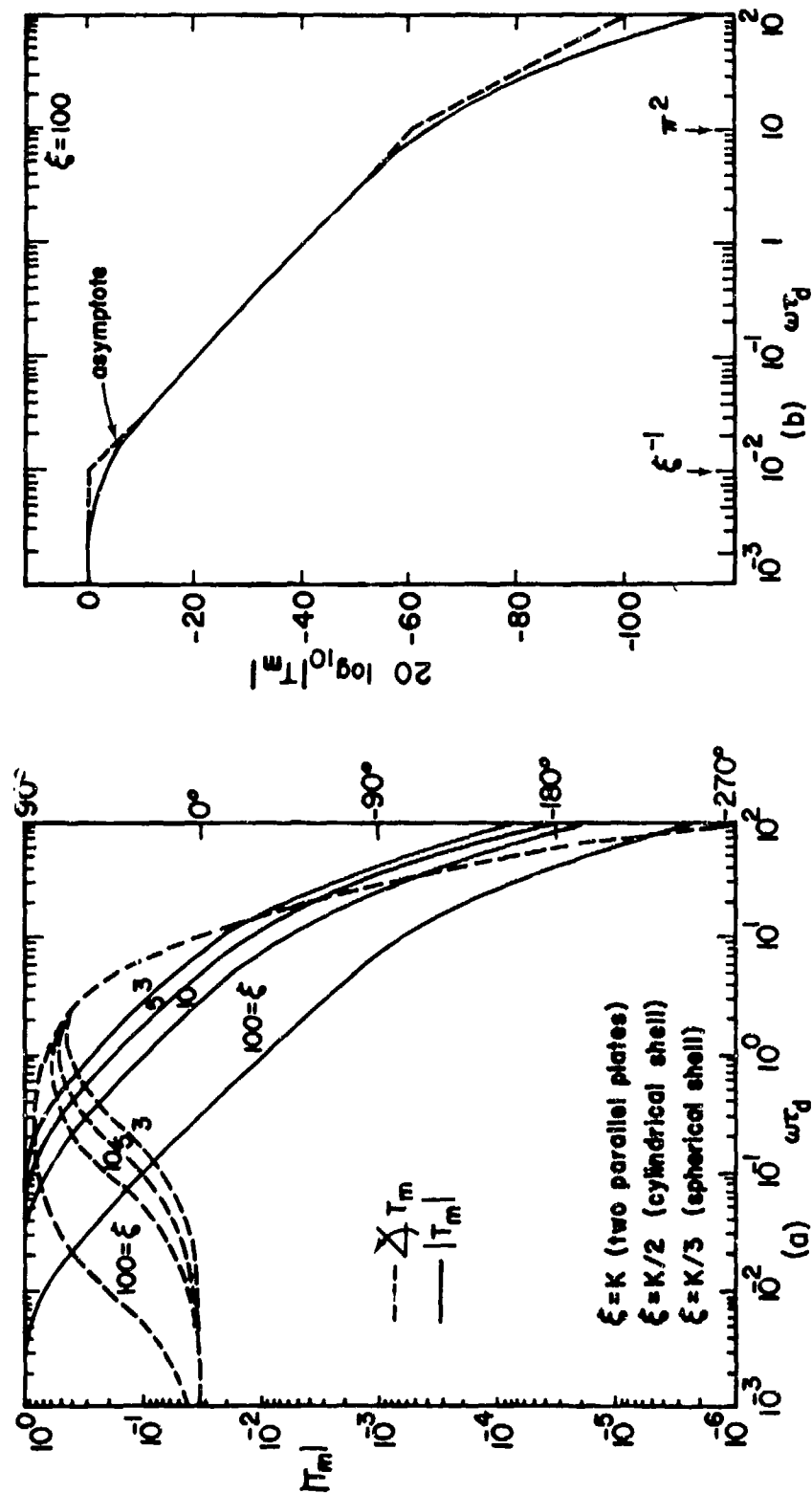


Fig. 35. (a) Magnitude and phase of transfer function versus normalized frequency ($\tau_d = \mu\sigma\Delta^2$),
 (b) Bode diagram for shielding effectiveness showing the frequency break points and
 asymptotes; higher break points occur at $(n\pi)^2$, $n = 2, 3, 4, \dots$

$$T_p(s) \rightarrow \frac{2\mu\Delta}{\mu_0 a} \frac{e^{-\sqrt{s}\tau_d}}{\sqrt{s}\tau_d} \quad (56)$$

$$T_c(s) \rightarrow \frac{4\mu\Delta}{\mu_0 a} \frac{e^{-\sqrt{s}\tau_d}}{\sqrt{s}\tau_d} \quad (57)$$

$$T_s(s) \rightarrow \frac{6\mu\Delta}{\mu_0 a} \frac{e^{-\sqrt{s}\tau_d}}{\sqrt{s}\tau_d} \quad (58)$$

Formulas (46) - (52) are valid for frequency $f \ll c/(2a)$, and $K \gg 1$, c being the vacuum speed of light. When $f \leq c/(16a)$ and $K \geq 5$ they are accurate to within 5%.

b. Time-Domain Solution

Since a typical nuclear EMP can be treated as an impulse so far as the penetrant cavity pulse $H^{in}(t)$ is concerned, one may write for the external pulse (Fig. 33)

$$H^{ex}(t, x) = H_0 \delta(t - x/c) \quad (59)$$

where H_0 is given by the time integral of H^{ex} as indicated in (41). Let the parameter ξ be introduced such that $\xi = K$ for two parallel plates, $\xi = K/2$ for a cylindrical shell, and $\xi = K/3$ for a spherical shell. Then, the transfer functions (46), (51) and (52) can be written in one single formula

$$T_m(s) = \frac{H^{in}(s)}{H_0} = \frac{1}{\cosh p + \xi p \sinh p}, \quad (p = \sqrt{s}\tau_d) \quad (60)$$

and the time history of the cavity field $H^{in}(t)$ is then given by

$$H^{in}(t) = \frac{H_0}{2\pi j} \int_{-j\infty-\Omega}^{j\infty+\Omega} \frac{e^{st} ds}{\cosh p + \xi p \sinh p} \quad (61)$$

This Laplace integral can be expressed in terms of an infinite series for computational purposes and the result is given in Fig. 36 for various values of ξ [28].

The early-time approximation of (61) is given by [28]

$$H^{in}(t) \approx \frac{2H_o}{\sqrt{\pi} \xi \tau_d} \sqrt{\frac{\tau_d}{t}} e^{-\tau_d/(4t)}, \quad \text{for } t/\tau_d \leq 0.1 \quad (62)$$

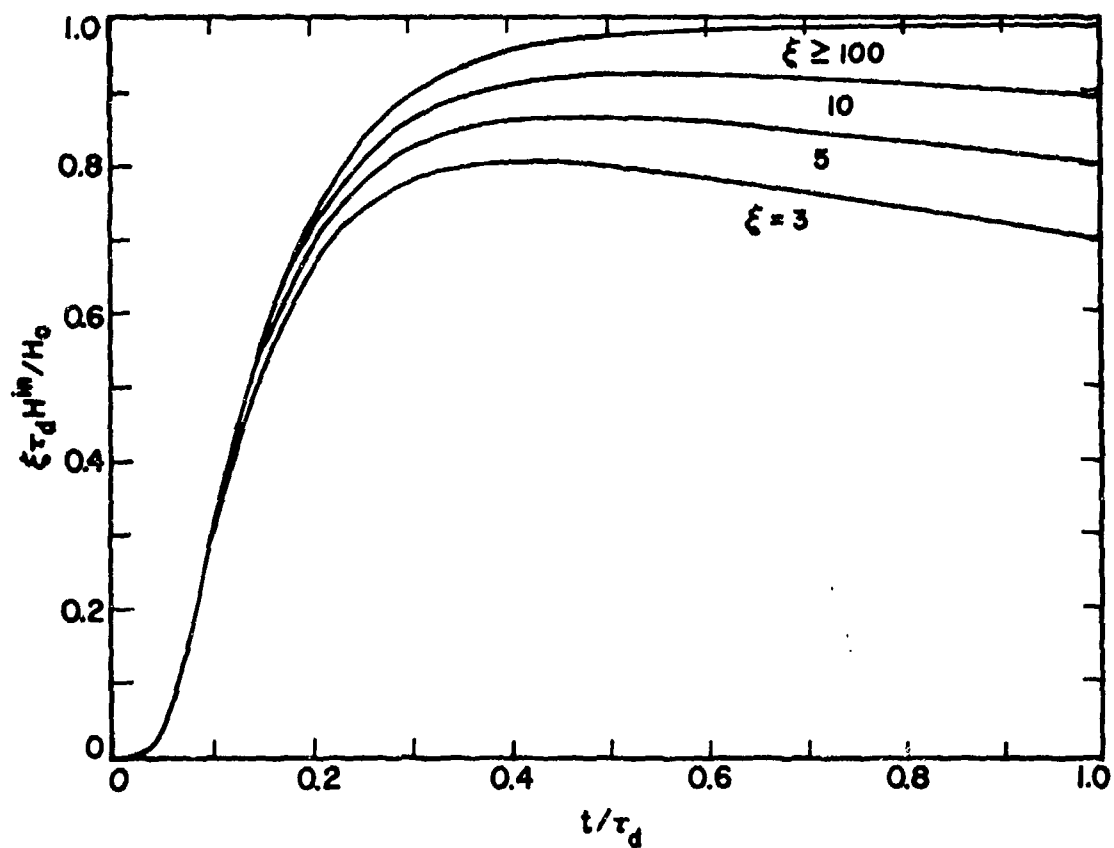


Fig. 36. Time variations of the penetrant EMP for various values of ξ .

whereas the intermediate and late-time approximation of (61) is

$$H^{in}(t) \approx \frac{H_0}{\xi \tau_d} \left[e^{-\xi^{-1} t/\tau_d} - 2e^{-\pi^2 t/\tau_d} + 2e^{-4\pi^2 t/\tau_d} \right], \text{ for } t/\tau_d \geq 0.1 \quad (63)$$

Since $\xi^{-1} \ll \pi^2$, the second and third exponentials can be dropped for $t \geq \tau_d$. The approximations (62) and (63) are plotted in Fig. 37 with the exact solution for $\xi \geq 100$. These two approximate formulas together describe the entire time history of the cavity field to a 0.1% accuracy.

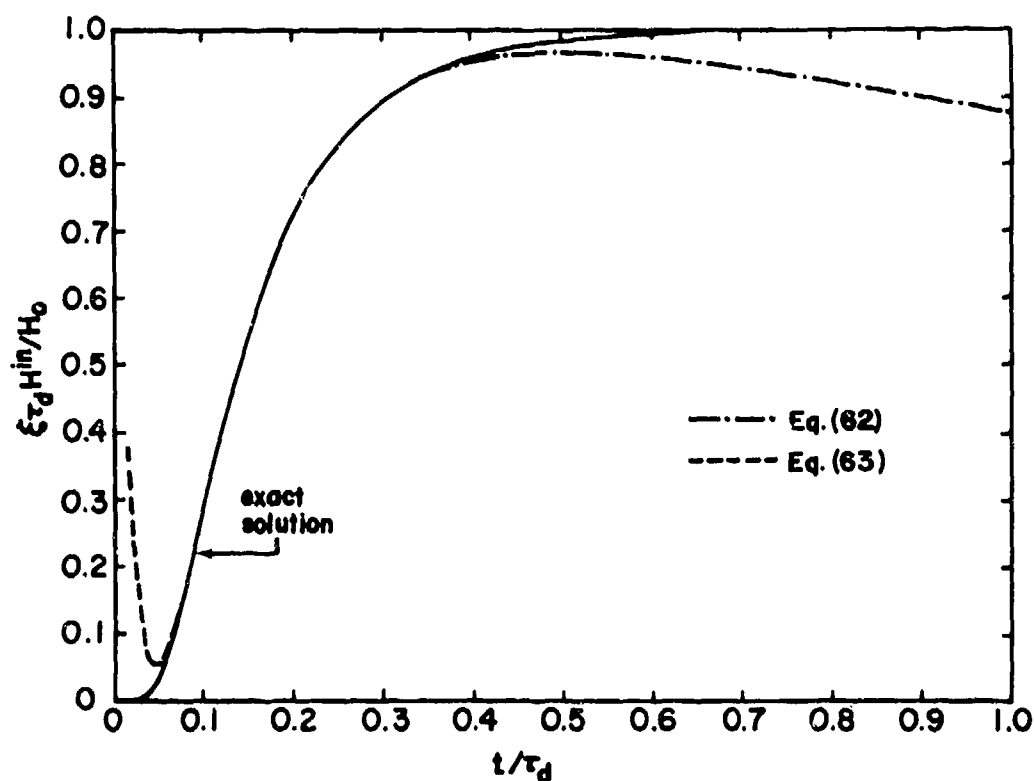


Fig. 37. Approximate and exact solutions for a penetrant EMP for $\xi \geq 100$.

Formulas (62) and (63) are valid for (i) $\xi \gg 1$ (physically thin shells), (ii) $t > \tau_a$ (observation time is greater than the transit time across the cavity which varies from a few to tens of nanoseconds), and (iii) $\tau_d \gg \tau_o$ (the diffusion time across the wall is much greater than the EMP pulse width; typically, $\tau_d \approx$ tens of microseconds and $\tau_o \approx$ hundreds of nanoseconds). When these three assumptions are met, formulas (62) and (63) describe the time history of the penetrant pulse to a 0.1% accuracy.

2.3.2.2.3 Arbitrarily Shaped Enclosures

Formulas (60), (62) and (63) can be readily generalized to an arbitrarily shaped enclosure if the parameter ξ can be expressed in terms of the global quantities of the geometry of the enclosure, such as the volume V and the surface area S of the enclosure. Indeed, one can write [28]

$$\xi = \frac{1}{\mu_r} \frac{V}{S\Delta} \quad (64)$$

where μ_r is the relative permeability and Δ the thickness of the wall. Define (see Fig. 33)

$$R = 1/(\sigma\Delta) = \text{dc wall resistance}$$

$$L = \mu_o V/S = \text{cavity inductance}$$

$$\tau_f = L/R = \text{fall time}$$

$$\tau_d = \mu\sigma\Delta^2 = \text{diffusion time}$$

Then, ξ can be rewritten as

$$\xi = \frac{L}{R\tau_d} = \frac{\tau_f}{\tau_d} \quad (65)$$

With ξ interpreted as (64) or (65), formulas (60), (62) and (63) can readily be applied to enclosures of any shape provided that the assumptions of the preceding section are satisfied. Table 2 summarizes

the important parameters of the interior cavity pulse $H^{in}(t)$, where $\dot{H}^{in}(\text{peak})$ means the peak value of the time derivative of $H^{in}(t)$.

TABLE 2. QUANTITIES CHARACTERIZING THE PENETRANT PULSE $H^{in}(t)$

$H^{in}(\text{peak})$	$\dot{H}^{in}(\text{peak})$	Rise Time (10 - 90%)	Decay Time (1/e)
$\frac{RH_o}{L}$	$\frac{6RH_o}{L\tau_d}$	$\frac{\tau_d}{4}$	$\frac{L}{R}$

2.3.2.2.4 Enclosures With Other Wall Materials

There are cavities whose walls are made of high- μ metals. Typical values of the relative permeability μ_r are $10^3 - 10^4$. For these types of cavities one must resort to (46-49), the inverse Laplace transform of which gives [28], by the method of residues, the penetrant cavity pulse shown in Fig. 38.

There are also cavities with walls made of ferromagnetic material whose μ is a function of the exciting field, or advanced composite material whose conductivity is a tensor. Cavities with these types of wall materials have received almost no attention, although EMP penetration through a single slab has been investigated [28, 37 - 38]. However, shielding by a single slab is not in general the same as shielding by an enclosure against low-frequency magnetic field. Fig. 39 shows an example from which one can see that a single slab is 6 orders of magnitude (or 120 dB) more effective in shielding than a spherical enclosure of 3-meter radius and of the same wall material and thickness as the slab.

2.3.3 PENETRATION

The cavity fields discussed in Sec. 2.3.2 are created by the coupling sources described in Sec. 2.3.1. These fields may in turn penetrate through

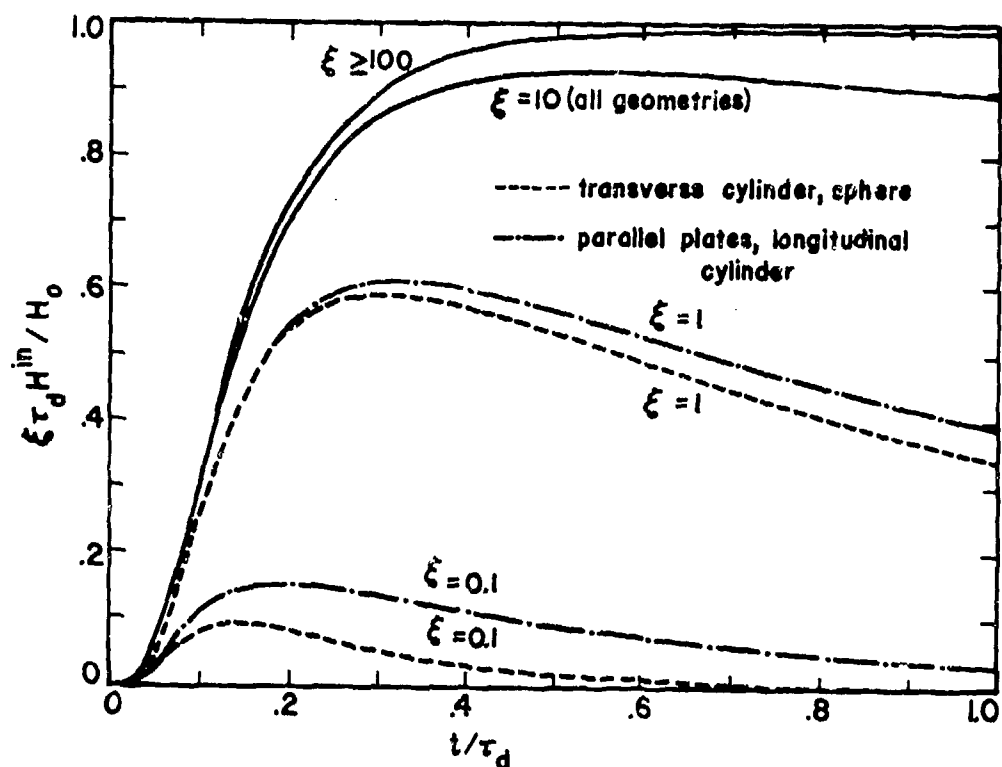


Fig. 38. Effect of geometry on enclosure response. $\xi = K$ for two parallel plates, $\xi = K/2$ for cylindrical shell, $\xi = K/3$ for spherical shell.

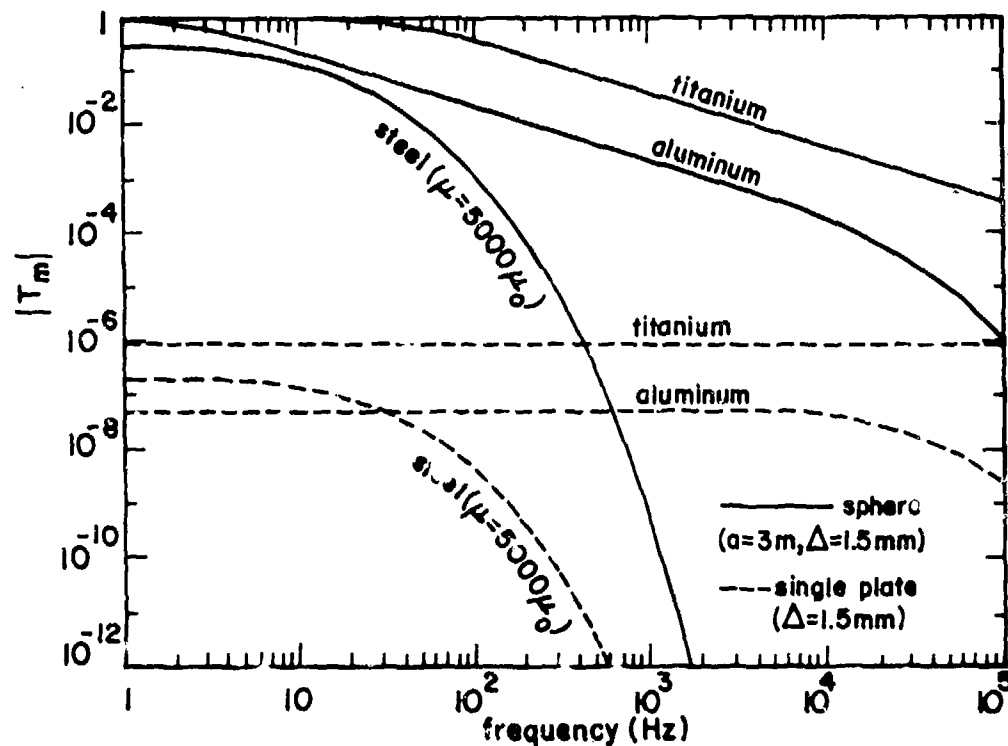


Fig. 39. Single-plate and enclosure transfer function versus frequency, where T_m is defined by (45).

the next layer into an interior region of, for example, an aircraft via the three different types of penetration treated in Sec. 2.1.3, namely, the deliberate penetration via antennas, the inadvertent penetration via apertures, and the diffusive penetration through conductive walls. These penetration sources are illustrated in Fig. 40 and tabulated in table 3.

The various symbols in table 3 are defined as follows:

\vec{E}_c, \vec{H}_c = cavity electric and magnetic fields (see Sec. 2.3.2)

$\vec{h}_{ef}, \vec{A}_{ef}$ = effective height and effective area (see Sec. 2.1.3.1)

$\vec{l}_{eq}, \vec{A}_{eq}$ = equivalent length and equivalent area (see Sec. 2.1.3.1)

Z_{in}, Y_{in} = input impedance and admittance (see Sec. 2.1.3.1)

$\vec{\alpha}_e, \vec{\alpha}_m$ = electric and magnetic polarizabilities defined with a ground plane (see Secs. 1.4.1.4 and 2.1.3.2)

$\vec{T}_{cm}, \vec{T}_{ce}$ = magnetic and electric current transfer functions (see Sec. 2.1.3.3)

V_{oc}, I_{sc} = open-circuit voltage and short-circuit current at the antenna's terminals (see Sec. 2.1.3.1)

\vec{p}, \vec{m} = electric and magnetic dipoles (see Sec. 2.1.3.2)

$\vec{J}_{eq}, \vec{J}_{m,eq}$ = equivalent electric and magnetic surface currents (see Sec. 2.1.3.3)

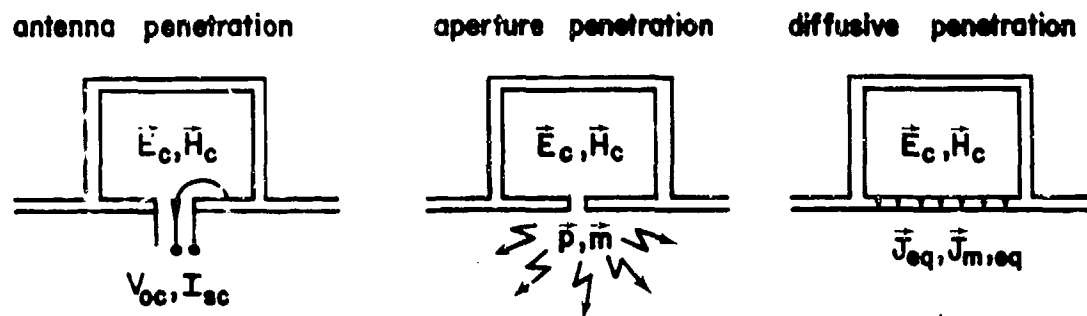


Fig. 40. Three types of penetration sources.

TABLE 3. PENETRATION SOURCES

Penetration	Excitation	Transfer Function	Penetration Source
Antenna	\vec{E}_c, \vec{H}_c	$\vec{h}_{ef}, \vec{A}_{ef}, \vec{h}_{eq}, \vec{A}_{eq}$ Z_{in}, Y_{in}	V_{oc}, I_{sc}
Aperture	\vec{E}_c, \vec{H}_c	$\vec{\alpha}_e, \vec{\alpha}_m$	\vec{p}, \vec{m}
Conductive Wall	\vec{E}_c, \vec{H}_c	$\vec{T}_{ce}, \vec{T}_{cm}$	$\vec{J}_{eq}, \vec{J}_{m,eq}$

The penetration sources in the third column of table 3 can be obtained by multiplying the appropriate excitation in the first column by the appropriate transfer function in the second column. It must be remembered that the transfer functions discussed previously are calculated on the assumption of an infinite ground plane, and hence, they do not contain the characteristics of the cavity. The properties of the cavity, however, show up in the excitation fields \vec{E}_c, \vec{H}_c .

REFERENCES

- [1] K.S.H. Lee, "Localized penetration through cable shields," Proc. of 1974 Spring FULMEN Meeting, Air Force Weapons Laboratory, April 16 - 17, 1974.
- [2] R.W. Latham, "Small holes in cable shields," IN 118, September 1972. In Eqs. (8.5), (8.7) and (8.9) of this reference the factor $2 \cos(x/4) / [1 + \cos(x/4)]$ has been left out.
- [3] R.W. Latham and K.S.H. Lee, "A study of some factors affecting the interior field of a semi-infinite pipe exposed to a low-frequency magnetic field," IN 10, August 1967, and also "Magnetic field leakage into a semi-infinite pipe," Canad. J. Phys., Vol. 46, 1968, pp.1455 - 1462.
- [4] R.W. Latham and K.S.H. Lee, "Theory of inductive shielding," IN 12, March 1968, and also Canad. J. Phys., Vol. 46, 1968, pp.1745 - 1752.
- [5] H. Kaden, Wirbelströme und Schirmung in der Nachrichtentechnik, Springer-Verlag, Berlin, 1959.
- [6] T. Teichmann and E.P. Wigner, "Electromagnetic field expansion in loss-free cavities excited through holes," Journal of Applied Physics, Vol. 24, No. 3, March 1953, pp.262 - 267.
- [7] S.A. Schelkunoff, "On representation of electromagnetic fields in cavities in terms of natural modes of oscillation," Journal of Applied Physics, Vol. 26, No. 10, October 1955, pp.1231 - 1234.
- [8] F.E. Borgnis and C.H. Papas, Electromagnetic Waveguides and Resonators, Handbuch der Physik, Vol. XVI, 1958.
- [9] J. Van Bladel, Electromagnetic Fields, McGraw-Hill, 1964.
- [10] K.S.H. Lee, F.C. Yang and K.C. Chen, "Cavity excitation via apertures," IN 316, February 1977.
- [11] C.D. Taylor, "Electromagnetic pulse penetration through small apertures," IN 74, March 1971.

- [12] C.D. Taylor, "Electromagnetic pulse penetration through small apertures," EMC-15, February 1973, pp.17 - 23.
- [13] J. Lam, "Analysis of EMP penetration through skin panel joints," AFWL-TR-77-170, December 1977.
- [14] C.M. Butler and E. Yung, "Properties of a slotted parallel-plate waveguide excited by an incident TEM wave," 1976 IEEE/AP-S Symposium, Amherst, Massachusetts, October 1976.
- [15] J.N. Bombardt, "Magnetic field shielding degradation due to circular apertures in long hollow cylinders," IN 3, September 1966.
- [16] J.N. Bombardt, "Quasi-static magnetic field transmission through circular apertures," IN 9, July 1967.
- [17] T.B.A. Senior, "Electromagnetic field penetration into a cylindrical cavity," IN 221, January 1975.
- [18] K.S.H. Lee, "Shields with periodic apertures," IN 89, January 1972.
- [19] T.B.A. Senior and G.A. Desjardins, "Electromagnetic field penetration into a spherical cavity," IN 142, August 1973, and also EMC-16, No. 4, November 1974, pp.205 - 208.
- [20] F.C. Yang and K.S.H. Lee, "EMP penetration into a closed wheel well," AFWL-TR-77-165, December 1977.
- [21] F.C. Yang, K.S.H. Lee, and L. Marin, "Analysis of EMP penetration into a weapons bay," AFWL-TR-77-133, December 1977.
- [22] L. Marin, "Quasi-static field penetration into a two-dimensional rectangular well in a ground plane," IN 171, March 1974.
- [23] J. Lam, "Analysis of EMP penetration into an open wheel well," AFWL-TR-77-139, December 1977.
- [24] J. Lam, "Exact solution of the problem of quasi-static electric field penetration into a hemispherical indentation in an infinite conducting plane," IN 175, April 1974.
- [25] J. Lam, "Quasi-static magnetic field penetration into a hemispherical indentation in an infinite conducting plane," IN 179, May 1974.

- [26] R.W. Latham, "Shielding by closed shells," Proc. of 1974 Spring FULMEN Meeting, Air Force Weapons Laboratory, April 16 - 17, 1974.
- [27] W.R. Smythe, Static and Dynamic Electricity, McGraw-Hill, New York, 1950, Chap. 11.
- [28] G. Bedrosian and K.S.H. Lee, "EMP penetration through metal skin panels and into aircraft cavities," IN 314, August 1976, and "EMP diffusion into specific aircraft configurations on the B-1, EC-135, and E-4," AFWL-TR-77-166, December 1977.
- [29] C.W. Harrison, Jr., M.L. Houston, R.W.P. King, and T.T. Wu, "The propagation of transient electromagnetic fields into a cavity formed by two imperfectly conducting sheets," IN 31, April 1964, and also AP-13, No. 1, January 1965, pp.149 - 158.
- [30] J.C. Jaeger, "Magnetic screening by hollow circular cylinders," Phil. Mag., Vol. 29, 1940, pp.18 - 31.
- [31] C.W. Harrison, Jr., "Transient electromagnetic field propagation through infinite sheets, into spherical shells, and into hollow cylinders," IN 32, May 1964.
- [32] C.W. Harrison, Jr. and C.H. Papas, "On the attenuation of transient fields by imperfectly conducting spherical shells," IN 34, July 1964.
- [33] L.V. King, "Electromagnetic shielding at radio frequencies," Phil. Mag. and J. Sci., Vol.15, No. 97, February 1933, pp.201 - 223.
- [34] C.E. Baum, "Unpublished notes on EMP shielding," 1967.
- [35] C.D. Taylor and C.W. Harrison, Jr., "On the attenuation of a plane-wave electromagnetic field by an imperfectly conducting prolate spheroidal shell," IN 35, October 1966.
- [36] R.W.P. King and C.W. Harrison, Jr., "Cylindrical shields," IN 30, March 1961.
- [37] K.F. Casey, "EMP penetration through advanced composite skin panels," IN 341, June 1978.

- [38] W.J. Karzas and Charles T.C. Mo, "Linear and nonlinear EMP diffusion through a ferromagnetic conducting slab," AP-26, No. 1, January 1978, pp.118 - 129.
- [39] D.E. Merewether, "EMP transmission through a thin sheet of saturable ferromagnetic material of infinite surface area," EMC-11, November 1969, p.139.

CHAPTER 2.4

CABLE INTERACTION

Engineering formulas and data describing the interaction of EMP-induced fields with cables are presented in this chapter. The cable interior usually represents the final shielded volume of a given shield topology; the cable guides electromagnetic energy from its penetration point(s) to the load which terminates it. The formulation of the differential equations governing the behavior of the currents and voltages on transmission lines has been described in Sec. 1.3.2. The parameters entering these equations and the solution of the transmission-line equations are given in this chapter.

Two distinct types of cable configurations commonly occur in this interaction problem: shielded cables, which are treated in Sec. 2.4.1, and unshielded or open cables, which are treated in Sec. 2.4.2.

2.4.1 SHIELDED CABLES

A shielded cable comprises one or more conductors within a cylindrical conducting shell which serves to shield the inner conductor(s) from the effects of external fields, in addition to serving as a return conductor. When there is only a single conductor within the shield and coaxial with it, the cable is a coaxial cable. When there are two or more conductors within the shield, the cable is referred to as a shielded multiconductor cable.

Engineering data and formulas are readily available for coaxial cables but exceedingly sparse for shielded multiconductor cables. Accordingly, most of this section deals only with coaxial cables. Available data and formulas for shielded multiconductor cables apply only to the propagation problem for such cables, and the penetration problem is formally identical to that for open transmission lines (see Sec. 2.4.2). The coupling problem for shielded multiconductor cables has not been extensively studied.

2.4.1.1 Coupling to Coaxial Cables

The source terms in the transmission-line equations for coaxial cables are presented in the following two sections. In Sec. 2.4.1.1.1 the source terms for distributed coupling are given; source terms for discrete coupling are given in Sec. 2.4.1.1.2.

2.4.1.1.1 Distributed Voltage and Current Sources per Unit Length

The distributed voltage and current source terms in the s-domain transmission-line equations (117) of Chap. 1.3 are respectively $V'^{(s)}(z,s)$ and $I'^{(s)}(z,s)$. For coaxial cables these source quantities are related to the total cable current $I_t(z,s)$ (the algebraic sum of the currents carried by the center conductor and the shield) and the total charge per unit length $Q'_t(z,s)$ by

$$V'^{(s)}(z,s) = Z'_T(s)I_t(z,s) \quad (1)$$

$$I'^{(s)}(z,s) = \Omega_T(s)Q'_t(z,s) \quad (2)$$

in which $Z'_T(s)$ is the shield transfer impedance per unit length and $\Omega_T(s)$ is the charge transfer frequency. I_t and Q'_t are related by equation

$$\frac{dI_t(z,s)}{dz} + sQ'_t(z,s) = 0 \quad (3)$$

Additional source terms associated with direct coupling to the external field exist for eccentrically shielded "coaxial" cables and multi-conductor cables in general. These terms do not occur in a truly coaxial cables [1,2].

The parameters $Z'_T(s)$ and $\Omega_T(s)$ for tubular, braided, and tape-helical cable shields are discussed in the following.

a. Tubular Cable Shields

A tubular cable shield is a cylindrical shell of conducting material. The inner and outer radii are denoted by b and c respectively,

the shell's thickness is $d = c - b$, and σ denotes the conductivity of the shield material, which is assumed to be non-ferromagnetic. For such a shield, the transfer impedance Z_T' has been given by (35) of Chap. 2.2, and the charge transfer frequency $\Omega_T = 0$. In practical shields $b/d \gg 1$ and $c/d \gg 1$. An accurate approximate expression for Z_T' under these conditions has been given by (37) of Chap. 2.2 and is repeated here for easy reference

$$Z_T'(s) \approx R_{dc}' \sqrt{s\tau_d} \operatorname{csch} \sqrt{s\tau_d} \quad (4)$$

$$R_{dc}' \approx \frac{1}{2\pi\sigma d \sqrt{bc}} \approx \frac{1}{2\pi\sigma b d} \quad (5)$$

where $\tau_d = \mu_0 \sigma d^2$. Curves of the magnitude and phase of Z_T'/R_{dc}' as functions of normalized frequency $f\tau_d$ are shown plotted on different scales in Fig. 1. A linear-scale plot can be found in Fig. 21 of Chap. 2.2. When $f\tau_d \gg 1$, accurate approximate expressions for the magnitude and phase of Z_T'/R_{dc}' are

$$|Z_T'/R_{dc}'| \approx 2\sqrt{2\pi f\tau_d} \exp(-\sqrt{\pi f\tau_d}) \quad (6)$$

$$\arg[Z_T'/R_{dc}'] \approx \frac{\pi}{4} - \sqrt{\pi f\tau_d} \quad (7)$$

The relative error in the expressions (4) and (5) is approximately 50 d/b% over the EMP frequency spectrum. When $f\tau_d > 4$ the approximate expressions given in (6) and (7) are accurate to within 0.1%.

b. Braided Cable Shields

A braided shield is shown in Fig. 2. The radius of the shield is b and the pitch angle of the woven braid is ψ . The dimension of each of the braid apertures in the direction parallel to the cable axis is δ and the circumferential separation between apertures at constant axial position is $w = 4\pi b/N$, where N is the number of carriers (bands of shield wires) in the braid (in Fig. 2, $N = 8$).

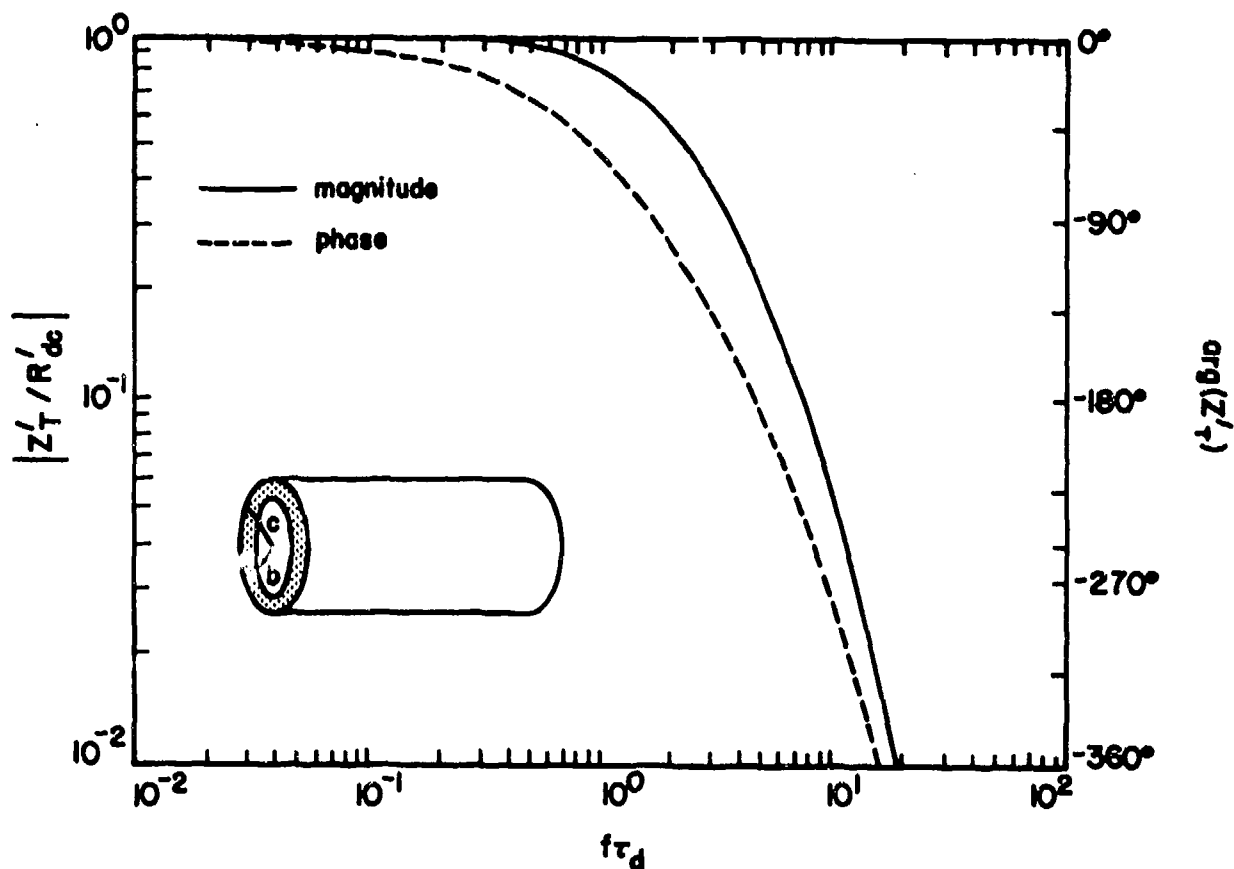


Fig. 1. Magnitude and phase of Z_T'/R'_{dc} versus $f\tau_d$ for tubular shields.

The source coefficients Z_T' and Ω_T for braided cable shields are given by [3-5]

$$Z_T'(s) = Z_{Td}'(s) + sL_T' \quad (8)$$

$$\Omega_T(s) = -sC'/C_T' \quad (9)$$

in which Z_{Td}' is the diffusion contribution to Z_T' , L_T' is the transfer inductance per unit length, C' is the capacitance per unit length between the center conductor of the cable and the shield, and C_T' is the transfer capacitance per unit length.

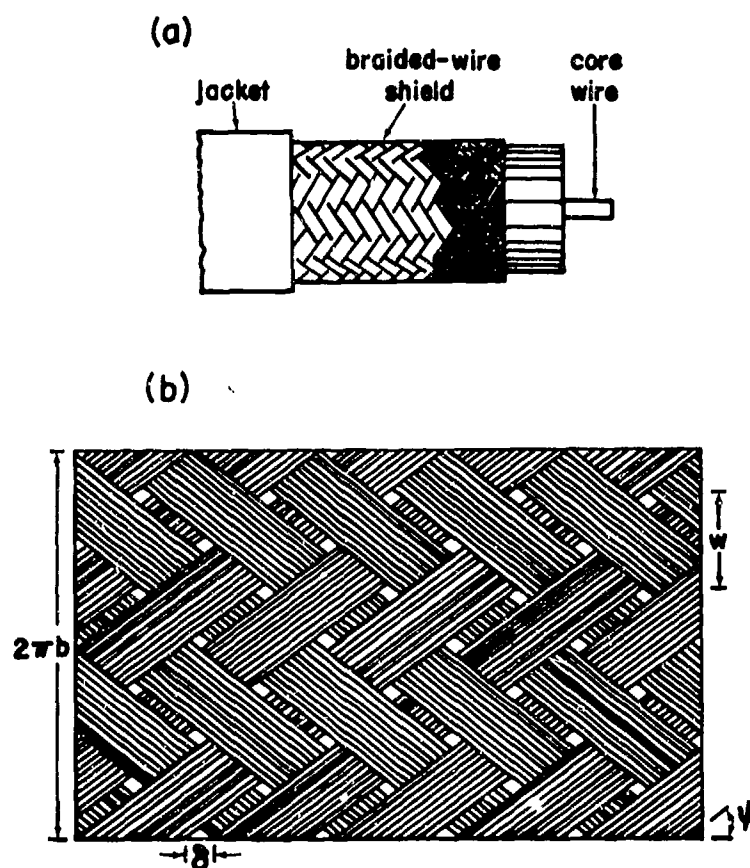


Fig. 2. (a) A braided shield, (b) developed surface.

The diffusion term Z'_{Td} is given by (see Eq.(4))

$$Z'_{Td}(s) = R'_b \sqrt{s\tau_d} \operatorname{csch} \sqrt{s\tau_d} \quad (10)$$

in which R'_b denotes the shield dc resistance per unit length of the braid

$$R'_b = \frac{1}{2\pi\sigma b d K} \quad (11)$$

where σ is the conductivity of the braid material, d is the shield thickness (typically taken equal to the diameter of the shield wires), and K is the optical coverage of the braid, i.e., the fraction of the

total shield area covered by the shield conductors. Curves of the magnitude and phase of Z'_{Td}/R'_b are shown in Fig. 1.

The transfer inductance per unit length L'_T may be expressed in terms of N , K , and ψ as follows [4]:

$$L'_T = \frac{2\mu_0}{N} \frac{(1-K)^{3/2} \bar{\alpha}_m(\psi) \cos \psi}{4 + (1-K)^{3/2} \bar{\alpha}_m(\psi) \Sigma_h(\psi) \cos^3 \psi \csc 2\psi} \quad (12)$$

in which $\bar{\alpha}_m(\psi)$ is a normalized magnetic polarizability of the shield apertures and $\Sigma_h(\psi)$ is an interaction sum which accounts for the effects of neighboring apertures in the shield. $\bar{\alpha}_m(\psi)$ is related to the magnetic polarizability $\alpha_m(\psi)$ of an isolated aperture by

$$\alpha_m(\psi) = \left(\frac{\delta}{2}\right)^3 \frac{\sin^2 \psi}{\cos \psi} \bar{\alpha}_m(\psi) \quad (13)$$

$\bar{\alpha}_m(\psi)$ and $\cos^3 \psi \Sigma_h(\psi)$ are tabulated in table 1 and shown plotted as functions of ψ in Figs. 3 and 4. The transfer inductance per unit length L'_T may also be written in the abbreviated form

$$L'_T = \frac{\mu_0}{2N} g \left[(1-K)^{3/2}, \psi \right] \quad (14)$$

The function $g \left[(1-K)^{3/2}, \psi \right]$ is given in tabular form in table 2.

The transfer capacitance per unit length C'_T is conveniently expressed as [4]

$$\frac{1}{C'_T} = \frac{2}{N\epsilon} \frac{f_d (1-K)^{3/2} \bar{\alpha}_e(\psi) \cos \psi}{4 + f_d (1-K)^{3/2} \bar{\alpha}_e(\psi) \Sigma_e(\psi) \cos^3 \psi \csc 2\psi} \quad (15)$$

in which $\bar{\alpha}_e(\psi)$ is a normalized electric polarizability of the shield apertures and $\Sigma_e(\psi)$ is an interaction sum which accounts for the effects

TABLE 1. $\bar{\alpha}_m(\psi)$ AND $\cos^3 \psi \Sigma_h(\psi)$ FOR DIAMOND-SHAPED APERTURES

ψ (Degrees)	$\bar{\alpha}_m(\psi)$	$\cos^3 \psi \Sigma_h(\psi)$
0	0.524	-1.531
5	0.533	-1.511
10	0.552	-1.456
15	0.582	-1.370
20	0.619	-1.264
25	0.665	-1.166
30	0.725	-1.123
35	0.805	-1.167
40	0.907	-1.286
45	1.041	-1.420

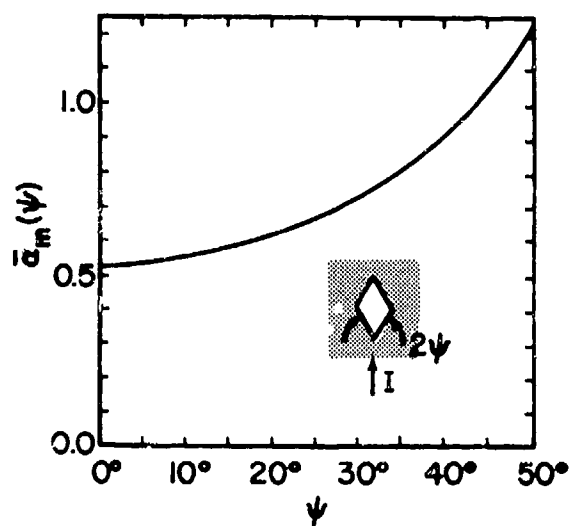


Fig. 3. $\bar{\alpha}_m(\psi)$ versus ψ .

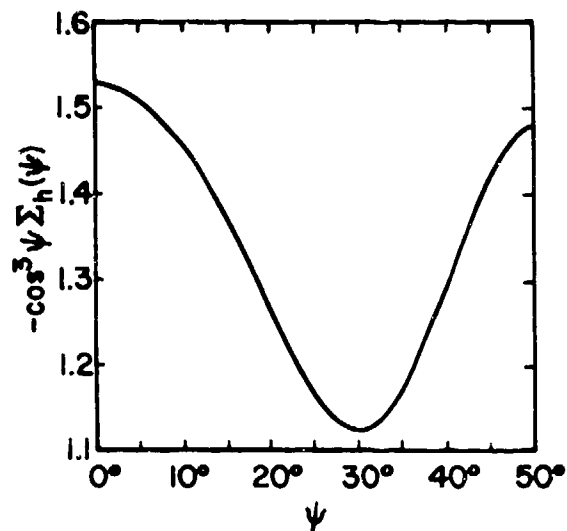


Fig. 4. $-\cos^3 \psi \Sigma_h(\psi)$ versus ψ .

TABLE 2. $g [(1-K)^{3/2}, \psi]$

$\psi \backslash (1-K)^{3/2}$	0.01	0.02	0.03	0.04	0.05
	$(\times 10^{-2})$				
5°	0.539	1.091	1.657	2.236	2.829
10°	0.555	1.117	1.686	2.261	2.844
15°	0.584	1.173	1.767	2.366	2.969
20°	0.621	1.246	1.874	2.507	3.143
25°	0.667	1.337	2.010	2.687	3.368
30°	0.727	1.457	2.190	2.928	3.668
35°	0.807	1.618	2.433	3.253	4.076
40°	0.910	1.825	2.745	3.671	4.603
45°	1.045	2.098	3.158	4.226	5.303

of neighboring apertures in the shield. $\bar{\alpha}_e(\psi)$ is related to the electric polarizability $\alpha_e(\psi)$ of an isolated aperture by

$$\alpha_e(\psi) = \left(\frac{\delta}{2}\right)^3 \frac{\sin^2 \psi}{\cos \psi} \bar{\alpha}_e(\psi) \quad (16)$$

The permittivity of the dielectric between the center conductor and the shield is ϵ . The factor f_d depends on ϵ and upon the permittivity and thickness of the cable's dielectric outer jacket. For practical cables, f_d is given by [6]

$$f_d = \begin{cases} \frac{2\epsilon}{\epsilon + \epsilon_0} & \text{if no jacket is present} \\ \frac{2\epsilon}{\epsilon + \epsilon_j} & \text{if a jacket is present} \end{cases} \quad (17)$$

The permittivity of the cable jacket is denoted by ϵ_j .

$\bar{\alpha}_e(\psi)$ and $\cos^3 \psi \Sigma_e(\psi)$ are tabulated in table 3 and shown plotted as functions of ψ in Figs. 5 and 6. The transfer capacitance per unit length C'_T may also be written in the abbreviated form

$$\frac{1}{C'_T} = \frac{1}{2N\epsilon} h \left[(1-K)^{3/2} f_{d,\psi} \right] \quad (18)$$

The function $h \left[(1-K)^{3/2} f_{d,\psi} \right]$ is tabulated in table 4. Thus the charge transfer frequency is, according to (9),

$$\Omega_T(s) = \frac{-\pi s}{N \ln(b/a)} h \left[(1-K)^{3/2} f_{d,\psi} \right] \quad (19)$$

where $C' = 2\pi\epsilon/\ln(b/a)$ has been used (see Sec. 2.4.1.2.1), and where a denotes the radius of the center conductor of the coaxial cable.

The expressions given in (10) and (11) are accurate within approximately 50 d/b% for a "perforated conducting tube" model of the braid. The expressions in (12) and (15) are based upon the assumption that the aperture separation is small in comparison to the shield radius, so that a planar model of the cylindrical shields can be used for analysis. It is estimated that for commonly encountered braid shields these results are accurate within 10%.

c. Tape-Helix Cable Shields

A tape-helical cable shield is shown in Fig. 7. The shield has radius b , thickness d ($d \ll b$), and pitch angle ψ . The width of the gap between tapes is denoted by w . The number of separate helical conductors in the shield is M (in Fig. 7, $M=2$).

The source coefficients Z'_T and Ω_T are given by [7,8]

$$Z'_T(s) = Z'_{Td}(s) + sL'_T \quad (20)$$

$$\Omega_T(s) = -sC'/C'_T \quad (21)$$

TABLE 3. $\bar{\alpha}_e(\psi)$ AND $\cos^3 \psi \Sigma_e(\psi)$ FOR DIAMOND-SHAPED APERTURES

ψ (Degrees)	$\bar{\alpha}_e(\psi)$	$\cos^3 \psi \Sigma_e(\psi)$
0	0.524	0.765
5	0.516	0.820
10	0.504	0.980
15	0.492	1.232
20	0.481	1.555
25	0.472	1.919
30	0.464	2.281
35	0.459	2.591
40	0.456	2.801
45	0.455	2.875

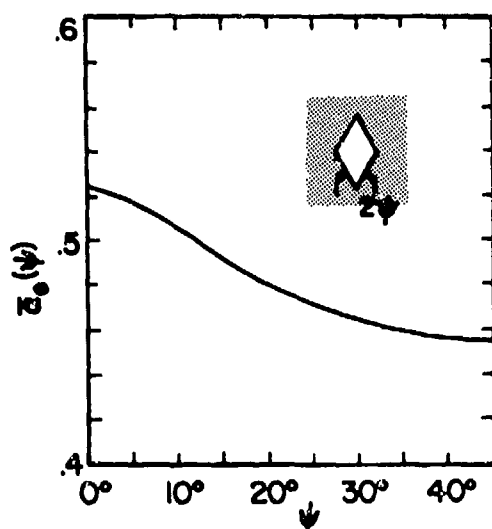


Fig. 5. $\bar{\alpha}_e(\psi)$ versus ψ .

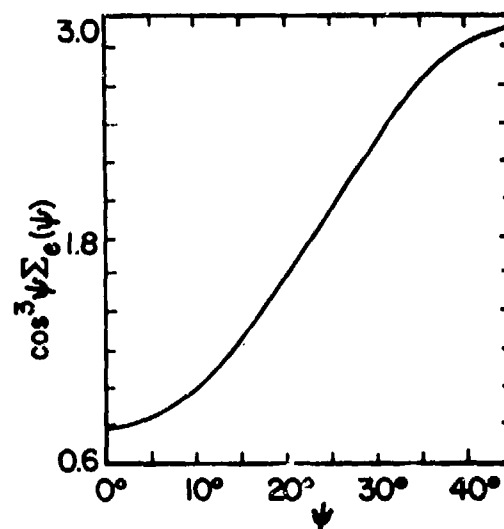


Fig. 6. $\cos^3 \psi \Sigma_e(\psi)$ versus ψ .

TABLE 4. $h [(1-K)^{3/2} f_d, \psi]$

$\psi \backslash (1-K)^{3/2} f_d$	0.01	0.02	0.03	0.04	0.05
	$(\times 10^{-2})$				
5°	0.521	1.036	1.545	2.049	2.547
10°	0.502	1.001	1.496	1.987	2.475
15°	0.491	0.987	1.463	1.944	2.423
20°	0.480	0.956	1.431	1.902	2.371
25°	0.471	0.939	1.404	1.866	2.326
30°	0.463	0.922	1.379	1.834	2.285
35°	0.458	0.912	1.364	1.813	2.259
40°	0.455	0.906	1.355	1.801	2.244
45°	0.454	0.904	1.352	1.796	2.238

in which Z'_{Td} is the diffusion contribution to Z'_T , L'_T is the transfer inductance per unit length, C' is the capacitance per unit length between the center conductor and the shield, and C'_T is the transfer capacitance per unit length.

The diffusion term Z'_{Td} is given by

$$Z'_{Td}(s) = R'_{dc} \sqrt{s\tau_d} \operatorname{csch} \sqrt{s\tau_d} \left[1 + \tan^2 \psi \cosh \sqrt{s\tau_d} \right] \quad (22)$$

Curves of the magnitude and phase of Z'_{Td}/R'_{dc} are given in Fig. 8 for various values of ψ . When $f\tau_d \gg 1$ and $\psi > 0$, accurate approximate expressions for Z'_{Td}/R'_{dc} are

$$|Z'_{Td}/R'_{dc}| \approx \sqrt{2\pi f\tau_d} \tan^2 \psi \quad (23)$$

$$\arg[Z'_{Td}/R'_{dc}] \approx \pi/4 \quad (24)$$

When $\psi = 0$, (6) and (7) may be used.

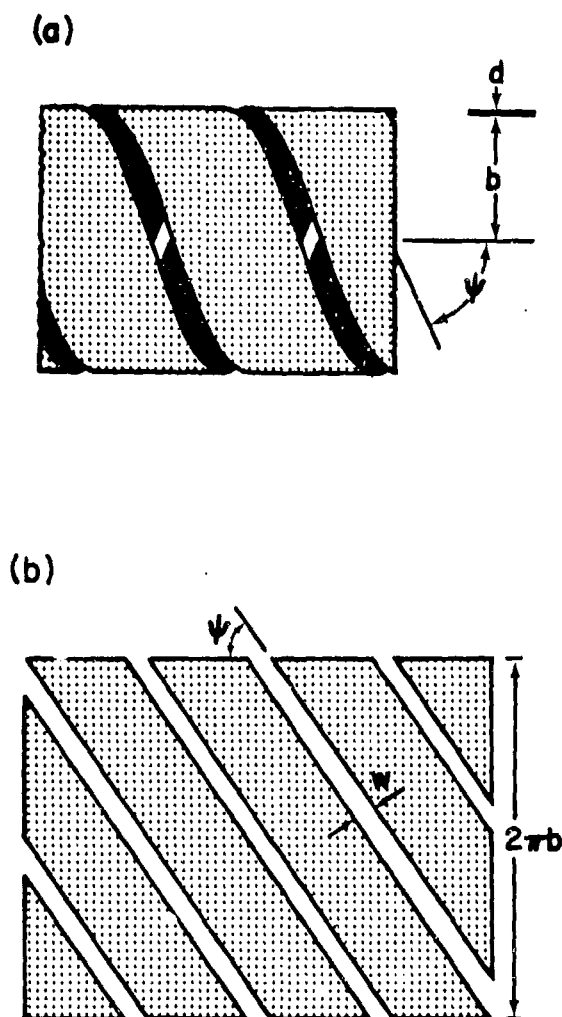


Fig. 7. (a) A tape-helical shield, (b) developed surface.

The transfer inductance per unit length L_T^i is expressed as

$$L_T^i = \frac{\mu_0}{4\pi} \left[(1 - a^2/b^2) \tan^2 \psi + \frac{1}{M} (w/4b)^2 \sec \psi \right] \quad (25)$$

where a denotes the radius of the center conductor of the coaxial cable. When $\psi > 0$ and $w/4b \ll 1$, the first term in the square brackets in (25) is much larger than the second term. This is the situation most commonly encountered in practice.

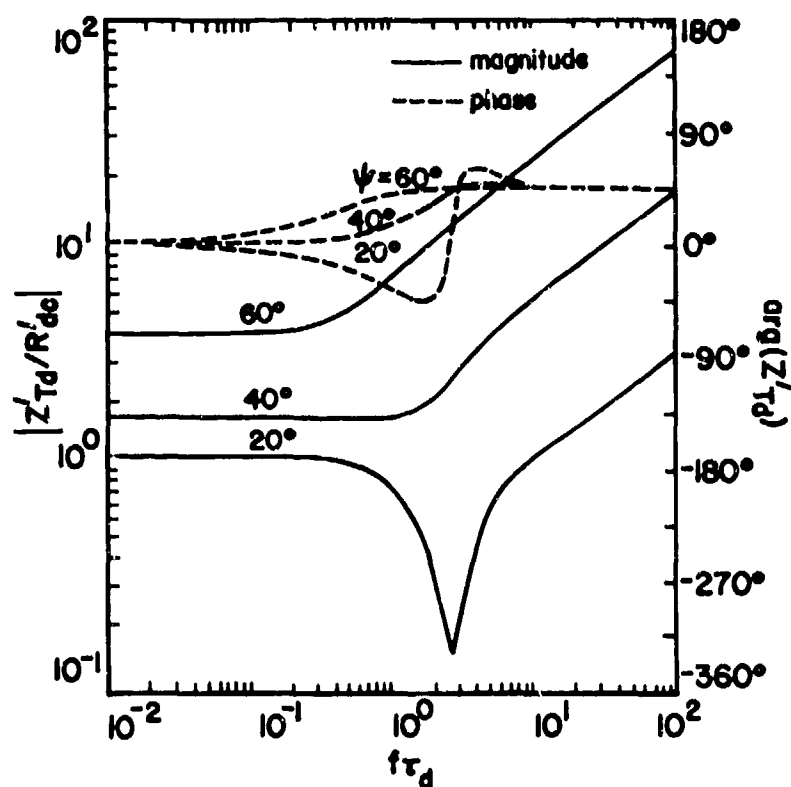


Fig. 8. Magnitude and phase of Z'_{Td}/R'_{dc} versus $f\tau_d$ for tape-helical shields; $\psi = 20^\circ, 40^\circ, 60^\circ$.

The quantity $1/C'_T$ is given by

$$\frac{1}{C'_T} = \frac{f_d}{4\pi\epsilon M} (w/4b)^2 \sec \psi \quad (26)$$

where ϵ is the permittivity of the dielectric between the center conductor and the shield, and f_d is the factor defined in (17). The charge transfer frequency Ω_T is given by

$$\Omega_T(s) \approx \frac{-s}{2n(b/a)} (w/4b)^2 \frac{\epsilon \sec \psi}{\epsilon + \epsilon_0} \quad (27)$$

for a helical shield with $M=1$ and without an outer dielectric jacket.

The result in (22) is analytically exact when $d \rightarrow 0$ and the gap width $w \rightarrow 0$. Typically w is very small and the error is negligible. The most important contribution to L_T' comes from the first term in square brackets in (25). The first term represents the contribution to Z_T' due to the circumferential currents in the shield. That term is analytically exact under the assumption that the current density is uniform across the tape. The remaining contributions to Z_T' and Ω_T are accurate to within 1% when $w/4b < 0.1$.

2.4.1.1.2 Discrete Voltage and Current Sources

The discrete voltage and current sources $V^{(s)}(z_0, s)$ and $I^{(s)}(z_0, s)$ due to the presence of an isolated aperture or connector at $z = z_0$ are given by [4,9]

$$V^{(s)}(z_0, s) = \frac{Z'(s)Z_w \alpha_m}{(2\pi b)^2 Z_c(s)} I_t(z_0, s) \quad (28)$$

$$I^{(s)}(z_0, s) = \frac{-s Z_w \alpha_e}{(2\pi b)^2 Z_c(s)} Q_t'(z_0, s) \quad (29)$$

in which Z' denotes the cable's series impedance per unit length, Z_c the characteristic impedance of the line, and $Z_w = \sqrt{\mu_0/\epsilon}$ the wave impedance of the dielectric material between the center conductor and the shield. The magnetic and electric polarizabilities of the aperture are denoted by α_m and α_e respectively.

The discrete voltage source $V^{(s)}$ appears, in an incremental transmission-line circuit model, in series with an impedance Z_a given by

$$Z_a(s) = \frac{s Z_w \alpha_m L'}{(2\pi b)^2 Z_c(s)} \quad (30)$$

where L' denotes the cable's series inductance per unit length. The discrete current source $I^{(s)}$ appears shunted by an admittance Y_a , given by

$$Y_a(s) = \frac{-s Z_w \alpha C'}{(2\pi b)^2 Z_c(s)} \quad (31)$$

in which C' denotes the shunt capacitance per unit length of the coaxial cable. When the isolated aperture is used to model a connector, a contact resistance term R_a whose value must be determined from measurements is added to the right-hand side of (30). An equivalent circuit representation of these discrete sources and their associated immittances is shown in Fig. 9.

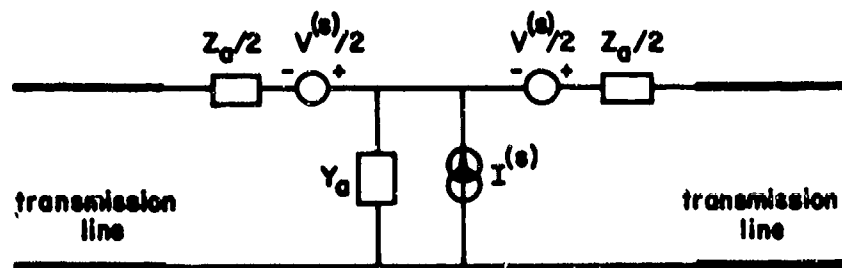


Fig. 9. Current and voltage sources and their associated immittances for discrete excitation.

In practice, one may use the ideal values for Z' , Z_c , L' , and C' (cf. 2.4.1.2) in (28) - (31) to obtain for tubular or braided-shield cables the following formulas

$$V^{(s)}(z_0, s) \approx \frac{s\mu_0}{(2\pi b)^2} \alpha_m I_t(z_0, s) \quad (32)$$

$$I^{(s)}(z_0, s) \approx \frac{-2\pi s \alpha_e}{(2\pi b)^2 \ln(b/a)} Q'_t(z_0, s) \quad (33)$$

$$Z_a(s) \approx \frac{s\mu_0}{(2\pi b)^2} \alpha_m \quad (34)$$

$$Y_a(s) \approx \frac{-s(2\pi)^2 \epsilon}{(2\pi b)^2 \ln^2(b/a)} \alpha_e \quad (35)$$

For tape-helix shield cables, $V^{(s)}$ and Z_a given in (32) and (34) should be multiplied by the factor

$$\left[1 + \frac{\tan^2 \psi}{2 \ln(b/a)} \left(1 - a^2/b^2 \right) \right]^{1/2}$$

and $I^{(s)}$ and Y_a given in (33) and (35) should be divided by this factor. Polarizabilities α_e and α_m for apertures of various shapes are given in Sec. 2.1.3.2.

The results in (28) - (31) are analytically exact for apertures whose dimensions are electrically small. Thus they may be regarded as exact in practice. The expressions in (32) - (35) are as accurate as the approximations used (see Sec. 2.4.1.2).

2.4.1.2 Propagation

The total series impedance per unit length Z' and the total shunt admittance per unit length Y' for coaxial cables with tubular, braided-wire, or tape-helical shields and shielded multiconductor cables are presented in 2.4.1.2.1. The solutions of the transmission-line equations are presented in 2.4.1.2.2 for coaxial cables with distributed shield coupling and for coaxial cables excited at an isolated aperture.

2.4.1.2.1 Series Impedance and Shunt Admittance per Unit Length

The series impedance per unit length Z' for coaxial as well as shielded multiconductor cables contains terms arising from the finite resistance per unit length of the shield and of the conductor or conductors within the shield, and terms arising from the inductance

of the region between the shield and the center conductor or conductors. In well shielded low-loss cables, neglect of the resistive contributions is a standard engineering approximation which leads to conservative estimates of the induced voltages and currents on the cable interior. This approximation is adopted throughout this section. In the following paragraphs, Z' and Y' are presented for coaxial cables with tubular, braided-wire, and tape-helical shields, as well as for shielded multi-conductor cables.

a. $Z'(s)$ and $Y'(s)$ for Tubular-Shielded Coaxial Cables

The internal immittances per unit length Z' and Y' for a tubular-shielded cable are given by [10]

$$Z'(s) = \frac{s\mu_0}{2\pi} \ln(b/a) \quad (36)$$

$$Y'(s) = \frac{2\pi\epsilon s}{\ln(b/a)} \quad (37)$$

when resistive contributions to Z' are neglected.

b. $Z'(s)$ and $Y'(s)$ for Braided-Shield Coaxial Cables

The internal immittances per unit length Z' and Y' for a braided-shield cable are given by [2,11]

$$Z'(s) = \frac{s\mu_0}{2\pi} \ln(b/a) + sL'_T \quad (38)$$

$$Y'(s) = \left[\frac{1}{2\pi\epsilon s} \ln(b/a) + \frac{1}{sC'_T} \right]^{-1} \quad (39)$$

where L'_T and $1/C'_T$ are given in (12) and (15) respectively. Resistive contributions to Z' have been neglected.

If the second terms in the above expressions are neglected with respect to the first, then (38) and (39) reduce to (36) and (37)

respectively. The relative errors in Z' and Y' incurred by neglecting the terms in L_T' and $1/C_T'$ are respectively

$$\frac{\pi g}{N \ln(b/a)} \quad \text{and} \quad \frac{\pi h}{N \ln(b/a)}$$

where g and h are given in tables 2 and 4. For typical braided-shield cables, these relative errors are less than 1%.

c. $Z'(s)$ and $Y'(s)$ for Tape-Helix Shielded Coaxial Cables

The internal immittances per unit length Z' and Y' for tape-helix shielded cables are given by [8]

$$Z'(s) = \frac{s\mu_0}{2\pi} \ln(b/a) + \frac{s\mu_0}{4\pi} \left[(1 - a^2/b^2) \tan^2 \psi + \frac{1}{M} (w/4b)^2 \sec \psi \right] \quad (40)$$

$$Y'(s) = 2\pi s \epsilon \left[\ln(b/a) + \frac{f_d}{2M} (w/4b)^2 \sec \psi \right]^{-1} \quad (41)$$

when resistive contributions to Z' are neglected. The terms proportional to $(w/4b)^2$ may generally be omitted with negligible error, yielding

$$Z'(s) \approx \frac{s\mu_0}{2\pi} \ln(b/a) + \frac{s\mu_0}{4\pi} (1 - a^2/b^2) \tan^2 \psi \quad (42)$$

$$Y'(s) \approx \frac{2\pi s \epsilon}{\ln(b/a)} \quad (43)$$

for the tape-helix shielded cable. The relative error incurred by neglecting terms in $(w/4b)^2$ is less than 0.1% if $w/b < 0.1$ and $\psi < 60^\circ$.

d. $Z'(s)$ and $Y'(s)$ for Eccentrically Shielded Cables

When the center conductor is not coaxial with the shield, the results given above must be modified. Let the distance between the axes of the shield and the internal conductor be D . Then (36) becomes

$$Z'(s) \approx \frac{s\mu_0}{2\pi} \operatorname{arccosh} \left(\frac{a^2 + b^2 - D^2}{2ab} \right) \quad (44)$$

and (37) becomes

$$Y'(s) \approx 2\pi s\epsilon / \operatorname{arccosh} \left(\frac{a^2 + b^2 - D^2}{2ab} \right) \quad (45)$$

Eq. (42) becomes

$$Z'(s) \approx \frac{s\mu_0}{2\pi} \operatorname{arccosh} \left(\frac{a^2 + b^2 - D^2}{2ab} \right) + \frac{s\mu_0}{4\pi} \left(1 - a^2/b^2 \right) \tan^2 \psi \quad (46)$$

It is noted that

$$\lim_{D \rightarrow 0} \operatorname{arccosh} \left(\frac{a^2 + b^2 - D^2}{2ab} \right) = \operatorname{arccosh} \left(\frac{a^2 + b^2}{2ab} \right) = \ln(b/a) \quad (47)$$

e. $Z'_{ij}(s)$ and $Y'_{ij}(s)$ for Shielded Multiconductor Cables

For a shielded multiconductor cable the per-unit-length series impedance (Z'_{ij}) and shunt admittance (Y'_{ij}) are matrices. Tables 5 and 6 give respectively the elements Z'_{ij} and Y'_{ij} for two- and three-conductor cables. To obtain those quantities it is assumed that the dielectric medium inside the shield is homogeneous and lossless, and that the inner conductors and the solid tubular shield are perfectly conducting.

2.4.1.2.2 Solutions of the Transmission-Line Equations

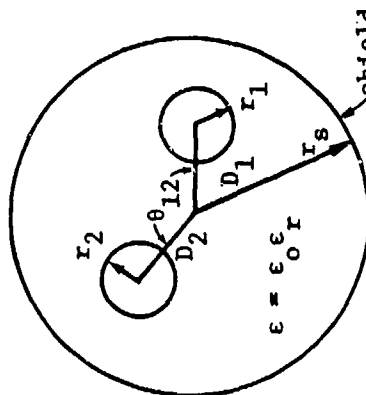
Let a cable run between $z=0$ and $z=l$ and be terminated by impedances Z_{t0} at $z=0$ and Z_{tl} at $z=l$. The characteristic impedance of the line Z_c and the complex propagation constant $\gamma_c(s)$ are related to Z' and Y' by

$$Z_c(s) = [Z'(s)/Y'(s)]^{1/2} \quad (48)$$

$$\gamma_c(s) = [Z'(s)Y'(s)]^{1/2} \quad (49)$$

The terminal voltages and currents will be given in terms of the total current I_t for distributed excitation, and in terms of $V^{(s)}$ and $I^{(s)}$ for discrete excitation.

TABLE 5. (Z'_{ij}) AND (Y'_{ij}) FOR A SHIELDED TWO-CONDUCTOR CABLE

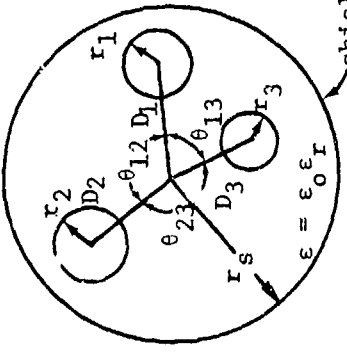
Two Wires Enclosed by a Circular Shield	Line Parameters
 <p><u>Assumption:</u> conductor radii are small compared to distances between conductors and between conductors and shield</p>	$(Z'_{ij}) = \frac{8\mu_0}{2\pi} \begin{bmatrix} a_{11} & a_{12} \\ a_{21} & a_{22} \end{bmatrix}$ $(Y'_{ij}) = \frac{2\pi\epsilon}{l} \begin{bmatrix} a_{22} & -a_{12} \\ -a_{21} & a_{11} \end{bmatrix}$

$$\Delta = a_{11}a_{22} - a_{12}a_{21}$$

$$a_{ii} = \ln \left(\frac{r_s^2 - D_i^2}{r_i r_1} \right) \quad (i = 1, 2)$$

$$a_{ij} = \ln \sqrt{\frac{(D_i D_j / r_s)^2 + r_s^2 - 2D_i D_j \cos \theta_{ij}}{D_i^2 + D_j^2 - 2D_i D_j \cos \theta_{ij}}} \quad (i \neq j)$$

TABLE 6. (Z'_{ij}) AND (Y'_{ij}) FOR A SHIELDED THREE-CONDUCTOR CABLE

Three Wires Enclosed by a Circular Shield	Line Parameters
	$(Z'_{ij}) = \frac{\mu_0}{2\pi} \begin{bmatrix} a_{11} & a_{12} & a_{13} \\ a_{12} & a_{22} & a_{23} \\ a_{13} & a_{23} & a_{33} \end{bmatrix}$ $(Y'_{ij}) = \frac{2\pi\epsilon}{\Delta} \begin{bmatrix} (a_{22}a_{33} - a_{23}^2) & -(a_{12}a_{33} - a_{13}a_{23}) & -(a_{13}a_{22} - a_{12}a_{23}) \\ -(a_{12}a_{33} - a_{13}a_{23}) & (a_{11}a_{33} - a_{13}^2) & -(a_{11}a_{23} - a_{13}a_{12}) \\ -(a_{13}a_{22} - a_{12}a_{23}) & -(a_{11}a_{23} - a_{13}a_{12}) & (a_{11}a_{22} - a_{12}^2) \end{bmatrix}$

Assumption: Same as the preceding case of two wires in a shield.

$$\Delta = a_{11}(a_{22}a_{33} - a_{23}^2) - a_{12}(a_{12}a_{33} - a_{13}a_{23}) + a_{13}(a_{12}a_{23} - a_{22}a_{13})$$

$$a_{ii} = \ln \left(\frac{r_s^2 - D_i^2}{r_s r_i} \right) \quad (i = 1, 2, 3)$$

$$a_{ij} = \ln \sqrt{\frac{(D_i D_j / r_s)^2 + r_s^2 - 2D_i D_j \cos \theta_{ij}}{D_i^2 + D_j^2 - 2D_i D_j \cos \theta_{ij}}} \quad (i \neq j)$$

a. Distributed Excitation

General formulas for the currents and voltages at the terminating impedances of a cable externally excited along its length are [8]

$$I(0,s) = \frac{-V(0,s)}{Z_{to}(s)} = I_m(0,s) + I_e(0,s) \quad (50)$$

$$I(l,s) = \frac{V(l,s)}{Z_{tl}(s)} = I_m(l,s) + I_e(l,s) \quad (51)$$

with

$$I_m(0,s) = (1 - \Gamma_o) \frac{f_m e^{\gamma_c l} - \Gamma_l g_m e^{-\gamma_c l}}{e^{\gamma_c l} - \Gamma_o \Gamma_l e^{-\gamma_c l}} \quad (52)$$

$$I_e(0,s) = \frac{-(1 + \Gamma_o)}{Z_{to}} \frac{f_e e^{\gamma_c l} + \Gamma_l g_e e^{-\gamma_c l}}{e^{\gamma_c l} - \Gamma_o \Gamma_l e^{-\gamma_c l}} \quad (53)$$

$$I_m(l,s) = (1 - \Gamma_l) \frac{g_m - \Gamma_o f_m}{e^{\gamma_c l} - \Gamma_o \Gamma_l e^{-\gamma_c l}} \quad (54)$$

$$I_e(l,s) = \frac{1 + \Gamma_l}{Z_{tl}} \frac{g_e + \Gamma_o f_e}{e^{\gamma_c l} - \Gamma_o \Gamma_l e^{-\gamma_c l}} \quad (55)$$

Γ_o and Γ_l are the voltage reflection coefficients at $z=0$ and $z=l$

$$\Gamma_o = \frac{Z_{to} - Z_c}{Z_{to} + Z_c} \quad (56)$$

$$\Gamma_l = \frac{Z_{tl} - Z_c}{Z_{tl} + Z_c} \quad (57)$$

and f_m , g_m , f_e , and g_e are the source quantities given by

$$f_m = \frac{Z_T'}{2Z_c} Q_1 \quad (58)$$

$$g_m = \frac{Z_T'}{2Z_c} Q_2 \quad (59)$$

$$f_e = \frac{-Z_c \Omega_T}{2s} \left[e^{-\gamma_c l} I_t(l) - I_t(0) + \gamma_c Q_1 \right] \quad (60)$$

$$g_e = \frac{-Z_c \Omega_T}{2s} \left[e^{\gamma_c l} I_t(l) - I_t(0) - \gamma_c Q_2 \right] \quad (61)$$

where

$$Q_1 = \int_0^l e^{-\gamma_c u} I_t(u, s) du \quad (62)$$

$$Q_2 = \int_0^l e^{\gamma_c u} I_t(u, s) du \quad (63)$$

When the line is terminated at each end in its characteristic impedance,

$$I(0, s) = (Z_T'/2Z_c) Q_1 + \frac{\Omega_T}{2s} \left[e^{-\gamma_c l} I_t(l) - I_t(0) + \gamma_c Q_1 \right] \quad (64)$$

$$I(l, s) = e^{-\gamma_c l} \left\{ (Z_T'/2Z_c) Q_2 - \frac{\Omega_T}{2s} \left[e^{\gamma_c l} I_t(l) - I_t(0) - \gamma_c Q_2 \right] \right\} \quad (65)$$

When $Z_{to} = Z_c$ and $Z_{tl} = 0$, the short-circuit current at $z = l$ is twice that given in (65) and when $Z_{to} = Z_c$ and $Z_{tl} = \infty$, the open-circuit voltage at $z = l$ is $(2Z_c)$ times the current given in (65). Terminal currents and voltages may be obtained for any other desired special case by appropriate manipulation of (50) - (63).

b. Discrete Excitation

The point of entry of the externally excited signals is taken to be $z = z_0$ ($0 < z_0 < l$). The general formulas for the currents and voltages at the terminating impedances are

$$I(0, s) = \frac{-V(0, s)}{Z_{to}(s)} = I_0(s) \frac{1 - \Gamma_0}{\gamma_c z_0 e - \Gamma_0 e^{-\gamma_c z_0}} \quad (66)$$

$$I(l, s) = \frac{V(l, s)}{Z_{tl}(s)} = I_l(s) \frac{1 - \Gamma_l}{\gamma_c (l - z_0) e - \Gamma_l e^{-\gamma_c (l - z_0)}} \quad (67)$$

where Γ_0 and Γ_l have been defined in (56) and (57) and

$$I_0(s) = \frac{-I^{(s)}(Z_{el} + Z_a/2) + V^{(s)}(Z_{el} + Z_a/2 + 2/Y_a)Y_a/2}{(Z_{eo} + Z_a/2)(Z_{el} + Z_a/2)Y_a + (Z_{el} + Z_{eo} + Z_a)} \quad (68)$$

$$I_l(s) = \frac{I^{(s)}(Z_{eo} + Z_a/2) + V^{(s)}(Z_{eo} + Z_a/2 + 2/Y_a)Y_a/2}{(Z_{eo} + Z_a/2)(Z_{el} + Z_a/2)Y_a + (Z_{el} + Z_{eo} + Z_a)} \quad (69)$$

The source quantities $I^{(s)}$, $V^{(s)}$, Z_a , and Y_a are given in (28) - (31) and Z_{eo} and Z_{el} are the impedances seen at $z = z_0$ looking toward $z = 0$ and $z = l$ respectively

$$Z_{eo} = Z_c \frac{\gamma_c z_0 e + \Gamma_0 e^{-\gamma_c z_0}}{\gamma_c z_0 e - \Gamma_0 e^{-\gamma_c z_0}} \quad (70)$$

$$Z_{el} = Z_c \frac{\gamma_c (l - z_0) e + \Gamma_l e^{-\gamma_c (l - z_0)}}{\gamma_c (l - z_0) e - \Gamma_l e^{-\gamma_c (l - z_0)}} \quad (71)$$

Eqs.(68) and (69) for I_0 and I_l may be considerably simplified by neglecting terms involving products of $I^{(s)}$, $V^{(s)}$, Z_a , and Y_a ; under this approximation

$$I_o(s) \approx \frac{V(s) - Z_{el} I(s)}{Z_{el} + Z_{eo} + (Z_a + Y_a Z_{el} Z_{eo})} \quad (72)$$

$$I_l(s) \approx \frac{V(s) + Z_{eo} I(s)}{Z_{el} + Z_{eo} + (Z_a + Y_a Z_{el} Z_{eo})} \quad (73)$$

where the denominator terms in parentheses can be dropped if $|Z_{el} + Z_{eo}|$ is large in comparison to $|Z_a + Y_a Z_{el} Z_{eo}|$.

The internal signals induced by the sources at $z = z_o$ when the line is terminated in its characteristic impedance at each end are

$$I(0,s) = \frac{V(s) - Z_c I(s)}{2Z_c} e^{-\gamma_c z_o} \quad (74)$$

$$I(l,s) = \frac{V(s) + Z_c I(s)}{2Z_c} e^{-\gamma_c (l - z_o)} \quad (75)$$

When $Z_{to} = Z_c$ and $Z_{tl} = 0$, the short-circuit current at $z = l$ is

$$I_{sc}(l,s) = \frac{1}{Z_c} \left[V(s) + I(s) Z_c \right] e^{-\gamma_c (l - z_o)} \quad (76)$$

When $Z_{to} = Z_c$ and $Z_{tl} = \infty$, the open-circuit voltage at $z = l$ is

$$V_{oc}(l,s) = \left[V(s) + I(s) Z_c \right] e^{-\gamma_c (l - z_o)} \quad (77)$$

Terminal currents and voltages may be obtained for any other desired special cases by appropriate manipulation of (66) - (73).

The approximation involved in obtaining (72) and onward yields negligible errors, owing to the small magnitude of the quantities involved for typical cases.

2.4.1.3 Penetration

The voltages and currents appearing at the terminations of a coaxial cable which is excited from its exterior through imperfections in the shield may be calculated from a knowledge of the Thévenin and/or Norton equivalent circuits which represent the cable. Such equivalent circuits are given in the following two sections. In 2.4.1.3.1 equivalent circuit models for a cable with distributed coupling are presented; models for a cable excited at a single point are given in 2.4.1.3.2. In each case equivalent sources and immittances are given for the $z = l$ termination of a cable which extends from $z = 0$ to $z = l$.

2.4.1.3.1 Penetration Resulting From Distributed Excitation

The parameters of the Thévenin equivalent circuit for the cable termination at $z = l$ are

$$Z_{Th}(\ell, s) = Z_c \frac{\gamma_c^\ell e^{\gamma_c \ell} + \Gamma_o e^{-\gamma_c \ell}}{\gamma_c^\ell e^{\gamma_c \ell} - \Gamma_o e^{-\gamma_c \ell}} \quad (78)$$

$$V_{Th}^{(s)}(\ell, s) = \frac{2Z_c(g_m - \Gamma_o f_m) + 2(g_e + \Gamma_o f_e)}{\gamma_c^\ell e^{\gamma_c \ell} - \Gamma_o e^{-\gamma_c \ell}} \quad (79)$$

where Γ_o has been defined in (56) and f_m , g_m , f_e , and g_e have been defined in (58) - (63).

The parameters of the corresponding Norton equivalent circuit are

$$Y_N(\ell, s) = \frac{1}{Z_{Th}(\ell, s)} \quad (80)$$

$$I_N^{(s)}(\ell, s) = \frac{V_{Th}^{(s)}(\ell, s)}{Z_{Th}(\ell, s)} \quad (81)$$

Results for three special cases are given below.

$$(a) \quad Z_{to} = 0$$

$$Z_{Th}(l, s) = Z_c \tanh \gamma_c l \quad (82)$$

$$V_{Th}^{(s)}(l, s) = \frac{Z_c (g_m + f_m) + (g_e - f_e)}{\cosh \gamma_c l} \quad (83)$$

$$(b) \quad Z_{to} = Z_c$$

$$Z_{Th}(l, s) = Z_c \quad (84)$$

$$V_{Th}^{(s)}(l, s) = 2(Z_c g_m + g_e) e^{-\gamma_c l} \quad (85)$$

$$(c) \quad Z_{to} = \infty$$

$$Z_{Th}(l, s) = Z_c \coth \gamma_c l \quad (86)$$

$$V_{Th}^{(s)}(l, s) = \frac{Z_c (g_m - f_m) + (g_e + f_e)}{\sinh \gamma_c l} \quad (87)$$

2.4.1.3.2 Penetration Resulting From Discrete Excitation

The parameters of the Thévenin equivalent circuit for the cable termination at $z = l$ are

$$Z_{Th}(l, s) = Z_c \frac{e^{\gamma_c l} + \Gamma_o e^{-\gamma_c l}}{e^{\gamma_c l} - \Gamma_o e^{-\gamma_c l}} \quad (88)$$

$$V_{Th}^{(s)}(l, s) = V^{(s)} \frac{e^{\gamma_c z_o} - \Gamma_o e^{-\gamma_c z_o}}{e^{\gamma_c l} - \Gamma_o e^{-\gamma_c l}} + Z_c I^{(s)} \frac{e^{\gamma_c z_o} + \Gamma_o e^{-\gamma_c z_o}}{e^{\gamma_c l} - \Gamma_o e^{-\gamma_c l}} \quad (89)$$

The parameters of the corresponding Norton equivalent circuit are

$$Y_N(l, s) = \frac{1}{Z_{Th}(l, s)} \quad (90)$$

$$I_N^{(s)}(l, s) = \frac{V_{Th}^{(s)}(l, s)}{Z_{Th}(l, s)} \quad (91)$$

Results for three special cases are given below.

$$(a) \quad Z_{to} = 0$$

$$Z_{Th}(l, s) = Z_c \tanh \gamma_c l \quad (92)$$

$$V_{Th}^{(s)}(l, s) = V^{(s)} \frac{\cosh \gamma_c z_o}{\cosh \gamma_c l} + Z_c I^{(s)} \frac{\sinh \gamma_c z_o}{\cosh \gamma_c l} \quad (93)$$

$$(b) \quad Z_{to} = Z_c$$

$$Z_{Th}(l, s) = Z_c \quad (94)$$

$$V_{Th}^{(s)}(l, s) = \left[V^{(s)} + Z_c I^{(s)} \right] e^{-\gamma_c (l - z_o)} \quad (95)$$

$$(c) \quad Z_{to} = \infty$$

$$Z_{Th}(l, s) = Z_c \coth \gamma_c l \quad (96)$$

$$V_{Th}^{(s)}(l, s) = V^{(s)} \frac{\sinh \gamma_c z_o}{\sinh \gamma_c l} + Z_c I^{(s)} \frac{\cosh \gamma_c z_o}{\sinh \gamma_c l} \quad (97)$$

2.4.2 OPEN TRANSMISSION LINES

Another class of cables often encountered within an aeronautical system consists of open or unshielded wires, as opposed to the coaxial lines treated in the previous section. Engineering information pertinent to the analysis of open transmission lines is presented in this section.

2.4.2.1 Determination of Line Parameters

The analysis of transmission lines described in Sec. 1.3.2 requires a knowledge of the line capacitance and inductance per unit length, or equivalently, the characteristic impedance Z_c and propagation constant γ_c . For simple two-conductor systems (one conductor plus reference conductor, i.e., $N=1$), the usual line description is in terms of Z_c and γ_c . For multiconductor lines, however, the inductance and capacitance coefficients are more useful, especially when modes of different velocities can exist on the line.

It is assumed in the following that the transmission lines are in a homogeneous medium and that all losses can be neglected.

2.4.2.1.1 Isolated Transmission Lines

One type of transmission line found in EMP applications is an isolated bundle of conductors containing $N+1$ wires. For the $N=1$ case, we have the conventional two-wire line, and for $N \geq 2$ the line is said to be a multiconductor line. It will be assumed that the total current on the wire bundle is zero at every cross section. Fig. 10 illustrates a typical $(N+1)$ -wire line, with the $(N+1)$ st wire serving as a reference conductor.

The inductance per-unit-length matrix (L'_{ij}) of this line has elements [12]

$$L'_{ii} = \frac{\mu_0}{2\pi} \ln \left(\frac{D_{in}^2}{r_i r_n} \right), \quad n = N+1 \quad (98)$$

and

$$L'_{ij} = \frac{\mu_0}{2\pi} \ln \left(\frac{D_{in} D_{jn}}{D_{ij} r_n} \right), \quad i \neq j, \quad n = N+1 \quad (99)$$

for $i, j = 1, \dots, N$. It is assumed that all values of D and r satisfy the relation $D \gg r$. Here D_{ij} represents the distance between the centers of the i th and j th wires, and r_j is the radius of the j th wire. Note that the matrix (L'_{ij}) is of order $N \times N$.

With the assumption of a homogeneous dielectric of relative permittivity ϵ_r surrounding the line, the capacitance coefficient matrix may be evaluated as

$$(C'_{ij}) = \frac{1}{v^2} (L'_{ij})^{-1} \quad (100)$$

where the velocity v is given by $v = c/\sqrt{\epsilon_r}$ and $c = 3 \times 10^8$ m/sec is the free-space wave velocity. Under this restriction the characteristic impedance matrix may be written

$$(Z_{c_{ij}}) = v(L'_{ij}) \quad (101)$$

and the propagation constant is

$$(\gamma_{c_{ij}}) = \frac{s\sqrt{\epsilon_r}}{c} (\delta_{ij}) \quad (102)$$

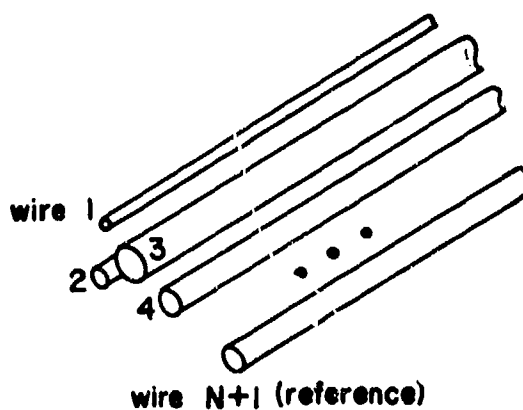


Fig. 10. Isolated $(N+1)$ -wire transmission line.

Table 7 gives these values for a two-, three-, and four-wire isolated line, each of which has wire radii much smaller than the wire separations.

2.4.2.1.2 Transmission Line Over a Ground Plane

Another transmission-line configuration frequently encountered in EMP problems is that of a bundle of N wires located near a perfectly conducting ground plane (Fig. 11). For this configuration TEM modes can exist on the transmission line without the requirement that the total current on the N wires be zero; the return current flows in the ground plane. One can regard this as an $(N+1)$ -wire transmission line by considering the ground plane to be an additional wire.

The inductance term for a single wire over a ground plane is [12]

$$L' = \frac{\mu_0}{2\pi} \ln(2h/r) \quad (103)$$

where r is the wire radius, h is the wire height above the ground plane, and $r \ll h$. Similarly, the mutual inductance between two wires above the ground is

$$L'_{ij} = \frac{\mu_0}{2\pi} \ln(D_{ij}/D_{ij}') \quad (104)$$

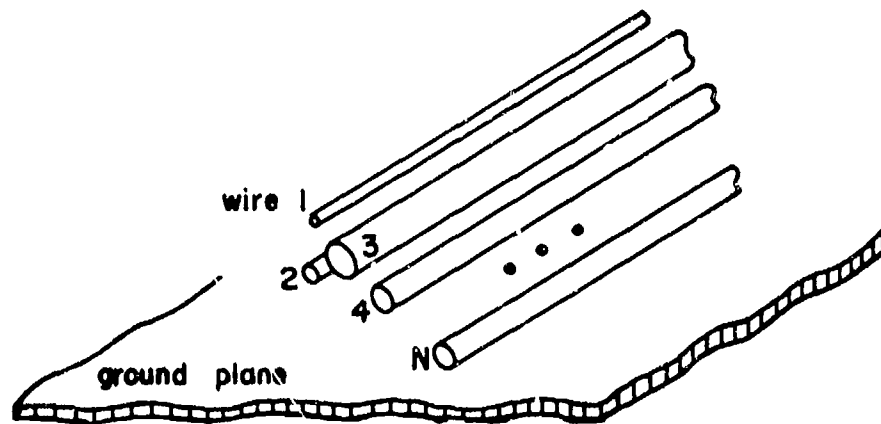


Fig. 11. N -wire transmission line over ground plane.

TABLE 7. ISOLATED TRANSMISSION LINE PARAMETERS (LOSSES NEGLECTED)

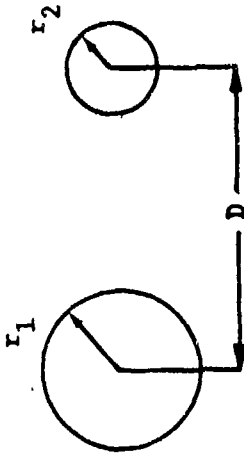
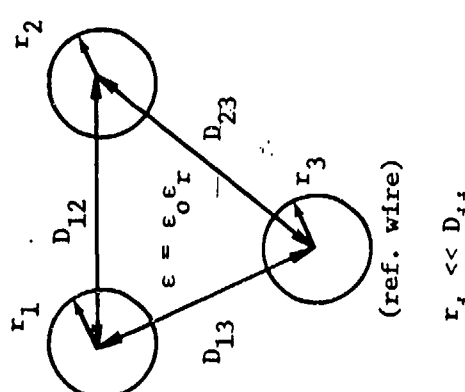
Isolated Two-Wire Line ($N = 1$)	Line Parameters
$\epsilon = \epsilon_0 \epsilon_r$  $r_1 \ll D$	$L' = \frac{\mu_0}{2\pi} \ln \left(\frac{D^2}{r_1 r_2} \right)$ $C' = 2\pi\epsilon / \ln \left(\frac{D^2}{r_1 r_2} \right)$ $\gamma_c = s\sqrt{\epsilon_r}/c$ $Z_c = \frac{60}{\sqrt{\epsilon_r}} \ln \left(\frac{D^2}{r_1 r_2} \right)$

TABLE 7. ISOLATED TRANSMISSION LINE PARAMETERS (LOSSES NEGLECTED) (Continued)

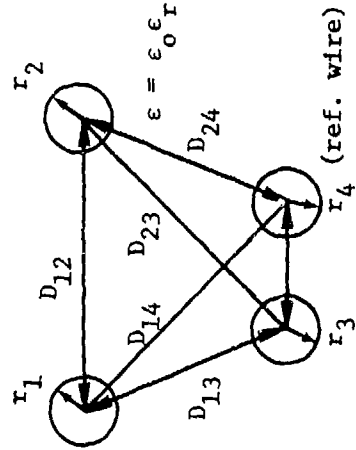
Isolated Three-Wire Line ($N = 2$)	Line Parameters
 <p style="text-align: center;">(ref. wire)</p> <p style="text-align: center;">$r_1 \ll D_{1j}$</p>	$(L'_{ij}) = \frac{\mu_0}{2\pi} \begin{bmatrix} a_{11} & a_{12} \\ a_{21} & a_{22} \end{bmatrix}$ $(C'_{ij}) = \frac{2\pi\epsilon}{\Delta} \begin{bmatrix} a_{22} & -a_{12} \\ -a_{21} & a_{11} \end{bmatrix}$ $(Y_{c_{ij}}) = \frac{s\sqrt{\epsilon}}{c} \begin{bmatrix} 1 & 0 \\ 0 & 1 \end{bmatrix}$ $(Z_{c_{ij}}) = \frac{60}{\sqrt{\epsilon}} \begin{bmatrix} a_{11} & a_{12} \\ a_{21} & a_{22} \end{bmatrix}$

$$\Delta = a_{11}a_{22} - a_{12}a_{21}$$

$$a_{ii} = \ln \left[(D_{13}^2) / (r_i r_3) \right] \quad (i = 1, 2)$$

$$a_{ij} = \ln \left[(D_{13}^D) / (D_{ij} r_3) \right] \quad (i \neq j)$$

TABLE 7. ISOLATED TRANSMISSION LINE PARAMETERS (LOSSES NEGLECTED) (Continued)

Isolated Four-Wire Line (N = 3)	Line Parameters
 <p style="text-align: center;">$r_1 \ll D_{1j}$</p>	$(L'_{ij}) = \frac{\mu_0}{2\pi} \begin{bmatrix} a_{11} & a_{12} & a_{13} \\ a_{12} & a_{22} & a_{23} \\ a_{13} & a_{23} & a_{33} \end{bmatrix}$ $(C'_{ij}) = \frac{2\pi\epsilon}{\Delta} \begin{bmatrix} (a_{22}a_{33} - a_{23}^2) & -(a_{12}a_{33} - a_{13}a_{23}) & -(a_{13}a_{22} - a_{12}a_{23}) \\ -(a_{12}a_{33} - a_{13}a_{23}) & (a_{11}a_{33} - a_{13}^2) & -(a_{11}a_{23} - a_{13}a_{12}) \\ -(a_{13}a_{22} - a_{12}a_{23}) & -(a_{11}a_{23} - a_{13}a_{12}) & (a_{11}a_{22} - a_{12}^2) \end{bmatrix}$ $(\gamma_{cij}) = \frac{s\sqrt{\epsilon}}{c} \begin{bmatrix} 1 & 0 & 0 \\ 0 & 1 & 0 \\ 0 & 0 & 1 \end{bmatrix} \quad (Z_{cij}) = \frac{60}{\sqrt{\epsilon_r}} \begin{bmatrix} a_{11} & a_{12} & a_{13} \\ a_{12} & a_{22} & a_{23} \\ a_{13} & a_{23} & a_{33} \end{bmatrix}$

$$\Delta = a_{11}(a_{22}a_{33} - a_{23}^2) - a_{12}(a_{12}a_{33} - a_{13}a_{23}) + a_{13}(a_{12}a_{23} - a_{22}a_{13})$$

$$a_{11} = \ln \left[\frac{(D_{14}^2)}{(r_1 r_4)} \right] \quad (i = 1, 2, 3)$$

$$a_{ij} = \ln \left[\frac{(D_{i4} D_{j4})}{(D_{ij} r_4)} \right] \quad (i \neq j)$$

where D_{ij} is the distance between the two wires and D_{ij}' is the distance from one wire to the image of the other in the ground plane. With (103) and (104) the capacitance coefficient matrix, the impedance matrix and the propagation matrix can be calculated from (100) - (102). Table 8 presents these quantities for one-, two-, and three-wire lines over a ground plane.

2.4.2.2 Coupling to Open Lines

The lumped or distributed equivalent voltage and current sources which drive the transmission-line equations of open lines are discussed in this section. Two types of excitation illumination by a plane wave (Sec. 2.4.2.2.1) and coupling from a parallel wire (Sec. 2.4.2.2.2) are discussed in detail; excitation by an aperture is briefly discussed (Sec. 2.4.2.2.3).

2.4.2.2.1 Transmission Line Illuminated by Plane Wave

The distributed voltage and current sources for TEM excitation of an open $(N+1)$ -wire transmission line are related to the incident magnetic and electric fields, respectively. One of the assumptions made is that the separation of the conductors is small compared with a wavelength. With this assumption the general source terms for TEM modes on an N -line are (see Sec. 1.3.2)

$$(V_i'(s)) = s \mu_0 (\vec{d}_i \times \vec{I}_z) \cdot \vec{H}^i \quad (105)$$

$$(I_i'(s)) = -s (C_{ij}') (\vec{d}_j \cdot \vec{E}^i) \quad (106)$$

where \vec{d}_i is a displacement vector between the electrical centers of the i th conductor and the reference conductor [13] and \vec{E}^i and \vec{H}^i are the incident electric and magnetic fields. For wires with radii much smaller than the wire separations, these distances become equal to the geometrical separation between centers of the wires.

For the two-wire line illustrated in Fig. 12 the per-unit-length voltage and current sources take the form

TABLE 8. TRANSMISSION LINES OVER GROUND PLANE (LOSSES NEGLECTED)

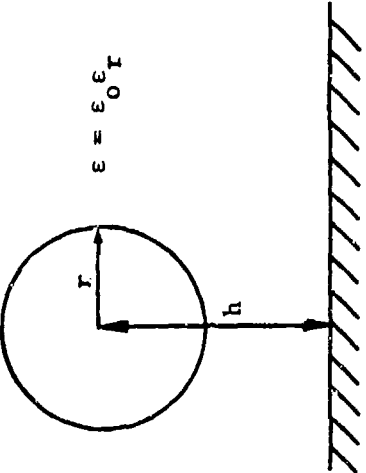
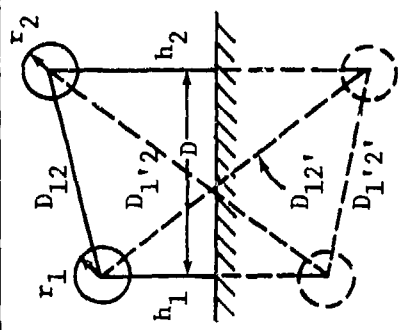
Single Wire (N = 1)	Line Parameters
 <p>$\epsilon = \epsilon_0 \epsilon_r$</p> <p>$r$</p> <p>$h$</p> <p>$\gamma \ll h$</p>	$L' = \frac{\mu_0}{2\pi} \ln(2h/r)$
	$C' = 2\pi\epsilon / \ln(2h/r)$
	$\gamma_c = s\sqrt{\epsilon_r}/c$
	$Z_c = \frac{60}{\sqrt{\epsilon_r}} \ln(2h/r)$

TABLE 8. TRANSMISSION LINES OVER GROUND PLANE (LOSSES NEGLECTED) (Continued)

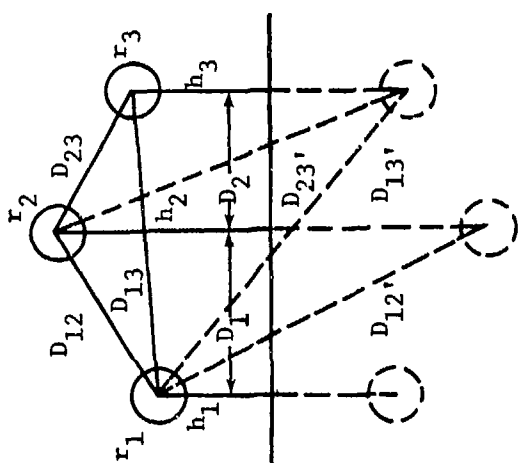
Two Wires (N = 2)	Line Parameters
 <p style="text-align: center;">$r_1 < D_{1j}, h_1$</p> <p>$D_{1j} = D_{j1}, D_{1j}' = D_{i'j}, D_{1j} = D_{i'j}'$ (This also applies for the three-wire line on the following page.)</p>	$(L_{1j}') = \frac{\mu_0}{2\pi} \begin{bmatrix} a_{11} & a_{12} \\ a_{21} & a_{22} \end{bmatrix}$
	$(C_{1j}') = \frac{2\pi\epsilon}{\Delta} \begin{bmatrix} a_{22} & -a_{12} \\ -a_{21} & a_{11} \end{bmatrix}$
	$(\gamma_{c1j}) = \frac{s\sqrt{\epsilon_r}}{c} \begin{bmatrix} 1 & 0 \\ 0 & 1 \end{bmatrix}$
	$(Z_{c1j}) = \frac{60}{\sqrt{\epsilon_r}} \begin{bmatrix} a_{11} & a_{12} \\ a_{21} & a_{22} \end{bmatrix}$

$$\Delta = a_{11}a_{22} - a_{12}a_{21}$$

$$a_{1i} = \ln(2h_i/r_i) \quad (i = 1, 2)$$

$$a_{ij} = \ln(D_{ij}'/D_{ij}) \quad (i \neq j)$$

TABLE 8. TRANSMISSION LINES OVER GROUND PLANE (LOSSES NEGLECTED) (Continued)

Three Wires (N = 3)	Line Parameters
	$(L'_{ij}) = \frac{\mu_0}{2\pi} \begin{bmatrix} a_{11} & a_{12} & a_{13} \\ a_{21} & a_{22} & a_{23} \\ a_{31} & a_{32} & a_{33} \end{bmatrix}$ $(C'_{ij}) = \mu_0 \epsilon (L'_{ij})^{-1}$ $(\gamma_{cij}) = \frac{s\sqrt{\epsilon_r}}{c} \begin{bmatrix} 1 & 0 & 0 \\ 0 & 1 & 0 \\ 0 & 0 & 1 \end{bmatrix}$ $(Z_{cij}) = \frac{60}{\sqrt{\epsilon_r}} \begin{bmatrix} a_{11} & a_{12} & a_{13} \\ a_{21} & a_{22} & a_{23} \\ a_{31} & a_{32} & a_{33} \end{bmatrix}$

$$a_{ii} = \ln(2h_i/r_i) \quad (i = 1, 2, 3)$$

$$a_{ij} = \ln(D_{ij}/D_{ij}') \quad (i \neq j)$$

$$V'(s)(z) = s \mu_0 d_1 H^1 \sin \theta e^{-\gamma z \sin \theta} \quad (107)$$

$$I'(s)(z) = -s C' d_1 E^1 e^{-\gamma z \sin \theta}$$

where $\gamma = s\sqrt{\epsilon_r}/c$,

$$d_1 = D \sqrt{\left[1 - \left(\frac{r_1 + r_2}{D}\right)^2\right] \left[1 - \left(\frac{r_1 - r_2}{D}\right)^2\right]} \quad (108)$$

and the line capacitance is given by

$$C' = 2\pi\epsilon \left[\operatorname{arccosh} \left(\frac{D^2 - r_1^2 - r_2^2}{2r_1 r_2} \right) \right]^{-1} \quad (109)$$

with r_1, r_2 being the wire radii and D the wire separation. For $D \gg r_1, r_2$, (109) reduces to

$$C' \approx 2\pi\epsilon / \ln(D^2/r_1 r_2) \quad (110)$$

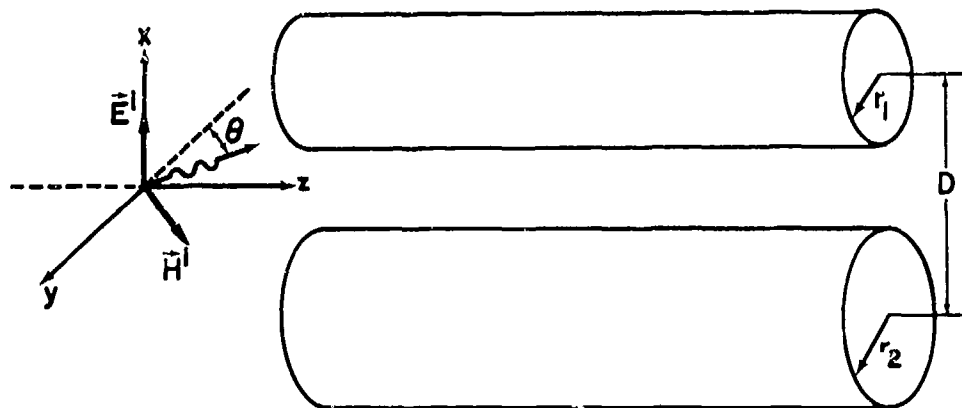


Fig. 12. Section of two-wire transmission line illuminated by an incident plane wave. \vec{H}^1 and the direction of propagation lie in the y, z plane.

2.4.2.2.2 Excitation of Transmission Line by a Parallel Line

A common type of transmission-line excitation in internal EMP interaction problems is that shown in Fig. 13. A wire with a large current (the exciting wire) is located near a second bundle of N wires over a ground plane. This entire internal interaction problem can be viewed as $N+1$ wires over a ground plane in multiconductor transmission-line theory. The capacitance and inductance coefficients for the entire line may be computed or estimated using (100) - (104). It will be assumed that the parasitic currents in the N wires do not substantially modify the driving current in the $(N+1)$ st wire.

Defining the inductance and capacitance coefficients for the entire $(N+2)$ -wire system as $(L'_{ij})_{N+1}$ and $(C'_{ij})_{N+1}$ respectively, the voltage and current sources on the i th wire of the wire bundle can be expressed as

$$\begin{aligned} I'_i(s)(s,z) &= -s C'_{i,N+1} V_{N+1}(s,z), \quad i=1, \dots, N \\ V'_i(s)(s,z) &= -s L'_{i,N+1} I_{N+1}(s,z), \quad i=1, \dots, N \end{aligned} \quad (111)$$

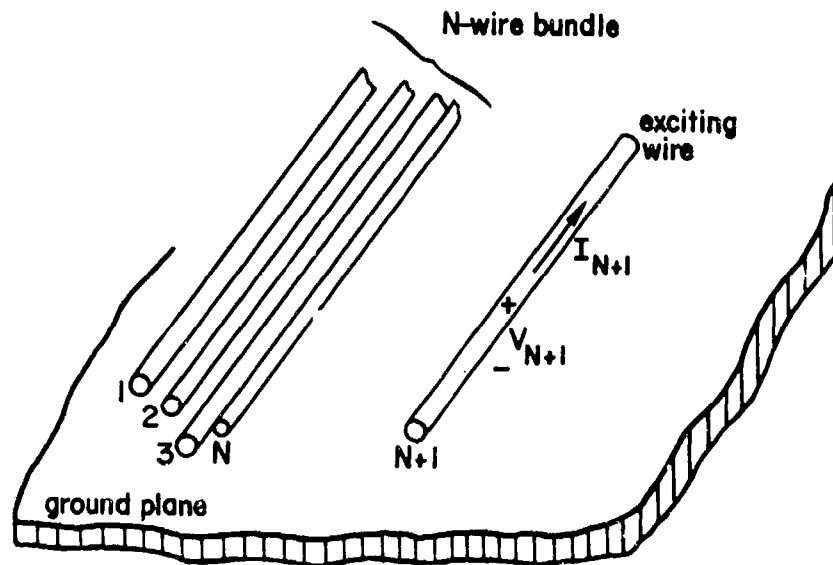


Fig. 13. Wire driving N -wire bundle.

where $V_{N+1}(s,z)$ and $I_{N+1}(s,z)$ are the voltage and current at position z on the driving line, and $C'_{i,N+1}$ and $L'_{i,N+1}$ are the individual capacitance and inductance coefficients between the i th wire and the driving wire.

The N -wire bundle can now be treated as a multiconductor line and the presence of the $(N+1)$ st wire ignored. For this approach to be valid it is necessary that the loading impedance of the driving line be connected only to the reference conductor and not to other wires within the N -wire bundle; otherwise the driving wire is strongly coupled to the N -wire bundle through the load.

In Fig. 14 is shown the cross-section of a two-wire line located over a ground plane and excited by a third wire. From table 8 the inductance coefficients are

$$L'_{13} = \frac{\mu_0}{4\pi} \ln \left(\frac{(D_1 + D_2)^2 + (h_3 + h_1)^2}{(D_1 + D_2)^2 + (h_3 - h_1)^2} \right) \quad (112)$$

$$L'_{23} = \frac{\mu_0}{4\pi} \ln \left(\frac{D_2^2 + (h_3 + h_2)^2}{D_2^2 + (h_3 - h_2)^2} \right) \quad (113)$$

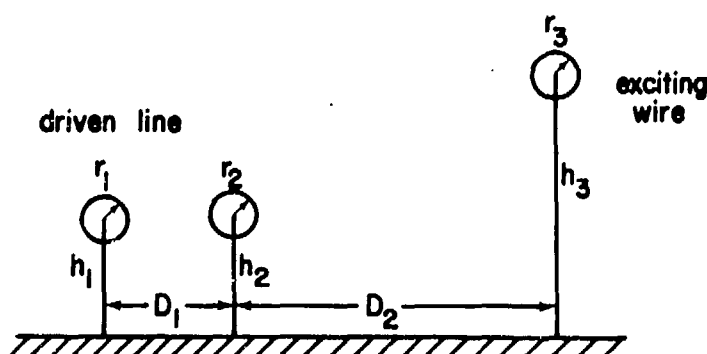


Fig. 14. Two-wire line excited by a parallel wire.

The corresponding capacitance coefficients are

$$C'_{13} = \frac{\pi\epsilon \ln \left(\frac{(D_1 + D_2)^2 + (h_3 + h_1)^2}{(D_1 + D_2)^2 + (h_3 - h_1)^2} \right)}{\ln \left(\frac{2h_1}{r_1} \right) \ln \left(\frac{2h_3}{r_3} \right)} \quad (114)$$

$$C'_{23} = \frac{\pi\epsilon \ln \left(\frac{D_2^2 + (h_3 + h_2)^2}{D_2^2 + (h_3 - h_2)^2} \right)}{\ln \left(\frac{2h_2}{r_2} \right) \ln \left(\frac{2h_3}{r_3} \right)} \quad (115)$$

The voltage and current sources on wires 1 and 2 can be determined from (111), once the response of wire 3 is known.

2.4.2.2.3 Transmission Lines Excited Through Apertures

Another important coupling mechanism results from an aperture in a ground plane and illuminating a multiconductor transmission line.

In general, the presence of the aperture will not only provide excitation to the line, but will also modify the transmission-line parameters in the vicinity of the line. Engineering formulas are presented in Secs. 2.2.1 and 2.2.2 for the equivalent sources and circuit parameters of an aperture in a ground plane passing under a single conductor. No comparable results for multiconductor lines are available.

The case of a transmission line excited by a localized source, e.g., a small electric or magnetic dipole in the vicinity of the line, can be treated in exactly the same way as the aperture coupling problem. The principal difference is that any orientation of the dipole moments is permitted, and the dipoles need not reside on a ground plane. There exist no readily available general results for the source term for this type of excitation.

2.4.2.3 Propagation Along Open Transmission Lines

When the equivalent voltage and current sources have been determined, it is possible to evaluate the currents and voltages along the line, as described in Sec. 1.3.2. In this section data for a number of cases of excited transmission lines are given. Particular emphasis is given to the behavior of the transmission-line load currents.

2.4.2.3.1 Two-Wire Line Response to Plane Waves

A two-wire line illuminated by a plane wave is shown in Fig. 15. The incident electric field is parallel to the load terminations (the x-direction). The current flowing in the load at $z = l$ is given by [16]

$$I(l, s) = \frac{E^i(s)b}{2M(s)} \left[2Z_c - (Z_c - Z_1)e^{-\gamma l(1 + \sin \theta)} - (Z_c + Z_1)e^{\gamma l(1 - \sin \theta)} \right] \quad (116)$$

where Z_c = characteristic impedance of the line, $\gamma = s/c$, and

$$M(s) = Z_c(Z_1 + Z_2)\cosh(\gamma l) + (Z_c^2 + Z_1Z_2)\sinh(\gamma l)$$

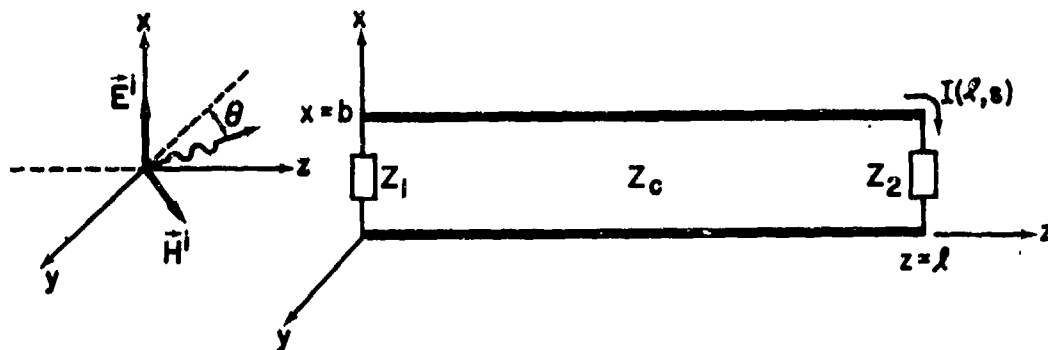


Fig. 15. Two-wire line illuminated by plane wave with \vec{E}^i parallel to x-axis.

For the special case of grazing incidence ($\theta = 90^\circ$), Fig. 16a shows the frequency response of the load current normalized with respect to the incident field for a 1-meter line having a characteristic impedance of 635Ω . Fig. 16b shows the same quantity for broadside incidence ($\theta = 0^\circ$).

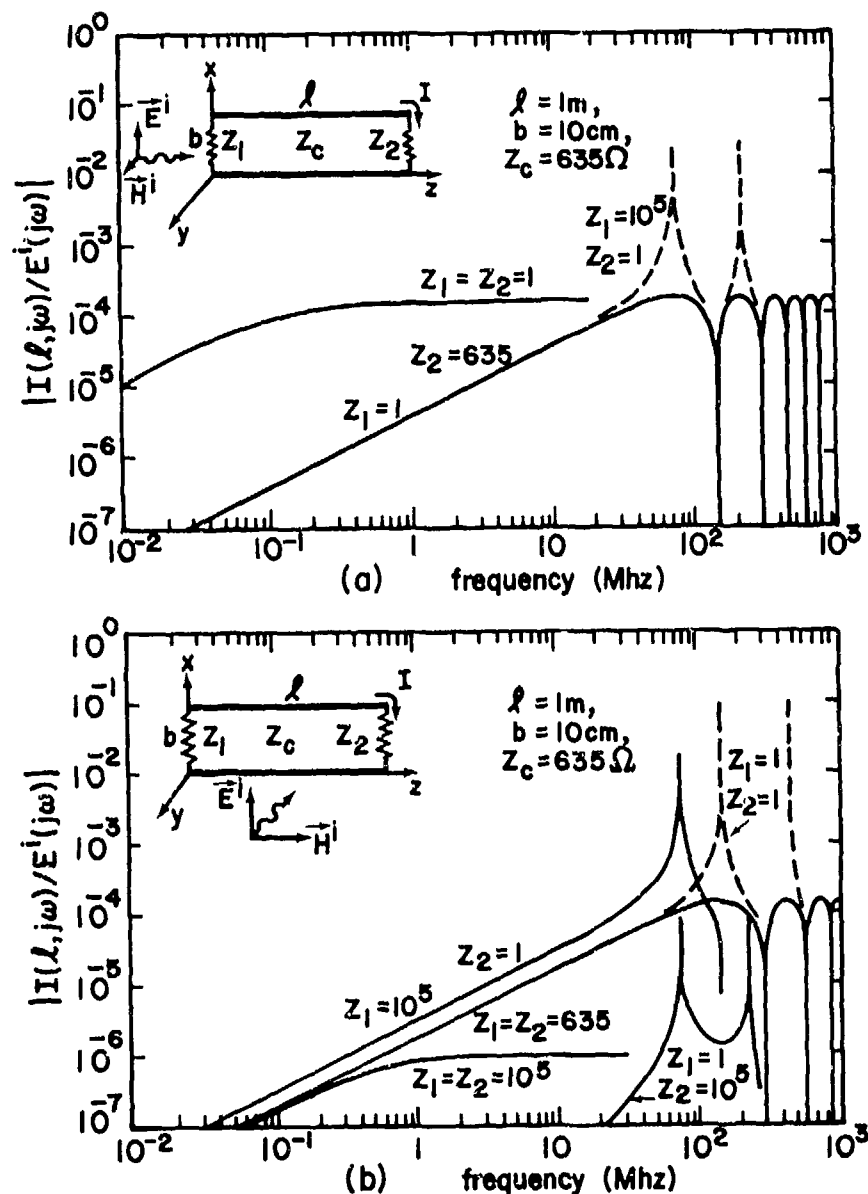


Fig. 16. Normalized load current for a 1 meter line excited by a plane wave with $\vec{E}^i = E^i \hat{x}$, traveling (a) in z -direction ($\theta = 90^\circ$) and (b) in $-y$ -direction ($\theta = 0^\circ$) [16].

Note that for each of these figures, various combinations of load impedance Z_1 and Z_2 are used.

The load current for the case shown in Fig. 17 is given by [16]

$$I(\ell, s) = \frac{K(s)}{\gamma M(s)} \left[\frac{(Z_c + Z_1)}{2} e^{\gamma \ell} - \frac{(Z_c - Z_1)}{2} e^{-\gamma \ell} - Z_1 \right] \quad (117)$$

where $K(s)$ is the difference of the two incident electric fields on the two parallel wires of the transmission line and is given by

$$K(s) = E^i(b, s) - E^i(0, s) \quad (118)$$

The other symbols are the same as in (116).

Fig. 18 shows the ratio $|I/E^i|$ as a function of frequency for the same transmission line used in Fig. 16a, for the case where the wave travels in the x -direction ($\theta = 90^\circ$).

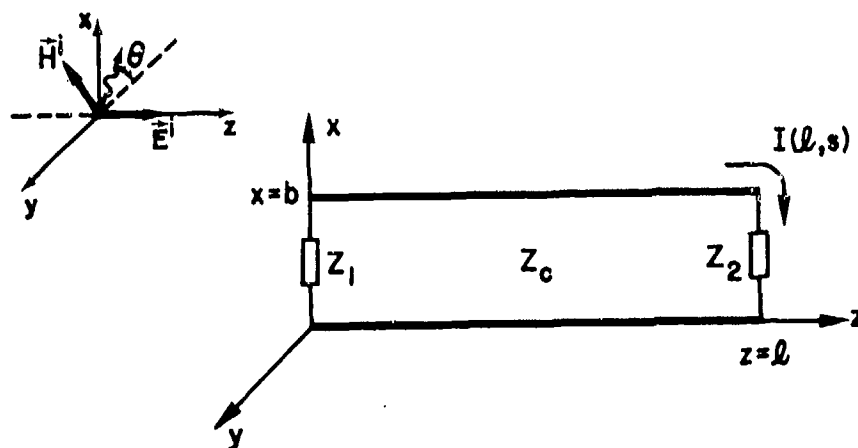


Fig. 17. Two-wire line illuminated by plane wave with \vec{E}^i parallel to z -axis and \vec{H}^i in x, y plane.

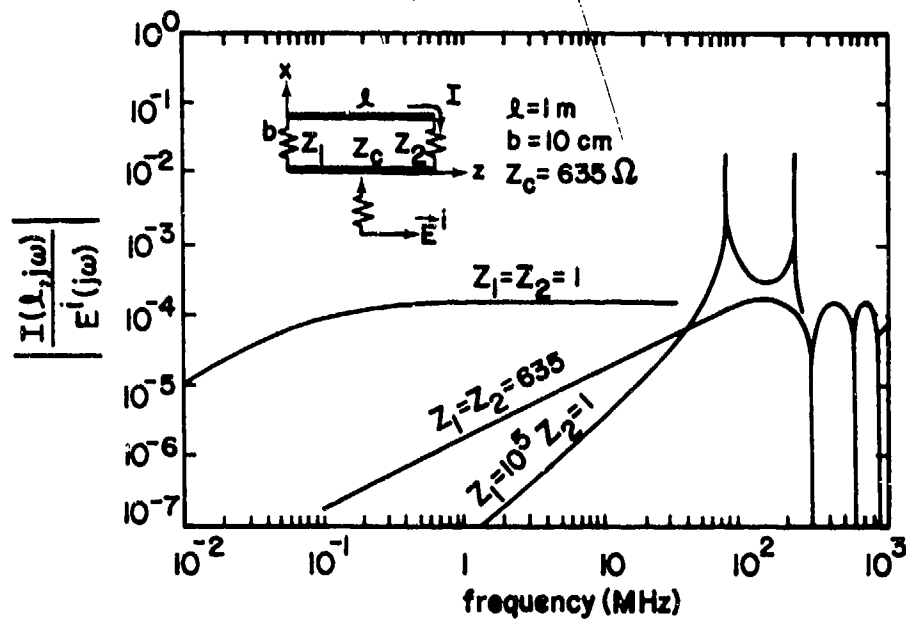


Fig. 18. Load current for 1 meter line excited by plane wave with $\vec{E}^i = \hat{z} E^i$ traveling in x-direction [16].

The current $I(0, s)$ for the configuration shown in Fig. 19 is given for various values of Z_1 and Z_2 in table 9 [17].

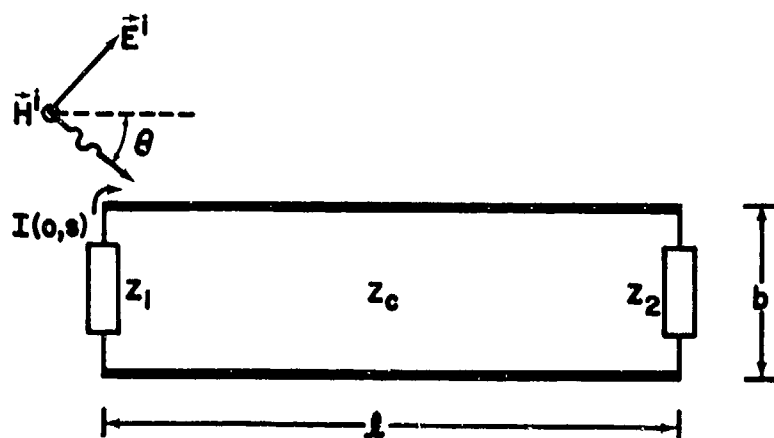


Fig. 19. Two-wire line illuminated by plane wave with \vec{H}^i normal to the plane of the line.

TABLE 9. LOAD CURRENT $I(0,s)$ FOR CONFIGURATION OF FIG. 19

Terminating Impedances	Normalized Current $(2Z_c/E^1_b)I(0,s)$
$Z_1 = Z_c$ $Z_2 = Z_c$	$1 - e^{-\gamma l(1 + \cos \theta)}$
$Z_1 = Z_c$ $Z_2 = 0$	$1 - e^{-2\gamma l}$
$Z_1 = Z_c$ $Z_2 = \infty$	$1 + e^{-2\gamma l} - 2e^{-\gamma l(1 + \cos \theta)}$
$Z_1 = 0$ $Z_2 = 0$	2
$Z_1 = 0$ $Z_2 = \infty$	$2 - 2e^{-\gamma l \cos \theta} \operatorname{sech}(\gamma l)$
$Z_1 = 0$ $Z_2 = Z_c$	$2 - 2e^{-\gamma l(1 + \cos \theta)}$

2.4.2.3.2 Two-Wire Line Response to Localized Sources

Fig. 20 shows the load current response at $z = \ell$ for a 10 meter line which is excited by a current loop located a distance $R = 2$ meters away from the center of the line. The loop is located along the midpoint of

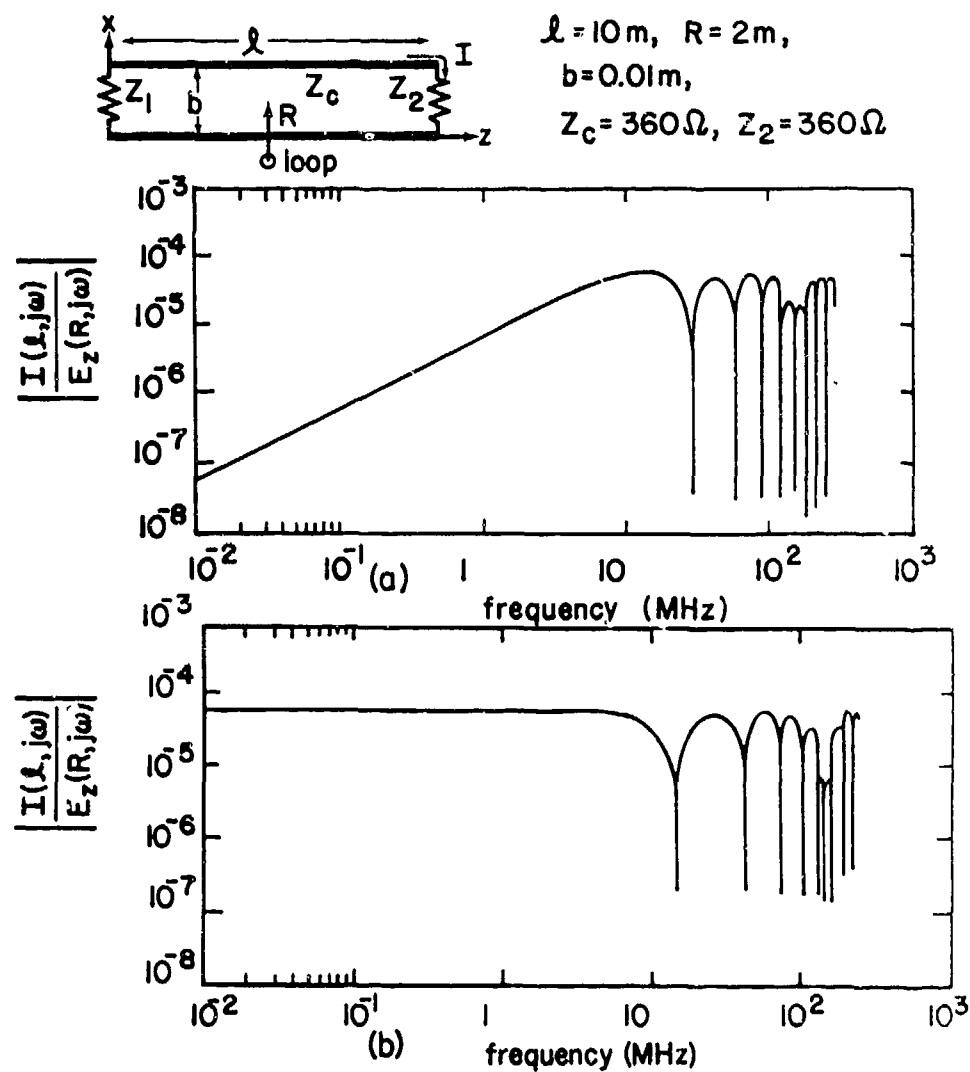


Fig. 20. Current transfer function for a 10 meter line excited by a current loop. (a) $Z_1 = 10^7\Omega$; (b) $Z_1 = 1\Omega$.

the transmission line at the point $z = 5$ meters and lies in the plane of the wires of the transmission line. The corresponding results for a small point electric dipole are illustrated in Fig. 21.

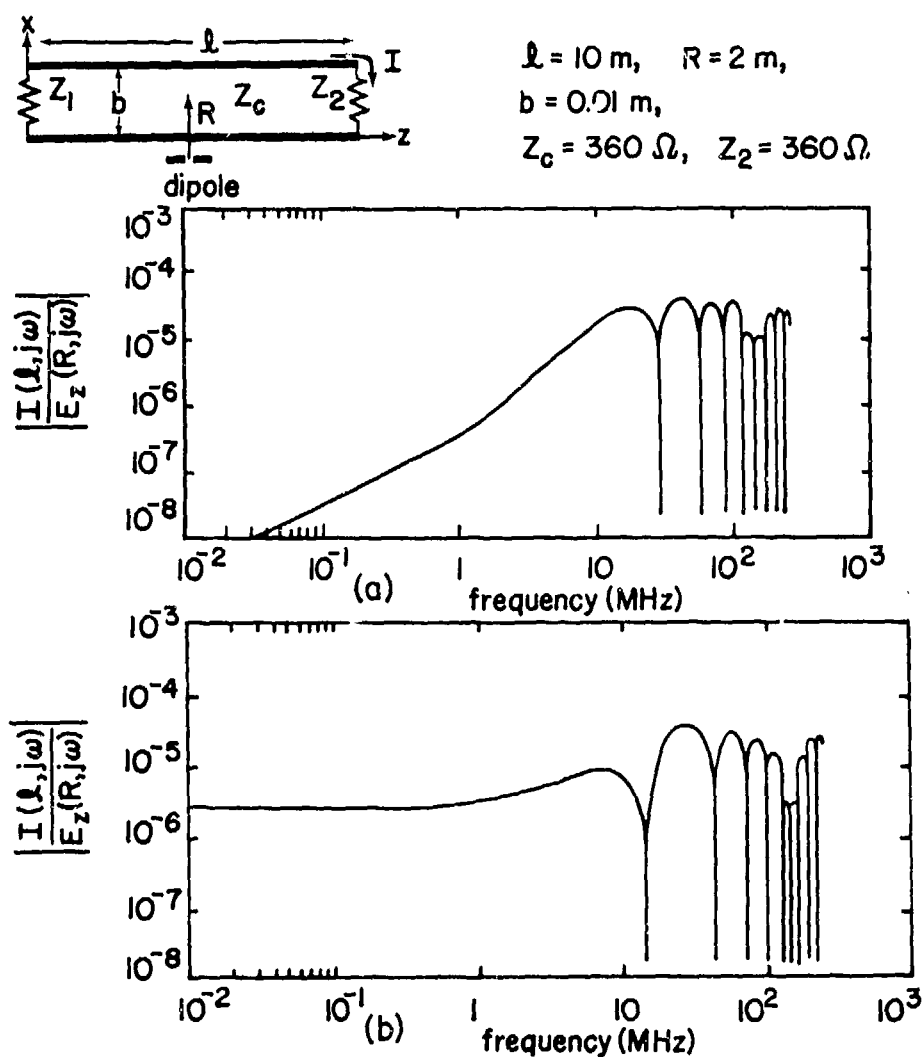


Fig. 21. Current transfer function for a 10 meter line excited by an electric dipole. (a) $Z_1 = 10^7 \Omega$; (b) $Z_1 = 1 \Omega$.

2.4.2.3.3 Multiconductor Line Response

In this section, we present the analysis of a rather simple network, a single section of multiconductor transmission line, using the BLT formalism outlined in Sec. 1.3.2.3.

A two-wire line above a ground plane is illustrated in Fig. 22. The corresponding linear graph for this simple network is illustrated in Fig. 22a. Because the region around the multiconductor line is homogeneous,

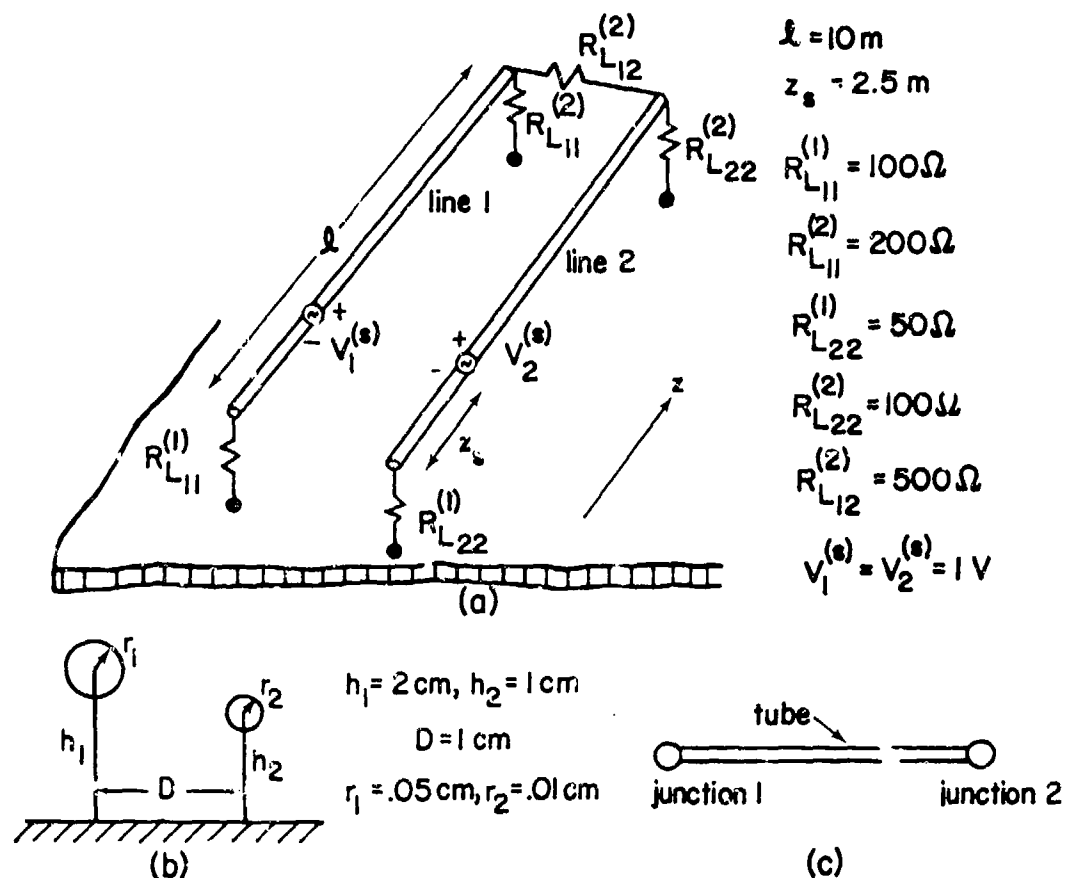


Fig. 22. (a) Two-wire line over ground, excited by voltage sources; (b) cross-sectional view; and (c) linear graph representation.

isotropic, and lossless, the per-unit-length inductance matrix (L'_{nm}) is directly proportional to the inverse of the capacitance matrix $(C'_{nm})^{-1}$. All current modes propagate at the same velocity and the transformation matrix (T_{nm}) of Sec. 1.3.2.2.3 may be taken to be the unit matrix, (δ_{nm}) .

For this special case the tube propagation matrix (P_{nm}) is given by

$$(P_{nm}) = \begin{bmatrix} e^{\gamma l} & 0 \\ 0 & e^{\gamma l} \end{bmatrix} \quad (119)$$

Since this network consists of only one tube, the propagation supermatrix in Sec. 1.3.2.3 is just a 2×2 block supermatrix which, when expressed in terms of its scalar components, has the form

$$\begin{bmatrix} I_1^{(r)}(0) \\ I_2^{(r)}(0) \\ I_1^{(r)}(l) \\ I_2^{(r)}(l) \end{bmatrix} = \begin{bmatrix} \begin{pmatrix} 0 & 0 \\ 0 & 0 \end{pmatrix} & \begin{pmatrix} e^{\gamma l} & 0 \\ 0 & e^{\gamma l} \end{pmatrix} \\ \begin{pmatrix} e^{\gamma l} & 0 \\ 0 & e^{\gamma l} \end{pmatrix} & \begin{pmatrix} 0 & 0 \\ 0 & 0 \end{pmatrix} \end{bmatrix} \begin{bmatrix} I_1^{(i)}(0) \\ I_2^{(i)}(0) \\ I_1^{(i)}(l) \\ I_2^{(i)}(l) \end{bmatrix} + \begin{bmatrix} \vartheta_1 \\ \vartheta_2 \\ \vartheta_1 \\ \vartheta_2 \end{bmatrix} \quad (120)$$

where the subscripts on the reflected or incident current components refer to actual wire components, due to the degeneracy of current modes and the particular choice of the transform matrix (T_{nm}) .

The combined current sources in the above equation are due only to the physical voltage sources $V_1^{(s)}$ and $V_2^{(s)}$ on the line. Following (145) of Chap. 1.3, these terms are expressible as

$$\begin{bmatrix} \vartheta_1 \\ \vartheta_2 \\ \vartheta_1 \\ \vartheta_2 \end{bmatrix} = \frac{1}{2} \begin{bmatrix} e^{\gamma z_s} & 0 \\ 0 & e^{\gamma z_s} \end{bmatrix} \begin{bmatrix} Z_{c_{nm}} \end{bmatrix}^{-1} \begin{bmatrix} V_1^{(s)} \\ V_2^{(s)} \end{bmatrix} \quad (121)$$

$$\begin{bmatrix} \varphi_1 \\ \varphi_2 \end{bmatrix} = \frac{1}{2} \begin{bmatrix} e^{\gamma(\ell - z_s)} & 0 \\ 0 & e^{\gamma(\ell - z_s)} \end{bmatrix} \begin{bmatrix} Z_{c_{nm}} \end{bmatrix}^{-1} \begin{bmatrix} V_1^{(s)} \\ V_2^{(s)} \end{bmatrix} \quad (122)$$

where z_s is the source location, as illustrated in Fig. 21, and $(Z_{c_{nm}})$ is the characteristic impedance matrix for the multiconductor line.

From table 8 this impedance matrix can be calculated to be

$$(Z_{c_{nm}}) = \begin{bmatrix} 262.9 & 48.3 \\ 48.3 & 317.9 \end{bmatrix} \text{ ohms} \quad (123)$$

Its inverse, for use in (121) and (122), is

$$(Z_{c_{nm}})^{-1} = \begin{bmatrix} 3.9 & -0.59 \\ -0.59 & 3.2 \end{bmatrix} \times 10^{-3} \text{ mhos} \quad (124)$$

At the $z = 0$ end of the tube, the current reflection coefficient matrix $(\Gamma_{1_{nm}})$ is given by

$$(\Gamma_{1_{nm}}) = \left((Z_{c_{nm}}) + (Z_{L_{nm}}^{(1)}) \right)^{-1} \left((Z_{c_{nm}}) - (Z_{L_{nm}}^{(1)}) \right) \quad (125)$$

where $(Z_{L_{nm}}^{(1)})$ is the load impedance matrix at $z = 0$

$$(Z_{L_{nm}}^{(1)}) = \begin{bmatrix} 100 & 0 \\ 0 & 50 \end{bmatrix} \text{ ohms} \quad (126)$$

The reflected and incident currents at this junction are thus related by

$$\begin{bmatrix} I_1^{(r)}(0) \\ I_2^{(r)}(0) \end{bmatrix} = (\Gamma_{1_{nm}}) \begin{bmatrix} I_1^{(i)}(0) \\ I_2^{(i)}(0) \end{bmatrix} \quad (127)$$

and an evaluation of (125) gives numerical values for $(\Gamma_{1_{nm}})$

$$(\Gamma_{1_{nm}}) = \begin{bmatrix} .44 & .04 \\ .07 & .72 \end{bmatrix} \quad (128)$$

A similar relation exists for the reflection coefficient $(\Gamma_{2_{nm}})$ at $z = l$, involving the load impedance at that point. From Fig. 22 the load impedance can be found to be

$$(Z_{I_{nm}}^{(2)}) = \begin{bmatrix} 150 & 50 \\ 50 & 87.5 \end{bmatrix} \text{ ohms} \quad (129)$$

and the corresponding current reflection coefficient is

$$(\Gamma_{2_{nm}}) = \begin{bmatrix} .29 & -.15 \\ -.07 & .60 \end{bmatrix} \quad (130)$$

Hence, using (128) and (130) the scattering equations given in Chap. 1.3 take the form

$$\begin{bmatrix} \begin{pmatrix} I_1^{(r)}(0) \\ I_2^{(r)}(0) \end{pmatrix} \\ \begin{pmatrix} I_1^{(r)}(l) \\ I_2^{(r)}(l) \end{pmatrix} \end{bmatrix} = \begin{bmatrix} \begin{pmatrix} .44 & .04 \\ .07 & .72 \end{pmatrix} & \begin{pmatrix} 0 & 0 \\ 0 & 0 \end{pmatrix} \\ \begin{pmatrix} 0 & 0 \\ 0 & 0 \end{pmatrix} & \begin{pmatrix} .29 & -.15 \\ -.07 & .60 \end{pmatrix} \end{bmatrix} \begin{bmatrix} \begin{pmatrix} I_1^{(i)}(0) \\ I_2^{(i)}(0) \end{pmatrix} \\ \begin{pmatrix} I_1^{(i)}(l) \\ I_2^{(i)}(l) \end{pmatrix} \end{bmatrix} \quad (131)$$

and the final BLT equation for the incident currents given in Chap. 1.3 becomes

$$\begin{bmatrix} \begin{pmatrix} I_1^{(i)}(0) \\ I_2^{(i)}(0) \end{pmatrix} \\ \begin{pmatrix} I_1^{(i)}(l) \\ I_2^{(i)}(l) \end{pmatrix} \end{bmatrix} = \begin{bmatrix} \begin{pmatrix} .44 & .04 \\ .07 & .72 \end{pmatrix} \begin{pmatrix} e^{\gamma l} & 0 \\ 0 & e^{\gamma l} \end{pmatrix} \\ \begin{pmatrix} e^{\gamma l} & 0 \\ 0 & e^{\gamma l} \end{pmatrix} \begin{pmatrix} .29 & -.15 \\ -.07 & .60 \end{pmatrix} \end{bmatrix}^{-1} \begin{bmatrix} \begin{pmatrix} \vartheta_1 \\ \vartheta_2 \end{pmatrix}_1 \\ \begin{pmatrix} \vartheta_1 \\ \vartheta_2 \end{pmatrix}_2 \end{bmatrix} \quad (132)$$

with the sources \mathcal{S} given by (121) and (122).

This BLT equation may be solved for the incident currents and the total load currents by evaluating (131). Fig. 23a illustrates the normalized currents at $z = \ell$ in wires 1 and 2 as a function of frequency for voltage excitation on line 1 only. Fig. 23b shows the corresponding curves for excitation on line 2 only.

Representative numerical results are shown in Figs. 24 and 25 for a terminated two-wire line located over a perfectly conducting ground plane and excited by a normally incident plane wave whose electric vector is parallel to the axis of the line [18].

2.4.2.4 Penetration

The penetration problem is considered to be the transfer of energy from the transmission line to the load impedance connected to the line. The effects of the transmission line and sources are represented by a Thévenin equivalent circuit at the load in question.

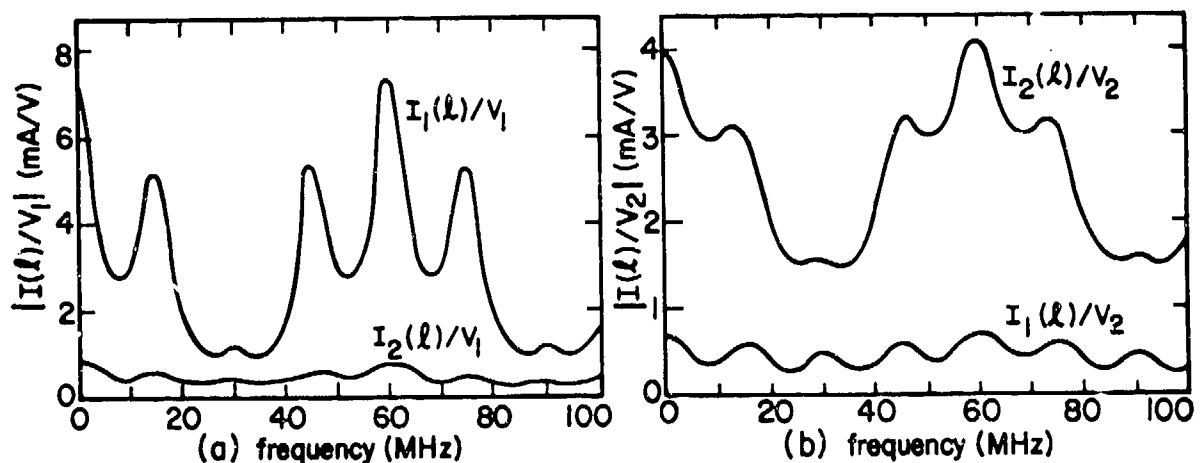


Fig. 23. Response of currents in wires 1 and 2 for a 10-m line in Fig. 22 as a function of frequency. (a) $V_1(s)$ excited, $V_2(s) = 0$; (b) $V_1(s) = 0$, $V_2(s)$ excited.

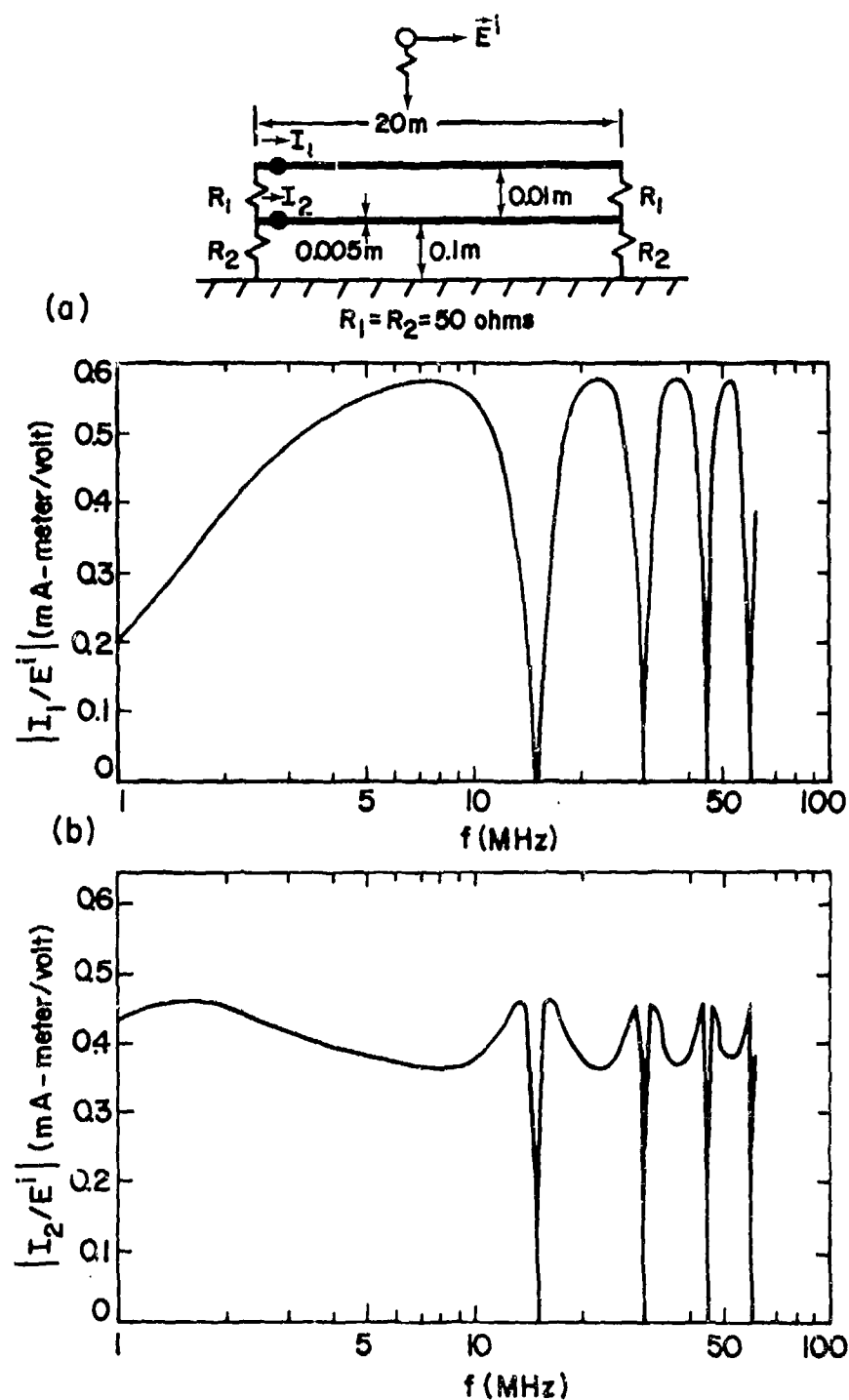


Fig. 24. Two-wire transmission line oriented parallel to a perfect ground plane and illuminated by a plane electromagnetic wave. (a) $|I_1/E^i|$ vs. f ; (b) $|I_2/E^i|$ vs. f .

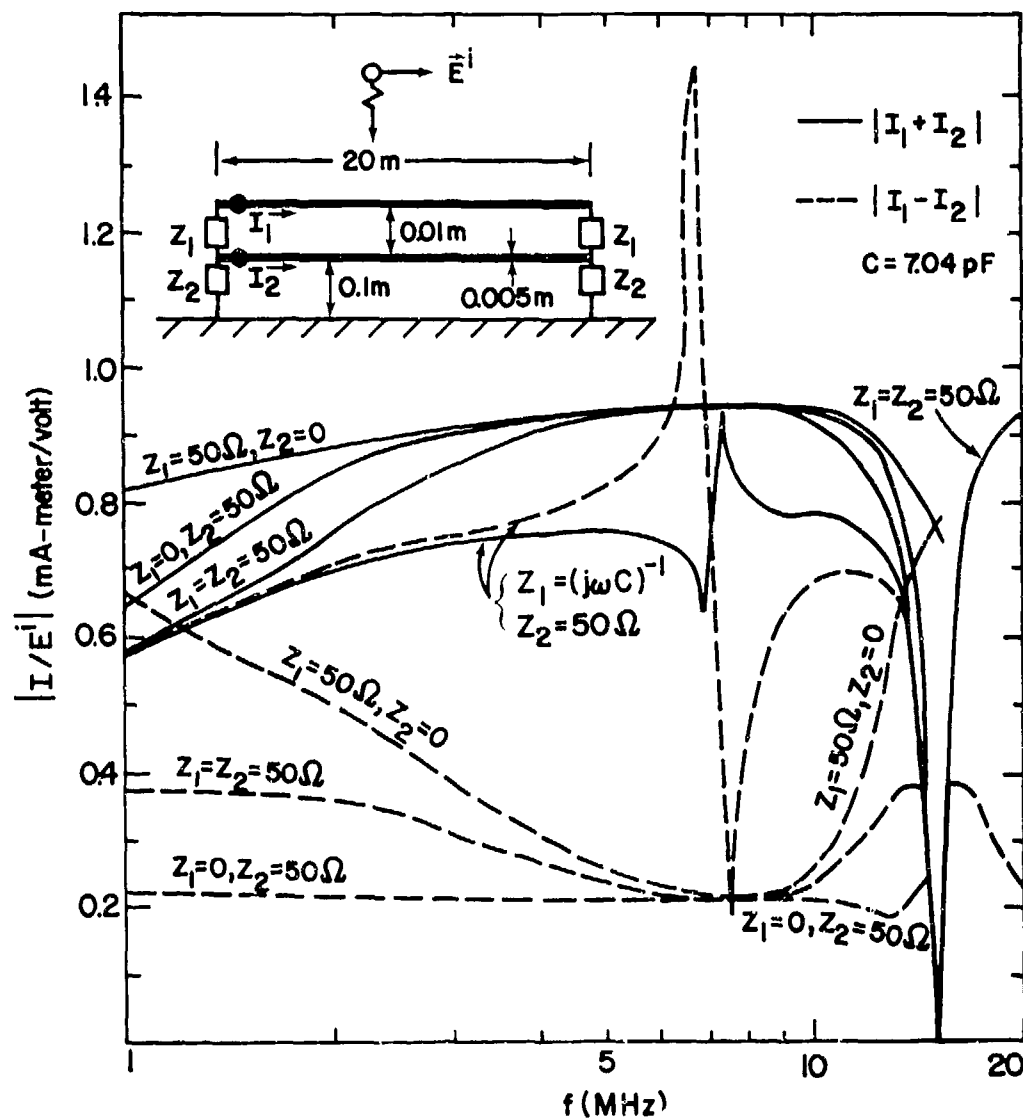


Fig. 25. Two-wire transmission line oriented parallel to a perfect ground plane and illuminated by a plane electromagnetic wave.

2.4.2.4.1 Two-Conductor Transmission Line

For the case of a single-wire line over a ground plane, or for an isolated two-wire line, the Thévenin impedance and voltage source for a point excitation on the line is given in Sec. 2.4.1.3.2, which deals with the coaxial line. For distributed excitation the Thévenin impedance remains the same, and the Thévenin voltage source can be obtained by integrating that of a point source excitation.

2.4.2.4.2 Multiconductor Lines

For a multiconductor line the Thévenin impedance seen at the end of a line of length l can be expressed as

$$(Z_{Th_{nm}}) = (Z_{c_{nm}}) \left(e^{\gamma_c l} (\delta_{nm}) + e^{-\gamma_c l} (\Gamma_{nm}) \right)^{-1} \left(e^{\gamma_c l} (\delta_{nm}) - e^{-\gamma_c l} (\Gamma_{nm}) \right) \quad (133)$$

where the term (Γ_{nm}) is the current reflection coefficient matrix given by (125).

The Thévenin voltage source for the multiconductor line is given by

$$\begin{aligned} (V_{Th_n}^{(s)}) = & \left(e^{\gamma_c l} (\delta_{nm}) + e^{-\gamma_c l} (\Gamma_{nm}) \right)^{-1} \left[\left(e^{\gamma_c z_s} (\delta_{nm}) + e^{-\gamma_c z_s} (\Gamma_{nm}) \right) (V_n^{(s)}(z_s)) \right. \\ & \left. + (Z_{c_{nm}}) \left(e^{\gamma_c z_s} (\delta_{nm}) - e^{-\gamma_c z_s} (\Gamma_{nm}) \right) (I_m^{(s)}(z_s)) \right] \quad (134) \end{aligned}$$

where, as before, $(V_n^{(s)}(z_s))$ and $(I_m^{(s)}(z_s))$ represent the localized voltage and current sources on the transmission line at the position $z = z_s$.

More general expressions can be derived for the Thévenin impedance and voltage using the general results in section 1.3.2, which take into account the multivelocity nature of energy propagation on the lines.

a. Open-Circuit Termination

For the special case in which the load at the end of the multi-conductor line is open circuited, the reflection coefficient becomes the negative of the unit matrix and the Thévenin impedance and voltage source become

$$\begin{aligned} (Z_{Th_{nm}}) &= (Z_{c_{nm}}) \coth(\gamma_c \ell) \\ (V_{Th_n}^{(s)}) &= \left(V_n^{(s)}(z_s) \right) \frac{\sinh(\gamma_c z_s)}{\sinh(\gamma_c \ell)} + (Z_{c_{nm}}) \left(I_m^{(s)}(z_s) \right) \frac{\cosh(\gamma_c z_s)}{\sinh(\gamma_c \ell)} \end{aligned} \quad (135)$$

where z_s is the source location, ℓ is the line length.

b. Short-Circuit Termination

Here the termination impedance is zero, giving a reflection coefficient of unity. The resulting Thévenin quantities are

$$\begin{aligned} (Z_{Th_{nm}}) &= (Z_{c_{nm}}) \tanh(\gamma_c \ell) \\ (V_{Th_n}^{(s)}) &= \left(V_n^{(s)}(z_s) \right) \frac{\cosh(\gamma_c z_s)}{\cosh(\gamma_c \ell)} + (Z_{c_{nm}}) \left(I_m^{(s)}(z_s) \right) \frac{\sinh(\gamma_c z_s)}{\cosh(\gamma_c \ell)} \end{aligned} \quad (136)$$

c. Matched Termination

For a matched line, $(Z_{L_{nm}}) = (Z_{c_{nm}})$, and the reflection coefficient is zero. The Thévenin quantities then become

$$\begin{aligned} (Z_{Th_{nm}}) &= (Z_{c_{nm}}) \\ (V_{Th_n}^{(s)}) &= \left[\left(V_n^{(s)}(z_s) \right) + (Z_{c_{nm}}) \left(I_m^{(s)}(z_s) \right) \right] e^{-\gamma_c (\ell - z_s)} \end{aligned} \quad (137)$$

REFERENCES

- [1] C.E. Baum, "Coupling into coaxial cables from currents and charges on the exterior," 1976 USNC/URSI Meeting, Amherst, Massachusetts, October 1976.
- [2] R.W. Latham, "An approach to certain cable shielding calculations," IN 90, January 1972.
- [3] E.F. Vance, "Shielding effectiveness of braided wire shields," EMC-17, May 1975, pp. 71 - 77.
- [4] R.W. Latham, "Small holes in cable shields," IN 118, September 1972.
- [5] K.S.H. Lee and C.E. Baum, "Application of modal analysis to braided wire shields," IN 132, January 1973, and EMC-17, August 1975, pp. 159 - 169.
- [6] L. Marin, "Effects of a dielectric jacket of a braided-shield cable on EMP coupling calculations," IN 178, May 1974.
- [7] H. Kaden, Wirbelströme und Schirmung in der Nachrichtentechnik, Springer-Verlag, Berlin, 1959.
- [8] E.F. Vance, "Coupling to cables," DNA Handbook Revision, Ch. 11, Stanford Research Institute, 1974.
- [9] K.S.H. Lee, "Localized penetration through cable shields," Proceedings of the 1974 FULMEN Meeting, Air Force Weapons Laboratory, 1974.
- [10] S.A. Schelkunoff, "The electromagnetic theory of coaxial transmission lines and cylindrical shields," Bell Syst. Tech. J., vol. 13, October 1934, pp. 535 - 579.
- [11] K.F. Casey and E.F. Vance, "EMP coupling through cable shields," AP-26, January 1978, pp. 100 - 106.
- [12] W.D. Stevenson, Jr., Elements of Power System Analysis, McGraw-Hill, New York, 1962.
- [13] K.S.H. Lee, "Balanced transmission lines in external fields," IN 115, July 1972.

- [14] C.M. Butler, et. al., "Selected topics in EMP interaction," IN 339, August 1976.
- [15] K.S.H. Lee and F.C. Yang, "A wire passing by a circular aperture in an infinite ground plane," IN 317, February 1977.
- [16] A.A. Smith, Jr., Coupling of External Electromagnetic Fields to Transmission Lines, John Wiley and Sons, New York, 1977.
- [17] K.S.H. Lee, "Two parallel terminated conductors in external fields," EMC-20, May 1978, pp. 288 - 295.
- [18] C.D. Taylor and J.P. Castillo, "On the electromagnetic field excitation of unshielded multiconductor cables," IN 348, January 1978.

PART 3

SYSTEM APPLICATIONS

CHAPTER 3.1

ASSESSMENT AND HARDENING

The purpose of this part of the document is to illustrate the application of the interaction technology described in Parts 1 and 2 to composite problems representative of system hardening or assessment problems. In Chap. 1.2 the process of decomposing a complex system into volumes, surfaces, transmission lines, apertures and antennas is discussed, and in Part 2 the responses of these elementary components to electrical excitations are presented in detail. In Part 3 we illustrate the recombination of the solutions for these elementary components to obtain a system response, with error estimates on the calculations.

In this chapter we discuss the assessment and hardening problem and hardening concepts in general terms. Then in Chap. 3.2 are presented several illustrative system examples. In each of these example analyses we begin with a general description of the system components in order to identify the system topology. We then decompose the system into principal surfaces, principal volumes and elementary components, and illustrate with numerical examples the system response to the EMP. In addition, where system susceptibility to the EMP is identified or postulated, techniques for reducing the susceptibility are illustrated.

3.1.1 THE ASSESSMENT AND HARDENING PROBLEM

The analysis of system susceptibility or the synthesis of system immunity to the EMP are classical source-interaction-response problems. In susceptibility analysis one seeks to determine the response for given source characteristics and intervening structure, whereas in synthesizing hardness one seeks to limit the response to an acceptable level for a given source by appropriate manipulation of the intervening structure. In either case, an understanding of the EMP interaction with the intervening structure is crucial. A fundamental difficulty in acquiring this understanding, as well as for many other interference analyses, is that the electromagnetic properties of the intervening structure are often not

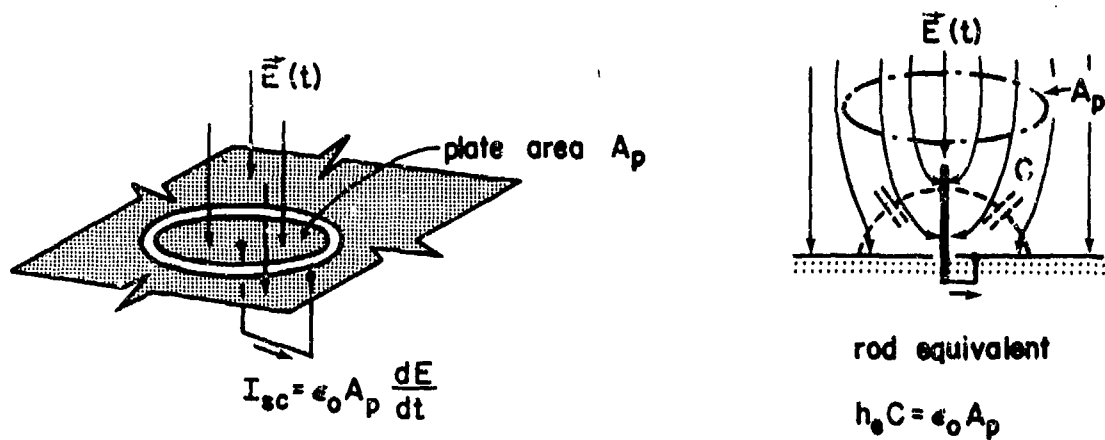
specified (e.g., structural materials, plumbing, etc.), or they are not specified for the entire spectrum of interest (e.g., 60 Hz power components or voice frequency communication equipment, etc.). Thus for susceptibility analysis one must identify the intervening structure and estimate or measure its electromagnetic properties, while for hardening one must specify and control its procedures.

In addition to understanding the structure, one must also know the sensitivity of critical circuits to the response. This sensitivity to upset or damage varies over a wide range and depends on the input-output circuit design and the shielding quality of the equipment cabinet or housing. Thus, considerations of circuit design and shielding also enter into an integrated approach to system hardening.

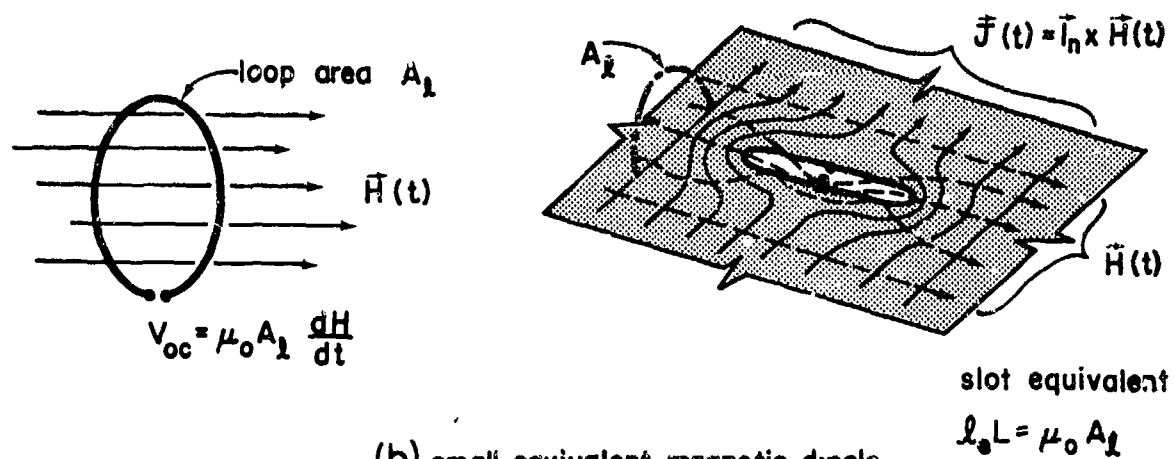
4.1.1.1 Severity of the Problem

To put the EMP interaction and hardening problem in perspective, we observe that the high-altitude EMP can induce open-circuit voltages of the order of MV or short-circuit currents of the order of 10 kA in overhead conductors such as power lines. Small-signal electronic circuits for data processing typically operate with switching signals of a few volts or a few tens of mA. Thus, to prevent EMP-induced transients on power lines from producing circuit upset, sufficient shielding, attenuation, or other interference reduction must be provided to reduce these transient peaks by a factor of 10^6 between the power lines and the small-signal circuits operated therefrom.

For airborne systems that do not possess long exposed conductors, one may gain a similar perspective by deriving the effective area of a plate or loop antenna (Fig. 1) that will produce the switching voltage or current when exposed to the incident high-altitude EMP. The quantities of interest are the short-circuit current induced in a small plate antenna, which has a large source impedance, and the open-circuit voltage induced in a small loop antenna, which has a small source impedance. These effective areas are approximately 1 cm^2 . That is, a plate (or loop) antenna of this area connected directly to the small-signal circuits will have sufficient current



(a) small equivalent electric dipole



(b) small equivalent magnetic dipole

Fig. 1. Dipole current and loop voltage induced by external fields.

(or voltage) induced on it by the incident EMP to produce switching-level transients in these circuits. Therefore, one must virtually eliminate electronic circuit exposure with shielding and insert sufficient attenuation between exposed conductors and the small-signal circuits to limit the transients delivered to those circuits to tolerable levels.

3.1.1.2 Shielding Surfaces

Because of the great disparity between the EMP source strength and the circuit sensitivity, compatibility between them can only be achieved through a systematic approach to interference control. The foundation for such an approach is described in Sec. 1.2.1. The space about the sensitive electronic circuits or devices is partitioned by shield surfaces. As illustrated in Fig. 2, shielding surfaces may be used to control interference of external origin, such as EMP, lightning, power switching transients, etc., or to control interference of internal origin such as emanations from transmitters, rectifiers, counters, and other switched high-current or inductive loads. Hence, the fundamental approach is applicable to controlling the EMP and all other types of interference,

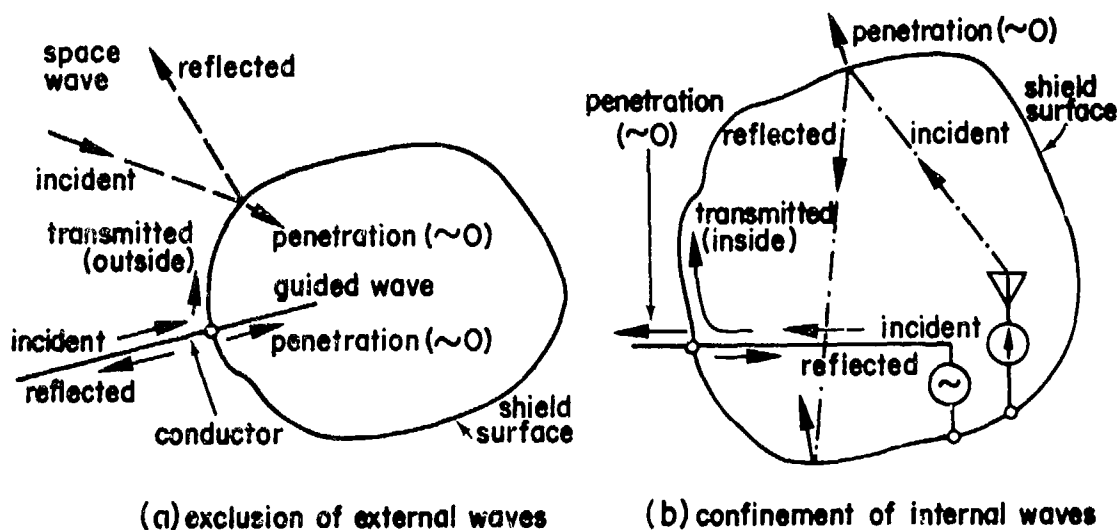


Fig. 2. Shielding surfaces.

which is an important consideration since it permits an integrated approach to interference control and tends to eliminate situations in which correction of one interference problem aggravates another. The control of internal and external interference sources with a two-layer shield system is illustrated in Fig. 3.

3.1.1.3 Penetration of Shields

The shielding surfaces may be compromised by conductors that pass through them. Such conductors are usually necessary to supply operating power and to communicate with the shielded circuit (i.e., to accommodate input and output data). Other conductors having non-electrical functions may also pass through the shielding surfaces. Pipes and tubes for utilities, hydraulic and pneumatic systems, and steel cables for controls and hoists fall into this category.

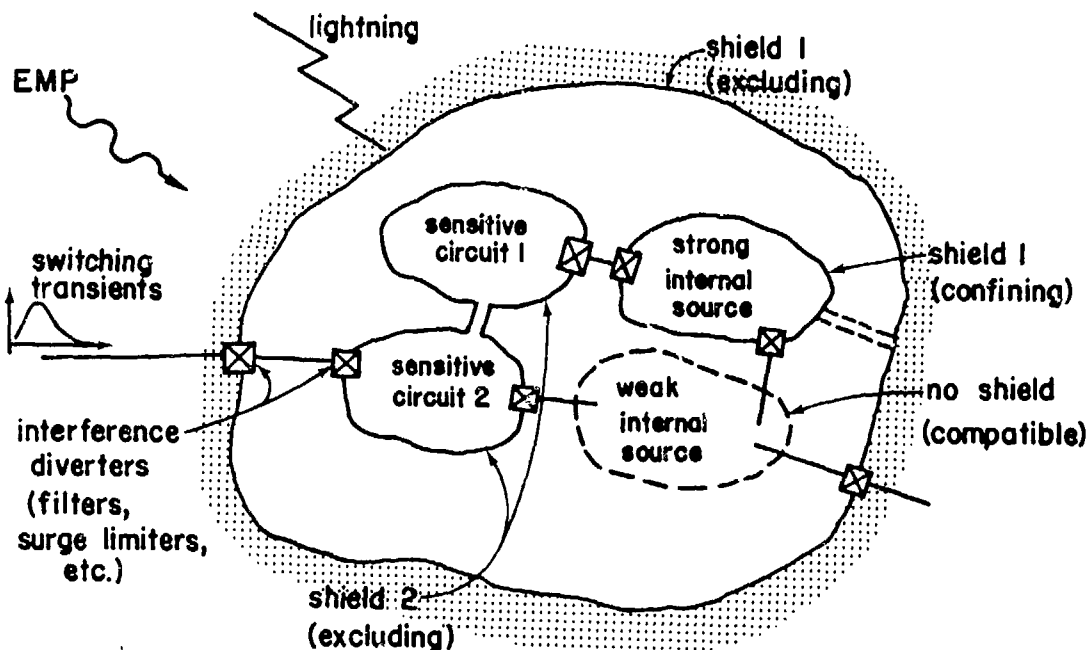


Fig. 3. Two-layer shielding topology for controlling internal and external interference sources.

The shields may also be compromised by openings for personnel entrance and egress, ventilation, light, and access for assembly or maintenance. Smaller, but often numerous, openings occur at riveted, bolted, or spot-welded joints in shield surfaces. All such openings (or apertures) permit some of the interference fields to penetrate through the shield surfaces.

Finally, because all practical shielding materials are imperfect conductors, some of the interference fields may diffuse through the shield. Except for very long slender structures such as cable shields, such diffusion is usually important only at low frequencies or for electrically thin shields.

In summary, interference fields may penetrate shields

- (a) along insulated conductors passing through the shields;
- (b) through openings or imperfections (apertures) in the shields;
- (c) by diffusion through imperfectly conducting shields.

The objective of system hardening is to control these interference penetrations at each shield, so that the interference reaching the sensitive circuit is within the tolerance of the circuit.

3.1.1.4 Coupling and Propagation

For a quantitative analysis of hardness, the current and charge distributions on conducting appendages (power lines, trailing wire antennas, missile plumes, etc.) and on the shield surfaces must be determined. The interaction of the EMP source fields with these shield and with cables and other elements outside the shield produces these current and charge distributions, which in turn are the excitation sources for the three shield penetration mechanisms listed above. The penetrant fields interact with structures inside the shield to produce the current and charge distributions on cables and other structures enclosed by the shield and on the surface of the next inward shield. The latter is the first step of the next layer of the interaction problem that deals with the second shield surface.

These coupling and propagation analyses, which are the subject of Part 2 of this document, often become more complex as the layer of shielding increases. Outside the first principal shielding surface (e.g., outside

the building shield or aircraft skin) there are only a few power lines, cables and antennas which are often of a simple geometry that is amenable to analysis. Between the first and second shields (i.e., inside the building or aircraft skin), the number of cables and other structures is much greater and their geometry is more complicated. Because of this complexity, the engineering approach is frequently that of "scoping" the intermediate interaction problem rather than obtaining an analytic solution to it. Thus representative but greatly simplified examples, such as an insulated wire passing through both shields, or a cavity-backed aperture, may be analyzed to obtain representative wire currents or cavity fields. These analyses may then be used to estimate the surge limiting or filtering required on wires.

3.1.2 HARDENING CONCEPTS

3.1.2.1 System Topology

The essence of interference control, whether for the EMP or for other sources, is to establish shielding integrity, thereby limiting the interference currents and fields that can penetrate the shield surfaces. A first step in interference analysis or control is, therefore, to identify the system topology, as discussed in Chap. 1.2. That is, the principal shielding surfaces at which the barrier to penetrating interference will be established must be identified and examined for compromising apertures and penetrating conductors. In practical systems, there are often several layers of shielding that form a set of nested shield surfaces, as shown in Fig. 4, each of which serves as a barrier to penetrating interference. In ground-based systems, the first principal surface might be a building or room shield, and the second principal surface might be an equipment cabinet, and the third principal surface might be a box that contains the small-signal circuits. In airborne systems, the first surface would usually be the aircraft or rocket skin, and the second surface would be the housings for the avionics equipment. These surfaces usually serve as successively more exclusive barriers to the interference, so that as one progresses from the outside toward the inside of Fig. 4 where line penetrations are absent, the interference environment becomes less severe.

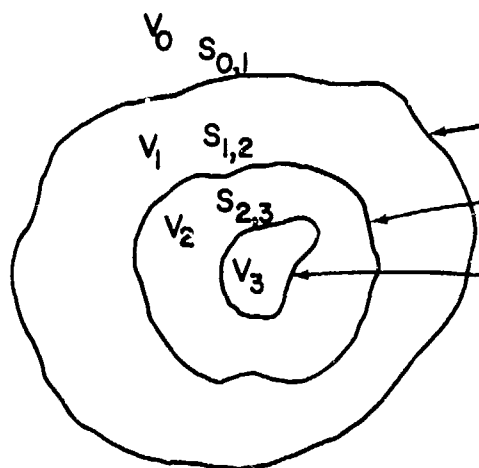


Fig. 4. Principal surfaces and volumes.

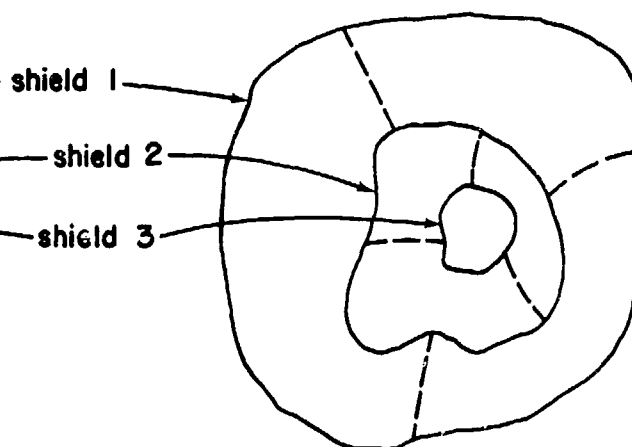


Fig. 5. Elementary surfaces and volumes.

In addition to the partitioning of space into principal volumes by the nested shield surfaces illustrated in Fig. 4, the principal volumes may be partitioned into elementary volumes by internal dividers as illustrated in Fig. 5 by the dashed lines. This cellular topology is common in aircraft and ships, where the interior regions are partitioned by bulkheads and decks. The cellular topology permits controlled gradations of interference environment within a region between shield layers.

For nearly perfect shields (thickness large compared to skin depth) it is sometimes convenient to visualize the shield as two independent surfaces — an outside surface on which reside the externally induced current and charge densities and an internal surface on which reside the internally induced current and charge densities. This concept is depicted in Fig. 6, where the two-surface idea for the shield layers is shown. For uncompromised shields (no penetrating conductors or apertures), each cell is electromagnetically independent of every other cell and of the external environment.

3.1.2.2 Penetrating Conductors

The two-surface idea is particularly useful for determining how interference-carrying conductors should be connected to the shield to

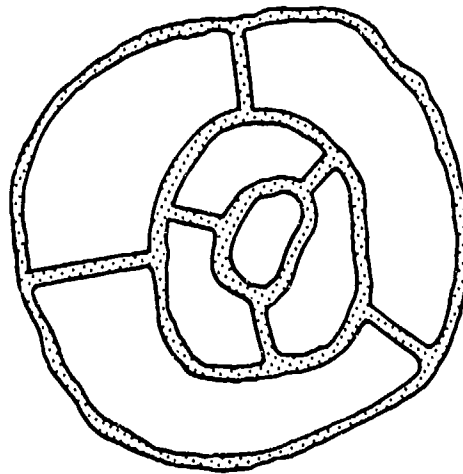


Fig. 6. Two-surface idea for nested cellular shields.

preserve its integrity. If an external interference-carrying conductor is connected to the outside surface of the shield, as illustrated in Fig. 7, the interference current flows onto the outside surface of the shield and thus has little effect on the volume enclosed by the shield. However, if the conductor is connected to the inside surface of the shield as in Fig. 8, the interference current flows onto the inside surface of the shield and contaminates the volume enclosed by the shield. To preserve the integrity of the shield, therefore, interference current of external origin must be diverted to the outside surface of the shield as illustrated in Fig. 7.

Several examples of the proper application of this principle are given in Fig. 9 together with some common compromises and violations of the shield. Note that each of the compromises and violations permits the currents on the outside conductors to flow into the protected region inside the shield. It should also be observed that filters and surge arrestors behave in the same way as any other connection of a penetrating conductor to the shield; that is, they divert the interference currents to the outside surface of the shield, thereby preventing these currents from entering the protected region. Because power and signal-carrying conductors cannot be continuously connected to the shield, they must be momentarily connected (when a certain threshold is exceeded) or connected only at frequencies not used for power or signals (i.e., through a filter). In

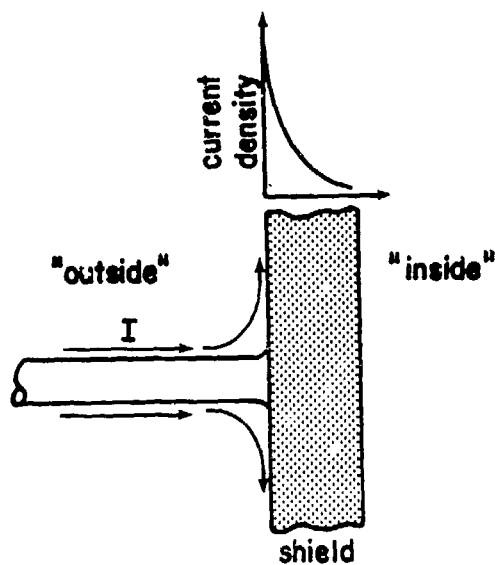


Fig. 7. Confinement of conductor current to the outside surface by skin effect.

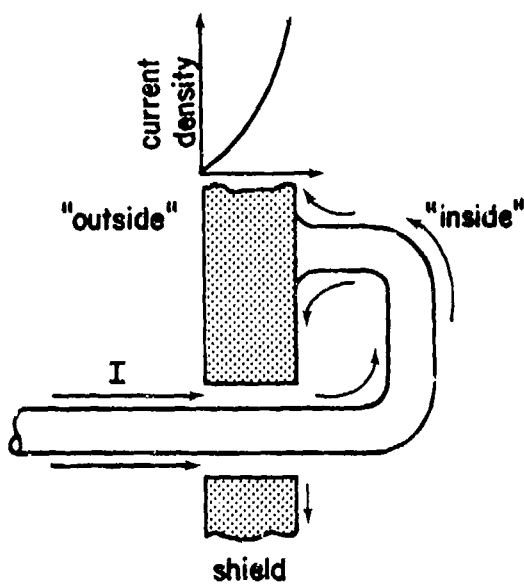


Fig. 8. Conductor current injected on the "inside" of a shield.

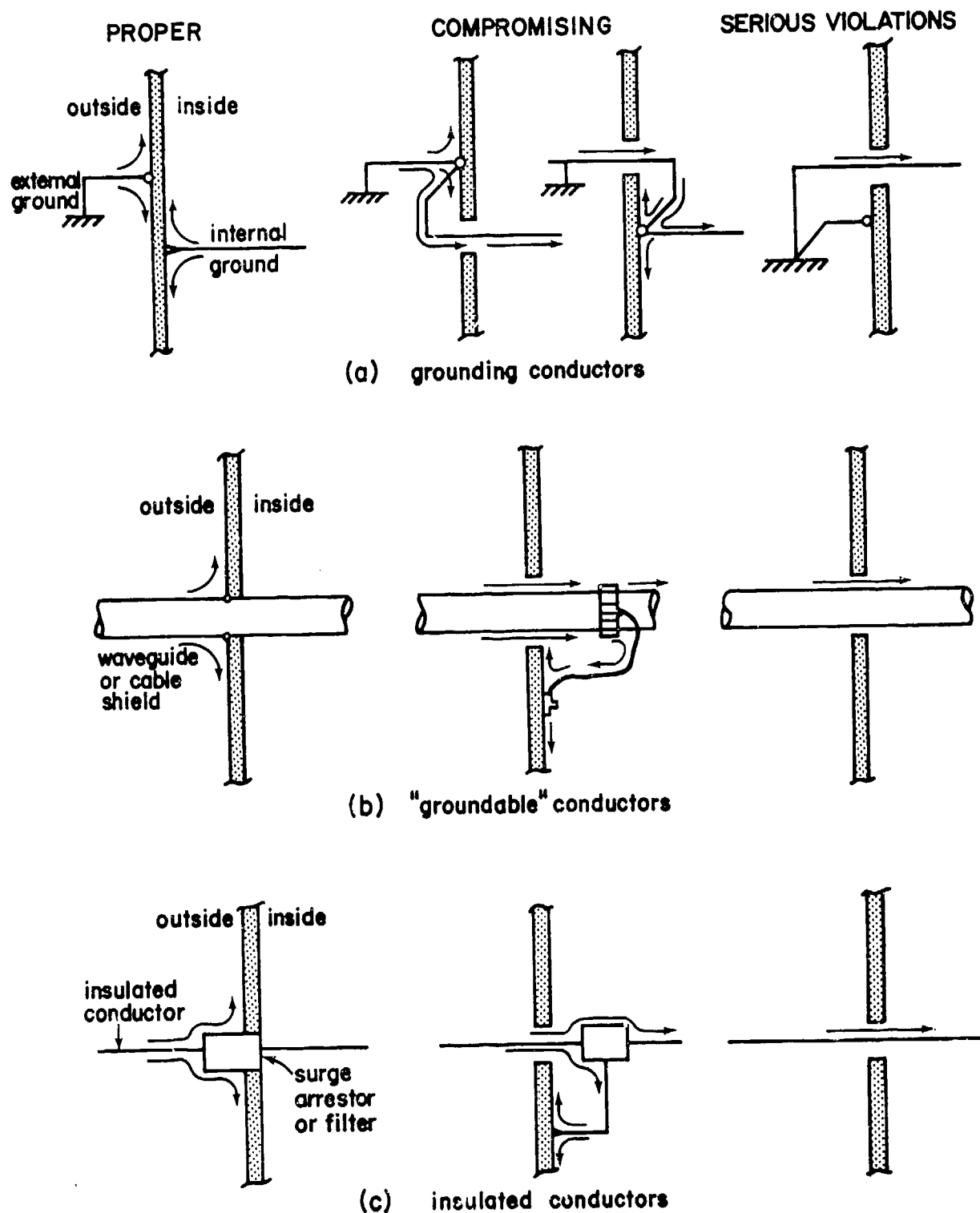


Fig. 9. Shielding integrity near interference-carrying external conductors.

either case, the diverted interference currents must flow to the outside surface of the shield, as illustrated in Fig. 9c, if shield integrity is to be preserved.

Each of the "proper" methods of preserving shielding integrity shown in Fig. 9 involves diverting the external conductor current to the outside surface of the shield. Methods of interrupting the current could also be employed, but at the first layer of shielding the current-diversion method may be more reliable and less expensive than the current-interruption approach. This is particularly so for ground-based systems for which the external conductors may be power lines and communication cables that can carry tens of kA of lightning or EMP-incuded currents toward the shield. Since the open-circuit voltages associated with these currents are of the order of MV, current-interruption techniques for treating these conductors would require insulation capable of withstanding these extremely high voltages without flashover. Such insulation is expensive to install and it requires considerable maintenance to ensure reliability. (However, dielectric pipes can be economical for water, sewer, and other plumbing penetrations.)

At secondary and tertiary shields where the open-circuit voltages are less severe (i.e., hundreds of volts instead of MV), current-interruption techniques are illustrated in Fig. 10, where the open-circuit voltage impressed across the current-interruption device is also indicated. Such techniques are usually applied only to insulated conductors such as power and signal conductors; "groundable" conductors such as cable shields, plumbing, and waveguides are economically and reliably treated with the current-diversion approach of Fig. 9b.

There are, of course, many other input/output circuits that can serve as buffers or isolators at the secondary and tertiary shields. Many of these are functional components of the system or electronic circuit that can be adapted to shielding purposes. Rectifier power supplies and dc-to-dc converters may serve to isolate the primary power conductors from the conditioned power supplied to the small-signal circuits. Tuned

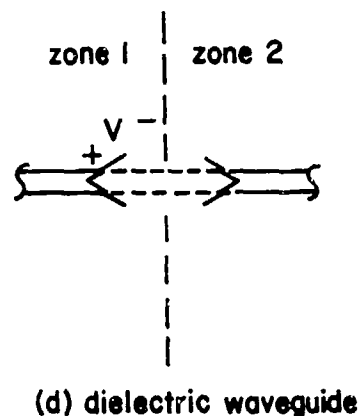
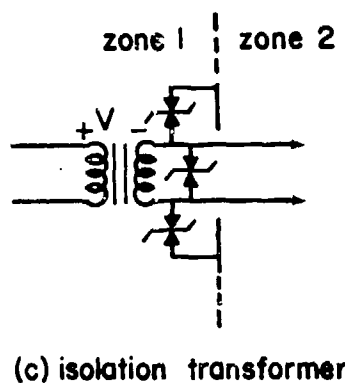
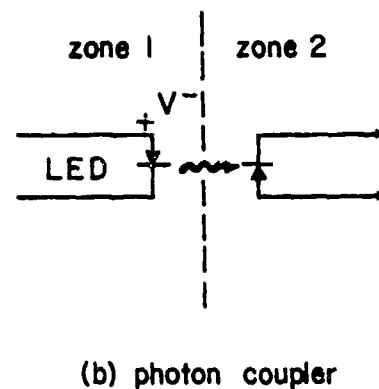
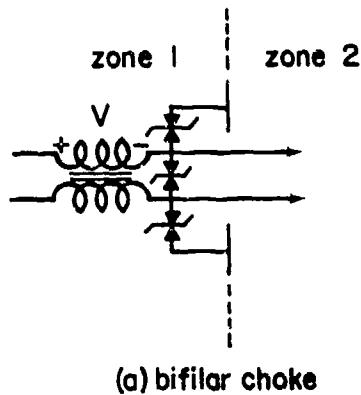


Fig. 10. Current-interruption treatments for secondary and tertiary shield penetrations.

RF amplifiers and mixers serve as narrow-band filters to exclude interference on the input conductors. Well-designed electronic equipment often contains balanced transmitters and receivers, emitter followers, or other high-tolerance buffer stages to protect the small-signal circuits from interference propagating toward the input/output terminals. Indeed, one approach to interference control is to make the electronic equipment "inherently immune" by providing high-integrity shielding in the cabinets and using high-tolerance input/output circuits.

3.1.2.3 Aperture Control

Most facilities require windows, doors, ventilation openings, access hatches, etc., which may also compromise the integrity of the shield. The penetration of external fields through apertures that are small compared to a wavelength is illustrated in Fig. 11. As shown in Fig. 11a, part of the electric field that would otherwise terminate on the outside surface of the shield fringes through the aperture where it may induce charges on internal cables. Similarly, some of the magnetic field that would otherwise be bounded by the surface current in the shield is permitted to fringe through the aperture, link an internal cable, and thereby induce a voltage in the cable (Fig. 11b). If the aperture is large compared to a wavelength, the incident wave can shine through the aperture as illustrated in Fig. 12. Because the shortest wavelengths of concern

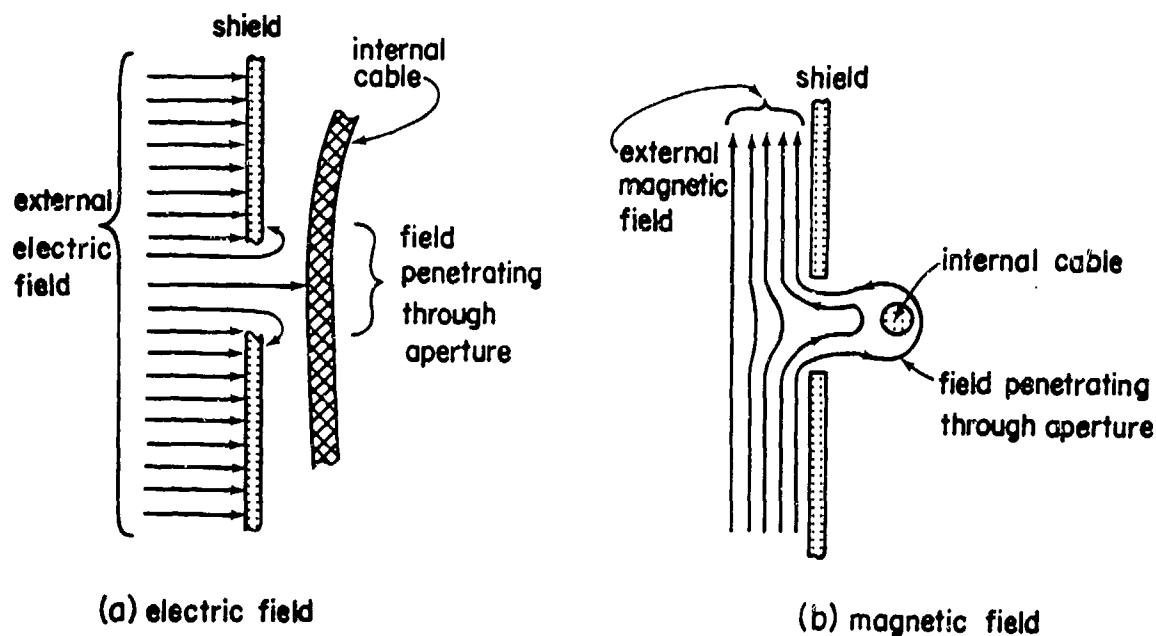


Fig. 11. Electromagnetic penetration of small apertures.

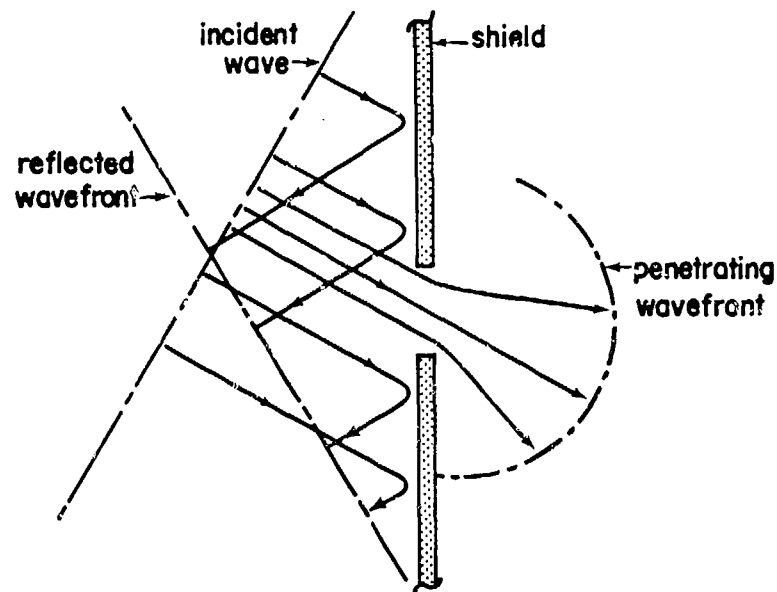


Fig. 12. Electromagnetic penetration of a large aperture.

in EMP hardening are of the order of 1 meter, the shine-through penetration mechanism usually occurs only at large windows and doors. Because the shine-through wave is attenuated very little in the direction of propagation of the incident wave, however, almost the full incident EMP peak field strength may be transmitted to the interior of the shield through large apertures.

The fields penetrating a small aperture depend on the aperture size. Therefore, if a given area of wall opening is subdivided into small openings, the penetrating fields at an interior point will be reduced. Thus one common treatment for such openings is to cover them with a conducting screen or mesh, so that the large opening is converted into a multitude of small openings.

More reduction can be obtained with sacrifices in optical transparency and increased resistance to air flow by adding thickness to the screen. Then each small aperture becomes a tube through the wall and behaves as a waveguide beyond cutoff. Fields transmitted through a waveguide beyond cutoff are attenuated exponentially with distance along the guide, so that

very large attenuation may be achieved by using many small tubes welded or brazed together in a honeycomb structure. Sketches of the magnetic field in the vicinity of a single aperture, an array of small apertures, and an array of waveguides beyond cutoff are shown in Fig. 13.

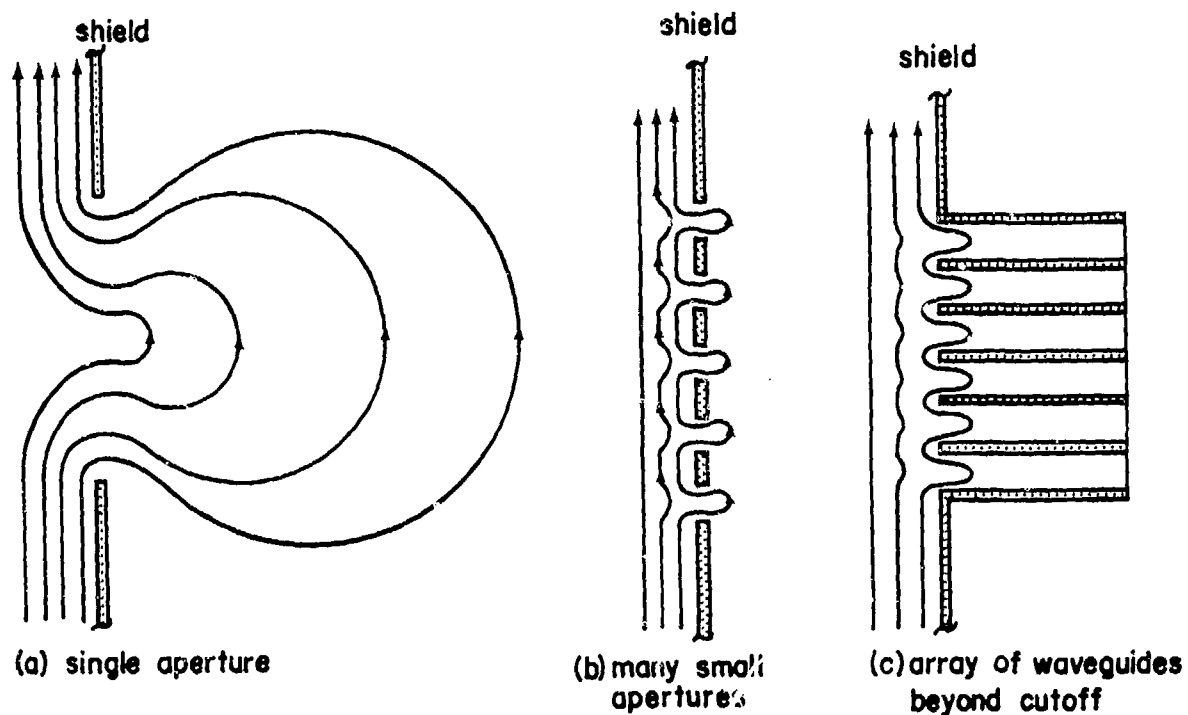


Fig. 13. Magnetic field penetration of apertures.

CHAPTER 3.2

ILLUSTRATIVE SYSTEM EXAMPLES

In this chapter we present illustrative analyses for four example systems: a rocket vehicle in flight, an aircraft, a ground-based system, and a satellite. In each case we discuss the system in general terms, decompose the system topologically, and then illustrate with numerical examples the system response to the EMP.

3.2.1 ROCKET VEHICLES IN FLIGHT

Typical elements of a multistage long-range rocket vehicle are shown in Fig. 1 together with a representative electrical wire harness and external cable raceway. The external cable raceway for interconnecting the guidance and control system with the downstage components is commonly used with monocoque motor construction. The raceway cable is used by the guidance and control system to control motor ignition, thrust vector (or other steering), stage separation, interstage jettison, and in some cases engine shutdown or thrust termination. The cable is also used to provide feedback on engine pressure, nozzle position, and other status or performance parameters to the control system. At staging, the wiring associated with the expended motor is jettisoned with the motor casing. The cable is usually provided with pull-away connectors to accommodate this operation, but mechanical and explosive cable cutters have also been used.

Smaller rocket vehicles used for ground-to-air, air-to-air, or air-to-ground missiles have similar components, but these are often one or two-stage vehicles and are usually smaller than the long-range, multistage vehicle. Smaller vehicles using forward-looking radar, infrared, or other target-seeking systems may also have the guidance and control package forward of the payload, rather than aft of the payload, as is usual in long-range vehicles. Finally, because the time of flight of the smaller vehicles is short, the in-flight characteristics of these vehicles are often less important than the pre-launch characteristics, insofar as interaction with the EMP is concerned. The electromagnetic characteristics of the long-range multistage vehicle will be examined in this section.

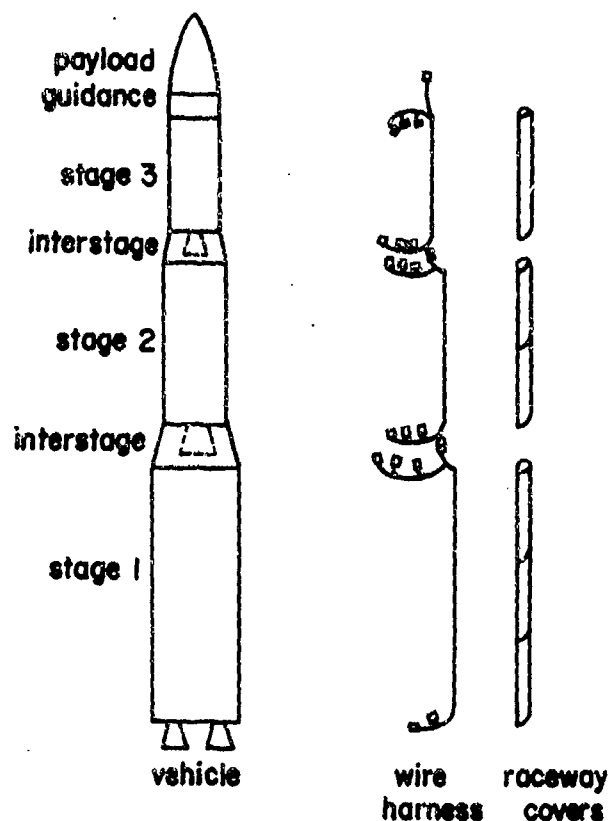


Fig. 1. Multistage rocket vehicle, wiring, and cable raceway.

Representative wiring in the vicinity of the payload and guidance and control system is illustrated in Fig. 2. As illustrated, the raceway cable originates in the guidance and control system and then branches to supply the downstage motor and staging functions. Other wiring associated with the guidance and control system may include telemetry or communication antenna cables and cabling to provide payload cover-removal, activation, and ejection. An umbilical connector to accommodate ground checkout and pre-launch functions is also located on or near the guidance and control system. When the umbilical cable is removed during launch, the pins of the umbilical connector may be exposed to the EMP environment. Deadfacing connectors that cover, retract, or break contact with the pins may be used to reduce this exposure.

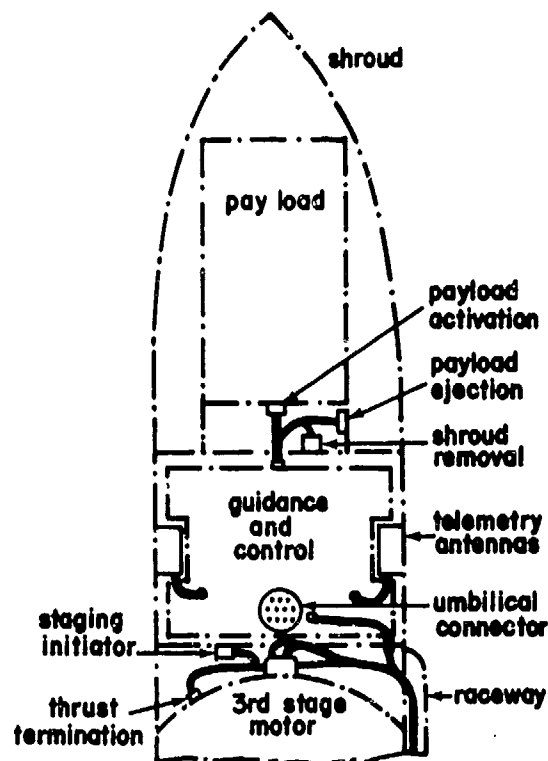


Fig. 2. Typical payload and guidance cabling.

Representative wiring in an interstage area is shown in Fig. 3. The wiring in this region supports engine ignition and engine pressure monitoring, staging ordnance initiation, and perhaps thrust termination or motor destruction (for aborting the mission) on the downstage motor, and nozzle or thrust vector control and interstage-removal ordnance initiation for the upstage motor.

The sensitive circuits in a rocket vehicle are mainly in the guidance and control package, which contains small-signal digital electronics for computing the vehicle trajectory and providing error-correction commands to the rocket steering system. Additional sensitive circuits may be found in the steering system (near the motor nozzles) and in the staging ordnance system (electro-explosive devices).

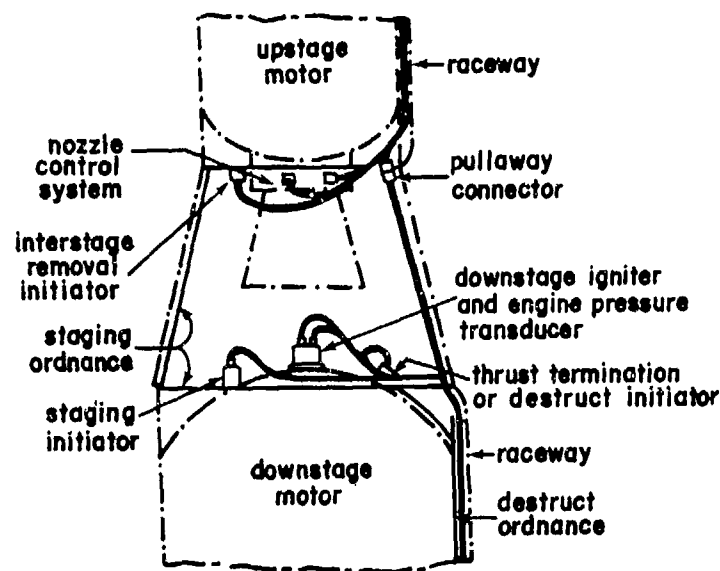


Fig. 3. Typical interstage cabling.

3.2.1.1 System Topology

The first principal shield for the all-metal rocket vehicle is the vehicle skin and raceway cover. Because high strength-to-weight-ratio composite materials are displacing metals for large motor casings, however, it is common for one or more of the motors to be electromagnetically transparent. As illustrated in Fig. 4, the first principal shield is then transferred from the metal motor casing shown on the left in the figure to the raceway and interstage structure shown on the right. The current density on the raceway will usually be larger on the nonmetallic rocket than on the all-metal vehicle, and unless particular care is exercised in maintaining the shielding integrity in the interstage area and at raceway joints, the effectiveness of the first principal shield on the nonmetallic vehicle may be considerably less than that on the all-metal rocket.

Compromises in the first principal shield often occur at joints in the vehicle skin between stages, at joints in the cable raceway covers, and

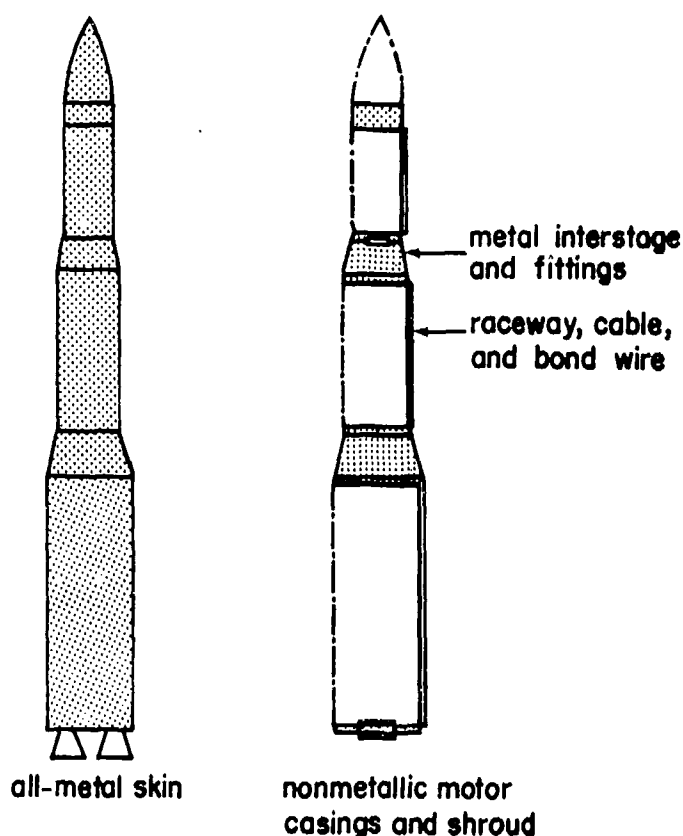


Fig. 4. First-layer shielding for rocket vehicles.

at access ports on the interstage structure or on the skin of the guidance and control system. The shield is also compromised at the aft end of the vehicle where the end of the raceway cable and some of its branches may be exposed. In addition, the umbilical connector and any openings for antennas on the vehicle are also potential penetration points.

A portion of the second principal shield for a typical rocket vehicle is illustrated in Fig. 5. The second principal shield is composed of the raceway cable shield; the housings for the electro-explosive devices, transducers, and nozzle control systems; and the guidance system container. The umbilical connector may constitute an abrogation of the two-layer shielding topology if conductors from this connector are connected directly

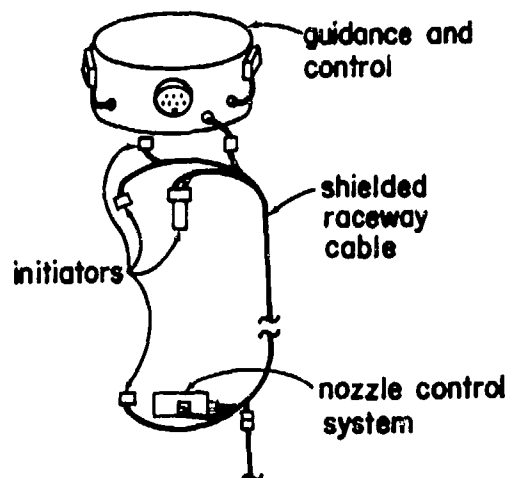


Fig. 5. Second-layer shielding for rocket vehicle circuits.

to small-signal circuits inside the guidance system. Deadfacing or wire-cutting operations may partially restore the two-layer shielding after the umbilical cable from the launch equipment is removed.

Leakage through the second principal shield may occur at connectors and along the raceway cable shield. EMP-induced interference penetrating the connector shells and cable shield can propagate along the internal conductors to the guidance and control system and to the electro-explosive initiators and nozzle control systems. EMP-induced interference can also enter the guidance and control system by means of leads from the umbilical connector and antennas.

In Sec. 3.2.1.2 through Sec. 3.2.1.4 numerical example calculations will be made for each of the events shown in the interaction sequence diagram (Fig. 6).

3.2.1.2 External Interaction

The interaction of an all-metal rocket with the incident EMP can be analyzed using the theory of cylindrical antennas. Because the configuration of the vehicle changes as the motors are expended and jettisoned, the antenna analysis may have to be repeated for several different

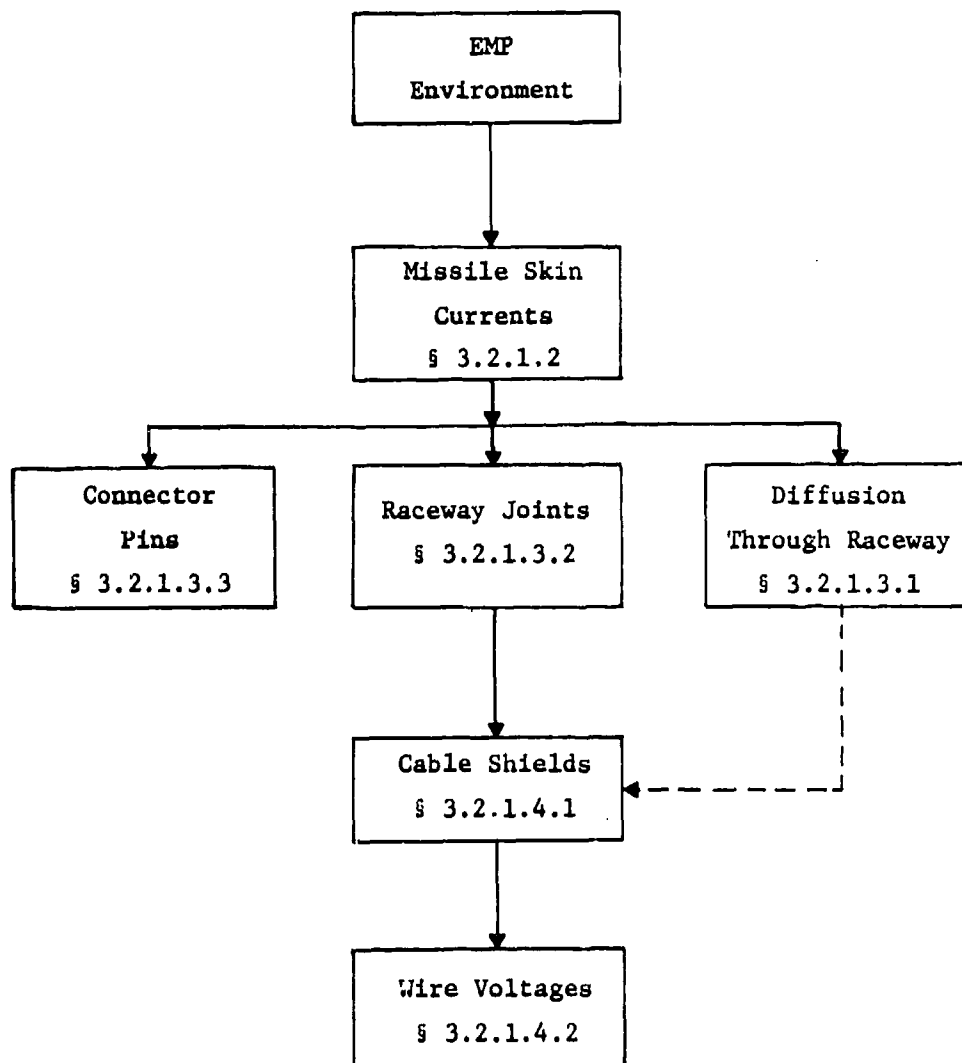


Fig. 6. Interaction sequence diagram for a rocket vehicle in flight.

configurations. A 3-stage rocket may have 3, 4, or 5 configurations during its flight (4 if the third stage is jettisoned, 5 if the payload cover or shroud is also removed). These configuration changes primarily affect the amount of analysis required, rather than the techniques to be used. In the final configuration with the third stage and shroud removed, however, the vehicle may be more accurately characterized as a satellite than as a rocket.

A serious complication of the analysis is encountered if the effects of the motor exhaust plume are to be included. This complication results from the facts that the conductivity of the plume is much smaller than that of the metal skin and varies spatially within the plume, that the size and shape of the plume vary with altitude (Fig. 7), and that the electrical properties of the plume are not thoroughly understood. Nevertheless, the plume has the effect of extending the effective length of the vehicle and causing the current density at the aft end of the vehicle to be enhanced (see Sec. 2.1.2.3.2), as illustrated in Fig. 8.

For the rocket-vehicle example discussed here, an all-metal vehicle is considered and the effects of the plume are neglected. In addition, it is assumed that all joints and access openings are optically opaque, so that only the magnetic field significantly penetrates the first principal shield. The external interaction problem then reduces to that of determining the surface current density on the vehicle skin.

The current density at low and intermediate frequencies consists of two parts. The first part is produced by the interaction of the incident magnetic field with the conducting skin and is given by (see Eq. (12) of Chap. 2.1)

$$J_o = \frac{2H^1}{2 - \alpha_o} \cos \phi \quad (1)$$

when the electric vector is parallel to the axis of the vehicle. The net axial current produced by this interaction is zero, since the current induced on the front side is in the direction opposite to that of the current on the back side.

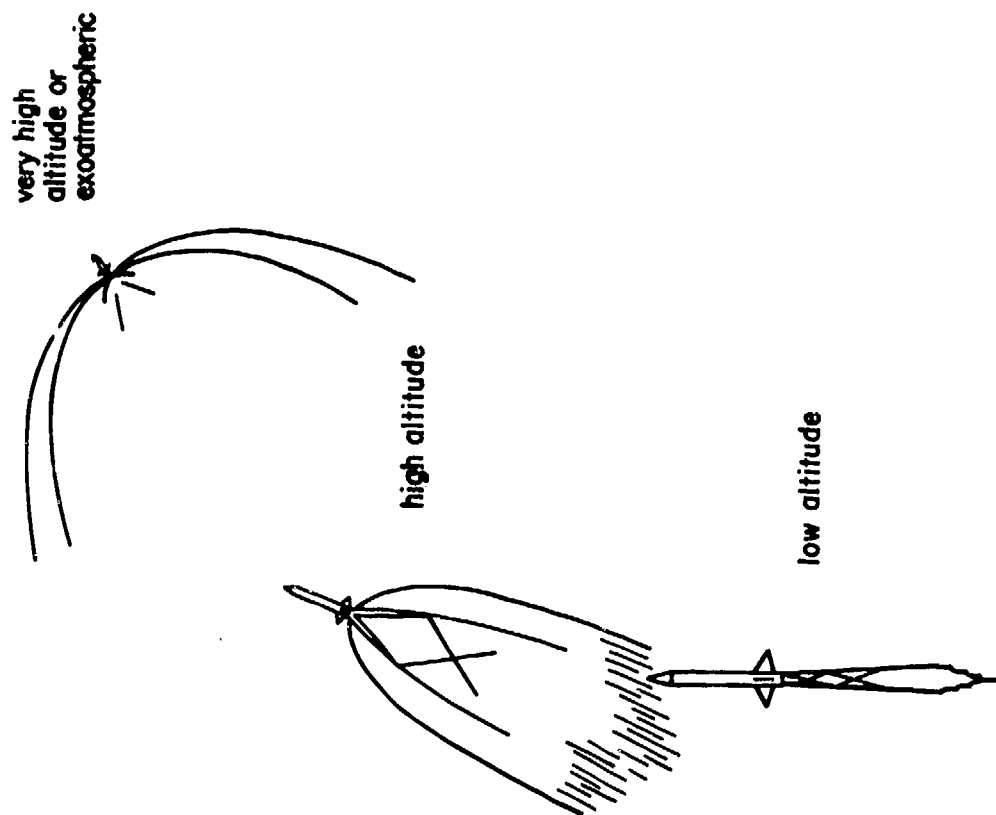


Fig. 7. Rocket motor exhaust plumes.

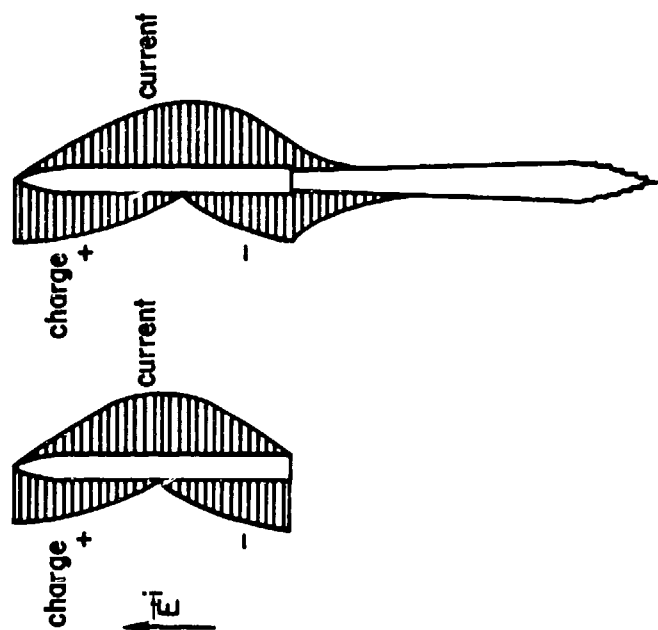


Fig. 8. Quasi-static current and charge distributions on rocket with and without plume (conceptual representation).

The second part of the induced current is the electric dipole current produced by interaction of the vehicle with the axial electric field. At low frequencies ($h \ll \lambda$), this current is of the form (see Eq.(12) of Chap. 2.1)

$$J_1 = \frac{j\omega\epsilon_0 a E^i}{2(1-\alpha_0)} \quad (2)$$

at the center of the vehicle, where a is the radius of the vehicle. For $E^i/H^i = Z_0 = 120\pi$, $\max(J_0) \geq |J_1|$ when

$$f \leq \frac{1}{60\pi \epsilon_0 a} \frac{1-\alpha_0}{2-\alpha_0} \quad (3)$$

For a typical ICBM ($L = 2h \approx 20\text{m}$, $a \approx 1\text{m}$), then α_0 is, according to (14) of Chap. 2.1, approximately 0.9797 and the skin interaction current density J_0 is greater than J_1 for $f \leq 4$ MHz. Thus, for fields that diffuse through the raceway cover, the current density J_0 induced by the magnetic field will dominate. On the other hand, the high-frequency penetration through joints and apertures and coupling to the raceway cable will be dominated by the dipole or "antenna" current J_1 , because the coupled voltage has the form $j\omega J_1$, which emphasizes the high frequencies.

The complete dipole current at intermediate frequencies is given by (17) of Chap. 2.1. The EMP spectrum displays a $1/f$ behavior in the vicinity of the half-wave resonance at 7.5 MHz. Hence, the first resonance response of the vehicle to the incident EMP can be represented by the step responses in Fig. 4 of Chap. 2.1. For our example we will assume $H^i = E^i/120\pi = 133$ A/m, and the peak current at the midpoint of the vehicle is then 5.8 kA, from Fig. 4 of Chap. 2.1.

3.2.1.3 Penetration of First Shield and Intermediate Interaction

The intermediate internal interaction problem is to determine the current induced on the shield of the raceway cable. The cable and raceway are treated as a leaky coaxial transmission line in which the shield is

the raceway and covers, and the center conductor is the raceway cable. This model is illustrated schematically in Fig. 9 for three vehicle configurations. The leakage through the shield occurs by diffusion through the covers, by a distributed longitudinal polarizability per unit length

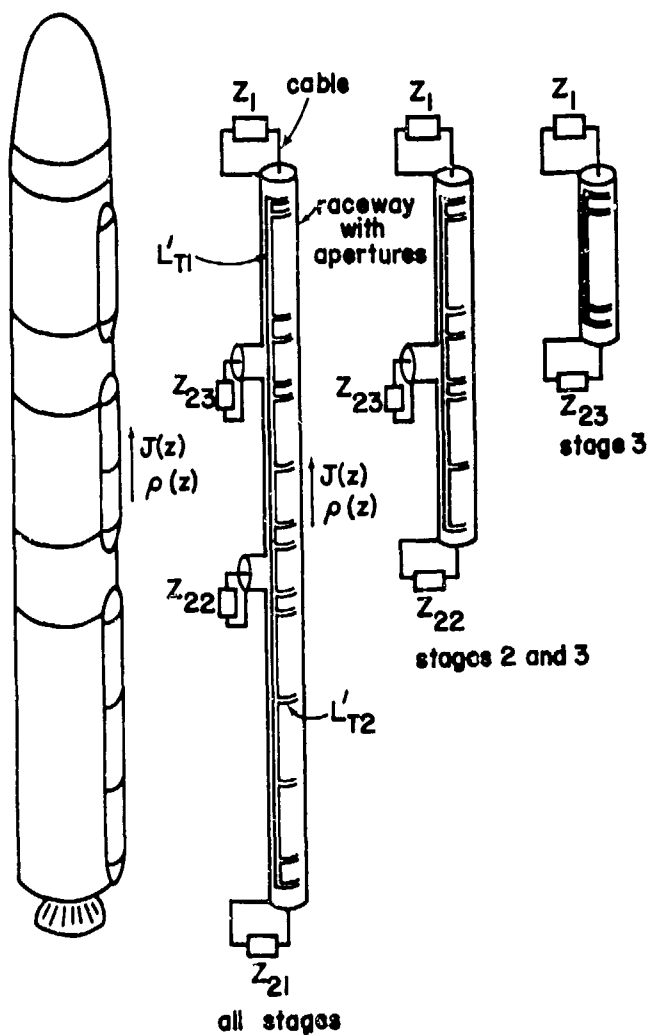
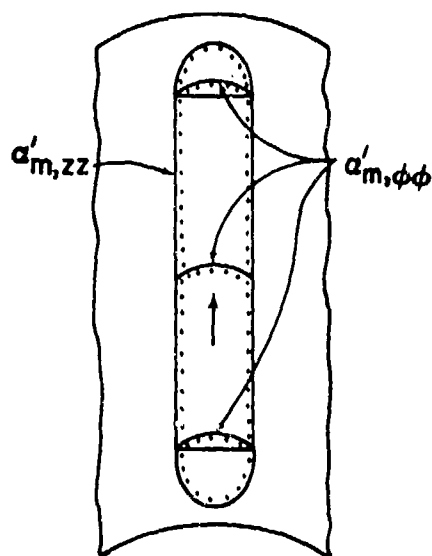


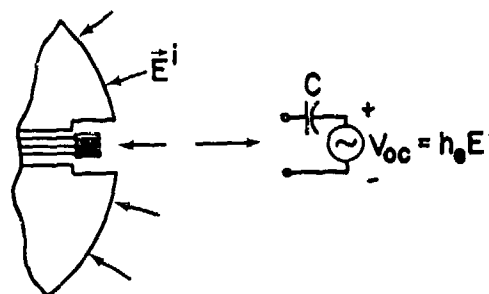
Fig. 9. Excitation of raceway cable through apertures at cover joints.

$\alpha'_{m,zz}$ representing the longitudinal raceway joints, and by a distributed polarizability per unit length $\alpha'_{m,\phi\phi}$ representing the annular joints between adjacent sections of the raceway cover, as illustrated in Fig. 10a.

The joint polarizabilities and the skin current density are used together with transmission-line theory to obtain the voltage and current induced on the raceway cable. Two solutions, one for distributed longitudinal joints and one for each of the distributed annular joints can be obtained for the raceway cable illustrated in Fig. 10a. However, for illustrative purposes we will use only one uniformly distributed transfer inductance L'_T to represent all leakage through the shield. To further simplify this example, we will ignore the interstage regions and the associated lumped impedances Z_{23} and Z_{21} in Fig. 9. Thus we will model the three-stage vehicle raceway as a single segment of a leaky transmission line, instead of three segments as illustrated in Fig. 9.



(a) polarizability per unit length of raceway cover joints



(b) small dipole equivalent of umbilical connector pins

Fig. 10. Coupling parameters for raceway cover and umbilical connector.

In addition, we will make an estimate of the open-circuit voltage induced on the pins of the umbilical connector illustrated in Fig. 10b.

3.2.1.3.1 Diffusion Through Skin

For a continuous metal raceway cover, the penetration of the missile current through the raceway cover is by diffusion only. To examine this effect we can use (4) of Chap. 2.4. The diffusion time constant τ_d for a 40 mil (1 mm) thick aluminum cover is

$$\tau_d = \mu \sigma d^2 = 44.5 \text{ } \mu\text{s} \quad (4)$$

and from Fig. 1 of Chap. 2.4 the frequencies that freely penetrate the cover are

$$f \leq 1/\tau_d = 22.5 \text{ kHz} \quad (5)$$

Therefore, we are primarily concerned with frequencies well below the missile resonance frequency of 7.5 MHz (the diffused fields at 7.5 MHz are smaller by a factor of 10^{13} than those below 22.5 kHz because of shield attenuation at 7.5 MHz). Furthermore, at 22.5 kHz, the 20-m long vehicle is electrically short, and because the EMP pulse-width τ_o is short compared to τ_d the EMP appears to be an impulse of magnitude $H_o \tau_o$, where H_o is the peak incident magnetic field strength.

The open-circuit voltage induced at one end of the raceway cable when the other end is connected to the missile skin is then

$$V_{oc} = J w Z_T^i \ell \quad (6)$$

where w is the perimeter of the raceway cover, ℓ is the length of the missile and Z_T^i is the transfer impedance of the raceway cover given by (4) of Chap. 2.4 with w replacing $2\pi b$. Making this substitution one gets

$$V_{oc}(s) = \frac{2H_o \tau_o \ell}{\sigma d} \sqrt{s \tau_d} \text{csch } \sqrt{s \tau_d} \quad (7)$$

which has the spectral form shown in Fig. 1 of Chap. 2.4. The time-domain curve for $V_{oc}(t)\sigma d\tau_d/(2H_o\tau_o\ell)$ is given in Fig. 113b of Chap. 2.1, from which

$$V_{pk} \approx 5.9 \frac{2H_o\tau_o\ell}{\sigma d\tau_d} \approx 4.56 \times 10^{-3} V, \quad \text{at } t \approx 4.0 \mu s \quad (8)$$

It is thus evident that a continuous flawless raceway cover would provide adequate shielding for the raceway cable, since 4.6 mV on this cable should cause no damage or upset in the missile electronic equipment. A similar conclusion can be reached if a flawless cylindrical raceway cable shield (or conduit) were used instead of the raceway cover.

3.2.1.3.2 Leakage Through Joints

In practical applications the raceway covers are attached with threaded fasteners or quick-disconnect fasteners. Thus the cover is not electromagnetically flawless because the cracks between fasteners permit the magnetic field to penetrate the covers. Such bolted joints characteristically permit magnetic fields to penetrate through the seam. This effect can be represented by a transfer impedance $Z_T' = j\omega L_T'$, as described in Sec. 2.4.1, Eq.(8). Note that in contrast to the diffusion case discussed above, this $j\omega L_T'$ leakage increases with frequency; hence the high-frequency part of the spectrum is more important for this case.

Although the value of L_T' is not calculable for bolted and riveted joints, a typical value for the equivalent polarizability $\alpha'_{m,zz}$ is $10^{-6} m^2$, which implies values of L_T' of the order of 1.0 - 1000 pH/m.

The voltage induced per unit length on raceway cable is of the form

$$V'(t) = L_T' \frac{dI}{dt} \quad (9)$$

where I is the raceway current, a fraction of the total current on the missile. At the midpoint of the missile, this current is a damped 7.5 MHz sinusoid of 5.8 kA peak amplitude. Approximately 1/20 of this current would flow on a 1-foot wide raceway. Thus the peak raceway current is approximately 290 A, and

$$\left. \frac{dI}{dt} \right|_{\text{peak}} \approx 2\pi f_1 I_{\text{peak}} = 1.37 \times 10^{10} \text{ A/s} \quad (10)$$

Hence, the voltage induced per meter is 13.7 V/m for the larger value of L_T' .

Because of propagation delays and nonuniform current distribution, the total open-circuit voltage induced on the cable is less than $\ell \times 13.7$ volts = 274 volts; nevertheless, a voltage of this magnitude is large enough to be of concern for small-signal electronic circuits operating at signal levels of the order of 1 volt. Therefore, it is apparent that the second layer of shielding is necessary to provide a safe margin of protection for circuits at the ends of the raceway cable.

Usually the cable shield, which forms the second principal shield for the raceway cable conductors, is connected to the vehicle structure at both ends. The current and voltage (or charge) on the shielded cable short-circuited at both ends must thus be known in order to perform the next stage of the analysis — the penetration of the cable shield and interaction with the internal conductors. Although straightforward, the analysis of the transmission line with distributed sources is long and tedious (see Chap. 2.4) and is best performed with the aid of a computer.

We may obtain an estimate of the current in the shield at low frequencies ($\ell \ll \lambda$) by observing that the impedance of the cable shield shorted at both ends is primarily inductive and is approximately given by

$$j\omega L = j\omega \ell L' \quad (11)$$

where L' is the inductance per unit length of the cable and raceway. For broadside incidence the induced voltage in the loop formed by the cable shield and its short-circuit terminations is

$$V(\omega) = j\omega \ell L_T' I \quad (12)$$

where I is the current flowing in the raceway. Hence the cable current at low frequencies is

$$I_t = \frac{V}{j\omega L} = \frac{L'_T I}{L'} \quad (13)$$

For a typical characteristic impedance of 40 ohms, L' is 0.133 $\mu\text{H}/\text{m}$, and for $L'_T \approx 10^{-9} \text{H}/\text{m}$, the total cable current is

$$I_t \approx 7.5 \times 10^{-3} I_{\text{peak}} \approx 2.2 \text{A} \quad (14)$$

If the cable were not shielded, this current would flow on the wire bundle.

As the first resonance frequency f_1 is approached, however, the cable shield circuit can no longer be accurately represented by a lumped source V driving a lumped inductance $\mathcal{L}L'$.

3.2.1.3.3 Voltage on Connector Pins

If the umbilical connector is not deadfaced when the umbilical cable is removed, the pins may behave as small electric dipole antennas interacting with the surface electric field (or the surface charge density $\rho = \epsilon E$) as illustrated in Fig. 10b. To estimate the open-circuit voltage induced on the pins, we need to know the effective height h_e of the pins (as dipole antennas) and the surface electric field strength E . From the dimensions of typical umbilical connectors, we can estimate the effective height of the pins to be about 1 cm. Also, from the properties of cylinders having aspect ratios (ℓ/a) of 20 it is known that the surface field is on the order of the incident axial field except very near the ends or corners (where it is larger than the incident field) and near the center (where the surface field vanishes). If the umbilical connector is at neither of these locations, the open-circuit voltage induced on the pins is on the order of

$$V_{\text{oc}} = h_e E^1 \quad (15)$$

$$\approx 500 \text{ volts (peak)}$$

for the canonical 50 kV/m EMP. The antenna impedance $(j\omega C)^{-1}$ is very large at most frequencies of interest ($C \approx 0.3 - 1 \text{ pF}$) and the antenna is loaded

with the characteristic impedance of the internal wire (≈ 100 ohms), so that the decay time-constant for the voltage delivered to the wire is 30 to 100 ps (i.e., much less than the EMP rise time). Hence, even though the induced voltage on the pin is much larger than that induced by the raceway cover leakage, its effect on internal components may be less important because of the very short time-constant of the circuit. The use of deadfaced umbilical connectors ensures that this penetration path will be ineffective.

3.2.1.4 Penetration of Second Shield and Internal Interaction

As illustrated in Fig. 11a, the internal interaction analysis for the rocket vehicle consists of repeating the transmission line analysis using the raceway cable shield transfer characteristics driven by the cable current to obtain the voltage and current of the internal conductors of the raceway cable. For the internal conductors, only the current and voltage at the cable-ends (i.e., those delivered to the sensitive components) are of interest. These quantities arise from distributed diffusion and aperture leakage through the cable shield (Fig. 11b), and from discrete leakage at the cable connectors (Fig. 11c). As was noted in the intermediate interaction analysis, however, only the aperture leakage is significant for the EMP. The distributed transfer impedance and transfer admittance for most cable shield configurations are given in Sec. 2.4.1. The discrete transfer impedance for connectors may be obtained from empirical data.

Although the raceway cable is a multiconductor cable, it will be treated as a single-conductor cable (with shield) to simplify the analysis, and only the common-mode open-circuit voltage at the end of the cable will be determined. This voltage induced by the interaction of the incident EMP with the rocket vehicle will constitute the final result for this analysis. In addition, as was the case for the raceway, the current in the cable varies with position and frequency (or time). Because the solution of the transmission-line equations for the distributed raceway, shield, and internal wire currents calculated at sufficient frequencies to obtain an inverse Fourier transform is very cumbersome, only a rough

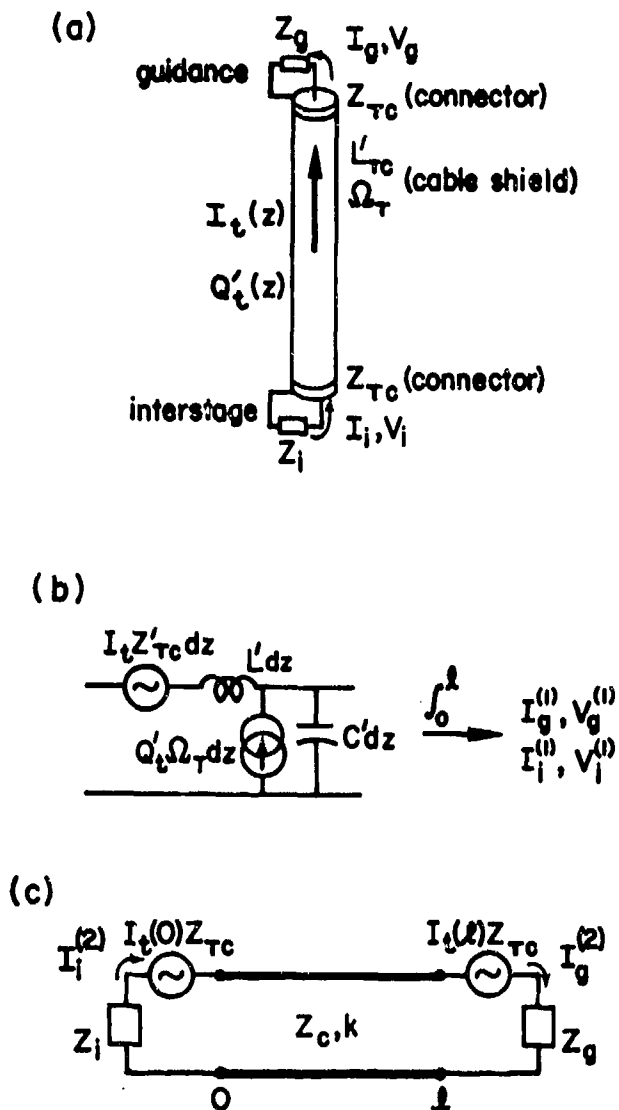


Fig. 11. Voltage and current delivered to loads in guidance system and interstage components. (a) Shielded raceway cable and connectors; (b) voltage and current from distributed coupling (cable shield); and (c) voltage and current from discrete coupling (connectors).

estimate of the currents will be made. Estimates similar to those made above for the voltage and current induced in the raceway cable will also be made for the internal wire current and voltage.

3.2.1.4.1 Cable Shield Parameters

The leakage through the braided wire shield of the raceway cable is determined by the transfer inductance and the charge transfer frequency defined in Sec. 2.4.1. For our example, we will assume the following cable shield properties:

cable radius $b = 1$ cm	wire size in braid $d = 0.15$ mm
weave angle $\psi = 30^\circ$	no. wires per carrier $n = 10$
coverage $K = 0.9$	no. carriers in shield $N = 50$

Then from (14) and table 2 of Chap. 2.4, the transfer inductance is

$$L'_{Tc} = 0.275 \text{ nH/m}$$

and from (19) and table 4 of Chap. 2.4 ($\epsilon_r = 2.3$) the charge transfer frequency is

$$\Omega_T = j 9.9 \times 10^6 \omega C'$$

where C' is the capacitance per unit length between the inner conductors and the shield. These transfer parameters are used to define the series and shunt sources driving the internal conductors in the cable. These sources, given by (1) and (2) of Chap. 2.4 are

$$\begin{aligned} V'(s) &\approx j\omega L'_{Tc} I'_t(z,s), & (\omega L'_{Tc} \gg R'_b) \\ I'(s) &= \Omega_T Q'_t(z,s) \end{aligned} \tag{16}$$

where I'_t and Q'_t are the total current and total charge per unit length on the cable.

3.2.1.4.2 Internal Wire Voltage

The driving sources given by (16) are space- and frequency-dependent, and because the cable is electrically long at the frequencies that freely penetrate the shield, a transmission-line solution of the type described in Sec. 2.4.2 is required to obtain the current and voltage on the internal conductor. A crude estimate of the internal wire voltage is obtained from the low-frequency approximation

$$\begin{aligned} V_{oc}(t) &\approx 2L'_{Tc} \frac{dI_t}{dt} \\ &\approx 2L'_{Tc} \frac{L'_T}{L'} \frac{dI}{dt} \end{aligned} \quad (17)$$

where I is the raceway current which is approximated by a 290A sinusoid. Using (10) for the value of dI/dt one finds the peak open-circuit voltage to be

$$V_{oc}(t) \Big|_{\text{peak}} \approx 0.57 \text{ volts} \quad (18)$$

This is to be compared with 274 volts calculated earlier for the unshielded raceway cable. The addition of the braided wire shield has thus reduced the open-circuit induced voltage on the raceway conductors by a factor of almost 500.

This example has provided some insight into the interaction of a rocket vehicle with the EMP and some representative excitation levels at points of interest in the vehicle. However, the low-frequency approximations used for the internal conductor analysis are very crude and should be used only for a rough estimate of the response. In a rigorous application to a system, the skin current density and the raceway cable current and voltage must be determined at enough points along the vehicle to define standing waves at the highest frequency of interest. That is, the distributed driving sources must be defined and the transmission-line theory must be used to calculate

the internal wire current or voltage. Such an approach is particularly important in the rocket vehicle example because the resonances of the vehicle and the cable shield occur at approximately the same frequencies, and may have the effect of a double-tuned transformer in enhancing the interaction of the interior wire with the EMP field at selected frequencies.

3.2.2 AIRCRAFT

3.2.2.1 General Description of Aircraft

3.2.2.1.1 Airframe and Equipment

Although aircraft interaction with the EMP has some similarities with rocket vehicle interaction, there are many significant differences. Aircraft undergo fewer configuration changes in flight than do multistage rocket vehicles; their principal axes (wing and fuselage) are horizontal rather than vertical; their engines produce no conductive plume; and their flight trajectory in the atmosphere is predominantly horizontal rather than vertical. Until recently, most military and commercial aircraft were of all-metal construction. While the all-metal airframe is still the norm, the introduction of composite materials such as glass fiber or carbon fiber-reinforced epoxy is an increasingly common deviation from this norm.

Aircraft are also equipped with extensive systems designed to accommodate the flight personnel — a fact that, on the one hand, makes the aircraft more complicated than the rocket vehicle and, on the other hand, makes the aircraft somewhat less dependent on automatic navigation and control systems. In the intermediate interaction regions, aircraft are considerably more complex than rocket vehicles because of the ubiquitous wiring, hydraulic tubing, control cables, and heat and ventilation ducting. In addition to elaborate environmental control systems, the aircraft contains a power plant and its derivatives, flight controls, and radio systems for communication and navigation. Except for some of the radio antennas, these systems are all within the mold lines of the airframe.

In addition to these flight systems, the aircraft will have "payload" systems related to its mission. Thus, for example, the aircraft may be equipped with fire control systems, bomb sights, terrain following systems, electronic countermeasures, IFF transponders, and many other mission-oriented systems. Fighters and bombers may carry external stores of weapons or fuel in pods on wing tips or on pylons under the wings. Such external stores may be jettisoned, thereby altering the shape of the vehicle, and they may contain electronic circuits that are critical to the aircraft mission.

Although the wide variety of mission payloads precludes a detailed description of each here, it is observed that the systems that require greatest EMP immunity are those containing small-signal electronic circuits. Since many of these circuits are digital in modern systems, they tend to be more susceptible to transients than the older analog circuits. It is also remarked that mission-oriented systems have grown increasingly sophisticated and susceptible to EMP effects with the development of high-performance, low-power integrated circuit components. The same remarks apply to flight systems. Hence, ensuring the ability of the aircraft to perform its intended functions in an EMP environment (or after exposure to one) is made more difficult by these advances in technology.

3.2.2.1.2 Power Plant and its Derivatives

The power plant usually consists of one or more turbine engines which provide the power for propelling the aircraft as well as for generating electricity, hydraulic power, and auxiliary power in the form of compressor bleed air. Supporting the power plant are: (a) the fuel system, which consists of the fuel tanks, pumps, gauges, and purging or venting systems; (b) engine controls such as the throttle, afterburner, and thrust reverser controls; (c) performance monitoring systems for engine pressure ratio, temperature, oil pressure, engine speed, etc.; and (d) protection systems such as fire warning sensors and fire extinguishers. Some of these items are illustrated in Fig. 12. The power plant is composed of mechanical and

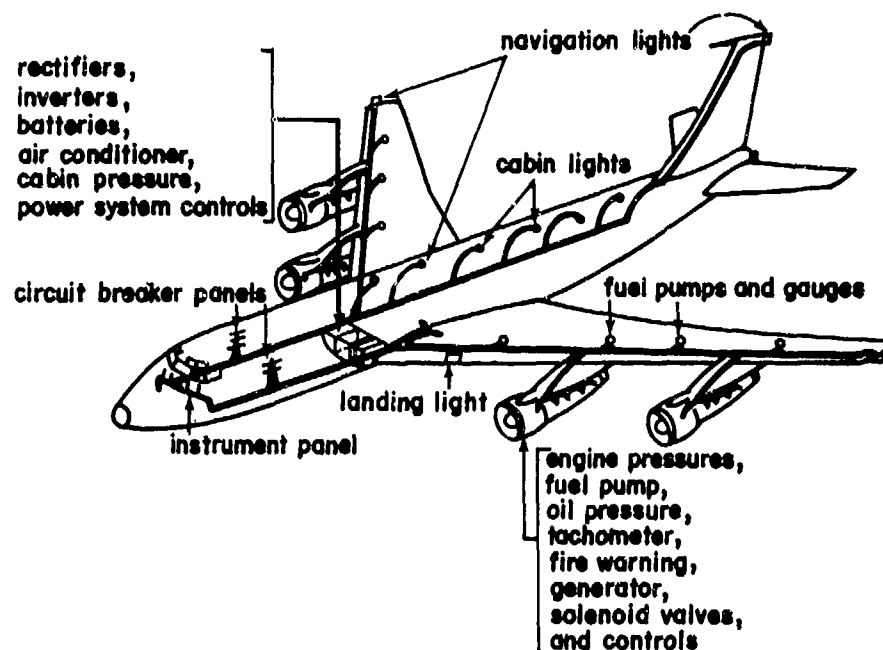


Fig. 12. Typical elements and cabling associated with the aircraft power system.

electromechanical components that are relatively immune to electrical transients. However, alternator controls, rectifiers, and controls for aircraft electrical power derived from the engine power often contain small-signal electronic circuits that require considerable protection.

3.2.2.1.3 Flight Control

The flight control system is made up of the control surfaces, control cables, the stick, rudder pedals, trim controls and servomechanisms associated with flight control. The control surfaces are shown in Fig. 13 and include the ailerons, elevators, rudder and speed brakes used in flight, and the flaps and spoilers used in takeoff and landing. Steel cables from the crew cabin to the control surfaces are used as the primary link between the crew and the control surfaces. However, actual movement of a control surface may be done by hydraulic or electrical actuators or by an aerodynamic boost device. In addition, because human reflexes are

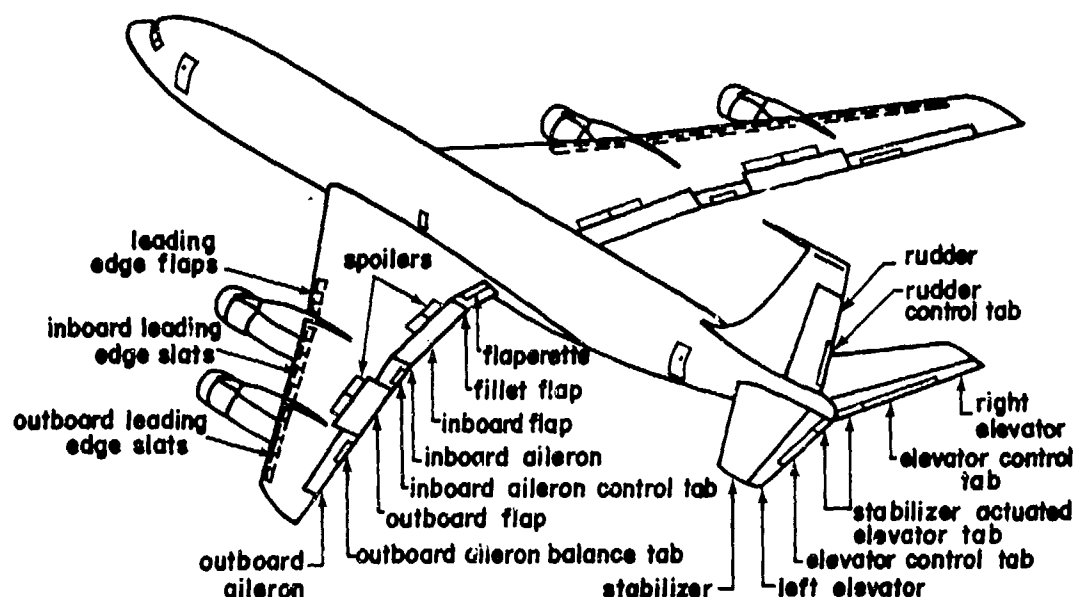


Fig. 13. Control surfaces on a modern jet transport.

often incompatible with the aerodynamic responses of the aircraft, servomechanisms and autopilots are used to aid the crew in maintaining stable flight. Gyros, compasses, altimeters, and other instruments used with these servomechanisms thus become a part of the flight control system. The flight controls are typically mechanical or electromechanical systems, but servomechanisms and autopilots contain small-signal electronic circuits that require protection from EMP-induced currents.

3.2.2.1.4 Radio Systems

The radio communication and navigation systems permit the crew to communicate with the ground and with other aircraft, and assist in fixing the aircraft position and in identifying and avoiding flight hazards such as thunderstorms, enemy aircraft, or other aircraft on a collision course. The communication systems in common use are VHF and UHF radio, but HF is often used on over-the-ocean flights, and VLF radio is used on some special-purpose aircraft. The antennas for some of these systems are

illustrated in Fig. 14. Navigation aids in common use are radio direction and range-finding systems (VOR, ADF, DME). Sophisticated ground-mapping and terrain-following systems are found on some advanced military aircraft. Most aircraft also carry weather radar, and military aircraft often have IFF and ECM systems. All of these systems contain extensive small-signal

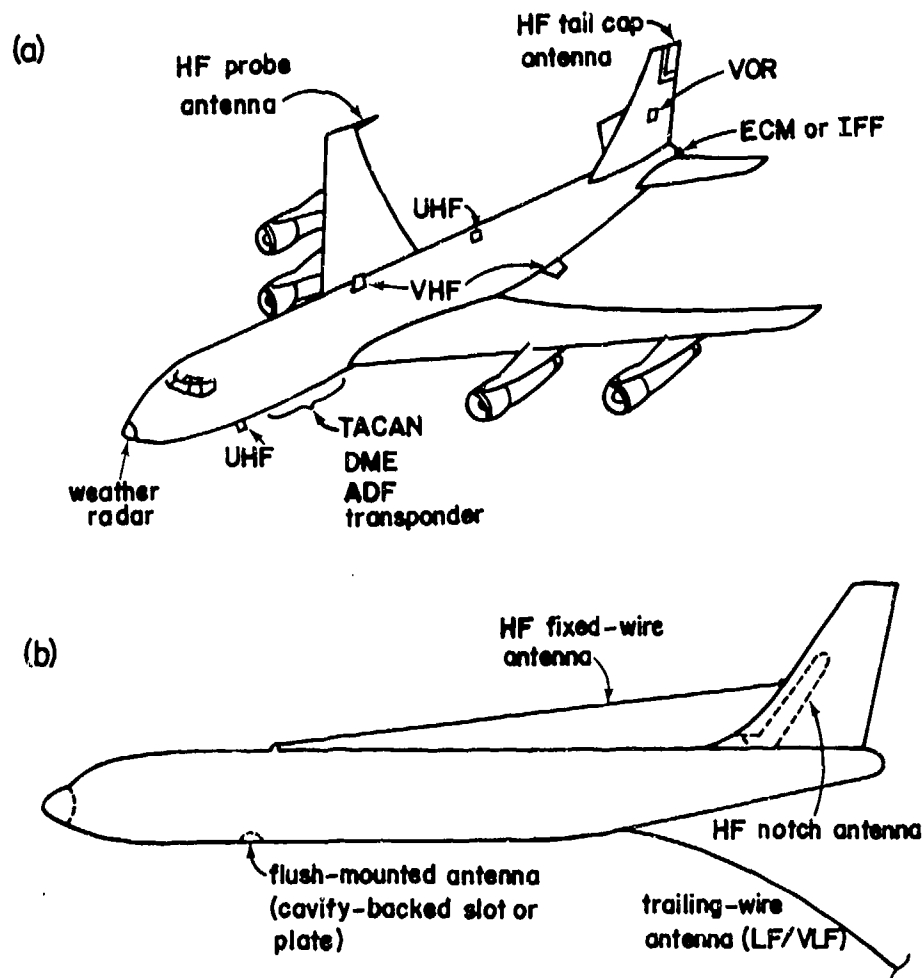


Fig. 14. (a) Some antennas on aircraft; (b) wire antennas and flush-mounted antennas.

electronic circuits that require protection from the EMP. Furthermore, all of these systems use antenna elements that are directly exposed to the external charges and currents induced on the airframe by the EMP.

3.2.2.1.5 Environmental Control Systems

Environmental control equipment required to accommodate the flight crew and passengers includes cabin pressurization, heating and air conditioning, oxygen supply systems, lavatories, ejection systems, windows and similar accouterments. Most of these items are relatively immune to the EMP, and many are not critical to the aircraft mission. Nevertheless, examination of these components is always prudent. For example, a window may be presumed to be immune to the EMP, but the compromise it makes in the shielding ability of the skin may be important to other onboard equipment. Also, seemingly unimportant changes in technology may produce significant ramifications in the susceptibility of the aircraft to the EMP. As an example, the low-cost and flexibility of microprocessors has led to widespread applications of these components in areas not heretofore considered. Therefore, many devices that were formerly mechanically or electromechanically operated and were therefore immune to the EMP are now electronically controlled and potentially susceptible.

3.2.2.2 Aircraft Topology

Most electronic components in conventional all-metal aircraft can be viewed as having two principal electromagnetic shielding surfaces. The first principal shield is provided by the metal skin of the aircraft, and the second is provided by the metal equipment cases. For structural and functional reasons, the volume inside the skin is often partitioned by bulkheads and decks, as illustrated in Fig. 15. Thus the volume inside the first principal shielding surface is cellular, or in the terminology of Part 1, it is divided into elementary volumes or subvolumes. For example, the equipment bays near the nose of the aircraft, the pressurized crew compartments, the bomb bays, the wheel wells, etc. are each nominally closed elementary volumes inside the first shield. Similar partitions

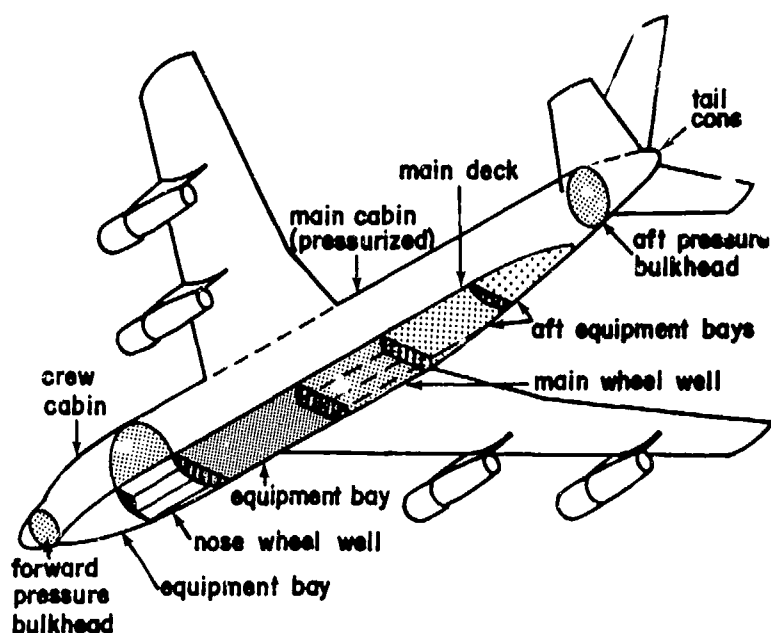


Fig. 15. Elementary volumes within the aircraft.

occur in the wings and empennage between the fixed and moving parts (see Fig. 13) and between the fuel cells and the leading and trailing edge regions of the wings.

Compromises of the first principal shield occur at windows, doors, cable and plumbing penetration points, and at riveted joints in the skin. The pressurized main cabin in Fig. 15, although potentially well shielded, may receive EMP fields through windows and imperfect door seals and skin joints, but probably more important will be the currents entering the cabin on electrical wiring and control cables that are exposed to the external EMP in the wings or under non-metallic skin sections or fairings. In the equipment bays, electrical wiring, hydraulic tubing, heating and ventilation pipes, control cables, and other plumbing may permit interference to propagate from one elementary volume to another. Therefore, the environments in elementary volumes that are potentially independent of one another may in fact be closely related because of the many conducting wires and tubes passing through the separating walls.

The second principal shield, the equipment cases, houses the small-signal circuits. The equipment is packaged for installation in equipment racks in the crew cabin or is mounted in one of the equipment bays. Therefore, each item of equipment is usually small enough to be hand-placed and each carries its own shield. A typical avionic system is made up of several such packages interconnected with cables as illustrated in Fig. 16. The second principal shield is thus composed of several potentially independent regions; however, unlike the first principal shield, these regions do not often share a common wall, although they may be separated by a common first wall as in Fig. 16. Alternatively, the individual equipment shields may be interconnected through the cable shields to form a single shield of irregular shape, as shown in Fig. 17.

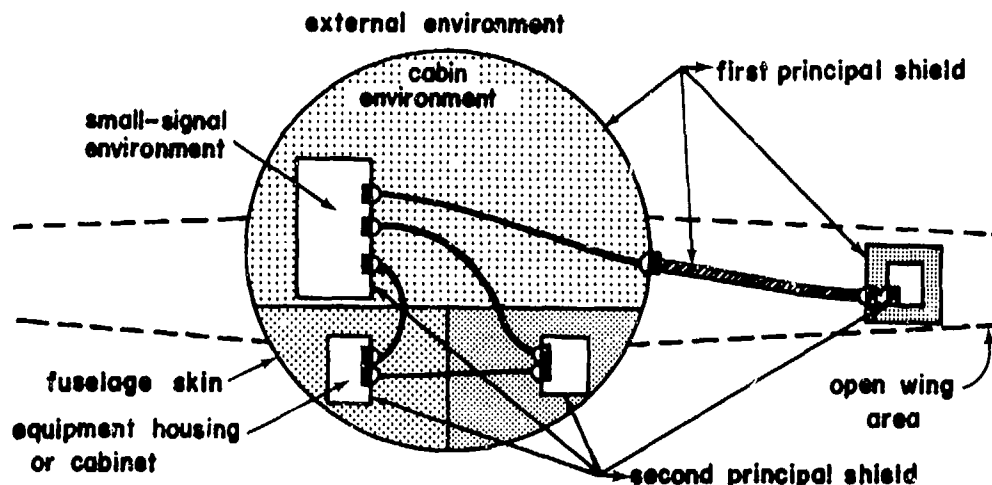


Fig. 16. Typical aircraft topology with unshielded interconnection cables.

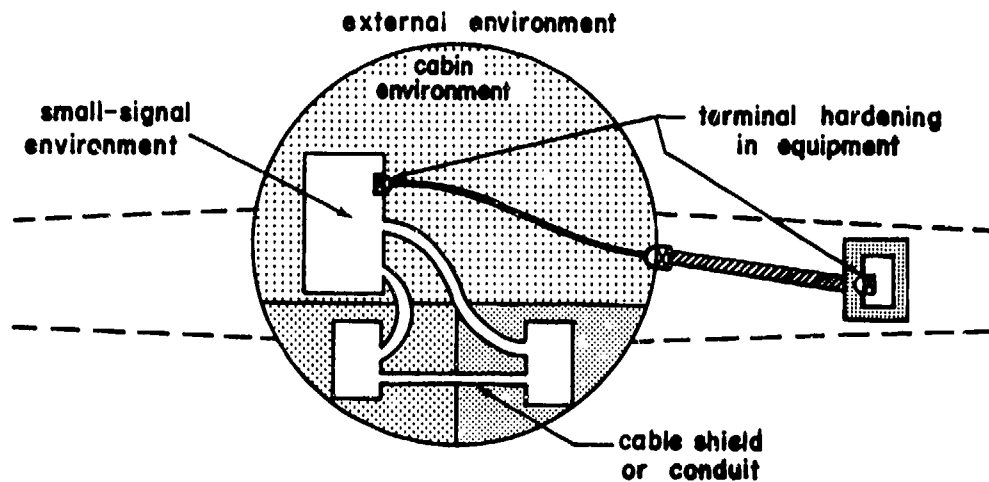


Fig. 17. Typical aircraft topology with shielded interconnecting cables in the cabin.

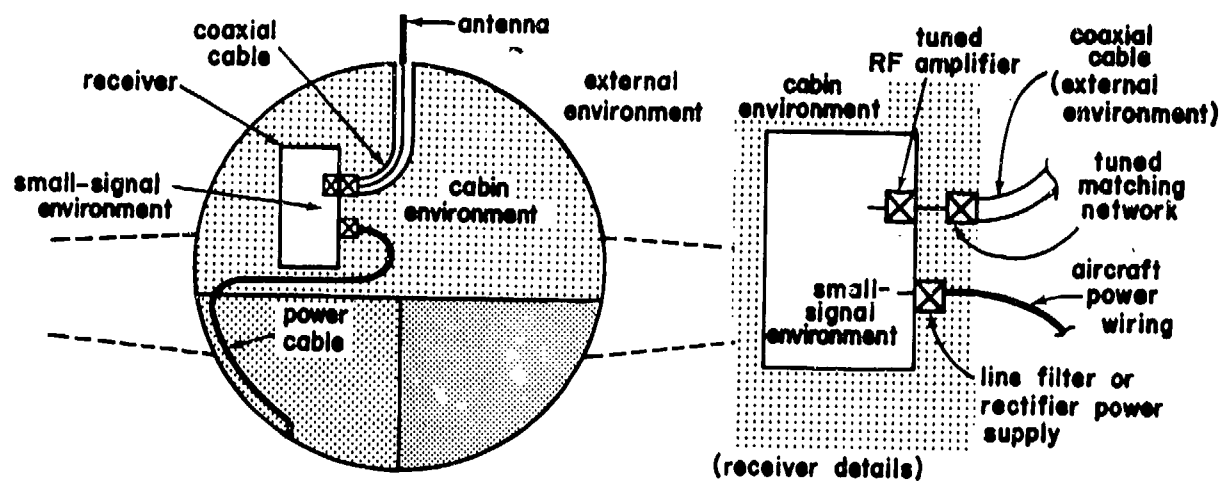


Fig. 18. Topology for a radio system.

The topology for a radio system with an external antenna is particularly interesting because of the external environment inside the antenna cable. Fig. 18 illustrates a radio receiver with a dipole antenna connected to the receiver by a coaxial cable. The receiver cabinet and RF terminal structure must provide two layers of shielding to be topologically consistent with the remainder of the two-layer shield system. As shown in Fig. 18, this may be achieved by employing a tuned matching network or coupler and a tuned RF stage, although in practice these shield-preserving components may not be as distinct as those shown in the illustration.

Because avionic equipment is often supplied, already packaged and ready to mount, the airframe manufacturer may have little control over the equipment case and its interior. He usually controls the interconnecting cable design and installation, however, so that he may be required to determine whether the cables should be unshielded, as in Fig. 16, or shielded as in Fig. 17. The correct choice will depend on the sensitivity of the equipment, the quality of the environment inside the first shield, and on the cost and weight of cable shielding compared to equipment terminal protection (or other techniques for maintaining the integrity of the second principal shield).

To provide further EMP hardness for certain components a third principal shield may be required, an example of which is the cable shield with a cable conduit. In principle, one may introduce a third principal shield, and so on, to reduce the interference to as small an amount as one pleases, but the penalty of cost and weight of shielding will be increased.

In the two sections that immediately follow, example calculations will be made for several interaction paths. Fig. 19 is the interaction sequence diagram that threads all the example calculations together.

3.2.2.3 External Interaction

3.2.2.3.1 Airframe

The interaction of a flying aircraft with the EMP induces current flow, and therefore charge displacement, on the airframe. Typical quasi-static

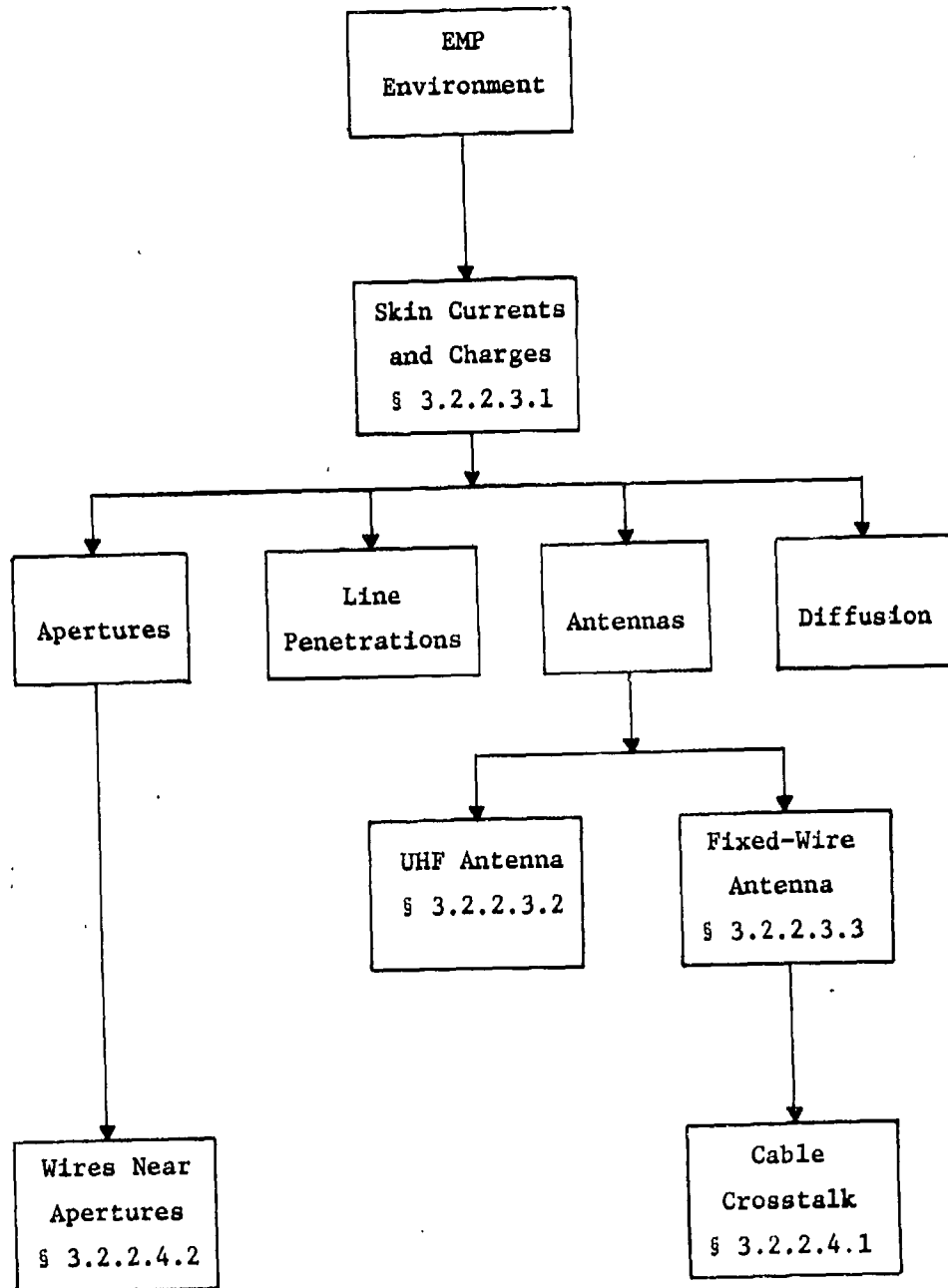


Fig. 19. Interaction sequence diagram for the aircraft example calculations.

airframe currents and charge displacements are shown in Fig. 20 for the fuselage and wing excitations. Because the airframe of a medium-sized transport aircraft resonates at a few MHz (e.g., the KC-135 resonates at about 2.5 MHz), the high-altitude EMP spectrum excites the first resonance and many higher-order natural modes.

These induced skin currents and charges determine the interaction of the EMP with the aircraft's interior. That is, the penetration of the EMP through a window, the excitation of a small antenna, and the diffusion of fields through the skin are all dependent on the nature of the local EMP-induced currents and charges on the airframe. Because the aircraft's outer skin is for the most part composed of a highly conducting metal, such as aluminum or titanium, the metal skin can be considered a perfect conductor for determining the skin current and charge density. The mathematical problem of calculating the skin currents and charges is then

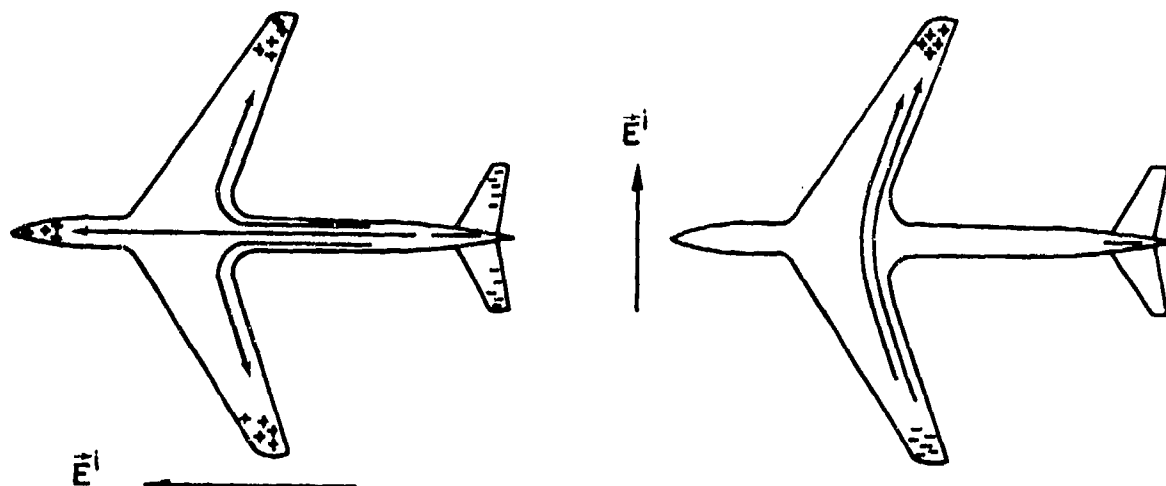


Fig. 20. Quasi-static current paths and charge distributions induced on an airframe.

a problem in electromagnetic scattering by a perfectly conducting body. The difficulty of such a problem depends on the complexity of the scattering object, which in the case of aircraft is very great. In aircraft external interaction analysis, one is usually limited to modeling an aircraft with simple geometrical shapes such as crossed pipes. For the stick (or crossed pipe) model illustrated in Fig. 21, computer codes have been developed to predict the values of induced currents and charges at low and intermediate frequencies (see Sec. 2.1.2.1.4).

If a substantial fraction of the skin is composed of partially conducting composite materials such as carbon fiber laminates, the resulting reduction of the skin conductivity complicates the response characteristics of the aircraft skin to an EMP. Consequently, the external interaction problem for an aircraft equipped with a partially composite skin is more difficult than the corresponding problem for an entirely metallic skin. Nonconducting composites such as glass or aramid fiber laminates are, of course, transparent to the EMP. Small nonconducting composite sections may be treated as apertures in the metal skin.

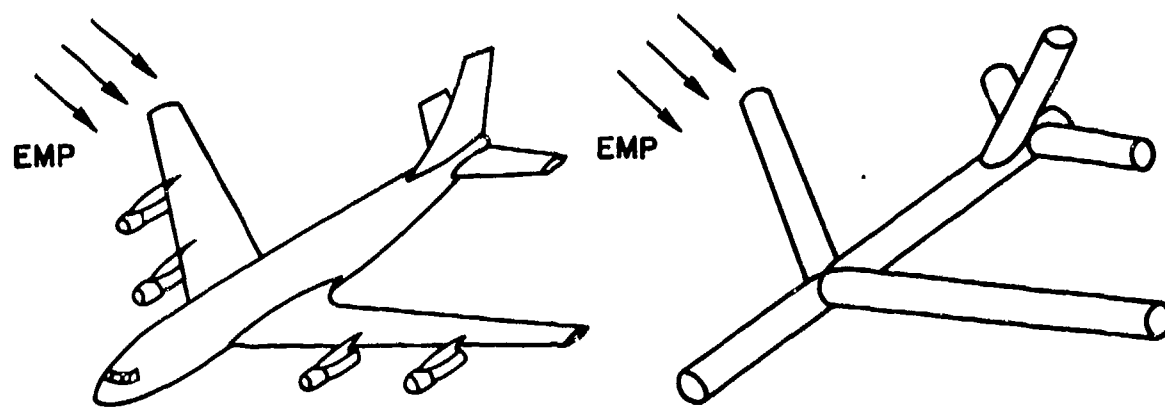


Fig. 21. A stick model of an aircraft used in the aircraft EMP external interaction calculation.

The external interaction of aircraft equipped with long trailing-wire antennas for low-frequency communication systems (e.g., LF-VLF) is unique because in this case, the characteristics of the antenna rather than the airframe dominate the low-frequency response. In the context of electromagnetic scattering, the airframe behaves as a small blob at the end of a very long wire (Fig. 22). Thus wavelengths of several kilometers, which are associated with low-frequency and quasi-static responses for most aircraft, are associated with the intermediate frequencies on aircraft with trailing-wire antennas (see Sec. 2.1.2.3.1).

Another important configuration to be considered is the "ground-alert" configuration in which the aircraft is parked on the ground with ground support equipment attached. In this configuration, the wheels are down, the external stores are installed, the canopy (or cabin door) is open, and a ground power cable and ground wire are attached. The excitation of the parked aircraft by the EMP also differs from that of the aircraft in flight in that the incident wave is reflected by the ground, after which the reflected wave also interacts with the aircraft (see Sec. 2.1.2.1.4d).

In either the flight or ground-alert configurations, the complete response of the airframe to the EMP is very complex and difficult to describe comprehensively. This difficulty results from the complex shape of the aircraft and the broadband spectrum of the EMP excitation. Because of these factors, a complete description of the surface charge and current



Fig. 22. Aircraft with LF/VLF trailing-wire antenna deployed.

densities everywhere on the aircraft is almost never attempted. It is adequate for EMP interaction studies to obtain the charge and current densities at a few specific points on the airframe, such as the points where antennas are mounted, where windows or albedo or sextant ports are located, where there are doors or access plates, or where there are cracks, seams, or nonmetallic skin sections.

3.2.2.3.2 UHF Antenna

As an example we will examine the current and charge in the vicinity of an antenna such as a UHF blade antenna near the nose of the aircraft. The charge density at the nose of an EC-135 aircraft is shown in Fig. 30 of Chap. 2.1. From Fig. 65 of Chap. 2.1 one can find the effective height h_e and the impedance Z_{in} of the UHF blade antenna. The open-circuit voltage induced at the terminals of the antenna's connector is

$$V_{oc} = h_e \rho / \epsilon_0 \quad (19)$$

where ρ is the charge density which would exist on the skin of the aircraft at the location of the antenna if the antenna were removed.

It is apparent from Fig. 65 of Chap. 2.1 that the effective height of the UHF antenna is small (less than 0.5 cm) for frequencies below 100 MHz. It is also apparent from Fig. 30 of Chap. 2.1 that the charge density ρ is very large ($10\epsilon_0 E^1 - 100\epsilon_0 E^1$ for the frequencies shown). Because the EMP source spectrum is weak above 20 - 100 MHz, the antenna response in this region of the spectrum is also weak. However, in the vicinity of 2.5 MHz, the source is significant and the charge density on the skin is enhanced by the fuselage first resonance.

Because of the shunt across the UHF blade antenna (Fig. 64, Chap. 2.1) the antenna characteristic at low frequencies is

$$h_e = h'_e (j\omega)^2 L C_a \quad (20)$$

where L is the inductance of the shunt ($L = 27.6$ nH), C_a is the antenna capacitance ($C_a \approx 2$ pF), and h'_e is the effective height of the antenna

before shunting ($h'_e \approx 0.2\text{m}$). Because L , C_a and h'_e are all nearly independent of frequency at frequencies below 20 MHz, h_e increases approximately as ω^2 in this region, whereas the EMP spectrum is falling as ω^{-1} throughout most of this region. Thus, if the normalized $\bar{\rho}(\omega)$ in Fig. 30 of Chap. 2.1 represents the impulse spectrum of the charge density, the antenna response to the EMP will look like the derivative of the impulse response; that is,

$$V_{oc}(\omega) \approx K j\omega \bar{\rho}(\omega) \quad (21)$$

$$V_{oc}(t) \approx K \frac{d}{dt} \bar{\rho}(t)$$

where $K = E_0 h'_e LC_a \approx 5.5 \times 10^{-16}$ and $E_0 = 5 \times 10^4 \text{V/m}$ = amplitude of $\bar{E}^1(t)$.

While the inverse transform of the charge density spectrum can be obtained numerically, an estimate of the transient charge density can be obtained from the spectral peak magnitudes and bandwidths of the two resonances displayed in Fig. 30 of Chap. 2.1.

A simple resonant circuit may be represented by the transfer function

$$\frac{V(s)}{V_o} = \frac{1}{s^2 + 2\zeta\omega_o s + \omega_o^2} \quad (22)$$

$$\frac{V(t)}{V_o} = \frac{1}{\omega_o \sqrt{1-\zeta^2}} e^{-\zeta\omega_o t} \sin(\omega_o \sqrt{1-\zeta^2} t) u(t)$$

where ω_o is the undamped natural frequency and ζ is the damping ratio for the circuit (e.g., for an RLC circuit, $\omega_o = (LC)^{-1/2}$ and $\zeta = 1/(2Q) = RC\omega_o/2 = R/(2\omega_o L)$). The properties of the resonance that are important are the magnitude of the spectrum at the peak ($s = j\omega_o$), namely

$$|V(j\omega_o)| = \frac{V_o}{2\zeta\omega_o^2} = \frac{V_o}{\omega_o \Delta\omega} \quad (23)$$

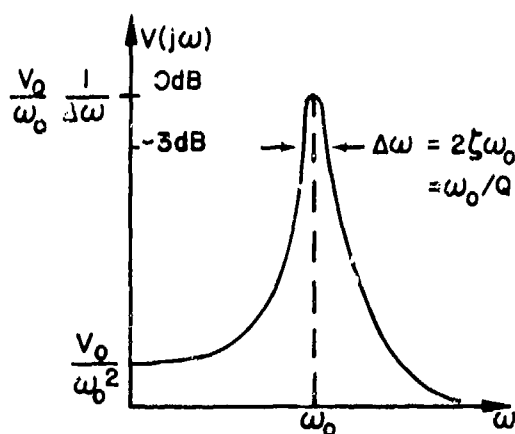
the resonance frequency ω_0 , and the bandwidth $\Delta\omega$ at 3 dB below the peak. These properties are illustrated in Fig. 23a. The impulse response of the circuit is shown in Fig. 23b where it is apparent that the impulse response is a damped sinusoid with a peak value of about V_0/ω_0 .

For the two resonances shown in Fig. 30 of Chap. 2.1 for $\bar{p}(\omega)$, we have

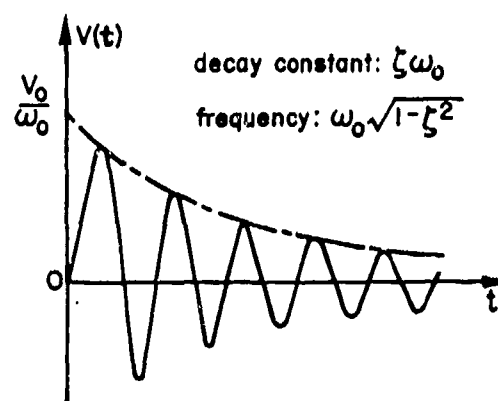
	#1	#2
magnitude	110	90
bandwidth	0.4 MHz	1 MHz
frequency	2.5 MHz	4.2 MHz

and in the time domain we have two damped sinusoids superimposed on one another. The damped sinusoids stimulated by the incident field have the properties

	#1	#2
peak amplitude	276×10^6	565×10^6
damping time constant	$0.795 \times 10^{-6} \text{ sec}$	$0.318 \times 10^{-6} \text{ sec}$
fundamental frequency	2.5 MHz	4.2 MHz



(a) impulse spectrum



(b) impulse response

Fig. 23. Simple resonant-circuit spectrum and impulse response.

The time derivatives of these impulse responses, which approximate the open-circuit voltage at the antenna terminals, give the EMP responses:

	<u>#1</u>	<u>#2</u>
peak amplitude	2.4 volts	8.2 volts
damping time constant	0.795×10^{-6} sec	0.318×10^{-6} sec
fundamental frequency	2.5 MHz	4.2 MHz

Therefore, it appears that the response of the UHF antenna to the EMP is dominated by the aircraft resonances and has a peak open-circuit voltage of a few volts. This result is consistent with the observations that the antenna is small and effectively shorted by the transmission-line stub throughout most of the EMP spectrum. The response calculated is for the antenna mounted on the nose where the charge density is enhanced. At more common locations on the fuselage, the charge density is lower by an order of magnitude.

This behavior is fairly typical of small antennas with built-in lightning protection and coupling networks. The few volts delivered to the coaxial center conductor are usually well within the tolerance of the receiver/transmitter terminals; furthermore, this signal is shielded from the interior of the aircraft by the coaxial cable shield. Thus EMP coupling to such antennas is usually not a major problem.

3.2.2.3.3 HF Fixed-Wire Antennas

To estimate the response of the HF fixed-wire antenna to an incident EMP let us examine Fig. 91 of Chap. 2.1 and the spectrum of a double-exponential pulse. The asymptotic behavior of a double-exponential pulse is shown in Fig. 24, where it is noted that for frequencies below f_1 (times greater than τ_f), the incident pulse behaves as an impulse of magnitude $E_0 \tau_f$, while for frequencies between f_1 and f_2 (times between τ_r and τ_f), the pulse behaves as a step function of magnitude E_0 . For the double-exponential EMP, $f_1 \approx 0.6$ MHz and $f_2 \approx 40$ MHz, so that the large 5 MHz resonance in h_c in Fig. 91 of Chap. 2.1 falls in the step-function region of the EMP spectrum. Thus we may estimate the antenna response by obtaining

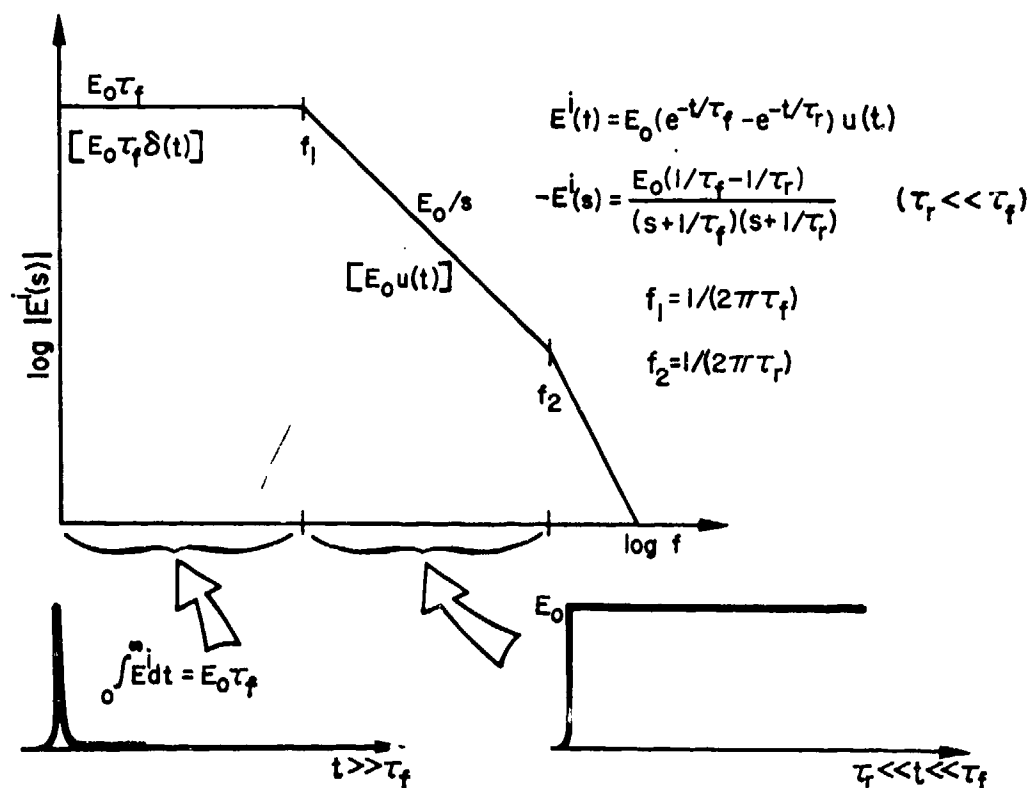


Fig. 24. Double-exponential pulse spectrum in log-log scale.

the step-function response of the simple resonant circuit described above. For the unit-step function excitation, the response is

$$V(t) = \frac{V_0}{\omega_0} \left[1 + \frac{1}{\sqrt{1-\zeta^2}} e^{-\zeta\omega_0 t} \sin(\omega_0 \sqrt{1-\zeta^2} t - \varphi) \right] u(t) \quad (24)$$

where $\varphi = \tan^{-1}(\sqrt{1-\zeta^2}/\zeta)$. For high-Q circuits ($\zeta \ll 1$) the step-function response consists of a sinusoid of peak magnitude V_0/ω_0^2 superimposed on a step of the same amplitude as illustrated in Fig. 25.

The "resonance" of h_e in Fig. 91 of Chap. 2.1 at 5.2 MHz has a peak magnitude of about 1000 m and a bandwidth of about 0.2 MHz. The bandwidth

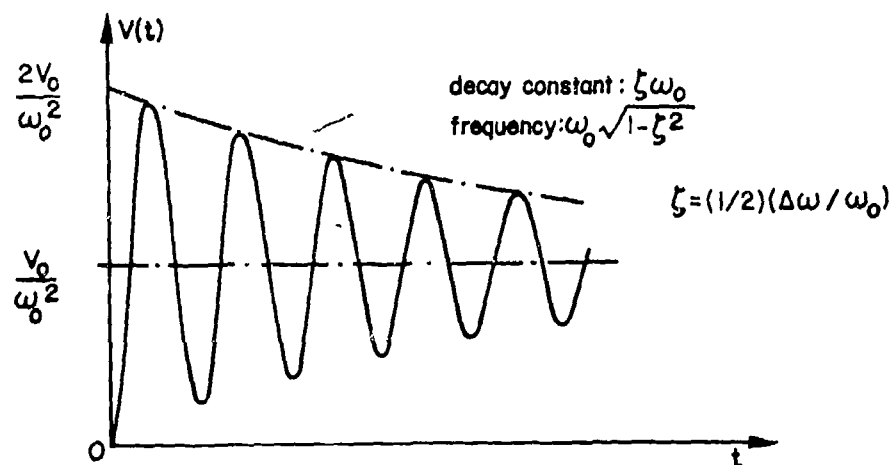


Fig. 25. Step-function response of a simple resonant circuit.

and resonance frequency lead to a damping ratio $\zeta \approx 0.02$ ($Q = 26$), and so the high- Q approximation can be used. Also, 5.2 MHz is in the "step-function" region of the EMP spectrum; thus the response to a 5×10^4 V/m step excitation will be used. Since

$$\frac{V_0}{\omega_0 \Delta \omega} = 1000 \quad \text{when } \omega_0 = 2\pi \times 5.2 \times 10^6$$

we have $V_0/\omega_0^2 = 38.5$. The peak open-circuit voltage induced at the terminals of the fixed-wire antenna by the 50 kV/m incident EMP is then

$$V(t) \Big|_{\text{pk}} \approx 5 \times 10^4 \times 2V_0/\omega_0^2 = 3.85 \text{ MV} \quad (25)$$

There is also a smaller, broader resonance at 1.7 MHz in Fig. 91 of Chap. 2.1; this is apparently the airframe first resonance, and the peak induced voltage at this frequency is about 0.4 MV. Thus the response at 5.2 MHz dominates the antenna response.

In Fig. 91a of Chap. 2.1 it is seen that the antenna input impedance is approximately 6×10^4 ohms at 5.2 MHz. Hence the antenna behaves as a current source supplying a short-circuit current $V_{\text{oc}}/Z_{\text{in}} = 3.85 \times 10^6 / 6 \times 10^4 = 64$ A to any load impedance small compared to 6×10^4 ohms. If a

50-ohm matched coaxial cable is used between the antenna and the receiver, this cable will carry 64A on the center conductor and the braided-wire shield. As indicated in Fig. 26, the voltage between the center conductor and the shield would be 3.2 kV, certainly enough to damage the receiver if the TR switch was not activated by the EMP induced pulse.

3.2.2.4 Internal Interaction

3.2.2.4.1 Fixed-Wire Cable Crosstalk

A question remains regarding the effect this EMP-induced voltage might have on other avionics on the same aircraft. Some of the EMP-induced signal will leak out of the braided wire shield used on typical coaxial transmission line and excite other nearby cables. A typical leakage inductance for the 50-ohm RG-213 cable is 0.25 nH/m. The voltage per meter developed outside the cable by the 64A current inside is

$$V' \approx \omega_0 L'_l I = 0.52 \text{ V/m} \quad (26)$$

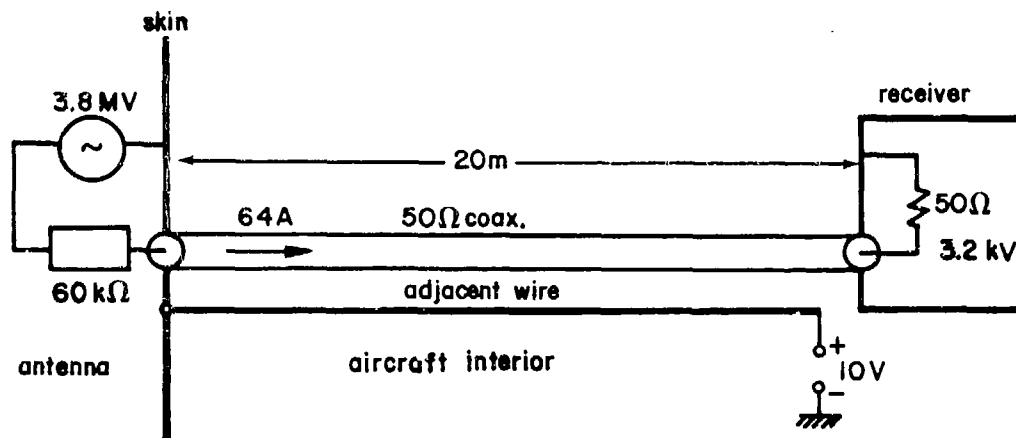


Fig. 26. Voltages and current induced by a 50 kV/m double-exponential pulse on HF fixed-wire antenna components.

Electric coupling between the braid shield and the external conductor has been neglected in this analysis. For the E-4 aircraft, 20 m of this cable may be required between the antenna and the receiver, so that as much as 10 volts could be developed on other conductors in the same bundle by leakage out of the antenna feed cable as indicated in Fig. 26. This assumes no coupler at the antenna terminals; a coupler is usually installed near the antenna terminals which, unless it were tuned to ω_0 , would attenuate the EMP-induced signal.

Although 10 volts is not a large transient for the interior of the aircraft, it is large enough to upset logic circuits unless the circuits are protected by an additional layer of shielding. Furthermore, because of uncertainties in the estimates leading to the 10-volt result, a safety margin of perhaps an order of magnitude is desired.

3.2.2.4.2 Wires Near Aperture

Interaction of the EMP with conductors inside the aircraft by means of fields penetrating apertures, such as windows, hatches, or doors, is also of interest. Such interaction is particularly likely in the vicinity of the cockpit where windows or canopies are required for operator visibility, and in wheel wells and bomb bays where large doors and poor electromagnetic seals can permit significant penetration.

Let us consider a wire bundle routed near a window as illustrated in Fig. 27a. The window and wire bundle can be represented as an aperture and a wire as shown in Fig. 27b. For the wire close to the wall ($h/R_0 \approx 0.1$) and not too close to the edge of the window ($\ell/R_0 < 2$), the data of Figs. 2 and 3 of Chap. 2.2 can be used. The open-circuit voltage induced on the wire by a surface tangential magnetic field H_{sc} perpendicular to the wire is

$$V_{oc} = f_s j \omega \mu_0 h \alpha_m H_{sc} / (\pi R_0^2) \quad (27)$$

where f_s is the small-hole correction factor given in Fig. 3 of Chap. 2.2, and α_m is the magnetic polarizability of the aperture. For a round hole of diameter ℓ , the polarizability of the hole is

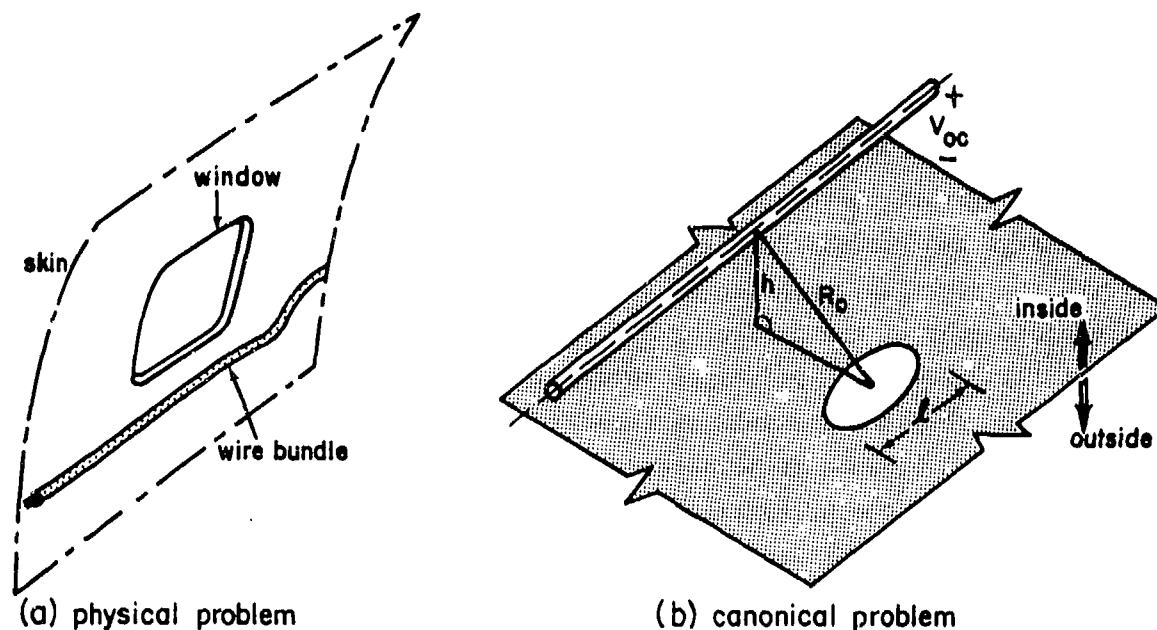


Fig. 27. Aperture penetration and interior wire interaction.

$$\alpha_m = \ell^3/6 \quad (28)$$

At airframe fundamental resonances, the short-circuit surface magnetic field H_{sc} is several times the incident magnetic field at points not too close to the extremities of the airframe.

For the EC-135 data of Fig. 32 of Chap. 2.1, the airframe first resonance occurs at about 2.5 MHz and the surface field is 20 times the incident field strength. Because the incident double-exponential EMP varies as $1/\omega$ at 2.5 MHz and the induced open-circuit voltage varies as ω , these frequency dependences cancel and the open-circuit voltage is directly proportional to the impulse response of the airframe. The impulse response whose frequency-domain properties are shown in Fig. 32 of Chap. 2.1 is a damped sinusoid of normalized peak magnitude $25\pi \times 10^6$ at the fundamental frequency of 2.5 MHz. For a 0.5 m diameter window, $\alpha_m = 0.0208 \text{ m}^3$, and for a typical wire position, the damped sinusoidal open-circuit voltage on the

wire has a peak value of about 110 volts. This is a significant voltage; it illustrates the importance of either treating windows to reduce the penetrating fields or routing wiring far from such openings.

3.2.2.5 Hardening Approaches

On aircraft there appears to be little that can be done to control the charge and current density induced on the skin by the incident EMP (with the possible exception of aircraft with trailing-wire antennas). Therefore most of the hardening concepts depend on establishing and controlling the first principal shield at the skin or at some other natural or deliberate shield surfaces. The pressure hull of the aircraft may be chosen because it is already a controlled surface and most sensitive avionics are in the pressurized region. Adding EMP control to the pressure barrier thus requires less special attention than imposing EMP requirements on otherwise uncontrolled skins and bulkheads.

As the above examples have illustrated, the principal offenders in EMP interaction are large antennas (or other line conductors that act as antennas) and large apertures. These devices allow the EMP energy to penetrate the first principal shield and to interact directly with equipment or indirectly through mutual coupling to other internal wiring. The topological approach to hardening requires that the apertures in the first principal shield be closed and that the currents on the penetrating conductors be diverted to the outer surface of the shield.

The apertures may be closed by covering them with metal skin if no penalty is incurred by doing this. For many apertures (notably the cockpit windows), however, visibility must be maintained. In such cases, several alternatives are available. A fine mesh that does not appreciably degrade visibility may be used to break the large aperture into many small apertures, thereby reducing the total aperture penetration. A conducting coating of stannous oxide having a surface resistivity of 2 to 5 ohms/square can be applied to significantly reduce the EMP penetration without seriously degrading transparency. Finally, one can simply avoid routing cables serving sensitive circuits near the large apertures. The latter approach may require somewhat more control over cabling practices than is normally exercised in aircraft manufacture.

Conductors that penetrate the first principal shield are often more serious compromises of the shield than the large apertures. It is important in EMP hardening to trace the system topology and identify all penetrating conductors, whether they are electrical cables or pipes, tubes, control cables, etc. Each must be treated in some manner to prevent externally induced currents from passing through the skin to the interior of the aircraft. Techniques for treating groundable stationary pipes and tubes and signal-carrying conductors are suggested in Fig. 9 of Chap. 3.1. An additional treatment for electrical wiring is to distort the first principal shield, so that the shield encloses the "external" wiring; that is, to enclose the external wiring in a conduit or other shield that is topologically part of the first shield. This approach can be used for wiring in the wings, bomb bays, and wheel wells where natural shielding afforded by the airframe is very poor during parts of the mission.

3.2.3 GROUND-BASED SYSTEM

Permanent ground-based installations such as rocket vehicle launchers and communication facilities are generally characterized by large external appendages such as power lines and communication cables, and by facility shields of various qualities. For the present example, we will use the rocket vehicle launcher illustrated in Fig. 28. Commercial power is normally used to operate the system and to perform expendable station-keeping operations. Communication and monitoring from a remote location is done through a buried, shielded communication cable. An alternative communication channel may be a radio system; hence, an external radio receiving antenna and feed cable may be provided.

The system illustrated in Fig. 28 is considerably simplified; operational systems often contain many other external elements such as outside lighting, WWV receivers, local radio communications systems, external power outlets, intrusion alarm sensors, radiation/EMP monitors, local telephone cables, etc., as well as plumbing for water, sewage, fuel, etc. However, the elements shown are representative of the external interaction elements, and they will be used to illustrate EMP interaction with long overhead conductors, long buried conductors, and "local" antennas and antenna feeds.

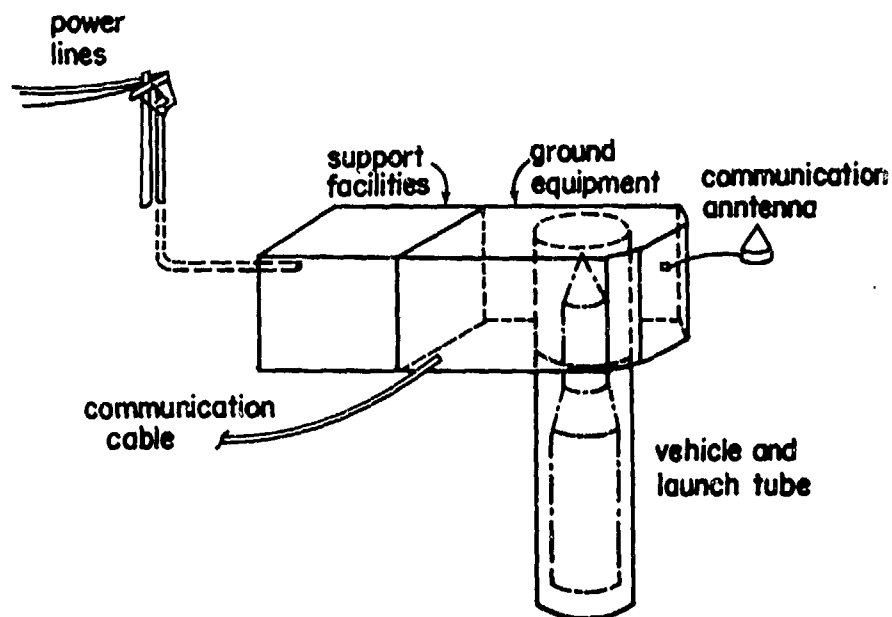


Fig. 28. Components of a ground-based launcher.

In addition, as will be discussed later, it will be assumed that the launch tube lid is imperfect, so that external magnetic fields may penetrate through the joints between the lid and the launch tube walls. Thus, this example will also demonstrate the effect of penetration through the apertures in the shield.

3.2.3.1 System Topology

The first principal shield for the system will be the welded steel walls of the launch tube and ground equipment compartment. This shield is identified in Fig. 29 as $S_{0,1}$. Except for the launch tube lid and the holes for cable entries, the outside envelope of $S_{0,1}$ is considered to be continuous steel plate.

Within $S_{0,1}$ there are secondary principal shields that form the housings for power and signal processing circuits. These secondary shields are identified as $S_{1,1}$ in Fig. 29, and are usually metal equipment cabinets.

Within the launch tube the vehicle skin $S_{1,2}$ is also a secondary principal shield that separates the rocket vehicle circuits from the environment of the equipment room and launch tube.

The pertinent system topology is illustrated in Fig. 30, where the left half of the diagram represents the equipment room and the right half represents the launch tube. The first principal shield on the left side is compromised by the penetrating cables, while on the right side the shield is compromised by the leaky lid apertures. The divider between the left and right sides represents the wall separating the launch tube from the ground equipment room; this divider is compromised by the umbilical cable between the support equipment and the vehicle.

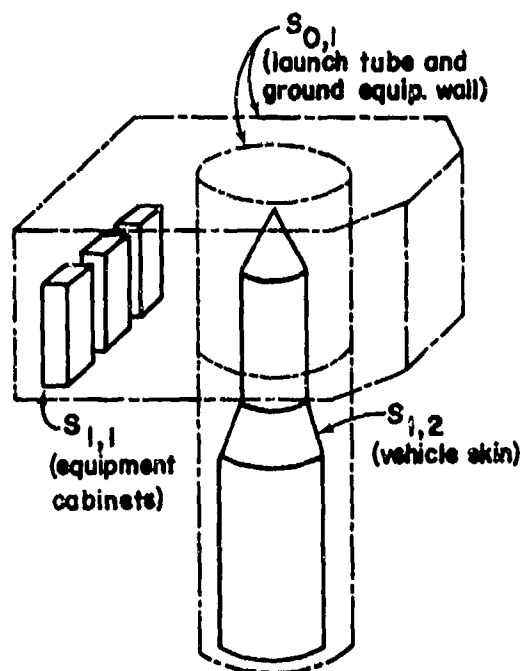


Fig. 29. Identification of shielding surfaces.

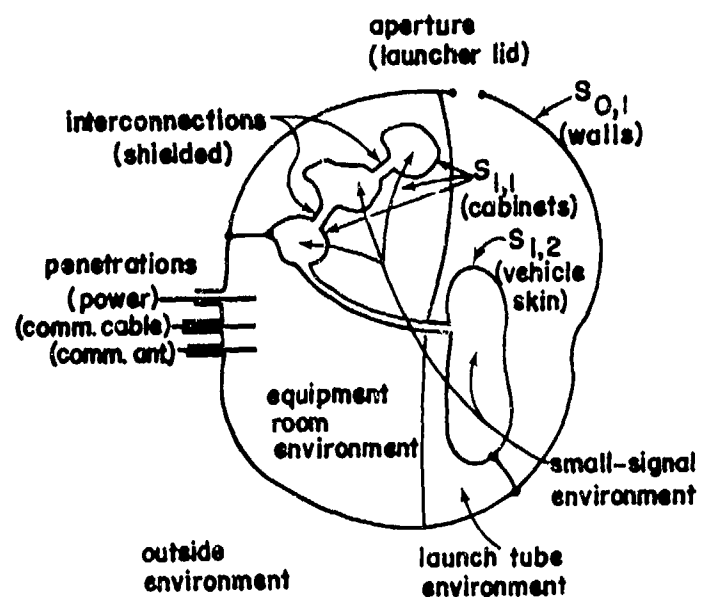


Fig. 30. System topology.

All sensitive circuits and components are presumed to be in the small-signal regions enclosed by the second principal shields. That is, all small-signal circuits are housed in the ground support equipment cabinets (shield $S_{1,1}$) or in the vehicle guidance and control compartment (shield $S_{1,2}$). Less susceptible circuits (lighting, heating/air conditioning, power conditioning) may be compatible with the equipment room environment.

3.2.3.2 External Interaction

Four important external interaction problems that can be identified on the first principal shield $S_{0,1}$ of Fig. 30 are (1) the overhead power lines, (2) the buried communication cable, (3) an on-site antenna and feed cable, and (4) the external fields exciting the apertures about the launch tube lid. These example problems will be worked out in this section.

3.2.3.2.1 AC Overhead Power Lines

The elements of the power line problem are illustrated in Fig. 31a. The exposed elements are a semi-infinite overhead conductor with a vertical down lead. These elements drive a shielded feeder that leads to the main distribution panel. At the main distribution panel the power circuits branch out to the various system loads, one of which is the equipment within the first principal shield. All circuits are assumed to be enclosed in tight metal conduit, so that negligible additional interaction occurs between the feeder and the facility shield. Within the main distribution panel the power conductors leave the conduit and are routed to circuit breaker terminals. This portion of the conductors has been represented by an inductance in Fig. 31a; it could also be represented by a segment of transmission line whose characteristic impedance is larger than that of the conductors in the conduit.

a. Overhead Line

Fig. 31b illustrates the problem geometry for the determination of the Norton equivalent source characteristic of the incident EMP and the exposed conductor. The induced terminal current can be obtained from scattering theory or approximated using transmission-line theory. In

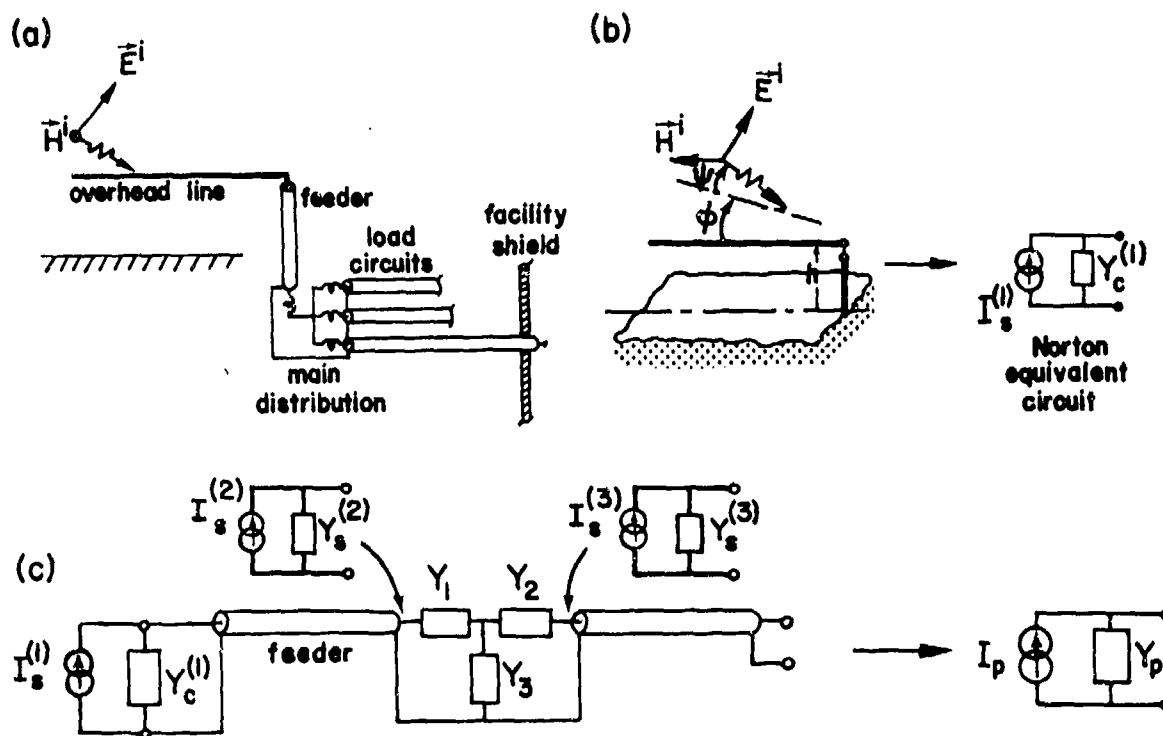


Fig. 31. External coupling and propagation through AC power system.
 (a) AC overhead power line circuits; (b) equivalent source for overhead lines; and (c) source transferred to facility shield penetration.

either case, the short-circuit current will depend on the incident EMP waveform and azimuth and elevation angles of incidence, and the current and admittance will depend on both the conductor size and height, and soil conductivity and permittivity.

For this example, consider a power line that extends to infinity (away from the facility) and is 10 m above soil of conductivity 10^{-3} mho/m. Also for simplicity, assume that the power lines can be represented by a single conductor of radius 0.1 m. Then for an exponential pulse $E_0 e^{-t/\tau}$ (with $\tau = 250$ ns) incident at an elevation angle of 20° ($\psi = 20^\circ$) end-on ($\phi = 0$), the line is characterized by (see Sec. 2.1.2.3.3a)

$$Z_c = \frac{Z_o}{2\pi} \ln(2h/a) = 317 \text{ ohms} \quad (29)$$

$$t_o/\tau = \frac{2h}{c\tau} \sin \psi = 0.0912 \quad (30)$$

$$\sigma\tau = 0.250 \times 10^{-9} \text{ mho} \cdot \text{sec/m}$$

$$D(\psi, \phi) = 5.67 \quad (\text{vertical polarization})$$

The short-circuit current at the terminals is given by (93) of Sec. 2.1.2.3.3a.4 and is plotted in Fig. 32 for $E_o = 10^4 \text{ V/m}$. The source admittance $Y_s^{(1)}$ is the inverse of the characteristic impedance Z_c , i.e., $Y_s^{(1)} = Y_c^{(1)} = 1/Z_c$. These define the Norton equivalent source representing the above-ground power line, as illustrated in Fig. 31b.

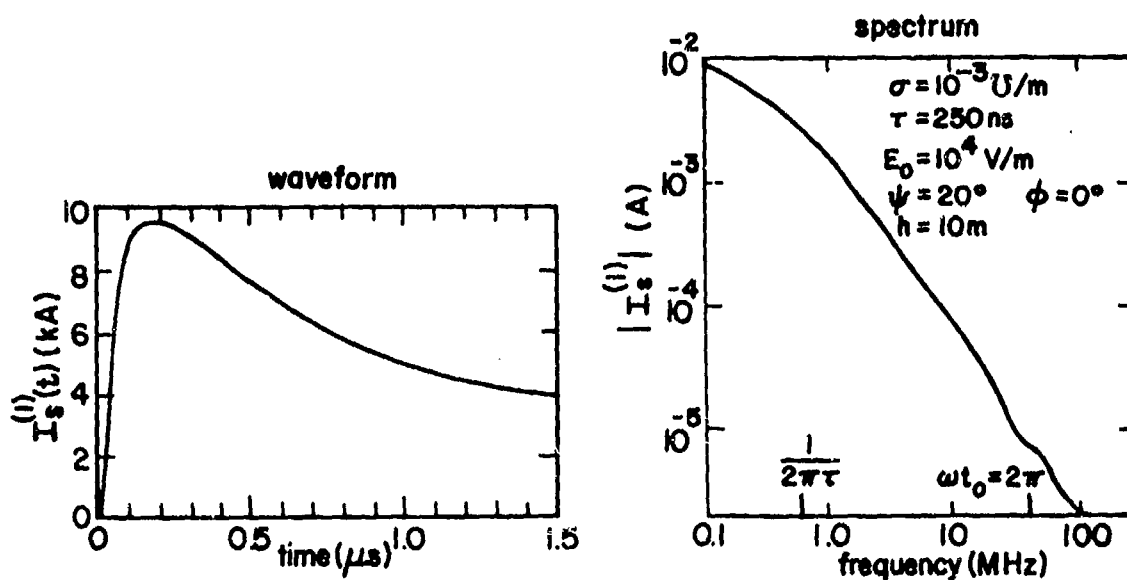


Fig. 32. Short-circuit current induced in power line by exponential pulse of incident field.

b. Low-Voltage Wiring

The propagation of the induced current through the feeder, distribution panel, and essential load conduit is illustrated in Fig. 31c. The stray inductances in the distribution panel and the other circuits in the support building (outside the first principal shield) are represented by a Tee network in Fig. 31c. Generally, the electrical wiring consists of several conductors in a conduit and thus the transmission lines shown in Figs. 31a and 31c are multiconductor transmission lines. As suggested in Fig. 31c, the transmission-line problem is solved as a two-conductor line to obtain the common-mode Norton equivalent source (I_p, Y_p) at the point where the conduit penetrates the first principal shield.

c. Service Entrance Conduit

The equivalent source $I_s^{(1)}$ drives the line end of the service entrance conduit conductors. For this example, we will consider only the common-mode currents on these conductors, and assume that the conductors and feeder conduit form a uniform, lossless transmission line. The Norton equivalent source $I_s^{(2)}, Y_s^{(2)}$ at the end of the service entrance conduit entering the main distribution panel is then

$$Y_s^{(2)} = Y_c^{(2)} \frac{1 - \rho(0)e^{-j2kl}}{1 + \rho(0)e^{-j2kl}} \quad (31)$$

$$I_s^{(2)} = I_s^{(1)} e^{-jkl} \frac{1 + \rho(0)}{1 + \rho(0)e^{-j2kl}} \quad (32)$$

where $\rho(0) = (Y_c^{(2)} - Y_c^{(1)}) / (Y_c^{(2)} + Y_c^{(1)})$, $Y_c^{(2)}$ and l are, respectively, the characteristic admittance and length of the conductors in the service entrance conduit, and $Y_c^{(1)}$ is the source admittance of the Norton equivalent source driving the conduit. Eqs.(31) and (32) above thus transfer the Norton current source from the line end of the conduit to the main distribution end.

For a feeder conduit 30-m long with a common-mode characteristic impedance of 25 ohms, $\rho(0) = 0.85$ and the conduit is a quarter-wavelength

long at 2.5 MHz. The waveform and spectrum of the short-circuit current $I_s^{(2)}$ are shown in Fig. 33.

d. Main Distribution Panel and Loads

The source $I_s^{(2)}$ drives the Tee network consisting of Y_1 , Y_2 , and Y_3 in Fig. 31c. We may represent the stray inductance of the incoming and outgoing wiring at the main distribution panel by lumped inductances Y_1 and Y_2 in series with the lines. The input admittances of non-essential station-keeping circuits are represented by a shunt admittance Y_3 as illustrated in Fig. 31c. The transfer function for the Tee network is then

$$\frac{I_s^{(3)}}{I_s^{(2)}} = \frac{Y_1 Y_2}{Y_s^{(2)} (Y_1 + Y_2 + Y_3) + Y_1 (Y_2 + Y_3)} \quad (33)$$

where $Y_s^{(2)}$ is the source admittance of the Norton equivalent source given in (31) above. Of particular interest here is the early-time effect of the Tee network on the transient. To examine this let

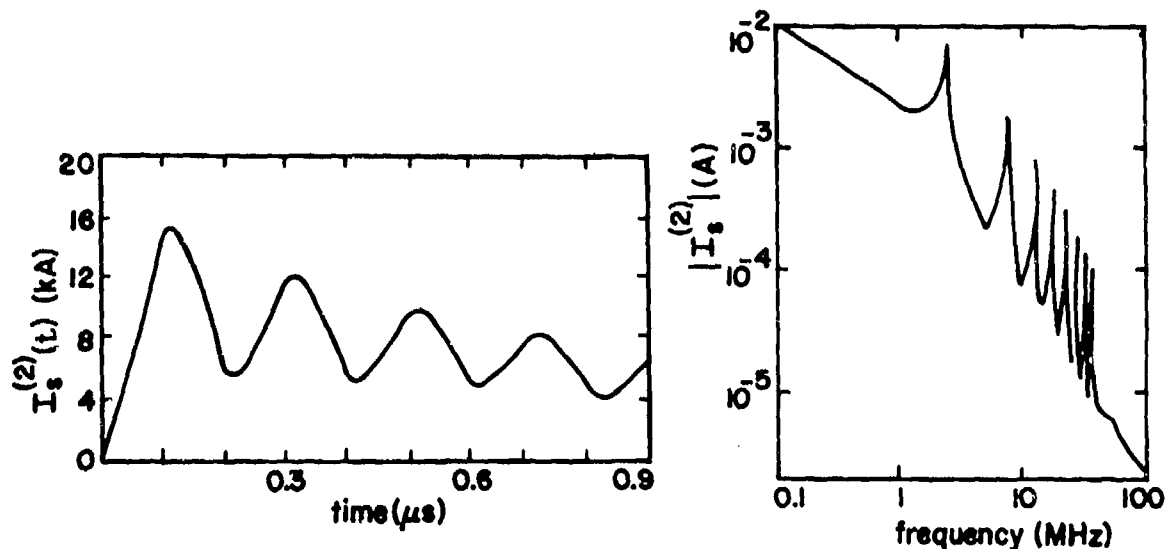


Fig. 33. Short-circuit current at end of feeder conduit.

$$Y_s^{(2)} \approx Y_c, \quad Y_3 \approx nY_c, \quad (t < 2 \ell/c) \quad (34)$$

$$Y_1 = Y_2 \approx (sL)^{-1}$$

where n is the number of parallel circuits that make up Y_3 (each has length ℓ and characteristic admittance Y_c), and L is the lumped inductance of the wiring inside the distribution panel. Then

$$\frac{I_s^{(3)}}{I_s^{(2)}} = \frac{1/\tau_s^2}{ns^2 + (2+n)s/\tau_s + 1/\tau_s^2} \quad (35)$$

where $\tau_s = LY_c$ and the inductance in series with the branch circuits has been neglected. This transfer function has poles at

$$s_{1,2} = \frac{-(2+n) \pm \sqrt{4+n^2}}{2n \tau_s} \quad (36)$$

For $L = 1 \mu\text{H}$, $1/Y_c = 25 \text{ ohms}$, and the number of station-keeping circuits $n=5$, the time constant $\tau_s = 40 \text{ ns}$. For these nominal values of characteristic impedance and wiring inductance, the poles occur at

$$f_1 = 0.64 \text{ MHz}, \quad f_2 = 4.9 \text{ MHz}$$

Although the transfer function may not be valid at frequencies as low as the pole frequencies, we have nevertheless demonstrated the effect of the stray inductance in rejecting the high-frequency content of the incoming transient (frequencies above f_2 are highly attenuated).

For very late times ($t \gg 2 \ell/c$), $Y_1 \approx Y_2 \rightarrow \infty$ and the n branch circuits appear to be open circuits (unless a green-wire ground is used), and

$$I_s^{(3)} \approx I_s^{(2)}, \quad Y_s^{(3)} \approx Y_3 + Y_s^{(2)} \quad (37)$$

That is, the short-circuit current at the output side of the distribution panel is the same as that at the input side, but the source admittance has changed because of the inclusion of the station-keeping circuits Y_3 .

At intermediate frequencies the natural resonances of the $n+1$ conduits will produce multiple oscillations superimposed on the oscillations shown in Fig. 33 which were caused by the service entrance conduit. Because the branch circuits are predominantly reactive in the common mode but possess a Q of less than 20, these oscillations are damped out rather rapidly. (The number of cycles required for a $1/e$ reduction in amplitude is Q/π .) For initial estimates, therefore, it will be assumed that $I_p \approx I_s^{(3)}$ and $Y_p \approx Y_s^{(3)}$.

3.2.3.2.2 Buried Communication Cable

The buried communication cable is assumed to be a shielded, multi-conductor cable buried at a uniform, shallow depth in the soil. As illustrated in Fig. 34a, the cable shield is in contact with the soil and is circumferentially connected to the first principal shield where the cable enters the facility.

The external interaction problem for the buried cable may be separated into three parts: (a) determination of the ambient fields in the soil (Fig. 34a), (b) determination of the total current induced in the cable by these fields (Fig. 34b), and (c) determination of the common-mode internal conductor currents from the total current and shield properties (Fig. 34c). For common installations, the cable can be treated as though it extended to infinity (away from the facility) and the shield is terminated in a short circuit at the facility shield. The cable shield may be composed of two or more shields; these are shorted together at the facility shield. The shields are usually continuous cylindrical shields (no apertures); thus, only diffusion through the shields need be considered.

The total current induced in the buried communication cable shown in Fig. 34 can be estimated from Figs. 59 and 60 of Sec. 2.1.2.3.3 b.2. For $\sigma = 10^{-3}$, $b = 1$ m, and the 50 kV/m exponential pulse ($\tau = 250$ ns) incident at $\psi = 90^\circ$, $\phi = 0$ on the soil, the following parameters are obtained:

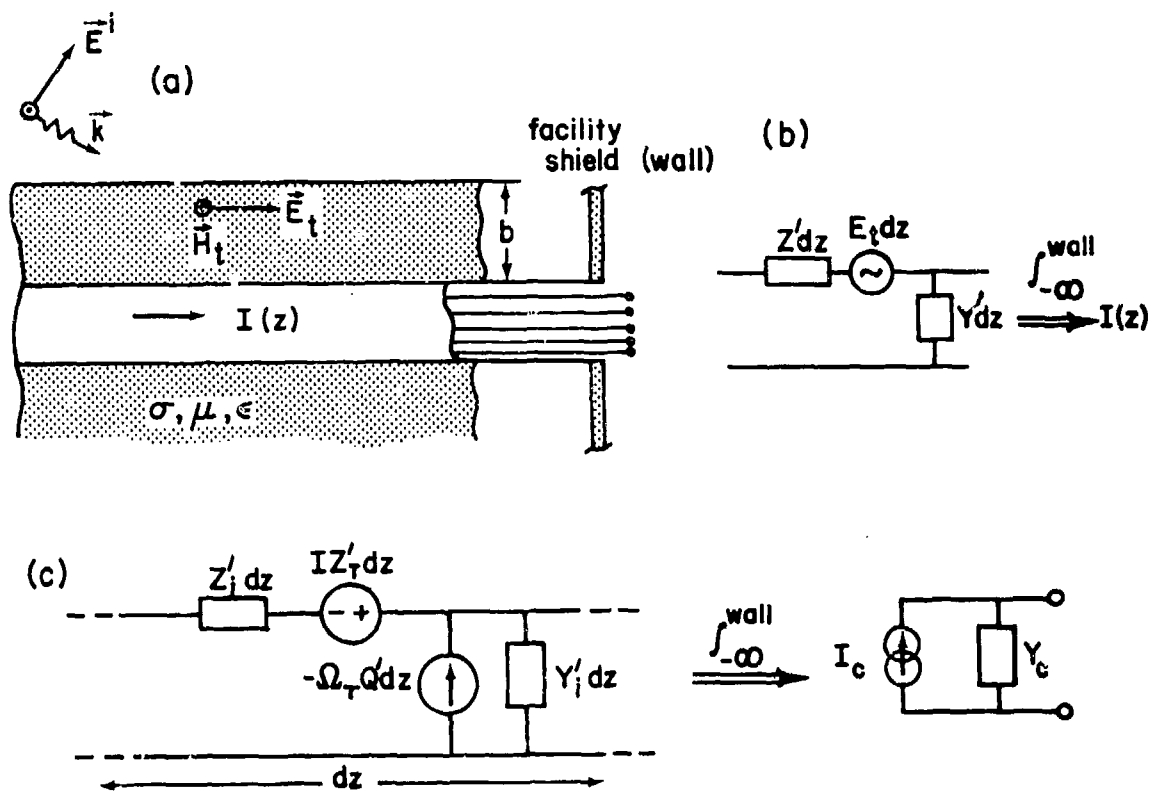


Fig. 34. External coupling and propagation through shielded underground communication cable. (a) Underground communication cable; (b) bulk current in cable; and (c) wire current at facility shield penetration.

$$\tau_b = \mu \sigma b^2 = 4\pi \times 10^{-10} \text{ sec}, \quad \tau_e = \epsilon_0 / \sigma = 8.85 \times 10^{-9} \text{ sec}$$

$$p = \tau_b / (4\tau) = 1.26 \times 10^{-3}, \quad D(\psi, \phi) = \cos \phi = 1 \quad (\text{vertical polarization})$$

and

$$I_{pk} \approx 1.33 \text{ kA} \quad (b = 1 \text{ m}) \quad (38)$$

The waveform of the current $I(t)$ is shown in Fig. 59 of Sec. 2.1.2.3.3 b.2.

Let us now assume that this cable has a single steel shield ($\mu_r = 100$, $\sigma = 6 \times 10^6 \text{ mho/m}$) which is 0.5 mm thick and 5 cm in diameter. Then the diffusion constant for the shield is

$$\tau_d = \mu \sigma d^2 = 37.7 \mu s \quad (39)$$

and the dc resistance per unit length of the cable shield is

$$R'_{dc} = (2\pi a \sigma d)^{-1} = 2.12 \times 10^{-3} \Omega/m \quad (40)$$

Therefore $\tau_d \gg \tau$ and the incident field $E_o e^{-t/\tau}$ produces the same response as an impulse $E_o \tau \delta(t)$. The short-circuit current induced in the core wires at the end of a cable of length ℓ matched at the opposite end is

$$I_{sc}(0) \approx I_{sc} Z'_T \ell / Z_c$$

$$\approx \frac{2R'_{dc} E_o \tau D(\psi, \phi) \ell}{Z_c L'_s} \frac{\sqrt{\tau_e \tau_d}}{\sinh \sqrt{s \tau_d}} \quad (41)$$

for $\ell \ll 2\pi c \tau_d = 71$ km. Here L'_s is the external inductance per unit length of the cable (see (102) of Sec. 2.1.2.3.3) and Z_c is the characteristic impedance of the core/shield transmission line. In the time domain, the current waveform is shown in Fig. 35a normalized to the coefficient given by (42) as a function of normalized time t/τ_d . For our example,

$$\frac{2E_o \tau D(\psi, \phi) R'_{dc}}{Z_c L'_s} \sqrt{\frac{\tau_e}{\tau_d}} = 0.0406 \text{ A/m} \quad (42)$$

Thus, a 10-km long cable would have a peak short-circuit current of $406 \text{ A} \times 1.85 = 751 \text{ A}$ induced on its core wires if $Z_c \approx 10 \Omega$ and $L'_s \approx 2 \mu\text{H/m}$.

For a wide pulse (step function or $\tau \gg \tau_d$), the current induced at the end of the cable is

$$I_{sc}(0) = \frac{2R'_{dc} \ell E_o D(\psi, \phi)}{Z_c L'_s} \sqrt{\tau_e \tau_d} \frac{1}{s \sinh \sqrt{s \tau_d}} \quad (43)$$

and the time-domain current waveform is shown in Fig. 35b, which evidently increases without limit as cable current is drawn from an ever-increasing

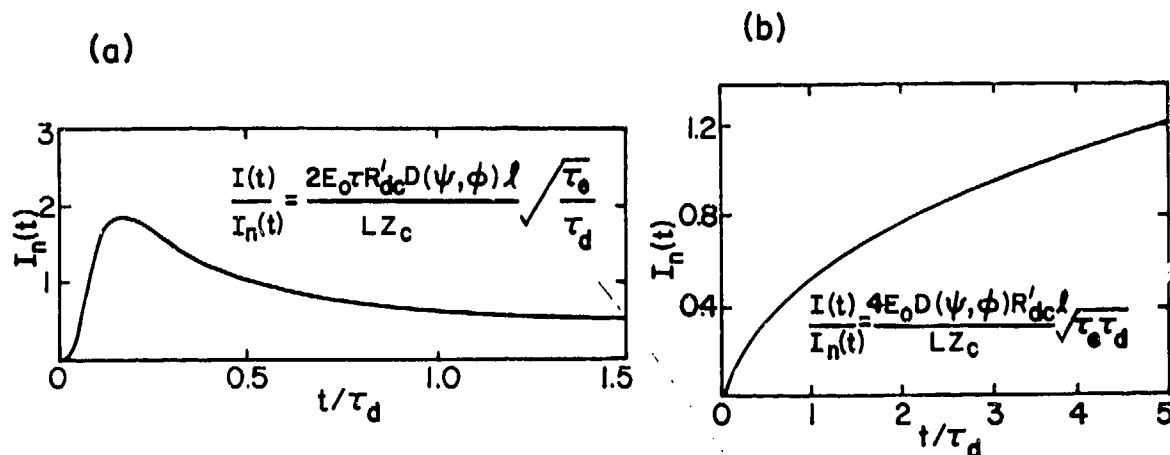


Fig. 35. Short-circuit current induced on core conductor of a buried shielded cable. (a) Short-pulse response, and (b) wide-pulse response.

radius in the soil and diffuses through the electrically thin shield. In practical problems, the finite dimensions of the cable and area of illumination, the finite pulse width, and the effects of propagation time place an upper limit on the induced short-circuit current. For most cables and soils, the impulse response of Fig. 35a is appropriate for high-altitude EMP excitation.

The Norton equivalent source just inside the facility shield thus consists of the current $I_{sc}(0)$ given by (43) and the characteristic admittance of the core/shield transmission line by $Y_c = (Z_c)^{-1}$.

3.2.3.2.3 Communication Antenna and Feed

The communication antenna and feed cable are illustrated in Fig. 36a. In this simplified model, the external interaction elements consist of the antenna and its base or ground plane, and the coaxial cable between the antenna and the facility shield. In practice, the antenna system may also contain an antenna coupler (matching network) and preamplifier at the base

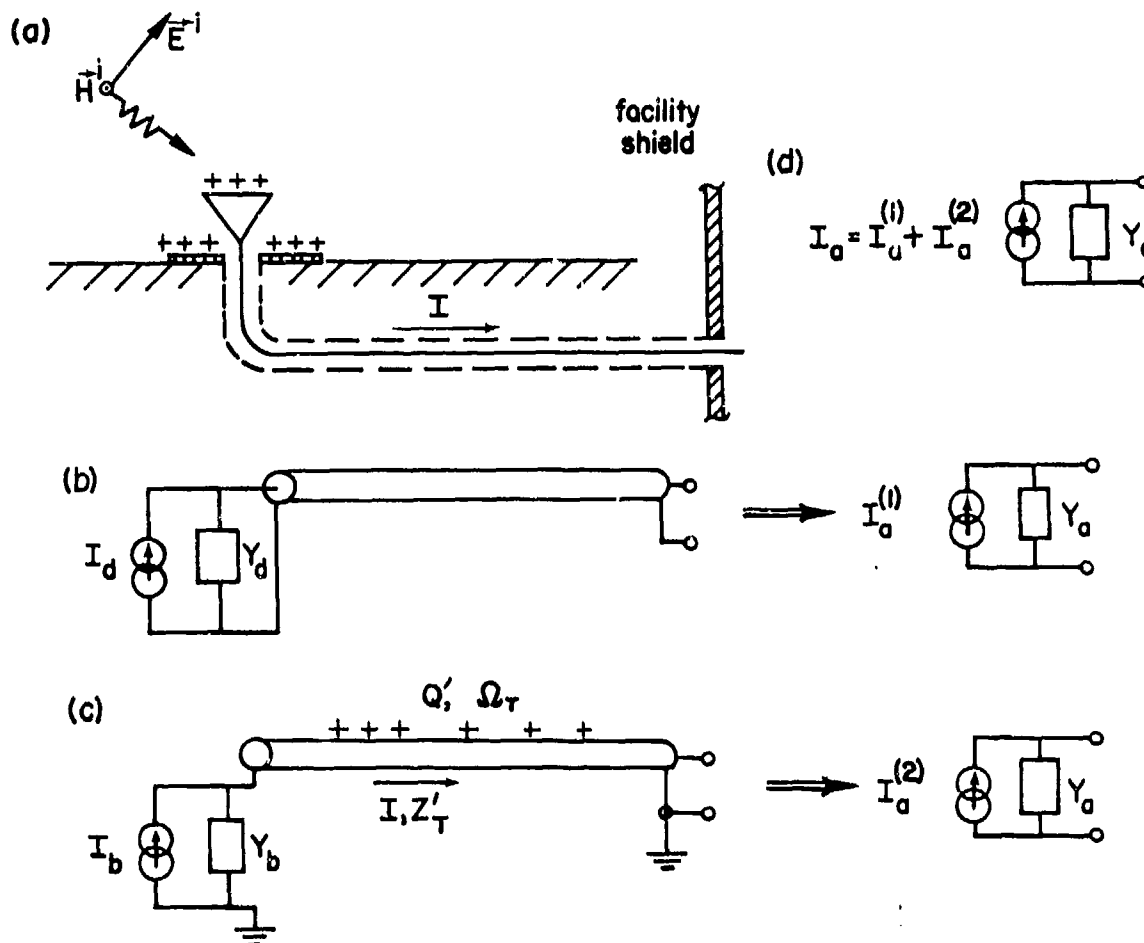


Fig. 36. External coupling and propagation through external antenna and feeds. (a) Communication antenna and feed; (b) contribution of antenna element; (c) contribution of antenna base and cable current and charge; and (d) equivalent source at facility shield penetration.

of the antenna; these components are not included in the example. The coaxial cable between the antenna and the facility shield is assumed to be RF coaxial transmission line with a braided-wire shield. Thus, aperture penetration through the cable shield will contribute to the externally induced current in the cable.

The EMP-induced current in the feed cable will consist of two parts: that induced in the antenna and propagated through the cable (Fig. 36b), and that induced through the cable shield along its exposed length between the antenna and the facility shield (Fig. 36c). For the first part, the transient response of the antenna is then used to transfer the antenna characteristics (I_d, Y_d) to the penetration point to obtain the Norton equivalent source $(I_a^{(1)}, Y_a)$ driving the internal cable.

For the second part of the problem the current and charge induced in the finite-length cable must be determined. This will include any current caused by interaction of the external fields with the antenna base (I_b, Y_b) as well as the distributed current induced by the fields along the cable. The cable current and charge and the shield transfer characteristics will then be used to determine the Norton equivalent source $(I_a^{(2)}, Y_a)$ at the penetration point. (It will be assumed that the leakiness of the shield has a negligible effect on the source admittance Y_a .) The resultant source (I_a, Y_a) at the penetration point is then obtained by superposition of the two sources (Fig. 36d).

a. Communication Antenna

If the antenna is a biconical antenna with a 30° cone half-angle and 0.3 m length, the antenna may be considered an electrically small dipole and its capacitance will be

$$C_a = \frac{2\pi\epsilon_0 d}{\ln(\cot 30^\circ)} \approx 30.4 \text{ pF} \quad (44)$$

The effective height h_e of the antenna will be approximately $d/2 = 0.15$ m and the short-circuit current available from the antenna will be

$$I_d = sC_a h_e E(s) \approx 4.56 \times 10^{-12} sE^i(s) \quad (45)$$

or

$$I_d(t) = h_e C_a \frac{dE^i}{dt} \approx 4.56 \times 10^{-12} \frac{dE^i}{dt} \quad (46)$$

and the source admittance is $Y_d = sC_a$.

b. Antenna Base

The current induced on the antenna base is the total current on the antenna structure less the current on the conical element (I_d above). The total current is approximately

$$I_t \approx \pi r_b^2 \epsilon_0 s E^1(s) \quad (47)$$

where r_b is the radius of the metal base plate. The net current to the base plate is thus

$$I_b = (\pi r_b^2 \epsilon_0 - h_e C_a) s E^1(s) \quad (48)$$

If $r_b \approx 0.6$ m, then $I_b \approx 5.45 \times 10^{-12} s E^1(s)$, which is about the same as the current in the antenna element. It turns out that the effect of this current is insignificant compared to that of the antenna current, because the base current flows to the cable shield rather than to the center conductor.

The Norton equivalent circuit (Fig. 36d) just inside the facility shield consists of the source I_d transferred to the opposite end of the coaxial cable through

$$I_a = I_d e^{-jk\ell} \frac{1 + \rho(0)}{1 + \rho(0) e^{-j2k\ell}} \quad (49)$$

where

$$\rho(0) = \frac{Y_c - sC_a}{Y_c + sC_a}$$

and the admittance Y_a is obtained from

$$Y_a = Y_c \frac{1 - \rho(0) e^{-j2k\ell}}{1 + \rho(0) e^{-j2k\ell}} \quad (50)$$

For the double-exponential EMP waveform, the current waveform $I_d(t)$ is

$$I_d(t) = E_0 h_e C_a \frac{d}{dt} (e^{-t/\tau_f} - e^{-t/\tau_r}) \quad (51)$$

For $E_0 = 5 \times 10^4$ V/m, $\tau_r = 2$ ns and $\tau_f = 250$ ns, this current has a peak value of 57 A and a very short duration, as illustrated in Fig. 37.

Because the significant current lasts for only about 10 ns, it occupies only about 10 feet of cable (air line). Thus, if the coaxial cable is over 10 feet long, the complete waveform is transmitted undistorted. However, the initial waveform will be followed by "echos" of the initial pulse as the reflections from the cable ends arrive at later times.

3.2.3.2.4 Summary of Penetration Currents

The peak currents and times to reach peak are summarized in table 1 for the three conductors penetrating the primary shield of the facility.

3.2.3.2.5 Lid Excitation

The aperture penetration problem associated with the launcher lid is illustrated in Fig. 38. An exact solution of the problem is very difficult because the apertures are at a discontinuity in the cylindrical

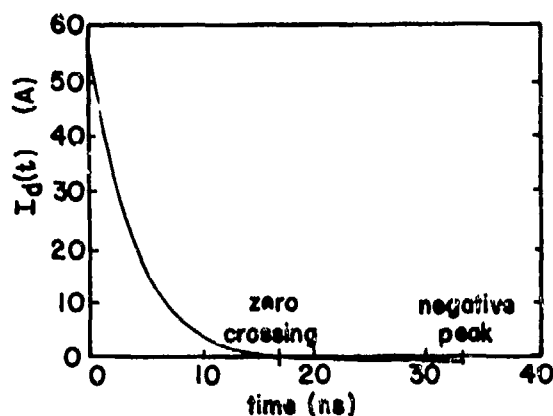


Fig. 37. Short-circuit current induced at antenna terminals.

Table 1. SUMMARY OF CURRENT SOURCES REPRESENTING CONDUCTORS
PENETRATING THE FIRST PRINCIPAL SHIELD

External Source	Peak Short-Circuit-Current	Time to Peak	Source Impedance	
			Early	Late
Power Lines	$\approx 15 \text{ kA}$	$\approx 100 \text{ ns}$	25 ohms	300 ohms
Communication Cable	$\approx 750 \text{ A}$	$\approx 6 \text{ } \mu\text{s}$	10 ohms	10 ohms
Communication Antenna	$\approx 50 \text{ A}$	$< 10 \text{ ns}$	50 ohms	-----

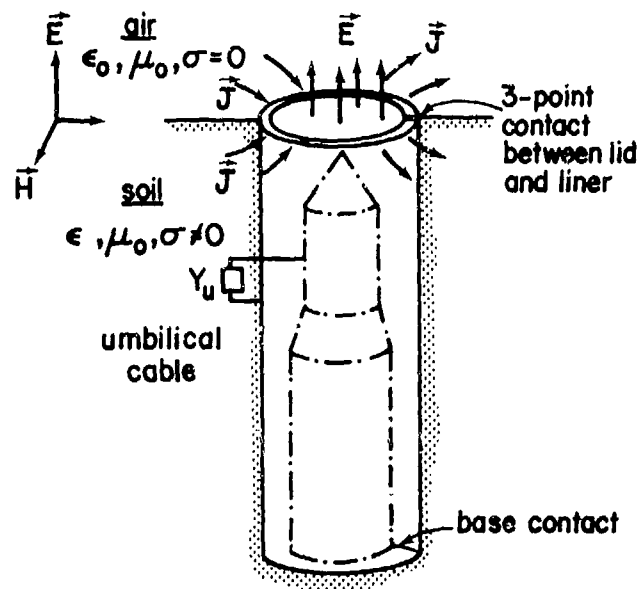


Fig. 38. Aperture coupling configuration.

surface. In an operational facility, the geometry is even more complicated because the lid makes a sliding contact with the top of the launch tube, so that the aperture has depth as well as area. In addition, the crack between the lid and the tube may be partially filled with lubricants and RFI gasket material. For this example, however, we will assume a simple circumferential aperture divided into three segments by the lid/tube contact.

The external interaction problem consists of determining the surface fields (Fig. 39a) and the current density \vec{J} flowing across the top surface of a metal cylinder immersed in the soil due to the incident EMP (Fig. 39b). A second mode of excitation is for longitudinal current to flow from the lid to the walls of the tube; this current will be driven by the vertical component of the electric field, whereas the current flowing across the top is driven by the horizontal component of the magnetic field.

The remainder of the external interaction problem is the calculation (or estimation) of the magnetic polarizability of the apertures of Fig. 39c (see table 15, Sec. 2.1.3.2). It will be assumed that the electric polarizability of the aperture is negligible in the practical case of a wide, low-impedance flange contact between the lid and the cylindrical launch tube.

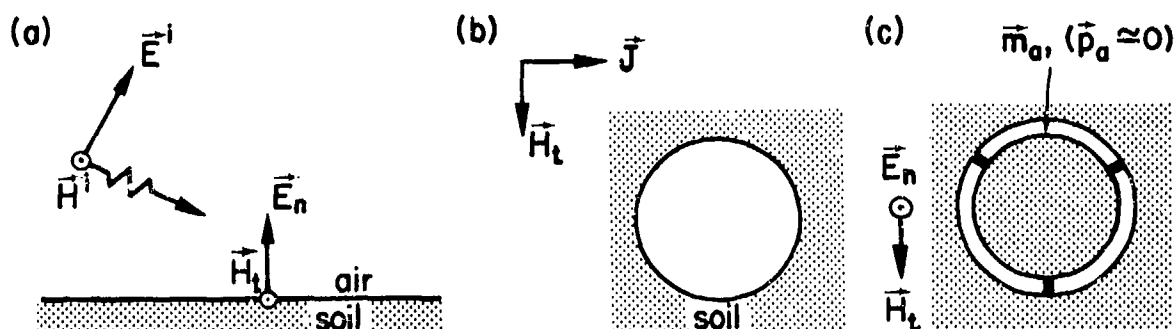


Fig. 39. External coupling to launcher lid apertures. (a) Surface fields, (b) surface magnetic field at lid, and (c) dipole moments of slots.

The radial current at the edge of the lid is

$$I_r \approx j\omega 2\epsilon_0 E^1 A \quad (52)$$

due to the vertical electric field when the elevation angle of incidence is small. The current across the lid produced by the horizontal magnetic field \vec{H}_t is, to the same degree of approximation,

$$I_z \approx a(2E^1/Z_0) \quad (53)$$

where a is the radius of the lid, $Z_0 = \sqrt{\mu_0/\epsilon_0}$ and $A = \pi a^2$. The ratio of these currents is

$$I_r/I_z \approx j\pi ka \quad (54)$$

where $k = \omega/c$. Thus, when $ka \ll 1$, for which these approximations are valid, the current I_z dominates. The surface current density exciting the lid apertures is predominantly given by $2E^1/Z_0$.

3.2.3.3 Internal Interaction

For the most part, the internal interaction consists of propagation along conductors; however, there are some special internal interaction cases that are of interest. The first is the case in which a coupling between the input and output cables occurs at a cabinet or junction box. This coupling occurs at high frequencies because of the capacitance between the input/output cables and the intervening circuit mass. Fig. 40 illustrates this coupling circuit in simplified form. The input

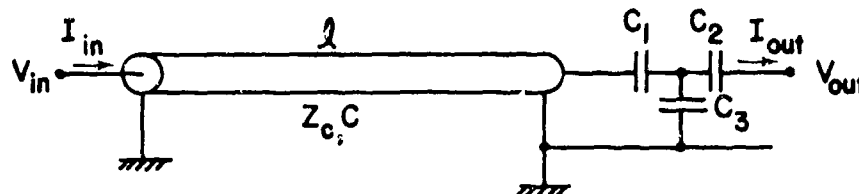


Fig. 40. Internal cable segment and capacitive coupling network.

cable is represented by a transmission line, and the capacitance between the input cable and the circuits in the cabinet circuits are represented by C_1 . The capacitance between the output cable and the cabinet circuits is represented by C_2 , and C_3 is the capacitance between the circuits and ground, or cabinet, chassis.

For illustrative purposes let us assume that $C_1 \approx C_2 \ll C_3$, and that the small capacitances C_1 and C_2 appear to be open-circuit terminations at the ends of the input/output cables for times of interest in the EMP analysis. Then

$$\frac{I_{out}}{I_{in}} \approx \frac{C_1 C_2}{C_3} Z_c \frac{2j\omega e^{-j\omega\ell/c}}{1 - e^{-j\omega 2\ell/c}} \quad (55)$$

where Z_c is the characteristic impedance of the cable and ℓ is its length. In the time domain

$$I_{out}(t) \approx \frac{2C_1 C_2}{C_3} Z_c \sum_{n=1}^{\infty} \left[\frac{d}{dt} I_{in}(t - m\ell/c) \right] u(t - m\ell/c) \quad (56)$$

where $m = 2n - 1$.

Note that if the input current I_{in} has a large derivative, the output current will be large. Consider, for example, a power lead with the current of Fig. 33 rising to 15 kA in 0.1 μ s. The rate of current rise is 15×10^{10} A/s, and for $C_1 = C_2 = 10$ pF, $C_3 = 200$ pF, and $Z_c = 100$ ohms, the peak output current is 15 A. Hence we have 15 A delivered to an output conductor that is ostensibly isolated from the power lead.

A second internal interaction phenomenon involves leakage out through cable shields, propagation along the shields, and leakage back through the shield to internal conductors. A simple example is illustrated in Fig. 41, where a larger EMP induced current I flowing on internal conductors induces currents I_{s1} and I_{s2} on the cable shields and a voltage V on the internal conductors of the second cable. This phenomenon is most effective at high frequencies because the braided-wire shields are leaky at high-frequencies and the inductance L_g of grounding conductors allows high-frequency components of the shield current I_{s1} to flow onto the second cable as I_{s2} .

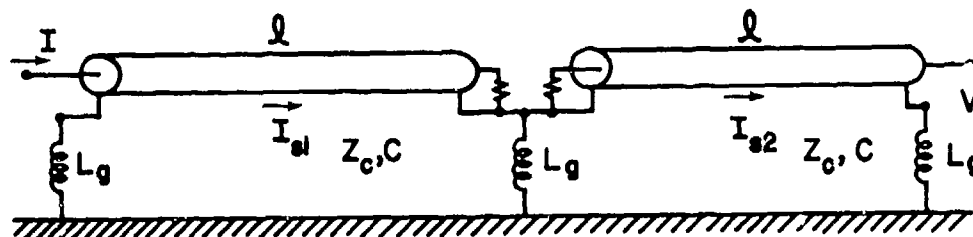


Fig. 41. Interference propagated on cable shields.

For a cable shield transfer impedance $Z_T' = j\omega L_T'$ per unit length, the current I_{s1} in the shield is approximately

$$I_{s1} \approx \frac{L_T'}{2L'} I(t) \quad (57)$$

at early times (i.e., before reflections from the ends) and for $IZ_c \ll L_g dI/dt$. If the second segment of cable is the same as the first, the early-time voltage induced on the internal conductor of the second cable will be

$$V_{oc}(t) \approx \frac{c(L_T')^2}{2L'} I(t) \quad (58)$$

For an inductance per unit length L' of 0.2 $\mu\text{H}/\text{m}$ and a leakage inductance per unit length L_T' of 1 nH/m , the open-circuit voltage impulse induced in the second cable by a 15 $\text{kA}\cdot\text{s}$ impulse in the first cable is 11 $\text{V}\cdot\text{s}$. For a cable impedance of about 100 ohms, this induced voltage would correspond to 0.1 A (for a short pulse) compared with 15 A for capacitive coupling between conductors. Such coupling phenomena as these are responsible for the apparent permeation of facilities by the high-

frequency responses even though stray series inductance and higher losses in dielectrics and conductors tend to attenuate the high frequencies.

It is also noteworthy that the leakage through the shields is significantly smaller than the capacitive coupling between cable ends. Topologically, the shielded conductors are separated by two layers of shielding, whereas the capacitively coupled conductors are in the same shielded volume.

3.2.4 SATELLITES

Satellites used as observation platforms or communication relay stations are rather complex vehicles topologically because of their solar cell arrays and their gossamer nature. Because the stresses on the vehicle structures in space are minimal and weight is at a premium, the satellite vehicles are often rather flimsy and skeletal in comparison to aircraft and rocket vehicles. Communication satellites may also contain large apertures to accommodate gimballed antennas or other adjustable-position components. These vehicles also often contain sensitive electronic systems to maintain the proper vehicle altitude and to store, relay, or read out data.

The basic features of a communication satellite are illustrated in Fig. 42. The main structure of the satellite is a hollow right circular cylinder. It spins steadily on its axis to maintain orientation stability. Its cylindrical surface is covered with solar cells. Two dish antennas are mounted on the cylinder's top end. This end is a movable platform detached from the rest of the cylinder. It is kept despun from the cylinder by a motor to achieve antenna aim control. A biconical horn antenna is mounted at the end of an axial shaft which extends through a circular aperture beyond the bottom end of the cylinder. Electronic components necessary for satellite operation are housed in the cylinder's interior. They are shown in Fig. 42 as "black boxes" connected to a circumferential cable bundle.

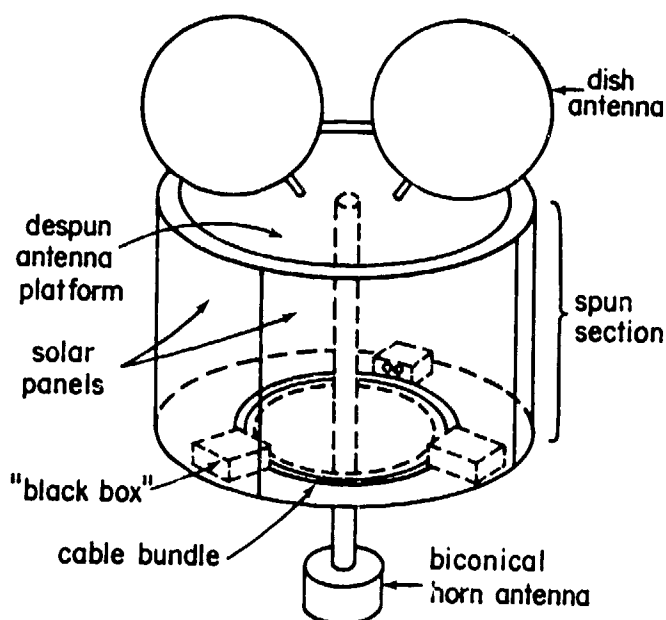


Fig. 42. Some basic features of a communication satellite model.

3.2.4.1 EMP Environment for Satellites

Because satellites are exoatmospheric vehicles, their EMP environment is significantly different from that of the surface and near-surface systems. The high-altitude EMP is generated in the lower, more dense region of the atmosphere well below the ionosphere. In order for this wave to reach satellite altitudes, it must propagate through the ionosphere; in so doing its characteristics are noticeably altered. For example, because the ionosphere is a good reflector for frequencies in or below the HF band, these components of the EMP spectrum incident on a satellite are largely filtered out by the ionosphere. For frequencies above the HF band, the electron inertia causes the effective dielectric constant and the electrical thickness of the ionosphere to vary with frequency, so that this portion of the EMP spectrum is dispersed by the ionosphere. The EMP waveform incident on the satellite therefore has a smaller peak field strength and is more oscillatory than the waveform observed below the ionosphere.

Perhaps more important than the dispersed EMP wave incident on the satellite is the flux of gamma and X-radiation produced by the nuclear detonation. Since there may be little intervening media between the weapon and the satellite for a high-altitude burst directly illuminating the satellite, there is little attenuation of the radiation propagating toward the satellite (except that caused by distance). This flux of radiation can interact with the satellite structure and components to cause system-generated EMP (SGEMP) and transient radiation effects on electronics (TREE). These effects are often more severe than the dispersed EMP itself on satellites. In the following discussion of satellite interaction, only the EMP interaction is considered.

3.2.4.2 EMP Interaction

The central problem of the satellite-EMP interaction analysis is to evaluate the voltages and currents induced on the cables by the EMP. One source of cable voltages and currents arises from the direct excitation of external wiring and antennas. The antennas pick up energy from the EMP and inject it directly into the cables. Note that the solar panels act like antennas. A second source of cable excitation arises from the penetration of the EMP fields through the open apertures on the satellite skin. These fields then interact with the cables in the satellite's interior.

The skin of the satellite in Fig. 42 can shield most of the energy of an impinging EMP from the satellite's interior. However, some EMP energy can penetrate through the skin by way of the antennas and the apertures. The apertures include the circumferential slot at the rim of the antenna platform, the vertical slits at the joints of adjacent solar panels, and the circular hole for the biconical horn antenna. These apertures are illustrated in Fig. 43.

Although the shape of the vehicle and its apertures are different from those of the rocket vehicle and aircraft, the electromagnetic interaction problem is quite similar to those already discussed. Furthermore,

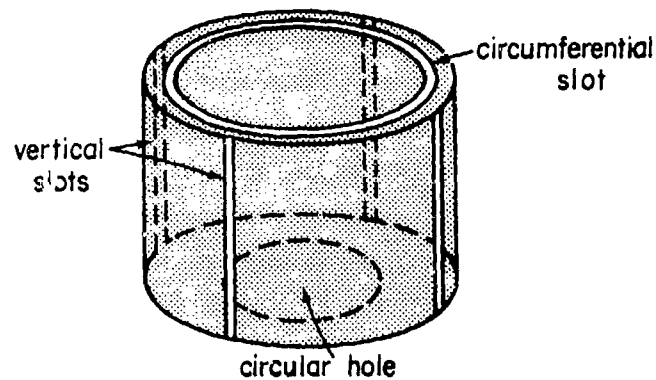


Fig. 43. A geometrical model applicable to the calculation of EMP penetration through the apertures on the satellite.

because the EMP problem is only part of the satellite interaction problem involving SGEMP and TREE considerations, only a simple numerical example will be worked out below.

When the satellite is illuminated by an incident EMP whose magnetic field is parallel to the satellite axis, significant magnetic-field penetration into the interior can occur via the slots and the hole shown in Fig. 43. The maximum open-circuit voltage that can be induced between the internal conductors and the shield of the circumferential cable bundle shown in Fig. 42 will be estimated in the following. It will be assumed that all of the magnetic flux which penetrates the satellite through the slots and hole also links the cable loop. The electromotive force associated with the rate of change of the magnetic flux will cause a total current I_t to flow in the cable loop; this total current will then induce currents and voltages on the internal conductors of the cable bundle. The open-circuit voltage is estimated by treating all the internal conductors as a single conductor and by ignoring the presence of the "black boxes" shown in Fig. 42.

The system topology for this elementary problem is shown in Fig. 44. The first principal shield is the outer skin of the satellite. The penetrations of this shield to be considered in this example calculation are the

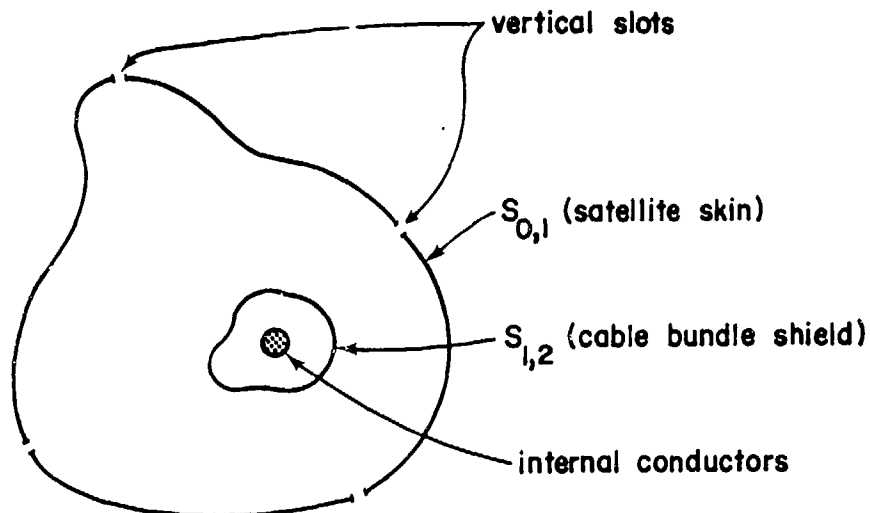


Fig. 44. Elementary satellite system topology.

vertical slot apertures in the outer skin. The second principal shield is the shield of the cable bundle. This shield is typically a mylar-aluminum film, penetration through which occurs via diffusion. An interaction sequence diagram for this elementary problem is given in Fig. 45. The following notations are used:

l = length of vertical slots

w = width of vertical slots

n = number of vertical slots

R_b = resistance of cable loop

L_b = inductance of cable loop

b = radius of cable loop

r_o = radius of cable bundle

Z_T' = transfer impedance per unit length of cable shield

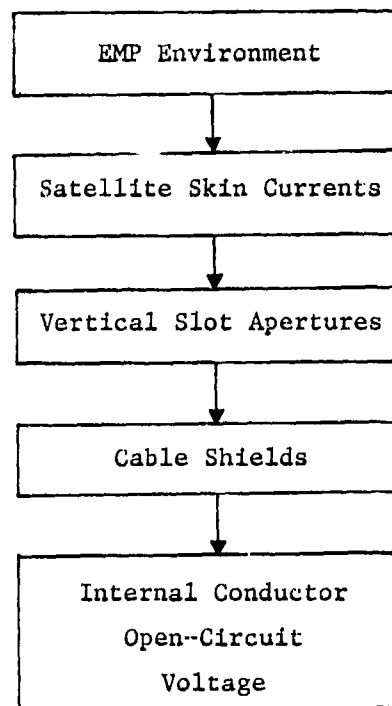


Fig. 45. Elementary interaction sequence diagram for satellite example calculation.

It is shown in table 8 of Sec. 2.1.2.1.2 that the short-circuit magnetic field H_{sc} on the outer surface of the satellite skin is approximately

$$H_{sc} \approx H^i \quad (59)$$

where H^i denotes the incident magnetic field. The magnetic flux Φ_m which penetrates the vertical slot apertures is related to H_{sc} and to α_m , the magnetic polarizability of a single aperture, by

$$\Phi_m = \frac{3n}{2\ell} \alpha_m \mu_o H_{sc} \approx \frac{3n}{2\ell} \alpha_m \mu_o H^i \quad (60)$$

The permeability of free space is denoted as usual by μ_o . The magnetic polarizability of a long slot aperture is given in table 14 of Chap. 2.1 by

$$\alpha_m = \frac{\pi \ell^3}{24 \ln(4\ell/w)} \quad (61)$$

Therefore, substitution of (61) into (60) yields

$$\phi_m = \frac{n\mu_o H_o^2 \pi \ell^2}{16 \ln(4\ell/w)} \quad (62)$$

which is an approximate expression for the total flux linking the interior of the satellite via the vertical slots.

It is assumed that all of the penetrant magnetic flux ϕ_m links the circumferential cable bundle. This assumption will lead to an overestimate of the total current induced in the cable loop. The electromotive force driving the cable loop is then simply $-s\phi_m$, and the current induced in the loop is this emf divided by the loop impedance $R_b + sL_b$. It can be shown that R_b may be neglected in comparison to sL_b in the frequency range of interest (i.e., $f \geq 30$ MHz because of the presence of the ionosphere between the source region and the satellite). From table 16 of Chap. 2.1, we have

$$L_b \approx \mu_o b \ln(8b/r_o) \quad (63)$$

so that the loop current I_t is

$$I_t = \frac{-n\pi \ell^2 H_o^2}{16b \ln(4\ell/w) \ln(8b/r_o)} \quad (64)$$

Now the maximum open-circuit voltage V_{oc} which can be developed between the shield and the internal conductors of the cable bundle is found from (117) of Chap. 1.3 and (1) of Chap. 2.4 to be

$$V_{oc} = 2\pi b Z_T' I_t \quad (65)$$

Using (5) of Chap. 2.4 and assuming that the cable bundle shield is electrically thin over the frequency range of interest, we find that V_{oc} is approximately

$$V_{oc} \approx \frac{-n\pi\ell^2 H^i}{16 r_o \sigma d \ln(8b/r_o) \ln(4\ell/w)} \quad (66)$$

in which σ and d denote the shield conductivity and thickness respectively. The time dependence of V_{oc} is thus seen to be identical to that of H^i ; and the peak value of V_{oc} is given by (66) when H^i is replaced by its peak value.

For purposes of numerical illustration, let $\ell = 2\text{m}$, $w = 0.5\text{ cm}$, $n = 4$, $b = 1\text{m}$, $r_o = 2\text{ cm}$, $\sigma = 3.7 \times 10^7\text{ mho/m}$, and $d = 0.025\text{ mm}$. Then the open-circuit voltage V_{oc} is given by

$$V_{oc} \approx -6.6 \times 10^{-3} [H^i] \text{ volts} \quad (67)$$

in which $[H^i]$ denotes the numerical value of H^i . It has already been pointed out that the presence of the ionosphere causes the incident EMP to have a smaller peak value than that which would be observed below the ionosphere. Thus the peak value of V_{oc} will be less than that which would occur were the ionosphere absent; choosing, for example, $[H^i] = 133$, which would correspond to a peak electric field strength below the ionosphere of 50 kV/m, we find that

$$|V_{oc, \text{peak}}| < 0.9 \text{ volts} \quad (68)$$

3.2.5 ERROR-ANALYSIS EXAMPLES

In this section we present the application of the error-analysis formulas described in Chap. 1.6 to some of the results obtained in the foregoing illustrative system analyses.

3.2.5.1 Induced Voltage on Rocket Raceway Cable (cf. Secs. 3.2.1.3.2, 3.2.1.4)

Eqs. (9) and (10) of Sec. 3.2.1.3.2 for the voltage induced per unit length of raceway cable on a rocket vehicle yield the following approximate expression for the peak value of this voltage:

$$V'_{pk} \approx L'_T f_1 I_{pk} w/a \quad (69)$$

in which w is the raceway perimeter and a is the missile radius. The quantity $w/(2\pi a)$ is a purely geometrical parameter used to estimate the fraction of the total missile current flowing on the raceway cover.

The root-mean-square (rms) relative errors in each of the quantities L'_T , f_1 , w/a and I_{pk} are respectively denoted by

$$\begin{aligned} \langle \tilde{x}_{L'_T}^2 \rangle^{1/2}, \quad \langle \tilde{x}_{f_1}^2 \rangle^{1/2}, \\ \langle \tilde{x}_{w/a}^2 \rangle^{1/2}, \quad \langle \tilde{x}_{I_{pk}}^2 \rangle^{1/2} \end{aligned}$$

and from (41), Chap. 1.6, the relative rms error in V'_{pk} , $\langle \tilde{x}_{V'_{pk}}^2 \rangle^{1/2}$, is given by

$$\langle \tilde{x}_{V'_{pk}}^2 \rangle^{1/2} = \left[(1 + \langle \tilde{x}_{L'_T}^2 \rangle) (1 + \langle \tilde{x}_{f_1}^2 \rangle) (1 + \langle \tilde{x}_{w/a}^2 \rangle) (1 + \langle \tilde{x}_{I_{pk}}^2 \rangle) - 1 \right]^{1/2} \quad (70)$$

We briefly discuss each of the input quantities in (70).

The transfer inductance per unit length L'_T represents the aggregate effect of the bolted and riveted raceway-cover joints. It is very difficult to calculate both L'_T itself and the effect of combining the axial and circumferential polarizabilities into a single equivalent L'_T . Thus, an optimistic estimate of $\langle \tilde{x}_{L'_T}^2 \rangle^{1/2}$ would be 0.5, or 50%. We use this value in the calculation of $\langle \tilde{x}_{V'_{pk}}^2 \rangle^{1/2}$.

The frequency f_1 can be accurately calculated for an idealized model of the rocket vehicle; measured natural-frequency data for given vehicles are also available. Thus we assign the value 0.05, or 5%, to $\langle \tilde{x}_{f_1}^2 \rangle^{1/2}$.

The fraction w/a can be determined almost exactly for a given vehicle, but it is used in (69) to denote the fraction of the total missile current

which flows in the raceway cover. This current fraction and the geometrical fraction may not be identical; thus we will use $\langle \tilde{x}_{w/a}^2 \rangle^{1/2} = 0.10$, or 10%, for the relative error in w/a .

The peak missile current I_{pk} , like the frequency f_1 , can be calculated quite accurately for an idealized model of the vehicle. Following the discussion in Sec. 2.1.2.1.1, we assign the value 0.15, or 15%, to $\langle \tilde{x}_{I_{pk}}^2 \rangle^{1/2}$.

It is now a simple matter to evaluate the relative error in V'_{pk} . We find that

$$\langle \tilde{x}_{V'_{pk}}^2 \rangle^{1/2} = 54\% \quad (71)$$

If the value of L'_T were exact, i.e., if $\langle \tilde{x}_{L'_T}^2 \rangle^{1/2}$ were set equal to zero, then $\langle \tilde{x}_{V'_{pk}}^2 \rangle^{1/2}$ would be less than 20%. It is apparent that the large relative error in L'_T is the dominant contribution to that in V'_{pk} , and that

$$\langle \tilde{x}_{V'_{pk}}^2 \rangle \approx \langle \tilde{x}_{L'_T}^2 \rangle \quad (72)$$

The open-circuit voltage developed on the internal cable conductor is approximately given by (17) of Sec. 3.2.1.4. The peak value of $V_{oc}(t)$ is approximately

$$\begin{aligned} V_{oc}(t) \Big|_{pk} &\approx f_1 L'_{Tc} \frac{L'_T}{L'} I_{pk} \frac{w}{a} \\ &\approx 2 L'_{Tc} \frac{1}{L'} V'_{pk} \end{aligned} \quad (73)$$

where V'_{pk} is given above in (69). Using the assumed relative error values

$$\begin{aligned} \langle \tilde{x}_0^2 \rangle^{1/2} &= 0.00, & \langle \tilde{x}_{L'_{Tc}}^2 \rangle^{1/2} &= 0.10 \\ \langle \tilde{x}_{1/L'}^2 \rangle^{1/2} &= 0.10, & \langle \tilde{x}_{V'_{pk}}^2 \rangle^{1/2} &= 0.54 \end{aligned} \quad (74)$$

we obtain

$$\langle \tilde{x}_{V_{oc}}^2 \rangle^{1/2} = 56\% \quad (75)$$

for the relative error in $V_{oc}(t)|_{pk}$.

It is apparent that calculations of relative error in a given quantity are straightforward when the relative errors in the constituents of that quantity are known. What is far more difficult to quantify is the error caused by the use of, say, a low-frequency approximation such as that used to obtain (12) of Sec. 3.2.1.3.2, when the solution to the same problem without the low-frequency approximation is not known. It is at this point where engineering judgement and experience, as well as analyses which are as accurate as possible, must be used to develop estimates of the errors incurred in approximate analyses.

3.2.5.2 Aircraft HF Fixed-Wire Antenna Response (cf. Sec. 3.2.2.3.3)

The peak open-circuit voltage developed at the terminals of an HF fixed-wire antenna is estimated in Sec. 3.2.2.3.3 to be

$$V_{oc}(t)|_{pk} \approx 4E_{pk}(\Delta\omega / 2\omega_o)h_e(\omega_o) \quad (76)$$

in which

E_{pk} = peak value of incident EMP electric field

ω_o = center frequency of resonant response of effective height h_e

$\Delta\omega$ = 3 dB bandwidth of resonance response

$h_e(\omega_o)$ = effective height at frequency ω_o

The principal assumptions used in obtaining this result are

- (a) The dominant contribution to the frequency-domain response arises from the resonance in effective height which occurs near $f = 5.2$ MHz.

- (b) An equivalent step-function response can be used to derive (76) since the resonance near 5.2 MHz lies in the "step-function" region of the EMP spectrum (cf. Sec. 3.2.2.3.3, Fig. 24).

The relative rms error in the peak voltage V_{oc} is given by

$$\langle \tilde{x}_{V_{oc}}^2 \rangle^{1/2} = \left[(1 + \langle \tilde{x}_{E_{pk}}^2 \rangle)(1 + \langle \tilde{x}_{\zeta}^2 \rangle)(1 + \langle \tilde{x}_{h_e}^2 \rangle) - 1 \right]^{1/2} \quad (77)$$

in which $\zeta \approx \Delta\omega_0/2\omega_0$. We assign example values to the rms relative errors in the input quantities as follows:

$$\langle \tilde{x}_{E_{pk}}^2 \rangle^{1/2} = 0.0, \quad \langle \tilde{x}_{\zeta}^2 \rangle^{1/2} = 0.25, \quad \langle \tilde{x}_{h_e}^2 \rangle^{1/2} = 0.50$$

yielding

$$\langle \tilde{x}_{V_{oc}}^2 \rangle^{1/2} = 0.57 \quad (78)$$

The short-circuit current I_{sc} will have peak value

$$I_{sc} \Big|_{pk} = V_{oc}/Z_{in}(\omega_0) \quad (79)$$

where $Z_{in}(\omega_0)$ is real. Assuming that the relative error in the admittance $1/Z_{in}(\omega_0)$ is 25%, we find the relative error in the current $I_{sc} \Big|_{pk}$ to be

$$\begin{aligned} \langle \tilde{x}_{I_{sc}}^2 \rangle^{1/2} &= \left\{ \left[1 + (0.57)^2 \right] \left[1 + (0.25)^2 \right] - 1 \right\}^{1/2} \\ &= 0.64 \end{aligned} \quad (80)$$

3.2.5.3 Satellite Cable-Bundle Induced Open-Circuit Voltage (cf. Sec. 3.2.4.2)

The open-circuit voltage developed between the shield and the internal conductors of the circumferential cable bundle shown in Fig. 42, due to electromagnetic penetrations of the vertical slot apertures in the satellite skin, is given in (66) of Sec. 3.2.4.2.

All quantities in (66) can presumably be determined exactly. The errors associated with that result arise, therefore, entirely from the modeling concept and the approximations used in its derivation. The principal assumptions used are that

- (a) The short-circuit magnetic field on the outer surface of the satellite can be approximated by the incident magnetic field.
- (b) The aperture penetrations can be treated as if the apertures were located in an infinite ground plane, rather than in the surface of a cylinder of finite length.
- (c) All the penetrant flux links the cable loop.

The first assumption is valid for a long cylinder whose length greatly exceeds its diameter. The satellite is modeled as a cylinder whose length and diameter are roughly equal; thus some error is introduced by assumption (a). This assumption leads to an underestimate of the true surface current density; the error could be as large as a factor of two.

Assumption (b) introduces error because the slots extend almost the entire length of the satellite. The curvature effect is probably not an important source of error, by virtue of the results in Sec. 2.3.1.1.1. However, the fact that the slots are comparable in length to that of the cylinder tends to yield a low estimate of the penetrant flux. This may be partly compensated by assumption (c), which would overestimate the flux linkages of the cable bundle. It is suggested that an error of ± 5 dB be associated with assumptions (b) and (c). Thus V_{oc} as given in (66) probably contains a systematic error of a factor of roughly 1.5 (i.e., V_{oc} as given in (66) is too low by a factor of 1.5) and an undetermined error of plus-or-minus a factor of 2.

SUPPLEMENTARY

INFORMATION



DEPARTMENT OF THE AIR FORCE

AIR FORCE WEAPONS LABORATORY (AFSC)
KIRTLAND AIR FORCE BASE, NM 87117

REPLY TO: NTAT (Robert Torres, 4-9758)
ATTN OF:

SUBJECT: Request for EMP Document

TO: BMO/MGEM
Norton AFB, CA 92409

1. The request for AFWL-TR-80-402, "EMP Interaction 2-1.." should be addressed to:

Defense Technical Information Center
ATTN: DTIC-DDR
Cameron Station
Alexandria, Virginia 22314

2. AFWL/NTAT no longer distributes AFWL-TR-80-402, "EMP Interaction 2-1..".

It is now handled by DTIC.

JAMES A. KEE, Major, USAF
Chief, Technology Branch

'AD-A100508

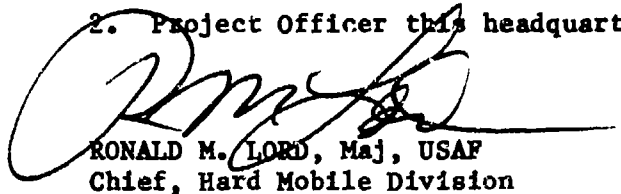
1st Endorsement

22 Oct 84

To: Defense Technical Information Center
Attn: DTIC-DDR

1. We request that the report number on "EMP Interaction 2-1" be changed from AFWL-TR-80-402 to BMO/TR-84-34. Also add OPR BMO/MGEM, Norton AFB, CA 92409 to block 16. Also please forward BMO/MGEM 2 copies as soon as possible.

2. Project Officer this headquarters is Lt Keith McBride, AV 876-7651.



RONALD M. LORD, Maj, USAF
Chief, Hard Mobile Division

UNCLASSIFIED

SECURITY CLASSIFICATION OF THIS PAGE (When Data Entered)

REPORT DOCUMENTATION PAGE		READ INSTRUCTIONS BEFORE COMPLETING FORM
1. REPORT NUMBER AFWL-TR-80-402 BMO/TR-84-34	2. GOVT ACCESSION NO.	3. RECIPIENT'S CATALOG NUMBER
4. TITLE (and Subtitle) EMP INTERACTION: PRINCIPLES, TECHNIQUES AND REFERENCE DATA (A COMPLETE CONCATENATION OF TECHNOLOGY FROM THE EMP INTERACTION NOTES) EMP INTERACTION 2-1		5. TYPE OF REPORT & PERIOD COVERED Final Report
7. AUTHOR(s) K.S.H. Lee, Editor		6. PERFORMING ORG. REPORT NUMBER DC-EH-1289
9. PERFORMING ORGANIZATION NAME AND ADDRESS Dikewood Industries, Inc. 1009 Bradbury Drive, S. E. Albuquerque, New Mexico 87106		8. CONTRACT OR GRANT NUMBER(s) F29601-76-C-0149
11. CONTROLLING OFFICE NAME AND ADDRESS Air Force Weapons Laboratory (NTMT) Kirtland AFB, New Mexico 87117		10. PROGRAM ELEMENT, PROJECT, TASK AREA & WORK UNIT NUMBERS 64711F/37630132
14. MONITORING AGENCY NAME & ADDRESS (if different from Controlling Office)		12. REPORT DATE December 1980
		13. NUMBER OF PAGES 762
		15. SECURITY CLASS. (of this report) Unclassified
		15a. DECLASSIFICATION/DOWNGRADING SCHEDULE
16. DISTRIBUTION STATEMENT (of this Report) Approved for public release; distribution unlimited. OPR BMO/NGEM, NORTON AFB, CA 92409		
17. DISTRIBUTION STATEMENT (of the abstract entered in Block 20, if different from Report)		
18. SUPPLEMENTARY NOTES		
19. KEY WORDS (Continue on reverse side if necessary and identify by block number) Aerospace System Ground Based Systems Aircraft Interaction Application Missile Coupling Satellites EMP		
20. ABSTRACT (Continue on reverse side if necessary and identify by block number) This work is divided into three parts. The first part, Principles and Techniques, concerns general concepts and calculational procedures from electro- magnetic theory relevant to EMP interaction. This contains a discussion of the concept of electromagnetic topology which is used to divide complex systems into somewhat natural smaller parts in an ordered way. This concept is fundamental to the organization and understanding of this work and is expected to lead to further insights and computational techniques [2-8]. Of course, there are many (over)		

NO. 473

UNCLASSIFIED

SECURITY CLASSIFICATION OF THIS PAGE (When Data Entered)